

JULY 2018

AJNR

VOLUME 39 • PP 1193–1384

AJNR

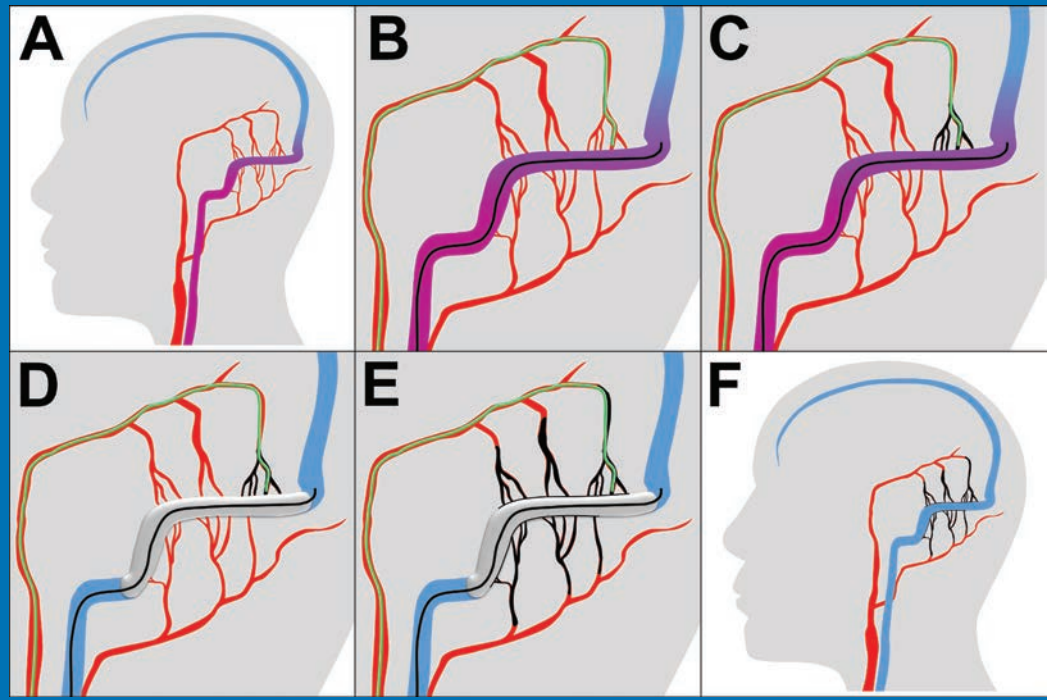
AMERICAN JOURNAL OF NEURORADIOLOGY

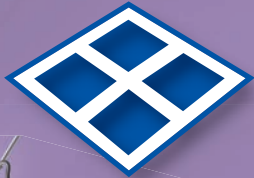
JULY 2018
VOLUME 39
NUMBER 7
WWW.AJNR.ORG

THE JOURNAL OF DIAGNOSTIC AND
INTERVENTIONAL NEURORADIOLOGY

Deep-learning classification of gliomas
Microhemorrhages in mild traumatic brain injury
Intraplaque hemorrhage in basilar artery stenosis

Official Journal ASNR • ASFNR • ASHNR • ASPNR • ASSR





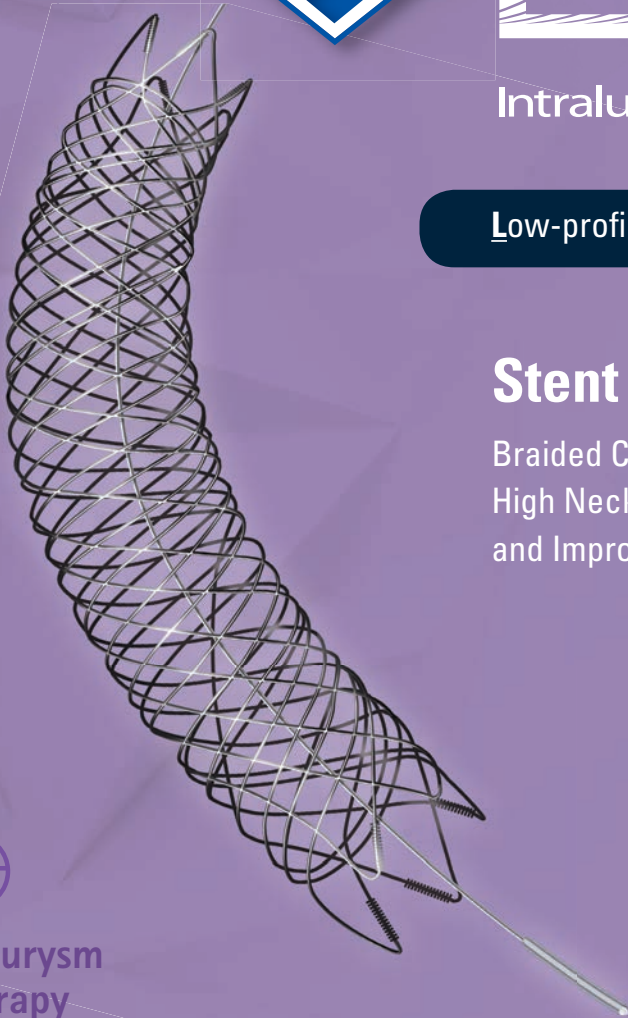
LVIS®

Intraluminal Support Device

Low-profile Visualized Intرالuminal Support

Stent Deployment. Refined.

Braided Coil Assist Stents with
High Neck Coverage, Excellent Visibility
and Improved Conformability*



Aneurysm
Therapy
Solutions



For more information or a product demonstration,
contact your local MicroVention representative:

MicroVention Worldwide
Innovation Center
35 Enterprise
Aliso Viejo, CA 92656 USA
MicroVention UK Limited
MicroVention Europe, S.A.R.L.
MicroVention Deutschland GmbH
microvention.com

PH +1.714.247.8000

PH +44 (0) 191 258 6777

PH +33 (1) 39 21 77 46

PH +49 211 210 798-0

**Humanitarian Device: Authorized by Federal Law for use with bare platinum embolic coils for the treatment of unruptured, wide neck (neck \geq 4 mm or dome to neck ratio $<$ 2), intracranial, saccular aneurysms arising from a parent vessel with a diameter \geq 2.5 mm and \leq 4.5 mm. The effectiveness of this device for this use has not been demonstrated.*

A Complete Coil Portfolio

MicroVention's comprehensive portfolio features clinically proven Hydrogel coils, which can be used exclusively or in combination with our trusted Platinum coils to treat a wide range of aneurysms and neurovascular lesions.



Aneurysm
Therapy
Solutions

Breakthrough Hydrogel Technology

- Less Recurrence
- Less Retreatment
- More Progressive Occlusion

Compared to platinum coils with comparable safety¹

REFERENCES:

1. Taschner et al. Second-Generation Hydrogel Coils for the Endovascular Treatment of Intracranial Aneurysm; A Randomized Controlled Trial. 2018;49:00-00. DOI:10.1161/STROKEAHA.117.018707



INDICATIONS FOR USE:

The HydroCoil® Embolic System (HES) and MicroPlex® Coil System (MCS) are intended for the endovascular embolization of intracranial aneurysms and other neurovascular abnormalities such as arteriovenous malformations and arteriovenous fistulae. The HES and MCS are also intended for vascular occlusion of blood vessels within the neurovascular system to permanently obstruct blood flow to an aneurysm or other vascular malformation and for arterial and venous embolizations in the peripheral vasculature.

The device should only be used by physicians who have undergone pre-clinical training in all aspects of HES/MCS procedures as prescribed by MicroVention.



**For more information or a product demonstration,
contact your local MicroVention representative:**



**MicroVention Worldwide
Innovation Center**
35 Enterprise
Aliso Viejo, CA 92656 USA
MicroVention UK Limited
MicroVention Europe, S.A.R.L.
MicroVention Deutschland GmbH
microvention.com

PH +1.714.247.8000

PH +44 (0) 191 258 6777

PH +33 (1) 39 21 77 46

PH +49 211 210 798-0



Bending expectations of conformability and stability.

Enhanced conformability – The hybrid cell structure is designed to enhance stent opening and conformability in bifurcations and tight curves.

Ease of use – All sizes of the Neuroform Atlas Stent are deliverable through Excelsior® SL-10® and Excelsior XT-17™ Microcatheters.

Higher deployment accuracy – The Neuroform Atlas Stent is designed to have very low foreshortening, which enables very high deployment accuracy.



Neuroform Atlas™

STENT SYSTEM

Balt USA.
The Future of Innovation is Here.

Introducing



Pushing Beyond the Boundaries of
Softness and Speed

Visit balt-usa.com to learn more

We're Inside Every Great Neuroradiologist!

ASNR MEMBERS RECEIVE

American Journal of Neuroradiology (AJNR)

The leading neuroradiology research journal, published monthly

Neurographics

Bimonthly educational journal with CME for members

ASNR Annual Meeting

Discounts for members on the field's premier conference

eCME

Online collection of lectures and articles with SA-CME and Category 1 credit

Advocacy

Coding/reimbursement, quality standards and practice guidelines; demonstrating neuroradiology's value!

Networking

Access to 5,000 peers

... And More!

TR 4730.0
TE 108.0
TA 03.27
BW 70.0
M/ND
A1
HL1.2;HS1.2
*tseR2d1_9 / 180
SP F17.7
SL 5.0
FoV 194*230
190*256s
Tra>Cor(8.7)
w 1469
c 705
MF 1.14
D
R
5cm
5cm

Join the leaders in neuroradiology today!

Learn more at www.asnr.org/join

ASNR

American Society of Neuroradiology

800 Enterprise Dr., Suite 205, Oak Brook, IL 60523 • (630)574-0220 • membership@asnr.org • www.asnr.org

Save the Date!!

The ASNR 57th Annual Meeting & The Foundation of the ASNR Symposium 2019

May 18-23, 2019 • Hynes Convention Center • Boston, Massachusetts



Images provided by Greater Boston Convention & Visitors Bureau



ASNR 57th Annual Meeting

c/o American Society of Neuroradiology

800 Enterprise Drive, Suite 205 | Oak Brook, Illinois 60523-4216

Phone: 630-574-0220 | Fax: 630 574-0661 | meetings@asnr.org



SAVE THE DATE 2018



12th Annual Meeting of the
American Society of

Functional Neuroradiology

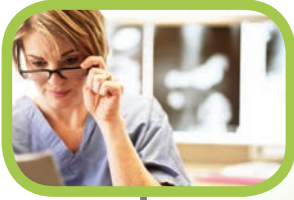
October 15-17, 2018

Hotel del Coronado, San Diego, CA

October 14, 2018

Optional Hands-on BOLD fMRI Workshop

For More Information, Visit www.asfnr.org



Simplify the MOC Process



Manage your CME Credits Online

CMEgateway.org

Available to Members of Participating Societies

American Board of Radiology (ABR)
American College of Radiology (ACR)
American Roentgen Ray Society (ARRS)
American Society of Neuroradiology (ASNR)
Commission on Accreditation of Medical
Physics Educational Programs, Inc. (CAMPEP)
Radiological Society of North America (RSNA)
Society of Interventional Radiology (SIR)
SNM
The Society for Pediatric Radiology (SPR)

It's Easy and Free!

Log on to CME Gateway to:

- View or print reports of your CME credits from multiple societies from a single access point.
- Print an aggregated report or certificate from each participating organization.
- Link to SAMs and other tools to help with maintenance of certification.

American Board of Radiology (ABR) participation!

By activating ABR in your organizational profile, your MOC-fulfilling CME and SAM credits can be transferred to your own personalized database on the ABR Web site.

Sign Up Today!

go to CMEgateway.org

Neuroform Atlas™ Stent System

See package insert for complete indications, contraindications, warnings and instructions for use.

Humanitarian Device. Authorized by Federal law for use with neurovascular embolic coils in patients who are ≥ 18 years of age for the treatment of wide neck, intracranial, saccular aneurysms arising from a parent vessel with a diameter of ≥ 2 mm and ≤ 4.5 mm that are not amenable to treatment with surgical clipping. Wide neck aneurysms are defined as having a neck to dome ratio of ≥ 4 mm or a dome-to-neck ratio < 2. The effectiveness of this device for this use has not been demonstrated.

INDICATIONS FOR USE

The Neuroform Atlas™ Stent System is indicated for use with neurovascular embolic coils in patients who are ≥ 18 years of age for the treatment of wide neck, intracranial, saccular aneurysms arising from a parent vessel with a diameter of ≥ 2 mm and ≤ 4.5 mm that are not amenable to treatment with surgical clipping. Wide neck aneurysms are defined as having a neck to dome ratio of ≥ 4 mm or a dome-to-neck ratio of < 2.

CONTRAINDICATIONS

Patients in whom antiplatelet and/or anticoagulation therapy is contraindicated.

POTENTIAL ADVERSE EVENTS

The potential adverse events listed below, as well as others, may be associated with the use of the Neuroform Atlas™ Stent System with or without the procedure:

Allergic reaction to nitinol metal and medications, Aneurysm perforation or rupture, Coil herniation through stent into parent vessel, Death, Embolus, Headache, Hemorrhage, In-stent stenosis, Infection, Ischemia, Neurological deficit/intracranial sequelae, Pseudoaneurysm, Stent fracture, Stent migration/embolization, Stent placement, Stent thrombosis, Stroke, Transient ischemic attack, Vasospasm, Vessel occlusion or closure, Vessel perforation/rupture, Vessel dissection, Vessel trauma or damage, Vessel thrombosis, Visual impairment, and other procedural complications including but not limited to anesthetic and contrast media risks, hypotension, hypertension, access site complications.

WARNINGS

- Contents supplied STERILE using an ethylene oxide (EO) process. Do not use if sterile barrier is damaged. If damage is found, call your Stryker Neurovascular representative.
- For single use only. Do not reuse, reprocess or resterilize. Reuse, reprocessing or resterilization may compromise the structural integrity of the device and/or lead to device failure which, in turn, may result in patient injury, illness or death. Reuse, reprocessing or resterilization may also create a risk of contamination of the device and/or cause patient infection or cross-infection, including, but not limited to, the transmission of infectious disease(s) from one patient to another. Contamination of the device may lead to injury, illness or death of the patient.
- After use, dispose of product and packaging in accordance with hospital, administrative and/or local government policy.
- This device should only be used by physicians who have received appropriate training in interventional neurodiology or interventional radiology and preclinical training on the use of this device as established by Stryker Neurovascular.
- Select a stent size (length) to maintain a minimum of 4 mm on each side of the aneurysm neck along the parent vessel. An incorrectly sized stent may result in damage to the vessel or stent migration. Therefore, the stent is not designed to treat an aneurysm with a neck greater than 22 mm in length.
- If excessive resistance is encountered during the use of the Neuroform Atlas™ Stent System or any of its components at any time during the procedure, discontinue use of the stent system. Continuing to move the stent system against resistance may result in damage to the vessel or a system component.
- Persons allergic to nickel titanium (Nitinol) may suffer an allergic response to this stent implant.
- Purge the system carefully to avoid the accidental introduction of air into the stent system.
- Confirm there are no air bubbles trapped anywhere in the stent system.

CAUTIONS / PRECAUTIONS

- Federal Law (USA) restricts this device to sale by or on the order of a physician.
- Use the Neuroform Atlas Stent System prior to the "Use By" date printed on the package.
- Carefully inspect the sterile package and Neuroform Atlas Stent System prior to use to verify that neither has been damaged during shipment. Do not use kinked or damaged components; contact your Stryker Neurovascular representative.
- The stent delivery microcatheter and the Neuroform Atlas Stent delivery system should not be used to recapture the stent.
- Exercise caution when crossing the deployed stent with adjunctive devices.
- After deployment, the stent may foreshorten from up to 6.3%.
- The max OD of the coiling microcatheter should not exceed the max OD of the stent delivery microcatheter.

Copyright © 2017 Stryker

AP001839 v1.0 | Page 2 of 2

Trevo® XP ProVue Retrievers

See package insert for complete indications, complications, warnings and instructions for use.

INDICATIONS FOR USE

1. The Trevo Retriever is indicated for use to restore blood flow in the neurovasculature by removing thrombus for the treatment of acute ischemic stroke to reduce disability in patients with a persistent, proximal anterior circulation, large vessel occlusion (IV t-PA) or who fail IV t-PA therapy who have first received intravenous tissue plasminogen activator (IV t-PA). Endovascular therapy with the device should start within 6 hours of symptom onset.
2. The Trevo Retriever is intended to restore blood flow in the neurovasculature by removing thrombus in patients experiencing ischemic stroke within 6 hours of symptom onset. Patients who are ineligible for intravenous tissue plasminogen activator (IV t-PA) or who fail IV t-PA therapy are candidates for treatment.
3. The Trevo Retriever is indicated for use to restore blood flow in the neurovasculature by removing thrombus for the treatment of acute ischemic stroke to reduce disability in patients with a persistent, proximal anterior circulation, large vessel occlusion of the internal carotid artery (ICA) or middle cerebral artery (MCA) M1 segments with smaller core infarcts (0-50cc for age < 80 years, 0-200cc for age ≥ 80 years). Endovascular therapy with the device should start within 6-24 hours of time last seen well in patients who are ineligible for intravenous tissue plasminogen activator (IV t-PA) or who fail IV t-PA therapy.

COMPLICATIONS

Procedures requiring percutaneous catheter introduction should not be attempted by physicians unfamiliar with possible complications which may occur during or after the procedure. Possible complications include, but are not limited to, the following: air embolism, hematoma or hemorrhage at puncture site; infection; distal embolism; pain/headache; vessel spasm, thrombosis, dissection, or perforation; emboli; acute occlusion; ischemia; intracranial hemorrhage; false aneurysm formation; neurological deficits including stroke; and death.

- Standard interventional devices with distal tips > 1.8 F may not be able to pass through the interstices of the stent.
- Safety of the Neuroform Atlas Stent System in patients below the age of 18 has not been established.
- In cases where multiple aneurysms are to be treated, start at the most distal aneurysm first.

MAGNETIC RESONANCE IMAGING (MRI)

Specific Information Magnetic Resonance Conditional

Non-clinical testing and analysis have demonstrated that the Neuroform Atlas Stent is MR Conditional alone, or when overlapped with a second stent, and adjacent to a Stryker Neurovascular coil mass. A patient with the Neuroform Atlas Stent can be safely scanned immediately after placement of this implant, under the following conditions:

- Static magnetic field of 1.5 and 3.0 Tesla
- Maximum spatial gradient field up to 2500 Gauss/cm (25 Tesla/m)
- Maximum MR system reported whole body averaged specific absorption rate of 2 W/kg (Normal Operating Mode) and head averaged specific absorption rate of 3.2 W/kg.

Under the scan conditions defined above, the Neuroform Atlas Stent is expected to produce a maximum temperature rise of 4°C after 15 minutes of continuous scanning. The Neuroform Atlas Stent should not migrate in this MRI environment.

In non-clinical testing, the image artifact caused by the device extends approximately 2 mm from the Neuroform Atlas Stent when imaged with a spin echo pulse sequence and 3 Tesla MRI System. The artifact may obscure the device lumen. It may be necessary to optimize MRI imaging parameters for the presence of this implant.

Excelsior® XT-17™ Microcatheter

See package insert for complete indications, contraindications, warnings and instructions for use.

INTENDED USE / INDICATIONS FOR USE

Stryker Neurovascular's Excelsior XT-17 Microcatheters are intended to assist in the delivery of diagnostic agents, such as contrast media, and therapeutic agents, such as occlusion coils, into the peripheral, coronary and neuro vasculature.

CONTRAINDICATIONS

None known.

POTENTIAL ADVERSE EVENTS

Potential adverse events associated with the use of microcatheters or with the endovascular procedures include, but are not limited to: access site complications, allergic reaction, aneurysm perforation, aneurysm rupture, death, embolism (air, foreign body, plaque, thrombus), hematoma, hemorrhage, infection, ischemia, neurological deficits, pseudoaneurysm, stroke, transient ischemic attack, vasospasm, vessel dissection, vessel occlusion, vessel perforation, vessel rupture, vessel thrombosis

WARNINGS

- The accessories are not intended for use inside the human body.
- Limited testing has been performed with solutions such as contrast media, saline and suspended embolic particles. The use of these microcatheters for delivery of solutions other than the types that have been tested for compatibility is not recommended. Do not use with glue or glue mixtures.
- Carefully inspect all devices prior to use. Verify shape, size and condition are suitable for the specific procedure.
- Exchange microcatheters frequently during lengthy procedures that require extensive guidewire manipulation or multiple guidewire exchanges.
- Never advance or withdraw an intravascular device against resistance until the cause of the resistance is determined by fluoroscopy. Movement of the microcatheter or guidewire against resistance could dislodge a clot, perforate a vessel wall, or damage microcatheter and guidewire. In severe cases, tip separation of the microcatheter or guidewire may occur.
- Contents supplied STERILE using an ethylene oxide (EO) process. Do not use if sterile barrier is damaged. If damage is found, call your Stryker Neurovascular representative.
- For single use only. Do not reuse, reprocess or resterilize. Reuse, reprocessing or resterilization may compromise the structural integrity of the device and/or lead to device failure which, in turn, may result in patient injury, illness or death. Reuse, reprocessing or resterilization may also create a risk of contamination of the device and/or cause patient infection or cross-infection, including, but not limited to, the transmission of infectious disease(s) from one patient to another. Contamination of the device may lead to injury, illness or death of the patient.
- After use, dispose of product and packaging in accordance with hospital, administrative and/or local government policy.
- These devices are intended for use only by physicians trained in performing endovascular procedures.
- Inspect product before use for any bends, kinks or damage. Do not use a microcatheter that has been damaged. Damaged microcatheters may rupture causing vessel trauma or tip detachment during steering maneuvers.
- The shaping mandrel is not intended for use inside the human body.

COMPATIBILITY

3x20mm retrievers are compatible with Trevo® Pro 14 Microcatheters (REF 90231) and Trevo® Pro 18 Microcatheters (REF 90238). 4x20mm retrievers are compatible with Trevo® Pro 18 Microcatheters (REF 90238). 4x30mm retrievers are compatible with Excelsior® XT-27™ Microcatheters (150cm x 6cm straight REF 275081) and Trevo® Pro 18 Microcatheters (REF 90238). 6x25mm Retriever are compatible with Excelsior® XT-27™ Microcatheters (150cm x 6cm straight REF 275081). Recommended minimum vessel ID for all Retriever sizes is 2.5mm. Compatibility of the Retriever with other microcatheters has not been established. Performance of the Retriever device may be impacted if a different microcatheter is used. Balloon Guide Catheters (such as Merzi® Balloon Guide Catheter and FlowGate® Balloon Guide Catheter) are recommended for use during thrombus removal procedures. Retrievers are compatible with the Abbott Vascular DOC® Guide Wire Extension (REF 22260).

Retrievers are compatible with Boston Scientific Rotating Hemostatic Valve (REF 421242).

SPECIFIC WARNINGS FOR INDICATION 1

• The safety and effectiveness of the Trevo Retrievers in reducing disability has not been established in patients with large core infarcts (i.e., ASPECTS ≤ 7). There may be increased risks, such as intracerebral hemorrhage, in these patients.

• The safety and effectiveness of the Trevo Retrievers in reducing disability has not been established or evaluated in patients with occlusions in the posterior circulation (e.g., basilar or vertebral arteries) or for more distal occlusions in the anterior circulation.

SPECIFIC WARNINGS FOR INDICATION 2

• To reduce risk of vessel damage, take care to appropriately size Retriever to vessel diameter at intended site of deployment.

SPECIFIC WARNINGS FOR INDICATION 3

• The safety and effectiveness of the Trevo Retrievers in reducing disability has not been established in patients with large core infarcts (i.e., ASPECTS ≤ 7). There may be increased risks, such as intracerebral hemorrhage, in these patients.

• The safety and effectiveness of the Trevo Retrievers in reducing disability has not been established or evaluated in patients with occlusions in the posterior circulation (e.g., basilar or vertebral arteries) or for more distal occlusions in the anterior circulation.

• Users should validate their imaging software analysis techniques to ensure robust and consistent results for assessing core infarct size.

- Discontinue use of microcatheter for infusion if increased resistance is noted. Resistance indicates possible blockage. Remove and replace blocked microcatheter immediately. DO NOT attempt to clear blockage by over-pressure. Doing so may cause the microcatheter to rupture, resulting in vascular damage or patient injury.
- Do not exceed 2,070 kPa (300 psi) infusion pressure. Excessive pressure could dislodge a clot, causing thromboemboli, or could result in a ruptured microcatheter or severed tip, causing vessel injury.

CAUTIONS / PRECAUTIONS

- To reduce the probability of occlusion in tortuous vasculature, use a guide catheter with a minimum internal diameter as specified in Table 1 above, and is recommended for use with Stryker Neurovascular hydrophilically coated microcatheters.
- To control the proper introduction, movement, positioning and removal of the microcatheter within the vascular system, users should employ standard clinical angiographic and fluoroscopic practices and techniques throughout the interventional procedure.
- Exercise care in handling of the microcatheter during a procedure to reduce the possibility of accidental breakage, bending or kinking.
- Use the product prior to the "Use By" date printed on the label.
- Limited testing indicates that Excelsior XT-17 Microcatheter is compatible with Dimethyl Sulfoxide (DMSO). The compatibility of Excelsior XT-17 Microcatheter with individual agents suspended in DMSO has not been established.
- Federal Law (USA) restricts this device to sale by or on the order of a physician.
- Wet dispenser coil or packaging tray and hydrophilically coated outer shaft of microcatheters prior to removal from packaging tray. Once the microcatheter has been wetted, do not allow to dry.
- The packaging mandrel is not intended for reuse. The packaging mandrel is not intended for use inside the human body.
- Check that all fittings are secure so that air is not introduced into guide catheter or microcatheter during continuous flush.
- In order to achieve optimal performance of Stryker Neurovascular Microcatheters and to maintain the lubricity of the Hydrolene® Coating surface, it is critical that a continuous flow of appropriate flush solution be maintained between the Stryker Neurovascular Microcatheter and guide catheter, and the microcatheter and any intraluminal device. In addition, flushing aids in preventing contrast crystal formation and/or clotting on both the intraluminal device and inside the guide catheter and/or the microcatheter lumen.
- Do not position microcatheter closer than 2.54 cm (1 in) from the steam source. Damage to the microcatheter may result.
- Excessive tightening of a hemostatic valve onto the microcatheter shaft may result in damage to the microcatheter. Removing the peel away introducer without a guidewire inserted in the microcatheter lumen might result in damage to the microcatheter shaft.
- To facilitate microcatheter handling, the proximal portion of the microcatheter does not have the hydrophilic surface. Greater resistance may be encountered when this section of the microcatheter is advanced into the RHV.

Excelsior® SL-10™ Microcatheter

See package insert for complete indications, contraindications, warnings and instructions for use.

INTENDED USE / INDICATIONS FOR USE

Stryker Neurovascular Excelsior SL-10 Microcatheter is intended to assist in the delivery of diagnostic agents, such as contrast media, and therapeutic agents, such as occlusion coils, into the peripheral, coronary, and neurovasculature.

CONTRAINDICATIONS

None known.

POTENTIAL ADVERSE EVENTS

Potential adverse events associated with the use of microcatheters or with the endovascular procedures include, but are not limited to: access site complications, allergic reaction, aneurysm perforation, aneurysm rupture, death, embolism (air, foreign body, plaque, thrombus), hematoma, hemorrhage, infection, ischemia, neurological deficits, pseudoaneurysm, stroke, transient ischemic attack, vessel dissection, vessel occlusion, vessel perforation, vessel rupture, vessel thrombosis.

WARNINGS

- Contents supplied STERILE using an ethylene oxide (EO) process. Do not use if sterile barrier is damaged. If damage is found, call your Stryker Neurovascular representative.
- For single patient use only. Do not reuse, reprocess or resterilize. Reuse, reprocessing or resterilization may compromise the structural integrity of the device and/or lead to device failure which, in turn, may result in patient injury, illness or death. Reuse, reprocessing or resterilization may also create a risk of contamination of the device and/or cause patient infection or cross-infection, including, but not limited to, the transmission of infectious disease(s) from one patient to another. Contamination of the device may lead to injury, illness or death of the patient.
- After use, dispose of product and packaging in accordance with hospital, administrative and/or local government policy.
- These devices are intended for use only by physicians trained in performing endovascular procedures.
- Inspect product before use for any bends, kinks or damage. Do not use a microcatheter that has been damaged. Damaged microcatheters may rupture causing vessel trauma or tip detachment during steering maneuvers.
- The shaping mandrel is not intended for use inside the human body.

WARNINGS APPLIED TO ALL INDICATIONS

- Administration of IV t-PA should be within the FDA-approved window (within 3 hours of stroke symptom onset).
 - To reduce risk of vessel damage, adhere to the following recommendations:
 - Do not perform more than six (6) retrieval attempts in same vessel using Retriever devices.
 - Maintain Retriever position in vessel when removing or exchanging Microcatheter.
 - To reduce risk of kinking/fracture, adhere to the following recommendations:
 - Immediately after unsheathing Retriever, position Microcatheter tip marker just proximal to shaped section. Maintain Microcatheter tip marker just proximal to shaped section of Retriever during manipulation and withdrawal.
 - Do not rotate or torque Retriever.
 - Use caution when passing Retriever through stented arteries.
- The Retriever is a delicate instrument and should be handled carefully. Before use and when possible during procedure, inspect device carefully for damage. Do not use a device that shows signs of damage. Damage may prevent device from functioning and may cause complications.
- Do not advance or withdraw Retriever against resistance or significant vasospasm. Moving or torquing device against resistance or significant vasospasm may result in damage to vessel or device. Assess cause of resistance using fluoroscopy and if needed reshape the device to withdraw.
- If Retriever is difficult to withdraw from the vessel, do not torque Retriever. Advance Microcatheter distally, gently pull Retriever back into Microcatheter, and remove Retriever and Microcatheter as a unit. If undue resistance is met when withdrawing the Retriever into the Microcatheter, consider extending the Retriever using the Abbott Vascular DOC guidewire extension (REF 22260) so that the Microcatheter can be exchanged for a larger diameter catheter such as a DAC® Catheter. Gently withdraw the Retriever into the larger diameter catheter.
- Administer anti-coagulation and anti-platelet medications per standard institutional guidelines.
- Users should take all necessary precautions to limit X-radiation doses to patients and themselves by using shielding sufficient, reducing fluoroscopy times, and modifying X-ray technical factors where possible.

- to injury, illness or death of the patient.
- After use, dispose of product and packaging in accordance with hospital, administrative and/or local government policy.
- **These devices are intended for use only by physicians trained in performing endovascular procedures.**
- Limited testing has been performed with solutions such as contrast media, saline and suspended embolic particles. The use of these catheters for delivery of solutions other than the types that have been tested for compatibility is not recommended. Do not use with glue or glue mixtures.
- The accessories are not intended for use inside the human body.
- Carefully inspect all devices prior to use. Verify shape, size and condition are suitable for the specific procedure.
- Exchange microcatheters frequently during lengthy procedures that require extensive guidewire manipulation or multiple guidewire exchanges.
- Never advance or withdraw an intravascular device against resistance until the cause of the resistance is determined by fluoroscopy. Movement of the microcatheter or guidewire against resistance could dislodge a clot, perforate a vessel wall, or damage microcatheter and guidewire. In severe cases, tip separation of the microcatheter or guidewire may occur.
- Inspect product before use for any bends, kinks or damage. Do not use a microcatheter that has been damaged. Damaged microcatheters may rupture causing vessel trauma or tip detachment during steering maneuvers.
- Shaping mandrel is not intended for use inside the human body.
- Discontinue use of microcatheter for infusion if increased resistance is noted. Resistance indicates possible blockage. Remove and replace blocked microcatheter immediately. DO NOT attempt to clear blockage by over-pressure. Doing so may cause the microcatheter to rupture, resulting in vascular damage or patient injury.
- Do not exceed 2,070 kPa (300 psi) infusion pressure. Excessive pressure could dislodge a clot, causing thromboemboli, or could result in a ruptured microcatheter or severed tip, causing vessel injury.

CAUTIONS / PRECAUTIONS

- Federal Law (USA) restricts this device to sale by or on the order of a physician.
- To facilitate microcatheter handling, the proximal portion of the microcatheter does not have the hydrophilic surface. Greater resistance may be encountered when this section of the microcatheter is advanced into the RHV.
- Exercise care in handling of the microcatheter during a procedure to reduce the possibility of accidental breakage, bending or kinking.
- To reduce the probability of coating damage in tortuous vasculature, use a guide catheter with a minimum internal diameter that is ≥ 1.00 mm (0.038 in) and is recommended for use with Stryker Neurovascular hydrophilically coated microcatheters.
- To control the proper introduction, movement, positioning and removal of the microcatheter within the vascular system, users should employ standard clinical angiographic and fluoroscopic practices and techniques throughout the interventional procedure.
- Flush dispenser coil of hydrophilically coated microcatheters prior to removal from guide cathet. Once the microcatheter has been wetted, do not allow to dry. Do not reinsert the microcatheter into dispenser coil.
- Do not position microcatheter closer than 2.54 cm (1 in) from the steam source. Damage to the microcatheter may result.
- Check that all fittings are secure so that air is not introduced into guide catheter or microcatheter during continuous flush.
- In order to achieve optimal performance of Stryker Neurovascular Microcatheters and to maintain the lubricity of the Hydrolene® Coating surface, it is critical that a continuous flow of appropriate flush solution be maintained between the Stryker Neurovascular Microcatheter and guide catheter, and the microcatheter and any intraluminal device. In addition, flushing aids in preventing contrast crystal formation and/or clotting on both the intraluminal device and inside the guide catheter and/or the microcatheter lumen.
- Excessive tightening of a hemostatic valve onto the microcatheter shaft may result in damage to the microcatheter.



Stryker Neurovascular
47900 Bayside Parkway
Fremont, CA 94538

strykerneurovascular.com

Date of Release: NOV/2017

EX_EN_US

PRECAUTIONS

- Prescription only – device restricted to use by or on order of a physician.
- Store in cool, dry, dark place.
- Do not use open or damaged packages.
- Use by "Use By" date.
- Exposure to temperatures above 54°C (130°F) may damage device and accessories. Do not autoclave.
- Do not expose Retriever to solvents.
- Use Retriever in conjunction with fluoroscopic visualization and proper anti-coagulation agents.
- To prevent thrombus formation and contrast media crystal formation, maintain a constant infusion of appropriate flush solution between guide catheter and Microcatheter and between Microcatheter and Retriever or guidewire.
- Do not attach a torque device to the shaped proximal end of DOC® Compatible Retriever. Damage may occur, preventing ability to attach DOC® Guide Wire Extension.

DOC is a trademark of Abbott Laboratories.



Stryker Neurovascular
47900 Bayside Parkway
Fremont, CA 94538

strykerneurovascular.com

Date of Release: APR/2018

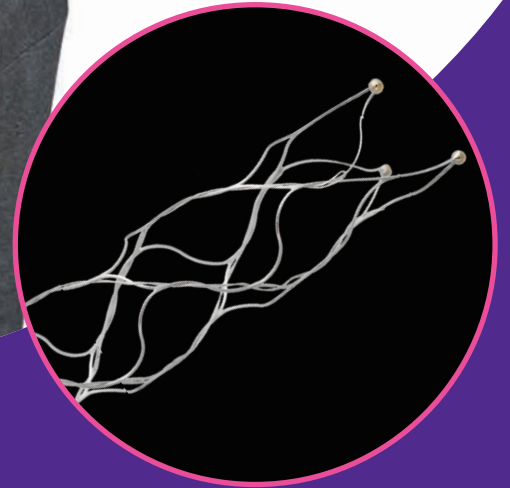
EX_EN_US

Copyright © 2018 Stryker

AP002078 v1.0 | Page 2 of 2

stryker

Now you have **24 hours** to make a lifetime of difference in stroke patients like Nora



The Trevo Retriever is the only device cleared to **reduce disability in stroke patients up to 24 hours** from time last seen well.

For more information, visit strykerneurovascular.com/trevo24hours

Trevo[®] XP
PROVUE RETRIEVER

Copyright © 2018 Stryker
AP002078 v1.0



Not for sale within the territory of the United States

PERFECT INTERPLAY

APERIO® Thrombectomy Device

Reliable stent retriever featuring a hybrid cell-design for fast flow restoration in acute ischemic strokes. Available in four sizes for tailored treatment.

RELIABLE. VARIABLE. SAFE.

www.acandis.com

acandis®

ENGINEERING STROKE SOLUTIONS

Official Journal:

American Society of Neuroradiology
American Society of Functional Neuroradiology
American Society of Head and Neck Radiology
American Society of Pediatric Neuroradiology
American Society of Spine Radiology

EDITOR-IN-CHIEF

Jeffrey S. Ross, MD

Professor of Radiology, Department of Radiology,
Mayo Clinic College of Medicine, Phoenix, AZ

SENIOR EDITORS

Harry J. Cloft, MD, PhD

Professor of Radiology and Neurosurgery,
Department of Radiology, Mayo Clinic College of
Medicine, Rochester, MN

Thierry A.G.M. Huisman, MD

Professor of Radiology, Pediatrics, Neurology, and
Neurosurgery, Chairman, Department of Imaging
and Imaging Science, Johns Hopkins Bayview,
Director, Pediatric Radiology and Pediatric
Neuroradiology, Johns Hopkins Hospital,
Baltimore, MD

Yvonne W. Lui, MD

Associate Professor of Radiology,
Chief of Neuroradiology,
New York University School of Medicine,
New York, NY

C.D. Phillips, MD, FACR

Professor of Radiology, Weill Cornell Medical
College, Director of Head and Neck Imaging,
New York-Presbyterian Hospital, New York, NY

Pamela W. Schaefer, MD

Clinical Director of MRI and Associate Director of
Neuroradiology, Massachusetts General Hospital,
Boston, Massachusetts, Associate Professor,
Radiology, Harvard Medical School, Cambridge, MA

Charles M. Strother, MD

Professor of Radiology, Emeritus, University of
Wisconsin, Madison, WI

STATISTICAL SENIOR EDITOR

Bryan A. Comstock, MS

Senior Biostatistician,
Department of Biostatistics,
University of Washington, Seattle, WA

EDITORIAL BOARD

Ashley H. Aiken, *Atlanta, GA*
Lea M. Alhilali, *Phoenix, AZ*
John D. Barr, *Dallas, TX*
Ari Blitz, *Baltimore, MD*
Barton F. Branstetter IV, *Pittsburgh, PA*
Jonathan L. Brisman, *Lake Success, NY*
Julie Bykowski, *San Diego, CA*
Keith Cauley, *Danville, PA*
Asim F. Choudhri, *Memphis, TN*
Alessandro Cianfoni, *Lugano, Switzerland*
J. Matthew Debnam, *Houston, TX*
Seena Dehkharghani, *New York, NY*
Colin Derdeyn, *Iowa City, IA*
Rahul S. Desikan, *San Francisco, CA*
Yonghong Ding, *Rochester, MN*
Clifford J. Eskey, *Hanover, NH*
Saeed Fakhraan, *Phoenix, AZ*
Massimo Filippi, *Milan, Italy*
Allan J. Fox, *Toronto, Ontario, Canada*
Wende N. Gibbs, *Los Angeles, CA*
Christine M. Glastonbury, *San Francisco, CA*
John L. Go, *Los Angeles, CA*
Allison Grayev, *Madison, WI*
Brent Griffith, *Detroit, MI*
Wan-Yuo Guo, *Taipei, Taiwan*
Ajay Gupta, *New York, NY*
Rakesh K. Gupta, *Lucknow, India*
Lotfi Hacein-Bey, *Sacramento, CA*
Christopher P. Hess, *San Francisco, CA*
Andrei Holodny, *New York, NY*
Benjamin Huang, *Chapel Hill, NC*
George J. Hunter, *Boston, MA*
Mahesh V. Jayaraman, *Providence, RI*
Valerie Jewells, *Chapel Hill, NC*
Christof Karmonik, *Houston, TX*
Timothy J. Kaufmann, *Rochester, MN*
Hillary R. Kelly, *Boston, MA*
Toshibumi Kinoshita, *Akita, Japan*
Kenneth F. Layton, *Dallas, TX*
Michael M. Lell, *Nürnberg, Germany*
Michael Lev, *Boston, MA*
Karl-Olof Lovblad, *Geneva, Switzerland*
Franklin A. Marden, *Chicago, IL*
M. Gisele Matheus, *Charleston, SC*
Joseph C. McGowan, *Merion Station, PA*
Stephan Meckel, *Freiburg, Germany*
Christopher J. Moran, *St. Louis, MO*
Takahisa Mori, *Kamakura City, Japan*
Suresh Mukherji, *Ann Arbor, MI*
Amanda Murphy, *Toronto, Ontario, Canada*
Alexander J. Nemeth, *Chicago, IL*
Sasan Partovi, *Cleveland, OH*
Laurent Pierot, *Reims, France*

Jay J. Pillai, *Baltimore, MD*
Whitney B. Pope, *Los Angeles, CA*
M. Judith Donovan Post, *Miami, FL*
Tina Young Poussaint, *Boston, MA*
Joana Ramalho, *Lisbon, Portugal*
Otto Rapalino, *Boston, MA*
Álex Rovira-Cañellas, *Barcelona, Spain*
Paul M. Ruggieri, *Cleveland, OH*
Zoran Rumboldt, *Rovinj-Rovigno, Croatia*
Amit M. Saindane, *Atlanta, GA*
Erin Simon Schwartz, *Philadelphia, PA*
Lubdha M. Shah, *Salt Lake City, UT*
Aseem Sharma, *St. Louis, MO*
J. Keith Smith, *Chapel Hill, NC*
Maria Vittoria Spampinato, *Charleston, SC*
Gordon K. Sze, *New Haven, CT*
Krishnamoorthy Thamburaj, *Hershey, PA*
Cheng Hong Toh, *Taipei, Taiwan*
Thomas A. Tomsick, *Cincinnati, OH*
Aquila S. Turk, *Charleston, SC*
Willem Jan van Rooij, *Tilburg, Netherlands*
Arastoo Vossough, *Philadelphia, PA*
Elysa Widjaja, *Toronto, Ontario, Canada*
Max Wintermark, *Stanford, CA*
Ronald L. Wolf, *Philadelphia, PA*
Kei Yamada, *Kyoto, Japan*
Carlos Zamora, *Chapel Hill, NC*

EDITORIAL FELLOW

Vahe Zohrabian, *New Haven, CT*

SPECIAL CONSULTANTS TO THE EDITOR

AJNR Blog Editor

Neil Lall, *Denver, CO*

Case of the Month Editor

Nicholas Stence, *Aurora, CO*

Case of the Week Editors

Juan Pablo Cruz, *Santiago, Chile*
Sapna Rawal, *Toronto, Ontario, Canada*

Classic Case Editor

Sandy Cheng-Yu Chen, *Taipei, Taiwan*

Health Care and Socioeconomics Editor

Pina C. Sanelli, *New York, NY*

Physics Editor

Greg Zaharchuk, *Stanford, CA*

Podcast Editor

Wende N. Gibbs, *Los Angeles, CA*

Twitter Editor

Jennifer McCarty, *Houston, Texas*

YOUNG PROFESSIONALS ADVISORY COMMITTEE

Asim K. Bag, *Birmingham, AL*
Anna E. Nidecker, *Sacramento, CA*
Peter Yi Shen, *Sacramento, CA*

Founding Editor
Juan M. Taveras

Editors Emeriti
Mauricio Castillo, Robert I. Grossman,
Michael S. Huckman, Robert M. Quencer

Managing Editor
Karen Halm

Assistant Managing Editor
Laura Wilhelm

Marketing and Social Media Manager
Kylie Mason

Executive Director, ASN
Mary Beth Hepp

AJNR

AMERICAN JOURNAL OF NEURORADIOLOGY

JULY 2018
VOLUME 39
NUMBER 7
WWW.AJNR.ORG

Publication Preview at www.ajnr.org features articles released in advance of print. Visit www.ajnrblog.org to comment on AJNR content and chat with colleagues and AJNR's News Digest at <http://ajnrdigest.org> to read the stories behind the latest research in neuroimaging.

1193 **PERSPECTIVES** *C.C. Green*

REVIEW ARTICLE

-  1194 **Cerebrovascular Manifestations of Neurosarcoidosis: An Underrecognized Aspect of the Imaging Spectrum** *G. Bathla, et al.* **ADULT BRAIN**

GENERAL CONTENTS

-    1201 **Deep-Learning Convolutional Neural Networks Accurately Classify Genetic Mutations in Gliomas** *P. Chang, et al.* **ADULT BRAIN**
-   1208 **Diffusion-Weighted Imaging and Diffusion Tensor Imaging for Differentiating High-Grade Glioma from Solitary Brain Metastasis: A Systematic Review and Meta-Analysis** *C.H. Suh, et al.* **ADULT BRAIN**
-   1215 **Quantitative Susceptibility Mapping after Sports-Related Concussion** *K.M. Koch, et al.* **ADULT BRAIN**
- 1222 **Prevalence of Cerebral Microhemorrhage following Chronic Blast-Related Mild Traumatic Brain Injury in Military Service Members Using Susceptibility-Weighted MRI** *E. Lotan, et al.* **ADULT BRAIN**
-   1226 **Improved Detection of New MS Lesions during Follow-Up Using an Automated MR Coregistration-Fusion Method** *A. Galletto Pregliasco, et al.* **ADULT BRAIN**
-    1233 **Identification of Chronic Active Multiple Sclerosis Lesions on 3T MRI** *M. Absinta, et al.* **ADULT BRAIN**
-    1239 **Imaging Differences between Neuromyelitis Optica Spectrum Disorders and Multiple Sclerosis: A Multi-Institutional Study in Japan** *H. Tatekawa, et al.* **ADULT BRAIN**
-   1248 **Visualization and Classification of Deeply Seated Collateral Networks in Moyamoya Angiopathy with 7T MRI** *T. Matsushige, et al.* **ADULT BRAIN**
- 1255 **Diffusion-Weighted Zonal Oblique Multislice-EPI Enhances the Detection of Small Lesions with Diffusion Restriction in the Brain Stem and Hippocampus: A Clinical Report of Selected Cases** *T. Sartoretti, et al.* **ADULT BRAIN**
-  1260 **Hematocrit Measurement with R2* and Quantitative Susceptibility Mapping in Postmortem Brain** *A.J. Walsh, et al.* **ADULT BRAIN**
-  1267 **Relationship between Cough-Associated Changes in CSF Flow and Disease Severity in Chiari I Malformation: An Exploratory Study Using Real-Time MRI** *A.F. Bezuidenhout, et al.* **ADULT BRAIN**

AJNR (Am J Neuroradiol ISSN 0195-6108) is a journal published monthly, owned and published by the American Society of Neuroradiology (ASNR), 800 Enterprise Drive, Suite 205, Oak Brook, IL 60523. Annual dues for the ASNR include \$170.00 for journal subscription. The journal is printed by Cadmus Journal Services, 5457 Twin Knolls Road, Suite 200, Columbia, MD 21045; Periodicals postage paid at Oak Brook, IL and additional mailing offices. Printed in the U.S.A. POSTMASTER: Please send address changes to American Journal of Neuroradiology, P.O. Box 3000, Denville, NJ 07834, U.S.A. Subscription rates: nonmember \$400 (\$470 foreign) print and online, \$320 online only; institutions \$460 (\$530 foreign) print and basic online, \$915 (\$980 foreign) print and extended online, \$380 online only (basic), extended online \$825; single copies are \$35 each (\$40 foreign). Indexed by PubMed/Medline, BIOSIS Previews, Current Contents (Clinical Medicine and Life Sciences), EMBASE, Google Scholar, HighWire Press, Q-Sensei, RefSeek, Science Citation Index, SCI Expanded, and Meta/CZI. Copyright © American Society of Neuroradiology.

-    1273 **Extent of Microstructural Tissue Damage Correlates with Hemodynamic Failure in High-Grade Carotid Occlusive Disease: An MRI Study Using Quantitative T2 and DSC Perfusion** *A. Seiler, et al.* **ADULT BRAIN
EXTRACRANIAL
VASCULAR**
-   1280 **Prediction of Borderzone Infarction by CTA in Patients Undergoing Carotid Embolization for Carotid Blowout** *B.-C. Lee, et al.* **ADULT BRAIN
EXTRACRANIAL
VASCULAR**
-   1286 **Clinical Significance of Intraplaque Hemorrhage in Low- and High-Grade Basilar Artery Stenosis on High-Resolution MRI** *C. Zhu, et al.* **ADULT BRAIN
INTERVENTIONAL**
- 1293 **Mobile Stroke Unit Reduces Time to Image Acquisition and Reporting** *E.M. Nyberg, et al.* **ADULT BRAIN
INTERVENTIONAL**
-  1296 **Endovascular Treatment of Dural Arteriovenous Fistulas Using Transarterial Liquid Embolization in Combination with Transvenous Balloon-Assisted Protection of the Venous Sinus** *D.F. Vollherbst, et al.* **INTERVENTIONAL**
-  1303 **Risk of Branch Occlusion and Ischemic Complications with the Pipeline Embolization Device in the Treatment of Posterior Circulation Aneurysms** *N. Adeeb, et al.* **INTERVENTIONAL**
- 1310 **Abnormal Blood Oxygen Level-Dependent Fluctuations in Focal Cortical Dysplasia and the Perilesional Zone: Initial Findings** *L. Gupta, et al.* **FUNCTIONAL**
-    1316 **Role of the Apparent Diffusion Coefficient as a Predictor of Tumor Progression in Patients with Chordoma** *T. Sasaki, et al.* **HEAD & NECK**
- 1322 **MSVAT-SPACE-STIR and SEMAC-STIR for Reduction of Metallic Artifacts in 3T Head and Neck MRI** *T. Hilgenfeld, et al.* **HEAD & NECK**
-   1330 **Cerebral Perfusion Is Perturbed by Preterm Birth and Brain Injury** *E.S. Mahdi, et al.* **PEDIATRICS**
- 1336 **β -Hydroxybutyrate Detection with Proton MR Spectroscopy in Children with Drug-Resistant Epilepsy on the Ketogenic Diet** *J.N. Wright, et al.* **PEDIATRICS**
-  1341 **Quantitative Assessment of Normal Fetal Brain Myelination Using Fast Macromolecular Proton Fraction Mapping** *V.L. Yarnykh, et al.* **PEDIATRICS**
-  1349 **Global and Widespread Local White Matter Abnormalities in Juvenile Neuronal Ceroid Lipofuscinosis** *U. Roine, et al.* **PEDIATRICS**
- 1355 **Balanced Steady-State Free Precession Sequence (CISS/FIESTA/3D Driven Equilibrium Radiofrequency Reset Pulse) Increases the Diagnostic Yield for Spinal Drop Metastases in Children with Brain Tumors** *K. Buch, et al.* **PEDIATRICS
SPINE**
-  1362 **MRI-Based Methods for Spinal Cord Atrophy Evaluation: A Comparison of Cervical Cord Cross-Sectional Area, Cervical Cord Volume, and Full Spinal Cord Volume in Patients with Aquaporin-4 Antibody Seropositive Neuromyelitis Optica Spectrum Disorders** *C. Chien, et al.* **SPINE**
- 1369 **A Qualitative and Quantitative Correlation Study of Lumbar Intervertebral Disc Degeneration Using Glycosaminoglycan Chemical Exchange Saturation Transfer, Pfirrmann Grade, and T1- ρ** *O. Togao, et al.* **SPINE**
- 1376 **Efficacy and Safety of Percutaneous Microwave Ablation and Cementoplasty in the Treatment of Painful Spinal Metastases and Myeloma** *M.A. Khan, et al.* **SPINE**
- 1384 **35 YEARS AGO IN AJNR**

ONLINE FEATURES

LETTERS

- E82** **Is Gd-DTPA Necessary in Clinical Practice for Peripheral Nerve Injury?**
M.I. Vargas, et al.
- E83** **Reply** *B. Hill, et al.*
- E84** **Neuroimaging in Dengue Seropositive Cases** *P. Sookaromdee, et al.*
- E85** **Reply** *H.A. Vanjare, et al.*
- E86** **Common Origin of Brachiocephalic and Left Common Carotid Arteries: Proposal of New Terminology** *A.M. Tawfik, et al.*

BOOK REVIEWS *R.M. Quencer, Section Editor*

Please visit www.ajnrblog.org to read and comment on Book Reviews.

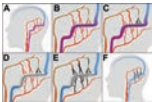


Illustration of embolization technique for dural fistula: After diagnostic angiography, a balloon catheter (in black) is navigated into the affected sinus, and a microcatheter (in green) is navigated into the feeder (B). After superselective diagnostic angiographies, Onyx is injected under balloon deflation until the Onyx cast (in black) reaches the sinus (C). The balloon is then inflated to prevent inadvertent embolization of the sinus and to enable retrograde embolization of the other arterial feeders (D). Onyx is injected until embolization of all feeders is achieved (E). After the intervention, all feeding arteries are embolized and the sinus is patent (F).



Indicates Editor's Choices selection



Indicates Fellows' Journal Club selection



Indicates open access to non-subscribers at www.ajnr.org



Indicates article with supplemental on-line table



Indicates article with supplemental on-line photo



Indicates article with supplemental on-line video



Evidence-Based Medicine Level 1



Evidence-Based Medicine Level 2



Title: There is Light at the End. A part of my medical practice in brain imaging includes the study of near-death experiences. This painting represents the light seen at the end of this tunnel, from one of my patients ... darkness of the trees of life through which we all pass to reach the Light at the End. It is executed using Oriental brushes and inks on fine rice paper, a method I've used exclusively since 1994, having studied these materials while practicing medicine in Singapore and China. I have been a professional artist since 1964, and a physician since 1978.

Christopher C. Green, MD, PhD, FAAFS, Detroit Medical Center, Harper University Hospital; Assistant Dean/Asia Pacific and Professor, Adjunct, Neuroimaging – MRI, Departments of Diagnostic Radiology & Psychiatry and Behavioral Neurosciences, Wayne State School of Medicine, Detroit, Michigan

Cerebrovascular Manifestations of Neurosarcoidosis: An Underrecognized Aspect of the Imaging Spectrum

G. Bathla, P. Watal, S. Gupta, P. Nagpal, S. Mohan, and T. Moritani



ABSTRACT

SUMMARY: Involvement of the central nervous system by sarcoidosis, also referred to as neurosarcoidosis, is seen clinically in about 5% of patients with systemic disease. CNS involvement most frequently affects the leptomeninges and cranial nerves, though the ventricular system, brain parenchyma, and pachymeninges may also be involved. Even though the involvement of the intracranial vascular structures is well-known on postmortem studies, there is scant literature on imaging manifestations secondary to the vessel wall involvement, being confined mostly to isolated case reports and small series. The authors present a review of various cerebrovascular manifestations of neurosarcoidosis, along with a brief synopsis of the existing literature.

ABBREVIATIONS: ICH = intracerebral hemorrhage; NS = neurosarcoidosis

Sarcoidosis is a noninfectious, idiopathic, inflammatory disorder that most frequently involves the lungs, skin, and lymph nodes.¹ It is more common in African Americans and patients with Scandinavian ancestry and is characterized pathologically by formation of noncaseating granulomas.¹ CNS imaging findings in neurosarcoidosis (NS) are seen in about 10% of patients with systemic sarcoidosis. This is less than the incidence of CNS involvement on postmortem studies (15%–25%), but more than the incidence of symptomatic CNS involvement (approximately 5%), implying that most patients with NS remain asymptomatic.^{1–4}

Common imaging manifestations of NS include meningitis, parenchymal granulomas, white matter signal abnormalities, ventriculitis, hydrocephalus, and spinal involvement.^{1,5} These have been previously well-described.^{1,6} However, patients with NS may rarely present with cerebrovascular manifestations such as hemorrhage and stroke. These are thought to result from involvement of the arterial and venous structures and are only sporadically described in the literature, mostly through case reports and small case series. Although rare, these are of considerable importance, given the associated morbidity and mortality. Herein, the authors present a review of the existing literature on

the pathophysiology, pathology, and imaging findings of cerebrovascular manifestations of NS.

Evolution and Pathogenesis

The pathogenesis of sarcoidosis remains elusive, though it is generally believed that it represents an exaggerated response by a genetically predisposed individual to a specific-yet-unidentified antigen, which may be environmental or occupational.¹ The scattered reports of occurrence of clusters of sarcoidosis (or sarcoid-like disease) in different population groups (health care workers, teachers, automobile manufacturers), including more recently in the firefighters exposed to World Trade Center “dust” during the collapse, again support some role for antigenic exposure.⁷

The offending antigens are likely airborne, which would explain the high incidence of lung involvement in sarcoidosis. Postmortem studies by Iwai et al⁸ demonstrated granulomatous dissemination by hematogenous and lymphatic routes as well as through local extension in the heart and lung. In the brain however, perivascular and vessel wall granulomas were the dominant feature.^{8–11} CNS involvement in systemic sarcoidosis is therefore presumably hematogenous, given the preferential perivascular distribution and paucity of a well-defined intracranial lymphatic system.

Besides the vascular involvement, postmortem studies have also documented prominent granulomatous involvement of the perivascular connective tissue, especially along the basal meninges, brain sulci, and the deep brain substance.^{8,12–14} The involvement of the deep gray nuclei likely results from extension along the lenticulostriate perforators or Virchow-Robin spaces.^{5,14,15} Over the cerebral convexities, the inflammation

From the Division of Neuroradiology (G.B., P.W., P.N., T.M.), Department of Radiology, and Department of Pathology (S.G.), University of Iowa Hospitals and Clinics, Iowa City, Iowa; and Division of Neuroradiology (S.M.), Department of Radiology, University of Pennsylvania, Philadelphia, Pennsylvania.

Please address correspondence to Girish Bathla, FRCP, MMed, 3960 JPP, Department of Radiology, University of Iowa Hospitals and Clinics, 200 Hawkins Dr, Iowa City, IA 52246; e-mail: girish-bathla@uiowa.edu

Indicates open access to non-subscribers at www.ajnr.org

<http://dx.doi.org/10.3174/ajnr.A5492>

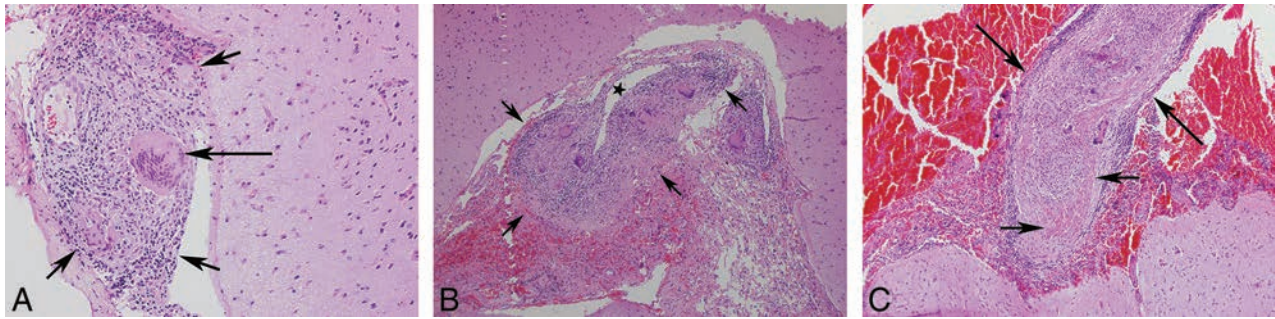


FIG 1. Brain biopsies from different patients showing typical sarcoid granuloma (*short arrows*) with a Langerhans-type giant cell (*long arrow*) (H&E, original magnification $\times 20$) (A), transmural granulomatous involvement of a meningeal vessel (*short arrows*, *star* represents the residual vessel lumen) (H&E, original magnification $\times 20$) (B), and granulomatous vessel wall involvement (*long arrows*) with fibrinoid necrosis (*short arrows*) (H&E, original magnification $\times 10$) (C).

again likely extends along the Virchow-Robin spaces into the cortex.

Although both arterial and venous involvement may be seen histopathologically, for unclear reasons, small arterial perforators are most frequently affected,^{12,14} while large-vessel involvement is the least common. Granulomatous phlebitis, on the contrary, most commonly involves the paraventricular veins along the lateral and third ventricles.^{12,14}

Even though the pathophysiology remains unclear, the vascular effects are unlikely to be purely secondary to vessel wall infiltration. Some studies have previously demonstrated significantly increased CNS endothelial immunoglobulin G binding in patients with NS.¹⁶ Similarly, patients with sarcoidosis have also been shown to have impaired endothelial function and elevated arterial stiffness, which tends to parallel disease activity.¹⁷ Additionally, elevated levels of endothelin-1, a compound with a strong mitogenic potential for smooth-muscle cells and fibroblasts, have been noted during active disease.¹⁸ Finally, recent studies have also noted widespread endothelial damage in patients with sarcoidosis, even in the absence of granuloma formation.¹⁹ Quite possibly, the cerebrovascular manifestations of NS are multifactorial.

Vascular involvement may result in cerebral ischemia or parenchymal or subarachnoid hemorrhage. Involvement of the larger venous sinuses has been reported, manifesting as sinus thrombosis with or without parenchymal hemorrhage. Involvement of the bigger arterial vessels may result in large or even recurrent strokes. For unclear reasons, the latter is exceptionally rare. Most interesting, the entire circumference of a large vessel is rarely involved by the granulomatous inflammation on postmortem examination, unlike smaller vessels where the inflammation is more likely to be circumferential and transmural.¹³

Histopathology

The histopathologic understanding of sarcoidosis has evolved with time. The classic description of a sarcoid granuloma recognizes the characteristic morphology as discrete, compact, epithelioid cell granulomas with minimal or no necrosis (Fig 1). Although the presence of fibrinoid necrosis was reported in isolated postmortem studies, the use of the term “necrotizing sarcoid granulomatosis” as a diagnostic entity was only introduced in the pathology literature in 1973 by Liebow.²⁰ Across time, these 2 relatively distinct morphologies have been thought to represent

the 2 ends of a histopathologic continuum. Some authors now advocate the use of the term “sarcoidosis with necrotizing sarcoid granulomatosis pattern” to describe the variable extent of necrosis, instead of “necrotizing sarcoid granulomatosis.”²¹

Another distinctive histopathologic feature is granulomatous vasculitis/angiitis, characterized by infiltration of the vessel by the epithelioid cell granulomas. Although it was previously considered to be more common in the CNS, recent studies show that extra-CNS granulomatous vasculitis also occurs with equal frequency, though the extent of involvement may be variable.²¹ Vascular infiltration may result in destruction of a part of the wall by intramural or transmural granulomas or result in compressive obliteration without destruction. The third and less frequently described pattern consists of vessel wall destruction by infiltrate of lymphocytes, plasma cells, and histiocytes without discrete granulomas.²² When fibrinoid necrosis is present, the lesions can closely mimic the picture seen in polyarteritis nodosa, though unlike polyarteritis nodosa, the findings may be confined to the CNS. Although there are no distinct clinical or imaging subtypes of patients with necrotizing sarcoid granulomatosis and fibrinoid necrosis, isolated case reports with postmortem correlation do seem to suggest that the conditions of these patients may follow a more aggressive course.^{9,14,23}

Role of Imaging

Traditionally, conventional angiography is considered the criterion standard for imaging vasculitis. However, because NS often involves the smaller perforating vessels and veins, it may not be well-evaluated.^{12,15,24} The utility of conventional angiography in patients with NS may therefore be limited to cases with large-vessel involvement. MR imaging, on the other hand, often plays a leading role. Although MR imaging does not directly depict small vessels, the superior ability to identify small infarcts and microhemorrhages not only increases the sensitivity for underlying vasculitis but also gives it a distinct advantage over CT. Additionally, noninvasive MR imaging (or CT) angiography and venography can often provide sufficient information about larger vessels to preclude invasive angiography. Given the rarity of large-vessel involvement and the inherent risks of invasive angiography, contrast-enhanced MR imaging and MR angiography are likely to remain the preferred imaging tests for suspecting and diagnosing cerebrovascular involvement in NS. Although CTA has the slight advantage of superior spatial resolution, given the low incidence

Table 1: Cases of NS with stroke in the reported English language literature^a

Author	Year	Age (yr)/Sex	Zajicek Criteria	CT/MRI	DWI	TIA	Stroke	Systemic Disease
Brown et al ¹²	1989	25/M	Probable	Y/NS	NS	Y	Left IC and corona radiata	Y
Corse and Stern ²⁶	1990	38/M	Probable	Y/Y	NS	Y	Right IC	Y
Michotte et al ⁴	1991	29/M	Probable	Y/Y	NS	N	Left BG, right frontal	Y
Zadra et al ²⁴	1996	30/M	Probable	Y/Y	NS	N	Multiple, anterior circulation	Y
Das et al ³⁰	1998	27/F	Probable	Y/NS	NS	N	Left MCA infarct	Y
Brisman et al ³	2006	41/M	Probable	NS/Y	Y	N	Multiple, anterior circulation	Y
Hodge et al ²	2007	36/F	Definite	NS/Y	Y	N	Left BG	N
Navi and DeAngelis ³¹	2009	35/M	Definite	NS/Y	N	N	Pons	Y
Navi and DeAngelis ³¹	2009	46/F	Definite	Y/Y	NS	N	Pons	Y
González-Aramburu et al ¹⁵	2012	27/M	Probable	Y/Y	Y	Y	Right IC and thalamus	Y
Campbell et al ³²	2015	26/M	Probable	Y/Y	Y	Y	Left centrum semiovale	Y
Raza and Schreck ²⁵	2017	73/F	Probable	NS/Y	NS	N	Recurrent left MCA strokes	Y
Macedo et al ⁵	2016	62/M	Possible	Y/Y	Y	Y	Multiple, anterior/posterior circulation	Y

Note:—BG indicates basal ganglia; IC, internal capsule; N, no; NS, not specified; Y, yes.

^a On the basis of the Zajicek criteria,¹ cases may be definite (neural tissue biopsy), probable (presence of CNS inflammation with evidence of systemic disease), or possible (clinical presentation consistent with NS with exclusion of alternate diagnosis).

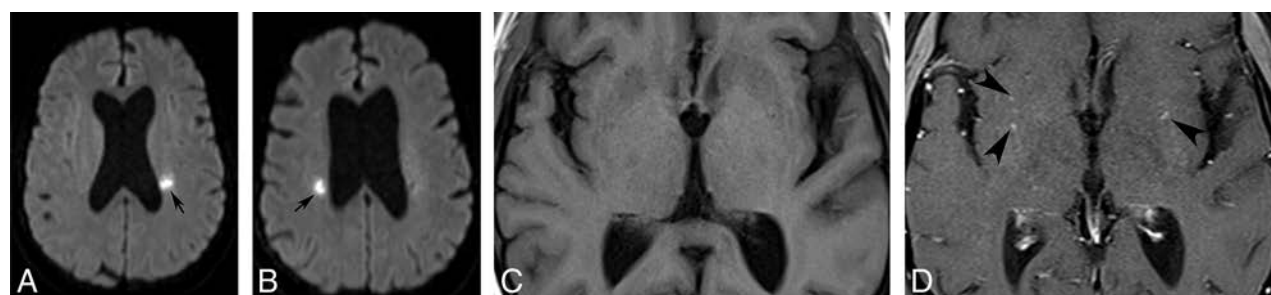


FIG 2. Axial DWIs at the level of the corona radiata obtained at 2 different time points (A and B) show recurrent periventricular infarcts. Axial magnified pre- (C) and postcontrast (D) images reveal subtle perivascular enhancement involving the bilateral basal ganglia (arrowheads, D).

of large-vessel vasculitis, it is unclear whether it adds any substantial value over MRA, which can be combined with an MR imaging study in a single session.

Ischemic Lesions

Ischemic insults in NS are intriguingly rare, despite the frequent granulomatous vascular infiltration on postmortem studies.^{3,4,12,15,25} The exact mechanism of infarction is likely multifactorial, resulting from a combination of small-vessel vasculitis, large-vessel inflammation, or cardioembolic phenomenon secondary to sarcoid cardiomyopathy.^{2,26} Because perforating arteries are most frequently involved, the infarcts are often small and commonly involve the basal ganglia, thalamus, and brain stem, though large-vessel and recurrent infarcts may also occur.²⁵

In the pre-CT era, most of the infarcts were diagnosed on postmortem studies. Commonly, these did not have a documented antemortem presentation.^{14,23,27-29} It is unclear whether the infarcts were clinically silent due to their small size or were overshadowed by the clinical manifestations of meningism, neurologic deficits, and hydrocephalus known to accompany NS. These predominantly involved the distribution of perforating arteries. Most of the described patients were young and male and had concurrent extracranial sarcoidosis.

At times, the ischemic insults in NS may be symptomatic and present as acute stroke with or without a preceding transient ischemic attack, or even as recurrent TIAs without stroke.^{2,5,10,25,26} Table 1 lists the cases of acute stroke reported in patients with NS in the English language literature.^{2-5,12,15,24-26,30-32} Like the asymp-

tomatic infarcts, most of the patients were young and nearly all had coexisting extracranial disease. Also, unlike sarcoidosis, which has a female predilection, cases with cerebrovascular findings showed a male predilection.

Given the existing literature, one may therefore expect to see both silent and symptomatic lesions on imaging, which is concordant with the institutional experience of the authors. The infarcts are often small and may be most apparent on diffusion-weighted images as foci of restricted diffusion, often in the deep brain substance. T2-weighted images may not be very useful and any surrounding parenchymal edema or white matter lesions tend to make them even more inconspicuous. Occasionally, the infarcts may be multiple, recurrent, or of varying ages (Fig 2).^{4,25} Rarely, lesions may be more superficial and subcortical, occurring secondary to involvement of the cortical vessels from surrounding meningeal inflammation (Fig 3). Although the presence of infarcts by itself is not specific for underlying NS, its occurrence, especially in young patients with coexisting intracranial findings of NS or known systemic sarcoidosis, may point to an underlying granulomatous etiology. Rarely, an ischemic insult may be the first manifestation of isolated NS without systemic involvement.² In such cases, the diagnosis may be especially challenging and eventually require histopathologic confirmation.

Large-vessel strokes in NS are exceptionally rare, as can be expected from the less severe and noncircumferential vessel wall involvement on pathology.^{13,25,26} MRA or conventional angiography in such cases may show focal vascular stenosis or occlu-

sion.^{4,5,15,26} A Moyamoya-like vasculopathy pattern has also been reported in association with NS and may be unilateral or bilateral.³³ Because the underlying etiology is vasculitis, one may see changes of both ischemia and hemorrhage in these patients at different time points (Fig 4).

In patients with ischemic strokes, the differential considerations include both embolic and nonembolic etiologies. Cardioembolic infarcts secondary to atheromatous disease are possible

but are statistically less likely among younger populations. The leading nonembolic consideration is the primary angiitis of the CNS, which can closely mimic vasculitis of NS on histopathology. Primary angiitis of the CNS, however, commonly affects patients in middle age, has an aggressive clinical course, and is confined to the CNS, unlike NS which invariably has extracranial disease. Additionally, primary angiitis of the CNS often has abnormal angiographic findings, reported in up to 50%–90% of patients.³⁴

CNS vasculitis may also be seen in association with collagen vascular diseases, drug abuse, or underlying infectious (HIV, herpes simplex virus, syphilis) or inflammatory lesions (Behçet disease, polyarteritis nodosa, Wegener disease).³⁵ In these cases, the constellation of clinical and imaging findings, presence of known systemic disease, or history of drug abuse may help narrow the differential considerations.

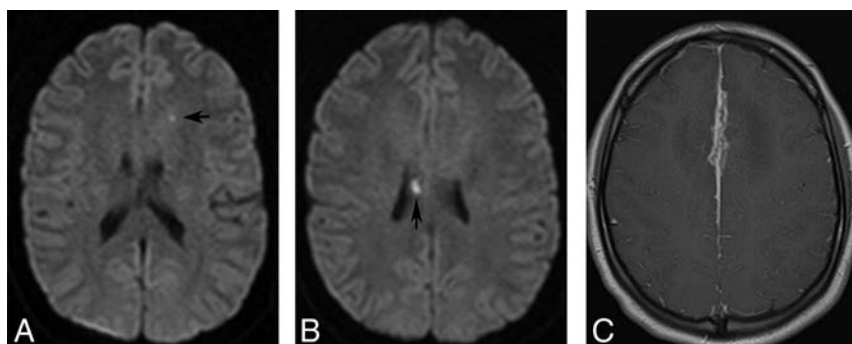


FIG 3. Axial DWIs reveal tiny subcortical infarcts (A and B) in a 22-year-old female patient. Axial postcontrast image (C) shows prominent involvement of the midline falx anteriorly. The infarcts were presumably secondary to involvement of the cortical vessels.

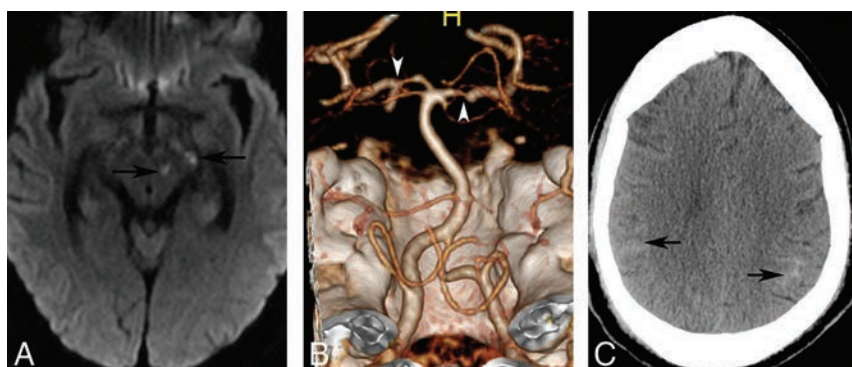


FIG 4. Axial DWI (A) in a 38-year-old male patient with NS reveals punctate infarcts involving the left cerebral peduncle and midbrain (arrows). A volume-rendered CT angiogram shows multifocal stenoses involving the P1 segments of the bilateral posterior cerebral arteries (B). The patient again presented after 2 months with severe headache. Noncontrast CT (C) image at this time shows acute subarachnoid hemorrhage over bilateral parietal convexities (arrows).

Hemorrhagic Lesions

Hemorrhagic lesions in NS are also rare, with a reported incidence of 0.6% in unselected sarcoidosis and series of patients with NS.^{36,37} Because the common denominator in both ischemic and hemorrhagic lesions is underlying vasculitis, it is not surprising that they both have a male predilection, unlike sarcoidosis, which is more common in females.^{36,38,39}

Table 2 lists the cases of NS with intracerebral hemorrhage (ICH) reported in the English language literature where imaging was performed.^{28,36–47} A review of these cases reveals that ICH in patients with NS is often intraparenchymal and is more likely to be supratentorial. Rarely, patients may also present with

Table 2: Cases of NS with ICH in the reported English language literature

Author	Year	Age (yr)/Sex	Zajicek Criteria	CT/MRI	MRA/DSA	Site	Systemic Disease
Caplan et al ²⁸	1983	21/M	Probable	Y/NS	NS	Left cerebellar	Y
Oksanen ⁴⁶	1986	NS/NS	NS	NS/NS	NS	NS	NS
Oksanen ⁴⁶	1986	NS/NS	NS	NS/NS	NS	NS	NS
Berek et al ⁴⁰	1993	35/M	Possible	Y/Y	Nm DSA	SAH on LP	N
Libman et al ⁴²	1997	48/F	Probable	Y/Y	+ DSA	Multiple, left cerebral hemisphere	Y
Eid et al ⁴³	1998	31/F	Probable	Y/NS	+ DSA	Right frontal	Y
Cipri et al ⁴⁷	2000	31/M	Definite	Y/Y	Nm DSA	Right occipital	N
Dakdouki et al ⁴⁵	2005	25/M	Probable	NS/Y	NS	Pons	Y
Tsappidi et al ³⁸	2011	43/M	Definite	Y/Y	Nm DSA/MRA	Multiple, supratentorial	N
O'Dwyer et al ³⁶	2013	41/M	Definite	Y/Y	Nm CTA	Cerebellum	N
O'Dwyer et al ³⁶	2013	41/M	Probable	Y/Y	Nm MRA	Pontomesencephalic	Y
O'Dwyer et al ³⁶	2013	36/M	Probable	Y/Y	Nm DSA	Left frontal	Y
Travers et al ⁴⁴	2014	37/M	Probable	NS/Y	Nm	Right temporal	Y
Pegat et al ⁴¹	2015	48/F	Probable	NS/Y	NS	Left frontoparietal	Y
Vargas et al ³⁷	2016	62/F	Probable	Y/Y	Nm MRA	Multiple microhemorrhages	Y
Vukojević et al ³⁹	2017	45/F	Probable	Y/Y	Nm CTA	Multiple, supra- and infratentorial	Y

Note:—Nm indicates normal findings; LP, lumbar puncture; N, no; NS, not specified; Y, yes; +, positive.

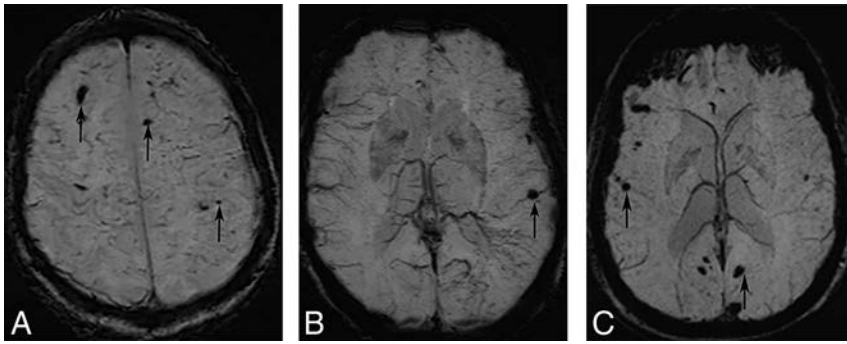


FIG 5. Axial SWI at the level of centrum semiovale (A) and basal ganglia (B) from 1 patient and at the level of basal ganglia in the other patient (C). There are multiple scattered foci of susceptibility involving bilateral subcortical white matter (arrows) with relative sparing of the basal ganglia in both patients.

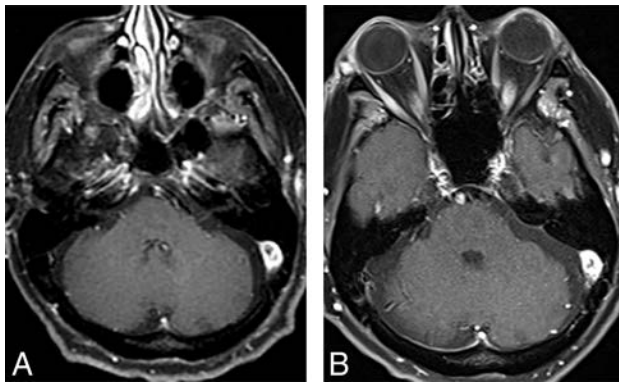


FIG 6. A and B, Axial postcontrast images through the posterior fossa obtained over an interval of 10 years. The prominent left sigmoid sinus enhancement remains essentially unchanged. The patient also had superior sagittal sinus involvement (not shown).

subarachnoid hemorrhage.⁴⁰ For unclear reasons, patients with symptomatic ICH seem to have a lobar predilection. This is somewhat counterintuitive because perivascular involvement in NS is most prominent in the basal ganglia, brain stem, and spinal cord.¹²⁻¹⁴ Isolated postmortem reports in patients with NS with ICH have also documented hemorrhages in the basal ganglia and posterior fossa compared with the cerebral hemispheres.^{14,28} Although some of the apparent lobar predilection may be from a reporting bias of larger symptomatic lesions, the reasons for relative sparing of the basal ganglia in the reported studies are unclear and unlikely to be entirely coincidental. Like some of the recently reported cases^{37,39,42} and the authors' personal experiences, distinct peripheral distribution of the ICH with sparing of the basal ganglia may be seen, though its significance is not clear (Fig 5).

The overall heterogeneity of the lesion distribution may be secondary to pathologically demonstrated "mixed" venous and arterial involvement.³⁶ As may be expected with predominantly small-vessel involvement, hemorrhagic lesions in patients with NS are often small and may be microhemorrhagic, though large parenchymal hematomas do rarely occur.^{36,37,43} Similar to ischemic strokes, multiple or recurrent hemorrhages may also be seen.^{37,39,42} Also analogous to cases with ischemic lesions, angiographic studies (DSA/MRA/CTA) are often unyielding. As shown

in Table 2, of the 11 cases in which an angiographic evaluation was performed, positive findings were only noted in 2 cases.

The initial diagnosis of NS in patients presenting with ICH can be very challenging, especially because almost half of these patients may not have known sarcoidosis.⁴⁶ Although it has been previously reported that about 31% of these patients have isolated NS, as noted in Table 2, most of these patients do have extra-CNS manifestations, though they may not be symptomatic.³⁶ Nevertheless, atypical locations of hemorrhage or multiple smaller or microhemorrhagic lesions, especially in the presence of other imaging signs of NS, should raise the suspicion in the appropriate clinical setting.^{36,44}

There is scarce literature on the impact of immunosuppressive therapy on patients with ischemic lesions. However, cases with hemorrhagic lesions do appear responsive to early aggressive antigranulomatous therapy, an important consideration because the microhemorrhages tend to increase with time and have been anecdotally associated with cognitive decline.^{36,37} An increase in intraparenchymal hemorrhages associated with steroid tapering or discontinuation has also been reported in multiple recent cases, highlighting the need for close follow-up while tapering immunosuppressive therapy.^{37,39,44,45}

The primary differential consideration of ICH in NS includes vasculitis, especially primary angiitis of the CNS, as discussed previously. Similar to the NS patients with ischemic lesions, the angiographic studies in patients with ICH are also often negative, though some cases may show large vessel vasculitis.^{36,42,43,46} Other differential considerations may include cerebral amyloid angiopathy, hypertensive angiopathy, and cerebral autosomal dominant arteriopathy with subcortical infarcts and leukoencephalopathy, though these tend to affect older patients in the first 2 instances and often have a predilection for the temporal lobes and external capsule in the latter.³⁷

Dural Sinus Involvement

Dural sinus thrombosis in NS is exceptionally rare, with only 5 cases reported in the literature.⁴⁸⁻⁵² The underlying mechanism is unclear and is presumably secondary to granulomatous meningeal involvement.^{51,52} Most patients present with symptoms of raised intracranial pressure. Given the rare occurrence, there is limited available imaging literature. The superior sagittal sinus is most frequently involved. Byrne and Lawton⁴⁹ reported a case of meningeal sarcoidosis in a 32-year-old woman with an obstructed straight sinus and bilateral transverse sinuses on angiography. They also noted meningeal enhancement along the occluded sinuses without any change in appearance on follow-up imaging at 5 years. The patient had imaging findings of intracranial hypertension, including an empty sella and erosion of the dorsum sella.

Leeds et al⁵² presented a case of superior sagittal sinus thrombosis, which they attributed to surrounding granulomatous inflammation. However, the images were presented as a part of

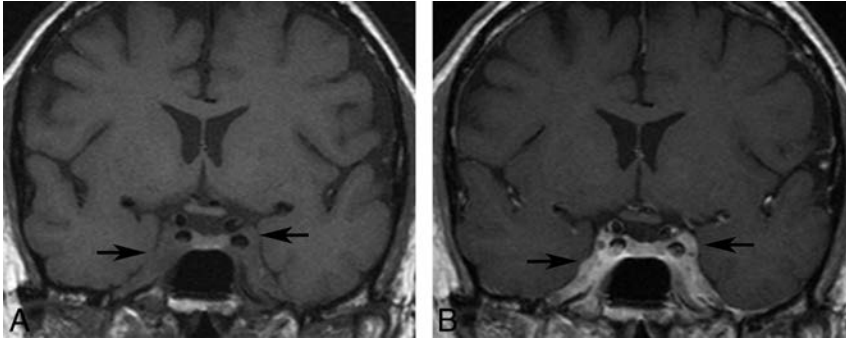


FIG 7. Coronal pre- (A) and postcontrast (B) images in a patient with NS show nodular thickening and enhancement of the cavernous sinuses bilaterally. The patient had additional intracranial stigmata of NS (not shown), and the cavernous sinus involvement was presumed to be secondary to NS.

an imaging review article with no additional patient-specific details. Chapelon et al⁵¹ also reported a case of a 26-year-old man with NS and superior sagittal sinus thrombosis in their review of 35 patients without much additional information.⁵¹ Akova et al⁴⁸ presented a case report of possible NS in a 35-year-old man with superior sagittal sinus thrombosis associated with meningeal sarcoidosis and clinical features of pseudotumor cerebri.

More recently, Degardin et al⁵⁰ presented a case of a 47-year-old man with superior sagittal sinus thrombosis. They also noted that the thrombosis persisted at 6-month follow-up despite satisfactory anticoagulation. The patient also had large-vessel involvement as well as multiple intraparenchymal hemorrhages of varying ages, which were attributed to granulomatous angiitis. We also encountered a similar case of thrombosis in a 61-year-old male patient involving the sagittal and left transverse sinuses over a background of multiple intraparenchymal hemorrhages of varying ages. Our patient also showed a persistently enlarged and enhancing sinus with surrounding collaterals that remained unchanged for 10 years (Fig 6). This feature contrasts with a bland thrombus, which is usually dissolved with anticoagulation, leaving behind a normal or attenuated vessel and a collateral network. The persistent imaging findings are possibly from continued granulomatous sinus involvement.

Cavernous Sinus Involvement

Cavernous sinus involvement in NS is again exceedingly rare, with only 2 prior reported cases.^{53,54} Chang et al⁵³ reported a case of left cavernous sinus involvement in a 54-year-old man with concurrent pulmonary sarcoidosis. The other reported case was by Kim et al⁵⁴ of a 40-year-old man with NS localized to the right cavernous sinus without any additional CNS or extra-CNS involvement. In both cases, the imaging findings were nonspecific and showed a T1-isointense, T2-hyperintense, enhancing cavernous sinus mass. We also encountered a case like that of Chang et al with nodular thickening of the cavernous sinus, most apparent on the contrast-enhanced images (Fig 7). Overall, the rarity of cavernous sinus involvement, the scarcity of literature, and nonspecific imaging findings preclude any meaningful conclusions about the expected MR imaging findings.

The differential considerations in such cases are invariably broad and include neoplasms, infective lesions, or inflammatory conditions such as Tolosa-Hunt syndrome. Coexisting CNS or

extra-CNS findings of sarcoidosis may be the only helpful clue in such cases.

CONCLUSIONS

The authors present a review of the various cerebrovascular manifestations that may be encountered in patients with NS. Although rare, these are of utmost importance, not only because of the associated morbidity but also because patients may present with isolated NS and pose considerable diagnostic challenges, especially when the manifestations are atypical. Vasculitic manifestations of NS should be considered in patients with recurrent hemorrhages or infarcts, espe-

cially when the patients are younger and demonstrate additional intracranial imaging findings that may support NS.

Disclosures: Suyash Mohan—UNRELATED: Grants/Grants Pending: Novocure, Radiological Society of North America, Guerbet, Comments: research grants*. *Money paid to the institution.

REFERENCES

1. Bathla G, Singh AK, Policeni B, et al. **Imaging of neurosarcoidosis: common, uncommon, and rare.** *Clin Radiol* 2016;71:96–106 CrossRef Medline
2. Hodge MH, Williams RL, Fukui MB. **Neurosarcoidosis presenting as acute infarction on diffusion-weighted MR imaging: summary of radiologic findings.** *AJNR Am J Neuroradiol* 2007;28:84–86 Medline
3. Brisman JL, Hinduja A, McKinney JS, et al. **Successful emergent angioplasty of neurosarcoid vasculitis presenting with strokes.** *Surg Neurol* 2006;66:402–04 CrossRef Medline
4. Michotte A, Dequenne P, Jacobovitz D, et al. **Focal neurological deficit with sudden onset as the first manifestation of sarcoidosis: a case report with MRI follow-up.** *Eur Neurol* 1991;31:376–79 Medline
5. Macedo PJ, da Silveira VC, Ramos LT, et al. **Isolated central nervous system vasculitis as a manifestation of neurosarcoidosis.** *J Stroke Cerebrovasc Dis* 2016;25:e89–e92 CrossRef Medline
6. Smith JK, Matheus MG, Castillo M, et al. **Imaging manifestations of neurosarcoidosis.** *AJR Am J Roentgenol* 2004;182:289–95 CrossRef Medline
7. Izbicki G, Chavko R, Banauch GI, et al. **World Trade Center “sarcoid-like” granulomatous pulmonary disease in New York City Fire Department rescue workers.** *Chest J* 2007;131:1414–23 CrossRef Medline
8. Iwai K, Takemura T, Kitalchi M, et al. **Pathological studies on sarcoidosis autopsy, II: early change, mode of progression and death pattern.** *Acta Pathol Jpn* 1993;43:377–85 Medline
9. Robert F. **Sarcoidosis of the central nervous system: report of a case and review of the literature.** *Arch Neurol* 1962;7:442–49 CrossRef Medline
10. Duffey P, Bates D. **Transient focal neurological deficit in sarcoidosis.** *Sarcoidosis Vasc Diffuse Lung Dis* 1997;14:171–72 Medline
11. Camp WA, Frierson JG. **Sarcoidosis of the central nervous system: a case with postmortem studies.** *Arch Neurol* 1962;7:432–41 CrossRef Medline
12. Brown MM, Thompson AJ, Wedzicha JA, et al. **Sarcoidosis presenting with stroke.** *Stroke* 1989;20:400–05 CrossRef Medline
13. Reske-Nielsen E, Harmsen A. **Periangiitis and panangiitis as a manifestation of sarcoidosis of the brain: report of a case.** *J Nerv Ment Dis* 1962;135:399–412 CrossRef Medline
14. Herring AB, Urich H. **Sarcoidosis of the central nervous system.** *J Neurol Sci* 1969;9:405–22 CrossRef Medline
15. González-Aramburu I, Ruiz-Pérez E, Gómez-Román J, et al. **Sarcoid-**

- osis presenting as transient ischemic attack status. *J Stroke Cerebrovasc Dis* 2012;21:515–17 CrossRef Medline
16. Tsukada N, Yanagisawa N, Mochizuki I. **Endothelial cell damage in sarcoidosis and neurosarcoidosis: autoantibodies to endothelial cells.** *Eur Neurol* 1995;35:108–12 Medline
 17. Siasos G, Tousoulis D, Gialafos E, et al. **Association of sarcoidosis with endothelial function, arterial wall properties, and biomarkers of inflammation.** *Am J Hypertens* 2011;24:647–53 CrossRef Medline
 18. Letizia C, Danese A, Reale MG, et al. **Plasma levels of endothelin-1 increase in patients with sarcoidosis and fall after disease remission.** *Panminerva Med* 2001;43:257–61 Medline
 19. Mochizuki I, Kubo K, Hond T. **Widespread heavy damage of capillary endothelial cells in the pathogenesis of sarcoidosis: evidence by monoclonal von Willebrand factor immunohistochemistry in the bronchus and lung of patients with sarcoidosis.** *Sarcoidosis Vasc Diffuse Lung Dis* 2014;31:182–90 CrossRef Medline
 20. Liebow AA. **The J Burns Amberson lecture: pulmonary angitis and granulomatosis.** *Am Rev Respir Dis* 1973;108:1–18 Medline
 21. Rosen Y. **Four decades of necrotizing sarcoid granulomatosis: what do we know now?** *Arch Pathol Lab Med* 2015;139:252–62 CrossRef Medline
 22. Churg A, Carrington CB, Gupta R. **Necrotizing sarcoid granulomatosis.** *Chest* 1979;76:406–13 CrossRef Medline
 23. Manz HJ. **Pathobiology of neurosarcoidosis and clinicopathologic correlation.** *Can J Neurol Sci* 1983;10:50–55 CrossRef Medline
 24. Zadra M, Brambilla A, Erli LC, et al. **Neurosarcoidosis, stroke and antiphospholipid antibodies: a case report.** *Eur J Neurol* 1996;3:146–48 CrossRef
 25. Raza N, Schreck KC. **Neurosarcoidosis presenting with recurrent strokes: a case report and literature review.** *Neurohospitalist* 2017;7:91–95 CrossRef Medline
 26. Corse AM, Stern BJ. **Neurosarcoidosis and stroke.** *Stroke* 1990;21:152–53 Medline
 27. Schonell ME, Gillespie WJ, Maloney AF. **Cerebral sarcoidosis.** *Br J Dis Chest* 1968;62:195–99 CrossRef Medline
 28. Caplan L, Corbett J, Goodwin J, et al. **Neuro-ophthalmologic signs in the angitic form of neurosarcoidosis.** *Neurology* 1983;33:1130–35 CrossRef Medline
 29. Meyer JS, Foley JM, Campagna-Pinto D. **Granulomatous angitis of the meninges in sarcoidosis.** *AMA Arch Neurol Psychiatry* 1953;69:587–600 CrossRef Medline
 30. Das SK, Sinha I, Kundu TN, et al. **Two cases of neurosarcoidosis presenting as peripheral neuropathy and stroke in young.** *J Assoc Physicians India* 1998;46:479–81 Medline
 31. Navi BB, DeAngelis LM. **Sarcoidosis presenting as brainstem ischemic stroke.** *Neurology* 2009;72:1021–22 CrossRef Medline
 32. Campbell J, Kee R, Bhattacharya D, et al. **Systemic sarcoidosis presenting with headache and stroke-like episodes.** *Case Rep Immunol* 2015;2015:619867 CrossRef Medline
 33. Ko JK, Lee SW, Choi CH. **Moyamoya-like vasculopathy in neurosarcoidosis.** *J Korean Neurosurg Soc* 2009;45:50–52 CrossRef Medline
 34. Birnbaum J, Hellmann DB. **Primary angitis of the central nervous system.** *Arch Neurol* 2009;66:704–09 CrossRef Medline
 35. Grossman RI, Yousem DM. *Neuroradiology: The Requisites.* St Louis: Mosby; 2003:196–204
 36. O'Dwyer JP, Al-Moyeed BA, Farrell MA, et al. **Neurosarcoidosis-related intracranial haemorrhage: three new cases and a systematic review of the literature.** *Eur J Neurol* 2013;20:71–78 CrossRef Medline
 37. Vargas A, Gorelick PB, Testai FD. **Progressive central nervous system vasculopathy in sarcoidosis: a case report.** *J Neurol Sci* 2016;362:153–54 CrossRef Medline
 38. Tsappidi S, Hui F, Turan TN, et al. **Intracerebral hemorrhage: an unusual presentation of neurosarcoidosis.** *Neurologist* 2011;17:292–96 CrossRef Medline
 39. Vukojević Z, Ilić TV, Dominović-Kovačević A, et al. **Neurosarcoidosis and multiple intracerebral hematomas: an unusual clinical presentation.** *J Neurol Sci* 2017;379:22–24 CrossRef Medline
 40. Berek K, Kiechl S, Willeit J, et al. **Subarachnoid hemorrhage as presenting feature of isolated neurosarcoidosis.** *Clin Investig* 1993;71:54–56 Medline
 41. Pegat B, Drapier S, Morandi X, et al. **Spinal cord hemorrhage in a patient with neurosarcoidosis on long-term corticosteroid therapy: case report.** *BMC Neurol* 2015;15:123 CrossRef Medline
 42. Libman RB, Sharfstein S, Harrington W, et al. **Recurrent intracerebral hemorrhage from sarcoid angitis.** *J Stroke Cerebrovasc Dis* 1997;6:373–75 CrossRef Medline
 43. Eid H, O'Connor CR, Catalano E, et al. **Life-threatening vasculitis associated with sarcoidosis.** *J Clin Rheumatol* 1998;4:338–43 CrossRef Medline
 44. Travers F, Maltête D, Morisse-Pradier H. **Intracranial hemorrhage in neurosarcoidosis.** *J Neurol Sci* 2014;341:185–86 CrossRef Medline
 45. Dakdouki GK, Kanafani ZA, Ishak G, et al. **Intracerebral bleeding in a patient with neurosarcoidosis while on corticosteroid therapy.** *South Med J* 2005;98:492–95 CrossRef Medline
 46. Oksanen V. **Neurosarcoidosis: clinical presentations and course in 50 patients.** *Acta Neurol Scand* 1986;73:283–90 Medline
 47. Cipri S, Gambardella G, Campolo C, et al. **Unusual clinical presentation of cerebral-isolated sarcoidosis: case report and review of the literature.** *J Neurosurg Sci* 2000;44:140–44 Medline
 48. Akova YA, Kansu T, Duman S. **Pseudotumor cerebri secondary to dural sinus thrombosis in neurosarcoidosis.** *J Clin Neuroophthalmol* 1993;13:188–89 Medline
 49. Byrne JV, Lawton CA. **Meningeal sarcoidosis causing intracranial hypertension secondary to dural sinus thrombosis.** *Br J Radiol* 1983;56:755–57 CrossRef Medline
 50. Degardin A, Devos P, Vermersch P, et al. **Cerebrovascular symptomatic involvement in sarcoidosis.** *Acta Neurol Belg* 2010;110:349–52 Medline
 51. Chapelon C, Ziza JM, Piette JC, et al. **Neurosarcoidosis: signs, course and treatment in 35 confirmed cases.** *Medicine* 1990;69:261–76 CrossRef Medline
 52. Leeds NE, Zimmerman RD, Elkin CM, et al. **Neurosarcoidosis of the brain and meninges.** *Semin Roentgenol* 1985;20:387–92 CrossRef Medline
 53. Chang CS, Chen WL, Li CT, et al. **Cavernous sinus syndrome due to sarcoidosis: a case report.** *Acta Neurol Taiwan* 2009;18:37–41 Medline
 54. Kim DH, Cho WH, Cho KS, et al. **Solitary cavernous sinus neurosarcoidosis mimicking neurosyphilis.** *J Korean Neurosurg Soc* 2014;55:61–63 CrossRef Medline

Deep-Learning Convolutional Neural Networks Accurately Classify Genetic Mutations in Gliomas

 P. Chang,  J. Grinband,  B.D. Weinberg,  M. Bardis,  M. Khy,  G. Cadena,  M.-Y. Su,  S. Cha,  C.G. Filippi,  D. Bota,  P. Baldi,  L.M. Poisson,  R. Jain, and  D. Chow



ABSTRACT

BACKGROUND AND PURPOSE: The World Health Organization has recently placed new emphasis on the integration of genetic information for gliomas. While tissue sampling remains the criterion standard, noninvasive imaging techniques may provide complimentary insight into clinically relevant genetic mutations. Our aim was to train a convolutional neural network to independently predict underlying molecular genetic mutation status in gliomas with high accuracy and identify the most predictive imaging features for each mutation.

MATERIALS AND METHODS: MR imaging data and molecular information were retrospectively obtained from The Cancer Imaging Archives for 259 patients with either low- or high-grade gliomas. A convolutional neural network was trained to classify *isocitrate dehydrogenase 1 (IDH1)* mutation status, 1p/19q codeletion, and *O6-methylguanine-DNA methyltransferase (MGMT)* promoter methylation status. Principal component analysis of the final convolutional neural network layer was used to extract the key imaging features critical for successful classification.

RESULTS: Classification had high accuracy: *IDH1* mutation status, 94%; 1p/19q codeletion, 92%; and *MGMT* promoter methylation status, 83%. Each genetic category was also associated with distinctive imaging features such as definition of tumor margins, T1 and FLAIR suppression, extent of edema, extent of necrosis, and textural features.

CONCLUSIONS: Our results indicate that for The Cancer Imaging Archives dataset, machine-learning approaches allow classification of individual genetic mutations of both low- and high-grade gliomas. We show that relevant MR imaging features acquired from an added dimensionality-reduction technique demonstrate that neural networks are capable of learning key imaging components without prior feature selection or human-directed training.

ABBREVIATIONS: CNN = convolutional neural network; *IDH* = *isocitrate dehydrogenase*; *MGMT* = *O6-methylguanine-DNA methyltransferase*; VASARI = Visually AcceSable Rembrandt Images

Diffuse infiltrating gliomas are a heterogeneous group of primary tumors with highly variable imaging characteristics, response to therapy, clinical course, and prognoses. This well-

known heterogeneity is, in part, attributed to the multiple variations in the genetic and epigenetic mutations that occur early in tumorigenesis.¹ For example, *isocitrate dehydrogenase 1* and/or 2 (*IDH1* and/or 2)–mutant glioblastomas demonstrate significantly improved survivorship compared with *IDH* wild-type glioblastomas (31 months versus 15 months).^{2,3} Similarly, patients with anaplastic oligodendrogliomas with 1p/19q codeletion benefit from combined procarbazine/lomustine/vincristine therapy and radiation therapy compared with patients without the mutation.^{4,5} Regarding chemotherapy response, glioblastomas with *O6-methylguanine-DNA methyltransferase (MGMT)* promoter methylation demonstrate improved response to the combination of temozolomide and radiation therapy versus radiation therapy

Received November 29, 2017; accepted after revision March 20, 2018.

From the Department of Radiology (P.C., S.C.), University of California, San Francisco, San Francisco, California; Department of Radiology (J.G.), Columbia University, New York, New York; Department of Radiology (B.D.W.), Emory University School of Medicine, Atlanta, Georgia; Departments of Radiology (M.B., M.K., M.-Y.S., D.C.), Neurosurgery (G.C.), and Neuro-Oncology (D.B.) and School of Information and Computer Sciences (P.B.), University of California, Irvine, Irvine, California; Department of Radiology (C.G.F.), North Shore University Hospital, Long Island, New York; Department of Public Health Sciences (L.M.P.), Henry Ford Health System, Detroit, Michigan; and Departments of Radiology and Neurosurgery (R.J.), New York University, New York, New York.

This work was supported by Canon Medical Systems USA. The work of P.B. was supported, in part, by the following grants: Defense Advanced Research Projects Agency D17AP00002 and National Institutes of Health GM123558. The work of P.C. was in part supported by the National Institutes of Health training grant T32EB001631.

Please address correspondence to Daniel Chow, MD, University of California, Irvine Medical Center, 101 The City Drive South, Douglas Hospital, Route 140, Room 0115, Orange, CA 92868-3201; e-mail: chowd3@uci.edu; @DanChow01

 Indicates open access to non-subscribers at www.ajnr.org

 Indicates article with supplemental on-line appendix.

 Indicates article with supplemental on-line photo.

<http://dx.doi.org/10.3174/ajnr.A5667>

alone (21.7 versus 15.3 months).⁶ The World Health Organization has recently placed new emphasis on the integration of genetic and molecular information for CNS tumor-classification schemes, including *IDH1* status and 1p/19q codeletion and several other molecular or genetic markers.⁷ Thus, knowledge of tumor genetic information is needed to accurately monitor patients with gliomas and guide personalized therapies.

At present, information regarding underlying genetic and molecular alterations of gliomas is based on analysis of tumor tissue obtained during an operation. However, although high-grade gliomas are known to infiltrate widely into the surrounding non-enhancing peritumoral region,⁸ biopsies are often limited to the easily accessible areas of the enhancing tumor. Additionally, molecular genetic testing can be costly or not widely available, and the results may take weeks, thereby delaying important therapeutic decisions. Noninvasive imaging techniques that can provide complimentary insight into clinically relevant genetic mutations may expedite and coordinate care among clinicians, minimizing these delays.

MR imaging can noninvasively assess the entire tumor, allowing both a global and regional (voxelwise) characterization of molecular genetics, in contrast to the spatially limited assessment of tissue biopsy. Specifically, both spatial and temporal variations in genetic expression are known to result in heterogeneous alterations in tumor biology, including changes in angiogenesis, cellular proliferation, cellular invasion, and apoptosis.⁹ These biologic changes are reflected in the complex imaging features of gliomas, manifest by varying degrees of enhancement, infiltration, hemorrhage, reduced diffusion, edema, and necrosis. Attempts to standardize visual interpretation of malignant gliomas for tissue classification have led to the Visually AcceSable Rembrandt Images (VASARI) feature set, a rule-based lexicon to improve the reproducibility of interpretation.¹⁰ However, a limitation of such approaches is the need for a priori feature selection and human visual interpretation, which innately distills a complex dataset of over a million voxels per MR imaging to a handful of numeric descriptors—a “big data” challenge.

The purpose of this study was to classify genetic variations of diffuse infiltrating gliomas using deep-learning/machine-learning approaches implemented with convolutional neural networks (CNNs). CNN approaches model the animal visual cortex by applying a feed-forward artificial neural network to simulate multiple layers of neurons organized in overlapping regions within a visual field, with each layer acting to transform the raw input image into more complex, hierarchic, and abstract representations.¹¹ Thus, it is natural to consider applying deep-learning methods to biomedical images. We hypothesized the following: 1) A CNN can be trained to independently predict underlying molecular genetic mutation status in gliomas with high accuracy, and 2) a trained CNN can identify predictive imaging features for a given mutation.

MATERIALS AND METHODS

Subjects

MR imaging data were retrospectively obtained from The Cancer Imaging Archives for patients with either low- or high-grade gliomas.¹² Corresponding molecular genetic information was ob-

tained from The Cancer Genome Atlas. Only patients with full preoperative MR imaging, including T2, FLAIR, and T1-weighted pre- and postcontrast acquisitions, were included in the analysis. Corresponding molecular information for each patient was obtained, including *IDH1* status, 1p/19q codeletion, and *MGMT* promoter methylation.¹³

Image Preprocessing

For each patient, all imaging modalities were coregistered using the FMRIB Linear Image Registration Tool (FLIRT; <http://www.fmrib.ox.ac.uk/fsl/fslwiki/FLIRT>).^{14,15} Registration was implemented with a linear affine transformation algorithm using 12 *df*, trilinear interpolation, and a mutual-information cost function. The reference volume for coregistration was the highest resolution sequence, most commonly the postcontrast T1-weighted acquisition. The average time for coregistration was approximately 1 minute per volume. On a typical multicentral processing unit core workstation, the required total of 3 registrations per patient can be performed simultaneously as separate processes, thus allowing all modalities to be coregistered in approximately 1 minute.

Each input technique was independently normalized using *z*-score values ($\mu = 0$, $\sigma = 1$). From these, a custom in-house fully automated whole-brain extraction tool-based 3D convolutional neural network was used to remove extracranial structures. Next, a fully automated brain tumor segmentation tool was used to identify lesion margins. This algorithm was the top-performing tool as evaluated in the international 2016 Multimodal Brain Tumor Segmentation Challenge.¹⁶ It is based on a serial fully convolutional neural network architecture with residual connections and performs whole-tumor segmentation in approximately 1 second. These masks were used to generate cropped slice-by-slice images of the tumor on all modalities, each of which were subsequently resized to a $32 \times 32 \times 4$ input.

No other form of preprocessing was necessary for this study. Specifically, the flexibility of CNNs allows robust classification, even in the absence of conventional image-preprocessing steps such as histogram normalization or bias field correction.

Convolutional Neural Networks

CNNs are an adaption of the traditional artificial neural network architecture whereby banks of 2D convolutional filter parameters and nonlinear activation functions act as a mapping function to transform a multidimensional input image into a desired output.¹⁷ Network overview and details are provided in the On-line Appendix.

Feature Analysis

The final feature vector produced by a neural network through serial convolutions often encodes for redundant information, given the flexibility of the algorithm to choose any feature necessary to produce accurate classification. In the architecture used for this study, this means that many of 64 features in the final hidden layer will be highly correlated to each other. To decompose this encoded information and gain insight into features learned by the algorithm, we applied principal component analysis to the final feature vector with various dimensionally reduced

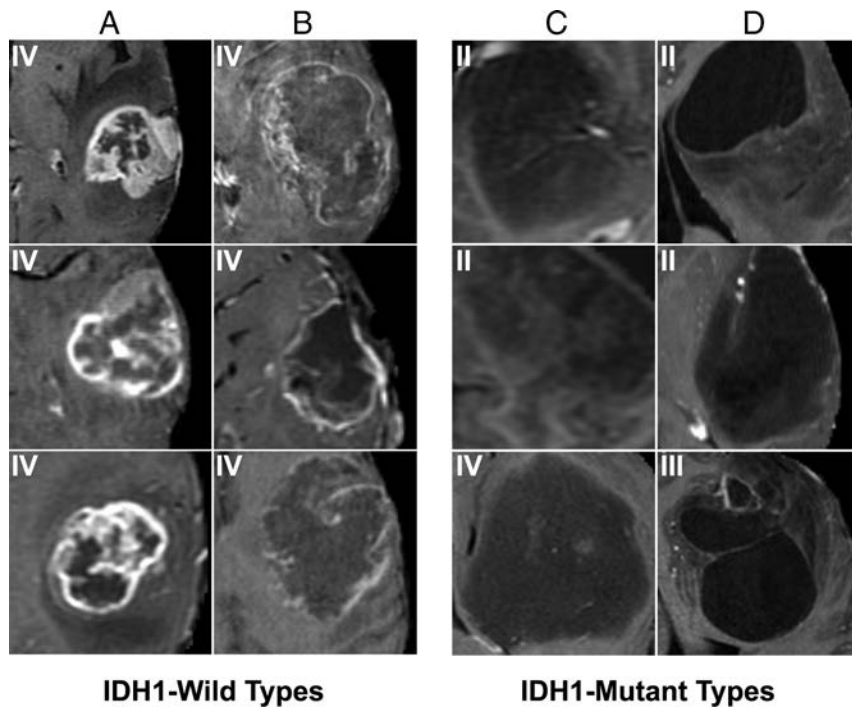


FIG 1. T1 postcontrast features most highly correlated with *IDH1* mutation status. Prototypical cases as identified by our convolutional neural network imaging features associated with *IDH* wild types (A and C) and mutation (B and D). Specifically, *IDH* wild types demonstrate thick and irregular enhancement (A) or thin, irregular poorly marginated peripheral enhancement (B). In contrast, patients with *IDH* mutation demonstrate absent or minimal enhancement (C) with well-defined tumor margins (D).

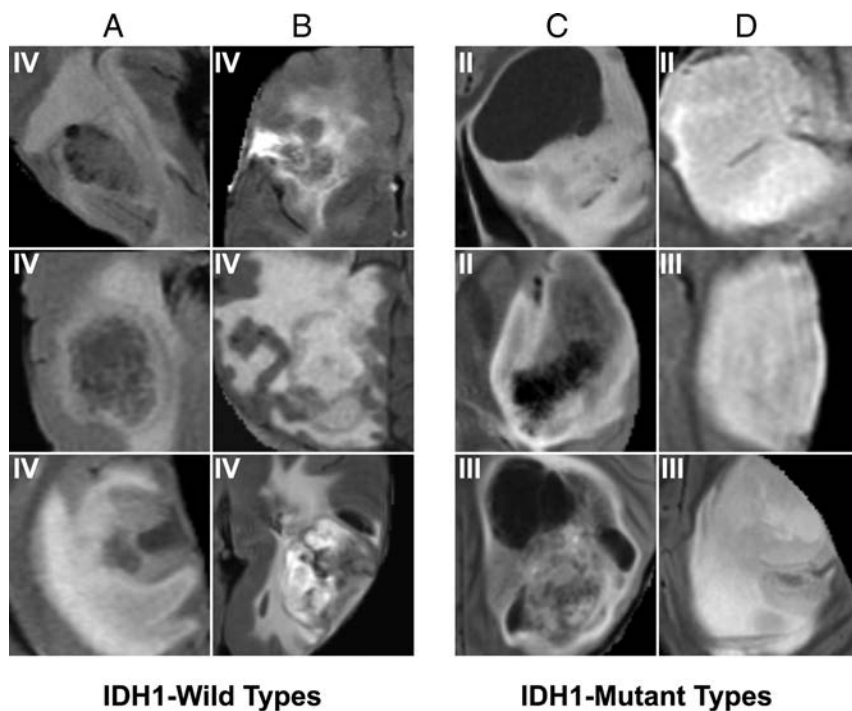


FIG 2. FLAIR features most highly correlated with *IDH1* mutation status. Prototypical cases as identified by our convolutional neural network imaging features are associated with *IDH* wild types (A and B) and mutation (C and D). *IDH* wild types demonstrate infiltrative patterns of edema, seen as more irregular (A) and ill-defined (B) margins of FLAIR signal abnormality. Patients with *IDH* mutation demonstrate central areas of cysts with FLAIR suppression (C) and well-defined tumor margins (D).

subspaces, $L \in \epsilon^{1-5}$. By means of this approach, the principal component analysis-reduced features, whose weights have the largest absolute value magnitude with respect to the final classification, can be identified. These features can be interpreted as those automatically learned by the algorithm that are most influential in classification of any given mutation status. These final imaging features identified by the algorithm are shown in Figs 1–4.

Statistical Analysis

To evaluate overall per-patient accuracy, we pooled mean softmax scores across all image slices, with a threshold of 0.5 used to determine mutation classification. As an example of *IDH* status, an average softmax score of >0.5 represents prediction of mutant status, while an average softmax score of <0.5 represents prediction of wild-type status. While a softmax score of 0.5 is the standard threshold for neural network classification, it is possible to arbitrarily change this cutoff to between 0 and 1 to alter the sensitivity and specificity of the network. By means of this approach, overall algorithm performance on a wide range of thresholds is reported as an area under the curve calculation for each mutation.

To assess algorithm generalization, we used a 5-fold cross-validation approach. For each of the 5 experimental iterations, 20% of the data were used for validation, while the remaining 80% of the data were used for training. Results are reported for only patients in the validation cohort after 5-fold cross-validation.

RESULTS

Subjects

A total of 5259 axial slices of tumor from 259 patients with gliomas (135 men/122 women/2 unknown; mean age, 53.2 years; mean survival, 18.8 years) were included for analysis. The distribution of gliomas included the following: 21.2% (55/259) grade II, 22.8% (59/259) grade III, and 55.2% (143/259) grade IV gliomas. There were 2 gliomas that had available genetic information but no World Health Organization grade assignment. *IDH1* mutant and wild-type tumors accounted for 45.9% (119/259) and 54.1% (140/259) of patients, respectively; 1p/19q codeletions and nondele-

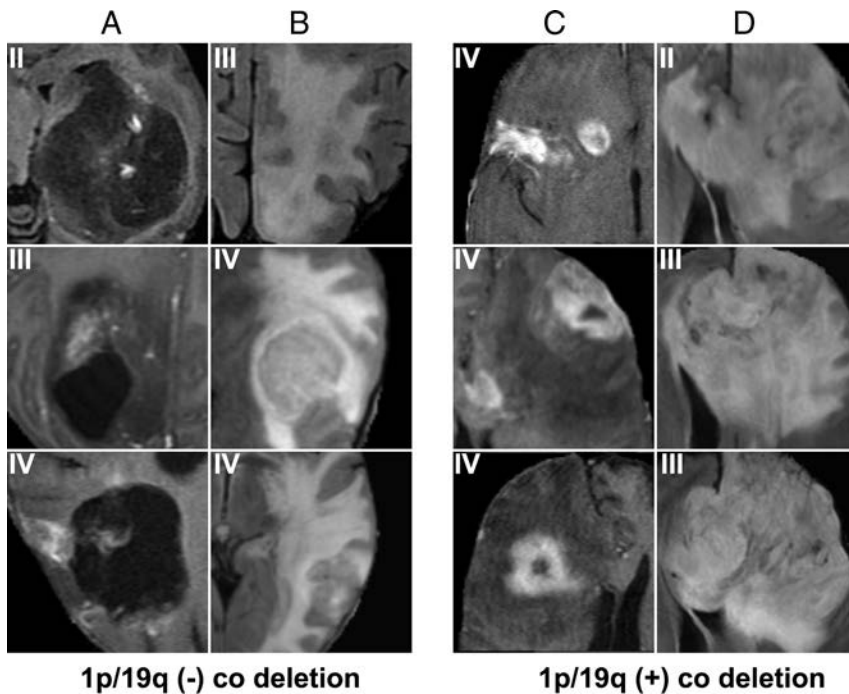


FIG 3. MR imaging features most highly correlated with 1p/19q codeletion. Prototypical cases as identified by our convolutional neural network imaging features are associated with 1p/19q absence (A and B) and presence (C and D) codeletion status. Features predictive of the absence of 1p/19q codeletion are poor enhancement (A) and increased vasogenic edema (B). Features predictive of the presence of 1p/19q codeletion are increased enhancement (C) and a left frontal predominance and ill-defined FLAIR margins with mass effect (D).

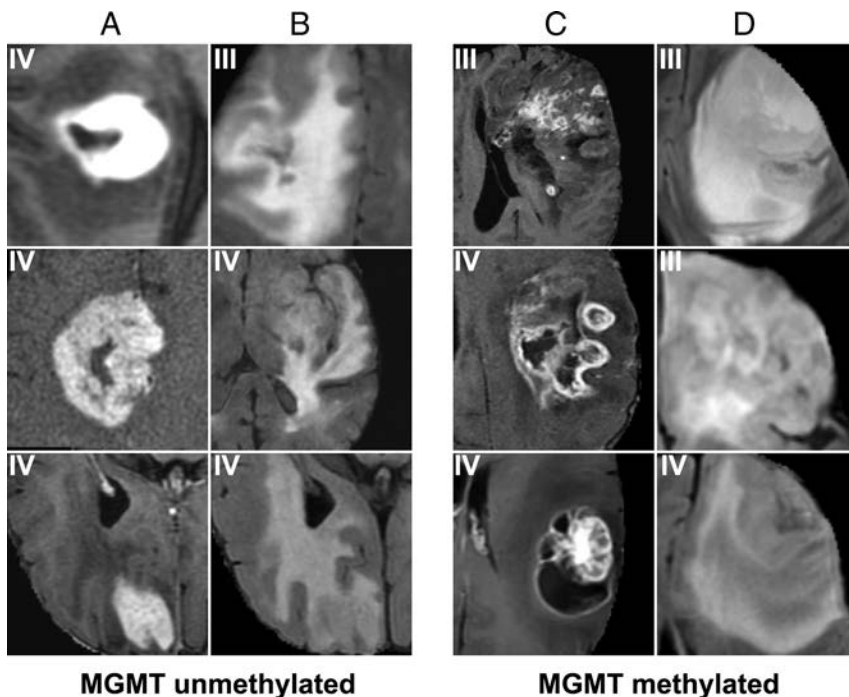


FIG 4. Features most highly correlated with MGMT methylation. Prototypical cases as identified by our convolutional neural network imaging features associated with unmethylated (A and B) and methylated (C and D) MGMT statuses. Features predictive of MGMT unmethylated status include thick enhancement with central necrosis (A) with infiltrative edema patterns (B). In contrast, features predictive of MGMT promoter methylated status include nodular and heterogeneous enhancement (C) with masslike FLAIR edema (D).

tions accounted for 12.0% (31/259) and 88.0% (228/259) of patients, respectively. MGMT promoter methylated and unmethylated accounted for 56.4% (146/259) and 43.6% (113/259) of patients, respectively. The mean tumor size determined by automated segmentation masks was 105.6 cm³.

CNN Accuracy

Overall, the algorithm correctly predicted IDH1 mutation (mean, 94%; range between cross validations, 90%–96%), 1p/19q codeletion (mean, 92%; range, 88%–95%), and MGMT promoter methylation (mean, 83%; range, 76%–88%) on 5-fold cross-validation. The area under the curve for IDH mutation (mean, 0.91; range, 0.89–0.92), 1p/19q codeletion (mean, 0.88; range, 0.85–0.90), and MGMT promoter methylation (mean, 0.81; range, 0.76–0.84) also reflected high performance. The CNN was trained for 25,000 iterations (approximately 3000 epochs with batch sizes ranging from 12 to 48) before convergence. A single forward pass during test time for classification of new cases can be achieved in 0.0043 seconds. Overall, the imaging workflow takes 5.12 seconds per patient (4–5 seconds for detection and preprocessing and the remaining 0.0043 seconds for classification).

Feature Analysis

For IDH1 mutation (Figs 1 and 2), the most predictive features were the following: absent or minimal areas of enhancement (the presence of a larger portion of nonenhancing tumor), central areas of cysts with low T1 and FLAIR suppression, and well-defined tumor margins. By comparison, IDH1 wild-type tumors tended to demonstrate a larger portion of enhancing tumor with thick enhancement; thin, irregular, poorly marginated peripheral enhancement with central necrosis; and an infiltrative pattern of edema (seen as more irregular and ill-defined margins of T2/FLAIR signal abnormality).

For 1p19 codeletion (Fig 3), the most predictive features were left frontal lobe location, ill-defined tumor margins, and larger portion of enhancement. Compared with either IDH1 mutation or MGMT promoter methylation, many features learned by the CNN for 1p19

codeletion were highly correlated to each other; this finding resulted in an overall smaller number of differentiable features.

For *MGMT* promoter methylation (Fig 4), the most predictive features were a heterogeneous, nodular enhancement; the presence of an eccentric cyst; more masslike edema (larger lesions with a higher portion of nonenhancing tumor component) with cortical involvement; and slight frontal and superficial temporal predominance. By comparison, unmethylated tumors tended to demonstrate thin rim enhancement, central areas of necrosis, solid enhancement, more vasogenic edema, and a slight, deep temporal predominance.

DISCUSSION

The variability of clinical outcomes in patients with diffuse infiltrating gliomas is, in part, predicated on molecular and genetic heterogeneity, which has spurred the development and study of noninvasive tools to better classify these tumors. In this study, we used a deep-learning approach to classify individual somatic mutations of diffuse infiltrating gliomas, World Health Organization II–IV, including *IDH1* status; 1p/19q codeletion; and the presence of *MGMT* promoter methylation with an accuracy of 94% (90%–96%), 92% (88%–95%), and 83% (76%–88%), respectively. We were able to implement the entire preprocessing pipeline from tumor detection to tissue segmentation to mutation classification without human supervision. Furthermore, neural networks have been criticized for being “black boxes” that generate uninterpretable feature vectors, which limits insight into the underlying mechanism for image classification. In this study, we applied a dimensionality-reduction approach to visually display the highest ranking features of each mutation category.

Molecular analysis of tumors has significantly impacted the diagnosis of glial tumors, with important implications for both prognosis and therapy guidance. The recently published 2016 World Health Organization Classification of Tumors of the Central Nervous System included several molecular genetic alterations as important features of tumor classification.⁷ One of the significant changes has been in the classification of oligodendrogliomas, in which mutations of *IDH1* or 2 and 1p/19q codeletion are the defining and diagnostic markers. Additionally, hypermethylation of the *MGMT* promoter, an enzyme involved in DNA de-alkylation and mediation of DNA damage, is a positive prognostic factor.⁶ Patients with a methylated *MGMT* promoter have improved survival and better response to radiation therapy with concurrent temozolomide.^{6,18}

Prior classic machine-learning approaches for linking imaging features to these genetic alternations in gliomas have typically relied on human-derived feature extraction such as textural analysis approaches or rule-based systems such as VASARI. For example, Ryu et al¹⁹ applied texture analysis to evaluate glioma heterogeneity to distinguish low- and high-grade gliomas with an 80% accuracy. Additionally, Drabycz et al²⁰ described a textural analysis approach to classifying *MGMT* promoter methylation status in patients with glioblastomas with 71% accuracy. More recently, Kanas et al²¹ achieved a 74% accuracy in distinguishing the *MGMT* promoter methylation status from gliomas acquired from The Cancer Genome Atlas using a multivariate prediction model based on qualitative imaging features from the VASARI lexicon.

While these approaches have improved the reproducibility and accuracy of classification, the need for manual a priori feature selection remains an inherently limiting factor, a process dependent on expert opinion and an assumption of relevant features.²²

As a result, there has been a recent paradigm shift toward end-to-end machine learning using CNNs, which are rapidly outperforming conventional benchmarks on various computer vision tasks.^{11,23} These models are capable of automatically identifying patterns in complex imaging datasets, thus combining both feature selection and classification into 1 algorithm and removing the need for direct human interaction during the training process. With deep-learning approaches, classification error rates of popular computer vision benchmarks have been significantly lower and now outperform humans on the same task.^{24–26}

Recent use of CNNs has started to yield promising results in multiple medical imaging disciplines, including the detection of pulmonary nodules,²⁷ colon cancer,²⁸ and cerebral microbleeds.²⁹ For example, Lakhani and Sundaram³⁰ applied a CNN approach to automatically identify patients with pulmonary tuberculosis with an area under the curve of 0.99, allowing radiologists to achieve a 97% sensitivity and 100% specificity. This outcome is in comparison with an area under the curve of up to 0.84 using classic machine-learning approaches such as texture and shape analysis.³¹ Additionally, Chang et al³² developed a CNN approach to automatically identify and count tumor cells from localized biopsy samples of patients with glioblastomas with an accuracy of 96.2%. Zhang et al³³ observed that a CNN approach performed significantly better than other techniques for brain segmentation in infants, including random forest, support vector machine, coupled level sets, and most voting.

Given the potential advantages of deep learning, a few studies have also started to explore the use of CNN-based approaches in the determination of glioma mutation status from MR imaging. Recently, Chang et al³⁴ used a 34-layer residual neural network to predict *IDH* status with up to 89% accuracy using MR imaging in combination with patient age. Compared with the current study, the network used by Chang et al has several million parameters (>1 order magnitude larger than the customized network used in this study), in part limiting overall accuracy through compensatory measures needed to prevent overfitting. Furthermore, only several prototypical slices of the tumor were used (compared with the entire volume in this study), which were then combined in all 3 orthogonal planes (requiring high-resolution isotropic imaging). Korfiatis et al³⁵ also recently described a 50-layer residual network architecture to predict *MGMT* status. However, the reported classification accuracy of 94.9% comprising 2027 of 2612 images (78%) used for testing contained no tumor at all. Furthermore, the 155 patients used in that study were derived completely from just a single academic center. Finally, in comparison with these prior works, the current study is the first to demonstrate the feasibility of a single neural network architecture to simultaneously predict the status of multiple different mutations (*IDH1* status, 1p/19q codeletion, *MGMT* promoter methylation) with minimal preprocessing in an efficient, fully automated approach.

Despite high accuracy, a commonly cited limitation of CNNs is the apparent difficulty in understanding the underlying black box analytic engine of a network. Several recent studies, however,

have proposed novel techniques such as deconvolutional neural networks and occlusion saliency maps to develop a deeper mechanistic understanding of the classification process.³⁶ In this study, we introduced a new technique to visualize the imaging features most relevant to the classification of genetic mutation status using principal component analysis as a means of dimensionality reduction and disentanglement of the final feature vector layer. This approach is useful in medical imaging domains in which the differentiating characteristics of the various disease classes may not be well-established, helping to identify clusters of imaging findings that can be used to guide practicing physicians (Figs 1–4).

In general, the clusters of imaging features identified by the neural network in this study represent a composite of various qualitative descriptions found elsewhere in the literature. For example, MR imaging features predictive of *IDH1* mutant status included absent or minimal areas of enhancement, central areas of cystlike necrosis with low T1 and FLAIR suppression, and well-defined tumor margins. This result is in line with existing literature, in which *IDH1* mutants have been reported to demonstrate absent or minimal enhancement^{37–39} and well-defined tumor margins.^{38,40} By contrast, we observed that *IDH1* wild-type tumors demonstrated thick and irregular enhancement with an infiltrative pattern of edema.

For 1p/19q codeletion, the most predictive features were frontal lobe location, ill-defined tumor margins, and increased enhancement. This finding is also in line with existing literature, which has demonstrated that tumors with 1p/19q codeletion are more likely to be found in the frontal cortex.⁴¹ Additionally, Sonoda et al³⁹ demonstrated that codeleted tumors are more likely to show contrast enhancement. Finally, the margins of 1p/19q codeleted tumors have also been characterized as poorly circumscribed.⁴²

With regard to *MGMT* promoter methylation, the most predictive features were a mixed, nodular enhancement; the presence of an eccentric cyst or area of necrosis; more masslike edema with cortical involvement; and slight frontal and superficial temporal predominance. Existing literature has similarly observed that tumors with *MGMT* promoter methylation tend to have a frontal lobe location^{43,44} (often colocalization with the *IDH1* mutation in this region⁴³) and the presence of an eccentric necrotic cyst.^{20,45} By comparison, we observed that nonmethylated tumors tended to demonstrate rim enhancement with central areas of necrosis. This observation is also congruent with other literature that has used subjective visual assessment, in which nonmethylated tumors are observed to demonstrate either ring enhancement with central necrosis,^{20,46} solid enhancement,²¹ and ill-defined margins.⁴⁵

When one interprets the results of our study, several limitations should be kept in mind. First, this is a relatively small sample size ($n = 259$) compared with the neural network studies within the nonmedical domains, which typically include tens of thousands. To address this limitation, we designed a tailor-made neural network architecture with a relatively small number of parameters/layers and high normalization. Additionally, all imaging input was resampled to a relatively small size ($32 \times 32 \times 4$) to prevent overfitting. Therefore, input for prediction is limited to 4096 voxels on any given slice of tumor as opposed to the potential tens of thousands of voxels. Second, this study is a retrospective

study of The Cancer Imaging Archives dataset, a heterogeneous dataset from multiple different contributing sites. However, the success of our network on this dataset suggests that the underlying CNN approach in this study is capable of handling nonuniform imaging protocols. Last, this study is limited by lack of an independent dataset. While the cross-fold validation technique used in this study ensures that the model generalizes well to held-out cohorts from The Cancer Imaging Archives dataset, generalization to unseen datasets remains to be determined. Future studies will need to expand the training set to include a variety of cancer sites and MR imaging scanners.

CONCLUSIONS

The results of our study show the feasibility of a deep-learning CNN approach for the accurate classification of individual genetic mutations of both low- and high-grade gliomas. Furthermore, we demonstrate that the relevant MR imaging features acquired from an added dimensionality-reduction technique are concordant with existing literature, showing that neural networks are capable of learning key imaging components without prior feature selection or human directed training.

Disclosures: Peter Chang—RELATED: Grant: National Institutes of Health (National Institute of Biomedical Imaging and Bioengineering) T32 Training Grant, T32EB001631*. Christopher G. Filippi—UNRELATED: Consultancy: KOL Philips Healthcare, Comments: part of a Key Opinion Leaders consortium in which I have advocated for CNNs in advanced imaging including neoplasms; Payment for Lectures Including Service on Speakers Bureaus: Visiting Professor, Comments: In a talk on advanced imaging of tumor, some of the preliminary work was included. Pierre Baldi—RELATED: Grant: National Institutes of Health*; UNRELATED: Royalties: MIT Press, Cambridge University Press, Wiley. Daniel Chow—RELATED: Grant: funding support from Canon Medical Systems USA. *Money paid to the institution.

REFERENCES

1. Cohen AL, Holmen SL, Colman H. **IDH1 and IDH2 mutations in gliomas.** *Curr Neurol Neurosci Rep* 2013;13:345 CrossRef Medline
2. Nobusawa S, Watanabe T, Kleihues P, et al. **IDH1 mutations as molecular signature and predictive factor of secondary glioblastomas.** *Clin Cancer Res* 2009;15:6002–07 CrossRef Medline
3. Yan H, Parsons DW, Jin G, et al. **IDH1 and IDH2 mutations in gliomas.** *N Engl J Med* 2009;360:765–73 CrossRef Medline
4. van den Bent MJ, Brandes AA, Taphoorn MJ, et al. **Adjuvant procarbazine, lomustine, and vincristine chemotherapy in newly diagnosed anaplastic oligodendroglioma: long-term follow-up of EORTC brain tumor group study 26951.** *J Clin Oncol* 2013;31:344–50 CrossRef Medline
5. Cairncross G, Wang M, Shaw E, et al. **Phase III trial of chemoradiotherapy for anaplastic oligodendroglioma: long-term results of RTOG 9402.** *J Clin Oncol* 2013;31:337–43 CrossRef Medline
6. Hegi ME, Diserens AC, Gorlia T, et al. **MGMT gene silencing and benefit from temozolomide in glioblastoma.** *N Engl J Med* 2005;352:997–1003 CrossRef Medline
7. Louis DN, Perry A, Reifenberger G, et al. **The 2016 World Health Organization Classification of Tumors of the Central Nervous System: a summary.** *Acta Neuropathol* 2016;131:803–20 CrossRef Medline
8. Gill BJ, Pisapia DJ, Malone HR, et al. **MRI-localized biopsies reveal subtype-specific differences in molecular and cellular composition at the margins of glioblastoma.** *Proc Natl Acad Sci U S A* 2014;111:12550–55 CrossRef Medline
9. Belden CJ, Valdes PA, Ran C, et al. **Genetics of glioblastoma: a window into its imaging and histopathologic variability.** *Radiographics* 2011;31:1717–40 CrossRef Medline

10. National Cancer Institute. Wiki for the VASARI feature set. <https://wiki.nci.nih.gov/display/CIP/VASARI>. Accessed August 30, 2017
11. LeCun Y, Bengio Y, Hinton G. **Deep learning.** *Nature* 2015;521:436–44 CrossRef Medline
12. Clark K, Vendt B, Smith K, et al. **The Cancer Imaging Archive (TCIA): maintaining and operating a public information repository.** *J Digit Imaging* 2013;26:1045–57 CrossRef Medline
13. Ceccarelli M, Barthel FP, Malta TM, et al. **Molecular profiling reveals biologically discrete subsets and pathways of progression in diffuse glioma.** *Cell* 2016;164:550–63 CrossRef Medline
14. Jenkinson M, Smith S. **A global optimisation method for robust affine registration of brain images.** *Med Image Anal* 2001;5:143–56 CrossRef Medline
15. Jenkinson M, Bannister P, Brady M, et al. **Improved optimization for the robust and accurate linear registration and motion correction of brain images.** *Neuroimage* 2002;17:825–41 CrossRef Medline
16. Chang PD. **Fully convolutional deep residual neural networks for brain tumor segmentation.** In: Crimi A, Menze B, Maier O, et al, eds. *Brainlesion: Glioma, Multiple Sclerosis, Stroke and Traumatic Brain Injuries: Second International Workshop, BrainLes 2016, with the Challenges on BRATS, ISLES and mTOP 2016, Held in Conjunction with MICCAI 2016*, Athens, Greece, October 17, 2016, Revised Selected Papers. Cham: Springer-Verlag International Publishing; 2016:108–18
17. LeCun Y, Bengio Y. **Convolutional networks for images, speech, and time-series.** In: Arbib MA, ed. *The Handbook of Brain Theory and Neural Networks*. Cambridge: MIT Press; 1998:255–58
18. Gorlia T, van den Bent MJ, Hegi ME, et al. **Nomograms for predicting survival of patients with newly diagnosed glioblastoma: prognostic factor analysis of EORTC and NCIC trial 26981–22981/CE.3.** *Lancet Oncol* 2008;9:29–38 CrossRef Medline
19. Ryu YJ, Choi SH, Park SJ, et al. **Glioma: application of whole-tumor texture analysis of diffusion-weighted imaging for the evaluation of tumor heterogeneity.** *PLoS One* 2014;9:e108335 CrossRef Medline
20. Drabycz S, Roldán G, de Robles P, et al. **An analysis of image texture, tumor location, and MGMT promoter methylation in glioblastoma using magnetic resonance imaging.** *Neuroimage* 2010;49:1398–405 CrossRef Medline
21. Kanas VG, Zacharaki EI, Thomas GA, et al. **Learning MRI-based classification models for MGMT methylation status prediction in glioblastoma.** *Comput Methods Programs Biomed* 2017;140:249–57 CrossRef Medline
22. Kassner A, Thornhill RE. **Texture analysis: a review of neurologic MR imaging applications.** *AJNR Am J Neuroradiol* 2010;31:809–16 CrossRef Medline
23. Simonyan K, Vedaldi A, Zisserman A. **Deep inside convolutional networks: visualising image classification models and saliency maps.** *CoRR* 2013;abs/1312.6034. <https://arxiv.org/abs/1312.6034>. Accessed August 30, 2017
24. He K, Zhang X, Ren S, et al. **Delving deep into rectifiers: surpassing human-level performance on ImageNet classification.** In: *Proceedings of the IEEE International Conference on Computer Vision*, Santiago, Chile. December 7–13, 2015:1026–34
25. He K, Zhang X, Ren S, et al. **Deep residual learning for image recognition.** *CoRR* 2015;abs/1512.03385. <https://arxiv.org/abs/1512.03385>. Accessed August 30, 2017
26. Krizhevsky A, Sutskever I, Hinton G. **ImageNet classification with deep convolutional neural networks.** <https://www.nvidia.cn/content/tesla/pdf/machine-learning/imagenet-classification-with-deep-convolutional-nn.pdf>. Accessed August 30, 2017
27. Setio AA, Ciompi F, Litjens G, et al. **Pulmonary nodule detection in CT images: false positive reduction using multi-view convolutional networks.** *IEEE Trans Med Imaging* 2016;35:1160–69 CrossRef Medline
28. Roth HR, Lu L, Liu J, et al. **Improving computer-aided detection using convolutional neural networks and random view aggregation.** *IEEE Trans Med Imaging* 2016;35:1170–81 CrossRef Medline
29. He K, Zhang X, Ren S, et al. **Deep residual learning for image recognition.** In: *Proceedings of the IEEE Conference on Computer Vision and Pattern Recognition*, Las Vegas, Nevada. June 27–30, 2016
30. Lakhani P, Sundaram B. **Deep learning at chest radiography: automated classification of pulmonary tuberculosis by using convolutional neural networks.** *Radiology* 2017;284:574–82 CrossRef Medline
31. Pande T, Cohen C, Pai M, et al. **Computer-aided detection of pulmonary tuberculosis on digital chest radiographs: a systematic review.** *Int J Tuberc Lung Dis* 2016;20:1226–30 CrossRef Medline
32. Chang PD, Malone HR, Bowden SG, et al. **A multiparametric model for mapping cellularity in glioblastoma using radiographically localized biopsies.** *AJNR Am J Neuroradiol* 2017;38:890–98 CrossRef Medline
33. Zhang W, Li R, Deng H, et al. **Deep convolutional neural networks for multi-modality iso-intense infant brain image segmentation.** *Neuroimage* 2015;108:214–24 CrossRef Medline
34. Chang K, Bai HX, Zhou H, et al. **Residual convolutional neural network for the determination of IDH status in low- and high-grade gliomas from MR imaging.** *Clin Cancer Res* 2018;24:1073–81 CrossRef Medline
35. Korfiatis P, Kline TL, Lachance DH, et al. **Residual deep convolutional neural network predicts MGMT methylation status.** *J Digit Imaging* 2017;30:622–28 CrossRef Medline
36. Zeiler MD, Fergus R. **Visualizing and understanding convolutional networks.** In: Fleet D, Pajdla T, Schiele B, et al, eds. *Proceedings of the European Conference on Computer Vision*, Zurich, Switzerland. September 6–12, 2014
37. Carrillo JA, Lai A, Nghiemphu PL, et al. **Relationship between tumor enhancement, edema, IDH1 mutational status, MGMT promoter methylation, and survival in glioblastoma.** *AJNR Am J Neuroradiol* 2012;33:1349–55 CrossRef Medline
38. Qi S, Yu L, Li H, et al. **Isocitrate dehydrogenase mutation is associated with tumor location and magnetic resonance imaging characteristics in astrocytic neoplasms.** *Oncol Lett* 2014;7:1895–902 CrossRef Medline
39. Sonoda Y, Shibahara I, Kawaguchi T, et al. **Association between molecular alterations and tumor location and MRI characteristics in anaplastic gliomas.** *Brain Tumor Pathol* 2015;32:99–104 CrossRef Medline
40. Metellus P, Coulibaly B, Colin C, et al. **Absence of IDH mutation identifies a novel radiologic and molecular subtype of WHO grade II gliomas with dismal prognosis.** *Acta Neuropathol* 2010;120:719–29 CrossRef Medline
41. Xiong J, Tan W, Wen J, et al. **Combination of diffusion tensor imaging and conventional MRI correlates with isocitrate dehydrogenase 1/2 mutations but not 1p/19q genotyping in oligodendroglial tumours.** *Eur Radiol* 2016;26:1705–15 CrossRef Medline
42. Johnson DR, Diehn FE, Giannini C, et al. **Genetically defined oligodendroglioma is characterized by indistinct tumor borders at MRI.** *AJNR Am J Neuroradiol* 2017;38:678–84 CrossRef Medline
43. Ellingson BM, Lai A, Harris RJ, et al. **Probabilistic radiographic atlas of glioblastoma phenotypes.** *AJNR Am J Neuroradiol* 2013;34:533–40 CrossRef Medline
44. Paldor I, Pearce FC, Drummond KJ, et al. **Frontal glioblastoma multiforme may be biologically distinct from non-frontal and multilobar tumors.** *J Clin Neurosci* 2016;34:128–32 CrossRef Medline
45. Moon WJ, Choi JW, Roh HG, et al. **Imaging parameters of high grade gliomas in relation to the MGMT promoter methylation status: the CT, diffusion tensor imaging, and perfusion MR imaging.** *Neuroradiology* 2012;54:555–63 CrossRef Medline
46. Eoli M, Menghi F, Bruzzone MG, et al. **Methylation of O6-methylguanine DNA methyltransferase and loss of heterozygosity on 19q and/or 17p are overlapping features of secondary glioblastomas with prolonged survival.** *Clin Cancer Res* 2007;13:2606–13 CrossRef Medline

Diffusion-Weighted Imaging and Diffusion Tensor Imaging for Differentiating High-Grade Glioma from Solitary Brain Metastasis: A Systematic Review and Meta-Analysis

C.H. Suh, H.S. Kim, S.C. Jung, and S.J. Kim



ABSTRACT

BACKGROUND: Accurate diagnosis of high-grade glioma and solitary brain metastasis is clinically important because it affects the patient's outcome and alters patient management.

PURPOSE: To evaluate the diagnostic performance of DWI and DTI for differentiating high-grade glioma from solitary brain metastasis.

DATA SOURCES: A literature search of Ovid MEDLINE and EMBASE was conducted up to November 10, 2017.

STUDY SELECTION: Studies evaluating the diagnostic performance of DWI and DTI for differentiating high-grade glioma from solitary brain metastasis were selected.

DATA ANALYSIS: Summary sensitivity and specificity were established by hierarchic logistic regression modeling. Multiple subgroup analyses were also performed.

DATA SYNTHESIS: Fourteen studies with 1143 patients were included. The individual sensitivities and specificities of the 14 included studies showed a wide variation, ranging from 46.2% to 96.0% for sensitivity and 40.0% to 100.0% for specificity. The pooled sensitivity of both DWI and DTI was 79.8% (95% CI, 70.9%–86.4%), and the pooled specificity was 80.9% (95% CI, 75.1%–85.5%). The area under the hierarchical summary receiver operating characteristic curve was 0.87 (95% CI, 0.84–0.89). The multiple subgroup analyses also demonstrated similar diagnostic performances (sensitivities of 76.8%–84.7% and specificities of 79.7%–84.0%). There was some level of heterogeneity across the included studies ($I^2 = 36\%$); however, it did not reach a level of concern.

LIMITATIONS: The included studies used various DWI and DTI parameters.

CONCLUSIONS: DWI and DTI demonstrated a moderate diagnostic performance for differentiation of high-grade glioma from solitary brain metastasis.

ABBREVIATIONS: FA = fractional anisotropy; HSROC = hierarchic summary receiver operating characteristic; MD = mean diffusivity; PRISMA = Preferred Reporting Items for Systematic Reviews and Meta-Analyses; QUADAS-2 = Quality Assessment of Diagnostic Accuracy Studies-2

The accurate diagnosis of high-grade glioma and solitary brain metastasis is clinically important because it affects the patient's outcome and alters patient management.^{1,2} Because

high-grade glioma and solitary brain metastasis have similar findings on conventional MR imaging, the clinical context or patient history could be helpful. In addition, advanced MR imaging techniques have been introduced to assist in their differentiation.

Multiple studies report on the use of DWI and DTI for differentiating high-grade glioma from solitary brain metastasis.^{3–16} High-grade glioma typically shows an infiltrative growth pattern with invasion of the surrounding brain tissues, whereas brain metastasis shows an expansive growth pattern causing displacement of the surrounding brain tissue.^{17,18} In addition, high-grade glioma cells tend to produce large amounts of extracellular matrix, which play an important role in tumor growth and infiltration.^{19,20} Therefore, assessment of the enhancing tumor and perienhancing area with DWI and DTI parameters has been intro-

Received December 15, 2017; accepted after revision March 7, 2018.

From the Department of Radiology and Research Institute of Radiology, University of Ulsan College of Medicine, Asan Medical Center, Seoul, Republic of Korea.

This study was supported by a grant from the National R&D Program for Cancer Control, Ministry of Health and Welfare, Republic of Korea (1720030).

Please address correspondence to Ho Sung Kim, MD, PhD, Department of Radiology and Research Institute of Radiology, University of Ulsan College of Medicine, Asan Medical Center, 86 Asanbyeongwon-Gil, Songpa-Gu, Seoul 138-736, Republic of Korea; e-mail: radhskim@gmail.com

Indicates open access to non-subscribers at www.ajnr.org

Indicates article with supplemental on-line tables.

Indicates article with supplemental on-line photos.

<http://dx.doi.org/10.3174/ajnr.A5650>

duced. However, the results have been quite varied, and the utility of these techniques is still an issue under debate.^{7,9,12} Some studies have reported a high diagnostic performance for DWI or DTI; however, other studies have reported a low diagnostic performance or no added value of DWI or DTI compared with conventional MR imaging.

Therefore, we considered it appropriate to assess the diagnostic performance of DWI and DTI for differentiating high-grade glioma from solitary brain metastasis using the currently available published resources. We thus performed a systematic review and meta-analysis evaluating the diagnostic performance of DWI and DTI for differentiating high-grade glioma from solitary brain metastasis.

MATERIALS AND METHODS

The current systematic review and meta-analysis are reported according to the Preferred Reporting Items for Systematic Reviews and Meta-Analyses (PRISMA) guidelines.²¹ The following research question was established²¹: What are the diagnostic performances of DWI and DTI for differentiating high-grade glioma from solitary brain metastasis?

Literature Search

A literature search of Ovid MEDLINE and EMBASE was conducted to find relevant original articles up to November 10, 2017. The search query combined equivalents for “glioma,” “brain metastasis,” “DWI,” and “DTI” as follows: ((brain metastasis) OR (brain metastases) OR (metastatic brain tumor*) OR (intraaxial metastatic tumor*) OR (cerebral metastasis) OR (cerebral metastases) OR (solitary metasta*)) AND ((glioblastoma) OR (glioma)) AND ((diffusion-weighted imaging) OR (diffusion-weighted imaging) OR (DWI) OR (“apparent diffusion coefficient”) OR (diffusion tensor imaging) OR (DTI)). The literature search was restricted to English language publications. Any additional relevant articles identified were also investigated.

Literature Selection

Inclusion Criteria. We used the following inclusion criteria: 1) population: patients with a solitary enhancing brain lesion; 2) index test: DWI and DTI scans available; 3) reference standard: histopathologic diagnosis; 4) outcomes: differentiation of high-grade glioma (glioblastoma and/or anaplastic astrocytoma) from solitary brain metastasis, with sufficient data provided to establish 2×2 tables for sensitivity and specificity; and 5) articles published as original articles.

Exclusion Criteria. We applied the following exclusion criteria: 1) case reports/series (a sample size of <10 patients), conference abstracts, reviews, and notes; 2) studies including patients with low-grade gliomas; 3) studies including patients with recurrent brain metastasis; 4) insufficient information for reconstruction of 2×2 tables; and 5) a partially overlapping patient population. In the case of an overlapping study population, the study with the largest study population was selected. When 2×2 tables could not be established, authors of the eligible studies were contacted for further data.

Data Extraction and Quality Assessment

The following data were extracted from the included studies: 1) study characteristics: authors, year of publication, institution, duration of patient recruitment, study design (prospective versus retrospective), study enrollment (consecutive versus nonconsecutive), and reference standard; 2) patient characteristics: number of patients, number of patients with high-grade glioma, mean age, age range, and male/female ratio; 3) MR imaging characteristics: magnet field strength, scanner vendor, scanner model, channels of head coil, and MR imaging techniques including DWI, DTI, b-value ($s\text{ mm}^{-2}$), ROI placement, parameters, and cutoff values; and 4) MR imaging interpretation: number of readers, experience of readers, and blinding of readers to the reference standard.

The study quality was assessed using the Quality Assessment of Diagnostic Accuracy Studies-2 (QUADAS-2) tool.²² The literature search, literature selection, data extraction, and quality assessment were performed independently by 2 reviewers (C.H.S. and H.S.K.).

Data Synthesis and Statistical Analysis

The primary aim of this study was to determine the diagnostic performance of DWI and DTI for differentiating high-grade glioma from solitary brain metastasis. We obtained 2×2 tables from the studies to identify their individual sensitivities and specificities. Summary sensitivity and specificity were established by hierarchic logistic regression modeling (bivariate random-effects model and hierarchic summary receiver operating characteristic [HSROC] model).²³⁻²⁵ An HSROC curve with 95% confidence and prediction regions was obtained, and the area under the HSROC curve was also calculated. Publication bias was investigated using the Deeks asymmetry test.²⁶

Heterogeneity across the studies was evaluated as follows: 1) Cochran Q test ($P < .05$ indicating the presence of heterogeneity); 2) Higgins inconsistency index (I^2 test)²⁷ ($I^2 = 0\%–40\%$, heterogeneity might not be important; $30\%–60\%$, moderate heterogeneity may be present; $50\%–90\%$, substantial heterogeneity may be present; and $75\%–100\%$, considerable heterogeneity); 3) visual assessment of a coupled forest plot or a Spearman correlation coefficient (>0.6 indicating a threshold effect) to assess a threshold effect (positive correlation between sensitivity and the false-positive rate)²⁸; and 4) visual assessment of the difference in the 95% confidence and prediction regions in the HSROC.

Multiple subgroup analyses were performed as follows: 1) studies using DWI, 2) studies using DTI, 3) studies including glioblastoma only, 4) studies including both glioblastoma and anaplastic astrocytoma, 5) studies using enhancing tumor for ROI placement, 6) studies using perienhancing area for ROI placement, 7) studies using fractional anisotropy (FA), 8) studies using mean diffusivity (MD), and 9) studies using perienhancing ADC or MD. Statistical analyses for the meta-analysis were performed by one of the reviewers (C.H.S., with 4 years of experience in performing systematic reviews and meta-analyses), using the metandi and midas modules in STATA 15.0 (StataCorp, College Station, Texas) and the mada package in R statistical and computing software, Version 3.4.1 (<http://www.r-project.org/>). $P < .05$ indicated statistical significance.

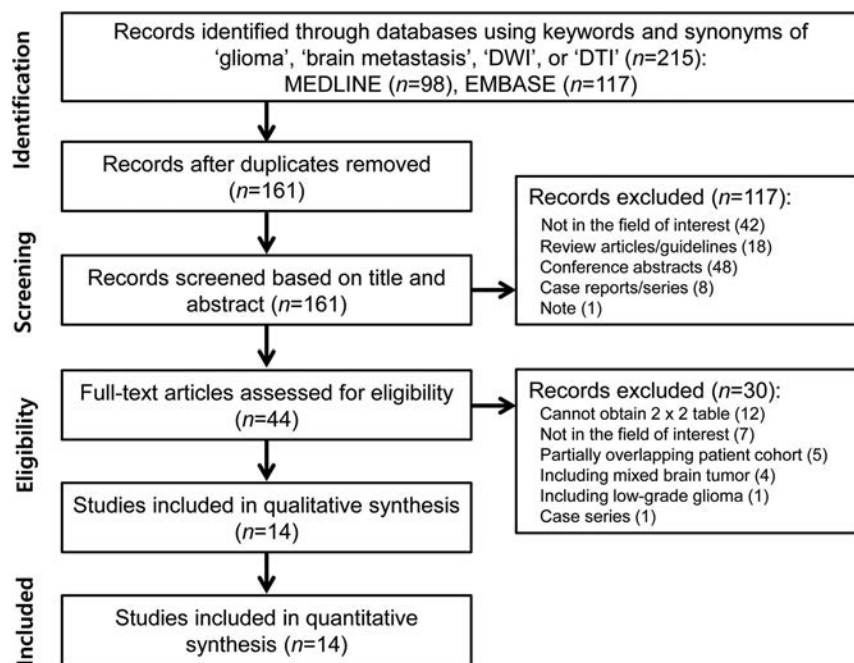


FIG 1. Flow diagram illustrating the study-selection process for the systematic review and meta-analysis.

RESULTS

Literature Search

The detailed literature-selection process is illustrated in Fig 1. The literature search identified 215 articles. After we removed 54 duplicate articles, screening of the titles and abstracts of the remaining 161 articles yielded 44 potentially eligible articles. Full-text reviews were performed, and 30 studies were excluded because of the following: 1) twelve studies because the 2×2 table could not be obtained²⁹⁻⁴⁰; 2) seven studies not in the field of interest⁴¹⁻⁴⁷; 3) five studies with a partially overlapping patient cohort⁴⁸⁻⁵²; 4) four studies with mixed brain tumors⁵³⁻⁵⁶; 5) one study with a low-grade glioma⁵⁷; and 6) one case series.⁵⁸ Fourteen studies evaluating the diagnostic performance of DWI and DTI for differentiating high-grade glioma from solitary brain metastasis,³⁻¹⁶ covering 1143 patients, were included in the analyses.

Characteristics of the Included Studies

The detailed study and patient characteristics are shown in On-line Table 1. Nine studies enrolled patients with glioblastoma only,^{3-7,10-12,15} while 5 studies enrolled patients with high-grade gliomas.^{8,9,13,14,16} Twelve studies used histopathology as the reference standard,^{3-5,7-13,15,16} and 1 study used histopathology and clinical diagnosis only for brain metastasis.¹⁴

The detailed MR imaging characteristics are described in On-line Table 2. DWI was used in 7 studies^{6,8,10-13,16}; and DTI, in 7 studies.^{3-5,7,9,14,15} A quantitative ADC value was used in 7 studies using DWI,^{6,8,10-13,16} Five of the 7 DTI studies used both FA and MD,^{3,5,9,14,15} whereas 2 studies used FA only.^{4,7} In terms of ROI placement, both enhancing tumor and perienhancing area were selected in 12 studies^{3,5-11,13-16}; enhancing tumor only, in 1 study⁴; and perienhancing area only, in 1 study.¹²

Quality Assessment

The results of the quality assessment are illustrated in On-line Fig 1. In the patient-selection domain, 10 studies revealed an unclear risk of bias because of nonconsecutive enrollment.^{3,5-7,9,11-15} In the index test domain, 6 studies revealed an unclear risk of bias because it was unclear whether imaging analysis had been conducted blinded to the reference standard.^{3,5,7,9,15,16} In the reference standard domain, 2 studies revealed a high risk of bias, with 1 study not mentioning the reference standard⁶ and 1 study using both histopathology and clinical diagnosis.¹⁴ In the flow and timing domain, 13 studies revealed an unclear risk of bias because the time intervals between MR imaging and the reference standard were not mentioned.^{3,4,6-16} However, there were no concerns regarding the applicability of all 3 domains.

Diagnostic Accuracy

The individual sensitivities and specificities of the 14 included studies showed a wide variation, ranging from 46.2% to 96.0% for sensitivity and 40.0% to 100.0% for specificity. The pooled sensitivity was 79.8% (95% CI, 70.9%–86.4%), and the pooled specificity was 80.9% (95% CI, 75.1%–85.5%) (Fig 2 and On-line Table 3). The area under the HSROC curve was 0.87 (95% CI, 0.84–0.89; On-line Fig 2). The Deeks funnel plot demonstrated that no publication bias was present ($P = .98$; On-line Fig 3).

In the investigation of heterogeneity, a Cochran Q test showed that heterogeneity was not present ($Q = 3.117$, $df = 2$, $P = .104$), and there was some level of heterogeneity across the included studies ($I^2 = 36\%$); however, it did not reach a level of concern. Visual assessment of the coupled forest plots revealed no threshold effect (Fig 2), and the Spearman correlation coefficient was 0.188 (95% CI, -0.653 – 0.381), also indicating no threshold effect. The HSROC curve illustrated a small difference between the 95% confidence prediction regions, indicating a low possibility of heterogeneity (On-line Fig 2).

Multiple Subgroup Analyses

On-line Table 4 shows the results of multiple subgroup analyses. In the subgroup analysis according to MR imaging technique, those studies using DWI showed a pooled sensitivity of 81.4% (95% CI, 70.6%–88.9%) and a pooled specificity of 81.8% (95% CI, 69.5%–89.9%).^{6,8,10-13,16} Studies using DTI showed a pooled sensitivity of 77.0% (95% CI, 62.3%–87.1%) and a pooled specificity of 80.3% (95% CI, 73.5%–85.7%).^{3-5,7,9,14,15} There was no statistical difference between DWI and DTI ($P = .59$). In the subgroup analysis according to study population, the studies including glioblastoma showed only a pooled sensitivity of 82.2% (95% CI, 71.9%–89.3%) and a pooled specificity of 81.4% (95% CI,

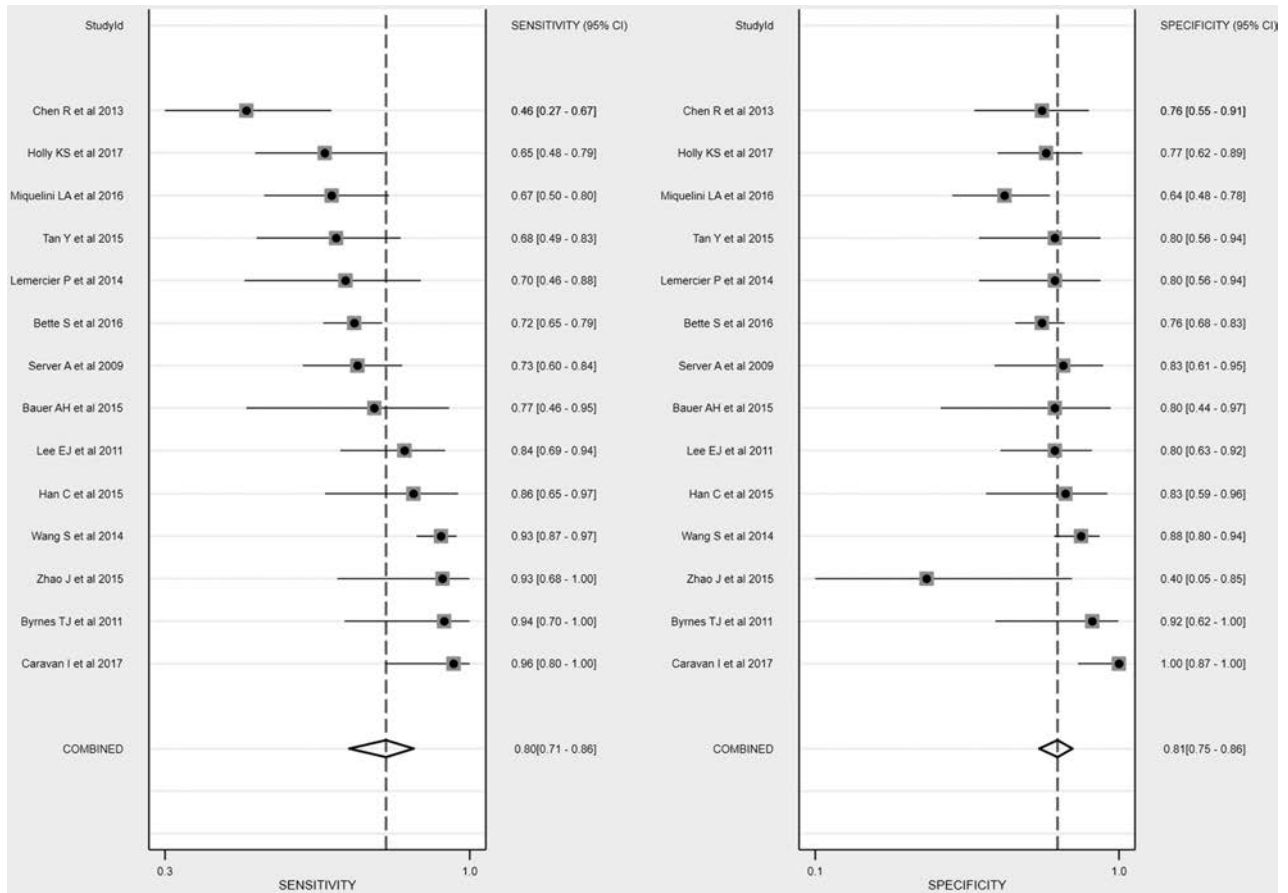


FIG 2. Coupled forest plots of pooled sensitivity and specificity. Numbers are pooled estimates with 95% confidence intervals in parentheses.

74.8%–86.6%).^{3,5,13–16} Studies including both glioblastoma and anaplastic astrocytoma showed a pooled sensitivity of 76.8% (95% CI, 61.45%–87.4%) and a pooled specificity of 81.2% (95% CI, 69.9%–88.9%).^{6–12}

In the subgroup analysis according to the ROI placement, studies using enhancing tumor showed a pooled sensitivity of 72.6% (95% CI, 63.4%–80.3%) and a pooled specificity of 77.0% (95% CI, 71.7%–81.6%).^{3,4,7,11,13,15} Studies using a perienhancing area showed a pooled sensitivity of 80.1% (95% CI, 69.1%–87.9%) and a pooled specificity of 81.0% (95% CI, 70.6%–88.3%).^{3,6,8–10,12,14,16} In the subgroup analysis according to DTI parameters, studies using FA showed a pooled sensitivity of 70.8% (95% CI, 61.0%–79.0%) and a pooled specificity of 74.5% (95% CI, 69.0%–79.3%).^{3,4,7,9,14,15} MD showed a pooled sensitivity of 84.5% (95% CI, 71.7%–92.1%) and a pooled specificity of 81.3% (95% CI, 72.0%–88.1%).^{3,9,14,15} Studies using perienhancing ADC or MD showed a pooled sensitivity of 84.7% (95% CI, 73.6%–91.6%) and a pooled specificity of 84.0% (95% CI, 71.8%–91.6%).^{3,6,8,10,14,16}

DISCUSSION

We identified 14 studies providing the diagnostic performance of DWI and DTI for differentiating high-grade glioma from solitary brain metastasis. DWI and DTI showed not only a wide range of individual sensitivities and specificities but also only a moderate diagnostic performance (ie, a pooled sensitivity of 79.8% [95% CI, 70.9%–86.4%] and a pooled specificity of 80.9% [95% CI,

75.1%–85.5%]). Multiple subgroup analyses also demonstrated similar diagnostic performances (sensitivities of 76.8%–84.7% and specificities of 79.7%–84.0%). DWI and DTI are rarely used as a single sequence, whereas DWI and DTI are usually part of a multiparametric MR imaging protocol for differentiating high-grade glioma from solitary brain metastasis. Therefore, DWI and DTI could actually be helpful in the context of multiparametric MR imaging.

High-grade glioma typically shows an infiltrative growth pattern with invasion of the surrounding brain tissues. However, brain metastasis shows an expansive growth pattern and displaces the surrounding brain tissue.¹⁰ Therefore, many researchers have used various advanced MR imaging techniques in attempts to differentiate the infiltrative edema of glioma from metastatic vasogenic edema. DWI and DTI have been used for testing the perienhancing area of solitary enhancing brain lesions; however, the results are conflicting. Two studies reported that the mean minimum perienhancing ADC values in high-grade glioma were significantly higher than those in brain metastases,^{6,8} whereas 1 study reported lower mean minimum perienhancing ADC values in high-grade glioma.¹⁰ Two studies also reported that perienhancing MD was significantly lower in high-grade glioma than in brain metastasis.^{3,14}

The current meta-analysis revealed a moderate diagnostic performance in 6 studies that used perienhancing ADC or MD as a parameter to determine optimal cutoff values, with a pooled sen-

sitivity of 84.7% (95% CI, 73.6%–91.6%) and a pooled specificity of 84.0% (95% CI, 71.8%–91.6%).^{3,6,8,10,14,16} Assessment of the perienhancing area with DWI or DTI presents several limitations or challenges. First, primary (de novo) glioblastoma shows minimal microscopic tumor infiltration in the perienhancing area. Therefore, a differentiation from brain metastasis could be challenging. Second, secondary glioblastoma, anaplastic astrocytoma, and oligodendroglioma generally show definite microscopic tumor infiltration in the perienhancing area, even on conventional MR imaging sequences such as FLAIR. Therefore, the added value of advanced MR imaging is controversial. Third, when it comes to extensive peritumoral edema, microscopic tumor infiltration in the perienhancing area could be overestimated on advanced MR imaging.

Glioma cells tend to produce large amounts of extracellular matrix components.^{19,20} This extracellular matrix serves as a substrate for adhesion and subsequent migration of the tumor cells along the enlarged extracellular space.¹⁹ These molecules are concentrated and are oriented in the extracellular matrix, which results in high FA.^{15,59} In the current meta-analysis, 3 studies demonstrated that high-grade glioma showed higher FA values in enhancing tumor than brain metastases; in 2 of these studies, the difference was statistically significant,^{4,15} though the difference did not reach statistical significance in the other one.³ However, 2 further studies did not show any meaningful differences between the 2 groups.^{9,14} A recent systematic review also revealed no significant changes in the FA of enhancing tumor between high-grade glioma and brain metastasis.⁶⁰ The underlying mechanism for this discrepancy is not fully understood, and further studies are required.

Although all the studies using DWI used ADC, the exact parameters varied and included minimum ADC, ADC ratio, gradient of ADC, or a combination of these. Despite the use of these various parameters, DWI is available in most institutions with MR imaging facilities, and the benefit is fast acquisition and easy image processing.¹¹ A variety of parameters were also used for DTI, including perienhancing MD and FA of the enhancing tumor. DTI had several drawbacks, including low spatial resolution and image distortion.⁶¹ Therefore, considerable effort is required to achieve standardization, and further studies are needed.

This study has several limitations. First, only 21.4% (3 of 14) of the included studies were prospective.^{5,13,16} However, the included studies are the only currently available ones. Second, we combined the MR imaging techniques used for diagnostic performance (ie, DWI and DTI). Third, the included studies used various parameters. However, we demonstrated the absence of heterogeneity across the included studies. In addition, we also performed multiple subgroup analyses. Furthermore, we conducted this study using robust methodology (hierarchical logistic regression modeling²³) and have reported the results in accordance with several guidelines (PRISMA,²¹ the Handbook for Diagnostic Test Accuracy Reviews published by the Cochrane Collaboration,⁶² and the Agency for Healthcare Research and Quality⁶³). Nevertheless, caution is required in applying our results to daily clinical practice.

CONCLUSIONS

DWI and DTI demonstrated a moderate diagnostic performance for differentiating high-grade glioma from solitary brain metastasis.

REFERENCES

- O'Neill BP, Buckner JC, Coffey RJ, et al. **Brain metastatic lesions.** *Mayo Clin Proc* 1994;69:1062–68 CrossRef Medline
- Giese A, Westphal M. **Treatment of malignant glioma: a problem beyond the margins of resection.** *J Cancer Res Clin Oncol* 2001;127:217–25 CrossRef Medline
- Bauer AH, Erly W, Moser FG, et al. **Differentiation of solitary brain metastasis from glioblastoma multiforme: a predictive multiparametric approach using combined MR diffusion and perfusion.** *Neuroradiology* 2015;57:697–703 CrossRef Medline
- Bette S, Huber T, Wiestler B, et al. **Analysis of fractional anisotropy facilitates differentiation of glioblastoma and brain metastases in a clinical setting.** *Eur J Radiol* 2016;85:2182–87 CrossRef Medline
- Byrnes TJ, Barrick TR, Bell BA, et al. **Diffusion tensor imaging discriminates between glioblastoma and cerebral metastases in vivo.** *NMR Biomed* 2011;24:54–60 CrossRef Medline
- Caravan I, Ciortea CA, Contis A, et al. **Diagnostic value of apparent diffusion coefficient in differentiating between high-grade gliomas and brain metastases.** *Acta Radiol* 2017;59:599–605 CrossRef Medline
- Chen R, Wang S, Poptani H, et al. **A Bayesian diagnostic system to differentiate glioblastomas from solitary brain metastases.** *Neuroradiol J* 2013;26:175–83 CrossRef Medline
- Han C, Huang S, Guo J, et al. **Use of a high b-value for diffusion weighted imaging of peritumoral regions to differentiate high-grade gliomas and solitary metastases.** *J Magn Reson Imaging* 2015;42:80–86 CrossRef Medline
- Holly KS, Barker BJ, Murcia D, et al. **High-grade gliomas exhibit higher peritumoral fractional anisotropy and lower mean diffusivity than intracranial metastases.** *Front Surg* 2017;4:18 CrossRef Medline
- Lee EJ, terBrugge K, Mikulis D, et al. **Diagnostic value of peritumoral minimum apparent diffusion coefficient for differentiation of glioblastoma multiforme from solitary metastatic lesions.** *AJR Am J Roentgenol* 2011;196:71–76 CrossRef Medline
- Lemercier P, Paz Maya S, Patrie JT, et al. **Gradient of apparent diffusion coefficient values in peritumoral edema helps in differentiation of glioblastoma from solitary metastatic lesions.** *AJR Am J Roentgenol* 2014;203:163–69 CrossRef Medline
- Miquelini LA, Pérez Akly MS, Funes JA, et al. **Usefulness of the apparent diffusion coefficient for the evaluation of the white matter to differentiate between glioblastoma and brain metastases.** *Radiologia* 2016;58:207–13 CrossRef Medline
- Server A, Kulle B, Maehlen J, et al. **Quantitative apparent diffusion coefficients in the characterization of brain tumors and associated peritumoral edema.** *Acta Radiol* 2009;50:682–89 CrossRef Medline
- Tan Y, Wang XC, Zhang H, et al. **Differentiation of high-grade astrocytomas from solitary-brain-metastases: comparing diffusion kurtosis imaging and diffusion tensor imaging.** *Eur J Radiol* 2015;84:2618–24 CrossRef Medline
- Wang S, Kim SJ, Poptani H, et al. **Diagnostic utility of diffusion tensor imaging in differentiating glioblastomas from brain metastases.** *AJNR Am J Neuroradiol* 2014;35:928–34 CrossRef Medline
- Zhao J, Yang ZY, Luo BN, et al. **Quantitative evaluation of diffusion and dynamic contrast-enhanced MR in tumor parenchyma and peritumoral area for distinction of brain tumors.** *PLoS One* 2015;10:e0138573 CrossRef Medline
- Watanabe M, Tanaka R, Takeda N. **Magnetic resonance imaging and histopathology of cerebral gliomas.** *Neuroradiology* 1992;34:463–69 CrossRef Medline
- Strugar J, Rothbart D, Harrington W, et al. **Vascular permeability factor in brain metastases: correlation with vasogenic brain edema**

- and tumor angiogenesis. *J Neurosurg* 1994;81:560–66 CrossRef Medline
19. Zamecnik J. The extracellular space and matrix of gliomas. *Acta Neuropathol* 2005;110:435–42 CrossRef Medline
 20. Vargová L, Homola A, Zámečník J, et al. Diffusion parameters of the extracellular space in human gliomas. *Glia* 2003;42:77–88 CrossRef Medline
 21. Liberati A, Altman DG, Tetzlaff J, et al. The PRISMA statement for reporting systematic reviews and meta-analyses of studies that evaluate health care interventions: explanation and elaboration. *Ann Intern Med* 2009;151:W65–94 Medline
 22. Whiting PF, Rutjes AW, Westwood ME, et al; QUADAS-2 Group. QUADAS-2: a revised tool for the quality assessment of diagnostic accuracy studies. *Ann Intern Med* 2011;155:529–36 CrossRef Medline
 23. Suh CH, Park SH. Successful publication of systematic review and meta-analysis of studies evaluating diagnostic test accuracy. *Korean J Radiol* 2016;17:5–6 CrossRef Medline
 24. Kim KW, Lee J, Choi SH, et al. Systematic review and meta-analysis of studies evaluating diagnostic test accuracy: a practical review for clinical researchers, Part I: general guidance and tips. *Korean J Radiol* 2015;16:1175–87 CrossRef Medline
 25. Lee J, Kim KW, Choi SH, et al. Systematic review and meta-analysis of studies evaluating diagnostic test accuracy: a practical review for clinical researchers, Part II: statistical methods of meta-analysis. *Korean J Radiol* 2015;16:1188–96 CrossRef Medline
 26. Deeks JJ, Macaskill P, Irwig L. The performance of tests of publication bias and other sample size effects in systematic reviews of diagnostic test accuracy was assessed. *J Clin Epidemiol* 2005;58:882–93 CrossRef Medline
 27. Higgins J, Green S, eds. *Cochrane Handbook for Systematic Reviews of Interventions*. Version 5.1.0 [updated March 2011]. The Cochrane Collaboration, 2011. Available from <http://handbook.cochrane.org>. Accessed October 2, 2017
 28. Devillé WL, Buntinx F, Bouter LM, et al. Conducting systematic reviews of diagnostic studies: didactic guidelines. *BMC Med Res Methodol* 2002;2:9 CrossRef Medline
 29. Calli C, Kitis O, Yuntun N, et al. Perfusion and diffusion MR imaging in enhancing malignant cerebral tumors. *Eur J Radiol* 2006;58:394–403 CrossRef Medline
 30. Chiang IC, Kuo YT, Lu CY, et al. Distinction between high-grade gliomas and solitary metastases using peritumoral 3-T magnetic resonance spectroscopy, diffusion, and perfusion imaging. *Neuroradiology* 2004;46:619–27 Medline
 31. Darwiesh AM, Maboud NM, Khalil AM, et al. Role of magnetic resonance spectroscopy & diffusion weighted imaging in differentiation of supratentorial brain tumors. *Egyptian Journal of Radiology and Nuclear Medicine* 2016;47:1037–42 CrossRef
 32. Guzman R, Altrichter S, El-Koussy M, et al. Contribution of the apparent diffusion coefficient in perilesional edema for the assessment of brain tumors. *J Neuroradiol* 2008;35:224–29 CrossRef Medline
 33. Kitis O, Altay H, Calli C, et al. Minimum apparent diffusion coefficients in the evaluation of brain tumors. *Eur J Radiol* 2005;55:393–400 CrossRef Medline
 34. Lu S, Ahn D, Johnson G, et al. Diffusion-tensor MR imaging of intracranial neoplasia and associated peritumoral edema: introduction of the tumor infiltration index. *Radiology* 2004;232:221–28 CrossRef Medline
 35. Papageorgiou TS, Chourmouzi D, Drevelengas A, et al. Diffusion tensor imaging in brain tumors: a study on gliomas and metastases. *Phys Med* 2015;31:767–73 CrossRef Medline
 36. Pavlisa G, Rados M, Pavlisa G, et al. The differences of water diffusion between brain tissue infiltrated by tumor and peritumoral vasogenic edema. *Clin Imaging* 2009;33:96–101 CrossRef Medline
 37. Shim WH, Kim HS, Choi CG, et al. Comparison of apparent diffusion coefficient and intravoxel incoherent motion for differentiating among glioblastoma, metastasis, and lymphoma focusing on diffusion-related parameter. *PLoS One* 2015;10:e0134761 CrossRef Medline
 38. Svolos P, Tsolaki E, Kapsalaki E, et al. Investigating brain tumor differentiation with diffusion and perfusion metrics at 3T MRI using pattern recognition techniques. *Magn Reson Imaging* 2013;31:1567–77 CrossRef Medline
 39. Tsougos I, Svolos P, Kousi E, et al. Differentiation of glioblastoma multiforme from metastatic brain tumor using proton magnetic resonance spectroscopy, diffusion and perfusion metrics at 3 T. *Cancer Imaging* 2012;12:423–36 CrossRef Medline
 40. Wang W, Steward CE, Desmond PM. Diffusion tensor imaging in glioblastoma multiforme and brain metastases: the role of p, q, L, and fractional anisotropy. *AJNR Am J Neuroradiol* 2009;30:203–08 CrossRef Medline
 41. Bobek-Billewicz B, Stasik-Pres G, Majchrzak K, et al. Fibre integrity and diffusivity of the pyramidal tract and motor cortex within and adjacent to brain tumour in patients with or without neurological deficits. *Folia Neuropathol* 2011;49:262–70 Medline
 42. Bulakbasi N, Guvenc I, Onguru O, et al. The added value of the apparent diffusion coefficient calculation to magnetic resonance imaging in the differentiation and grading of malignant brain tumors. *J Comput Assist Tomogr* 2004;28:735–46 CrossRef Medline
 43. Bulakbasi N, Kocaoglu M, Ors F, et al. Combination of single-voxel proton MR spectroscopy and apparent diffusion coefficient calculation in the evaluation of common brain tumors. *AJNR Am J Neuroradiol* 2003;24:225–33 Medline
 44. Cho NS, Jenabi M, Arevalo-Perez J, et al. Diffusion tensor imaging shows corpus callosum differences between high-grade gliomas and metastases. *J Neuroimaging* 2018;28:199–205 CrossRef Medline
 45. Jones TL, Byrnes TJ, Yang G, et al. Brain tumor classification using the diffusion tensor image segmentation (D-SEG) technique. *Neuro Oncol* 2015;17:466–76 CrossRef Medline
 46. Kolakshyapati M, Adhikari RB, Karlowee V, et al. Nonenhancing peritumoral hyperintense lesion on diffusion-weighted imaging in glioblastoma: a novel diagnostic and specific prognostic indicator. *J Neurosurg* 2018;128:667–78 CrossRef Medline
 47. Zolal A, Hejcl A, Malucelli A, et al. Distant white-matter diffusion changes caused by tumor growth. *J Neuroradiol* 2013;40:71–80 CrossRef Medline
 48. Lu S, Ahn D, Johnson G, et al. Peritumoral diffusion tensor imaging of high-grade gliomas and metastatic brain tumors. *AJNR Am J Neuroradiol* 2003;24:937–41 Medline
 49. Wang S, Kim S, Chawla S, et al. Differentiation between glioblastomas, solitary brain metastases, and primary cerebral lymphomas using diffusion tensor and dynamic susceptibility contrast-enhanced MR imaging. *AJNR Am J Neuroradiol* 2011;32:507–14 CrossRef Medline
 50. Wang S, Kim S, Chawla S, et al. Differentiation between glioblastomas and solitary brain metastases using diffusion tensor imaging. *Neuroimage* 2009;44:653–60 CrossRef Medline
 51. Yang G, Jones TL, Barrick TR, et al. Discrimination between glioblastoma multiforme and solitary metastasis using morphological features derived from the p:q tensor decomposition of diffusion tensor imaging. *NMR Biomed* 2014;27:1103–11 CrossRef Medline
 52. Yang G, Jones TL, Howe FA, et al. Morphometric model for discrimination between glioblastoma multiforme and solitary metastasis using three-dimensional shape analysis. *Magn Reson Med* 2016;75:2505–16 CrossRef Medline
 53. Min ZG, Niu C, Rana N, et al. Differentiation of pure vasogenic edema and tumor-infiltrated edema in patients with peritumoral edema by analyzing the relationship of axial and radial diffusivities on 3.0T MRI. *Clin Neurol Neurosurg* 2013;115:1366–70 CrossRef Medline
 54. Oh J, Cha S, Aiken AH, et al. Quantitative apparent diffusion coefficients and T2 relaxation times in characterizing contrast enhancing brain tumors and regions of peritumoral edema. *J Magn Reson Imaging* 2005;21:701–08 CrossRef Medline
 55. van Westen D, Latt J, Englund E, et al. Tumor extension in high-grade

- gliomas assessed with diffusion magnetic resonance imaging: values and lesion-to-brain ratios of apparent diffusion coefficient and fractional anisotropy. *Acta Radiol* 2006;47:311–19 CrossRef Medline
56. Vandendries C, Ducreux D, Lacroix C, et al. **Statistical analysis of multi-b factor diffusion weighted images can help distinguish between vasogenic and tumor-infiltrated edema.** *J Magn Reson Imaging* 2014;40:622–29 CrossRef Medline
57. Hoefnagels FW, De Witt Hamer P, Sanz-Arigita E, et al. **Differentiation of edema and glioma infiltration: proposal of a DTI-based probability map.** *J Neurooncol* 2014;120:187–98 CrossRef Medline
58. Rollin N, Guyotat J, Streichenberger N, et al. **Clinical relevance of diffusion and perfusion magnetic resonance imaging in assessing intra-axial brain tumors.** *Neuroradiology* 2006;48:150–59 CrossRef Medline
59. Pope WB, Mirsadraei L, Lai A, et al. **Differential gene expression in glioblastoma defined by ADC histogram analysis: relationship to extracellular matrix molecules and survival.** *AJNR Am J Neuroradiol* 2012;33:1059–64 CrossRef Medline
60. Jiang R, Du FZ, He C, et al. **The value of diffusion tensor imaging in differentiating high-grade gliomas from brain metastases: a systematic review and meta-analysis.** *PLoS One* 2014;9:e112550 CrossRef Medline
61. Mori S, Zhang J. **Principles of diffusion tensor imaging and its applications to basic neuroscience research.** *Neuron* 2006;51:527–39 CrossRef Medline
62. Deeks JJ, Bossuyt PM, Gatsonis C, eds. *Cochrane Handbook for Systematic Reviews of Diagnostic Test Accuracy*. Version 1.0.0. The Cochrane Collaboration, 2013. <http://methods.cochrane.org/sdt/handbook-dta-reviews>. Accessed October 9, 2017
63. Trikalinos TA, Balion CM, Coleman CI, et al. **Chapter 8: meta-analysis of test performance when there is a “gold standard.”** *J Gen Intern Med* 2012;27(Suppl 1):S56–66 CrossRef Medline

Quantitative Susceptibility Mapping after Sports-Related Concussion

K.M. Koch, T.B. Meier, R. Karr, A.S. Nencka, L.T. Muftuler, and M. McCrea



ABSTRACT

BACKGROUND AND PURPOSE: Quantitative susceptibility mapping using MR imaging can assess changes in brain tissue structure and composition. This report presents preliminary results demonstrating changes in tissue magnetic susceptibility after sports-related concussion.

MATERIALS AND METHODS: Longitudinal quantitative susceptibility mapping metrics were produced from imaging data acquired from cohorts of concussed and control football athletes. One hundred thirty-six quantitative susceptibility mapping datasets were analyzed across 3 separate visits (24 hours after injury, 8 days postinjury, and 6 months postinjury). Longitudinal quantitative susceptibility mapping group analyses were performed on stability-thresholded brain tissue compartments and selected subregions. Clinical concussion metrics were also measured longitudinally in both cohorts and compared with the measured quantitative susceptibility mapping.

RESULTS: Statistically significant increases in white matter susceptibility were identified in the concussed athlete group during the acute (24 hour) and subacute (day 8) period. These effects were most prominent at the 8-day visit but recovered and showed no significant difference from controls at the 6-month visit. The subcortical gray matter showed no statistically significant group differences. Observed susceptibility changes after concussion appeared to outlast self-reported clinical recovery metrics at a group level. At an individual subject level, susceptibility increases within the white matter showed statistically significant correlations with return-to-play durations.

CONCLUSIONS: The results of this preliminary investigation suggest that sports-related concussion can induce physiologic changes to brain tissue that can be detected using MR imaging–based magnetic susceptibility estimates. In group analyses, the observed tissue changes appear to persist beyond those detected on clinical outcome assessments and were associated with return-to-play duration after sports-related concussion.

ABBREVIATIONS: CV = coefficient of variation; MNI = Montreal Neurological Institute; mTBI = mild traumatic brain injury; QSM = quantitative susceptibility mapping; RTP = return to play; SAC = Standardized Assessment of Concussion; SCAT-3 = Sport Concussion Assessment Tool, 3rd ed; SRC = sports-related concussion

Mild traumatic brain injury (mTBI) is an issue of increasing importance in the medical, sports, and military communities. Despite the increasing scope of this issue, the role of diagnos-

tic imaging in its assessment and management remains limited. Although CT and MR imaging can detect hemorrhages, contusions, or edema indicative of complicated mTBI,¹ conventional diagnostic imaging assessments of uncomplicated mTBI have limited sensitivity to the subtle physiologic and morphologic changes in brain function and structure.

MR imaging has recently shown accelerated improvement in performing quantitative assessments of soft-tissue characteristics. As a nonionizing radiative imaging technique, quantitative MR imaging is well-suited for use as a longitudinal scientific probe of the subtle physiologic changes resulting from mTBI. Previous studies have explored mTBI-induced changes in MR imaging dif-

Received September 5, 2017; accepted after revision April 8, 2018.

From the Departments of Radiology (K.M.K., R.K., A.S.N.) and Neurosurgery (T.B.M., L.T.M., M.M.), Medical College of Wisconsin, Milwaukee, Wisconsin.

This work was supported, in part, by the GE-NFL Head Health Challenge I and the U.S. Army Medical Research and Materiel Command under award number W81XWH-12-1-0004. This publication was also supported by the Clinical and Translational Science Institute grant IUL1-RR031973 (-01) and by the National Center for Advancing Translational Sciences, National Institutes of Health grant 8UL1TR000055. It was also supported by the Advancing a Healthier Wisconsin Research and Education Committee.

The contents of this publication are the sole responsibility of the authors and do not necessarily represent the official views of the National Institutes of Health. Opinions, interpretations, conclusions, and recommendations are those of the authors and are not necessarily endorsed by the NFL, GE, or the U.S. Army.

Please address correspondence to Kevin M. Koch, PhD, Medical College of Wisconsin, Department of Radiology, 8701 Watertown Plank Rd, Milwaukee, WI 53226; e-mail: kmkoch@mcw.edu; @KevinMatKoch

Indicates open access to non-subscribers at www.ajnr.org

Indicates article with supplemental on-line tables.

<http://dx.doi.org/10.3174/ajnr.A5692>

fusion tensor imaging,² diffusional kurtosis imaging,³ arterial spin-labeling,⁴ and functional connectivity.⁵

Here, we present a preliminary application of another emerging MR imaging quantitative metric, quantitative susceptibility mapping (QSM), in the assessment of mTBI. Conventional susceptibility-weighted imaging, which uses magnetic susceptibility as a contrast mechanism, is well-established as a useful diagnostic tool.⁶ As a quantitative extension of SWI, QSM uses off-resonance information extracted from multiecho MR imaging acquisitions to estimate an isotropic magnetic susceptibility tensor for each tissue voxel. Quantifying the isotropic magnetism of brain tissue can reveal changes in components such as ferritin, hemosiderin, water content, myelin, and calcium.^{7,8} Along with conventional SWI, QSM has already been used to identify regions of focal tissue damage in complicated mTBI in cohorts of military personnel⁹ and civilians.¹⁰

The present report summarizes preliminary results from QSM MR imaging analysis after sports-related concussion (SRC) in high school and collegiate football athletes. This study is unique compared with previous QSM mTBI studies in that it examines QSM of injured and control subjects longitudinally at 3 visits beginning at the acute injury phase (ie, within 24 hours) and ending 6 months postinjury.

MATERIALS AND METHODS

Subjects

Collegiate and high school football athletes were recruited at pre-season team meetings at 10 local institutions. Subjects provided written consent or assent and parental consent if minors for a study approved by the local institutional human research review. A subset of 56 subjects, split evenly across injured and matched control athletes, were enrolled into an advanced MR imaging component of the study during the season. Athletes were imaged within 24 hours after injury, followed by examinations at 8 days and 6 months postinjury. The injured athlete return-to-play (RTP) timeframe was not fixed to the MR imaging session schedule.

One hundred thirty-six QSM datasets collected across the 3 visits were used for the present analysis. Details of longitudinal data composition are provided in On-line Table 1. The Sport Concussion Assessment Tool, 3rd ed (SCAT-3) symptom checklist, the Standardized Assessment of Concussion (SAC), and the Balance Error Scoring System were also collected at each visit.

Imaging and Mapping Technique

Imaging was performed on a clinical 3T MR imaging scanner using a 32-channel head receive array. QSM data were collected by saving the raw k -space data from a commercially available SWI application. SWI data acquisition parameters were as follows: in-plane data matrix, 320×256 ; FOV, 24 cm; slice thickness, 2 mm; echo spacing, 7 ms; number of echoes, 4; TEs, 10.4, 17.4, 24.4, 31.4 ms; TR, 58.6 ms; autocalibrated parallel imaging factors, 3×1 ; acquisition time, 4 minutes.

Following background field removal using the regularization-enabled sophisticated harmonic artifact reduction for phase data (RESHARP)¹¹ algorithm, susceptibility inversion was performed using an adapted localized processing formulation¹² of the morphology-enabled dipole inversion (MEDI) algorithm.¹³

Streaking artifacts are a well-known confounding factor in QSM.⁷ To mitigate these potential artifacts from erroneous field estimates on the periphery of the brain, we applied tissue segmentations and aggressive (4 mm) erosions to construct a tissue mask. This conservative approach largely eliminated boundary field discontinuities and kept streaking below any qualitatively visible threshold. In addition, a localized processing adaptation of the MEDI algorithm was used to further reduce the streaking impact.¹² Because of these measures, no datasets were excluded due to streaking artifacts in the manual quality control analysis. Of the 143 acquired QSM datasets, only 7 were removed due to motion-related quality control checks.

Image Analysis

Group analyses were performed via a triple-stage registration process implemented in FSL (<http://www.fmrib.ox.ac.uk/fsl>).¹⁴ First, magnitude images from a 3D T1-weighted scan collected on each subject were nonlinearly registered to a 2-mm isotropic Montreal Neurological Institute (MNI) space T1-weighted template image.¹⁵ Next, a magnitude image constructed from each subject's QSM acquisition was affine-registered to the subject's T1-weighted image. All QSMs were then transformed to MNI space and registered to a single common QSM dataset in MNI space using FSL.¹⁵

Group changes in susceptibility were identified through the following processing pipeline: First, brain regions of sufficient QSM stability were identified by computing coefficients of variation (CVs) within the control cohort. A stability mask was then constructed from this CV map at a threshold of $CV < 0.8$. Next, global white matter and iron-rich subcortical gray matter compartments were defined using susceptibility thresholds computed on a mean susceptibility map of the control subjects. White matter was defined as $\chi < -0.03$ ppm,¹⁶ and subcortical iron-rich regions were defined as $\chi > 0.05$ ppm.

ROI analysis within the compartments was performed using anatomic segmentations extracted from the Johns Hopkins University and Harvard MNI space atlases.^{17,18} Primary analyses focused on 2 global compartments (ie, white matter and subcortical gray matter). Twenty-eight additional ROIs within the global compartments were assessed as secondary analyses. These regions are summarized in Table 1.

Statistical Analysis

Statistical processing was performed using the Statistics Toolbox in Matlab (MathWorks, Natick, Massachusetts). Mean susceptibility values were computed within each gray and white matter ROI for each subject. Group differences between the means were computed using 2-tailed independent samples t tests with unequal variances at each visit. In addition, effect sizes between the groups were estimated by computing the Cohen D at each visit. Longitudinal trends of the susceptibility means were assessed using a linear mixed effects model with random effects terms. In the linear mixed effects model, the mean ROI susceptibility was the response variable and the direct fixed predictor terms were group (injured versus control) and visit. An interaction fixed predictor term, group \times visit, was also included in the model. Finally, random effects terms were modeled for subject variation by group and subject variation by visit. Pearson correlations between sus-

ceptibility measurements and clinical symptoms (SCAT-3, SAC, Balance Error Scoring System) were performed for each region at each visit. RTP outcome measures were also correlated with the 24-hour susceptibility measurements. For the subregional analyses, multiple comparison corrections were performed using the Benjamini-Hochberg false discovery rate correction at a false discovery rate of 10%.

RESULTS

Tables 2 and 3 provide general characteristics of the complete study population. None of the reported physical or general

metrics showed statistically significant group differences, though the history of prior diagnosed sports-related concussions between the groups nearly reached significance ($P = .07$, Mann-Whitney U test). SCAT-3, SAC, Balance Error Scoring System, and RTP measures on the full study cohort are also presented in Tables 2 and 3. A breakdown of the cohort characteristics based on QSM data inclusion at each visit is provided in On-line Table 2.

Figure 1 presents control group susceptibility mean (A), SD (B), and coefficient of variation (C) maps across several axial slices. The CV maps provide an estimate of QSM stability, as measured across the control group. This stability assessment reflects physiologic, acquisition, and algorithmic variations. The susceptibility estimate is reliable in particular brain regions comprising deep gray matter structures and deep white matter tracts.

Figure 1D shows subcortical gray matter (blue) and white matter (red) regions that were identified on MNI atlases and masked to reflect regions of sufficient susceptibility measurement stability ($CV < 0.8$). Table 1 provides descriptions for each of the assessed ROIs.

Table 4 summarizes the group susceptibility effects for several regions, including the global white and gray matter compartments. The global white matter compartment showed statistically significant susceptibility increases relative to the control group at both the 24-hour and 8-day visits. This effect was diminished and was no longer statistically significant at the 6-month visit. Several displayed individual white matter regions showed similar trends. Eleven of the 20 white matter subregions showed a statistically significant positive increase at 1 or both of the 24-hour and/or 8-day visits. One subregion (the right cingulum) showed significant group differences remaining at the 6-month visit. Adjustment of these results by at 10% false discovery rate correction

Table 1: Description of additional ROIs in white matter and subcortical gray matter

White Matter ROI	Gray Matter ROI
L anterior thalamic radiation	L thalamus
R anterior thalamic radiation	L caudate
L corticospinal tract	L putamen
R corticospinal tract	L pallidum
L cingulum (cingulate gyrus)	R thalamus
R cingulum (cingulate gyrus)	R caudate
L cingulum (hippocampus)	R putamen
R cingulum (hippocampus)	R pallidum
Forceps major	
Forceps minor	
L inferior fronto-occipital fasciculus	
R inferior fronto-occipital fasciculus	
L inferior longitudinal fasciculus	
R inferior longitudinal fasciculus	
L superior longitudinal fasciculus	
R superior longitudinal fasciculus	
L uncinate fasciculus	
R uncinate fasciculus	
L superior longitudinal fasciculus (temporal)	
R superior longitudinal fasciculus (temporal)	

Note:—R indicates right; L, left.

Table 2: General characteristics of complete control and injured study cohorts (N = 56)^a

	Physical			General			
	Age (n = 28) (yr)	Weight (n = 28) (lbs)	Height (n = 28) (in)	Y.I.S. (n = 28) (yr)	G.P.A. (n = 28) (4.0)	P.SRC (n = 28) (Total)	RTP (n = 24) (days)
C	17.9 (17.3–18.5)	202 (188–217)	72.0 (71.0–73.0)	8.3 (7.2–9.5)	3.3 (3.1–3.5)	8	NA
I	17.7 (17.2–18.3)	221 (199–243)	71.6 (70.4–72.8)	8.6 (7.3–9.8)	3.1 (2.8–3.3)	16	13.9 (11.3–16.5) range, 4–28
P	.66	.15	.64	.76	.11	.07	NA

Note:—Y.I.S. indicates years in sport; G.P.A., academic grade point average on a 4.0-point scale; P.SRC, number of previous sports-related concussions; C, control; I, injured; NA, not applicable.

^a When appropriate, values are shown as mean and 95% confidence intervals of the distribution. P values from 2-tailed independent samples between the 2 cohorts are reported for all metrics. Due to skewness of the distribution, the P.SRC test statistics were computed using a Mann-Whitney U test. Return to play: 3 of the 24 injured subjects returned to play prior to the 8-day imaging visit.

Table 3: Clinical characteristics of complete control and injured study cohorts (N = 56)^a

	SCAT Severity			SAC Total Score			BESS Score		
	24 Hours (n = 28)	8 Days (n = 28)	6 Months (n = 19)	24 Hours (n = 28)	8 Days (n = 28)	6 Months (n = 22)	24 Hours (n = 27)	8 Days (n = 27)	6 Months (n = 22)
C	3.2 (1.9–4.5)	2.9 (1.2–4.6)	2.1 (0.8–3.4)	26.1 (25.4–26.8)	27.6 (27.0–28.2)	27.2 (26.4–28.0)	12.3 (10.5–14.0)	10.8 (8.8–12.8)	11.4 (9.5–13.2)
I	27.8 (21.4–34.2) ^b	5.0 (1.9–8.2)	3.1 (–1.1–7.4)	24.6 (23.7–25.5)	26.8 (25.9–27.7)	26.9 (25.8–27.9)	28.9 (11.8–15.7)	5.5 (10.2–13.7)	1.2 (9.9–14.4)
P	<.001 ^b	.22	.64	.01 ^b	.14	.63	.25	.36	.57

Note:—BESS indicates Balance Error Scoring System; C, control; I, injured.

^a When appropriate, values are shown as mean and 95% confidence intervals of the distribution. P values from 2-tailed independent samples between the 2 cohorts are reported for all metrics.

^b Significant.

yielded 10 statistically significant subregions at the 8-day visit. None of the *t* tests of the control visit groups relative to the full control group showed any significant differences (before any false discovery rate correction). Although there were not any

statistically significant effects in the subcortical gray matter compartments, the measured subcortical susceptibility differences generally showed opposing effect signs compared with the white matter.

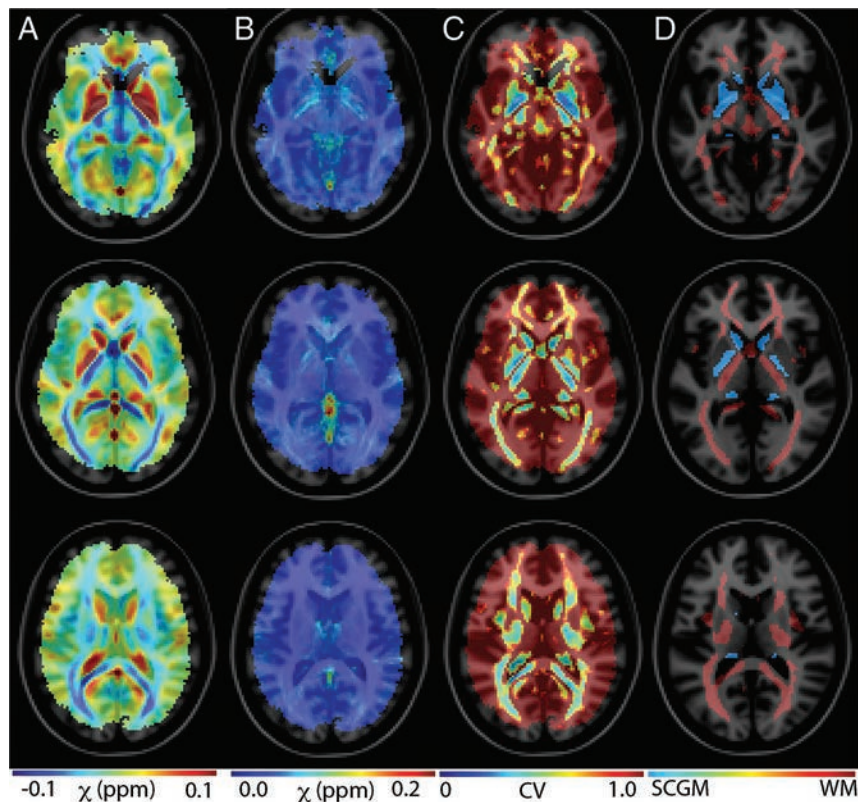


FIG 1. Assessment of QSM stability across the control group. Maps of mean (A), SD (B), and coefficients of variation (C) are shown across 4 axial slices throughout the brain. The stability of the QSM measurement varies across brain compartments. Deep gray and white matter structures show the most prominent stability. D, Subcortical gray matter (blue) and white matter (red) regions that were identified on MNI atlases and masked to reflect regions of sufficient susceptibility measurement stability (CV < 0.8).

Figure 2 presents boxplots of 4 representative white matter regions. The global white matter compartment is shown in A. A general upward trend in susceptibility values is observed in the injured group, which has statistical significance relative to the controls at the 24-hour and 8-day visits. This difference is removed by the 6-month visit. Plots B, C, and D, respectively, provide similar analysis within 2 longitudinal fasciculus regions and 1 thalamic radiation subregion. Similar longitudinal trends are observed in these areas.

Neither of the global or subregional tissue compartments showed statistically significant correlations between the acute (24 hour) visit susceptibility and the SCAT-3, SAC, or Balance Error Scoring System metrics within the injured group. However, there was a significant positive correlation (after false discovery rate correction) between the injured acute susceptibility measurements and RTP in several white matter compartments that showed significant group susceptibility differences (Table 4).

Linear mixed effects model results are shown in Table 5. The global white matter and several subregions (2 re-

Table 4: Statistical report comparing means of susceptibility values within injured and control groups^a

ROI	Susceptibility Group Differences (Injured vs Control)						RTP vs 24-Hour Suscept	
	24 Hours		8 Days		6 Months		P	ρ
	P	D	P	D	P	D		
White matter	.032 ^b	0.65 ^b	.001 ^b	1.01 ^b	.463	0.25	.022 ^b	0.55
Gray matter	.980	-0.01	.255	-0.34	.382	-0.30	.146	-0.26
L ATR	.017 ^b	0.72 ^b	.069	0.55	.735	-0.11	.146	0.37
R cing (hipp)	.072	0.53	.011 ^{b,c}	0.79 ^b	.012 ^b	0.91 ^b	.015 ^{b,c}	0.58 ^b
Forceps minor	.017 ^b	0.75 ^b	.008 ^{b,c}	0.82 ^b	.738	0.11	.989	<0.01
L IFOF	.127	0.46	.037 ^{b,c}	0.63 ^b	.730	0.12	.015 ^{b,c}	0.58 ^b
R IFOF	.073	0.55	.019 ^{b,c}	0.72 ^b	.783	0.09	.480	0.18
L ILF	.194	0.39	.027 ^{b,c}	0.67 ^b	.650	0.15	.146	0.37
R ILF	.187	0.40	.034 ^{b,c}	0.64 ^b	.814	0.08	.003 ^{b,c}	0.67 ^b
L SLF	.334	0.28	.014 ^{b,c}	0.75 ^b	.550	0.21	.019 ^{b,c}	0.56 ^b
R SLF	.021 ^b	0.72 ^b	.002 ^{b,c}	1.00 ^b	.819	0.08	.015 ^{b,c}	0.58 ^b
L SLF (temp)	.847	0.06	.035 ^{b,c}	0.64 ^b	.510	0.23	.034 ^{b,c}	0.52 ^b
R SLF (temp)	.010 ^b	0.82 ^b	.007 ^{b,c}	0.83 ^b	.576	0.19	.412	0.21

Note:—ATR indicates anterior thalamic radiation; cing, cingulum; hipp, hippocampus; IFOF, inferior fronto-occipital fasciculus; ILF, inferior longitudinal fasciculus; SLF, superior longitudinal fasciculus; temp, temporal; RTP, return to play temporal duration; D, effect sizes; Suscept, susceptibility; L, left; R, right.

^a White matter regions showing significant trends and the global gray matter compartment are shown. At each visit, group differences are characterized with *P* values computed using 2-tailed independent samples *t* tests and effect sizes are computed using the Cohen *D*. The Pearson correlation of RTP temporal duration vs 24-hour susceptibility values for individual injured subjects is also presented. *P* values and effect sizes (ρ) are displayed. *P* values for the subregional analyses are reported without multiple-comparison corrections.

^b Effects that showed statistical significance (*P* < .05).

^c Statistically significant after correction for multiple comparisons.

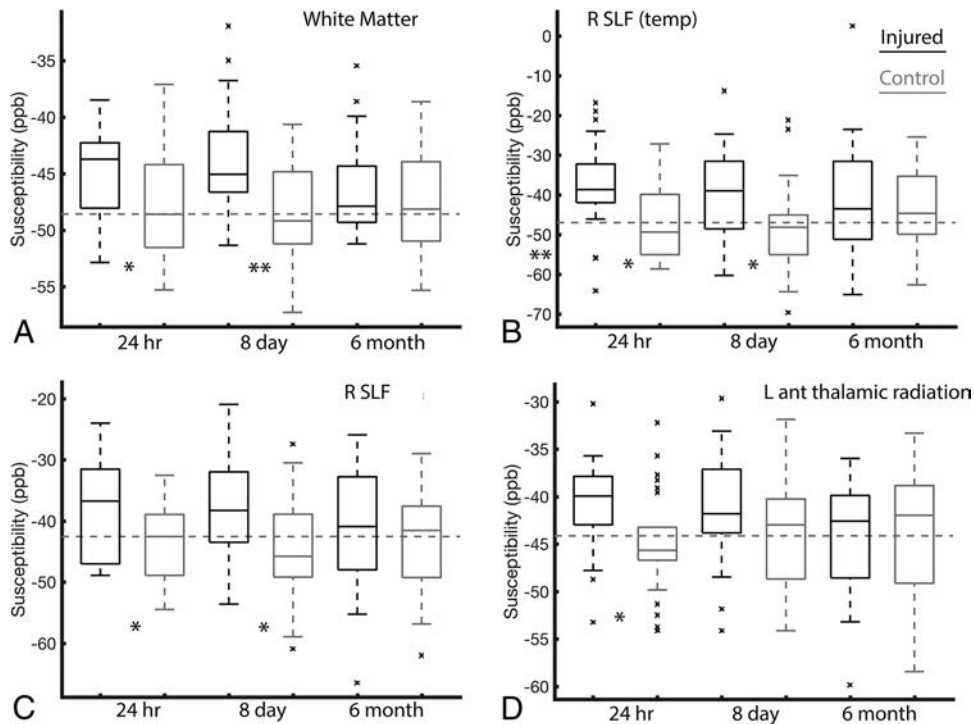


FIG 2. Boxplots of susceptibility means across 4 representative white matter regions. Indices for each region, as defined in Table 1, are provided for each boxplot. The displayed boxplots provide *median lines*, *boxes* across the interquartile range, and *bars* across the 95th confidence interval regions. Outliers are plotted as *x*'s. The *dashed horizontal line* provides a visual of the full control cohort mean susceptibility value. Statistical significance of the injured-versus-control *t* tests at each visit are indicated for *P* < .05 (*asterisk*) and *P* < .01 (*double asterisks*). SLF indicates superior longitudinal fasciculus; ant, anterior; temp, temporal; L, left; R, right.

Table 5: Linear mixed effects modeling results^a

ROIs	Direct		Interact
	Time	Injury	Time × Injury
Primary			
White matter	.874	.016 ^b	.659
Gray matter	.390	.711	.175
Additional			
L ant. thal. rad.	.416	.003 ^{b,c}	.053
Forceps minor	.767	.004 ^{b,c}	.256
L IFOF	.986	.043 ^b	.226
R SLF	.903	.023 ^b	.671
R SLF (temp)	.498	.024 ^b	.500

Note:—ant. thal. rad. indicates anterior thalamic radiation; L, left; R, right; IFOF, inferior fronto-occipital fasciculus; SLF, superior longitudinal fasciculus; temp, temporal.

^a *P* values are reported for white matter and gray matter compartments, as well as for additional ROIs with significant effects. Interaction terms indicate longitudinal susceptibility variations of one group relative to the other.

^b Statistical significance (*P* < .05).

^c Significant after multiple-comparison correction.

gions, post-false discovery rate correction) showed statistically significant effects of the injured group relative to the controls. None of the regions showed statistically significant interaction terms, which would have indicated statistical recovery patterns within the measurement visits.

DISCUSSION

Because QSM is very sensitive to blood products, it can clearly identify local damage in complicated mTBI, whereby shearing forces can cause diffuse axonal injury patterns that manifest as hemorrhages and contusions.⁹ The potential utility of QSM in assessing uncomplicated mTBI is more nuanced. In a recent

study by Lin et al,¹⁰ a cohort of clinical subjects admitted for hospital care with mTBI were analyzed with QSM within 2 weeks of injury. In agreement with the results of the present study, Lin et al found susceptibility increases associated with injury in white matter regions. In addition, Lin et al found substantial decreases of susceptibility in subcortical gray matter compartments. Although the present study did not find statistically significant differences in these regions, the general gray matter trends (Table 4) show a negative correlation between susceptibility and injury, thus adding support to recent QSM studies that have found that susceptibility decreases in deep gray matter regions correlated with complicated mTBI.¹⁹

The magnitude of group susceptibility differences observed in this study is nearly an order of magnitude less than that reported by Lin et al.¹⁰ This finding is expected, given the reduced magnitude of head trauma in the present sports concussion cohort and could be one reason that the observed subcortical gray matter susceptibility reduction trends did not reach statistical significance. In addition, compared with deep gray matter structures, white matter structures may be more sensitive to shear strain forces experienced during mTBI and therefore exhibit detectable differences at a lower injury threshold.

The stability analysis shown in Fig 1 illustrates the practical limitations of QSM in reliably detecting small changes in tissue susceptibility. This expected result shows that QSM estimates will predominantly be most reliable in deep gray and white matter structures. Outside these regions, the control susceptibility estimates are highly variable. This result is not surprising because QSM is known to be dependent on the white matter in tract ori-

entation with respect to the main MR imaging magnetic field direction.²⁰

The physiologic and physical causes of the observed susceptibility changes will require further scientific investigation. Increases in white matter susceptibility could be due to demyelination or increased water content (swelling). Qualitative correlation of QSM and diffusion tensor imaging results from the athlete cohort analyzed in this study³ has shown localized agreement in white matter regions of QSM increases and decreased axial diffusion, which support the white matter swelling hypothesis. Preliminary studies suggest that the observed gray matter decreases could be due to calcium (which is a diamagnetic [negative susceptibility] ion) influx after brain trauma.²¹

In recent years, there has been increased attention paid to the assessment and management of SRC.²²⁻²⁸ Although large-cohort studies have already informed SRC best practices,^{29,30} management of its progression remains a substantial challenge in the sports medicine community. Several studies^{29,31-33} have provided insight into elements of SRC progression but did not uncover an objective biomarker that relates the acute physiologic effects of SRC on brain structure and function. Without such a biomarker, it is difficult to identify the windows of cerebral vulnerability that may extend beyond the point of clinical recovery.³⁴ This period of vulnerability is of major translational significance because it may point to a physiologically compromised brain state, which potentially increases the risk of repetitive injury. As shown in Tables 2 and 3, the group SCAT-3 differences in this study are resolved by the 8-day postinjury assessment. The global white matter compartment and several subregions, however, still show substantial statistically significant group differences at this assessment point. Linear mixed effects models, which accounted for individual subject variations and random effects, showed substantial group susceptibility differences correlating with injury.

The present study had several limitations. First, as with many longitudinal studies of nonclinical cohorts, subject compliance for the MR imaging examination component of the study was not perfect (On-line Table 1) and showed attrition at the last visit point. A necessary mathematic assumption applied to the statistical analysis in this study is that the missing data are randomly distributed between the analysis groups. However, this data attrition could partially explain the lack of a significant interaction term in the linear mixed effects model.

A second limitation of the study is that baseline imaging measurements were not performed. This lack of data acquisition was due to the substantial additional resources that would be required to perform an MR imaging examination on every enrolled subject in the study, >3000 athletes. To address this limitation, future studies may target baseline imaging in smaller cohorts that are more likely to experience injury. Although no injured subjects experienced a second diagnosed concussion during the context of the study, injured subjects were exposed to subconcussive impacts throughout the duration of the study after their return to normal activity. In addition, control subjects in this study were also contact sport athletes experiencing subconcussive impacts throughout their participation in the study. Thus, this study was not well-positioned to study the effects of subconcussive events on tissue-susceptibility measurements.

The lack of baseline imaging highlights another potential confounding factor in the study: the near statistically significant ($P = .07$) difference in prior SRC history between the injured and control groups. Although this study excluded subjects who had ongoing neurocognitive effects from past brain injuries, injured subjects were not excluded solely on the basis of prior concussions. Control subjects were excluded if they had a diagnosed prior concussion within 6 months of their initial imaging session. To further study the effects of prior concussion on the results of this study, Pearson correlations between the first time point susceptibility values and prior SRC history were computed for both cohort groups. Neither the global white matter region nor any of the subregions with statistically significant group differences showed a statistically significant correlation in these tests. This finding suggests that the history of prior concussion is not a strong determinant of the observed susceptibility changes.

Finally, this study did not analyze highly localized variations of tissue susceptibility within individual subjects. Such effects will not be captured in the ROI analyses used. Future work will apply localized extremum analyses to identify patterns of susceptibility changes within individual subjects.

CONCLUSIONS

The presented analysis of QSM MR imaging group differences in SRC has shown encouraging preliminary results. Consistent susceptibility differences have been identified in the injured cohort. The directionality of the observed susceptibility changes is in general agreement with larger military and civilian studies of mTBI using QSM, including those studies of more severe TBI. Furthermore, the identified group changes in susceptibility appear to outlast symptom-recovery patterns and correlate with RTP time after SRC. Further work will be required to assess the effect of head impact exposure on the observed tissue-susceptibility recovery patterns.

Disclosures: Timothy B. Meier—RELATED: Grant: GE Head-Health Initiative, Comments: Work was completed as part of the GE-NFL Head Health Challenge I award (Principal Investigator, Mike McCrea).* Andrew S. Nencka—RELATED: Grant: GE Healthcare, Comments: salary support; Principal Investigator, Mike McCrea*; UNRELATED: Grants/Grants Pending: GE Healthcare*; Patents (Planned, Pending or Issued): Medical College of Wisconsin, Comments: The author is listed as an inventor on MRI-related patents owned by Medical College of Wisconsin.* Michael McCrea—RELATED: Grant: National Collegiate Athletic Association and Department of Defense.* *Money paid to the institution.

REFERENCES

1. Williams DH, Levin HS, Eisenberg HM. **Mild head injury classification.** *Neurosurgery* 1990;27:422–28 CrossRef Medline
2. Shenton ME, Hamoda HM, Schneiderman JS, et al. **A review of magnetic resonance imaging and diffusion tensor imaging findings in mild traumatic brain injury.** *Brain Imaging Behav* 2012;6:137–92 CrossRef Medline
3. Lancaster MA, Olson DV, McCrea MA, et al. **Acute white matter changes following sport-related concussion: a serial diffusion tensor and diffusion kurtosis tensor imaging study.** *Hum Brain Mapping* 2016;37:3821–34 CrossRef Medline
4. Wang Y, Nelson LD, LaRoche AA, et al. **Cerebral blood flow alterations in acute sport-related concussion.** *J Neurotrauma* 2016;33:1227–36 CrossRef Medline
5. Mayer AR, Bellgowan PS, Hanlon FM. **Functional magnetic resonance imaging of mild traumatic brain injury.** *Neurosci Biobehav Rev* 2015;49:8–18 CrossRef Medline

6. Mittal S, Wu Z, Neelavalli J, et al. **Susceptibility-weighted imaging: technical aspects and clinical applications, part 2.** *AJNR Am J Neuroradiol* 2009;30:232–52 CrossRef Medline
7. Wang Y, Liu T. **Quantitative susceptibility mapping (QSM): decoding MRI data for a tissue magnetic biomarker.** *Magn Reson Med* 2015;73:82–101 CrossRef Medline
8. Reichenbach JR, Schweser F, Serres B, et al. **Quantitative susceptibility mapping: concepts and applications.** *Clin Neuroradiol* 2015; 25(Suppl 2):225–30 CrossRef Medline
9. Liu W, Soderlund K, Senseney JS, et al. **Imaging cerebral microhemorrhages in military service members with chronic traumatic brain injury.** *Radiology* 2016;278:536–45 CrossRef Medline
10. Lin HH, Liu HS, Tsai PH, et al. **Quantitative susceptibility mapping in mild traumatic brain injury.** In: *Proceedings of the Annual Meeting and Exhibition of the International Society for Magnetic Resonance in Medicine*, Honolulu, Hawaii. April 22–27, 2017:2395
11. Sun H, Wilman AH. **Background field removal using spherical mean value filtering and Tikhonov regularization.** *Magn Reson Med* 2014;71:1151–57 CrossRef Medline
12. Anderson C, Nencka A, Muftuler T, et al. **Volume-parcellated quantitative susceptibility mapping.** In: *Proceedings of the Annual Meeting and Exhibition of the International Society for Magnetic Resonance in Medicine*, Singapore. May 7–13, 2016:1108
13. Liu J, Liu T, de Rochefort L, et al. **Morphology enabled dipole inversion for quantitative susceptibility mapping using structural consistency between the magnitude image and the susceptibility map.** *Neuroimage* 2012;59:2560–68 CrossRef Medline
14. Jenkinson M, Beckmann CF, Behrens TE, et al. **FSL.** *Neuroimage* 2012;62:782–90 CrossRef Medline
15. Mazziotta J, Toga A, Evans A, et al. **A four-dimensional probabilistic atlas of the human brain.** *J Am Med Assoc* 2001;286:401–30 CrossRef Medline
16. Li W, Wu B, Batrachenko A, et al. **Differential developmental trajectories of magnetic susceptibility in human brain gray and white matter over the lifespan.** *Hum Brain Mapp* 2014;35:2698–713 CrossRef Medline
17. Desikan RS, Ségonne, Fischl B, et al. **An automated labeling system for subdividing the human cerebral cortex on MRI scans into gyral based regions of interest.** *Neuroimage* 2006;31:968–80 CrossRef Medline
18. Mori S, Wakana S, van Zijl PC, et al. *MRI Atlas of Human White Matter*. Boston: Elsevier; 2005
19. Liu W, Riedy G, Yeh PH, et al. **Patients with cerebral microhemorrhage exhibit increased magnetic susceptibility in the cerebral hemispheres, but reduced magnetic susceptibility in the basal ganglia.** In: *Proceedings of the Annual Meeting and Exhibition of the International Society for Magnetic Resonance in Medicine*, Honolulu, Hawaii. April 22–27, 2017:4534
20. Li Wei, Liu C. **Comparison of magnetic susceptibility tensor and diffusion tensor of the brain.** *J Neurosci Neuroeng* 2013;2:431–40 CrossRef Medline
21. Schweser F. **9.4 Tesla in vivo quantitative susceptibility mapping (QSM) detects thalamic calcium influx associated with repeated mild traumatic brain injury (mTBI).** In: *Proceedings of the Annual Meeting and Exhibition of the International Society for Magnetic Resonance in Medicine*, Honolulu, Hawaii. April 22–27, 2017:4517
22. McCrory P, Meeuwisse WH, Aubry M, et al. **Consensus statement on concussion in sport: the 4th International Conference on Concussion in Sport held in Zurich, November 2012.** *Br J Sports Med* 2013; 47:250–58 CrossRef Medline
23. McCrory P, Meeuwisse W, Johnston K, et al. **Consensus statement on concussion in sport: the 3rd International Conference on Concussion in Sport held in Zurich, November 2008.** *J Athl Train* 2009; 44:434–48 CrossRef Medline
24. McCrory P, Johnston K, Meeuwisse W, et al. **Summary and agreement statement of the 2nd International Conference on Concussion in Sport, Prague 2004.** *Br J Sports Med* 2005;39:196–204 Medline
25. DeKosky ST, Ikonomic MD, Gandy S. **Traumatic brain injury: football, warfare, and long-term effects.** *N Engl J Med* 2010;363: 1293–96 CrossRef Medline
26. Kelly JP. **Traumatic brain injury and concussion in sports.** *JAMA* 1999;282:989–91 CrossRef Medline
27. Langlois JA, Rutland-Brown W, Wald MM. **The epidemiology and impact of traumatic brain injury: a brief overview.** *J Head Trauma Rehabil* 2006;21:375–78 CrossRef Medline
28. Centers for Disease Control and Prevention (CDC). **Nonfatal traumatic brain injuries from sports and recreation activities: United States, 2001–2005.** *MMWR Morb Mortal Wkly Rep* 2007;56:733–37 Medline
29. McCrea M, Guskiewicz KM, Marshall SW, et al. **Acute effects and recovery time following concussion in collegiate football players: the NCAA Concussion Study.** *JAMA* 2003;290:2556–63 CrossRef Medline
30. Guskiewicz KM, McCrea M, Marshall SW, et al. **Cumulative effects associated with recurrent concussion in collegiate football players: the NCAA Concussion Study.** *JAMA* 2003;290:2549–55 CrossRef Medline
31. McCrea M, Barr WB, Guskiewicz K, et al. **Standard regression-based methods for measuring recovery after sport-related concussion.** *J Int Neuropsychol Soc* 2005;11:58–69 Medline
32. McCrea M, Guskiewicz K, Randolph C, et al. **Effects of a symptom-free waiting period on clinical outcome and risk of reinjury after sport-related concussion.** *Neurosurgery* 2009;65:876–82; discussion 882–83 CrossRef Medline
33. McCrea M, Pritchep L, Powell MR, et al. **Acute effects and recovery after sport-related concussion: a neurocognitive and quantitative brain electrical activity study.** *J Head Trauma Rehabil* 2010;25: 283–92 CrossRef Medline
34. McCrory P, Meeuwisse W, Dvořák J, et al. **Consensus statement on concussion in sport: the 5th International Conference on Concussion in Sport held in Berlin, October 2016.** *Br J Sports Med* 2017;51: 838–47 CrossRef Medline

Prevalence of Cerebral Microhemorrhage following Chronic Blast-Related Mild Traumatic Brain Injury in Military Service Members Using Susceptibility-Weighted MRI

E. Lotan, C. Morley, J. Newman, M. Qian, D. Abu-Amara, C. Marmar, and Y.W. Lui

ABSTRACT

BACKGROUND AND PURPOSE: Cerebral microhemorrhages are a known marker of mild traumatic brain injury. Blast-related mild traumatic brain injury relates to a propagating pressure wave, and there is evidence that the mechanism of injury in blast-related mild traumatic brain injury may be different from that in blunt head trauma. Two recent reports in mixed cohorts of blunt and blast-related traumatic brain injury in military personnel suggest that the prevalence of cerebral microhemorrhages is lower than in civilian head injury. In this study, we aimed to characterize the prevalence of cerebral microhemorrhages in military service members specifically with chronic blast-related mild traumatic brain injury.

MATERIALS AND METHODS: Participants were prospectively recruited and underwent 3T MR imaging. Susceptibility-weighted images were assessed by 2 neuroradiologists independently for the presence of cerebral microhemorrhages.

RESULTS: Our cohort included 146 veterans (132 men) who experienced remote blast-related mild traumatic brain injury (mean, 9.4 years; median, 9 years after injury). Twenty-one (14.4%) reported loss of consciousness for <30 minutes. Seventy-seven subjects (52.7%) had 1 episode of blast-related mild traumatic brain injury; 41 (28.1%) had 2 episodes; and 28 (19.2%) had >2 episodes. No cerebral microhemorrhages were identified in any subject, as opposed to the frequency of SWI-detectable cerebral microhemorrhages following blunt-related mild traumatic brain injury in the civilian population, which has been reported to be as high as 28% in the acute and subacute stages.

CONCLUSIONS: Our results may reflect differences in pathophysiology and the mechanism of injury between blast- and blunt-related mild traumatic brain injury. Additionally, the chronicity of injury may play a role in the detection of cerebral microhemorrhages.

ABBREVIATIONS: CMH = cerebral microhemorrhages; CTE = chronic traumatic encephalopathy; mTBI = mild traumatic brain injury; TBI = traumatic brain injury

Blast-related traumatic brain injury (TBI) is of considerable interest in the study of military head trauma due to ongoing United States military deployments in the Middle East and the frequency of exposure to improvised explosive devices.^{1,2} Ten-to-twenty percent of veterans returning from Iraq and Afghanistan are estimated to have had TBI with blast exposure, with >75% of these classified as mild traumatic brain injury (mTBI) by the

American Congress of Rehabilitative Medicine criteria.²⁻⁴ Blast-related TBI results from blast wave-induced changes in atmospheric pressure.⁵ It is clear from several recent studies that blast-related mTBI is associated with remarkable clinical impact,⁶ and chronic traumatic encephalopathy (CTE) has been described on postmortem examinations in individuals with exposure to repeat episodes.⁷ How a pressure wave damages the brain is the subject of debate dating back to the post-World War II period.⁸⁻¹⁰ A few recent reports using in vivo diffusion MR imaging showed a reduction in white matter fractional anisotropy in patients with blast-related mTBI¹¹⁻¹⁵ in a pattern that may be distinct from civilian blunt-related mTBI.¹⁶ It has been suggested that blast-related mTBI represents a unique injury mechanism distinct from blunt head trauma.^{9,17,18} There is current interest in specifically characterizing patients who have experienced blast-related mTBI and in determining whether there are unique features of this type of injury.

Cerebral microhemorrhage is a clear imaging biomarker associated with mTBI seen distinctly on conventional MR imaging using susceptibility-weighted imaging.^{19,20} Studies in civilians

Received February 3, 2018; accepted after revision April 4.

From the Departments of Radiology (E.L., C.M., Y.W.L.) and Psychiatry (J.N., M.Q., D.A.-A., C.M.), Steven and Alexandra Cohen Veterans Center for Posttraumatic Stress and Traumatic Brain Injury, New York University Langone Medical Center, New York, New York; and Sackler Faculty of Medicine (E.L.), Tel Aviv University, Tel Aviv, Israel.

Eyal Lotan is a recipient of Fellowship Grants from the American Physicians Fellowship for Medicine in Israel and from the Dr. Pinchas Borenstein Talpiot Medical Leadership Program 2013.

Main findings previously presented at: Annual Meeting of the American Society of Neuroradiology and the Foundation of the ASNR Symposium, April 20–27, 2017; Long Beach, California.

Please address correspondence to Yvonne W. Lui, MD, 660 1st Ave, Room 336, New York, NY 10016; e-mail: yvonne.lui@nyumc.org

<http://dx.doi.org/10.3174/ajnr.A5688>

following acute and subacute blunt mTBI have reported that the frequency of SWI-detected cerebral microhemorrhages (CMH) ranged from 19% to 28%.²¹⁻²⁴ A few recent works have suggested a lower prevalence in military personnel with chronic mTBI compared with civilians,^{3,25,26} though these studies were of mixed cohorts, including both blast- and blunt-related TBI and a range of injury severity.^{3,25} Riedy et al³ and Liu et al²⁵ found an approximately 3%–4% prevalence of CMH in subjects with a mixed history of blast- and blunt-related mTBI. The true prevalence of CMH in blast-related mTBI is not known. The purpose of the current study was to characterize CMH in military service members with chronic blast-related mTBI.

MATERIALS AND METHODS

Participants and Measures

Subjects in this study were drawn from an ongoing prospective study of military veterans performed at the NYU Langone Medical Center. The study was approved by the local institutional review board. All participants provided written informed consent. Inclusion criteria for this study were the following: military service in Operation Enduring Freedom, Operation Iraqi Freedom, and/or Operation New Dawn; between 18 and 70 years; and clinical diagnosis of mTBI in conjunction with close proximity to a blast explosion without concomitant blunt traumatic head injury based on the Department of Veterans Affairs and the Department of Defense definition of mTBI²⁷ (including altered mental state for <24 hours and no or <30 minutes loss of consciousness) as elicited by the Ohio State University TBI Identification Method–Short Form.²⁸ Subjects were excluded with a history of comorbid major neurologic disorder or systemic illness, a history of severe drug use disorder, psychosis, suicidality, homicidality, a history of prior moderate or severe head injury, or contraindications to MR imaging. All participants completed a formal, self-report measure of postconcussion symptoms. Symptom severity and quantity were measured using the Concussion Symptom Inventory, a list of 12 symptoms that are graded in severity by the patient on a 7-point Likert scale.²⁹ The maximum Concussion Symptom Inventory score is 72, indicating maximum overall symptom severity. Additionally, to assess the impact of headache, we used the Headache Impact Test-6 score.³⁰ This score ranges between 36 and 78, with larger scores reflecting greater impact and a score of >50 considered an abnormal finding. All participants were administered the 2-factor model from the Wechsler Adult Intelligence Scale, 2nd ed,³¹ which uses vocabulary and matrix reasoning subtests to estimate intelligence quotient.

MR Imaging

Participants were imaged at 3T (Skyra; Siemens, Erlangen, Germany) using a 20-channel head coil. SWI was performed with the following parameters: TR = 29 ms, TE = 20 ms, flip angle = 15°, slice thickness = 2 mm, intersection gap = 0 mm, FOV = 158 × 220 mm, matrix = 261 × 448, generalized autocalibrating partially parallel acquisition factor = 2. Conventional MR imaging, including T1-weighted imaging, T2-weighted imaging, T2-weighted FLAIR imaging, and diffusion-weighted imaging, was also performed. SWI and conventional MR imaging sequences were reviewed independently by 2 neuroradiologists (1 second-

Table 1: Demographic and clinical characteristics (N = 146)

Variable	No.	%
Ethnicity		
White	84	57.5
Hispanic	31	21.2
African American	17	11.6
Asian	9	6.2
Other	5	3.4
Tours of duty		
0	7	4.8
1	55	37.7
2	48	32.9
3	19	13.0
≥4	17	11.6
Episodes of blast-related mTBI		
1	77	52.7
2	41	28.1
≥3	28	19.2
Hypertension	19	13.0

Table 2: Demographic and clinical characteristics (N = 146)^a

Variable	Mean	SD
Time since mTBI (yr)	9.4	6.2
Deployment time (yr)	5.7	3.5
WASI-II IQ (standard score)	106.6	13.3
HIT-6 score	45.8	9.3
CSI	12.5	14.0

Note:—WASI-II indicates Wechsler Adult Intelligence Scale, 2nd ed; IQ, intelligence quotient; HIT-6 = Headache Impact Test-6; CSI = Concussion Symptom Inventory.
^a The maximum CSI and HIT-6 score is 72, indicating maximum symptom severity.

year neuroradiology fellow [E.L.] and 1 attending neuroradiologist with >10 years of experience [Y.W.L.]). Susceptibility-weighted images were reviewed for quality in terms of susceptibility seen in expected locations such as venous structures and calcification of the choroid plexus, or for the presence of any artifacts. The presence of CMH was determined using the Greenberg criteria, including a round or ovoid signal at least half surrounded by brain parenchyma with a dipole effect on SWI phase imaging and distinct from other potential mimics (calcium deposits, bone, air, or vessel flow voids).^{32,33}

RESULTS

One-hundred forty-six subjects were identified with a history of blast-related mTBI (132 men, 14 women). Demographic and clinical data for the present sample are reported in Tables 1 and 2. The mean age was 32.8 ± 7.4 years (median, 31 years; range, 22–66 years). The time interval from the last injury to MR imaging ranged from 1 to 31 years (mean, 9.4 ± 6.2 years; median, 9 years). Sixty-nine subjects (47.3%) had ≥2 episodes. Twenty-one (14.4%) reported loss of consciousness with their injury of <30 minutes, and 85.6% had altered mental status. Subjects had a normal distribution of IQ and demonstrated mild headache pain and postconcussive symptoms (Tables 1 and 2). No CMH were detected by either neuroradiologist. One subject (1%) had cerebellar ectopia, 7 (5%) had developmental venous anomalies, 48 (33%) had some degree of white matter abnormality (ie, T2 hyperintensity), 3 (2%) had arachnoid cysts, and 54 (37%) had sinus disease. No other structural abnormalities were identified. No images demonstrated artifacts warranting exclusion.

Table 3: Prevalence of CMH in civilian and military populations

Authors	Population	Mechanism of mTBI	Prevalence of CMH	Time since mTBI	MRI	Voxel Size (mm)
van der Horn et al (2017) ²⁴	Civilian	Blunt	15/54 (28%)	33 days	SWI (3T)	0.9 × 0.9 × 2
Trifan et al (2017) ³⁴	Civilian	Blunt	26/150 (17%)	29 months	SWI (3T)	0.5 × 0.5 × 2
Toth et al (2018) ³⁵	Civilian	Blunt	1/13 (8%)	2 years	SWI (3T)	1.0 × 0.9 × 1.5
Huang et al (2015) ²²	Civilian	Blunt	23/111 (23%)	25 days	SWI (3T)	0.5 × 0.5 × 2
Wang et al (2014) ²³	Civilian	Blunt	32/165 (19%)	≤3 days	SWI (3T)	0.7 × 0.7 × 1.2
Yuh et al (2013) ²¹	Civilian	Blunt	23/98 (23%)	12 days	T2*-weighted GRE (1.5/3T)	NA
Topal et al (2008) ³⁶	Civilian	Blunt	4/40 (10%)	<1 day	T2*-weighted GRE (1.5T)	NA
Tate et al (2017) ²⁶	Military members	Mixed blunt and blast	9/77 (12%)	309 days	SWI (3T)	1.0 × 0.9 × 1.5
Liu et al (2016) ²⁵	Military members	Mixed blunt and blast	18/559 (3%)	1325 days	SWI (3T)	0.5 × 0.9 × 1.5
Riedy et al (2016) ³	Military members	Mixed blunt and blast	29/768 (4%)	1381 days	SWI (3T)	0.5 × 0.9 × 1.5
Current study (2018)	Military members	Blast	0/146 (0%)	9 years	SWI (3T)	0.5 × 0.6 × 2

Note:—NA indicates not applicable; GRE, gradient recalled-echo.

DISCUSSION

In this cohort of 146 veterans with exposure to chronic blast-related mTBI, with approximately half exposed to multiple blast episodes in multiple tours during 5 years of deployment time, no foci of CMH were detected at 3T MR imaging using SWI. The overall prevalence of CMH in our cohort of well-characterized subjects with a history of chronic military blast-related mTBI was low compared with previous reports of civilian blunt-related mTBI.^{21-24,34-36} There is a mix of literature and findings in terms of the mechanism of injury (blunt or mixed population of blunt- and blast-related mTBI), prevalence of CMH, variable cohorts (military or civilian), variable time since injury, and the MR imaging techniques used for CMH detection. The literature is summarized in Table 3.^{3,21-26,34-36} Our findings are in keeping with Liu et al²⁵ and Riedy et al,³ who reported 3%–4% prevalence of CMH in a mixed group of military service members with a chronic history of either blunt- or blast-related mTBI. Technical differences between the current study and prior studies do not account for differences in CMH prevalence. The acquisition and protocol used in the current study are comparable with those in multiple other recent studies (Table 3).

The undetectable prevalence of CMH in the current cohort of 146 subjects with blast-related mTBI supports the evolving notion that blast-related mTBI has not only a unique mechanism of injury but also a unique pathophysiology that may be distinct from blunt trauma-induced mTBI.^{9,17,18} In addition, despite the longstanding idea that brain hemosiderin remains in clusters of iron-laden macrophages in perivascular spaces for the long term,³⁷⁻³⁹ there may be variability in the detection of CMH relating to the evolution of blood products, particularly in the acute and sub-acute phases after injury.⁴⁰ The sensitivity for CMH may diminish with time as has been suggested by Liu et al.²⁵ Furthermore, in an 8-year longitudinal study of nontraumatic CMH using SWI, the hemorrhages persisted across time, with a slight decrease in volume.⁴¹ Nevertheless, 2 recently published studies on civilian patients with chronic blunt-related mTBI demonstrated a CMH prevalence of 8%–17%.^{34,35} This suggests that while CMH may evolve between the acute and chronic phases after injury, the prevalence of chronic blast-related mTBI CMH that we report here remains lower than in previous reports of blunt-related injury.

Limitations of this study include a retrospective self-report of injury, though a prospective study including acutely injured subjects is challenging due to the limitations of MR imaging availability in remote military sites. Furthermore, the Ohio State University TBI Identification Method is considered a reliable and valid tool for assessing TBI and was selected on the basis of its high interrater reliability.²⁸ An additional limitation is the variability of the time since injury compared with the previous studies, particularly because there is evidence that CMH may evolve.

CONCLUSIONS

We found that no individuals in the 146 subjects with chronic blast-related mTBI had evidence of CMH on 3T SWI. This finding may suggest a substantially lower prevalence of CMH in this cohort of subjects with blast-related mTBI compared with previous reports, primarily in civilian chronic blunt-related mTBI,^{34,35} and may reflect differences in the mechanism and pathophysiology of injury. However, due to possible degradation of CMH with time, the chronicity of injury may play a role in the detection of CMH, and future studies will be needed to assess the prevalence of CMH in the more acute settings.

Disclosures: The project described was made possible with support by grants from the Steven A. and Alexandra M. Cohen Foundation, Inc. and Cohen Veterans Bioscience, Inc. (CVB) to NYU School of Medicine. The content is solely the responsibility of the authors and does not necessarily represent the official views of the Foundation or CVB.

REFERENCES

- Shively SB, Perl DP. **Traumatic brain injury, shell shock, and post-traumatic stress disorder in the military: past, present, and future.** *J Head Trauma Rehabil* 2012;27:234–39 CrossRef Medline
- Hoge CW, McGurk D, Thomas JL, et al. **Mild traumatic brain injury in U.S. soldiers returning from Iraq.** *N Engl J Med* 2008;358:453–63 CrossRef Medline
- Riedy G, Senseney JS, Liu W, et al. **Findings from structural MR imaging in military traumatic brain injury.** *Radiology* 2016;279:207–15 CrossRef Medline
- Kay T, Harrington DE, Adams R, et al. **Definition of mild traumatic brain injury.** *J Head Trauma Rehabil* 1993;8:86–87 CrossRef
- DePalma RG, Burris DG, Champion HR, et al. **Blast injuries.** *N Engl J Med* 2005;352:1335–42 CrossRef Medline
- MacDonald CL, Barber J, Jordan M, et al. **Early clinical predictors of**

- 5-year outcome after concussive blast traumatic brain injury. *JAMA Neurol* 2017;74:821–29 CrossRef Medline
7. Mayer AR, Quinn DK, Master CL. **The spectrum of mild traumatic brain injury: a review.** *Neurology* 2017;89:623–32 CrossRef Medline
 8. Denny-Brown D. **Cerebral concussion.** *Physiol Rev* 1945;25:296–325 CrossRef
 9. Elder GA, Stone JR, Ahlers ST. **Effects of low-level blast exposure on the nervous system: is there really a controversy?** *Front Neurol* 2014; 5:269 CrossRef Medline
 10. Courtney A, Courtney M. **The complexity of biomechanics causing primary blast-induced traumatic brain injury: a review of potential mechanisms.** *Front Neurol* 2015;6:221 CrossRef Medline
 11. Ivanov I, Fernandez C, Mitsis EM, et al. **Blast exposure, white matter integrity, and cognitive function in Iraq and Afghanistan combat veterans.** *Front Neurol* 2017;8:127 CrossRef Medline
 12. Mac Donald CL, Barber J, Andre J, et al. **5-Year imaging sequelae of concussive blast injury and relation to early clinical outcome.** *Neuroimage Clin* 2017;14:371–78 CrossRef Medline
 13. Trotter BB, Robinson ME, Milberg WP, et al. **Military blast exposure, ageing and white matter integrity.** *Brain* 2015;138:2278–92 CrossRef Medline
 14. Mac Donald CL, Johnson AM, Cooper D, et al. **Detection of blast-related traumatic brain injury in U.S. military personnel.** *N Engl J Med* 2011;364:2091–100 CrossRef Medline
 15. Taber KH, Hurley RA, Haswell CC, et al. **White matter compromise in veterans exposed to primary blast forces.** *J Head Trauma Rehabil* 2015;30:E15–25 CrossRef Medline
 16. Davenport ND, Lim KO, Armstrong MT, et al. **Diffuse and spatially variable white matter disruptions are associated with blast-related mild traumatic brain injury.** *Neuroimage* 2012;59:2017–24 CrossRef Medline
 17. Bhattacharjee Y. **Neuroscience: shell shock revisited—solving the puzzle of blast trauma.** *Science* 2008;319:406–08 CrossRef Medline
 18. Fischer B, Parsons M, Durgerian S, et al. **Neural activation during response inhibition differentiates blast from mechanical causes of mild to moderate traumatic brain injury.** *J Neurotrauma* 2014;31: 169–79 CrossRef Medline
 19. Haacke EM, Mittal S, Wu Z, et al. **Susceptibility-weighted imaging: technical aspects and clinical applications, part 1.** *AJNR Am J Neuroradiol* 2009;30:19–30 CrossRef Medline
 20. Bigler ED, Maxwell WL. **Neuropathology of mild traumatic brain injury: relationship to neuroimaging findings.** *Brain Imaging Behav* 2012;6:108–36 CrossRef Medline
 21. Yuh EL, Mukherjee P, Lingsma HF, et al; TRACK-TBI Investigators. **Magnetic resonance imaging improves 3-month outcome prediction in mild traumatic brain injury.** *Ann Neurol* 2013;73:224–35 CrossRef Medline
 22. Huang YL, Kuo YS, Tseng YC, et al. **Susceptibility-weighted MRI in mild traumatic brain injury.** *Neurology* 2015;84:580–85 CrossRef Medline
 23. Wang X, Wei XE, Li MH, et al. **Microbleeds on susceptibility-weighted MRI in depressive and non-depressive patients after mild traumatic brain injury.** *Neurol Sci* 2014;35:1533–39 CrossRef Medline
 24. van der Horn HJ, de Haan S, Spikman JM, et al. **Clinical relevance of microhemorrhagic lesions in subacute mild traumatic brain injury.** *Brain Imaging Behav* 2017 Jun 29. [Epub ahead of print] CrossRef Medline
 25. Liu W, Soderlund K, Senseney JS, et al. **Imaging cerebral microhemorrhages in military service members with chronic traumatic brain injury.** *Radiology* 2016;278:536–55 CrossRef Medline
 26. Tate DF, Gusman M, Kini J, et al. **Susceptibility weighted imaging and white matter abnormality findings in service members with persistent cognitive symptoms following mild traumatic brain injury.** *Mil Med* 2017;182:e1651–58 CrossRef Medline
 27. O’Neil ME, Carlson K, Storzbach D, et al. **Complications of mild traumatic brain injury in veterans and military personnel: a systematic review [Internet].** Washington, DC: Department of Veterans Affairs; 2013
 28. Corrigan JD, Bogner J. **Initial reliability and validity of the Ohio State University TBI Identification Method.** *J Head Trauma Rehabil* 2007;22:318–29 CrossRef Medline
 29. Randolph C, Millis S, Barr WB, et al. **Concussion Symptom Inventory: an empirically-derived scale for monitoring resolution of symptoms following sports-related concussion.** *Arch Clin Neuropsychol* 2009;24:219–29 CrossRef Medline
 30. Kosinski M, Bayliss MS, Bjorner JB, et al. **A six-item short-form survey for measuring headache impact: the HIT-6.** *Qual Life Res* 2003; 12:963–74 CrossRef Medline
 31. Wechsler D. *Wechsler Test of Adult Reading: WTAR.* San Antonio; Psychological Corporation; 2001
 32. Greenberg SM, Vernooij MW, Cordonnier C, et al; Microbleed Study Group. **Cerebral microbleeds: a guide to detection and interpretation.** *Lancet Neurol* 2009;8:165–74 CrossRef Medline
 33. Greenberg SM, Finklestein SP, Schaefer PW. **Petechial hemorrhages accompanying lobar hemorrhage: detection by gradient-echo MRI.** *Neurology* 1996;46:1751–54 CrossRef Medline
 34. Trifan G, Gattu R, Haacke EM, et al. **MR imaging findings in mild traumatic brain injury with persistent neurological impairment.** *Magn Reson Imaging* 2017;37:243–51 CrossRef Medline
 35. Toth A, Kornyei B, Kovacs N, et al. **Both hemorrhagic and non-hemorrhagic traumatic MRI lesions are associated with the microstructural damage of the normal appearing white matter.** *Behav Brain Res* 2018;340:106–16 CrossRef Medline
 36. Topal NB, Hakyemez B, Erdogan C, et al. **MR imaging in the detection of diffuse axonal injury with mild traumatic brain injury.** *Neurol Res* 2008;30:974–78 CrossRef Medline
 37. Shoamanesh A, Kwok CS, Benavente O. **Cerebral microbleeds: histopathological correlation of neuroimaging.** *Cerebrovasc Dis* 2011; 32:528–34 CrossRef Medline
 38. Roob G, Fazekas F. **Magnetic resonance imaging of cerebral microbleeds.** *Curr Opin Neurol* 2000;13:69–73 CrossRef Medline
 39. Roob G, Lechner A, Schmidt R, et al. **Frequency and location of microbleeds in patients with primary intracerebral hemorrhage.** *Stroke* 2000;31:2665–69 CrossRef Medline
 40. Toth A, Kovacs N, Tamas V, et al. **Microbleeds may expand acutely after traumatic brain injury.** *Neurosci Lett* 2016;617:207–12 CrossRef Medline
 41. Daugherty AM, Raz N. **Incident risk and progression of cerebral microbleeds in healthy adults: a multi-occasion longitudinal study.** *Neurobiol Aging* 2017;59:22–29 CrossRef Medline

Improved Detection of New MS Lesions during Follow-Up Using an Automated MR Coregistration-Fusion Method

 A. Galletto Pregliasco,  A. Collin,  A. Guéguen,  M.A. Metten,  J. Aboab,  R. Deschamps,  O. Gout,  L. Duron,  J.C. Sadik,  J. Savatovsky, and  A. Lecler



ABSTRACT

BACKGROUND AND PURPOSE: MR imaging is the key examination in the follow-up of patients with MS, by identification of new high-signal T2 brain lesions. However, identifying new lesions when scrolling through 2 follow-up MR images can be difficult and time-consuming. Our aim was to compare an automated coregistration-fusion reading approach with the standard approach by identifying new high-signal T2 brain lesions in patients with multiple sclerosis during follow-up MR imaging.

MATERIALS AND METHODS: This prospective monocenter study included 94 patients (mean age, 38.9 years) treated for MS with dimethyl fumarate from January 2014 to August 2016. One senior neuroradiologist and 1 junior radiologist checked for new high-signal T2 brain lesions, independently analyzing blinded image datasets with automated coregistration-fusion or the standard scroll-through approach with a 3-week delay between the 2 readings. A consensus reading with a second senior neuroradiologist served as a criterion standard for analyses. A Poisson regression and logistic and γ regressions were used to compare the 2 methods. Intra- and interobserver agreement was assessed by the κ coefficient.

RESULTS: There were significantly more new high-signal T2 lesions per patient detected with the coregistration-fusion method (7 versus 4, $P < .001$). The coregistration-fusion method detected significantly more patients with at least 1 new high-signal T2 lesion (59% versus 46%, $P = .02$) and was associated with significantly faster overall reading time (86 seconds faster, $P < .001$) and higher reader confidence (91% versus 40%, $P < 1 \times 10^{-4}$). Inter- and intraobserver agreement was excellent for counting new high-signal T2 lesions.

CONCLUSIONS: Our study showed that an automated coregistration-fusion method was more sensitive for detecting new high-signal T2 lesions in patients with MS and reducing reading time. This method could help to improve follow-up care.

ABBREVIATIONS: CF = coregistration-fusion; HST2 = high-signal T2; IQR = interquartile range

MR imaging is the key examination in the diagnosis and follow-up of patients with MS, as emphasized by the McDonald Criteria^{1,2} or the more recent Magnetic Resonance Imaging in Multiple Sclerosis (MAGNIMS) guidelines.^{3,4} MR imaging is of great value during follow-up care when new high-signal T2 (HST2) intensity lesions provide an objective indication of an active disease process in addition to clinical presentation, requiring potential therapeutic changes from providers.^{5,6}

However, identifying new lesions when scrolling through 2

follow-up examinations is time-consuming and error-prone and can be extremely difficult in the case of high lesion burden. A few studies have shown that methods such as subtraction or registration could improve the detection of new HST2 lesions, but these approaches to imaging may not be practical in many clinical environments.⁷⁻¹²

The purpose of our study was to evaluate the efficacy of an automated coregistration-fusion (CF) approach during follow-up for patients with MS.

MATERIALS AND METHODS

Research Design

We conducted a retrospective study in a tertiary referral center specialized in treating neurologic diseases, based on a prospective study data base (Monitoring of Patients Followed for a Multiple Sclerosis and Treated by Dimethyl-fumarate, NCT02047097; www.clinicaltrials.gov). This study was approved by a National Research Ethics Board and adhered to the tenets of the Declara-

Received January 9, 2018; accepted after revision April 11.

From the Departments of Radiology (A.G.P., A.C., L.D., J.C.S., J.S., A.L.) and Neurology (A.G., J.A., R.D., O.G.) and Clinical Research Unit (M.A.M.), Fondation Ophtalmologique Adolphe de Rothschild, Paris, France.

Please address correspondence to Augustin Lecler, MD, Department of Radiology, Fondation Ophtalmologique Adolphe de Rothschild, 25 rue Manin, 75019 Paris, France; e-mail: alecler@for.paris

 Indicates article with supplemental on-line photo.

 Indicates article with supplemental on-line video.

<http://dx.doi.org/10.3174/ajnr.A5690>

Patient characteristics

Characteristics	
No. of patients	94
Sex ratio (male/female)	42:52
Mean age (yr)	38.9 ± 11.3
Median No. of MRIs per patient (IQR)	3.5 (2–13)
Type of MS (No.)	
RRMS	79 (84.0%)
SPMS	10 (10.7%)
PPMS	5 (5.3%)
Mean EDSS score	3.2 ± 2.1
Mean disease duration (yr)	13.6 ± 9.2

Note:—EDSS indicates Expanded Disability Status Scale; RRMS, relapsing-remitting MS; SPMS, secondary-progressive MS; PPMS, primary-progressive MS.

tion of Helsinki (institutional review board 2016-A00896-45). Signed informed consent was obtained from all subjects. This study follows the Strengthening the Reporting of Observational Studies in Epidemiology guidelines.¹³

Patients

Inclusion criteria were the following: older than 18 years of age with a confirmed diagnosis of MS and treatment with dimethyl fumarate and 2 MR imaging examinations, including 3D-FLAIR sequence, performed in our center on the same MR imaging machine, separated by an interval of at least 6 months.

From January 2014 to August 2016, ninety-four patients with MS were included in the study.

Chart Review

The following clinical data were noted at the time of inclusion: type of MS, year of symptom onset, duration of the disease, and the Expanded Disability Status Scale score.¹⁴ Clinical data are provided in the Table.

MR Imaging

All patients had the same MR imaging protocol, including 3D-FLAIR imaging, axial T2WI, 3D-spin-echo T1WI, and axial diffusion-weighted imaging. All imaging was performed on 2 machines: a 1.5T Achieva with a 16-channel head coil (Philips Healthcare, Best, the Netherlands) for 78 patients and a 3T Achieva with a 32-channel coil (Philips Healthcare) for 16 patients.

The 1.5T sequence parameters were as follows: 3D-FLAIR imaging (TR/TE = 7000/350 ms, TI = 2200 ms, voxel size = 1.15 × 1.14 × 1.3 mm³, FOV = 250 × 217 × 182 mm³, total acquisition time = 4 minutes 47 seconds) and 3D-spin-echo T1WI (TR/TE = 400/9.4 ms, voxel size = 1.1 × 1.1 × 1.1 mm³, FOV = 250 × 250 × 180 mm³, total acquisition time = 3 minutes 59 seconds).

The 3T sequence parameters were as follows: 3D-FLAIR imaging (TR/TE = 8000/388 ms, TI = 2400 ms, voxel size = 0.9 × 0.9 × 1 mm³, FOV = 240 × 240 × 175 mm³, total acquisition time = 4 minutes 24 seconds) and 3D-spin-echo T1WI (TR/TE = 500/27 ms, voxel size = 1 × 1 × 1 mm³, FOV = 252 × 252 × 200 mm³, total acquisition time = 3 minutes 37 seconds).

Coregistration-Fusion

We performed the CF process on the workstation that we routinely use during our clinical sessions (Advantage Workstation 4.6; GE Healthcare, Milwaukee, Wisconsin). The CF process available as standard on the Advantage Workstation console is

based on a software algorithm that normalizes examinations spatially using rigid body registration. Once the MR images are acquired, they are automatically transmitted to our usual reading console located in our usual reading room. The reader then manually selects the sequences, the 3D-FLAIR sequences in our study, of the current and previous examinations to be analyzed and launches the CF process.

The CF process is then carried out automatically. The 2 images are automatically coregistered and merged, and one of the images is artificially colored. We have arbitrarily chosen to color the old examination blue so that new lesions appear white while pre-existing lesions appear blue. The standard algorithm does not perform either suppression of healthy white matter or any preselection of the HST2 lesions before applying the colors. There is no automated thresholding. The degree of transparency and the intensity of the color applied are dependent on the MR imaging signal intensity and are set manually by the operator. Thus, the areas of lower MR imaging intensity correspond to the areas of maximal transparency and do not appear blue. The transparency ramp is globally linear. Globally, readers modify these settings so the healthy white matter has a minimal intensity, and the MS lesions have the highest intensity, as shown in On-line Video 1. In our study, readers could adjust the window width. The reading console finally displays 3 separate synchronized screens: 2 screens with the 3D-FLAIR sequences of the current and previous examination and a third screen with the fused sequences. The reader can thus analyze the images and check the native images to confirm the presence or absence of a new lesion. The merged images are automatically sent to the PACS to be available for clinicians or later review. Fig 1 artificially details the steps of the CF process, which are performed automatically by the workstation. On-line Video 1 shows a screenshot of the entire process being performed, and On-line Video 2 shows the final result after CF.

Image Analysis

In our 94 patients, we compared a single pair of separate MR imaging examinations spaced at least 6 months apart. Two radiologists, blinded to clinical data, read independently and in random order the MR imaging examinations using a standard method (ie, scrolling through a side-by-side comparison of the most recent and previous 3D-FLAIR images) or an automated coregistration-fusion method, with at least 3 weeks between the 2 readings to avoid recognition. The first senior neuroradiologist was specialized in neuroimaging with 3 years of experience (A.G.), and the second was a junior radiologist with no experience in neuroimaging (A.C.). They did not have a time limit on their reading but were instructed to read the examinations under conditions of current clinical practice, doing their best to detect new lesions. A dedicated consensus reading session was performed with a third reader, a second senior neuroradiologist with 8 years of experience (A.L.), 6 weeks later to serve as a criterion standard for analysis. He performed his reading independent of the other authors and before statistical analysis. He could use both standard and coregistration-fusion approaches. Conditions were replicated 3 months later to assess intrareader agreement. All examinations were read on the same dedicated workstation.

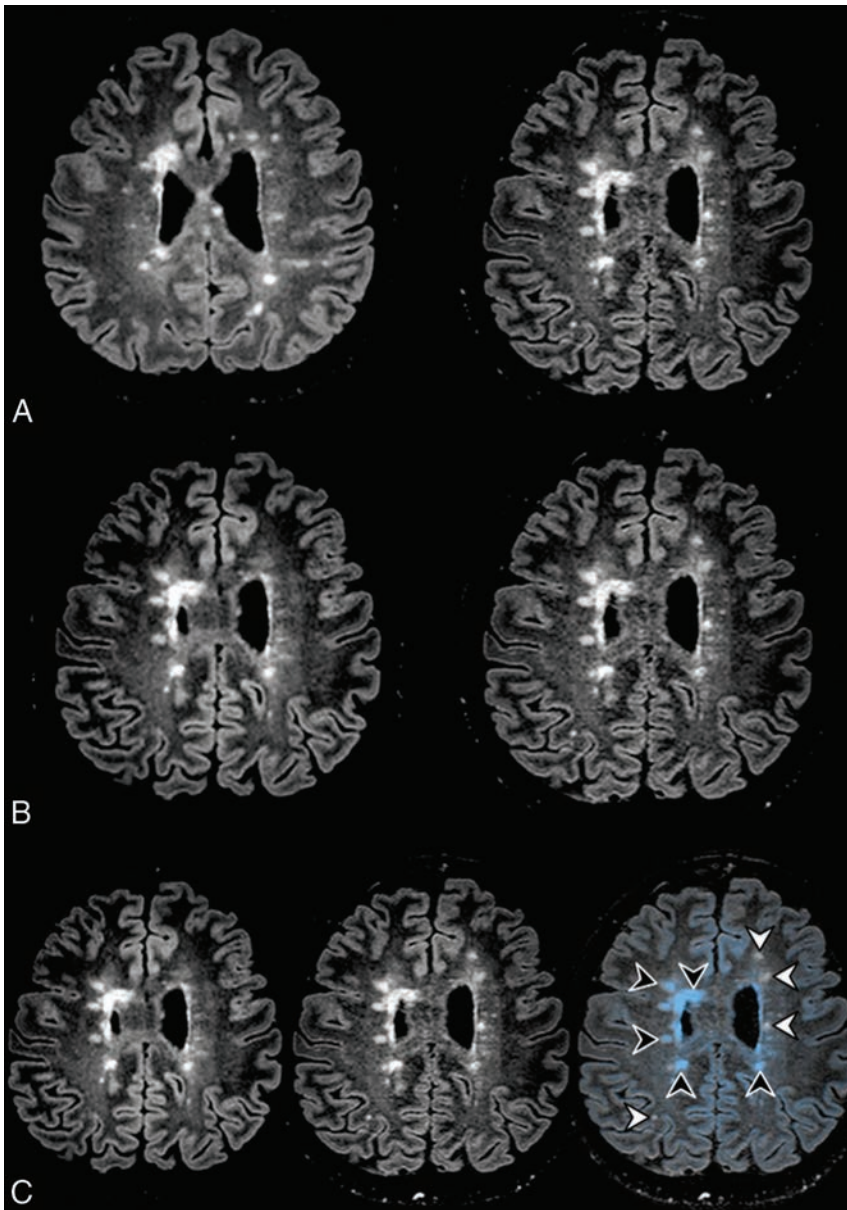


FIG 1. Automated MR imaging coregistration-fusion method. *A*, First step of the CF method: Two 3D-FLAIR images in the axial plane (the previous one on the *left* and the new one on the *right*) appear side by side. Note that the ventricles and cerebral sulci are different in size and orientation due to differences in laterolateral and anteroposterior orientation in the image acquisition. *B*, Second step of CF method: The 2 examinations are perfectly coregistered and linked so that the images can be scrolled together to display the same anatomic level. *C*, Third step: The previous (*left*) examination and the current one (*middle*) are merged, and the fusion image (*right*) is automatically artificially colored blue. All the pre-existing lesions are blue (*black arrowheads*), whereas the new ones are white (*white arrowheads*), highlighting their presence to the reader.

Readers assessed the following characteristics on a standardized report form:

- The presence and number of new HST2 lesions defined as nonartifactual, new, bright areas clearly visible against the background.
- The volume of lesion burden classified as low (<10 HST2) or high (>10 HST2).
- Repartition of the lesions classified as individual lesion spots and converging lesions.
- Reading time measured by an independent timekeeper, starting from the selection of the patient from electronic medical re-

ports up to the end of the reading. Reading time included CF processing time. The end of the reading was decided by the reader after identifying all the lesions.

- The quality of the examinations classified as excellent, moderate, or poor.
- The degree of reading confidence classified as excellent, moderate, or poor.
- Failure or success of coregistration-fusion.

Statistical Analysis

Quantitative variables were presented as means and medians (interquartile range [IQR]), and categorical variables, as percentages. Mixed models were fit to compare the 2 reading methods: A Poisson regression was used for the number of new HST2 lesions; a logistical regression, for binary variables such as the presence of at least 1 new HST2 lesion or the degree of confidence; and a γ regression, for the reading time. The Light κ coefficient¹⁵ and intraclass correlation coefficient¹⁶ were used to assess interobserver and intraobserver agreement for the presence of at least 1 new HST2 lesion and for the number of new HST2 lesions. According to the Landis and Koch¹⁵ guidelines, values of $\kappa < 0$ indicate no agreement; 0–0.20, slight; 0.21–0.40, fair; 0.41–0.60, moderate; 0.61–0.80, substantial; and 0.81–1, excellent agreement.

Poor, fair, good, and excellent agreement categories were qualified according to Cicchetti.¹⁶ A *P* value below .05 was considered statistically significant. Analyses were performed using R, Version 3.3.2 (<http://www.r-project.org/>).¹⁷ The statistical analysis was conducted by M.A.M.

RESULTS

Demographic and Clinical Characteristics

Ninety-four patients (188 paired MR imaging studies) with a confirmed diagnosis of treated MS (52 women and 42 men; mean age, 38.9 ± 11.3 years) were included in the study from January 2014 to August 2016. The mean Expanded Disability Status Scale score was 3.2 ± 2.1 . The mean disease duration was 13.6 ± 9.2 years. Demographic and clinical data are presented in the Table.

Imaging

Comparison of the Reading Methods. There were significantly more new HST2 lesions per patient discovered with the CF

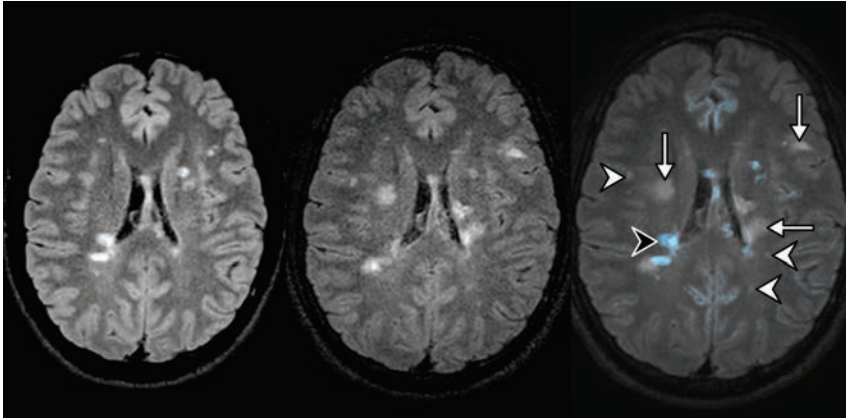


FIG 2. Previous and new 3D-FLAIR MR imaging of a 35-year-old woman with MS. The coregistration-fusion image (right) shows multiple new HST2 lesions; some of them are obvious (arrows), while others are discrete and potentially difficult to detect using the standard method (white arrowheads). Note that the CF method also allows the identification of a lesion that shrank during follow-up (black arrowhead).

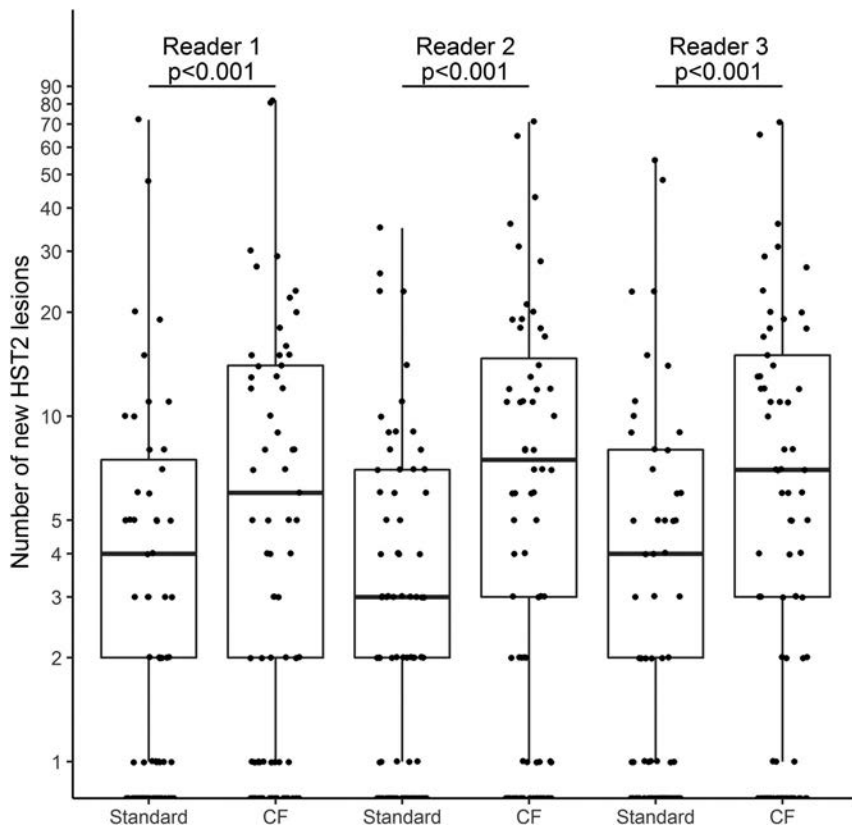


FIG 3. Comparison of the number of new HST2 lesions for each reader. Significant differences are indicated with the P value. The median number of new HST2 lesions is represented by the black line.

method as opposed to the standard one: 7 (IQR, 12) versus 4 (IQR, 6) ($P < .001$) (Figs 2 and 3). Forty-seven patients had more lesions discovered with the CF method compared with the standard method, whereas 6 patients had more lesions discovered with the standard method compared with the CF (On-line Figure).

There were significantly more patients with at least 1 new HST2 lesion discovered with the CF method compared with the standard method (57 [61%] versus 43 [46%], $P = .02$) (Fig 4).

Seventeen patients had at least 1 new HST2 lesion discovered with the CF method compared with the standard method, and 3 had at least 1 new HST2 discovered with the standard method compared with the CF method. Twenty-two (23.4%) patients had at least 3 new HST2 lesions detected with the CF method but fewer than 2 new HST2 lesions with the standard method. MR imaging data for all readers are presented in Fig 3.

Detection of new HST2 lesions was significantly higher among patients with a high lesion burden or with converging lesions with the CF method as opposed to the standard method ($P < .001$ and $P < .001$, respectively).

Reading time was significantly reduced with the CF method versus the standard one: 106 ± 31 seconds, including 20 ± 5 seconds of processing, versus 192 ± 54 seconds ($P < .001$). MR imaging data for all readers are presented in Fig 5.

The dichotomized degree of confidence (excellent and moderate versus poor) was significantly higher with the CF method as opposed to the standard one: 91% versus 40% ($P < 1 \times 10^{-4}$).

Inter- and Intraobserver Agreement

Interobserver agreement was substantial for the presence of at least 1 new HST2 lesion ($\kappa = 0.80$ [IQR, 0.67–0.88] and 0.75 [IQR, 0.63–0.84]) and excellent for counting new HST2 lesions (intraclass correlation coefficient = 0.97 [IQR, 0.94–0.98] and 0.88 [IQR, 0.83–0.92]) with the CF and the standard methods, respectively.

Intraobserver agreement was excellent for the presence of at least 1 new HST2 lesion ($\kappa = 1$) and counting new HST2 lesions (intraclass correlation coefficient = 0.95 [0.67–0.99]) using the CF method.

DISCUSSION

Our study showed that the CF method was significantly more sensitive when detecting new HST2 lesions as opposed to the standard method, with a helpful reduction in reading time and significantly higher reader-reported confidence.

Our results are in accordance with the literature in which different optimized reading techniques have been compared with scrolling through images, as in subtraction techniques^{7,9,11,18,19} or with semiautomated¹² or automated^{8,10} assistive software plat-

forms. These methods have shown improvement in detecting new lesions and reducing radiologists' false-negative errors. Some authors now consider them the criterion standard for detecting new

HST2 lesions in MS studies.²⁰ Despite their benefits, optimized readings remain time-consuming,⁷ require specific software and training,¹² and ultimately may not be practical for most clinical environments. In our study, the CF method detected 80% more lesions than the standard one, which is within the range of 1.5–2.1 times more detections in reports on the advantages of optimized methods.^{12,21,22} To the best of our knowledge, no one has yet investigated the feasibility and efficacy of combining a coregistration and fusion imaging method in follow-up examination of patients with MS.

Guidelines state that routine brain imaging should be considered every 6 months to 2 years for all patients with relapsing MS.²³ Conventional side-by-side comparison is tiring, inefficient,

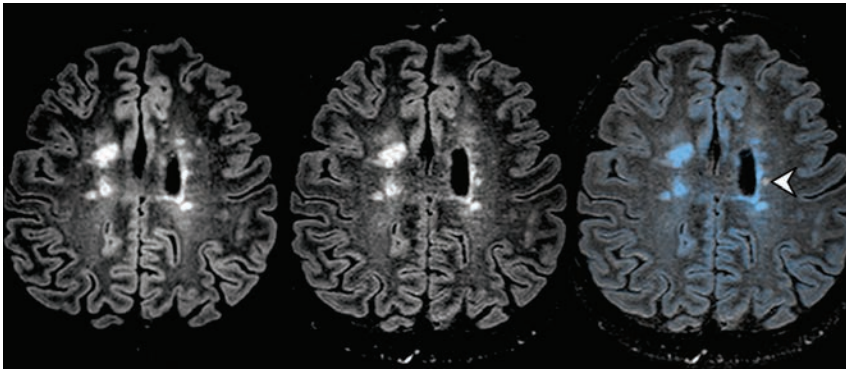


FIG 4. Previous and new 3D-FLAIR MR imaging of a 35-year-old woman with MS. The coregistration-fusion image (right) shows only 1 small HST2 lesion (white arrowhead) among several older blue ones.

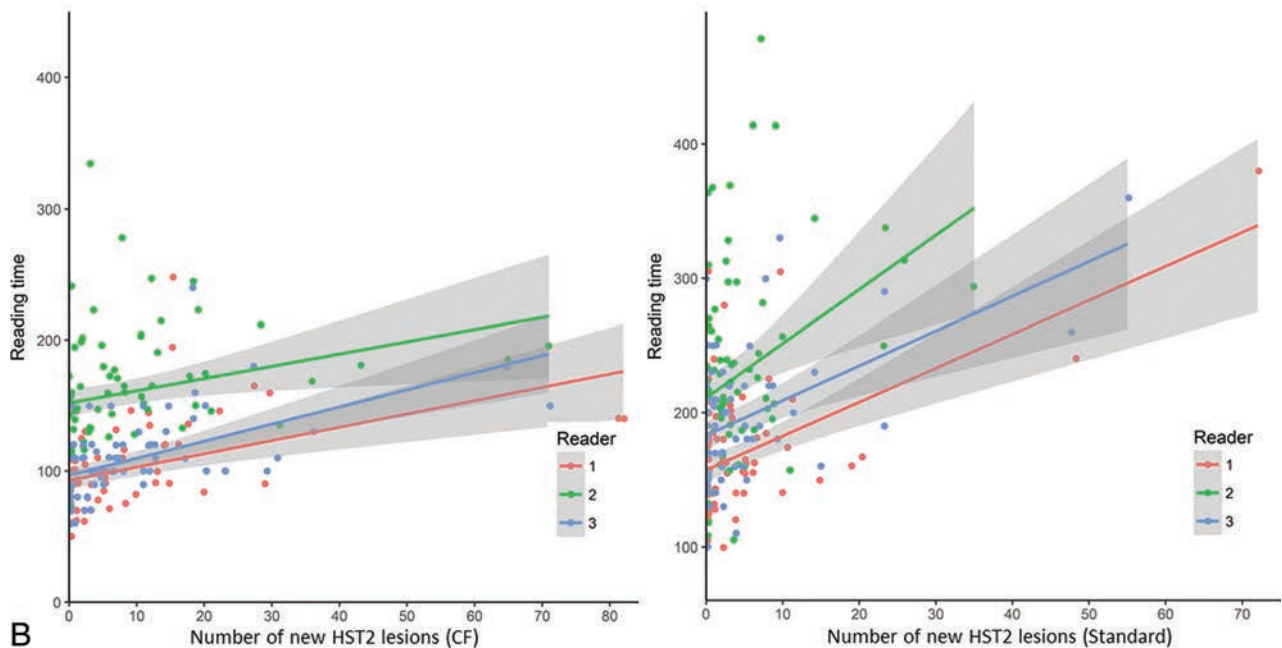
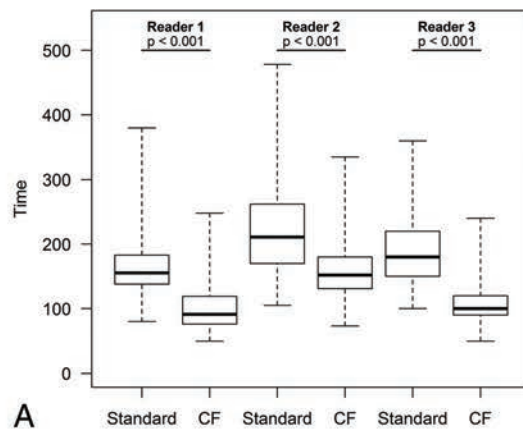


FIG 5. Comparison of the overall reading time for each reader. Significant differences are indicated with the *P* value (A). The reading time is indicated in seconds. Note the mild linear increase of the reading time for all readers when facing a higher lesion burden using the CF method as opposed to a much sharper increase with the standard method (B).

error-prone, and, moreover, not sufficiently reliable due to varying levels of training among readers.^{12,20} In our study, the CF method showed significantly reduced reading time with increased lesion detection. This kind of success supports accuracy and high-quality care in a frequently disrupted work environment.²⁴ The CF method is automated, can be easily performed in a few steps, and does not require any specific training. It is workable during routine clinical practice. This technique can be easily integrated into the workflow, unlike most assistive software and subtraction techniques. Furthermore, our study demonstrated a jump in reader confidence, suggesting that easier and more reliable answers could be integrated into care, especially in patients who already face a high lesion burden. Moreover, our results show that even a young radiologist not specialized in neuroradiology worked fast and accurately when looking for new HST2 lesions; this outcome is particularly interesting considering that non-neuroradiologists previously showed poorer detection rates when searching for new HST2 lesions compared with specialists.²⁰

Therapeutic decisions often hinge on searching for new lesions in patients with MS for whom positive detection normally indicates disease progression.²⁵⁻²⁷

Three or more new HST2 lesions were reported to be associated with a worse disability in patients treated with interferon- β ,²⁸ while a threshold of 5 new HST2 lesions has been used in the Modified Rio Score to predict therapeutic efficacy.²⁶ In our study, readers saw 23.4% of patients with at least 3 new HST2 lesions visible with the CF method but fewer than 2 using side-by-side comparison, meaning less advanced imaging leaves patients underdiagnosed and misclassified as having “no evidence of disease activity,” which is increasingly considered the treatment goal.²⁹

In addition to MR imaging, radiologists use gadolinium-based contrast agents when checking for new lesions indicating MS progression,²⁵ but the sensitivity and prognostic value of this marker alone are limited because lesions should have appeared in ≤ 3 weeks old to detect them.³⁰ Moreover, recent studies³¹ have suggested that gadolinium-based contrast agents could accumulate in the brains of patients who have undergone multiple contrast-enhanced MR imaging studies. Therefore, the most recent guidelines⁴ recommend that clinicians carefully evaluate the necessity of using gadolinium-based contrast agents. Therefore, an optimized HST2 lesion-detection method such as CF might be a sensitive way to assess lesion change during follow-up of patients with MS,³² while avoiding or reducing the use of gadolinium-based contrast agents.

European and American guidelines provide recommendations about MR imaging protocols for this patient population^{4,23} but lack consensus on how to use 3D sequences and offer nothing on advised reading methods. 3D sequences come highly recommended,^{23,33} largely because it is now feasible on most scanners to acquire 3D image datasets with isotropic resolution in clinically acceptable scan times. Our results support these recommendations, especially for 3D-FLAIR, because 3D sequences support accurate coregistration or subtraction methods³⁴ and increase accurate reading performance. New guidelines could include specific recommendations about improved reading methods such as CF.

Our study has limitations. First, the overall number of patients is relatively small. Second, we analyzed only MR imaging with 3D-FLAIR sequences, which are more easily coregistered than 2D sequences. The practice of using 3D sequences is not yet widespread in all hospitals or in private practice; thus, our results may not be applied in all centers. Third, a high number of patients were followed on a 1.5T MR machine, with performance reported to be less sensitive for detecting new HST2 lesions. Fourth, readers knew which method they were assessing, which could have led to a certain bias.

CONCLUSIONS

Our study showed that a CF method was significantly more sensitive when detecting new HST2 lesions as opposed to manually scrolling through 2 images, with significantly decreased reading time and significantly higher reader-reported confidence. It might be interesting to evaluate this method on different PACS and posttreatment systems in the future.

ACKNOWLEDGMENTS

Laura McMaster provided professional English-language medical editing of this article.

Disclosures: Antoine Guéguen—UNRELATED: Board Membership: Novartis, Merck, Roche; Consultancy: Novartis, Sanofi Genzyme; Grants/Grants Pending: CSL Bering; Payment for Lectures Including Service on Speakers Bureaus: Roche; Travel/Accommodations/Meeting Expenses Unrelated to Activities Listed: Teva Pharmaceutical Industries, Roche, Biogen, Sanofi Genzyme. Jennifer Aboab—UNRELATED: Board Membership: Merck Serono.

REFERENCES

1. Polman CH, Reingold SC, Banwell B, et al. **Diagnostic criteria for multiple sclerosis: 2010 revisions to the McDonald criteria.** *Ann Neurol* 2011;69:292–302 CrossRef Medline
2. Thompson AJ, Banwell BL, Barkhof F, et al. **Diagnosis of multiple sclerosis: 2017 revisions of the McDonald criteria.** *Lancet Neurol* 2018;17:162–73 CrossRef Medline
3. Filippi M, Rocca MA, Ciccarelli O, et al; MAGNIMS Study Group. **MRI criteria for the diagnosis of multiple sclerosis: MAGNIMS consensus guidelines.** *Lancet Neurol* 2016;15:292–303 CrossRef Medline
4. Wattjes MP, Rovira À, Miller D, et al; MAGNIMS study group. **Evidence-based guidelines: MAGNIMS consensus guidelines on the use of MRI in multiple sclerosis—establishing disease prognosis and monitoring patients.** *Nat Rev Neurol* 2015;11:597–606 CrossRef Medline
5. Erbayat Altay E, Fisher E, Jones SE, et al. **Reliability of classifying multiple sclerosis disease activity using magnetic resonance imaging in a multiple sclerosis clinic.** *JAMA Neurol* 2013;70:338–44 CrossRef Medline
6. Barkhof F, Simon JH, Fazekas F, et al. **MRI monitoring of immunomodulation in relapse-onset multiple sclerosis trials.** *Nat Rev Neurol* 2011;8:13–21 CrossRef Medline
7. Horsfield MA, Rocca MA, Pagani E, et al. **Estimating brain lesion volume change in multiple sclerosis by subtraction of magnetic resonance images.** *J Neuroimaging* 2016;26:395–402 CrossRef Medline
8. Battaglini M, Rossi F, Grove RA, et al. **Automated identification of brain new lesions in multiple sclerosis using subtraction images.** *J Magn Reson Imaging* 2014;39:1543–49 CrossRef Medline
9. Ganiler O, Oliver A, Diez Y, et al. **A subtraction pipeline for automatic detection of new appearing multiple sclerosis lesions in longitudinal studies.** *Neuroradiology* 2014;56:363–74 CrossRef Medline
10. Sweeney EM, Shinohara RT, Shea CD, et al. **Automatic lesion incidence estimation and detection in multiple sclerosis using multi-**

- sequence longitudinal MRI. *AJNR Am J Neuroradiol* 2013;34:68–73 CrossRef Medline
11. Patel N, Horsfield MA, Banahan C, et al. **Detection of focal longitudinal changes in the brain by subtraction of MR images.** *AJNR Am J Neuroradiol* 2017;38:923–27 CrossRef Medline
 12. van Heerden J, Rawlinson D, Zhang AM, et al. **Improving multiple sclerosis plaque detection using a semiautomated assistive approach.** *AJNR Am J Neuroradiol* 2015;36:1465–71 CrossRef Medline
 13. von Elm E, Altman DG, Egger M, et al; STROBE Initiative. **The Strengthening of Reporting of Observational Studies in Epidemiology (STROBE) statement: guidelines for reporting observational studies.** *Ann Intern Med* 2007;147:573–77 CrossRef Medline
 14. Kurtzke JF. **Rating neurologic impairment in multiple sclerosis: an Expanded Disability Status Scale (EDSS).** *Neurology* 1983;33:1444–52 CrossRef Medline
 15. Landis JR, Koch GG. **The measurement of observer agreement for categorical data.** *Biometrics* 1977;33:159–74 CrossRef Medline
 16. Cicchetti DV. **Guidelines, criteria, and rules of thumb for evaluating normed and standardized assessment instruments in psychology.** *Psychol Assess* 1994;6:284–90 CrossRef
 17. R statistical and computing software. <http://www.r-project.org/>. Accessed March 1, 2015
 18. Bilello M, Arkuszewski M, Nasrallah I, et al. **Multiple sclerosis lesions in the brain: computer assisted assessment of lesion load dynamics on 3D FLAIR MR images.** *Neuroradiol J* 2012;25:17–21 CrossRef Medline
 19. Tan IL, van Schijndel RA, Fazekas F, et al. **Image registration and subtraction to detect active T(2) lesions in MS: an interobserver study.** *J Neurol* 2002;249:767–73 CrossRef Medline
 20. Wang W, van Heerden J, Tacey MA, et al. **Neuroradiologists compared with non-neuroradiologists in the detection of new multiple sclerosis plaques.** *AJNR Am J Neuroradiol* 2017;38:1323–27 CrossRef Medline
 21. Moraal B, Meier DS, Poppe PA, et al. **Subtraction MR images in a multiple sclerosis multicenter clinical trial setting.** *Radiology* 2009;250:506–14 CrossRef Medline
 22. Tan IL, van Schijndel RA, Pouwels PJ, et al. **Serial isotropic three-dimensional fast FLAIR imaging: using image registration and subtraction to reveal active multiple sclerosis lesions.** *AJR Am J Roentgenol* 2002;179:777–82 CrossRef Medline
 23. Traboulsee A, Simon JH, Stone L, et al. **Revised recommendations of the Consortium of MS Centers Task Force for a standardized MRI protocol and clinical guidelines for the diagnosis and follow-up of multiple sclerosis.** *AJNR Am J Neuroradiol* 2016;37:394–401 CrossRef Medline
 24. Yu JP, Kansagra AP, Mongan J. **The radiologist's workflow environment: evaluation of disruptors and potential implications.** *J Am Coll Radiol* 2014;11:589–93 CrossRef Medline
 25. Trojano M, Tintore M, Montalban X, et al. **Treatment decisions in multiple sclerosis - insights from real-world observational studies.** *Nat Rev Neurol* 2017;13:105–18 CrossRef Medline
 26. Sormani MP, Rio J, Tintorè M, et al. **Scoring treatment response in patients with relapsing multiple sclerosis.** *Mult Scler* 2013;19:605–12 CrossRef Medline
 27. Freedman MS, Selchen D, Arnold DL, et al; Canadian Multiple Sclerosis Working Group. **Treatment optimization in MS: Canadian MS Working Group updated recommendations.** *Can J Neurol Sci* 2013;40:307–23 CrossRef Medline
 28. Sormani MP, Gasperini C, Romeo M, et al; MAGNIMS study group. **Assessing response to interferon- β in a multicenter dataset of patients with MS.** *Neurology* 2016;87:134–40 CrossRef Medline
 29. Bevan CJ, Cree BA. **Disease activity free status: a new end point for a new era in multiple sclerosis clinical research?** *JAMA Neurol* 2014;71:269–70 CrossRef Medline
 30. Cotton F, Weiner HL, Jolesz FA, et al. **MRI contrast uptake in new lesions in relapsing-remitting MS followed at weekly intervals.** *Neurology* 2003;60:640–46 CrossRef Medline
 31. Kanda T, Fukusato T, Matsuda M, et al. **Gadolinium-based contrast agent accumulates in the brain even in subjects without severe renal dysfunction: evaluation of autopsy brain specimens with inductively coupled plasma mass spectroscopy.** *Radiology* 2015;276:228–32 CrossRef Medline
 32. McNamara C, Sugrue G, Murray B, et al. **Current and emerging therapies in multiple sclerosis: implications for the radiologist, Part 1: mechanisms, efficacy, and safety.** *AJNR Am J Neuroradiol* 2017;38:1664–71 CrossRef Medline
 33. Vrenken H, Jenkinson M, Horsfield MA, et al; MAGNIMS Study Group. **Recommendations to improve imaging and analysis of brain lesion load and atrophy in longitudinal studies of multiple sclerosis.** *J Neurol* 2013;260:2458–71 CrossRef Medline
 34. Moraal B, Wattjes MP, Geurts JJ, et al. **Improved detection of active multiple sclerosis lesions: 3D subtraction imaging.** *Radiology* 2010;255:154–63 CrossRef Medline

Identification of Chronic Active Multiple Sclerosis Lesions on 3T MRI

M. Absinta, P. Sati, A. Fechner, M.K. Schindler, G. Nair, and D.S. Reich



ABSTRACT

BACKGROUND AND PURPOSE: MR imaging–pathologic studies have reported that paramagnetic rims on 7T susceptibility-based MR imaging identify, in vivo, the subset of MS lesions with compartmentalized inflammation at the lesion edge and associated remyelination failure. Here, we assessed the reliability of detecting these rims on high-resolution 3T phase images.

MATERIALS AND METHODS: High-resolution T2* and phase MR imaging was collected in 20 patients with MS at 3T (3D segmented EPI, 0.65 mm³) and 7T (2D gradient-echo, 0.2 × 0.2 × 1 mm) MR imaging. In each case, 5 discrete chronic (nonenhancing) MS lesions were selected on T2 FLAIR images for rim evaluation. Five raters experienced in MS imaging contributed to the rim assessment, of whom 3 worked independently on 3T data, and 2, on 7T data. Consensus agreement was reached for both 3T and 7T rim evaluations. Discrepancies between 3T and 7T were discussed, and consensus was reached.

RESULTS: Phase rims were seen in 34 lesions at 7T and in 36 lesions at 3T by consensus. Inter- and intrarater reliability were “substantial/good” both at 3T and 7T analysis (Cohen κ , >0.71). Based on consensus agreement, the reliability of rim visualization at 3T versus 7T was 0.78 (κ) with a pair-wise agreement of 90%. More lesions were judged to be false-positive or false-negative at 3T than at 7T.

CONCLUSIONS: Nearly all 7T paramagnetic rims can also be seen at 3T. Imaging at 3T opens the possibility of implementing paramagnetic rims as an outcome measure in multicenter, MR imaging–based clinical trials aimed at treating perilesional persistent inflammation and its potential effects on remyelination.

ABBREVIATIONS: EDSS = Expanded Disability Status Scale; QSM = Quantitative Susceptibility Mapping

In multiple sclerosis, plaques of demyelination, the hallmark of this disease, can present simultaneously at different pathologic stages.^{1,2} Especially relevant from a disease perspective are 2 types of chronic plaques that can be considered opposite ends of the pathologic spectrum: lesions in which, after active inflammatory demyelination, the repair process has been relatively efficient (leading to remyelination), and lesions in which

regeneration has completely failed, due, in part, to residual compartmentalized inflammation at the lesion margin (ie, chronic active/slowly expanding/smoldering lesions, henceforth denoted “chronic active”).^{1,2}

Chronic active lesions are pathologically characterized by a hypocellular demyelinated core and a hypercellular edge of activated microglia/macrophages related to smoldering inflammation and axonal degeneration.^{1,2} On MR imaging, these lesions have a characteristic paramagnetic rim on 7T susceptibility-based MR imaging sequences; the paramagnetic shift is due to the stable presence of iron-laden activated microglia/macrophages^{3–11} and, potentially, reactive astrocytes¹² at the lesion edge. Usually, paramagnetic rims are seen on 7T phase images, but a proportion can also be detected on 7T T2* magnitude images, mostly when iron content is higher.^{4–6,13,14} In the context of early lesion evolution, we recently reported that paramagnetic rims in active lesions colocalize with peripheral or centripetal gadolinium enhancement¹⁴ and that persistence of these rims after restoration of the blood-brain barrier (ie, approximately 3 months after initial demyelination) predicts failure of tissue repair and remyelination.¹⁰ There-

Received December 8, 2017; accepted after revision March 13, 2018.

From the Translational Neuroradiology Section (M.A., P.S., A.F., M.K.S., G.N., D.S.R.), Division of Neuroimmunology and Neurovirology, National Institute of Neurological Disorders and Stroke, National Institutes of Health, Bethesda, Maryland; and Department of Radiology (A.F.), Fondation Ophthalmologique Adolphe de Rothschild, Paris, France.

This work was supported by the Intramural Research Program of National Institute of Neurological Disorders and Stroke.

Please address correspondence to Daniel S. Reich, MD, PhD, Translational Neuroradiology Section/National Institute of Neurological Disorders and Stroke/National Institutes of Health, 10 Center Dr, MSC 1400, Building 10, Room 5C103, Bethesda, MD 20892; e-mail: daniel.reich@nih.gov

Indicates open access to non-subscribers at www.ajnr.org

Indicates article with supplemental on-line photo.

<http://dx.doi.org/10.3174/ajnr.A5660>

Table 1: Clinical and demographic data

Patient No.	Sex	Age (yr)	Clinical Phenotype	EDSS	Disease Duration (yr)	Disease-Modifying Treatment
1	Female	60	RR	1.5	11	Dimethyl fumarate
2	Female	66	Progressive	7	28	None
3	Male	56	Progressive	6	24	None
4	Male	47	RR	1.5	16	Daclizumab
5	Female	43	RR	2	43	None
6	Female	64	RR	1.5	9	None
7	Female	55	RR	1.5	2	Interferon β -1a
8	Male	36	RR	1	7	Glatiramer acetate
9	Male	61	Progressive	6.5	40	None
10	Female	51	Progressive	6.5	24	None
11	Female	35	RR	1	4	Dimethyl fumarate
12	Female	36	RR	2.5	18	Glatiramer acetate
13	Male	38	RR	0	1	None
14	Female	28	RR	1.5	1	None
15	Female	33	RR	2	1	None
16	Female	42	RR	2.5	10	Mycophenolate mofetil
17	Female	25	RR	2	1	Glatiramer acetate
18	Female	30	RR	1.5	8	None
19	Female	36	RR	1.5	9	Dimethyl fumarate
20	Female	71	RR	1	15	None

Note:—RR indicates relapsing-remitting.

after, in chronic lesions, rims have been shown to be stable during short-to-medium-term follow-up (up to 3.5 years)¹³⁻¹⁵ and are not known to be affected by current disease-modifying treatments. These results establish paramagnetic rims as potential outcome measures in MR imaging–based clinical trials of therapies that might treat perilesional persistent microglial-/macrophage-driven inflammation.

Because 7T MR imaging scanners remain relatively sparse and confined to major academic centers in developed countries, the ability to reliably identify paramagnetic rims on more widespread, lower field strength (3T) scanners seems to be a necessary step toward application in multicenter clinical trials and—as important—clinical practice. A proper investigation of the detection of paramagnetic rims on 3T susceptibility-based MR images is necessary to achieve this. Here, we aimed to assess the reliability of visualizing 7T paramagnetic rims (our criterion standard *in vivo*) on high-resolution 3T susceptibility-based MR images in 20 patients with MS. At 3T, we implemented a 0.65-mm isotropic voxel, whole-brain 3D segmented echo-planar imaging sequence that is already known in the MS imaging field for its benefits in assessing the central vein sign within MS lesions.¹⁶⁻²¹

MATERIALS AND METHODS

Participants

Under an institutional review board–approved natural history protocol, we recruited, from May 2012 to December 2016, twenty individuals with MS (15 women/5 men; mean age, 46 years; range, 28–71 years; all fulfilling the 2017 McDonald revised MS criteria²²). Sixteen had relapsing-remitting and 4 had progressive MS.²³ Experienced MS clinicians determined disability according to the Expanded Disability Status Scale (EDSS)²⁴ and obtained clinical data. The median EDSS score was 1.5 (range, 0–7), and mean disease duration was 14 years (range, 1–40 years); clinical data were collected at the first MR imaging acquisition (Table 1).

MR Imaging Acquisition

Participants underwent 2 MR imaging acquisitions approximately a year apart, one on a Magnetom Skyra (Siemens, Erlangen, Germany) 3T scanner (equipped with a body transmit coil and a 32-channel receive coil) and one on a Siemens Research System 7T MR imaging scanner (equipped with a birdcage-type transmit coil and a 32-channel receive coil). The mean time lapse between the first and second MR imaging was 0.9 years (median, 0.7 years; range, 2 days to 3.4 years). Because paramagnetic rims in chronic lesions have been shown to be stable with time,¹³⁻¹⁵ including in our cohort, we did not implement a maximum time lapse between 3T and 7T scans.

The following details the 3T MR imaging protocol for rim detection:

- Whole-brain 3D segmented echo-planar imaging providing T2* magnitude and phase contrasts (TR = 64 ms; TE = 35 ms; flip angle = 10°; acquisition time = 5 minutes 46 seconds; 256 sagittal slices; 0.65-mm isotropic voxels with a voxel size of 0.27 μ L).
- Whole-brain 3D T2 FLAIR (TR = 4800 ms; TE = 354 ms; TI = 1800 ms; flip angle = 120°; acquisition time = 6 minutes 30 seconds; 176 sagittal slices; 1-mm isotropic voxels with voxel size = 1 μ L).

The following details the 7T MR imaging protocol for rim detection:

- 2D high-resolution gradient recalled-echo providing T2* and phase contrasts (TR = 1300 ms; TE = 32 ms; 29 axial slices; flip angle = 50°; acquisition time = 8 minutes 36 seconds; in-plane resolution = 0.2 \times 0.2 mm; slice thickness = 1 mm; voxel size = 0.04 μ L). Three minimally overlapping slabs were acquired to allow coverage of most of the supratentorial brain.

Additional MR imaging sequences, including postcontrast T1-weighted images, were typically acquired for clinical or other research purposes at both 3T and 7T MR imaging and were examined qualitatively as part of this study.

Table 2: Intra- and interrater agreement for paramagnetic rim evaluation on 3T and 7T phase MRI

Raters	Percentage Agreement	Cohen κ	Agreement ²⁸
3T (3 raters)			
Intrarater (1 rater)	89%	0.77	Substantial
Interrater	86%	0.71 (Fleiss κ)	Substantial
Each rater vs 3T consensus	86%–90%	0.71–0.79	Substantial
7T (2 raters)			
Intrarater (1 rater)	89%	0.77	Substantial
Interrater	87%	0.72	Substantial
Each rater vs 7T consensus	91%–96%	0.81–0.91	Almost perfect
3T vs 7T			
3T vs 7T consensus	90%	0.78	Substantial

MR Imaging Analysis

Phase postprocessing and coregistration among images were performed as previously described.^{10,14} Postcontrast T1-weighted images were implemented to exclude enhancing lesions from the analysis.

As previously described,⁶ a chronic lesion was defined as “rim-positive” when it showed a paramagnetic rim signal on phase images while being either hyper- or isointense in its inner portion. The paramagnetic rim assessment included 5 investigators with experience in imaging MS, including 2 neurologists (M.A., M.K.S.), 2 neuroradiologists (A.F., D.S.R.), and an MR physicist (P.S.). On 3T T2 FLAIR images, an investigator (M.A.) selected 5 discrete supratentorial chronic MS lesions (largest diameter of >3 mm) from each case. The lesion location and largest lesion diameter were recorded. To remain masked to data acquired at 3T and 7T, we planned rim assessment as follows:

3T Paramagnetic Rim Assessment

- For each selected lesion, 3 investigators (A.F., M.K.S., D.S.R.) independently assessed the presence of paramagnetic rims on 3T phase MR images. T2 FLAIR and phase images were reviewed simultaneously by each investigator using OsiriX software (<http://www.osirix-viewer.com>). Lesions to be analyzed were marked on MR images with a number and an arrow. A binary code was implemented as 0 = no rim and 1 = rim.
- After 4 months, 1 rater repeated the analysis on 3T phase data.
- Consensus agreement was subsequently reached by all investigators, and comments were recorded.

7T Paramagnetic Rim Assessment

- Similar to the previous analysis, for each selected lesion, an investigator (M.A.) assessed the presence of paramagnetic rims on 7T phase MR imaging.
- After 5 months, a second investigator (P.S.) performed the analysis, and the first rater repeated the analysis.
- Consensus agreement was subsequently reached, and comments were recorded.

After consensus, discrepancies between rim visualization at 3T versus 7T were retrospectively investigated and discussed. The presence of rims on 3T T2* magnitude images (known to be less sensitive to susceptibility shifts) was assessed retrospectively by consensus of 2 investigators (M.A., P.S.).

Statistical Analysis

Intra- and interrater reliability for rim assessment was computed on the basis of the number of raters, using the Cohen κ (2 raters) and Fleiss κ (3 raters). MR imaging differences (lesion diameter and location) between lesions with-versus-without rims were assessed with a *t* test and Fisher exact test when appropriate.

RESULTS

One hundred discrete supratentorial chronic MS lesions were initially evaluated (5 lesions per patient). Two lesions were excluded from the final analysis, one for abutting a confluent lesion and one for obvious changes in size at the second time point (time lapse, 1.7 and 1.4 years, respectively). Of the remaining 98 lesions, 35 (36%) were periventricular; 39 (40%), in the deep white matter; and 24 (24%), juxtacortical/leukocortical.

Lesion Rim Assessment at 3T MR Imaging (Masked to the 7T Data)

Of 98 analyzed lesions, 36 had a paramagnetic rim on 3T phase images by consensus agreement. Rim lesions were larger than nonrim lesions (mean diameter, 8.1 ± 2.3 mm and 6.7 ± 2.3 mm, respectively; *t* test, *P* = .007). Overall, we did not notice any preferential lesion location: 13 lesions with rim were periventricular (38% of total periventricular lesions), 14 were in the deep white matter (38% of total deep white matter lesions), and 9 were juxtacortical/leukocortical (38% of total juxtacortical/leukocortical lesions).

The intrarater and interrater agreement results are provided in Table 2. The reliability between each rater and the final consensus agreement was “substantial/good,” with a Cohen κ ranging from 0.71 to 0.79 and a pair-wise agreement ranging from 86% to 90%.

Sixteen of 36 lesions with a phase rim (44%) also showed a rim on T2* magnitude images. The presence of a T2* rim was significantly associated with the detection of a rim on phase images by consensus (Fisher exact test, *P* < .0001).

Lesion Rim Assessment at 7T MR Imaging (Masked to the 3T Data)

Of 98 analyzed lesions, 34 had a paramagnetic rim on 7T phase images by consensus agreement. Twenty-one of 34 lesions with a phase rim (62%) also showed a rim on T2* magnitude images (Fig 1). The intrarater and interrater agreement results are provided in Table 2. The reliability between each rater and the final consensus agreement was “almost perfect,” with a Cohen κ ranging from 0.81 to 0.91 and a pair-wise agreement ranging from 91% to 96%.

Lesion Rim Assessment at 3T versus 7T and Analysis of Disagreements

Rims were seen in 34 lesions on 7T phase images and in 36 lesions on 3T phase images by consensus. The reliability between the consensus agreement at 3T versus 7T was substantial/good, with a Cohen κ of 0.78 and a pair-wise agreement of 90%. After discussion, discrepancies between 3T and 7T were seen in 10 lesions:

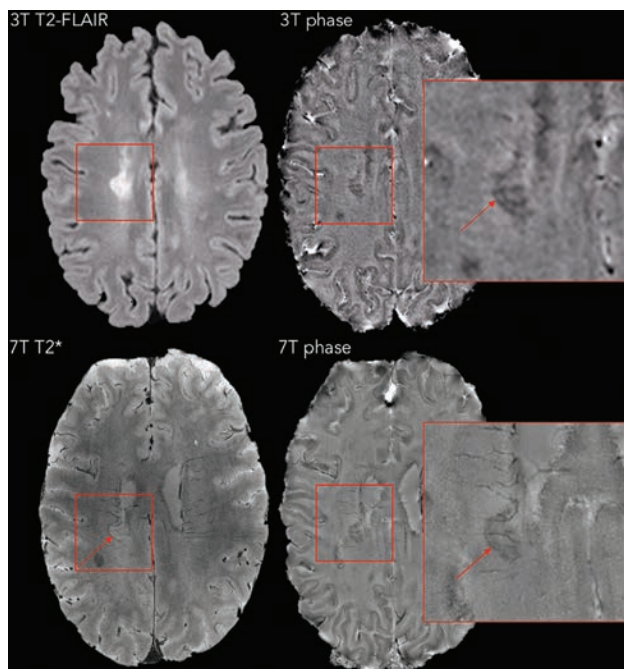


FIG 1. A right periventricular lesion in a 55-year-old woman with relapsing-remitting MS. A paramagnetic rim can be easily seen on 3T and 7T phase images (magnified view) as well as on the 7T T2* magnitude image (red arrows). On susceptibility images, medullary veins crossing the lesion are also prominent.

- Four lesions were considered to have been missed at 3T (“false-negative”). One possible explanation is a small susceptibility effect at the edge of these lesions because none had a T2* rim.
- Three lesions identified as having rims at 3T did not have rims at 7T and were therefore considered “false-positive” at 3T. On review, this misinterpretation was thought to be related to a “rim-like” configuration of vessels at the lesion edge.
- Two lesions were considered to have been missed at 7T. On review, this was thought to be due to the relatively thick slices in the 7T acquisition (1 mm versus 0.65 mm at 3T).
- One lesion, even after re-evaluation, was considered to have a rim at 3T but not at 7T. For this lesion, the 3T scan preceded the 7T scan by 1 month, and none of the other lesions in this case were discordant.

Representative concordant and discordant cases are shown in Figs 1–3.

DISCUSSION

In this study, we tested the reliability of 3T susceptibility-based imaging in visualizing 7T-detected paramagnetic rims in nonenhancing MS lesions. Anticipated difficulties revolved mainly around the lower sensitivity of 3T MR imaging to susceptibility effects, as well as the lower voxel volume of the 3T acquisition. At 7T MR imaging, the mean rim thickness in nonenhancing MS lesions has been estimated at $\sim 430 \mu\text{m}$ (range, 150–1200 μm),¹⁴ indicating the necessity of acquiring submillimeter susceptibility-based imaging. Here, we implemented a 3T whole-brain 3D segmented EPI sequence, providing 0.65-mm isotropic voxels and both T2* magnitude and phase contrasts. This is the optimized sequence for FLAIR* imaging¹⁶ and the related assessment of the

central vein sign in MS lesions.^{17–21} The potential of detecting central vein and paramagnetic rims with the same sequence would also be a clear advantage in terms of acquisition time in a clinical setting. In addition, like the central vein, small 7T MR imaging studies showed that lesions with rims are not frequently seen in other inflammatory disorders of the central nervous system such as neuromyelitis optica spectrum disorder^{25,26} and Susac syndrome.²⁷

Overall, detection of paramagnetic rims performed well at 3T; representative examples are shown in Figs 1 and 2. Intra- and interrater agreement was substantial/good or better²⁸ for both 3T and 7T. Most important, agreement was not perfect at 7T; this outcome suggests that a clear MR imaging definition of what constitutes a rim is necessary for future research studies (population analysis) and/or MR imaging–based clinical trials. In addition, our results suggest that dedicated training in MS MR imaging should be a prerequisite for assessing this important morphologic feature at both 3T and 7T.

The discussion that took place within our group during the consensus process highlighted several important observations about imaging of paramagnetic rim lesions at 3T. On the one hand, rim detection on 3T phase images was more reliable when the rim was seen: 1) on T2* magnitude and phase images, indicating stronger susceptibility effects; 2) on >1 consecutive slice; and 3) on multiple orthogonal views. On the other hand, rim detection was less reliable: 1) in areas with a high density of veins, such as around the ventricular horns; 2) within the corpus callosum; 3) when the rim was seen only partially around the lesion; 4) when the rim did not match the edge of the lesion seen on T2-FLAIR images; and 5) in areas with motion and/or bulk susceptibility artifacts.

One important limitation of phase imaging at both 3T and 7T is the presence of dipolar fields surrounding cerebral vessels and some MS lesions. These dipolar projections may hinder the detection of phase rims (especially thin ones) or may be misinterpreted as (false-positive) phase rims.^{29,30} One way to remove these dipolar fields is to apply an extra processing step called Quantitative Susceptibility Mapping (QSM), which computes the magnetic susceptibility of tissues by solving the field-to-source inversion problem using the dipole model.³¹ However, the appearance of QSM images depends heavily on the choice of the algorithm and parameters used for solving the inversion problem.³² Moreover, QSM images are typically smoothed. This step can result in a loss of conspicuity for fine structures such as the thin paramagnetic rims frequently observed in our study (On-line Figure). Therefore, further development is warranted for establishing a robust and effective QSM algorithm that can display all types of paramagnetic rims around MS lesions.

Potential limitations of our study are the limited number of lesions included in the analysis and the sometimes long time lapse between 3T and 7T MR imaging acquisitions, which ranged from 2 days to 3.4 years (mean, 0.9 years, median, 0.7 years). Because paramagnetic rims in chronic lesions have been consistently shown to remain stable for similar durations of follow-up,^{13–15} any detection difference is more likely to be

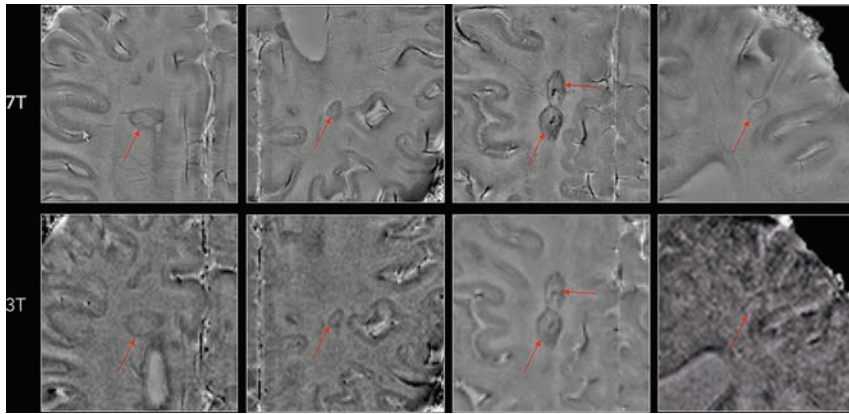


FIG 2. Representative examples of MS lesions in which a paramagnetic rim (red arrows) can be easily seen on both 7T and 3T phase images. Note the superior image quality at 7T in at least 3 of the 4 examples.

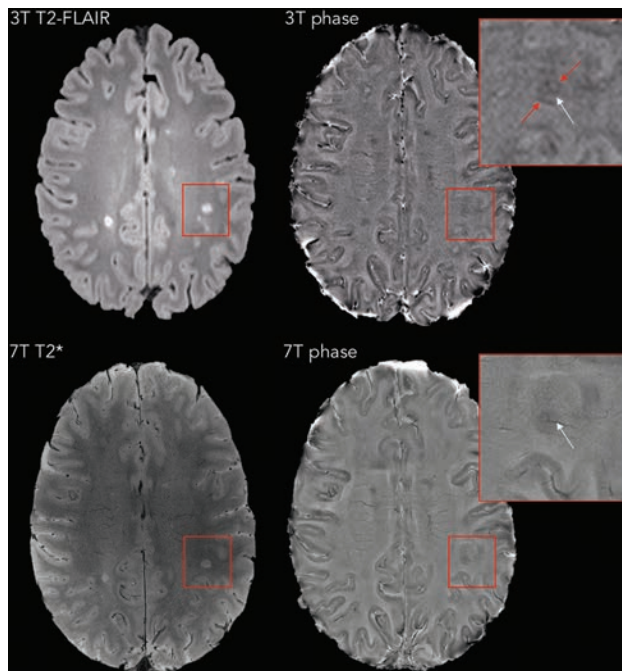


FIG 3. A left centrum semiovale lesion in a 30-year-old woman with relapsing-remitting MS; the time lapse between 3T and 7T scans was 6 months. In this case, the lesion was judged to have a rim on 3T (red arrows), but not on 7T phase images. The false-positive rim at 3T is related to the configuration of blood vessels at the lesion edge. On the other hand, the central vein of the lesion is prominent in both phase images (white arrows).

related to different magnetic strengths (3T versus 7T) than to the biologic variability of this feature.

CONCLUSIONS

Our results show that nearly all 7T paramagnetic rims can also be seen at 3T. This finding suggests the possibility of implementing paramagnetic rims for MS diagnosis and as outcome measures in MR imaging-based clinical trials, potentially affecting perilesional persistent microglial/macrophage-mediated inflammation.

ACKNOWLEDGMENTS

We thank the study participants, the Neuroimmunology Clinic for recruiting and evaluating the patients and for coordinating the

scans, and the National Institutes of Health Functional Magnetic Resonance Imaging Facility. We thank Souheil Inati, John A Derbyshire, and Sunil Patil for support with MR imaging sequences and Christian Langkammer for help with QSM image processing.

Disclosures: Martina Absinta—UNRELATED: Grant: National Multiple Sclerosis Society and Conrad N. Hilton Foundation.* Daniel S. Reich—UNRELATED: Grants/Grants Pending: Vertex Pharmaceuticals*; Payment for Lectures Including Service on Speakers Bureaus: At the Limits, Comments: Continuing Medical Education lecture; Travel/Accommodations/Meeting Expenses Unrelated to Activities Listed: Verily Life Sciences, Biogen, Comments: support for travel and accommodations to present scientific lectures.* *Money paid to the institution.

REFERENCES

1. Lassmann H, Raine CS, Antel J, et al. Immunopathology of multiple sclerosis: report on an international meeting held at the Institute of Neurology of the University of Vienna. *J Neuroimmunol* 1998;86: 213–17 CrossRef Medline
2. Kuhlmann T, Ludwin S, Prat A, et al. An updated histological classification system for multiple sclerosis lesions. *Acta Neuropathol* 2017;133:13–24 CrossRef Medline
3. Hammond KE, Metcalf M, Carvajal L, et al. Quantitative in vivo magnetic resonance imaging of multiple sclerosis at 7 Tesla with sensitivity to iron. *Ann Neurol* 2008;64:707–13 CrossRef Medline
4. Pitt D, Boster A, Pei W, et al. Imaging cortical lesions in multiple sclerosis with ultra-high-field magnetic resonance imaging. *Arch Neurol* 2010;67:812–18 CrossRef Medline
5. Bagnato F, Hametner S, Yao B, et al. Tracking iron in multiple sclerosis: a combined imaging and histopathological study at 7 Tesla. *Brain* 2011;134:3602–15 CrossRef Medline
6. Yao B, Bagnato F, Matsuura E, et al. Chronic multiple sclerosis lesions: characterization with high-field-strength MR imaging. *Radiology* 2012;262:206–15 CrossRef Medline
7. Hagemeyer J, Heininen-Brown M, Poloni GU, et al. Iron deposition in multiple sclerosis lesions measured by susceptibility-weighted imaging filtered phase: a case control study. *J Magn Reson Imaging* 2012;36:73–83 CrossRef Medline
8. Walsh AJ, Lebel RM, Eissa A, et al. Multiple sclerosis: validation of MR imaging for quantification and detection of iron. *Radiology* 2013;267:531–42 CrossRef Medline
9. Wisnieff C, Ramanan S, Olesik J, et al. Quantitative susceptibility mapping (QSM) of white matter multiple sclerosis lesions: interpreting positive susceptibility and the presence of iron. *Magn Reson Med* 2015;74:564–70 CrossRef Medline
10. Absinta M, Sati P, Schindler M, et al. Persistent 7-Tesla phase rim predicts poor outcome in new multiple sclerosis patient lesions. *J Clin Invest* 2016;126:2597–609 CrossRef Medline
11. Dal-Bianco A, Grabner G, Kronnerwetter C, et al. Slow expansion of multiple sclerosis iron rim lesions: pathology and 7 T magnetic resonance imaging. *Acta Neuropathol* 2017;133:25–42 CrossRef Medline
12. Popescu BF, Frischer JM, Webb SM, et al. Pathogenic implications of distinct patterns of iron and zinc in chronic MS lesions. *Acta Neuropathol* 2017;134:45–64 CrossRef Medline
13. Bian W, Harter K, Hammond-Rosenbluth KE, et al. A serial in vivo 7T magnetic resonance phase imaging study of white matter lesions in multiple sclerosis. *Mult Scler* 2013;19:69–75 CrossRef Medline
14. Absinta M, Sati P, Gaitán MI, et al. Seven-Tesla phase imaging of acute multiple sclerosis lesions: a new window into the inflammatory process. *Ann Neurol* 2013;74:669–78 CrossRef Medline

15. Dal-Bianco A, Hametner S, Grabner G, et al. **Veins in plaques of multiple sclerosis patients: a longitudinal magnetic resonance imaging study at 7 Tesla.** *Eur Radiol* 2015;25:2913–20 CrossRef Medline
16. Sati P, George IC, Shea CD, et al. **FLAIR*: a combined MR contrast technique for visualizing white matter lesions and parenchymal veins.** *Radiology* 2012;265:926–32 CrossRef Medline
17. Solomon A, Schindler M, Howard DB, et al. **“Central vessel sign” on 3T FLAIR* MRI for the differentiation of multiple sclerosis from migraine.** *Ann Clin Transl Neurol* 2015;3:82–87 CrossRef Medline
18. George IC, Sati P, Absinta M, et al. **Clinical 3-Tesla FLAIR* MRI improves diagnostic accuracy in multiple sclerosis.** *Mult Scler* 2016; 22:1578–86 CrossRef Medline
19. Sati P, Oh J, Constable RT, et al. **The central vein sign and its clinical evaluation for the diagnosis of multiple sclerosis: a consensus statement from the North American Imaging in Multiple Sclerosis Cooperative.** *Nat Rev Neurol* 2016;12:714–22 CrossRef Medline
20. Champion T, Smith RJ, Altmann DR, et al. **FLAIR* to visualize veins in white matter lesions: a new tool for the diagnosis of multiple sclerosis?** *Eur Radiol* 2017;27:4257–63 CrossRef Medline
21. Samaraweera AP, Clarke MA, Whitehead A, et al. **The central vein sign in multiple sclerosis lesions is present irrespective of the T2* sequence at 3 T.** *J Neuroimaging* 2017;27:114–21 CrossRef Medline
22. Thompson AJ, Banwell BL, Barkhof F, et al. **Diagnosis of multiple sclerosis: 2017 revisions of the McDonald criteria.** *Lancet Neurol* 2018;17:162–73 CrossRef Medline
23. Lublin FD, Reingold SC, Cohen JA, et al. **Defining the clinical course of multiple sclerosis: the 2013 revisions.** *Neurology* 2014;83:278–86 CrossRef Medline
24. Kurtzke JF. **Rating neurologic impairment in multiple sclerosis: an expanded disability status scale (EDSS).** *Neurology* 1983;33:1444–52 CrossRef Medline
25. Sinnecker T, Dörr J, Pfueller CF, et al. **Distinct lesion morphology at 7-T MRI differentiates neuromyelitis optica from multiple sclerosis.** *Neurology* 2012;79:708–14 CrossRef Medline
26. Sinnecker T, Schumacher S, Mueller K, et al. **MRI phase changes in multiple sclerosis vs neuromyelitis optica lesions at 7T.** *Neurol Neuroimmunol Neuroinflamm* 2016;3:e259 CrossRef Medline
27. Wuerfel J, Sinnecker T, Ringelstein EB, et al. **Lesion morphology at 7 Tesla MRI differentiates Susac syndrome from multiple sclerosis.** *Mult Scler* 2012;18:1592–99 CrossRef Medline
28. Landis JR, Koch GG. **The measurement of observer agreement for categorical data.** *Biometrics* 1977;33:159–74 CrossRef Medline
29. Eskreis-Winkler S, Deh K, Gupta A, et al. **Multiple sclerosis lesion geometry in quantitative susceptibility mapping (QSM) and phase imaging.** *J Magn Reson Imaging* 2015;42:224–29 CrossRef Medline
30. Cronin MJ, Wharton S, Al-Radaideh A, et al. **A comparison of phase imaging and quantitative susceptibility mapping in the imaging of multiple sclerosis lesions at ultrahigh field.** *MAGMA* 2016;29: 543–57 CrossRef Medline
31. Deistung A, Schweser F, Reichenbach JR. **Overview of quantitative susceptibility mapping.** *NMR Biomed* 2017;30 CrossRef Medline
32. Langkammer C, Schweser F, Shmueli K, et al. **Quantitative susceptibility mapping: report from the 2016 reconstruction challenge.** *Magn Reson Med* 2018;79:1661–73 CrossRef Medline

Imaging Differences between Neuromyelitis Optica Spectrum Disorders and Multiple Sclerosis: A Multi-Institutional Study in Japan

H. Tatekawa, S. Sakamoto, M. Hori, Y. Kaichi, A. Kunimatsu, K. Akazawa, T. Miyasaka, H. Oba, T. Okubo, K. Hasuo, K. Yamada, T. Taoka, S. Doishita, T. Shimono, and Y. Miki



ABSTRACT

BACKGROUND AND PURPOSE: Both clinical and imaging criteria must be met to diagnose neuromyelitis optica spectrum disorders and multiple sclerosis. However, neuromyelitis optica spectrum disorders are often misdiagnosed as MS because of an overlap in MR imaging features. The purpose of this study was to confirm imaging differences between neuromyelitis optica spectrum disorders and MS with visually detailed quantitative analyses of large-sample data.

MATERIALS AND METHODS: We retrospectively examined 89 consecutive patients with neuromyelitis optica spectrum disorders (median age, 51 years; range, 16–85 years; females, 77; aquaporin 4 immunoglobulin G–positive, 93%) and 89 with MS (median age, 36 years; range, 18–67 years; females, 68; relapsing-remitting MS, 89%; primary-progressive MS, 7%; secondary-progressive MS, 2%) from 9 institutions across Japan (April 2008 to December 2012). Two neuroradiologists visually evaluated the number, location, and size of all lesions using the Mann-Whitney *U* test or the Fisher exact test.

RESULTS: We enrolled 79 patients with neuromyelitis optica spectrum disorders and 87 with MS for brain analysis, 57 with neuromyelitis optica spectrum disorders and 55 with MS for spinal cord analysis, and 42 with neuromyelitis optica spectrum disorders and 14 with MS for optic nerve analysis. We identified 911 brain lesions in neuromyelitis optica spectrum disorders, 1659 brain lesions in MS, 86 spinal cord lesions in neuromyelitis optica spectrum disorders, and 102 spinal cord lesions in MS. The frequencies of periventricular white matter and deep white matter lesions were 17% and 68% in neuromyelitis optica spectrum disorders versus 41% and 42% in MS, respectively (location of brain lesions, $P < .001$). We found a significant difference in the distribution of spinal cord lesions between these 2 diseases ($P = .024$): More thoracic lesions than cervical lesions were present in neuromyelitis optica spectrum disorders (cervical versus thoracic, 29% versus 71%), whereas they were equally distributed in MS (46% versus 54%). Furthermore, thoracic lesions were significantly longer than cervical lesions in neuromyelitis optica spectrum disorders ($P = .001$), but not in MS ($P = .80$).

CONCLUSIONS: Visually detailed quantitative analyses confirmed imaging differences, especially in brain and spinal cord lesions, between neuromyelitis optica spectrum disorders and MS. These observations may have clinical implications.

ABBREVIATIONS: AQP4-IgG = aquaporin 4 immunoglobulin G; BS = brain stem; DGM = deep gray matter; DWM = deep white matter; IQR = interquartile range; NMO = neuromyelitis optica; NMOSD = neuromyelitis optica spectrum disorders; PVWM = periventricular white matter; SCWM = subcortical white matter

Neuromyelitis optica (NMO) is a central nervous system autoimmune disorder that commonly manifests as optic neuritis and longitudinal extensive transverse myelitis.¹ Historically,

Received January 16, 2018; accepted after revision March 18.

From the Department of Diagnostic and Interventional Radiology (H.T., S.S., S.D., T.S., Y.M.), Osaka City University Graduate School of Medicine, Osaka, Japan; Department of Radiology (M.H.), Graduate School of Medicine, Juntendo University, Tokyo, Japan; Department of Diagnostic Radiology (Y.K.), Graduate School and Institute of Biomedical and Health Sciences, Hiroshima University, Hiroshima, Japan; Department of Radiology (A.K.), Graduate School of Medicine, University of Tokyo, Tokyo, Japan; Department of Radiology (K.A., K.Y.), Graduate School of Medical Science, Kyoto Prefectural University of Medicine, Kyoto, Japan; Department of Radiology (T.M.), Nara Medical University, Nara, Japan; Department of Radiology (H.O.), Teikyo University School of Medicine, Tokyo, Japan; Department of Radiology (T.O.), Teikyo University Chiba Medical Center, Chiba, Japan; Department of Diagnostic Radiology (K.H.), National Center for Global Health and Medi-

cine, Tokyo, Japan; and Department of Radiology (T.T.), Nagoya University Graduate School of Medicine, Nagoya, Japan.

The institutions that had recruited the patients in this study received a grant from Bayer Yakuin Ltd (Osaka, Japan). The sponsor had no role in the study concept, study design, data analysis, and interpretation, or reporting of results.

Paper previously presented at: Annual Meeting of the Radiological Society of North America, November 26–December 1, 2017; Chicago, Illinois.

Please address correspondence to Shinichi Sakamoto, MD, PhD, Department of Diagnostic and Interventional Radiology, Osaka City University Graduate School of Medicine, 1-4-3, Asahi-machi, Abeno-ku, Osaka 545-8585, Japan; e-mail: s-sakamoto@med.osaka-cu.ac.jp

Indicates open access to non-subscribers at www.ajnr.org

Indicates article with supplemental on-line tables.

Indicates article with supplemental on-line photos.

<http://dx.doi.org/10.3174/ajnr.A5663>

NMO was known as Devic disease, and whether NMO is a subtype of multiple sclerosis was long debated. The discovery of aquaporin 4 immunoglobulin G (AQP4-IgG) allowed NMO and MS to be classified as separate conditions, and the 2006 revised NMO criteria and NMO spectrum disorders (NMOSD) with limited forms of NMO in patients seropositive for AQP4 antibodies were widely accepted.² These criteria and the 2010 revised McDonald criteria, which are used to diagnose MS, emphasize the requirement of MR imaging.¹⁻³ However, because of overlap in imaging features, NMOSD is still often misdiagnosed as MS. Nevertheless, differentiation of these 2 diseases is crucial because NMOSD requires long-term immunosuppression therapy to prevent devastating relapses, and MS therapies such as interferon- β and natalizumab may exacerbate NMOSD.⁴

Although initially NMO was not thought to involve the brain, brain abnormalities in regions with high AQP4 expression and longitudinal extensive transverse myelitis, preferentially in the central portion of the spinal cord, were revealed to be specific in NMOSD.⁵⁻⁷ In MS, some features such as ovoid lesions and isolated U-fiber lesions are considered characteristic, and spinal cord lesions tend to be shorter than those in NMOSD.⁸ These imaging features may be useful to differentiate these 2 diseases. Intensive investigations currently use diffusion tensor imaging and ultra-high-field MR imaging for differentiation.⁶⁻⁹

However, brain abnormalities such as periependymal lesions are only seen in a minority of patients with NMOSD, and ovoid lesions that are considered specific to MS may be common in Asian patients with NMOSD.⁹⁻¹² Furthermore, most studies included a limited number of patients, and some sequences used in these studies are not widely available for routine clinical examinations. Hence, validation and investigation of imaging differences on conventional MR imaging are needed using a large sample size. Visually detailed quantitative analyses about each lesion in NMOSD and MS have received little attention; thus, we especially focused on the number, size, and distribution of brain and spinal cord lesions.^{12,13}

The objectives of the present study were to confirm imaging differences between NMOSD and MS by performing detailed quantitative analyses and to validate characteristic features in a large sample size. The quantitative analysis approach was performed by 2 neuroradiologists who visually counted the number of lesions and recorded the size and location of all lesions on conventional MR imaging.

MATERIALS AND METHODS

Patients

This retrospective study was approved by the institutional review boards. Written informed consent was waived. We retrospectively examined the same number of consecutive patients with NMOSD and MS (older than 15 years of age) from 9 institutions across Japan between April 2008 and December 2012: eighty-nine patients with NMOSD (median age, 51 years; range, 16–85 years; females, 77; AQP4-IgG-positive, 93%; median disease duration, 4 years; median Expanded Disability Status Scale score, 6) and 89 patients with MS (median age, 36 years; range, 18–67 years; females, 68; relapsing-remitting MS, 89%; primary-progressive MS, 7%; secondary-progressive MS, 2%; median disease duration, 2

years; median Expanded Disability Status Scale score, 2). All patients with NMO/NMOSD were defined according to the NMO/NMOSD criteria published in 2006 and 2007, respectively, and fulfilled the 2015 International Panel for NMO Diagnosis criteria.¹⁴ For simplification, we referred to all patients with NMO/NMOSD as NMOSD.¹⁵ All patients with MS fulfilled the 2010 revised McDonald criteria.³ Because myelin oligodendrocyte glycoprotein-IgG was not well-recognized during the time in which patients were recruited (April 2008 to December 2012), we could not obtain and analyze myelin oligodendrocyte glycoprotein-IgG data. Eligibility criteria were the following: in brain analyses, inclusion criterion—axial T2-weighted images were obtained; exclusion criteria—1) imaging with motion artifacts that reduced diagnostic quality, 2) the presence of old vascular damage that involved ≥ 2 lobes and extended into the cerebral cortex; in spinal cord analyses, inclusion criterion—both cervical and thoracic (including conus medullaris) sagittal T2-weighted images were obtained; exclusion criterion—imaging with motion artifacts that reduced diagnostic quality; in optic nerve analyses, inclusion criterion—orbital coronal STIR, FLAIR, or T2-weighted images were obtained. We evaluated only the initial images that were obtained for each part during the recruitment period. The patient-selection flowchart and patient characteristics are shown in Fig 1 and Table 1, respectively.

Image Acquisition and Data Analyses

For brain analyses, detailed quantitative analyses were performed on axial T2-weighted fast spin-echo images. Morphologic features and characteristic signs were assessed on T2-weighted FSE images, along with FLAIR and/or T1-weighted images with/without gadolinium enhancement if these imaging examinations were performed. For spinal cord analyses, quantitative analyses and morphologic assessments were performed on sagittal T2-weighted FSE images and axial T2-weighted FSE or gradient-echo images. Optic nerve analyses were performed on orbital coronal STIR, FLAIR, or T2-weighted images. All MR imaging was performed with 1.5T or 3T scanners. Other imaging parameters and a summary of available MR images for each analysis are shown in On-line Tables 1 and 2. All image archives were reviewed with a DICOM viewer (OsiriX Version 3.2.1; <http://www.osirix-viewer.com>) on a Macintosh computer (Apple, Cupertino, California) and analyzed by 2 neuroradiologists (10 and 7 years of experience) who were blinded to the clinical diagnosis. All detailed quantitative analyses were performed by visually counting the number of lesions and recording the size and location of all lesions, and the raters performed these analyses independent of each other. Discrepancies in the assessment of morphologic features and signs were resolved by consensus.

Brain Analyses

For detailed quantitative analyses, we visually counted the number of T2 hyperintense lesions of ≥ 3 mm, measured the maximum diameter (millimeter), and identified the location (periventricular white matter [PVWM], deep white matter [DWM], subcortical white matter [SCWM], deep gray matter [DGM], brain stem [BS], and cerebellum). SCWM included the regions of the subcortical white matter and cortex because 94% of cortical

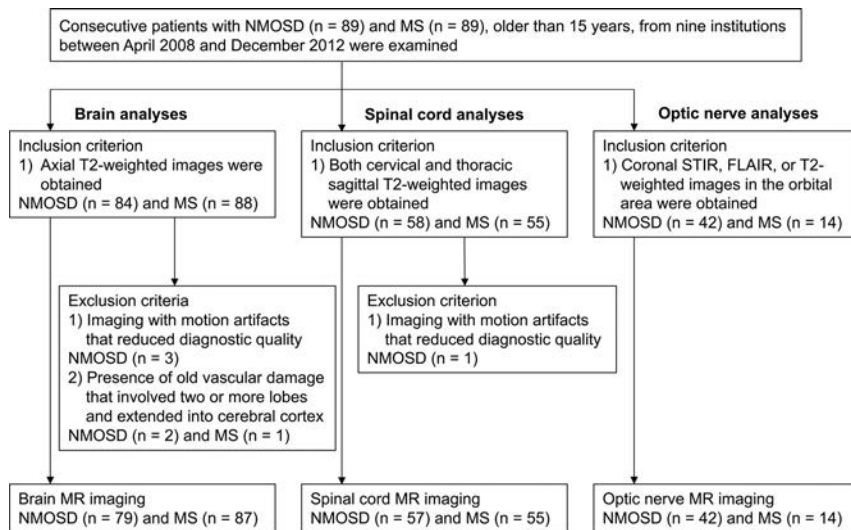


FIG 1. Patient selection flowchart. Consecutive patients, 89 with NMOSD and 89 with MS, are examined. According to the eligibility criteria, 79 patients with NMOSD and 87 with MS are assessed for brain analyses, 57 patients with NMOSD and 55 with MS are assessed for spinal cord analyses, and 42 patients with NMOSD and 14 with MS are assessed for optic nerve analyses.

Table 1: Patient demographics and characteristics in NMOSD and MS^a

	NMOSD	MS	P Value ^c
Demographics (NMOSD, n = 89) (MS, n = 89)			
Age (yr) (median) (IQR, range)	51 (39–61, 16–85)	36 (29–43, 18–67)	<.001
No. of females ^b	77 (86.5)	68 (76.4)	.12 ^d
Disease duration (yr) (median) (IQR, range)	4 (0–11, 0–73)	2 (1–7, 0–21)	.40
EDSS (median) (IQR, range)	6 (2–7.5, 1–9)	2 (1–3, 0–6)	<.001
AQP4-IgG ^b			
Positive	83 (93.3)		
Negative	5 (5.6)		
Unknown	1 (1.1)		
MS type ^b			
Relapsing-remitting MS		79 (88.8)	
Primary-progressive MS		6 (6.7)	
Secondary-progressive MS		2 (2.2)	
Unknown		2 (2.2)	
Brain MRI (NMOSD, n = 79) (MS, n = 87)			
Age (yr) (median) (IQR, range)	50 (38–61, 17–83)	36 (29–45, 19–67)	<.001
No. of females ^b	68 (86.1)	67 (77)	.16 ^d
Disease duration (yr) (median) (IQR, range)	4 (0–11, 0–41)	3 (1–7, 0–21)	.59
EDSS (median) (IQR, range)	6 (2–7.5, 1–9)	2 (1–3, 0–6)	<.001
Gadolinium enhancement ^b	51 (64.6)	68 (78.2)	
Spinal cord MRI (NMOSD, n = 57) (MS, n = 55)			
Age (yr) (median) (IQR, range)	53 (39–61, 25–78)	37 (29–43, 18–66)	<.001
No. of females ^b	51 (89.5)	36 (65.5)	.003 ^d
Disease duration (yr) (median) (IQR, range)	4 (0–12, 0–43)	2 (0–7, 0–19)	.18
EDSS (median) (IQR, range)	6 (2–7, 1–9)	2 (2–3.5, 0–6)	<.001
Optic nerve MRI (NMOSD, n = 42) (MS, n = 14)			
Age (yr) (median) (IQR, range)	50 (37–61, 17–79)	35 (34–39, 19–67)	.004
No. of females ^b	37 (88.1)	9 (64.3)	.10 ^d
Disease duration (yr) (median) (IQR, range)	5 (0–12, 0–42)	1 (0–6, 0–17)	.15
EDSS (median) (IQR, range)	6 (3–8, 1–9)	3 (2–3.5, 2–4)	.065

Note:—EDSS indicates Expanded Disability Status Scale.

^a Unless otherwise indicated, data are medians, with interquartile range and total range in parentheses.

^b Data in parentheses are percentages.

^c Mann-Whitney *U* test.

^d Fisher exact test.

lesions were identified as mixed cortical-subcortical lesions, and some cortical lesions cannot be identified without double inversion recovery images.^{16–18} We classified patients according to the number of lesions in bins of 10 lesions (0, 1–10, 11–20, 21–30,

31–40, 41–50, ≥51), categorized lesions according to the location (PVWM, DWM, SCWM, DGM, BS, cerebellum), and calculated the diameter in each region. For morphologic assessment, we evaluated the presence of visual aspects of brain atrophy and ventriculomegaly. For assessment of characteristic signs, we evaluated the presence of ovoid/Dawson finger lesions (oval or elliptic hyperintense lesions on T2-weighted images whose major axes were perpendicular to the anteroposterior axis of the head),¹⁹ T1 black hole lesions (areas that are hypointense compared with white matter on T1-weighted images and are concordant with hyperintense lesions on T2-weighted images),²⁰ callosal-septal-interface lesions/subcallosal striations (corpus callosum lesions oriented perpendicular [rather than parallel] to the ependyma),²¹ isolated U-fiber/juxtacortical lesions (lesions extending along the subcortical U-fibers),¹⁶ dirty white matter lesions (subtle, abnormal areas that showed patchy and slightly higher signal intensity than the surrounding normal-appearing white matter but lower signal intensity than the plaques),²² tumefactive MS lesions (lesions of >2 cm, mass effect, edema, and/or ring enhancement),²³ and cloudlike enhancement (multiple patchy enhancement with a blurred margin in adjacent regions, in comparison with isolated enhancing lesions)²⁴ according to the previously reported criteria.

Spinal Cord Analyses

For detailed quantitative analyses, we visually counted the number of T2 hyperintense lesions in the sagittal and axial T2-weighted images. We measured the longitudinal length (millimeter) and identified the spinal location (from the first cervical vertebra to the 12th thoracic vertebra) in the sagittal T2-weighted images. We defined the center of the T2 hyperintensity as the spinal location of the lesion. We classified patients according to the number of lesions (0, 1, 2, 3, 4, ≥5), categorized lesions from the first to seventh cervical verte-

Table 2: Number and size of brain lesions for rater 1 and assessment of brain morphologic features and characteristic signs

Quantitative Analyses	NMOSD (n = 79)	MS (n = 87)	P Value	Accuracy	κ Value
Total No. of lesions	911	1659			
Per patient ^a	5 (1–18, 0–81)	8 (3–28, 0–120)	.004 ^c		
Diameter of lesions (mm) ^a	5.7 (4.3–8.5, 3.0–45)	6.1 (4.6–8.3, 3.0–56)	.046 ^c		
In each region (mm) ^a					
PVWM	9.2 (5.3–14, 3.0–36)	6.8 (5.1–9.5, 3.0–47)	<.001 ^c		
DWM	5.5 (4.2–7.7, 3.0–45)	5.5 (4.3–7.4, 3.0–56)	.73 ^c		
SCWM	5.4 (3.7–7.2, 3.0–28)	5.9 (4.5–7.9, 3.0–25)	.054 ^c		
DGM	5.9 (4.3–8.3, 3.1–30)	6.7 (5.5–9.2, 3.5–48)	.31 ^c		
BS	6.2 (5.3–8.3, 3.3–22)	6.9 (5.2–8.1, 3.6–16)	.96 ^c		
Cerebellum	3.7 (3.7–3.7, 3.7–3.7)	7.3 (5.5–8.9, 3.4–21)	.17 ^c		
Morphologic assessment					
Brain atrophy ^b	4 (5.1)	5 (5.7)	1 ^d	0.48	0.52
Ventriculomegaly ^b	3 (3.8)	3 (3.4)	1 ^d	0.48	0.5
Characteristic signs					
Ovoid lesions ^b	17 (21.5)	55 (63.2)	<.001 ^d	0.71	0.68
T1 black hole lesions ^b	16 (20.3)	47 (54)	<.001 ^d	0.66	0.65
Callosal-septal-interface lesions ^b	23 (29.1)	48 (55.2)	.001 ^d	0.63	0.75
Isolated U-fiber lesions ^b	8 (10.1)	24 (27.6)	.005 ^d	0.57	0.56
Dirty white matter lesions ^b	13 (16.5)	23 (26.4)	.14 ^d	0.54	0.61
Tumefactive MS lesions ^b	1 (1.3)	2 (2.3)	1 ^d	0.48	0.74
Cloudlike enhancement ^b	0 (0)	0 (0)			

^a Data are medians, with interquartile range and total range in parentheses.

^b Data in parentheses are percentages.

^c Mann-Whitney *U* test.

^d Fisher exact test.

disease. We also visually measured the transverse maximum diameter (millimeter), identified the intramedullary location (central, peripheral, both), and calculated the transverse diameter in the cervical and thoracic regions in the axial T2-weighted images. For morphologic assessment, we evaluated the presence of visual aspects of spinal atrophy and swelling.

Optic Nerve Analyses

We identified the laterality (none, unilateral, bilateral) and location (optic nerve, optic chiasm, optic tract) of STIR/FLAIR/T2 hyperintense lesions and evaluated visual aspects of optic nerve atrophy and swelling.

Statistical Analyses

The Mann-Whitney *U* test was performed to evaluate differences in age, disease duration, Expanded Disability Status Scale, and number and size of lesions. The Fisher exact test was performed to evaluate the sex ratio, frequency of morphologic features and signs, and the presence of predominant locations of lesions. Multiple-comparison correction was not performed because this was exploratory research. *P* values < .05 were considered statistically significant. Diagnostic accuracies for differentiating MS from NMOSD were calculated for the assessment of each morphologic feature and sign. Interobserver variation of the existence of predominant distribution was analyzed by the κ or weighted κ coefficient (<0 = poor, 0–0.20 = slight, 0.21–0.40 = fair, 0.41–0.60 = moderate, 0.61–0.80 = substantial, 0.81–1.0 = almost perfect).²⁵ SPSS (Version 21.0) software (IBM, Armonk, New York) was used for all analyses.

RESULTS

According to the eligibility criteria, we enrolled 79 patients with NMOSD and 87 with MS for brain analyses, 57 with NMOSD and 55 with MS for spinal cord analyses, and 42 with NMOSD and 14

with MS for optic nerve analyses. The brain, spinal cord, and optic nerve analyses are summarized in Tables 2, 3, and 4, respectively. Detailed quantitative analyses of the brain and spinal cord for rater 2 are shown in On-line Tables 3 and 4 and On-line Figs. 1 and 2.

Brain Analyses

For quantitative analyses, 911 lesions in 79 patients with NMOSD and 1659 lesions in 87 patients with MS were identified. We found significant differences between NMOSD and MS in the number (NMOSD: median, 5; interquartile range [IQR], 1–18; MS: median, 8; IQR, 3–28; *P* = .004) and size of lesions (NMOSD: median diameter, 5.7 mm; IQR, 4.3–8.5 mm; MS: median diameter, 6.1 mm; IQR, 4.6–8.3 mm; *P* = .046). As shown in Fig 2A, the proportions of patients classified by the number of lesions were significantly different between NMOSD and MS (*P* = .015; weighted κ value, 0.92). More patients with NMOSD had no brain lesions of ≥ 3 mm, and patients with MS had a tendency to have more brain lesions than those with NMOSD. As shown in Fig 2B, the distribution of lesions categorized by location was significantly different between NMOSD and MS (*P* < .001). DWM lesions (68%) were more frequent than PVWM lesions (17%) in NMOSD, whereas PVWM lesions (41%) and DWM lesions (42%) were present at a similar frequency in MS.

For morphologic assessment, the frequencies of brain atrophy and ventriculomegaly were not significantly different between NMOSD and MS.

For assessment of characteristic signs, the frequencies of ovoid lesions (*P* < .001), T1 black hole lesions (*P* < .001), callosal-septal-interface lesions (*P* = .001), and isolated U-fiber lesions (*P* = .005) were significantly higher in MS than in NMOSD. The frequencies of dirty white matter lesions and tumefactive MS lesions were not significantly different between NMOSD

Table 3: Number, size, and location of spinal cord lesions for rater 1 and assessment of spinal cord morphologic features^a

Quantitative Analyses	NMOSD (n = 57)	MS (n = 55)	P Value ^c	Accuracy	κ Value
Total No. of lesions	86	102			
Per patient	1 (1–2, 0–6)	1 (0–3, 0–6)	.77		
Longitudinal length (mm)	47 (17–109, 4.5–408)	13 (9.0–20, 4.0–208)	<.001		
In cervical region (mm)	23 (9.5–36, 4.5–149)	13 (8.4–21, 4.0–110)	.077		
In thoracic region (mm)	63 (25–131, 6.0–408)	13 (9.4–20, 4.1–208)	<.001		
Transverse diameter (mm)	4.4 (3.2–6.2, 1.8–13)	4.4 (3.6–5.3, 1.9–11)	.99		
In cervical region (mm)	5.8 (3.6–7.5, 1.9–13)	4.7 (4.0–5.8, 1.9–11)	.55		
In thoracic region (mm)	4.2 (3.1–5.7, 1.8–10)	4.0 (3.5–4.8, 2.3–7.3)	.76		
Intramedullary location ^b					
Central	66 (76.7)	59 (57.8)	.007 ^d		
Peripheral	11 (12.8)	32 (31.4)			
Both	9 (10.5)	11 (10.8)			
Morphologic assessment					
Atrophy ^b	17 (29.8)	5 (9.1)	.008 ^d	0.40	0.53
Swelling ^b	19 (33.3)	8 (14.5)	.027 ^d	0.41	0.67

^a Unless otherwise indicated, data are medians, with interquartile range and total range in parentheses.

^b Data in parentheses are percentages.

^c Mann-Whitney *U* test.

^d Fisher exact test.

Table 4: Laterality and location of optic nerve lesions and assessment of optic nerve morphologic features^a

	NMOSD (n = 42)	MS (n = 14)	P Value ^b	Accuracy	κ Value
Laterality of lesions					
None	16 (38.1)	7 (50)	.67		0.73
Unilateral	18 (42.9)	4 (28.6)			
Bilateral	8 (19)	3 (21.4)			
Location of lesions					
Optic nerve	26 (61.9)	7 (50)	.54		0.7
Optic chiasm	2 (4.8)	2 (14.3)	.26		0.7
Optic tract	0 (0)	1 (7.1)	.25		0.49
Atrophy	5 (11.9)	0 (0)	.32	0.66	0.48
Swelling	10 (23.8)	5 (35.7)	.49	0.66	0.41

^a Data in parentheses are percentages.

^b Fisher exact test.

and MS, and none of the patients with NMOSD or MS showed cloudlike enhancement, even though 51 (64.6%) patients with NMOSD and 68 (78.2%) with MS underwent contrast-enhanced studies.

Spinal Cord Analyses

For quantitative analyses, 86 lesions in 57 patients with NMOSD and 102 lesions in 55 patients with MS were identified. We found no significant difference between NMOSD and MS in the number of lesions (NMOSD: median, 1; IQR, 1–2; MS: median, 1; IQR, 0–3; $P = .77$). The longitudinal length was significantly longer in NMOSD than in MS (NMOSD: median length, 47 mm; IQR, 17–109 mm; MS: median length, 13 mm; IQR, 9.0–20 mm; $P < .001$). As shown in Fig 3A, the proportions of patients classified by the number of lesions were not significantly different between NMOSD and MS ($P = .76$; weighted κ value, 0.94). Forty-seven (82%) patients with NMOSD and 37 (67%) patients with MS had ≥ 1 spinal cord lesion. As shown in Fig 3B, both NMOSD and MS showed bimodal distributions of lesions. The peak of the distribution in NMOSD was high in the thoracic regions, whereas the variation and peaks of the distribution were relatively smaller in MS than in NMOSD. The proportions of lesions in cervical and thoracic regions were significantly different between NMOSD and MS ($P = .024$); more thoracic lesions (71%) than cervical

lesions (29%) were present in NMOSD, whereas the difference between the frequency of cervical (46%) and thoracic lesions (54%) was small in MS. As shown in Fig 3C, thoracic lesions were significantly longer than cervical lesions in NMOSD (NMOSD: median length cervical, 23 mm; IQR, 9.5–36 mm; median length thoracic, 63 mm; IQR, 25–131 mm; $P = .001$), whereas the length was not significantly different between cervical and thoracic lesions in MS (MS: median length cervical, 13 mm; IQR, 8.4–21 mm; median length thoracic, 13 mm; IQR, 9.4–20 mm; $P = .80$). The transverse diameter was not significantly different between NMOSD and MS (NMOSD: median diameter, 4.4 mm; IQR, 3.2–6.2 mm; MS: median diameter 4.4 mm; IQR, 3.6–5.3 mm; $P = .99$). The intramedullary location was significantly different between NMOSD and MS ($P = .007$); central lesions were more frequent in NMOSD (76.7%) than in MS (57.8%).

For morphologic assessment, the frequencies of spinal atrophy ($P = .008$) and swelling ($P = .027$) were significantly higher in NMOSD than in MS.

Optic Nerve Analyses

We found no significant differences in the laterality or location of lesions between NMOSD and MS. The frequencies of optic nerve atrophy ($P = .32$) and swelling ($P = .49$) were not significantly different between NMOSD and MS.

DISCUSSION

Using a large sample size, we investigated the imaging features of NMOSD and MS. Two experienced neuroradiologists who were blinded to the clinical diagnosis evaluated every lesion. We found imaging differences between these 2 diseases, especially in brain and spinal cord lesions.

We evaluated the distribution of brain lesions between NMOSD and MS because different lesions in these 2 diseases are distributed in various areas of the brain parenchyma, including white matter, DGM, and BS, and differentiating between these 2 diseases is still difficult.¹¹ This study showed that the distribution of lesions was significantly different between NMOSD and MS. The difference in the frequencies between PVWM and DWM lesions was larger in NMOSD than in MS (frequencies in PVWM

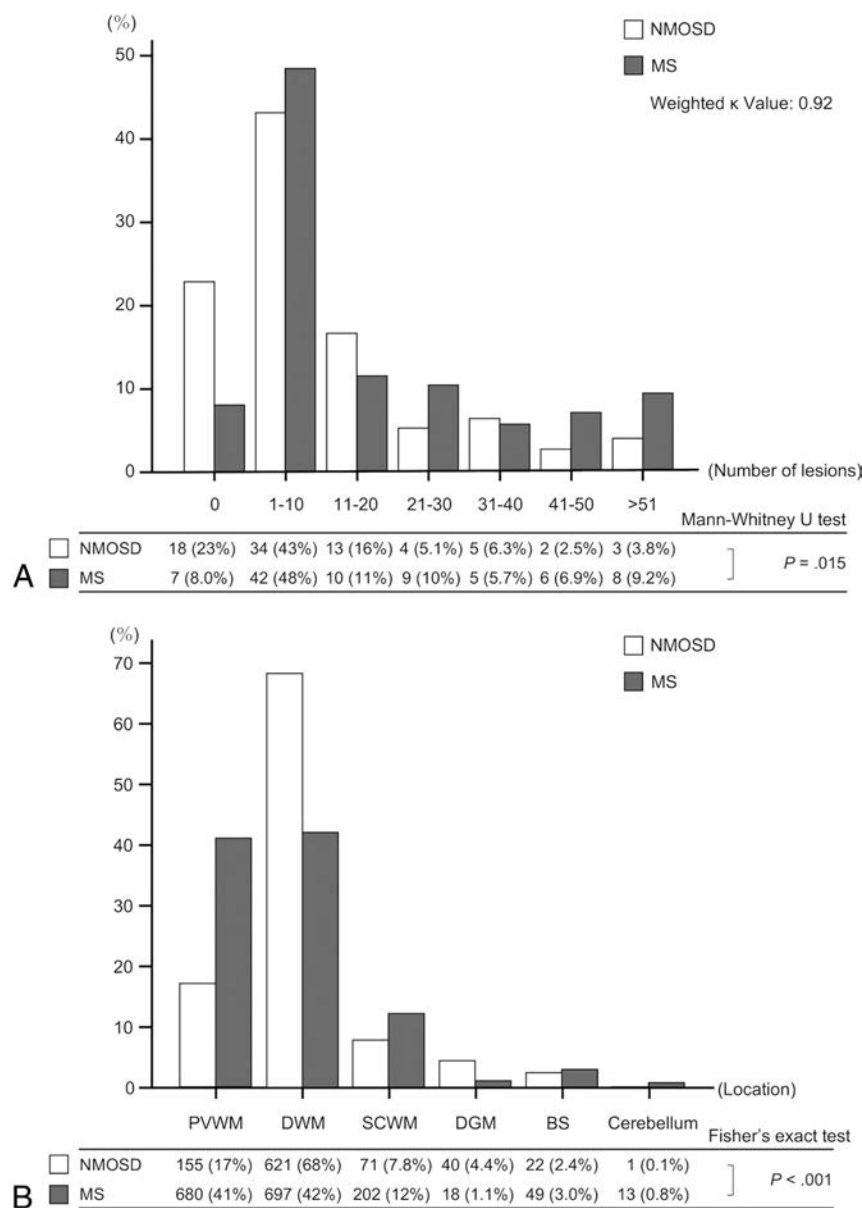


FIG 2. Bar graphs show the proportion of patients classified by the number of brain lesions in bins of 10 lesions (A), and the distribution of brain lesions categorized by the location (PVWM, DWM, SCWM, DGM, BS, cerebellum) (B) for rater 1. A total of 911 brain lesions in 79 patients with NMOSD and 1659 brain lesions in 87 patients with MS are identified. A, The proportion of patients is significantly different between NMOSD and MS ($P = .015$; weighted κ value, 0.92). More patients with NMOSD have no brain lesions of ≥ 3 mm, and a tendency for patients with MS to have more brain lesions than those with NMOSD is found. B, The distribution of lesions categorized by location is significantly different between NMOSD and MS ($P < .001$). DWM lesions (68%) are more frequent than PVWM lesions (17%) in NMOSD, whereas the difference in the frequencies of lesions in PVWM (41%) and DWM (42%) is small in MS.

and DWM: NMOSD, 17% and 68%; MS, 41% and 42%); this finding was consistent with a previous lesion probability map study.⁵ We speculate that characteristic immunoreactions associated with anatomic factors may cause the different distributions, especially in PVWM and DWM.

The pathogenesis of NMOSD lesions may differ in PVWM and DWM.^{10,11} Perivascular demyelination with loss of astrocytes associated with AQP4 expression is seen with PVWM lesions. These lesions are often accompanied by surrounding vasogenic edema but serially disappear or shrink, resulting in a decreased

number of PVWM lesions.²⁶ In contrast, DWM lesions were suspected to be caused by microvascular diseases regardless of AQP4 expression.^{13,27} Microvascular lesions were reported to include degeneration of neurons, gliosis, or perivascular spaces and persist across time. These different pathogeneses may affect the distribution of lesions.

In MS, the pathogenesis of both PVWM and DWM lesions involves local inflammation and myelin destruction, especially along medullary veins, which mostly run in DWM perpendicular to the lateral ventricles and gather conspicuously in PVWM.²⁸ This anatomic feature of medullary veins was suspected to influence the distribution of white matter lesions and may reflect the similar frequency of these lesions.^{29,30}

Although we found that ovoid/Dawson finger lesions and isolated U-fiber/juxtacortical lesions were present at significantly higher frequencies in MS than in NMOSD, compared with previous European studies, the frequencies of these lesions in NMOSD in this study (ovoid lesions, 21.5%; isolated U-fiber lesions, 10.1%) were higher.^{5,31} These European studies suggested that the presence of these lesions could distinguish MS from NMOSD with high sensitivity and specificity, but this may not apply to Asian patients with NMOSD.^{32,33} Genetic or environmental factors depending on different areas such as Asia and Europe were reported to affect imaging differences in patients with MS in different areas.³⁴ The imaging appearances of NMOSD may also differ between Asian and European patients. Further studies to reveal imaging appearances of NMOSD in different areas are required.

Although cloudlike enhancement was reported to be characteristic of NMOSD,²⁴ no patients with NMOSD in this study showed this sign. Cloudlike enhancement has been defined as "multiple patchy enhancement with blurred margin in adjacent regions, in comparison with isolated enhancing lesions,"²⁴ and we also evaluated this sign according to this definition. However, the diagnostic threshold for this sign may be slightly different depending on the rater, which may affect the results of this study. Further validation is needed.

NMOSD spinal cord lesions are known to be localized in regions of high AQP4 expression, and AQP4 expression was reported to be unchanged along all spinal levels in rats.³⁵ Therefore, spinal cord lesions in humans may also be unchanged along all

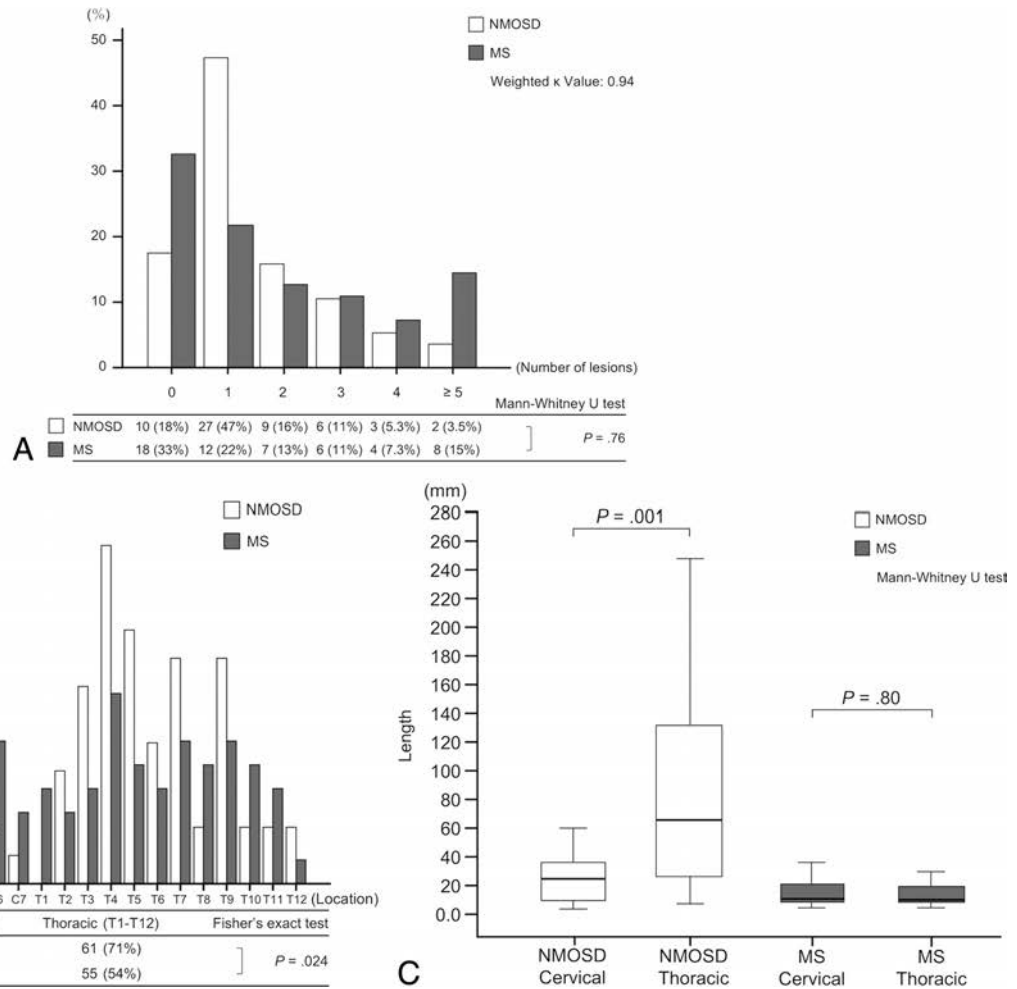


FIG 3. Graphs show the proportion of patients classified by the number of spinal cord lesions (A), the distribution and proportion of spinal cord lesions (B), and the length of spinal cord lesions in each location (C) for rater 1. A total of 86 spinal cord lesions in 57 patients with NMOSD and 102 spinal cord lesions in 55 patients with MS are identified. A, No significant difference is found in the number of lesions between NMOSD and MS ($P = .76$; weighted κ value, 0.94). Forty-seven (82%) patients with NMOSD and 37 (67%) with MS have ≥ 1 spinal cord lesion. B, Bimodal distributions of spinal cord lesions are present in both NMOSD and MS, but the peak of the distribution in NMOSD is high in thoracic regions, whereas the variation and peaks of the distribution are relatively smaller in MS than in NMOSD. The proportions of lesions categorized into cervical or thoracic regions are significantly different between NMOSD and MS ($P = .024$). More thoracic lesions (71%) than cervical lesions (29%) are found in NMOSD, whereas the difference in the frequencies of cervical (46%) and thoracic lesions (54%) is small in MS. C, In NMOSD, thoracic lesions are significantly longer than cervical lesions ($P = .001$), whereas in MS, the length is not significantly different between cervical and thoracic lesions ($P = .80$).

spinal levels. However, in this study, NMOSD spinal cord lesions showed a bimodal distribution with a high peak in thoracic regions, and more frequent (71%) and significantly longer lesions in thoracic regions than in cervical regions. Numerous thoracic lesions were also seen in a recent study.³⁶ In contrast, MS spinal cord lesions showed a small distribution variation and small differences in the frequency and length between cervical and thoracic lesions. We speculate that characteristic immunoreactions associated with anatomic factors may also cause the variation in spinal cord lesions.

We hypothesized that the ratio of gray matter in transverse sections may reflect the diversity of NMOSD spinal cord lesions. Much gray matter is present in cervical and lumbar intumescence, and the gray matter ratio tends to be higher in lower spinal levels.³⁷ Furthermore, lumbar intumescence, which is localized in thoracic vertebral levels, has a higher gray matter ratio than cervical intumescence. AQP4-IgG is known to destroy astrocytes,

which are abundant in gray matter. Thus, the peak distribution in thoracic regions and long, numerous thoracic lesions may be associated with the high gray matter ratio in thoracic levels. This hypothesis also explains the increased number of lesions in central compared with peripheral portions of the spinal cord. On the other hand, although NMOSD patients were considered to have spinal cord lesions longer than 3 vertebral segments,^{1,2,14} our results suggested that cervical lesions were not always long. Therefore, the spinal cord lesions may be short in some NMOSD patients who had spinal cord lesions in only cervical region.

MS spinal cord lesions were also reported to occur in perivenous regions, including both gray matter and white matter.³⁸ Unlike brain medullary veins, spinal intrinsic veins have numerous anastomoses and collateral networks in the spinal cord and may reflect the small differences in the distribution and length of lesions in the spinal cord.³⁹

We found that spinal cord atrophy and swelling were more frequent in NMOSD than in MS. It was reported that severe inflammatory reactions in NMOSD triggered demyelination, resulting in drastic spinal morphologic changes, whereas in MS, Wallerian degeneration mainly caused mild morphologic changes.⁴⁰ These different pathogeneses may affect morphologic features.

Bilateral optic neuritis and optic chiasm involvement were suggested to be specific features in NMOSD.⁴¹ However, we found no significant differences between NMOSD and MS. These discrepancies may be due to the following: First, we recruited consecutive patients in both acute and chronic phases, whereas the previous study included only patients in the acute phase; second, this retrospective optic nerve analysis examined a different number of patients between NMOSD and MS. Further prospective studies with distinct eligibility criteria are required.

This study had several limitations. First, the parameters and scanner types were not exactly matched among institutions. Because we cannot obtain reliable results of these analyses in this multi-institutional study,⁴² we did not perform automated analyses. To reduce variation, we only used T2-weighted images for detailed quantitative analyses. On the other hand, for the detection of lesions, FLAIR images may be slightly more sensitive than T2-weighted images, especially for detecting subcortical/cortical lesions, whereas total detectability and detected lesion size were reported to be almost the same between FLAIR and T2-weighted images.⁴³ Therefore, the results of lesion number and size were not significantly biased using T2-weighted images. Second, although different field strengths may cause different detectability of lesions, 1 study reported no apparent impact of brain 3T MR imaging compared with 1.5T MR imaging on the diagnosis of MS.⁴⁴ Therefore, analyses with different field strengths in NMOSD and MS did not seem to significantly influence differentiation of these diseases. Third, we could not analyze interobserver agreements regarding the lesion number, size, or location because the number of lesions detected differed between raters. However, some quantitative results, such as the number of spinal cord lesions per patient; the size of brain lesions in PVWM, DWM, and SCWM; and the longitudinal length of cervical lesions between NMOSD and MS, showed significant differences in only one rater but not the other. As a previous study reported that the reproducibility for detecting lesions was fair, and for evaluating lesion size, it was slight,⁴⁵ the statistically different results between raters may be due to independent evaluation of each lesion by the 2 raters. On the other hand, the proportion of patients categorized by lesion number showed almost perfect weighted κ values (brain, 0.92; spinal cord, 0.94). The other quantitative results showed the same statistical significance for both raters, and the distributions of lesions also showed similar tendencies between raters. Because these results were considered reliable and we emphasized and discussed these reliable results throughout this article, the statistically different results between raters did not affect the conclusions. Furthermore, 2 experienced neuroradiologists analyzed MR images, and the interobserver agreements of morphologic features (0.41–0.67) and signs (0.56–0.75) were moderate to sub-

stantial. Therefore, the assessments of the morphologic features and signs were also considered reliable.

CONCLUSIONS

Visually detailed quantitative analyses of all lesions in a large sample size showed imaging differences between NMOSD and MS in the number and location of brain lesions and the length and distribution of spinal cord lesions. This study confirmed previously observed differences in brain features and revealed longer and more thoracic lesions than cervical lesions in NMOSD in a large cohort of patients. These observations may have clinical implications.

Disclosures: Hiroyuki Tatekawa—RELATED: Grant: Bayer Yakuhin, Ltd (Osaka, Japan).* Shinici Sakamoto—RELATED: Grant: Bayer Yakuhin Ltd (Osaka, Japan).* Yoko Kaichi—RELATED: Grant: Bayer Yakuhin Ltd (Osaka, Japan).* Akira Kunimatsu—RELATED: Grant: Bayer Yakuhin Ltd (Osaka, Japan).* UNRELATED: Grants/Grants Pending: Daiichi-Sankyo Co Ltd (Tokyo, Japan), Eisai Co Ltd (Tokyo, Japan), Takeda Pharmaceutical Co Ltd (Tokyo, Japan)*; Payment for Lectures Including Service on Speakers Bureaus: Siemens Healthcare Diagnostics K.K. (Tokyo, Japan), Philips Electronics Japan (Tokyo), Toshiba Medical Systems (Tokyo, Japan); Payment for Manuscript Preparation: GE Healthcare Japan (Tokyo, Japan). Kentaro Akazawa—RELATED: Grant: Bayer Yakuhin Ltd (Osaka, Japan)*; UNRELATED: Grants/Grants Pending: Eisai (Tokyo, Japan), Daiichi Pharmaceutical (Tokyo, Japan), Fuji Pharma (Tokyo, Japan)*; Payment for Lectures Including Service on Speakers Bureaus: Daiichi Pharmaceutical (Tokyo, Japan), Eisai (Tokyo, Japan). Toshiteru Miyasaka—UNRELATED: Grants/Grants Pending: Bayer Yakuhin Ltd.* Toshiyuki Okubo—RELATED: Grant: Bayer Yakuhin Ltd (Osaka, Japan).* Kanehiro Hasuo—RELATED: Grant: Bayer Yakuhin Ltd (Osaka, Japan).* Kei Yamada—RELATED: Grant: Bayer Yakuhin Ltd*; UNRELATED: Grants/Grants Pending: Ministry of Health, Welfare and Labor*; Payment for Lectures Including Service on Speakers Bureaus: Eisai, Bayer, Daiichi-Sankyo. Satoshi Doishita—RELATED: Grant: Bayer Yakuhin Ltd (Osaka, Japan).* Taro Shimono—RELATED: Grant: Bayer Yakuhin Ltd (Osaka, Japan).* Yukio Miki—RELATED: Grant: Bayer Yakuhin Ltd (Osaka, Japan).* *Money paid to the institution.

ACKNOWLEDGMENTS

We thank Masahiro Fuchigami, Kondo Photo Process Co Ltd (Osaka, Japan), for his outstanding help and support with the statistical analyses.

REFERENCES

1. Wingerchuk DM, Lennon VA, Pittock SJ, et al. **Revised diagnostic criteria for neuromyelitis optica.** *Neurology* 2006;66:1485–89 CrossRef Medline
2. Wingerchuk DM, Lennon VA, Lucchinetti CF, et al. **The spectrum of neuromyelitis optica.** *Lancet Neurol* 2007;6:805–15 CrossRef Medline
3. Polman CH, Reingold SC, Banwell B, et al. **Diagnostic criteria for multiple sclerosis: 2010 revisions to the McDonald criteria.** *Ann Neurol* 2011;69:292–302 CrossRef Medline
4. Kitley J, Evangelou N, Küker W, et al. **Catastrophic brain relapse in seronegative NMO after a single dose of natalizumab.** *J Neurol Sci* 2014;339:223–25 CrossRef Medline
5. Matthews L, Marasco R, Jenkinson M, et al. **Distinction of seropositive NMO spectrum disorder and MS brain lesion distribution.** *Neurology* 2013;80:1330–37 CrossRef Medline
6. Pires CE, Silva CM, Lopes FC, et al. **Brain MRI abnormalities in Brazilian patients with neuromyelitis optica.** *J Clin Neurosci* 2012; 19:969–74 CrossRef Medline
7. Pittock SJ, Lennon VA, Krecke K, et al. **Brain abnormalities in neuromyelitis optica.** *Arch Neurol* 2006;63:390–96 CrossRef Medline
8. Filippi M, Rocca MA, Ciccarelli O, et al; MAGNIMS Study Group. **MRI criteria for the diagnosis of multiple sclerosis: MAGNIMS consensus guidelines.** *Lancet Neurol* 2016;15:292–303 CrossRef Medline
9. Huh SY, Min JH, Kim W, et al. **The usefulness of brain MRI at onset in the differentiation of multiple sclerosis and seropositive neuro-**

- myelitis optica spectrum disorders. *Mult Scler* 2014;20:695–704 CrossRef Medline
10. Tackley G, Kuker W, Palace J. **Magnetic resonance imaging in neuromyelitis optica.** *Mult Scler* 2014;20:1153–64 CrossRef Medline
 11. Kim W, Park MS, Lee SH, et al. **Characteristic brain magnetic resonance imaging abnormalities in central nervous system aquaporin-4 autoimmunity.** *Mult Scler* 2010;16:1229–36 CrossRef Medline
 12. Lu Z, Zhang B, Qiu W, et al. **Comparative brain stem lesions on MRI of acute disseminated encephalomyelitis, neuromyelitis optica, and multiple sclerosis.** *PLoS One* 2011;6:e22766 CrossRef Medline
 13. Sinnecker T, Dörr J, Pfueller CF, et al. **Distinct lesion morphology at 7-T MRI differentiates neuromyelitis optica from multiple sclerosis.** *Neurology* 2012;79:708–14 CrossRef Medline
 14. Wingerchuk DM, Banwell B, Bennett JL, et al; International Panel for NMO Diagnosis. **International consensus diagnostic criteria for neuromyelitis optica spectrum disorders.** *Neurology* 2015;85:177–89 CrossRef Medline
 15. Juryńczyk M, Craner M, Palace J. **Overlapping CNS inflammatory diseases: differentiating features of NMO and MS.** *J Neurol Neurosurg Psychiatry* 2015;86:20–25 CrossRef Medline
 16. Miki Y, Grossman RI, Udupa JK, et al. **Isolated U-fiber involvement in MS: preliminary observations.** *Neurology* 1998;50:1301–06 CrossRef Medline
 17. Geurts JJ, Pouwels PJ, Uitdehaag BM, et al. **Intracortical lesions in multiple sclerosis: improved detection with 3D double inversion-recovery MR imaging.** *Radiology* 2005;236:254–60 CrossRef Medline
 18. Mike A, Glanz BI, Hildenbrand P, et al. **Identification and clinical impact of multiple sclerosis cortical lesions as assessed by routine 3T MR imaging.** *AJNR Am J Neuroradiol* 2011;32:515–21 CrossRef Medline
 19. Horowitz AL, Kaplan RD, Grewe G, et al. **The ovoid lesion: a new MR observation in patients with multiple sclerosis.** *AJNR Am J Neuroradiol* 1989;10:303–05 Medline
 20. Sahraian MA, Radue EW, Haller S, et al. **Black holes in multiple sclerosis: definition, evolution, and clinical correlations.** *Acta Neurol Scand* 2010;122:1–8 CrossRef Medline
 21. Palmer S, Bradley WG, Chen DY, et al. **Subcallosal striations: early findings of multiple sclerosis on sagittal, thin-section, fast FLAIR MR images.** *Radiology* 1999;210:149–53 CrossRef Medline
 22. Ge Y, Grossman RI, Babb JS, et al. **Dirty-appearing white matter in multiple sclerosis: volumetric MR imaging and magnetization transfer ratio histogram analysis.** *AJNR Am J Neuroradiol* 2003;24:1935–40 Medline
 23. Lucchinetti CF, Gavriloa RH, Metz I, et al. **Clinical and radiographic spectrum of pathologically confirmed tumefactive multiple sclerosis.** *Brain* 2008;131:1759–75 CrossRef Medline
 24. Ito S, Mori M, Makino T, et al. **“Cloud-like enhancement” is a magnetic resonance imaging abnormality specific to neuromyelitis optica.** *Ann Neurol* 2009;66:425–28 CrossRef Medline
 25. Landis JR, Koch GG. **The measurement of observer agreement for categorical data.** *Biometrics* 1977;33:159–74 CrossRef Medline
 26. Lucchinetti CF, Guo Y, Popescu BF, et al. **The pathology of an autoimmune astrocytopathy: lessons learned from neuromyelitis optica.** *Brain Pathol* 2014;24:83–97 CrossRef Medline
 27. Cabrera-Gomez JA, Kister I. **Conventional brain MRI in neuromyelitis optica.** *Eur J Neurol* 2012;19:812–19 CrossRef Medline
 28. Taoka T, Fukusumi A, Miyasaka T, et al. **Structure of the medullary veins of the cerebral hemisphere and related disorders.** *Radiographics* 2017;37:281–97 CrossRef Medline
 29. Lee MA, Smith S, Palace J, et al. **Spatial mapping of T2 and gadolinium-enhancing T1 lesion volumes in multiple sclerosis: evidence for distinct mechanisms of lesion genesis?** *Brain* 1999;122(Pt 7):1261–70 CrossRef Medline
 30. Tallantyre EC, Dixon JE, Donaldson I, et al. **Ultra-high-field imaging distinguishes MS lesions from asymptomatic white matter lesions.** *Neurology* 2011;76:534–39 CrossRef Medline
 31. Juryńczyk M, Tackley G, Kong Y, et al. **Brain lesion distribution criteria distinguish MS from AQP4-antibody NMOSD and MOG-antibody disease.** *J Neurol Neurosurg Psychiatry* 2017;88:132–36 CrossRef Medline
 32. Matsushita T, Isobe N, Piao H, et al. **Reappraisal of brain MRI features in patients with multiple sclerosis and neuromyelitis optica according to anti-aquaporin-4 antibody status.** *J Neurol Sci* 2010;291:37–43 CrossRef Medline
 33. Liao MF, Chang KH, Lyu RK, et al. **Comparison between the cranial magnetic resonance imaging features of neuromyelitis optica spectrum disorder versus multiple sclerosis in Taiwanese patients.** *BMC Neurol* 2014;14:218 CrossRef Medline
 34. Kira J. **Multiple sclerosis in the Japanese population.** *Lancet Neurol* 2003;2:117–27 CrossRef Medline
 35. Oklinski MK, Lim JS, Choi HJ, et al. **Immunolocalization of water channel proteins AQP1 and AQP4 in rat spinal cord.** *J Histochem Cytochem* 2014;62:598–611 CrossRef Medline
 36. Dumrikarnlert C, Siritho S, Chulapimphan P, et al. **The characteristics of spinal imaging in different types of demyelinating diseases.** *J Neurol Sci* 2017;372:138–43 CrossRef Medline
 37. Goto N, Otsuka N. **Development and anatomy of the spinal cord.** *Neuropathology* 1997;17:25–31 CrossRef
 38. Gilmore CP, Bö L, Owens T, et al. **Spinal cord gray matter demyelination in multiple sclerosis—a novel pattern of residual plaque morphology.** *Brain Pathol* 2006;16:202–08 CrossRef Medline
 39. Griessenauer CJ, Raborn J, Foreman P, et al. **Venous drainage of the spine and spinal cord: a comprehensive review of its history, embryology, anatomy, physiology, and pathology.** *Clin Anat* 2015;28:75–87 CrossRef Medline
 40. Liu Y, Wang J, Daams M, et al. **Differential patterns of spinal cord and brain atrophy in NMO and MS.** *Neurology* 2015;84:1465–72 CrossRef Medline
 41. Khanna S, Sharma A, Huecker J, et al. **Magnetic resonance imaging of optic neuritis in patients with neuromyelitis optica versus multiple sclerosis.** *J Neuroophthalmol* 2012;32:216–20 CrossRef Medline
 42. Jovicich J, Czanner S, Han X, et al. **MRI-derived measurements of human subcortical, ventricular and intracranial brain volumes: reliability effects of scan sessions, acquisition sequences, data analyses, scanner upgrade, scanner vendors and field strengths.** *Neuroimage* 2009;46:177–92 CrossRef Medline
 43. Yousry TA, Filippi M, Becker C, et al. **Comparison of MR pulse sequences in the detection of multiple sclerosis lesions.** *AJNR Am J Neuroradiol* 1997;18:959–63 Medline
 44. Kataoka H, Kiriya T, Taoka T, et al. **Comparison of brain 3.0-T with 1.5-T MRI in patients with multiple sclerosis: a 6-month follow-up study.** *Clin Neurol Neurosurg* 2014;121:55–58 CrossRef Medline
 45. Tan IL, van Schijndel RA, Fazekas F, et al. **Improved interobserver agreement for visual detection of active T2 lesions on serial MR scans in multiple sclerosis using image registration.** *J Neurol* 2001;248:789–94 CrossRef Medline

Visualization and Classification of Deeply Seated Collateral Networks in Moyamoya Angiopathy with 7T MRI

T. Matsushige, M. Kraemer, T. Sato, P. Berlit, M. Forsting, M.E. Ladd, R. Jabbarli, U. Sure, N. Khan, M. Schlamann, and K.H. Wrede



ABSTRACT

BACKGROUND AND PURPOSE: Collateral networks in Moyamoya angiopathy have a complex angioarchitecture difficult to comprehend on conventional examinations. This study aimed to evaluate morphologic patterns and the delineation of deeply seated collateral networks using ultra-high-field MRA in comparison with conventional DSA.

MATERIALS AND METHODS: Fifteen white patients with Moyamoya angiopathy were investigated in this prospective trial. Sequences acquired at 7T were TOF-MRA with $0.22 \times 0.22 \times 0.41 \text{ mm}^3$ resolution and MPRAGE with $0.7 \times 0.7 \times 0.7 \text{ mm}^3$ resolution. Four raters evaluated the presence of deeply seated collateral networks and image quality in a consensus reading of DSA, TOF-MRA, and MPRAGE using a 5-point scale in axial source images and maximum intensity projections. Delineation of deeply seated collateral networks by different imaging modalities was compared by means of the McNemar test, whereas image quality was compared using the Wilcoxon signed-rank test.

RESULTS: The relevant deeply seated collateral networks were classified into 2 categories and 6 pathways. A total of 100 collateral networks were detected on DSA; 106, on TOF-MRA; and 73, on MPRAGE. Delineation of deeply seated collateral networks was comparable between TOF-MRA and DSA ($P = .25$); however, both were better than MPRAGE ($P < .001$).

CONCLUSIONS: This study demonstrates excellent delineation of 6 distinct deeply seated collateral network pathways in Moyamoya angiopathy in white adults using 7T TOF-MRA, comparable to DSA.

ABBREVIATIONS: DSCN = deeply seated collateral network; MMA = Moyamoya angiopathy; SEM = standard error of the mean

Moyamoya angiopathy (MMA) is a rare cerebral vasculopathy with progressive steno-occlusion of the intracranial portion of the internal carotid arteries.^{1,2} A secondary crucial pathophysiology is characterized by progressive formation of col-

lateral vessels at the base of the brain, so-called “Moyamoya vessels,” and mutual anastomoses to compensate hemodynamic insufficiency.¹⁻⁴ Considering these diagnostic criteria, MRA along with flow-void-based T2-weighted imaging, plays a primary role in addition to DSA in the current clinical work-up.^{2,5}

Recent reports suggested the importance of collateral networks in MMA for classifying disease severity.⁶⁻¹⁰ Despite these collaterals, MMA manifests with hemodynamic insufficiency with transient ischemic attacks, strokes, and choreoathetiform movements in early childhood and in young adults.¹¹⁻¹³ In contrast to the positive compensatory role of collateral networks, clinical presentation with cerebral bleeding has been attributed to the rupture of extensive fragile collateral vessels, and chronic headaches have been attributed to extensive dural anastomoses.^{14,15}

Received July 5, 2016; accepted after revision March 7, 2018.

From the Department of Neurosurgery (T.M., T.S., R.J., U.S., K.H.W.), University Hospital Essen, University Duisburg-Essen, Essen, Germany; Department of Neurosurgery (T.M.), Graduate School of Biomedical and Health Sciences, Hiroshima University, Hiroshima, Japan; Erwin L. Hahn Institute for Magnetic Resonance Imaging (T.M., T.S., M.E.L., K.H.W.), University Duisburg-Essen, Essen, Germany; Department of Neurology (M.K., P.B.), Alfried Krupp Hospital, Essen, Germany; Department of Neurology (M.K.), University Hospital Dueseldorf, Dueseldorf, Germany; Department of Neurosurgery (T.S.), Fukushima Medical University, Fukushima, Japan; Department of Diagnostic and Interventional Radiology and Neuroradiology (M.F., M.S.), University Hospital Essen, Essen, Germany; Medical Physics in Radiology (M.E.L.), German Cancer Research Center, Heidelberg, Germany; Faculty of Physics and Astronomy and Faculty of Medicine (M.E.L.), University of Heidelberg, Heidelberg, Germany; Moyamoya Center, Division of Pediatric Neurosurgery (N.K.), Department of Surgery, University Children's Hospital Zurich, Zurich, Switzerland; and Department of Neuroradiology (M.S.), University Hospital Cologne, Cologne, Germany.

Toshinori Matsushige, Markus Kraemer, Marc Schlamann, and Karsten H. Wrede contributed equally to this work.

This work received funding from the University of Duisburg-Essen (Programm zur internen Forschungsförderung Essen [IFORES grant] to K.H.W.).

Please address correspondence to Karsten H. Wrede, MD, University Hospital Essen, Department of Neurosurgery, Hufelandstr 55, 45147 Essen, Germany; e-mail: karsten.wrede@uk-essen.de

Indicates article with supplemental on-line tables.

<http://dx.doi.org/10.3174/ajnr.A5700>

While morphologic submillimeter studies of complex and tiny collateral vessels are still ongoing, assessment of these collaterals in most cases remains unfeasible with conventional 3T MR imaging and is challenging with DSA, the current clinical diagnostic standard. Nevertheless, proliferation of these fine anastomoses could be evaluated by MR imaging indirectly as a summation of high signal intensity in the basal ganglia,^{16,17} or, alternatively, by specific collateral pathways running adjacent to the ventricles.^{9,18}

Since Cho et al¹⁹ reported the application of ultra-high-field 7T MRA for excellent visualization of intracranial perforating arteries, depiction of intracranial submillimeter vessels has further advanced. Several studies have suggested the feasibility and diagnostic accuracy for delineation of submillimeter perforating arteries, microvascular structures, and vessel walls.²⁰⁻²⁶ Therefore, studies on collateral networks in MMA using ultra-high-field 7T MR imaging are warranted. Better visualization of deeply seated collateral networks (DSCNs) in MMA might improve our understanding of this rare and complicated pathophysiology and presumably facilitate treatment decisions. In the present study, morphologic visualization of collateral networks in adult patients with MMA using 7T MRA was evaluated in comparison with DSA. Moreover, this study aimed to delineate different types of collateral networks.

MATERIALS AND METHODS

The study patients were recruited consecutively at Alfried Krupp Hospital in Essen, Germany. There were no ethnic inclusion or exclusion criteria. All patients with Moyamoya angiopathy in the hospital cohort were of white ethnic background. Participation was voluntary and refusal to participate had no consequence for further treatment. The University of Duisburg-Essen ethics committee authorized the study, and all patients provided written informed consent before examination. The study was conducted according to the principles of the Declaration of Helsinki and was Health Insurance Portability and Accountability Act-compliant.

In addition to a standard clinical work-up with conventional MRA and selective DSA, 15 patients with MMA were prospectively recruited for a 7T TOF-MRA feasibility study commencing in October 2011.²⁷ Except in the case of patients with a second postoperative 7T MR imaging, the 7T MR imaging was performed within 1 week of DSA. In the current observational study, delineation of collateral networks has been further evaluated. Inclusion criteria were the following: 1) idiopathic MMA (classic Moyamoya disease and unilateral variants of Moyamoya angiopathy) previously diagnosed via DSA and conventional MR imaging, 2) 18 years of age and older, and 3) the ability to give informed consent. Exclusion criteria were the following: 1) a known concomitant disease (Moyamoya syndrome), ie, cerebral vasculitis, Down syndrome, or von Recklinghausen neurofibromatosis,² 2) the presence of a cardiac pacemaker or any other electronic implants, 3) pregnancy or breast-feeding, and 4) claustrophobia.

High-Resolution 7T MRA

All subjects were evaluated using a 7T whole-body MR imaging system (Magnetom 7T; Siemens, Erlangen, Germany) equipped with a 1-channel transmit/32-channel receive head radiofrequency coil (Nova Medical, Wilmington, Massachusetts) begin-

ning in October 2011 at the Erwin L. Hahn Institute for Magnetic Resonance Imaging, University of Duisburg-Essen, Essen, Germany. The system has a gradient system providing 40 mT/m maximum amplitude and a slew rate of 200 mT/m/ms. High-resolution MRA was acquired with a customized 3D fast low-angle shot TOF pulse sequence^{27,28} (voxel size, $0.22 \times 0.22 \times 0.41$ mm³) and with a modified MPRAGE sequence²⁹⁻³¹ (voxel size, $0.7 \times 0.7 \times 0.7$ mm³). Detailed sequence parameters for 7T MR imaging are listed in On-line Table 1.

DSA

Six-vessel DSA was performed using an Axiom Artis angiography suite (Siemens) in the Department of Neuroradiology of Alfried Krupp Hospital in Essen, Germany. After the standardized introduction, 45° oblique 2-plane projections of the posterior circulatory system and both internal carotid artery circulation areas were acquired.

Image Analysis

Image evaluation was performed using a freeware DICOM reader (Horos, Version 2.0.1; <http://www.horosproject.org/>). DSCNs were classified according to location and connecting vessels, referring to morphologic characteristics described by Baltsavias et al,³²⁻³⁴ who described collateral circulation in pediatric Moyamoya disease with superselective angiography. Images were analyzed by 1 experienced vascular neurologist (M.K.), 2 experienced vascular neurosurgeons (T.M. and K.H.W.), and 1 experienced neuroradiologist (M.S.) in a consensus reading. At first, all raters evaluated the images separately, and afterward, a consensus was found by discussion. Reading was performed in 9 sessions with at least a 2-week interval between each session (3 sessions for every imaging technique and 5 patients per session).

Overall image quality and image quality for anastomoses to major trunk vessels and collateral pathways to cortical vessels were rated on a 5-point scale (5 = excellent, 4 = good, 3 = moderate, 2 = poor, and 1 = nondiagnostic). Collateral networks were rated by a 3-stage evaluation process using a different 5-point scale (5 = excellent, collateral networks obviously detected with clear identification of the vessel course and high vessel-tissue contrast; 4 = good, collateral networks well-detected with lower vessel-tissue contrast; 3 = moderate, collateral networks partially obscured but still adequate for diagnosis; 2 = poor, collateral connections scarcely demonstrated but sufficient to presume their existence; and 1 = no collateral networks detected).

At first, each rater individually assessed the DSA images for the presence and image quality of collateral networks. Additionally, the Suzuki stages in DSA were rated by an experienced vascular neurosurgeon as a fifth rater (N.K.). In the second step, the transverse source images and MIPs with slab thicknesses of 10–20 mm obtained with TOF-MRA and MPRAGE were evaluated in the same way. Finally, all 4 raters discussed their individual evaluations to establish a consensus reading. To assess interobserver concordance, an experienced vascular neurosurgeon evaluated the data blinded to the consensus results as a fifth rater (T.S.). For analysis of image quality in collateral networks, subjects without detection on DSA were excluded.

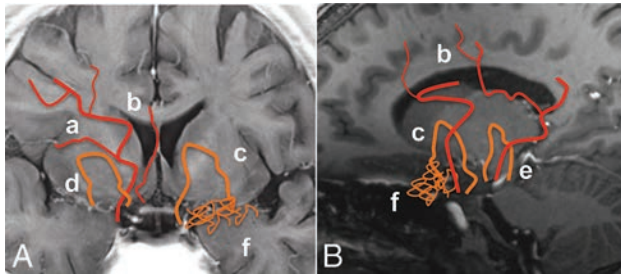


FIG 1. Schematic illustrations of deeply seated collateral networks are shown in coronal (A) and sagittal (B) MR imaging views. Six pathways of collateral vessels according to perfusing territories can be divided into collateral networks to cortical vessels (remote, type a and b) and to major trunk vessels (local, types c–f). Anastomoses between striate arteries or choroidal arteries and cortical arteries directly or via medullary arteries (a); septal transcallosal anastomoses between choroidal arteries with pericallosal arteries (b); anastomoses between choroidal arteries or the posterior communicating artery and thalamostriate arteries (c); intrastriate anastomosis among striate arteries (d); intrathalamic anastomosis among thalamic arteries (e); and focal Moyamoya vessels in the basal cistern (f).

Statistical Analysis

Delineation of collateral networks was analyzed by the McNemar test. Image quality was compared using Wilcoxon signed-rank tests. Corrections for multiple comparisons were performed with the Bonferroni method. Interobserver concordance was assessed using the κ coefficient. Statistical analyses were performed with the JMP statistical package (Version 10; SAS Institute, Cary, North Carolina) and the STATA software package (Version 14.2; StataCorp, College Station, Texas).

RESULTS

Patients comprised 4 men and 11 women with an average age of 36 years (range, 19–58 years). Two patients had a unilateral variant of MMA (cases 3 and 4). All were from white family backgrounds. Two patients underwent all examinations both before and up to 6 months after bypass surgery (cases 1 and 5). Clinical characteristics are summarized in On-line Table 2. All examinations were successfully performed without adverse events.

In total, 32 affected hemispheres were evaluated. According to the Suzuki angiographic staging, 7 hemispheres were rated as stage II, 20 were rated as stage III, and 5 were rated as stage IV. Overall image quality was rated excellent for most scans. The mean overall image quality was 4.7 (standard error of the mean [SEM] = 0.12; range, 4–5) in DSA, 4.9 (SEM = 0.07; range, 4–5) in TOF-MRA, and 4.5 (SEM = 0.13; range, 4–5) in MPRAGE.

Interobserver concordance was almost perfect for identification of collateral networks in DSA (0.9001), TOF-MRA (0.9243), and MPRAGE (0.8699). Interobserver concordance for the quality of collateral network delineation was moderate to substantial in DSA (0.4214), TOF-MRA (0.6143), and MPRAGE (0.4825), with only 1-point variability for most differing ratings.

DSCNs were classified into 2 major categories (connection to cortical vessels/major trunk vessels) with a total of 6 pathways (Fig 1, a–f). One hundred collateral networks were detected in DSA; 106, in TOF-MRA; and 73, in MPRAGE. Basic patient characteristics and scoring for DSCNs are summarized in On-line Tables 3 and 4.

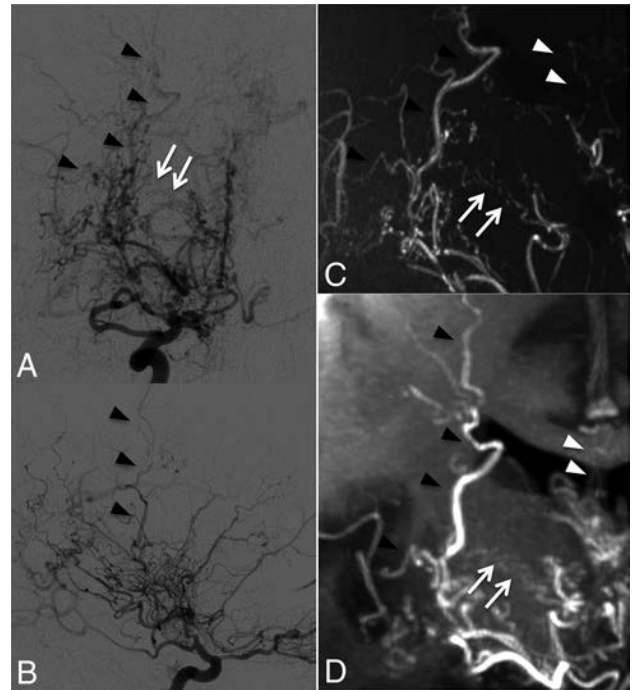


FIG 2. Case 1. Selective right internal carotid angiography (anteroposterior, A; lateral view, B) shows anastomotic connections to cortical arteries from the anterior choroidal artery (black arrowheads, type b) as well as from thalamostriate arteries (white arrows, type a). Collateral networks are excellently visualized in MIP from TOF-MRA with slab thickness of 20 mm (white arrows and black arrowheads) (C). Transcallosal connections to cortical arteries (white arrowheads) not detected by DSA are poorly visualized on MPRAGE (D).

Morphology of DSCNs

DSCNs had pathways connecting to 2 cortical vessels: either the peripheral MCA or the anterior cerebral artery. Most anastomoses were detected between either choroidal arteries or striate arteries and cortical arteries directly or via medullary arteries (type a: Fig 2). Septal transcallosal anastomoses between choroidal arteries and pericallosal arteries were also identified (type b: Fig 2).

Collateral networks among major trunk vessels (MCA, anterior cerebral artery, choroidal arteries, and communicating arteries) were also identified as having a U-shaped running course. Especially, anastomoses between either choroidal arteries or the posterior communicating artery and thalamostriate arteries were located in the basal ganglia running adjacent to the ventricles (type c: Fig 3). Intrastriate anastomoses among striate arteries were prominent in the basal ganglia (type d: Fig 4). Intrathalamic anastomoses among thalamic arteries from posterior cerebral arteries were relatively rare (type e: Fig 5). Anastomoses among Moyamoya vessels focally proliferated in the basal cistern were detected in all patients (type f: Fig 4).

Eighteen (type a, $n = 11$; type b, $n = 7$) collateral networks connecting to cortical arteries were detected in DSA; 25 (type a, $n = 16$; type b, $n = 9$), in TOF-MRA; and 12 (type a, $n = 8$; type b, $n = 4$), in MPRAGE. Whereas 82 (type c, $n = 21$; type d, $n = 21$; type e, $n = 8$; type f, $n = 32$) collateral networks connecting major trunk vessels were detected in DSA; 81 (type c, $n = 19$; type d, $n = 22$; type e, $n = 8$; type f, $n = 32$) were detected in TOF-MRA; and 61 (type c, $n = 9$; type d, $n = 16$; type e, $n = 6$; type f, $n = 30$), in MPRAGE.

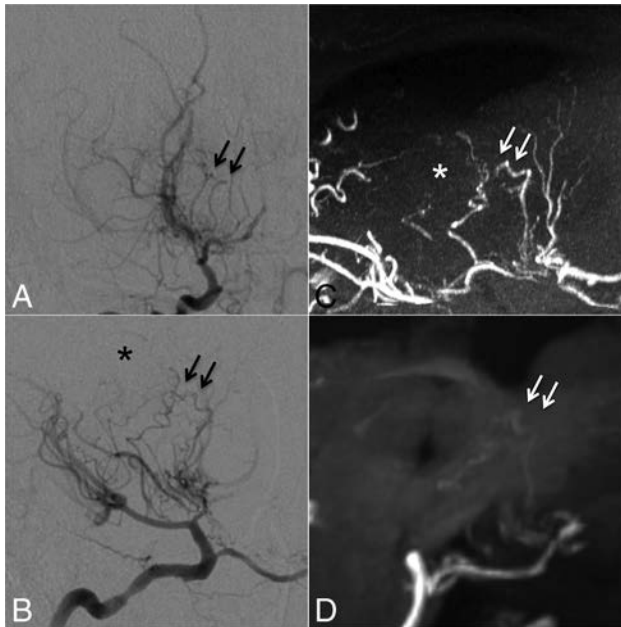


FIG 3. Case 8. Selective right internal carotid angiography (anteroposterior, *A*; right 45° oblique view, *B*) shows anastomosis between the posterior communicating artery and the thalamostriate arteries (arrows, type c). MIP from TOF-MRA (*C*) demonstrates this anastomosis clearly as well as connection with the anterior choroidal artery (asterisk). The latter anastomosis could neither be detected in DSA nor visualized by MIP from MPRAGE (*D*).

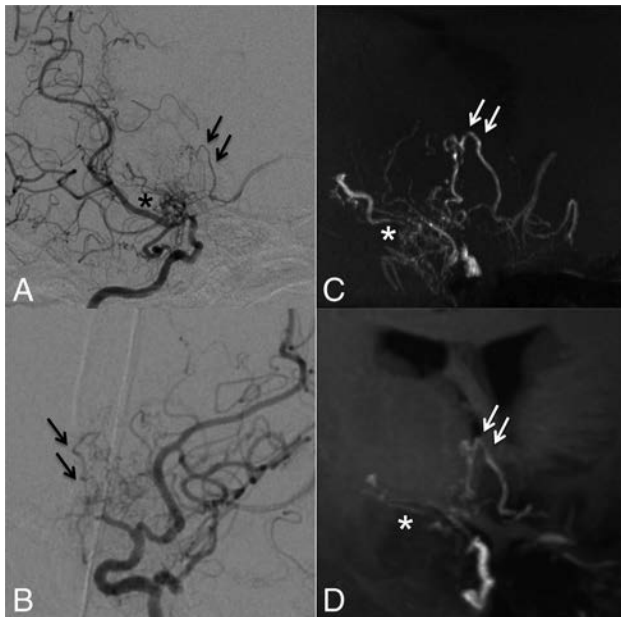


FIG 4. Case 5. Selective right internal carotid angiography (right 45° oblique, *A*; left 45° oblique view, *B*) shows intrastriatal anastomoses among thalamostriate arteries running through the periventricular space (arrows, type d). MIP from TOF-MRA (*C*) excellently demonstrates these networks as well as focal connections among Moyamoya vessels in the basal cistern (asterisk, type f). MIP from MPRAGE (*D*) moderately depicts the network; however, basal Moyamoya vessels are poorly visualized.

Regarding DSA as a clinical standard, 96 of 100 (96%) collateral networks were delineated in TOF-MRA, and 71 of 100 (71%), in MPRAGE. Figure 6 shows an example of an anastomosis delin-

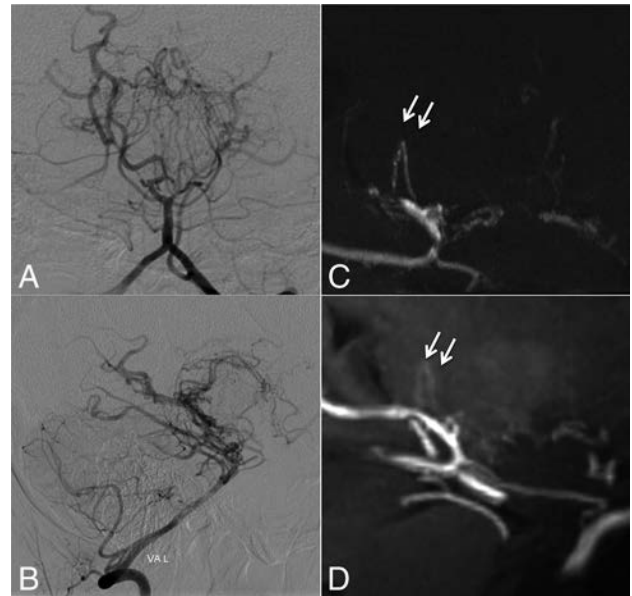


FIG 5. Case 6. Selective left vertebral angiography (anteroposterior, *A*; lateral view, *B*) shows no marked anastomosis. The MIP from TOF-MRA (*C*) demonstrates excellent visualization of inner thalamic anastomosis among posterior thalamostriate arteries (white arrows, type e), whereas the visualization is only moderate on MIP from MPRAGE (*D*).

ated by DSA, but not by TOF-MRA or MPRAGE. Conversely, 9 anastomoses were identified by MRA (TOF: $n = 9$; MPRAGE: $n = 3$) that were not visible in DSA images. Seven were anastomoses with cortical arteries, and the others were an inner-striatal and a thalamic anastomosis. These DSA false-negative cases were presumably due to contrast washout and limited viewing angles during the DSA examination. Delineation of DSCNs was comparable between TOF-MRA and DSA ($P = .25$); however, both were better than MPRAGE ($P < .001$). The morphologic characteristics and detected number of DSCNs as well as the image quality of each imaging technique are summarized in the Table.

Image-Quality Comparison among DSA, 7T TOF-MRA, and MPRAGE

Image quality of 100 collateral pathways detected on DSA (18 connecting to cortical arteries and 32 to major trunk vessels) was evaluated. In collateral pathways to cortical arteries, image quality in DSA, TOF-MRA, and MPRAGE was 4.0 (SEM = 0.28; range, 3–5), 4.8 (SEM = 0.10; range, 3–5), and 2.4 (SEM = 0.35; range, 1–5), respectively. The image quality of TOF-MRA proved to be significantly better than that of DSA ($P = .02$) or MPRAGE ($P < .001$); the image quality of DSA was better than that of MPRAGE ($P = .01$). For anastomoses to major trunk vessels, image quality of DSA and 7T TOF-MRA was comparable, 4.6 (SEM = 0.07; range, 2–5) versus 4.4 (SEM = 0.12; range, 3–5) ($P = .07$); however, both were better than MPRAGE 2.7 (SEM = 0.13; range, 1–5) ($P < .001$).

DISCUSSION

This study visualized collateral networks in MMA with ultra-high-field 7T MRA. The high spatial resolution of the applied 7T TOF-MRA sequence allowed comparable visualization of collat-

eral networks in MMA with standard selective DSA. The spatial resolution of conventional DSA is as high as 0.1 mm^2 ;³⁵ however, dynamic flow alterations and overlapping vessels can impair clear identification of small collateral networks. The lack of anatomic landmarks can further hamper understanding of the complex angioarchitecture of these networks. In contrast, MRA provides high-resolution 3D vessel delineation (TOF-MRA, $0.22 \times 0.22 \times 0.41 \text{ mm}^3$ in this study) in combination with visualization of adjacent brain structures, helping to comprehend the network morphology and its distinct location. Therefore, the current clinical standard DSA is complemented by 7T MR imaging.

In the presented study, 9 collateral networks not visible on DSA could be detected by 7T MRA, with most ($n = 7$) being collateral connections to cortical vessels. The impaired visualiza-

tion in DSA might be explained by flow interactions of various anastomotic collateral vessels (ie, leptomeningeal or durocortical collateral networks) predominantly in peripheral territories. A second explanation is visualization impairment due to overlapping vessel structures hiding small collateral networks. As reported in previous studies, TOF-MRA was significantly better for visualization of submillimeter vessels than nonenhanced MPRAGE.²⁴⁻²⁷ The main disadvantage of the MPRAGE sequence was the lower spatial resolution, which restricted detection of small collateral networks. Furthermore, visualization of the complete collateral network was also impaired in most cases. Although the applied MPRAGE sequence successfully visualized some collateral networks, it was inferior to 7T TOF-MRA and DSA and does not seem suitable for evaluation of the complex angioarchitecture in MMA.

In addition to the combination of high-resolution vessel delineation and depiction of adjacent brain structures by 7T MRA, application of MIP processing allows visualization of collateral networks comparable with superselective DSA. Nevertheless, collateral vessels in MMA have a very complex angioarchitecture and are difficult to investigate, even with superselective DSA. Recently, Baltsavias et al³²⁻³⁴ first and precisely demonstrated the collateral circulations in pediatric Moyamoya disease by superselective DSA with microcatheters. However, superselective DSA is accompanied by considerable risks for cerebral hemorrhage because of vessels that might be injured by the microcatheter, especially in fragile Moyamoya collaterals. Besides being noninvasive, 1 further major advantage of 7T MRA MIP over superselective angiography is the possibility of unrestricted 3D rotations.

The excellent depiction of the angioarchitecture by 7T TOF-MRA in combination with MIP allowed the establish-

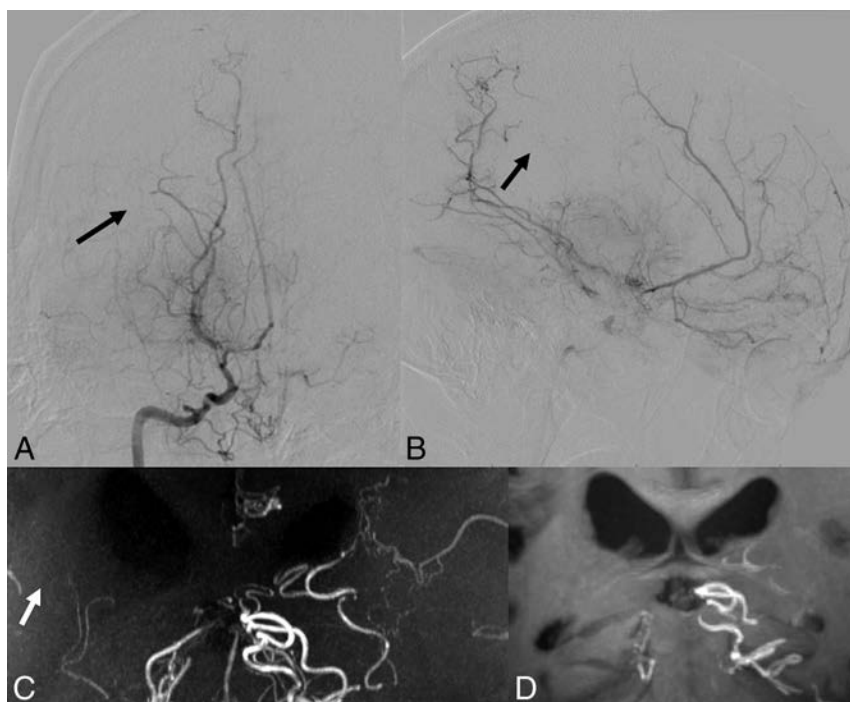


FIG 6. Case 10. Selective right vertebral angiography (anteroposterior, A; lateral view, B) shows a tiny, barely visible anastomosis (black arrows) between the posterior thalamostriate artery and a medullary-cortical artery. MIP from TOF-MRA (C) and MIP from MPRAGE (D) do not delineate the anastomosis. The white arrow (C) indicates the supposed anatomic location of the anastomosis.

Comparison of 7T MRA and DSA regarding the number of detected collateral networks and image quality for anastomoses to major trunk vessels and collateral pathways to cortical vessels

Type	Connecting Vessels in Collateral Networks	DSA	TOF-MRA	MPRAGE
Collateral networks connecting to cortical arteries				
a	Striate/choroidal arteries and medullary-cortical arteries	11	16	8
b	Striate/choroidal arteries and the pericallosal arteries	7	9	4
	Total	18	25	12
	Image quality ($n = 18$) ^a (mean) (SEM) (range)	4.0 (0.26, 3–5)	4.8 (0.10, 3–5)	2.4 (0.35, 1–5)
Collateral networks connecting to major trunk vessels				
c	Choroidal arteries or PcomA and thalamostriate arteries	21	19	9
d	Intraatrial arteries	21	22	16
e	Intrathalamic arteries	8	8	6
f	Moyamoya vessels in the basal cistern	32	32	30
	Total	82	81	61
	Image quality ($n = 82$) ^a (mean) (SEM) (range)	4.6 (0.07, 2–5)	4.4 (0.12, 3–5)	2.7 (0.13, 1–5)

Note.—PcomA indicates posterior communicating artery.

^aImage quality was evaluated in collateral networks detected by DSA as a clinical standard using a 5-point scale.

ment of a comprehensive classification of collateral networks in MMA. The classification comprises 2 main subtypes: collateral networks connecting the circle of Willis with cortical arteries (remote type) and collateral networks between major trunk vessels (local type). The latter are characterized by their U-shaped running course. In total, 6 distinct collateral network types were identified. So far, the clinical relevance of collateral vessels has been indirectly evaluated by depiction of dilated branching arteries (ie, of the posterior communicating artery and/or the anterior choroidal artery).^{6–8} Recently, 3T flow-sensitive black-blood MRA allowed Funaki et al¹⁸ to specify one of the deeply seated collateral pathways adjacent to the ventricles, the so-called “periventricular anastomosis” between either thalmo-perforating or choroidal arteries and medullary arteries. They suggested that this pathway is associated with vessel fragility and hemorrhagic presentation at onset in Moyamoya disease.⁹ A recent 7T TOF-MRA study on intraventricular submillimeter microaneurysms in collateral networks branching from the posterior choroidal artery supports this hypothesis.³⁶ Although the clinical relevance of the different collateral networks remains unclear, the presented classification can improve our understanding of the complex pathophysiology of MMA and might serve as a follow-up marker, especially after bypass surgery.

With regard to MRA, the better delineation of Moyamoya vessels in stronger magnets has been previously reported.^{16,17,37} However, these studies only analyzed summation of high-signal-intensity areas associated with Moyamoya vessels or pathophysiologic major trunks at the terminal portion of the internal carotid artery.^{16,17,37} Recent studies using ultra-high-field 7T MRA have enhanced the diagnostic accuracy of this neurovascular imaging technique to delineate microvascular structures and even vessel walls.^{20–23} The presented study used dedicated MRA sequences to identify possible collateral networks with up to 2.4- to 3.2-fold higher resolution than in recently reported studies on MMA using 7T MRA.^{17,37} This study shows the possible clinical application of 7T MRA to identify submillimeter collateral networks in MMA. Therefore, further studies including larger patient numbers at different Suzuki stages are warranted to investigate the clinical importance of each collateral pathway.

Nevertheless, the presented study has some limitations. The main limitation is the relatively small number of patients ($n = 15$) with MMA and different Suzuki stages. Ratings might be biased due to memory of collateral pathways from a previous evaluation. However, due to long intervals between reading sessions and the complex vascular anatomy, memory bias seemed to be a minor issue. Enlisting a substantially larger number of patients with MMA for a 7T MR imaging study remains challenging due to the low incidence of MMA and the limited availability of 7T MR imaging systems. A direct comparison of 7T MRA with superselective DSA would have been beneficial but was rejected because of the increased risk for the patients. Furthermore, conclusions derived from comparing high-resolution TOF-MRA with much lower resolution MPRAGE are limited, but scanning time for a MPRAGE sequence with comparable resolution would, by far, have exceeded typical patient tolerance. A lower resolution MPRAGE sequence was therefore included in the study protocol as previously applied in several cerebrovascular studies including

MMA studies.^{17,38} Finally, the study design did not include MRA at conventional field strengths (1.5T or 3T) due to heterogeneous previous imaging sessions, but numerous recent studies have already shown the superiority of 7T over 3T TOF-MRA for delineation of submillimeter vessels.^{17,37}

CONCLUSIONS

In the presented study, 7T MRA could delineate DSCNs in MMA in a clinical setting. With respect to submillimeter collateral vessels, visualization by 7T TOF-MRA was comparable with that in DSA. For further morphologic and pathophysiologic research on submillimeter collateral networks in MMA, 7T TOF-MRA is a very promising imaging technique.

Disclosures: Markus Kraemer—UNRELATED: Grants/Grants Pending: Novartis, German Neurological Society*; Payment for Lectures Including Service on Speakers Bureaus: Merck Serono; Travel/Accommodations/Meeting Expenses Unrelated to Activities Listed: Merck Serono, Novartis, Shire, Genzyme. Karsten H. Wrede—RELATED: Grant: Programm zur internen Forschungsförderung Essen. *Money paid to the institution.

REFERENCES

1. Suzuki J, Takaku A. Cerebrovascular “moyamoya” disease: disease showing abnormal net-like vessels in base of brain. *Arch Neurol* 1969;20:288–99 CrossRef Medline
2. Research Committee on the Pathology and Treatment of Spontaneous Occlusion of the Circle of Willis; Health Labour Sciences Research Grant for Research on Measures for Intractable Diseases. Guidelines for diagnosis and treatment of moyamoya disease (spontaneous occlusion of the circle of Willis). *Neurol Med Chir (Tokyo)* 2012;52:245–66 CrossRef Medline
3. Bersano A, Guey S, Bedini G, et al; European Moyamoya Disease Initiative. Research progresses in understanding the pathophysiology of Moyamoya disease. *Cerebrovasc Dis* 2016;41:105–18 CrossRef Medline
4. Bedini G, Blecharz KG, Nava S, et al. Vasculogenic and angiogenic pathways in Moyamoya disease. *Curr Med Chem* 2016;23:315–45 CrossRef Medline
5. Yamada I, Matsushima Y, Suzuki S. Moyamoya disease: diagnosis with three-dimensional time-of-flight MR angiography. *Radiology* 1992;184:773–78 CrossRef Medline
6. Morioka M, Hamada J, Kawano T, et al. Angiographic dilatation and branch extension of the anterior choroidal and posterior communicating arteries are predictors of hemorrhage in adult moyamoya patients. *Stroke* 2003;34:90–95 CrossRef Medline
7. Strother MK, Anderson MD, Singer RJ, et al. Cerebrovascular collaterals correlate with disease severity in adult North American patients with Moyamoya disease. *AJNR Am J Neuroradiol* 2014;35:1318–24 CrossRef Medline
8. Jang DK, Lee KS, Rha HK, et al. Clinical and angiographic features and stroke types in adult moyamoya disease. *AJNR Am J Neuroradiol* 2014;35:1124–31 CrossRef Medline
9. Funaki T, Takahashi JC, Yoshida K, et al. Periventricular anastomosis in moyamoya disease: detecting fragile collateral vessels with MR angiography. *J Neurosurg* 2016;124:1766–72 CrossRef Medline
10. Kronenburg A, Braun KP, van der Zwan A, et al. Recent advances in moyamoya disease: pathophysiology and treatment. *Curr Neurol Neurosci Rep* 2014;14:423 CrossRef Medline
11. Kraemer M, Diehl RR, Diesner F, et al. Differential diagnosis between cerebral ischemia, focal seizures and limb shaking TIAs in moyamoya disease. *Br J Neurosurg* 2012;26:896–98 CrossRef Medline
12. Kraemer M, Heienbrok W, Berlitz P. Moyamoya disease in Europeans. *Stroke* 2008;39:3193–200 CrossRef Medline
13. Kirschek B, Kasuya H, Khan N, et al. Genetic and clinical characteristics of Moyamoya disease in Europeans. *Acta Neurochir Suppl* 2011;112:31–34 CrossRef Medline

14. Ganesan V. **Moyamoya: to cut or not to cut is not the only question—a paediatric neurologist’s perspective.** *Dev Med Child Neurol* 2010;52:10–13 CrossRef Medline
15. Kraemer M, Lee SI, Ayzenberg I, et al. **Headache in Caucasian patients with moyamoya angiopathy: a systematic cohort study.** *Cephalalgia* 2017;160:137–41 CrossRef Medline
16. Fushimi Y, Miki Y, Kikuta K, et al. **Comparison of 3.0- and 1.5-T three-dimensional time-of-flight MR angiography in moyamoya disease: preliminary experience.** *Radiology* 2006;239:232–37 CrossRef Medline
17. Deng X, Zhang Z, Zhang Y, et al. **Comparison of 7.0- and 3.0-T MRI and MRA in ischemic-type moyamoya disease: preliminary experience.** *J Neurosurg* 2016;124:1716–25 CrossRef Medline
18. Funaki T, Fushimi Y, Takahashi JC, et al. **Visualization of periventricular collaterals in Moyamoya disease with flow-sensitive black-blood magnetic resonance angiography: preliminary experience.** *Neurol Med Chir (Tokyo)* 2015;55:204–09 CrossRef Medline
19. Cho ZH, Kang CK, Han JY, et al. **Observation of the lenticulostriate arteries in the human brain in vivo using 7.0T MR angiography.** *Stroke* 2008;39:1604–06 CrossRef Medline
20. van der Kolk AG, Zwanenburg JJ, Brundel M, et al. **Intracranial vessel wall imaging at 7.0-T MRI.** *Stroke* 2011;42:2478–84 CrossRef Medline
21. Kleinloog R, Korkmaz E, Zwanenburg JJ, et al. **Visualization of the aneurysm wall: a 7.0-Tesla magnetic resonance imaging study.** *Neurosurgery* 2014;75:614–22; discussion 622 CrossRef Medline
22. Matsushige T, Chen B, Ringelstein A, et al. **Giant intracranial aneurysms at 7T MRI.** *AJNR Am J Neuroradiol* 2016;37:636–41 CrossRef Medline
23. Matsushige T, Chen B, Dammann P, et al. **Microanatomy of the subcallosal artery: an in-vivo 7 T magnetic resonance angiography study.** *Eur Radiol* 2016;26:2908–14 CrossRef Medline
24. Bouvy WH, Biessels GJ, Kuijf HJ, et al. **Visualization of perivascular spaces and perforating arteries with 7 T magnetic resonance imaging.** *Invest Radiol* 2014;49:307–13 CrossRef Medline
25. Conijn MM, Hendrikse J, Zwanenburg JJ, et al. **Perforating arteries originating from the posterior communicating artery: a 7.0-Tesla MRI study.** *Eur Radiol* 2009;19:2986–92 CrossRef Medline
26. Hartevelde AA, De Cocker LJ, Dieleman N, et al. **High-resolution postcontrast time-of-flight MR angiography of intracranial perforators at 7.0 Tesla.** *PLoS One* 2015;10:e0121051 CrossRef Medline
27. Wrede KH, Johst S, Dammann P, et al. **Improved cerebral time-of-flight magnetic resonance angiography at 7 Tesla: feasibility study and preliminary results using optimized venous saturation pulses.** *PLoS One* 2014;9:e106697 CrossRef Medline
28. Johst S, Wrede KH, Ladd ME, et al. **Time-of-flight magnetic resonance angiography at 7 T using venous saturation pulses with reduced flip angles.** *Invest Radiol* 2012;47:445–50 CrossRef Medline
29. Wrede KH, Johst S, Dammann P, et al. **Caudal image contrast inversion in MPRAGE at 7 Tesla: problem and solution.** *Acad Radiol* 2012;19:172–78 CrossRef Medline
30. Umutlu L, Theysohn N, Maderwald S, et al. **7 Tesla MPRAGE imaging of the intracranial arterial vasculature: nonenhanced versus contrast-enhanced.** *Acad Radiol* 2013;20:628–34 CrossRef Medline
31. Wrede KH, Dammann P, Johst S, et al. **Non-enhanced MR imaging of cerebral arteriovenous malformations at 7 Tesla.** *Eur Radiol* 2016;26:829–39 CrossRef Medline
32. Baltasavias G, Khan N, Valavanis A. **The collateral circulation in pediatric moyamoya disease.** *Childs Nerv Syst* 2015;31:389–98 CrossRef Medline
33. Baltasavias G, Khan N, Filipce V, et al. **Selective and superselective angiography of pediatric moyamoya disease angioarchitecture in the posterior circulation.** *Interv Neuroradiol* 2014;20:403–12 CrossRef Medline
34. Baltasavias G, Valavanis A, Filipce V, et al. **Selective and superselective angiography of pediatric moyamoya disease angioarchitecture: the anterior circulation.** *Interv Neuroradiol* 2014;20:391–402 CrossRef Medline
35. Chang W, Huang M, Chien A. **Emerging techniques for evaluation of the hemodynamics of intracranial vascular pathology.** *Neuroradiol J* 2015;28:19–27 Medline
36. Matsushige T, Kraemer M, Schlamann M, et al. **Ventricular microaneurysms in Moyamoya angiopathy visualized with 7T MR angiography.** *AJNR Am J Neuroradiol* 2016;37:1669–72 CrossRef Medline
37. Dengler NF, Madai VI, Wuerfel J, et al. **Moyamoya vessel pathology imaged by ultra-high-field magnetic resonance imaging at 7.0 T.** *J Stroke Cerebrovasc Dis* 2016;25:1544–51 CrossRef Medline
38. Oh BH, Moon HC, Baek HM, et al. **Comparison of 7T and 3T MRI in patients with moyamoya disease.** *Magn Reson Imaging* 2017;37:134–38 CrossRef Medline

Diffusion-Weighted Zonal Oblique Multislice–EPI Enhances the Detection of Small Lesions with Diffusion Restriction in the Brain Stem and Hippocampus: A Clinical Report of Selected Cases

T. Sartoretti, E. Sartoretti, C. Binkert, A. Gutzeit, C. Reischauer, D. Czell, M. Wyss, E. Brüllmann, and S. Sartoretti-Schefer

ABSTRACT

SUMMARY: Diffusion restriction is the morphologic hallmark of acute ischemic infarcts and excitotoxic brain injury in various cerebral pathologies. Diffusion restriction is visible as hyperintensity on DWI and as hypointensity on ADC maps. Due to the vicinity of multiple anatomic structures in the brain stem and hippocampus, very small lesions with diffusion restriction may result in severe clinical symptomatology, but these small lesions easily go undetected on standard cerebral DWI due to insufficient spatial resolution, T2* blurring, and image artifacts caused by susceptibility-related image distortions. Diffusion-weighted zonal oblique multislice–EPI with reduced FOV acquisition permits a considerable increase in spatial resolution and enhances the visualization of very small pathologic lesions in the brain stem and hippocampus. Improved performance in the depiction of different pathologic lesions with diffusion restriction in the brain stem and hippocampus using this sequence compared with standard DWI in selected cases is presented.

ABBREVIATIONS: CN III = oculomotor nerve nucleus area; CN VI = abducens nerve nucleus area; DW = diffusion-weighted; sshot SE = single-shot spin-echo; TGA = transient global amnesia; ZOOM = zonal oblique multislice

Diffusion restriction is caused by different cerebral pathologies leading to cytotoxic edema by energy failure, altered intra- and extracellular ion and water concentrations, and excitotoxic brain injury due to extracellular increase of glutamate.^{1,2} These mechanisms may overlap in certain pathologies. Diffusion restriction is the main characteristic feature of an acute ischemic event²; therefore, DWI is the only reliable sequence for detecting an acute ischemic event.

DWI is routinely used in brain protocols for the evaluation of various cerebral pathologies characterized by diffusion restriction. The limited spatial resolution of a standard single-shot spin-echo (sshot SE) EPI DWI, called “standard DWI” in our work, is an enormous disadvantage if the clinical symptomatology indicates a lesion in the brain stem and hippocampus.

This clinical report shows how diffusion-weighted (DW) zonal oblique multislice (ZOOM)-EPI can improve the detection of DWI abnormalities in pathologies in the brain stem and hippocampus by increasing spatial resolution, allowing the visualization of small lesions with diffusion restriction not visible on standard DWI.

MATERIALS AND METHODS

In this clinical report, the MR images of 7 patients of a group with 44 patients (23 women and 21 men; 40–89 years of age; mean age, 76.4 years) are depicted. Informed and written consent for publication of patient data and images was obtained by all patients described in this study. All patients with various acute clinical symptoms all indicating a brain stem pathology (mainly characterized by nausea, vertigo, ataxia, nystagmus, gaze disorders) or hippocampal pathology with amnesic syndrome were examined by both standard transverse sshot SE EPI DWI (called “standard DWI”) and transverse DW ZOOM-EPI during the same examination. The acquisition of DW ZOOM-EPI followed immediately after the acquisition of the standard DWI on the same MR imaging scanner with an identical field strength. Identical image plane angulation was used in both transverse diffusion-weighted sequences.

Patient examinations were performed from October 2016 to August 2017 on a 1.5T Ingenia (Philips Healthcare, Best, the Netherlands) or a 3T Achieva (Philips Healthcare) scanner. Imaging parameters of DW ZOOM-EPI and of standard DWI are shown in Tables 1 and 2. In all patients, 3D FLAIR imaging and transverse T2 TSE sequences were added for possible confirmation of the suspected pathology.

In each patient, the presence or absence of acute ischemic lesions in the brain stem on standard DWI and on DW ZOOM-EPI was determined retrospectively. In 27 patients, no pathologic lesion was visible on both standard DWI and DW

Received October 19, 2017; accepted after revision March 5, 2018.

From the Institut für Radiologie (T.S., E.S., C.B., M.W., S.S.-S.), Kantonsspital Winterthur, Winterthur, Switzerland; Institut für Radiologie und Nuklearmedizin (A.G., C.R.), Hirslanden Klinik St. Anna, Luzern, Switzerland; Medizinische Klinik (D.C.), Abteilung für Neurologie, Uznach, Switzerland; and Philips HealthSystems (M.W., E.B.), Zürich, Switzerland.

Please address correspondence to Sabine Sartoretti-Schefer, MD, Institut für Radiologie, Kantonsspital Winterthur, Brauerstr 15, 8401 Winterthur, Switzerland; e-mail: sabine.sartoretti@ksw.ch

<http://dx.doi.org/10.3174/ajnr.A5635>

Table 1: Imaging parameters of DW ZOOM-EPI

	DW ZOOM-EPI on 1.5T MRI	DW ZOOM-EPI on 3T MRI
Sequence type	sshot SE-EPI	sshot SE-EPI
Slice orientation	Transversal	Transversal
FOV (RL × AP)	97 × 92 mm ²	180 × 64 mm ²
Acquisition voxel size (RL × AP × FH)	1.2 × 1.2 × 3.0 mm ³	1.0 × 1.15 × 3.0 mm ³
No. of slices	19	25
TR	3545 ms	2899 ms
TE	85 ms	64 ms
Flip angle	90°	90°
Half scan factor	0.6	0.6
Bandwidth	11.5 Hz/pixel	12.9 Hz/pixel
EPI factor	75	81
No. of signal averages	5	2
Acquisition duration (minutes:seconds)	05:39	03:04
Fat suppression	SPAIR	SPIR
b-values	0, 1000 s/mm ²	0, 1000 s/mm ²

Note:—SPIR indicates spectral presaturation with inversion recovery; SPAIR, spectral attenuated inversion recovery; RL, right left; AP, anterior posterior; FH, feet head.

Table 2: Imaging parameters of standard DWI

	Standard DWI on 1.5T MRI	Standard DWI on 3T MRI
Sequence type	sshot SE-EPI	sshot SE-EPI
Slice orientation	Transversal	Transversal
FOV (RL × AP)	230 × 230 mm ²	230 × 230 mm ²
Acquisition voxel size (RL × AP × FH)	1.4 × 2.0 × 3.0 mm ³	1.55 × 1.95 × 3.0 mm ³
No. of slices	47	50
TR	6642 ms	6224 ms
TE	97 ms	85 ms
Flip angle	90°	90°
Sensitivity encoding factor	2	2
Half scan factor	0.8	No
Bandwidth	16.6 Hz/pixel	20.7 Hz/pixel
EPI factor	57	59
No. of signal averages	1	1
Acquisition duration (minutes:seconds)	02:16	01:52
Fat suppression	SPIR	SPIR
b-values	0, 1000 s/mm ²	0, 1000 s/mm ²

Note:—SPIR indicates spectral presaturation with inversion recovery; RL, right left; AP, anterior posterior; FH, feet head.

ZOOM-EPI. In 9 patients both standard DWI and DW ZOOM-EPI showed an acute ischemic infarct with diffusion restriction, involving both the brain stem and cerebellum in 6 patients, only the cerebellum in 2 patients, and only the brain stem in 1 patient. All infarcts visible on both standard DWI and DW ZOOM-EPI had a minimum size of 1 cm. In 8 patients, mostly punctate acute ischemic foci, either in the brain stem, cerebellum, or hippocampi, were only visible on DW ZOOM-EPI.

Despite the acquisition time of the DW ZOOM-EPI (3 minutes to 5 minutes and 30 seconds), no visually evident movement artifacts in the patients examined were observed, but a quantification of movement artifacts was not performed.

Case Series

Transient Global Amnesia. A 65-year-old female patient presented with anterograde and retrograde amnesia due to clinically suspected transient global amnesia (TGA) lasting for 18 hours (Fig 1). Punctate diffusion restriction was demonstrated on DW ZOOM-EPI with ADC maps in the lateral hippocampal body as a specific TGA-associated lesion. No abnormality was visible on standard DWI or on FLAIR.

Hippocampal Ischemia. An 83-year-old woman with atrial fibrillation presented with acute hemiparesis on the left side and anterograde amnesia (Fig 2). Multiple punctate acute embolic ischemic infarcts with diffusion restriction were visible on DW ZOOM-EPI with ADC maps, namely in the mesencephalon along the pyramidal tract, in the left medial occipitotemporal gyrus, in the left hippocampus, and bilaterally in the pre- and postcentral area on the right. The punctate hippocampal infarct was not visible on standard DWI or FLAIR.

Acute Internuclear Ophthalmoplegia and Partial Oculomotor Nerve Palsy. A 44-year-old woman presented with acute internuclear ophthalmoplegia and a partial oculomotor nerve palsy on the left. The acute ischemic infarct in the oculomotor nerve nuclear area (CN III) and the medial longitudinal fascicle was visible on DW ZOOM-EPI and ADC maps but not on standard DW and was only faintly apparent on FLAIR (Fig 3). The ischemic infarct was caused by an acute embolus from a pulmonary arteriovenous malformation.

Acute Internuclear Ophthalmoplegia and Acute Abducens Palsy. A 71-year-old man presented with acute internuclear ophthalmoplegia/abducens nerve palsy of the left side, skew deviation, and nystagmus to the right side. An acute ischemic infarct with diffusion restriction was visible on DW ZOOM-EPI and ADC maps involving the left medial longitudinal fascicle and the abducens nerve nuclear area (CN VI). Standard DWI and FLAIR images did not show any abnormality (Fig 4).

Acute Ischemic Infarct in the Left Inferior Cerebellar Peduncle. A 57-year-old woman presented with severe intractable vertigo, nystagmus, and vomiting due to isolated vestibular syndrome lasting 3 days. A punctate diffusion abnormality on DW ZOOM-EPI and ADC maps (Fig 5) in the left inferior cerebellar peduncle was present, not visible on standard DWI or FLAIR.

Acute Ischemic Infarct in the Right Nucleus Prepositus Hypoglossi. A 40-year-old female patient presented with acute forward and backward vertigo and horizontal nystagmus. A punctate diffusion abnormality was visible on DW ZOOM-EPI and ADC maps (Fig 6) in the right nucleus prepositus hypoglossi; the lesion was not depicted on standard DWI and on FLAIR.

Acute Ischemic Infarct in the Right Flocculus. A 51-year-old woman presented with vertigo and saccadic eye movements during the last 5 days. A punctate diffusion abnormality representing her infarction

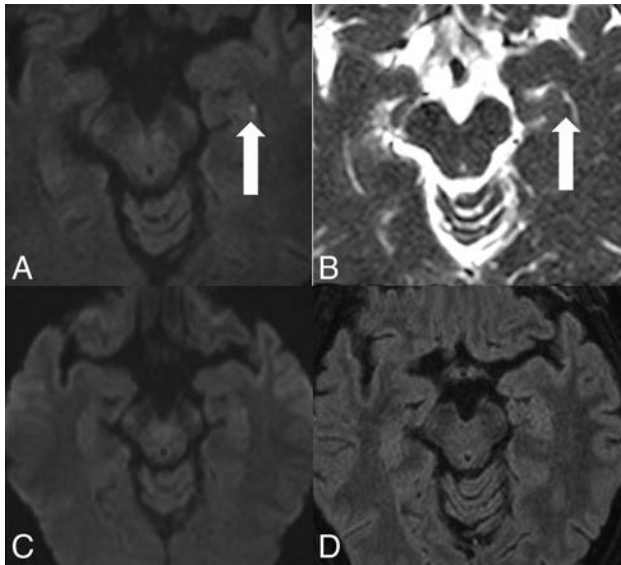


FIG 1. TGA. MR imaging was performed on a 1.5T scanner 24 hours after the beginning of the clinical symptomatology. On DWI ZOOM-EPI (white arrow in A), a punctate hyperintensity and, on DWI ZOOM-EPI ADC map (white arrow in B), a punctate hypointensity with an ADC of $0.915 \times 10^{-3} \text{ mm}^2/\text{second}$ were demonstrated in the left lateral hippocampal body as a specific TGA-associated lesion. ADC in the normal right hippocampus was $1.093 \times 10^{-3} \text{ mm}^2/\text{second}$. Standard DWI (C) did not show the abnormality nor was any signal intensity change visible on transverse FLAIR (D).

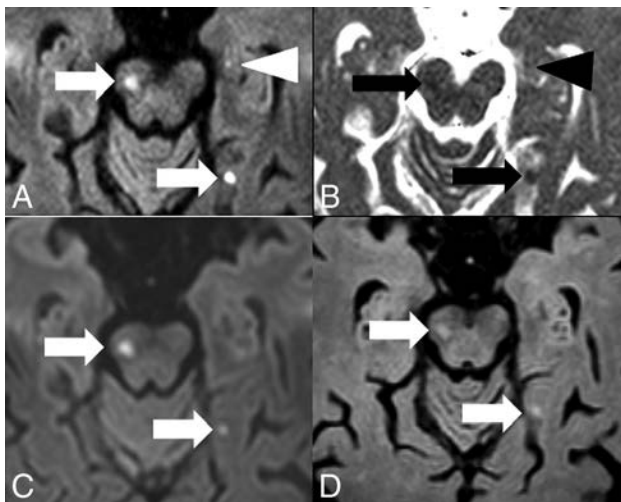


FIG 2. Hippocampal embolic ischemia. MR imaging was performed on a 1.5T scanner. On DW ZOOM-EPI, 3 acute ischemic infarcts in the right mesencephalon along the pyramidal tract (white arrow), in the left medial occipitotemporal gyrus (white arrow), and in the left hippocampus (white arrowhead) were visible as hyperintense foci in A. On DW ZOOM-EPI ADC, the same infarcts were hypointense in B marked with black arrows and a black arrowhead (with an ADC of $0.817 \times 10^{-3} \text{ mm}^2/\text{second}$ compared with the ADC of $1.03 \times 10^{-3} \text{ mm}^2/\text{second}$ in the normal right hippocampus). The punctate small hippocampal infarct on the left side was not visible on standard DWI (C) or FLAIR (D).

was present in the right flocculus on DW ZOOM-EPI and ADC maps (Fig 7). Standard DWI and FLAIR findings were normal.

DISCUSSION

Standard sshot SE EPI DWI is prone to geometric distortions, mainly due to the long readout time and low bandwidth in the

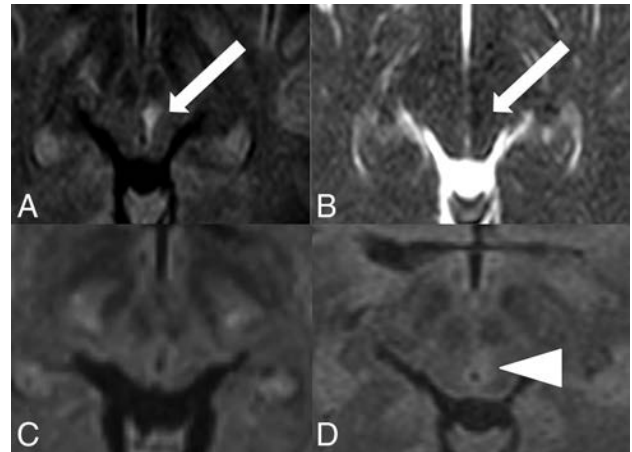


FIG 3. Acute internuclear ophthalmoplegia with partial oculomotor nerve palsy. MR imaging was performed on a 3T scanner. The acute ischemic infarct in left CN III and the medial longitudinal fascicle was visible as a hyperintensity (white arrow) on DW ZOOM-EPI (A), as a hypointensity (white arrow) on DW ZOOM-EPI ADC (B) with an ADC of $0.6 \times 10^{-3} \text{ mm}^2/\text{second}$ (compared with an ADC of $0.985 \times 10^{-3} \text{ mm}^2/\text{second}$ in the normal right CN III), and as very faintly hyperintense on transverse FLAIR (D, white arrowhead). No pathologic findings were seen on standard DWI (C).

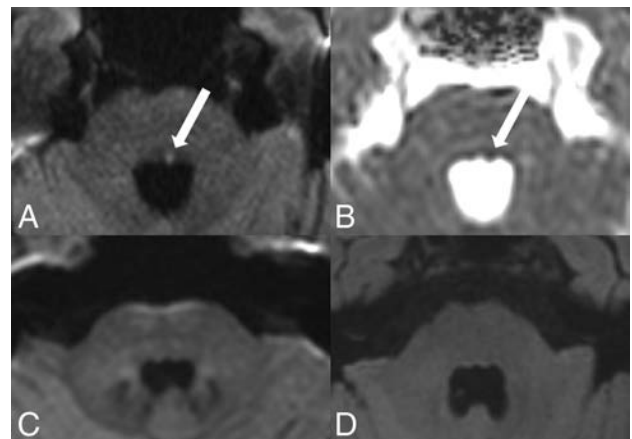


FIG 4. Acute internuclear ophthalmoplegia with abducens nerve palsy. MR imaging was performed on a 3T scanner. The punctate acute ischemic infarct in the left CN VI and the medial longitudinal fascicle, located in the inferior pons, was visible as hyperintensity (white arrow) on DW ZOOM-EPI (A) and as hypointensity (white arrow) on DW ZOOM-EPI ADC with an ADC of $0.707 \times 10^{-3} \text{ mm}^2/\text{second}$ (B) but was not visible on standard DWI (C, with slightly different angulation compared with DW ZOOM-EPI) and on FLAIR (D). ADC in the right CN VI area was $0.948 \times 10^{-3} \text{ mm}^2/\text{second}$. A local microangiopathic origin was suspected. No cardiovascular embolic source was found.

phase-encoding direction. Reduced-FOV imaging allows acquisition of a small FOV with either reduced geometric distortion (shorter readout time) or higher spatial resolution (same readout time) compared with standard EPI DWI. An FOV smaller than the object typically induces foldover artifacts. Numerous different techniques have been introduced in the past to prevent these, especially selective excitation methods that excite only the ROI such as “inner volume imaging” and suppression-based methods that apply bands to saturate signal external to the target FOV such as “outer volume suppression” or a combination of both.³⁻⁷

Reduced-FOV imaging or ZOOM imaging or small-FOV imaging is a commonly used technique in the context of data acqui-

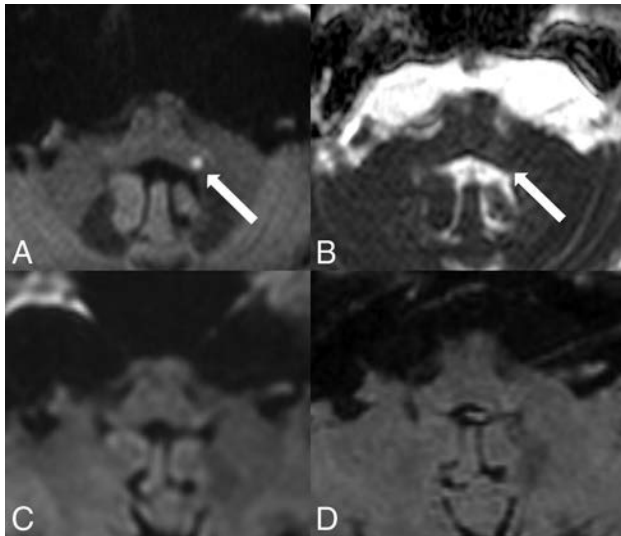


FIG 5. Acute ischemic infarct in the left inferior cerebellar peduncle. MR imaging was performed on a 3T scanner. Note a punctate area with hyperintensity in the inferior cerebellar peduncle on the left side on DW ZOOM-EPI (white arrow in A) and as a slight hypointensity on DW ZOOM-EPI ADC with an ADC of $0.562 \times 10^{-3} \text{ mm}^2/\text{second}$ (white arrow in B) compared with the ADC of $0.841 \times 10^{-3} \text{ mm}^2/\text{second}$ in the normal right inferior cerebellar peduncle. This diffusion abnormality was not visible on transverse standard DWI (C) or the transverse FLAIR image (D). Severe chronic microangiopathy was present in the supra- and infratentorial areas.

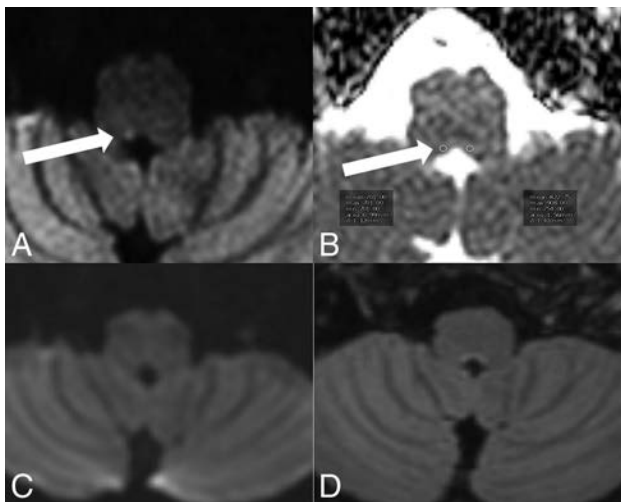


FIG 6. Acute ischemic infarct in the nucleus prepositus hypoglossi on the right side. MR imaging was performed on a 1.5T scanner. A punctate area with diffusion restriction was visible in the right nucleus prepositus hypoglossi. This lesion was hyperintense on DW ZOOM-EPI (white arrow in A) and slightly hypointense on DW ZOOM-EPI ADC with an ADC of $0.701 \times 10^{-3} \text{ mm}^2/\text{second}$ (white arrow in B) compared with an ADC of $0.822 \times 10^{-3} \text{ mm}^2/\text{second}$ in the normal left nucleus prepositus hypoglossi. The lesion was not visible on transverse standard DWI (C) and FLAIR (D) and was thought to be of local microangiopathic origin.

sition of small FOVs within larger objects. In this work, a non-coplanar excitation combined with outer volume suppression, originally presented by Wilm et al,⁸ was used. This technique is now referred to as DW ZOOM-EPI, and the main applications using small-FOV imaging are imaging of the prostate, spinal cord, pancreas, breast, and heart,⁵⁻¹¹ where a relatively small

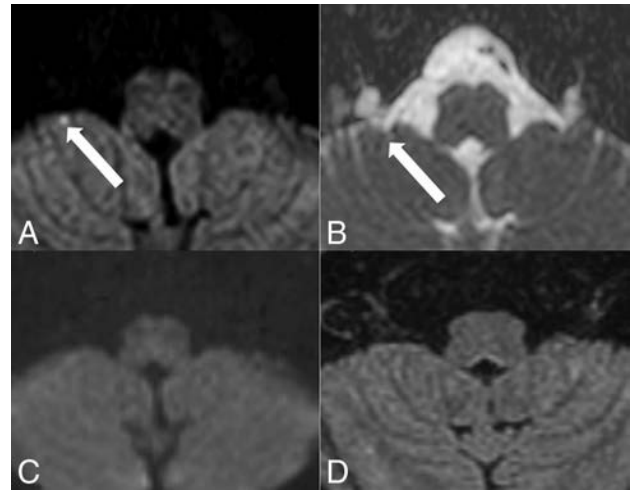


FIG 7. Subacute ischemic infarct in the right flocculus. MR imaging was performed on a 1.5T scanner. On DW ZOOM-EPI, a punctate hyperintensity (white arrow, A) with isointensity on DW ZOOM-EPI ADC and an ADC of $0.878 \times 10^{-3} \text{ mm}^2/\text{second}$ (white arrow, B) represents a subacute ischemic infarct in the right flocculus. In the normal left flocculus, the ADC was $0.926 \times 10^{-3} \text{ mm}^2/\text{second}$. Standard DWI (C) and FLAIR (D) findings were normal. The lesion was thought to be of local microangiopathic origin.

area of interest surrounded by tissue of less interest is depicted with high resolution. However, to date, the use of reduced-FOV imaging in the depiction of very small pathologic lesions with diffusion restriction in the brain stem and hippocampus has not yet been systematically evaluated.¹²⁻¹⁸ The imaging examples presented in this clinical report stress but do not prove the importance of reduced-FOV imaging for the visualization of small lesions in the brain stem and hippocampus.

The increased detectability of small lesions with diffusion restriction in the brain stem and hippocampus on DW ZOOM-EPI in comparison with standard DWI might have been influenced by several technical factors:

- 1) The registration effect: The standard DWI and the DW ZOOM-EPI slice selections may be slightly different. As a result, the comparison of visual lesion detectability may not entirely represent an effect of the sequence in these patients.
- 2) The difference in scan time: The total scan time and thus the signal-to-noise ratio differed between standard DWI and DW ZOOM-EPI. The increased scan time in DW ZOOM-EPI automatically increased the signal-to-noise ratio and could also affect the visibility of lesions.
- 3) The difference in the display window/level settings: Due to the differences in the imaging parameters between standard DWI and DW ZOOM-EPI, it was not possible to keep an identical display window/level. Window and level selection was at the discretion of the reviewer to optimally depict pathology.

Therefore, a next step might be a prospective study of standard DWI and DW ZOOM-EPI with constant imaging parameters to make a precise comparison of the 2 sequences. This would help clarify whether the improved visibility of small lesions originates from a higher SNR, higher resolution, reduced image distortion, or a combination of these factors.

CONCLUSIONS

Pathologies with diffusion restriction are routinely depicted by standard DWI. However, the visualization of very small lesions with diffusion restriction in the brain stem and hippocampus may be difficult on standard DWI. Tailored DW ZOOM-EPI enhances the visualization of very small lesions in the brain stem and hippocampus and thus can be the only MR image depicting the pathology. The acquisition of DW ZOOM-EPI may be recommended in selected patients presenting with specific brain stem syndromes or with clinical suspicion of hippocampal pathologies such as TGA or hippocampal ischemia and with negative standard DWI findings. The correct diagnosis of an ischemic-pathologic lesion can expedite correct subsequent therapy.

ACKNOWLEDGMENTS

The authors thank Dr Simon Rauch, Institute of Radiology, Kantonsspital Winterthur, Winterthur, Switzerland, for his support in the preparation of the manuscript.

Disclosures: Christoph Binkert—UNRELATED: Consultancy: Merit Medical Systems, Biotronik; Grants/Grants Pending: Cook, Merit Medical Systems. David Czell—UNRELATED: Payment for Development of Educational Presentations: University of Zürich. Michael Wyss—UNRELATED: Employment: My position in the hospital is paid by Philips within the framework of a collaboration agreement. Comments: €4000 per year.* Erika Brüllmann—OTHER RELATIONSHIPS: Philips HealthSystems employee. *Money paid to the institution.

REFERENCES

1. Moritani T, Smoker WRK, Sato Y, et al. **Diffusion-weighted imaging of acute excitotoxic brain injury.** *AJNR Am J Neuroradiol* 2005;26:216–28 Medline
2. Schaefer PW, Grant PE, Gonzalez RG. **Diffusion-weighted MRI imaging of the brain.** *Radiology* 2000;217:331–45 CrossRef Medline
3. Wargo CJ, Moore J, Gore JC. **A comparison and evaluation of reduced-FOV methods for multi-slice 7T human imaging.** *Magn Reson Imaging* 2013;31:1349–59 CrossRef Medline
4. Wheeler-Kingshott CA, Parker GJ, Symms MR, et al. **ADC mapping of the human optic nerve: increased resolution, coverage, and reliability with CSF-suppressed ZOOM-EPI.** *Magn Reson Med* 2002;47:24–31 CrossRef Medline
5. Andre JB, Bammer R. **Advanced diffusion-weighted magnetic resonance imaging techniques of the human spinal cord.** *Top Magn Reson Imaging* 2010;21:367–78 CrossRef Medline
6. Dowell NG, Jenkins TM, Ciccarelli O, et al. **Contiguous-slice zonally oblique multislice (COZOOM) diffusion tensor imaging: examples of in vivo spinal cord and optic nerve applications.** *J Magn Reson Imaging* 2009;29:454–60 CrossRef Medline
7. Samson RS, Lévy S, Schneider T, et al. **ZOOM or non-ZOOM? Assessing spinal cord diffusion tensor imaging protocols for multi-centre studies.** *PLoS One* 2016;11:e0155557 CrossRef Medline
8. Wilm BJ, Svensson J, Henning A, et al. **Reduced field-of-view MRI using outer volume suppression for spinal cord diffusion imaging.** *Magn Reson Med* 2007;57:625–30 CrossRef Medline
9. Dong H, Li Y, Li H, et al. **Study of the reduced field-of-view diffusion-weighted imaging of the breast.** *Clin Breast Cancer* 2014;14:265–71 CrossRef Medline
10. Kim H, Lee JM, Yoon JH, et al. **Reduced field-of-view diffusion-weighted magnetic resonance imaging of the pancreas: comparison with conventional single-shot echo-planar imaging.** *Korean J Radiol* 2015;16:1216–25 CrossRef Medline
11. Reischauer C, Wilm BJ, Froehlich JM, et al. **High-resolution diffusion tensor imaging of prostate cancer using a reduced FOV technique.** *Eur J Radiol* 2011;80:34–41 CrossRef Medline
12. Förster A, Griebel M, Gass A, et al. **Diffusion-weighted imaging for the differential diagnosis of disorders affecting the hippocampus.** *Cerebrovasc Dis* 2012;33:104–15 CrossRef Medline
13. Bartsch T, Deuschl G. **Transient global amnesia: functional anatomy and clinical implications.** *Lancet Neurol* 2010;9:205–14 CrossRef Medline
14. Weon YC, Kim JH, Lee JS, et al. **Optimal diffusion-weighted imaging protocol for lesion detection in transient global amnesia.** *AJNR Am J Neuroradiol* 2008;29:1324–28 CrossRef Medline
15. Dekezyer S, De Kock S, Nikoubashman O, et al. **“Unforgettable”: a pictorial essay on anatomy and pathology of the hippocampus.** *Insights Imaging* 2017;8:199–212 CrossRef Medline
16. Szabo K, Förster A, Jäger Th, et al. **Hippocampal lesion patterns in acute posterior cerebral artery stroke: clinical and MRI findings.** *Stroke* 2009;40:2042–45 CrossRef Medline
17. Kim HJ, Lee SH, Park JH, et al. **Isolated vestibular nuclear infarction: report of two cases and review of the literature.** *J Neurol* 2014;261:121–29 CrossRef Medline
18. Kim SH, Park SH, Kim HJ, et al. **Isolated central vestibular syndrome.** *Ann N.Y. Acad Sci* 2015;1343:2015:80–89 CrossRef Medline

Hematocrit Measurement with $R2^*$ and Quantitative Susceptibility Mapping in Postmortem Brain

A.J. Walsh, H. Sun, D.J. Emery, and A.H. Wilman



ABSTRACT

BACKGROUND AND PURPOSE: Noninvasive venous oxygenation quantification with MR imaging will improve the neurophysiologic investigation and the understanding of the pathophysiology in neurologic diseases. Available MR imaging methods are limited by sensitivity to flow and often require assumptions of the hematocrit level. In situ postmortem imaging enables evaluation of methods in a fully deoxygenated environment without flow artifacts, allowing direct calculation of hematocrit. This study compares 2 venous oxygenation quantification methods in in situ postmortem subjects.

MATERIALS AND METHODS: Transverse relaxation ($R2^*$) mapping and quantitative susceptibility mapping were performed on a whole-body 4.7T MR imaging system. Intravenous measurements in major draining intracranial veins were compared between the 2 methods in 3 postmortem subjects. The quantitative susceptibility mapping technique was also applied in 10 healthy control subjects and compared with reference venous oxygenation values.

RESULTS: In 2 early postmortem subjects, $R2^*$ mapping and quantitative susceptibility mapping measurements within intracranial veins had a significant and strong correlation ($R^2 = 0.805, P = .004$ and $R^2 = 0.836, P = .02$). Higher $R2^*$ and susceptibility values were consistently demonstrated within gravitationally dependent venous segments during the early postmortem period. Hematocrit ranged from 0.102 to 0.580 in postmortem subjects, with $R2^*$ and susceptibility as large as 291 seconds^{-1} and 1.75 ppm, respectively.

CONCLUSIONS: Measurements of $R2^*$ and quantitative susceptibility mapping within large intracranial draining veins have a high correlation in early postmortem subjects. This study supports the use of quantitative susceptibility mapping for evaluation of in vivo venous oxygenation and postmortem hematocrit concentrations.

ABBREVIATIONS: QSM = quantitative susceptibility mapping; $R2^*$ = transverse relaxation rate; RESHARP = regularization enabled sophisticated harmonic artifact reduction for phase data; SvO_2 = venous oxygen saturation

Determination of regional brain oxygen use is important for improved understanding of the pathophysiology of neurologic disease such as stroke,¹ malignancy,² and demyelinating conditions.³ MR imaging methods, which are noninvasive, can be used to calculate the oxygen extraction fraction to infer cellular oxygen use. Gradient-echo methods are advantageous because they have relatively fast imaging times for volume coverage. Sev-

eral gradient-echo methods have been proposed, including single-vessel-decay modeling,⁴ phase-signal difference analysis,⁵ and quantitative susceptibility mapping (QSM).⁶ QSM is a novel technique that extrapolates volumetric susceptibility values from gradient-echo phase images. QSM is promising for this application because unlike phase images, QSM venous oxygen saturation (SvO_2) measurements are not dependent on vessel orientation to the main magnetic field.

Several studies have shown that venous oxygen saturation calculations with a QSM approach yield close to expected average values in healthy controls.^{6,7} However, these studies had no criterion standard comparison, and to determine SvO_2 , they required exact knowledge of the local hematocrit level. Furthermore, flowing blood may introduce additional phase artifacts. In a postmortem environment, all blood vessels are 100% deoxygenated and blood is stationary, which enables direct noninvasive measurement of hematocrit.

In situ postmortem intravascular changes have been previ-

Received August 7, 2017; accepted after revision April 1, 2018.

From the Departments of Biomedical Engineering (A.J.W., H.S., A.H.W.) and Radiology and Diagnostic Imaging (A.J.W., D.J.E.), Faculty of Medicine and Dentistry, University of Alberta, Edmonton, Alberta, Canada.

This work was supported by the Canadian Institutes of Health Research grant MOP 102582.

Please address correspondence to Alan H. Wilman, PhD, 1098 RTF, Department of Biomedical Engineering, University of Alberta, Edmonton, AB, Canada, T6G 2V2; e-mail: wilman@ualberta.ca

Indicates open access to non-subscribers at www.ajnr.org

<http://dx.doi.org/10.3174/ajnr.A5677>

ously evaluated with CT⁸; however, they have not been studied with iron-sensitive MR imaging methods. Several physiologic changes occur in the early postmortem period, including a shift from oxy- to deoxyhemoglobin, cellular lysis and hemoglobin diffusion,⁹ and a settling (or hematocrit) effect as demonstrated with CT.^{8,10,11} Transverse relaxation rate ($R2^* = 1/T2^*$) and susceptibility mapping are robust methods for evaluating intracranial brain matter iron concentration but can be sensitive to motion artifacts from whole-head motion and from intravascular flow. Postmortem analysis allows accurate comparison of advanced iron-sensitive quantitative MR imaging methods, including $R2^*$ mapping and QSM imaging of veins, without the confounder of motion and flow artifacts.

This study compared QSM and $R2^*$ measurements within major intracranial draining veins in postmortem subjects. By means of QSM, variations in hematocrit with spatial location were examined. Susceptibility measurements were additionally performed with healthy in vivo subjects, and calculated SvO_2 values were compared between different intracranial venous vascular segments and previously reported values.^{6,12,13}

MATERIALS AND METHODS

Venous Oxygenation and Magnetic Susceptibility

The susceptibility shift between water and venous blood has been described as

$$1) \quad \Delta\chi_{\text{vein-water}} = (1 - SvO_2) \times \Delta\chi_{\text{do}} \times Hct + \Delta\chi_{\text{oxy-water}} \times Hct,$$

where SvO_2 is the percentage oxygen saturation of venous blood, Hct is the hematocrit, $\Delta\chi_{\text{do}}$ is the susceptibility shift per unit hematocrit between fully oxygenated and fully deoxygenated red blood cells, and $\Delta\chi_{\text{oxy-water}}$ is the susceptibility shift between oxygenated red blood cells and water.^{14,15} $\Delta\chi_{\text{do}}$ is assumed to be 0.27 ppm¹⁶ in centimeters-grams-second units. $\Delta\chi_{\text{oxy-water}}$ is assigned -0.03 ppm,¹⁴ and hematocrit (Hct) is set to 40% for in vivo subjects.

For postmortem subjects, this equation is simplified because the blood is fully deoxygenated; therefore, SvO_2 is set to zero. The hematocrit can therefore be calculated as

$$2) \quad Hct = \Delta\chi_{\text{vein-water}} / (\Delta\chi_{\text{do}} + \Delta\chi_{\text{oxy-water}}).$$

MR Imaging Acquisition

MR imaging data were acquired using a 4.7T whole-body imaging system (Unity Inova; Varian Medical Systems, Palo Alto, California). Ten healthy control subjects (age range, 24–54 years; average, 32 years) and 3 postmortem subjects were imaged after institutional review board approval. The 3 postmortem subjects were in a palliative state before death and were imaged in situ 7, 6, and 28 hours after death, respectively, for postmortem subjects 1, 2, and 3. These patients had been previously studied for deep gray matter tissue iron.^{17,18} The postmortem subjects had a relatively unchanged supine flat body and head position during the postmortem period. Hematocrit values from the most recent clinical laboratory tests were obtained, retrospectively, from the clinical charts.

The MR imaging protocol for each patient consisted of 2 axial MR imaging methods: multiecho gradient-echo $R2^*$

mapping (8.9 minutes) and single-echo gradient-echo QSM imaging (6.6 minutes). The healthy control subjects and postmortem subject 2 did not undergo imaging with the $R2^*$ mapping sequence.

Images were acquired with a standard birdcage head coil for transmission and a tight-fitting 4-element array coil for signal reception. Due to size limitations, the birdcage coil was used for reception and transmission in postmortem subject 3.

Axial 3D $R2^*$ mapping was acquired with full-brain coverage (160 mm) and parameters as follows: TR, 44 ms; 10 echoes with 4.0–4.2 ms echo spacing; first echo, 2.9–3.2 ms; flip angle, 11°; FOV, 256 × 128–160 × 160 mm; matrix, 256 × 160 × 80; voxel size, 1 × 0.8–1 × 2 mm.

Axial QSM imaging and magnitude gradient-echo imaging used a 2D single gradient-echo with first-order flow compensation acquired with parameters as follows: TR, 1540 ms; TE, 7–15 ms; 50 contiguous sections; section thickness, 2 mm; flip angle, 70°; FOV, 214–256 × 3 × 163–192 mm; matrix, 512 × 256–392; voxel size, 0.42–0.5 × 0.42–0.5 × 2 mm.

Image Processing

QSM. From the 2D single gradient-echo sequence, phase images from the 4 receiver channels were first optimally combined using the adaptive filter method.¹⁹ (This step was not needed in postmortem subject 3 due to the single birdcage receiver.) A binary brain volume mask was extracted from the magnitude images using the FSL Brain Extraction Tool (<http://fsl.fmrib.ox.ac.uk/fsl/fslwiki/BET>).²⁰ The fractional intensity threshold was set to 0.2, and the smoothness factor was set to 2 for the Brain Extraction Tool. Combined phase images were unwrapped in 3D using the Phase Region Expanding Labeller for Unwrapping Discrete Estimates/FMRIB Software Library (PRELUDE; https://fsl.fmrib.ox.ac.uk/fsl/fslwiki/FUGUE/Guide#PRELUDE_28phase_unwrapping.29) method. The residual phase offset from the receiver channel combination was removed using a 3D second-order polynomial fit. The large macroscopic background phase from the air-tissue susceptibility interface was removed using the regularization enabled sophisticated harmonic artifact reduction for phase data (RESHARP) method,²¹ resulting in a local phase map of the brain. The RESHARP spherical kernel was set to 3 mm, and the Tikhonov regularization parameter was set to 5×10^{-4} . Due to the implementation of the RESHARP method, a 3-mm brain edge was discarded. A local field map with units of parts-per-million was generated by normalizing the local phase with TE and field strength. A dipole field inversion was performed on the local field map using the total variation regularization method,^{6,22} with the regularization parameter set to 5×10^{-4} . Susceptibility values were calculated in Système International d'Unités units.

$R2^*$ Map. $R2^*$ maps were produced from the 3D multiecho gradient-echo sequence using a weighted least-squares mono-exponential fit of the 10 echoes.²³ Before fitting, a linear field-gradient correction algorithm was applied to recover signal losses from air-tissue interfaces.²⁴ Composite magnitude $T2^*$ -weighted images were created from the susceptibility-corrected images.²⁵

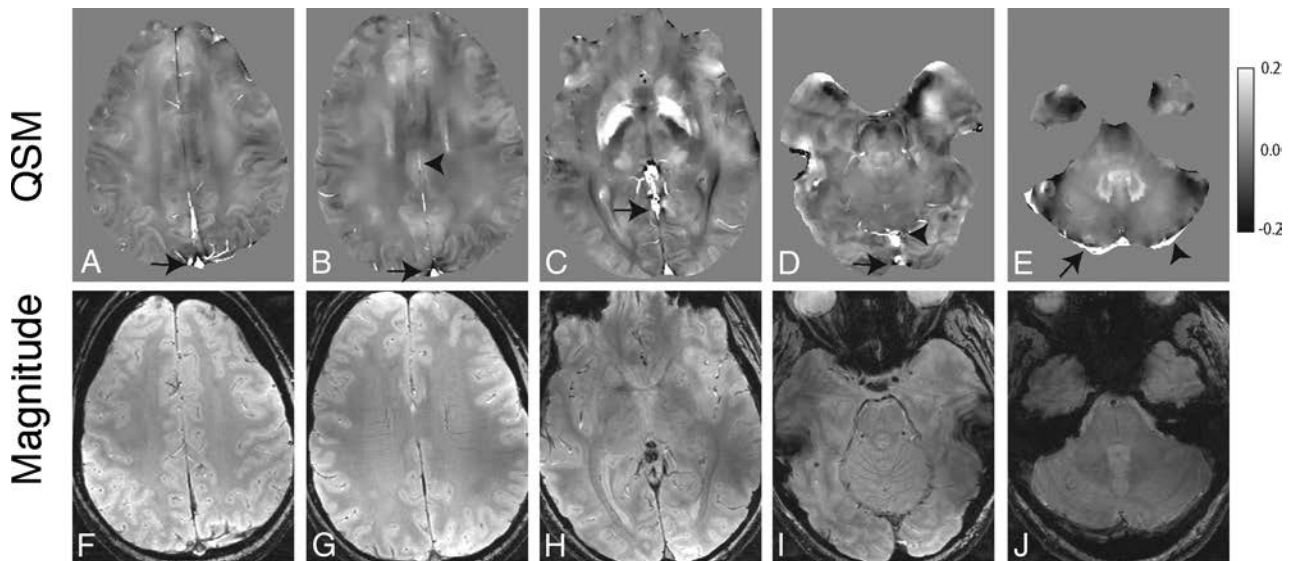


FIG 1. Axial QSM (A–E) and single-echo gradient-echo magnitude (F–J) images from 1 in vivo subject demonstrating representative venous segments from which we obtained ROI measurements: superior aspect of the superior sagittal sinus (arrow, A), inferior aspect of the superior sagittal sinus (arrow, B) and inferior sagittal sinus (arrowhead, B), anterior aspect of the straight sinus (arrow, C), inferior aspect of the superior sagittal sinus (arrow, D) and posterior aspect of the straight sinus (arrowhead, D), right transverse sinus (arrow, E), and left transverse sinus (arrowhead, E).

Table 1: Comparison among R2*, susceptibility measurements, and calculated hematocrit values in intracranial veins in 3 postmortem subjects

Venous Segment	Subject 1			Subject 2		Subject 3		
	Susceptibility (ppm)	Hematocrit	R2* (1/s)	Susceptibility (ppm)	Hematocrit	Susceptibility (ppm)	Hematocrit	R2* (1/s)
Superior aspect of superior sagittal sinus	0.963	0.319	141	0.677	0.225	0.927	0.308	155
Inferior aspect of superior sagittal sinus	NA	NA	NA	0.782	0.259	0.985	0.327	164
Left transverse sinus	1.749	0.580	291	0.780	0.259	1.142	0.379	176
Right transverse sinus	1.135	0.377	277	1.045	0.347	0.785	0.260	161
Anterior aspect of straight sinus	0.661	0.219	94	0.643	0.213	0.681	0.226	104
Posterior aspect of straight sinus	0.972	0.322	182	0.841	0.279	0.939	0.312	177
Inferior sagittal sinus	0.523	0.174	90	0.307	0.102	0.447	0.148	76

Note:—NA indicates not available.

Venous Susceptibility Measurements

ROI measurements from multiple venous segments were acquired from axial QSM and R2* images using the composite magnitude T2*-weighted gradient-echo images from both acquisitions, to identify venous anatomy. ImageJ²⁶ (National Institutes of Health, Bethesda, Maryland) was used to obtain ROI measurements from 2 to 8 axial images of each venous segment, depending on the length and orientation (Fig 1). In each subject, measurements were obtained from the following venous segments: superior sagittal sinus (posterior superior aspect), superior sagittal sinus (posterior inferior aspect), posterior right transverse sinus near the confluence, posterior left transverse sinus near the confluence, anterior aspect of the straight sinus, posterior aspect of the straight sinus, and inferior sagittal sinus.

For postmortem subjects, hematocrit values were calculated on the basis of Equation 2. SvO₂ values were calculated for in vivo subjects on the basis of Equation 1, assuming a hematocrit of 40%.

Linear regression analysis was performed using SPSS software (Version 24.0 for Macintosh; IBM, Armonk, New York) between R2* and QSM ROI measurements in the 2 postmortem subjects in whom both methods were implemented.

RESULTS

In the 3 postmortem subjects, intravenous susceptibility measurements and calculated hematocrit values were higher in more gravitationally dependent venous segments across all 3 subjects (Tables 1 and 2). Susceptibility in the superior aspect of the superior sagittal sinus was lower than in the inferior aspect of the superior sagittal sinus in the 2 subjects in whom it was compared, while subject 1 had artifacts within the inferior aspect of the superior sagittal sinus, precluding measurement. Susceptibility in the anterior aspect of the straight sinus was lower than in the posterior aspect in all 3 subjects. Although the postmortem subjects were imaged in the supine position, some had minor left/right rotation (Fig 2). Sagittal images in Fig 2 were first rotated in the axial plane to obtain a midsagittal projection.

R2* values had a strong and significant correlation (subject 1: $R^2 = 0.805$, $P = .004$; subject 3: $R^2 = 0.836$, $P = .02$) to susceptibility measurements within the 2 subjects in whom measurements were compared (Fig 3 and Table 1). The 2 regressions had a similar linear regression line slope (Fig 3). Visual comparison of axial images of the same territory demonstrates hyperintensity of veins

Table 2: Percentage decrease in hematocrit between contiguous venous segments in postmortem subjects

Venous Segments Compared	Subject 1 ^a	Subject 2 ^b	Subject 3 ^c
Superior aspect of superior sagittal sinus/inferior aspect of superior sagittal sinus	NA	13.4	5.8
Anterior aspect of straight sinus/posterior aspect of straight sinus	32.0	23.5	27.4

Note:—NA indicates not available.

^a Subject 1, imaged 7 hours after death.

^b Subject 2, imaged 6 hours after death.

^c Subject 3, imaged 28 hours after death.

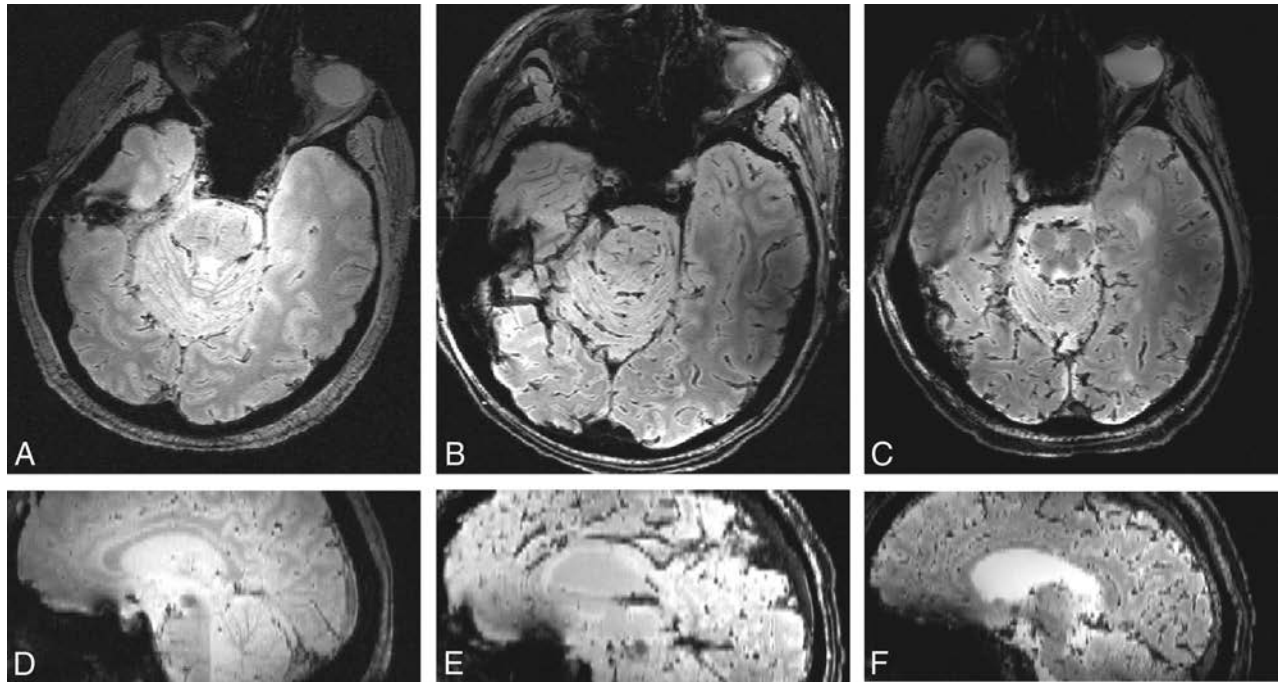


FIG 2. Axial T2*-weighted images and isotropically interpolated sagittal reformats using the single-echo gradient-echo sequence. Postmortem subjects 1 (A and D), 2 (B and E), and 3 (C and F) demonstrate head positioning in these planes (axial and sagittal, respectively).

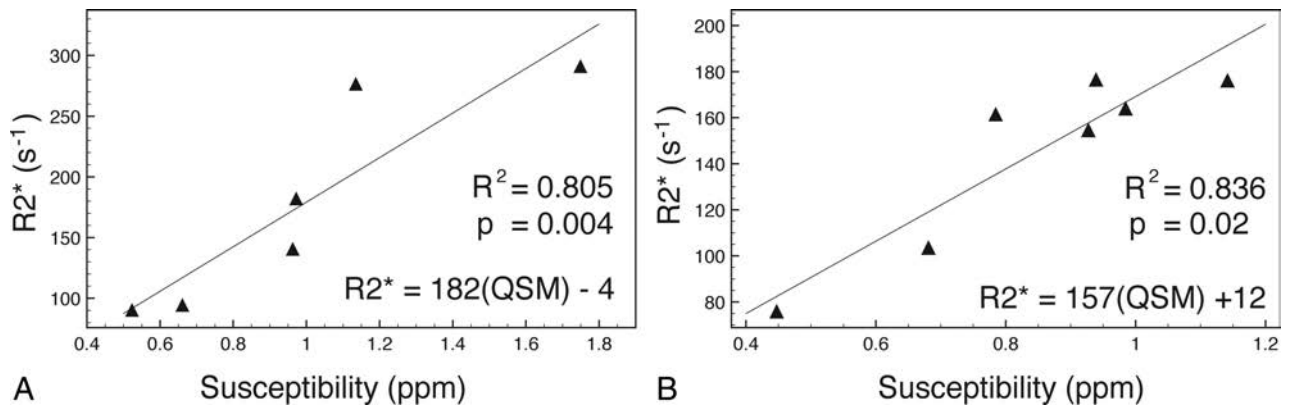


FIG 3. Scatterplot with linear regression of 2 postmortem subjects comparing QSM and R2* ROI measurements within venous segments. A, Subject 1. B, Subject 3.

on R2* maps and corresponding susceptibility maps in postmortem subjects (Fig 4). Calculated hematocrit values in the 3 postmortem subjects ranged from 0.102 to 0.580 (Table 1). This is comparable with the hematocrit values obtained before death (subject 1 = 0.40, acquired 5 days before death; subject 2 = 0.38, acquired 4 weeks before death; and subject 3 = 0.49, acquired 4 months before death).

Susceptibility values within the venous segments evaluated from in vivo subjects did not follow the same gravity-dependent

distribution compared with postmortem subjects (Table 3) in the contiguous venous segments of the superior sagittal sinus and the straight sinus. SvO₂ measurements in Table 4 were calculated using Equation 1.

DISCUSSION

This study is the first to evaluate and compare QSM and R2* mapping in postmortem intracranial venous vasculature.

In the postmortem period, intravascular blood undergoes

several changes, including hypostasis, which can lead to gravity-dependent hemoconcentration; hemolysis, which may depend on the circumstances surrounding death; cell-shape alteration; thrombosis; and thrombolysis.^{9,27} The relative contribution of each process has been previously studied and can be variable among individual patients.⁹ Despite these various changes, there is a strong linear correlation between R2* and susceptibility measurements, which is predicted by the static dephasing regime for geometric shapes.^{28,29} Dependent hemoconcentration is demonstrated with both R2* and QSM measurements in this study. This effect is seen as early as 6 hours and persists up to at least 28 hours after death. The supine head and body position of each subject throughout the postmortem period led to increased values in the more posterior segments of contiguous venous segments. The susceptibility measurements in the dependent venous segments are similar to suscep-

tibility measurements in in vivo intracranial hemorrhage at least 24 hours in age.³⁰

There was no appreciable difference in the percentage change in hematocrit within gravity-dependent portions of contiguous venous segments based on the time since death; however, the few subjects in this study preclude statistical analysis. This study differs from studies that directly evaluated hemoconcentration effects within the appendicular body, which showed that there may be an ongoing increase in hematocrit in dependent veins for up to 96 hours.^{27,31} This could indicate that intracranial gravity-dependent hemoconcentration occurs relatively early in the postmortem period and persists for at least 28 hours. The initial postmortem hematocrit is unknown in this study; however, it is likely less than the measured laboratory values when the patients were alive due to the long time interval between acquisition and death in subjects 2 and 3. The palliative state of the patients may have

resulted in a decrease in hematocrit during the interval. Additionally, Equation 2 may not be entirely valid because factors such as hemolysis, alteration in cell shape, and hemoglobin diffusion may change the susceptibility of deoxygenated hemoglobin. However, cellular lysis is likely not a major contributor in the early postmortem period of this study.²⁷ Additionally, these factors could contribute to the calculated hematocrit values being slightly less than direct laboratory measurements in subjects 2 and 3.

In vivo calculated SvO₂ measurements are slightly higher in this study compared with other recent studies^{6,7}; however, they follow a similar distribution within veins, with the straight sinus and transverse sinuses having the lowest SvO₂ and the inferior sagittal sinus having the largest SvO₂. Several invasive

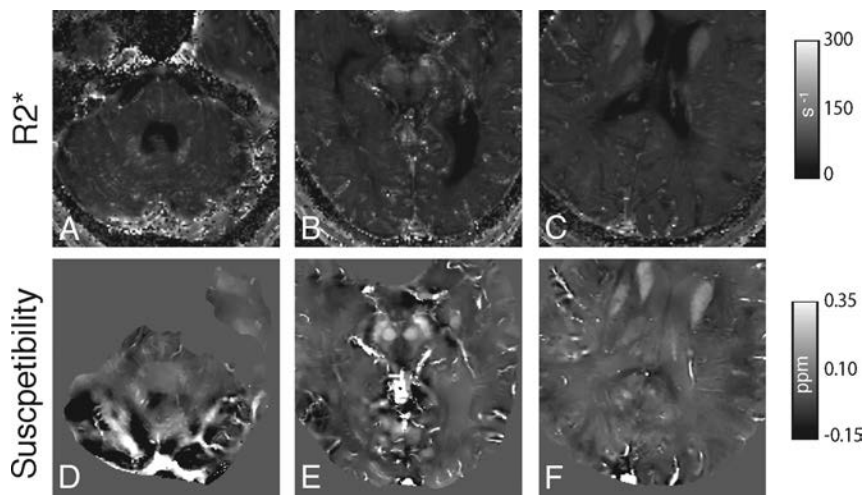


FIG 4. Axial R2* maps (A–C) and corresponding QSM (D–F) images depicting representative venous segments (right and left transverse sinus, A and D; inferior aspect of superior sagittal sinus and anterior aspect of straight sinus, B and E; superior aspect of superior sagittal sinus and inferior sagittal sinus, C and F) in postmortem subject 3 (A, C, D, F) and subject 2 (B and E). For the R2* images, values of >500 seconds⁻¹ were removed to reduce visual washout from bright R2* intravenous voxels and from bone/air.

Table 3: Susceptibility measurements (ppm) from intracranial venous segments in 10 healthy subjects

Venous Segment	Subject										Average ± SD
	1	2	3	4	5	6	7	8	9	10	
Superior aspect of superior sagittal sinus	0.202	0.212	0.179	0.263	0.188	0.239	0.205	0.172	0.234	0.227	0.212 ± 0.029
Inferior aspect of superior sagittal sinus	0.270	0.238	0.249	0.285	0.211	0.215	0.228	0.230	0.261	0.251	0.244 ± 0.024
Left transverse sinus	0.343	0.255	0.329	0.389	0.263	0.280	0.292	0.311	0.278	0.327	0.307 ± 0.041
Right transverse sinus	0.346	0.228	0.306	0.366	0.290	0.267	0.252	0.252	0.285	0.297	0.289 ± 0.043
Anterior aspect of straight sinus	0.393	0.286	0.369	0.329	0.287	0.287	0.290	0.326	0.325	0.272	0.316 ± 0.040
Posterior aspect of straight sinus	0.403	0.280	0.286	0.334	0.184	0.187	0.201	0.270	0.295	0.250	0.269 ± 0.069
Inferior sagittal sinus	0.190	0.145	0.194	0.295	0.184	0.173	0.172	0.227	0.226	0.155	0.196 ± 0.044

Table 4: Calculated percentage SvO₂ for intracranial venous segments in 10 healthy subjects

Venous Segment	Subject										Average ± SD
	1	2	3	4	5	6	7	8	9	10	
Superior aspect of superior sagittal sinus	74.0	73.3	75.7	69.5	75.0	71.3	73.8	76.2	71.7	72.1	73.3 ± 2.1
Inferior aspect of superior sagittal sinus	69.0	71.3	70.6	67.9	73.4	73.0	72.1	71.9	69.7	70.4	70.9 ± 1.8
Left transverse sinus	63.6	70.1	64.6	60.2	69.5	68.3	67.4	66.0	68.4	64.8	66.3 ± 3.1
Right transverse sinus	63.4	72.1	66.4	61.9	67.5	69.2	70.3	70.3	67.9	67.0	67.6 ± 3.2
Anterior aspect of straight sinus	60.0	67.8	61.7	64.7	67.7	67.7	67.5	64.9	65.0	68.8	65.6 ± 2.9
Posterior aspect of straight sinus	59.2	68.3	67.8	64.3	75.3	75.1	74.0	69.0	67.1	70.5	69.1 ± 5.1
Inferior sagittal sinus	74.9	78.2	74.6	67.1	75.3	76.1	76.2	72.1	72.2	77.5	74.4 ± 3.2

studies that measured SvO₂ within the jugular bulb and confluence of the sinuses^{13,32} suggest that the SvO₂ in these regions should exceed 55% in healthy individuals, which was not seen in some subjects in a recent QSM vein oxygen saturation study.⁶ This difference may be due to the RESHARP phase-removal method being more accurate at brain edges.²¹

Intravascular QSM and R2* venous oxygen measurements have benefits compared with intravascular SWI measurements⁶ or methods of measuring subvoxel vasculature oxygenation with T2*-weighted methods.⁴ These other methods are dependent on the angular orientation of the measured vessel to the main magnetic field. R2* mapping, however, requires several image acquisitions with varied TEs and therefore may be more sensitive to global patient motion due to the longer image-acquisition time. Flow compensation could be used with increased image-acquisition time. Postmortem imaging allows accurate comparison between motion-sensitive MR imaging methods. Modifications to this R2* mapping method can be applied to in vivo subjects with flow compensation or electrocardiography-gated acquisition³³ to reduce flow artifacts.

There are several limitations to this study. Although the correlation between R2* and susceptibility is strong and significant in the postmortem subjects, the number of postmortem subjects is limited. Using a larger number of subjects with varying time intervals of imaging after death could help evaluate measurement changes in the early postmortem period relative to the time of death. QSM was not applied to the full cerebral volume, and relatively large voxels were used to reduce image-acquisition times, to use methods appropriate for in vivo imaging. Laboratory hematocrit values from postmortem subjects were not obtained directly before death due to the patients' palliative state before imaging. As well, laboratory analysis of intravenous blood changes in the postmortem state were not evaluated and compared with MR imaging findings, which could be an important future investigation. This could elucidate the relative contribution of cell lysis, molecular degradation, cellular swelling, and hematocrit effect to quantitative MR imaging values. The R2* mapping method in this study did not use flow compensation to obtain sufficient echoes for accurate R2* calculations. Therefore, the method could not be used to evaluate venous oxygenation in in vivo subjects.

In the future, application of SvO₂ methods using QSM could be used in neurologic disease to assess altered cellular oxygen metabolism. Optimal phase removal and QSM methods need to be determined because several methods currently exist. R2* mapping methods and QSM imaging could be compared among in vivo subjects using flow-compensated R2* mapping techniques.

CONCLUSIONS

Quantitative intracranial venous measurements with MR imaging using R2* mapping and QSM have a high correlation in early postmortem subjects, and calculated hematocrit values are within the expected range. Both methods demonstrated a hemoconcentration effect in dependent venous segments in postmortem subjects, which is similar to direct hematocrit measurements and CT findings from prior postmortem studies.

Disclosures: Andrew J. Walsh—RELATED: Grant: Canadian Institutes of Health Research grant MOP 102582.* Derek J. Emery—RELATED: Grant: Canadian Institutes of Health Research.* Alan Wilman—RELATED: Grant: Canadian Institutes of Health Research.* *Money paid to the institution.

REFERENCES

1. Liu Z, Li Y. **Cortical cerebral blood flow, oxygen extraction fraction, and metabolic rate in patients with middle cerebral artery stenosis or acute stroke.** *AJNR Am J Neuroradiol* 2016;37:607–14 CrossRef Medline
2. Mohammed W, Xunning H, Haibin S, et al. **Clinical applications of susceptibility-weighted imaging in detecting and grading intracranial gliomas: a review.** *Cancer Imaging* 2013;13:186–95 CrossRef Medline
3. Dal-Bianco A, Hametner S, Grabner G, et al. **Veins in plaques of multiple sclerosis patients: a longitudinal magnetic resonance imaging study at 7 Tesla.** *Eur Radiol* 2015;25:2913–20 CrossRef Medline
4. Sedlacik J, Rauscher A, Reichenbach JR. **Obtaining blood oxygenation levels from MR signal behavior in the presence of single venous vessels.** *Magn Reson Med* 2007;58:1035–44 CrossRef Medline
5. Fernández-Seara MA, Techawiboonwong A, Detre JA, et al. **MR susceptometry for measuring global brain oxygen extraction.** *Magn Reson Med* 2006;55:967–73 CrossRef Medline
6. Fan AP, Bilgic B, Gagnon L, et al. **Quantitative oxygenation venography from MRI phase.** *Magn Reson Med* 2014;72:149–59 CrossRef Medline
7. Fan AP, Evans KC, Stout JN, et al. **Regional quantification of cerebral venous oxygenation from MRI susceptibility during hypercapnia.** *Neuroimage* 2015;104:146–55 CrossRef Medline
8. Smith AB, Lattin GE, Jr., Berran P, et al. **Common and expected postmortem CT observations involving the brain: mimics of antemortem pathology.** *AJNR Am J Neuroradiol* 2012;33:1387–91 CrossRef Medline
9. Jackowski C, Thali M, Aghayev E, et al. **Postmortem imaging of blood and its characteristics using MSCT and MRI.** *Int J Legal Med* 2006;120:233–40 CrossRef Medline
10. Takahashi N, Satou C, Higuchi T, et al. **Quantitative analysis of intracranial hypostasis: comparison of early postmortem and antemortem CT findings.** *AJR Am J Roentgenol* 2010;195:W388–93 CrossRef Medline
11. Ishida M, Gonoji W, Okuma H, et al. **Common postmortem computed tomography findings following atraumatic death: differentiation between normal postmortem changes and pathologic lesions.** *Korean J Radiol* 2015;16:798–809 CrossRef Medline
12. Krishnamurthy LC, Mao D, King KS, et al. **Correction and optimization of a T2-based approach to map blood oxygenation in small cerebral veins.** *Magn Reson Med* 2016;75:1100–09 CrossRef Medline
13. Lam JM, Chan MS, Poon WS. **Cerebral venous oxygen saturation monitoring: is dominant jugular bulb cannulation good enough?** *Br J Neurosurg* 1996;10:357–64 CrossRef Medline
14. Weisskoff RM, Kiihne S. **MRI susceptometry: image-based measurement of absolute susceptibility of MR contrast agents and human blood.** *Magn Reson Med* 1992;24:375–83 CrossRef Medline
15. He X, Yablonskiy DA. **Biophysical mechanisms of phase contrast in gradient echo MRI.** *Proc Natl Acad Sci U S A* 2009;106:13558–63 CrossRef Medline
16. Jain V, Abdulmalik O, Probert KJ, et al. **Investigating the magnetic susceptibility properties of fresh human blood for noninvasive oxygen saturation quantification.** *Magn Reson Med* 2012;68:863–67 CrossRef Medline
17. Walsh A, Lebel R, Eissa A, et al. **Multiple sclerosis: validation of MR imaging for quantification and detection of iron.** *Radiology* 2013;267:531–42 CrossRef Medline
18. Sun H, Walsh AJ, Lebel RM, et al. **Validation of quantitative susceptibility mapping with Perls' iron staining for subcortical gray matter.** *Neuroimage* 2015;105:486–92 CrossRef Medline
19. Walsh DO, Gmitro AF, Marcellin MW. **Adaptive reconstruction of phased array MR imagery.** *Magn Reson Med* 2000;43:682–90 Medline

20. Smith SM, Jenkinson M, Woolrich MW, et al. **Advances in functional and structural MR image analysis and implementation as FSL.** *Neuroimage* 2004;23(Suppl 1):S208–19 CrossRef Medline
21. Sun H, Wilman AH. **Background field removal using spherical mean value filtering and Tikhonov regularization.** *Magn Reson Med* 2014;71:1151–57 CrossRef Medline
22. Bilgic B, Pfefferbaum A, Rohlfing T, et al. **MRI estimates of brain iron concentration in normal aging using quantitative susceptibility mapping.** *Neuroimage* 2012;59:2625–35 CrossRef Medline
23. Baudrexel S, Volz S, Preibisch C, et al. **Rapid single-scan T2*-mapping using exponential excitation pulses and image-based correction for linear background gradients.** *Magn Reson Med* 2009;62:263–68 CrossRef Medline
24. Du YPP, Jin ZY, Hu YZ, et al. **Multi-echo acquisition of MR angiography and venography of the brain at 3 Tesla.** *J Magn Reson Imaging* 2009;30:449–54 CrossRef Medline
25. Volz S, Hattingen E, Preibisch C, et al. **Reduction of susceptibility-induced signal losses in multi-gradient-echo images: application to improved visualization of the subthalamic nucleus.** *Neuroimage* 2009;45:1135–43 CrossRef Medline
26. Rasband WS. ImageJ. Bethesda: National Institutes of Health; 1997–2011
27. Penttilä A, Laiho K. **Autolytic changes in blood cells of human cadavers, II: morphological studies.** *Forensic Sci Int* 1981;17:121–32 CrossRef Medline
28. Yablonskiy DA, Haacke EM. **Theory of NMR signal behavior in magnetically inhomogeneous tissues: the static dephasing regime.** *Magn Reson Med* 1994;32:749–63 CrossRef Medline
29. He X, Zhu M, Yablonskiy DA. **Validation of oxygen extraction fraction measurement by qBOLD technique.** *Magn Reson Med* 2008;60:882–88 CrossRef Medline
30. Chang S, Zhang J, Liu T, et al. **Quantitative susceptibility mapping of intracerebral hemorrhages at various stages.** *J Magn Reson Imaging* 2016;44:420–25 CrossRef Medline
31. Thomsen H, Kaatsch HJ, Krisch B. **How and why does the platelet count in postmortem blood change during the early postmortem interval?** *Forensic Sci Int* 1999;101:185–94 CrossRef Medline
32. Schell RM, Cole DJ. **Cerebral monitoring: jugular venous oximetry.** *Anesth Analg* 2000;90:559–66 CrossRef Medline
33. Li D, Waight DJ, Wang Y. **In vivo correlation between blood T2* and oxygen saturation.** *J Magn Reson Imaging* 1998;8:1236–39 CrossRef Medline

Relationship between Cough-Associated Changes in CSF Flow and Disease Severity in Chiari I Malformation: An Exploratory Study Using Real-Time MRI

A.F. Bezuidenhout, D. Khatami, C.B. Heilman, E.M. Kasper, S. Patz, N. Madan, Y. Zhao, and R.A. Bhadelia



ABSTRACT

BACKGROUND AND PURPOSE: Currently no quantitative objective test exists to determine disease severity in a patient with Chiari I malformation. Our aim was to correlate disease severity in symptomatic patients with Chiari I malformation with cough-associated changes in CSF flow as measured with real-time MR imaging.

MATERIALS AND METHODS: Thirteen symptomatic patients with Chiari I malformation (tonsillar herniation of ≥ 5 mm) were prospectively studied. A real-time, flow-sensitized pencil-beam MR imaging scan was used to measure CSF stroke volume during rest and immediately following coughing and relaxation periods (total scan time, 90 seconds). Multiple posterior fossa and craniocervical anatomic measurements were also obtained. Patients were classified into 2 groups by neurosurgeons blinded to MR imaging measurements: 1) nonspecific Chiari I malformation (5/13)—Chiari I malformation with nonspecific symptoms like non-cough-related or mild occasional cough-related headache, neck pain, dizziness, paresthesias, and/or trouble swallowing; 2) specific Chiari I malformation (8/13)—patients with Chiari I malformation with specific symptoms and/or objective findings like severe cough-related headache, myelopathy, syringomyelia, and muscle atrophy. The Spearman correlation was used to determine correlations between MR imaging measurements and disease severity, and both groups were also compared using a Mann-Whitney *U* test.

RESULTS: There was a significant negative correlation between the percentage change in CSF stroke volume (resting to postcoughing) and Chiari I malformation disease severity ($R = 0.59$; $P = .03$). Mann-Whitney comparisons showed the percentage change in CSF stroke volume (resting to postcoughing) to be significantly different between patient groups ($P = .04$). No other CSF flow measurement or anatomic measure was significantly different between the groups.

CONCLUSIONS: Our exploratory study suggests that assessment of CSF flow response to a coughing challenge has the potential to become a valuable objective noninvasive test for clinical assessment of disease severity in patients with Chiari I malformation.

ABBREVIATIONS: CMI = Chiari I malformation; NS-CMI = Chiari I malformation with nonspecific symptoms; PBI = pencil-beam imaging; S-CMI = Chiari I malformation with specific symptoms; SV_{CSF} = CSF stroke volume

Hans Chiari first described the spectrum of Chiari malformations during the end of the 19th century, and in 1985, Aboulezz et al¹ described the radiologic definition of Chiari I malformation (CMI) as a ≥ 5 -mm downward displacement of the cerebellar tonsils through the foramen magnum. Much controversy has arisen regarding the management of these patients since

then because CMI is not an infrequent MR imaging finding in the general population with a prevalence of 0.56%–0.77%.^{2,3} The conundrum exists because some patients who meet the MR imaging criteria for CMI are asymptomatic and some with < 5 -mm tonsillar herniation have typical CMI symptoms.^{4–10} It has been estimated that at present, only 20% of patients diagnosed as having CMI by current MR imaging criteria will have symptoms amenable to surgical intervention.¹¹ Because there is no reliable objective test available that correlates with the severity of clinical findings, the treatment of these patients largely depends on the management philosophy of the treating neurosurgeon. Reportedly, this has led to the overzealous use of surgical treatment with unfavorable outcomes being reported in up to 30% of patients.^{6,12}

Most of the symptoms and clinical findings associated with CMI are believed to be due either to neural compression or abnormal CSF circulation at the foramen magnum.^{5,7,13–23} Because

Received February 17, 2018; accepted after revision March 21.

From the Departments of Radiology (A.F.B., D.K., R.A.B.) and Neurosurgery (E.M.K.), Beth Israel Deaconess Medical Center, Boston, Massachusetts; Departments of Neurosurgery (C.B.H.) and Radiology (N.M.), Tufts Medical Center, Boston, Massachusetts; Department of Radiology (S.P.), Brigham and Woman's Hospital, Boston, Massachusetts; and Philips Healthcare (Y.Z.), Boston, Massachusetts.

This work was supported by a grant from the Conquer Chiari Foundation.

Please address correspondence to Fourie Bezuidenhout, MD, Department of Radiology, Beth Israel Deaconess Medical Center, WCB90, 330 Brookline Ave, Boston, MA 02215; e-mail: abezuide@bidmc.harvard.edu; @Fouriebez

<http://dx.doi.org/10.3174/ajnr.A5670>

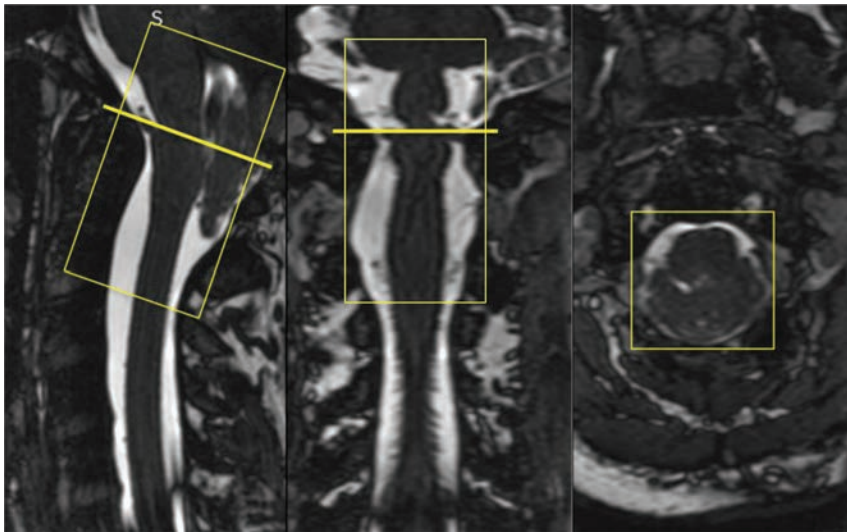


FIG 1. The position of the PBI cylinder (*rectangle*) and location of CSF flow evaluation (*line*) are shown in a patient with CMI.

both of these pathologic forces are likely to be interrelated within the bony confines of the foramen magnum, assessment of fluid dynamics by CSF pressure or flow measurements at the craniocervical junction may better reflect CMI disease severity than MR imaging–based anatomic measurements like tonsillar herniation or posterior fossa volume.^{21,23–26} Thus, both invasive simultaneous pressure measurements in the head and spinal canal and non-invasive CSF flow imaging using cine phase-contrast MR imaging have been used.^{5,7,13–16,27–31} However, none of the above methods have been widely accepted for presurgical evaluation of individual patients with CMI: pressure measurements due to their invasive nature and cine phase-contrast due to wide variability in quantitative CSF flow estimates between patients with CMI of different disease severities (as well as between healthy subjects and patients with CMI).

An important limitation of previous cine phase-contrast methods is that most assess CSF flow while the patient is breathing quietly in the MR imaging scanner and provide weighted averages of CSF flow pulsations over ≥ 15 cardiac cycles. Because physiologic challenges such as coughing or the Valsalva maneuver are known to transiently induce or exaggerate pressure dissociations at the craniocervical junction affecting CSF flow for only a few seconds, these weighted averages of CSF flow over many cardiac cycles measured by cine phase-contrast may not capture transient changes in CSF flow.^{21–23,32–35} In a recent study, Bhadelia et al³² proposed a real-time CSF flow imaging technique to assess the transient changes in CSF flow as a consequence of physiologic maneuvers. This technique was further used to compare CSF flow response to coughing in patients with CMI and healthy subjects.³³ In this exploratory study, we used real-time MR imaging to correlate disease severity among symptomatic patients with CMI with cough-associated changes in CSF flow.

MATERIALS AND METHODS

Institutional review board approval was obtained for this Health Insurance Portability and Accountability Act–compliant prospective study, and each patient signed an informed consent.

Patients

Thirteen symptomatic patients with CMI who agreed to participate in a research study at the initial neurosurgical consultation were prospectively evaluated between 2011 and 2013. Two board-certified neurosurgeons with >15 years of experience in Chiari care developed a grading scale for symptom severity by consensus (slightly modified from a previously published CMI study, Alperin et al 2014³⁶). Subsequently, this grading system was used by the neurosurgeons blinded to MR imaging measurements to classify patients into 2 groups: 1) nonspecific CMI (NS-CMI): CMI with nonspecific symptoms like non-cough-related or mild occasional cough-related headache, neck pain, dizziness, paresthesias, and/or dysphagia; 2) specific-CMI (S-CMI): patients with CMI with specific symptoms and/or objective

findings like severe cough-related headache, myelopathy, syringomyelia, and muscle atrophy.

MR Imaging

All patients underwent MR imaging on a 3T scanner (Achieva; Philips Healthcare, Best, the Netherlands).

For localization and anatomic measurements of the posterior fossa and craniocervical junction, sagittal 3D T1 and 3D T2-weighted images were obtained. To assess CSF flow, we used a real-time flow-sensitized pencil-beam imaging (PBI) method with ~ 50 -ms temporal resolution. PBI excites a narrow cylinder or “pencil” region and has been described in detail previously.^{32,37,38} A 25-mm-diameter and 64-mm-length cylinder with bipolar velocity-encoding and readout gradients applied along the long axis of the cylinder (pencil beam) was positioned along the long axis of the upper cervical spinal canal, extending from just above the level of the foramen magnum to the C3 level covering the entire thecal sac (Fig 1).^{32,33} The PBI scan provides a phase-encoded velocity measurement with a temporal resolution of ~ 50 ms and spatial resolution along the cylinder axis.³⁸ To avoid phase wrap, we used a velocity encoding of 5 cm/s along the superior-to-inferior direction. Other imaging parameters were TR, 25–28 ms; TE, 3.8 ms; and flip angle, 5°. The bipolar phase-encoding gradient was alternated on sequential TRs, making the effective temporal resolution $2 \times TR$ (ie, 50–56 ms). Heart rate and respiratory movements were continuously monitored using the physiologic recording system of the scanner. Cardiac gating was not required for this PBI study, which recorded pulsatile CSF flow motion in real-time and, therefore, was able to acquire data much faster than the gated phase-contrast MR imaging.

Each PBI scan was acquired for approximately 90 seconds, during which the patient was asked to do the following: 1) breathe quietly for the first 15–20 seconds (by counting from 1 to 20), 2) then cough as forcefully as possible consecutively 6 times, and 3) breathe quietly again after the end of coughing. Each 90-second scan set was repeated 3 times.

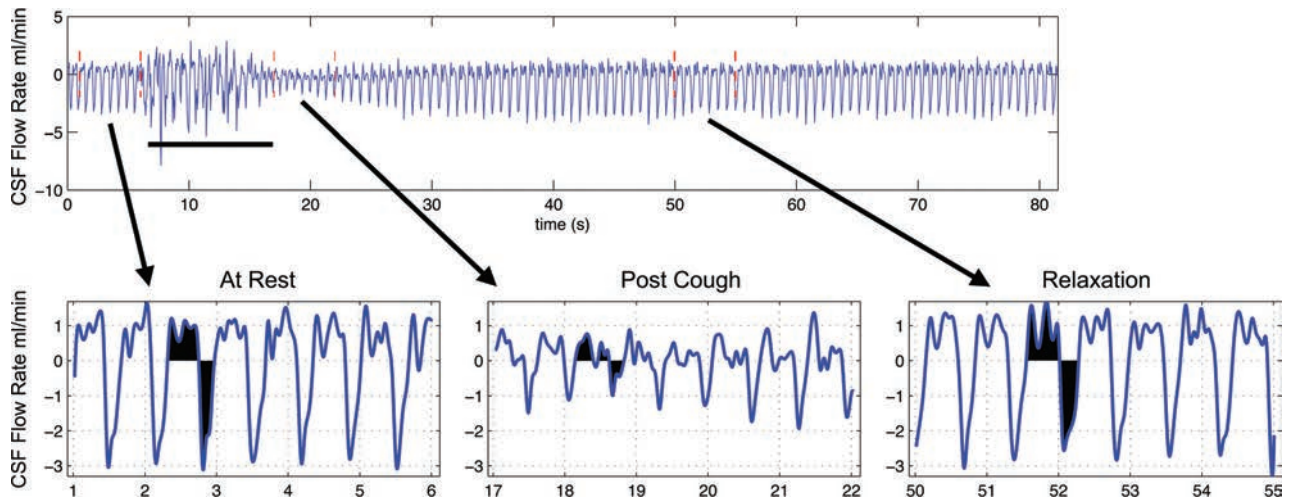


FIG 2. The effect of coughing on a cardiac cycle–related CSF flow waveforms is seen in a patient with CMI with specific symptoms. Left-to-right: resting, coughing (*underlined*), postcoughing, and relaxation waveforms are seen. CSF flow waveforms: craniocaudal CSF flow (*area colored in below the zero line*) and caudocranial CSF flow (*area colored in above the zero line*). CSF stroke volume is the average of absolute flow from craniocaudal and caudocranial CSF flow. In this patient with CMI with specific symptoms, the CSF flow-pulsation magnitude in the immediate postcoughing period decreases in comparison with the resting value before gradually returning to the resting level at relaxation. The x-axis indicates time in seconds; the y-axis, CSF flow rate in milliliters per minute. Arrows indicate a magnified view of the CSF flow waveforms during the respective actions performed by the patient.

Image Analysis

3D anatomic images were used to measure the amount of tonsillar herniation below the level of the foramen magnum as well as multiple posterior fossa and craniocervical dimensions and angles. Posterior fossa measurements included the length of the clivus (inferior boundary of the dorsum sellae to the basion), supraocciput (opisthion to the internal occipital protuberance), the McRae line (basion to the opisthion), and the Twining line (inferior boundary of the dorsum sellae to the internal occipital protuberance). Craniocervical measurements included the clivus-canal angle (clival-axis angle), odontoid retroversion angle (posterior inclination of the odontoid relative to the body of C2), skull base angle (from the nasion to the center of the pituitary fossa to the clivus/basion), and the pB-C2 line (perpendicular length between a line connecting the basion and the inferoposterior C2 body to the ventral dura).

The posterior fossa and craniocervical measurements were manually obtained using the midsagittal image on a PACS workstation.

CSF flow analysis was performed off-line using custom software developed in Matlab (MathWorks, Natick, Massachusetts), which allows simultaneous display of 3D anatomic and physiologic PBI data along with the heart rate and respiration. The cross-sectional area of the CSF flow channel of a patient within the PBI cylinder was determined on axial anatomic images by subtracting the area of the neural structures from the area of the thecal sac at that level.³⁹ The software then calculated CSF flow in milliliters per second by multiplying average PBI velocity by the area of CSF flow channel. CSF flow waveforms were plotted with CSF flow on the y-axis versus time (seconds) on the x-axis, thereby depicting cardiac cycle–related CSF flow pulsations over the entire 90-second data acquisition, encompassing resting, postcoughing, and relaxation (delayed) periods. The physiologic parameter measured was CSF stroke volume (SV_{CSF}) in milliliters, which was defined as the average of the absolute values of integrated crani-

caudal and caudocranial CSF flows during the entire cardiac cycle (Fig 2).⁴⁰

The SV_{CSF} for each period was calculated during a 5- to 6-second period. For postcoughing assessment, the period was selected approximately 5 seconds after the end of coughing to allow sufficient time for any motion related to coughing to subside. The relaxation assessment was performed about 20–25 seconds after coughing. We assessed CSF flow just below the level of foramen magnum along the PBI cylinder. No discontinuities were present on the phase images to indicate aliasing (no velocities exceeding 5 cm/s).

All anatomic and CSF flow measurements for this exploratory study were obtained by consensus by 2 radiologists with 25 and 3 years of clinical experience but without the knowledge of the clinical severity grade of the patients.

Data Analysis

Besides using resting, postcoughing, and relaxation values of SV_{CSF} as physiologic measurements, change in the SV_{CSF} between resting to postcoughing, postcoughing to relaxation, and resting to relaxation was also evaluated and expressed in a percentage of initial values for normalization of differences among patients. The Spearman correlation was used to determine relationships between anatomic and physiologic CSF flow measurements and CMI disease severity. A Mann-Whitney U test was used to compare anatomic and physiologic measurements between NS-CMI and S-CMI patient groups. A P value of $< .05$ was statistically significant.

RESULTS

Thirteen symptomatic patients with CMI were included. They were a mean of 38.6 ± 6.7 years of age, and 11/12 (92%) were women. The patients were divided into 2 groups based on symptoms by neurosurgeons as described in the “Materials and Methods” section. Group 1 included patients with nonspecific CMI

Anatomic and physiologic measurements in S-CMI and NS-CMI

	S-CMI (n = 8)	NS-CMI (n = 5)
Anatomic measurements (mean)		
Tonsillar herniation (mm)	17.5 ± 7.4	12.2 ± 6.2
Clivus length (mm)	34.3 ± 5.4	32.8 ± 2.5
Supraocciput length (mm)	42.4 ± 7.7	40.4 ± 2.5
Twining line (mm)	81.4 ± 4.8	81.8 ± 1.3
McRae line (mm)	36.6 ± 4.2	39 ± 3.4
Skull base angle	131.1° ± 6.9°	125.6° ± 4.8°
Odontoid retroversion angle	69.8° ± 9.3°	70.4° ± 8.7°
Clivus-canal angle	145.5° ± 10.4°	150.6° ± 6.9°
pB-C2 Line (mm)	6.1 ± 2	7.2 ± 1.5
Physiologic measurements (mean)		
SV _{CSF} resting (mL)	0.37 ± 0.27	0.48 ± 0.20
SV _{CSF} postcough (mL)	0.14 ± 0.13	0.29 ± 0.13
SV _{CSF} relaxation (mL)	0.36 ± 0.31	0.51 ± 0.20
ΔSV _{CSF} resting to postcough (%)	-64.9 ± 17.3 ^a	-35.1 ± 29.6 ^a
ΔSV _{CSF} postcough to relaxation (%)	190 ± 158	98.1 ± 115.7
ΔSV _{CSF} resting to relaxation (%)	-9.6 ± 37.6	9.3 ± 27.3

Note:—ΔSV_{CSF} resting to postcough indicates change in SV_{CSF} from resting to postcough in %; ΔSV_{CSF} postcough to relaxation, change in SV_{CSF} from postcough to relaxation in %; ΔSV_{CSF} resting to relaxation, change in SV_{CSF} from resting to relaxation in %.

^a *P* < .05, Mann-Whitney *U* test.

symptoms and consisted of 5 (5/13) patients. Group 2 included patients with specific CMI symptoms and consisted of 8 (8/13) patients.

No statistically significant relationship was observed between anatomic measurements and CMI disease severity. There was a statistically significant negative relationship observed between the percentage change in SV_{CSF} from resting to postcoughing and CMI disease severity (*R* = 0.59; *P* = .03).

Anatomic and physiologic CSF flow measurements of NS-CMI and S-CMI groups are shown in the Table. The Mann-Whitney *U* test showed the percentage change in the SV_{CSF} from resting to postcough to be the only MR imaging measurement significantly different between the groups (*P* = .04). The change in the SV_{CSF} is graphically demonstrated in a patient with S-CMI with cough and Valsalva-related headache and syringomyelia (Fig 2).

Figure 3 shows the effect of coughing in a patient with NS-CMI compared with S-CMI. No appreciable change in CSF flow is seen in a patient with NS-CMI after coughing, but in the patient with S-CMI, considerable decrease is clearly visualized.

DISCUSSION

In this exploratory study, real-time physiologic measurement of CSF flow demonstrated a significant decrease in flow across the foramen magnum in response to coughing in patients with CMI with severe specific symptoms compared with those with CMI with nonspecific symptoms. Real-time physiologic measurement of decreased CSF flow after coughing demonstrated better correlation with CMI disease severity than any of the anatomic measurements of the posterior fossa or craniocervical junction. Another important finding of the study was that no significant difference in the SV_{CSF} was seen between the 2 groups of patients with CMI in resting or relaxation periods and only a borderline significant difference (*P* = .07) was seen in the postcoughing values. The observation that only the percentage change in CSF flow from resting to postcoughing showed a significant difference between the 2 groups underscores the importance of the use of nor-

malized values of CSF flow in objective quantitative physiology-based assessment of CSF flow obstruction at the foramen magnum in an individual patient with CMI. In other words, each patient acted as his or her own control by using a physiologic challenge to assess his or her ability to handle compensatory flow across the foramen magnum and thereby negating confounding variables among patients. The results of this exploratory study are encouraging enough to pursue a larger prospective study of patients with CMI to determine whether this method can be used as an objective clinical test for assessing disease severity.

Previously published invasive pressure studies have shown that physiologic challenges such as coughing or Valsalva maneuver produce pressure dissociation between the head and spine in patients with CMI.^{21,23,24,32-35} The development of pressure dissociation is explained by a transient increase in spinal pressure (from increased intrathoracic pressure and consequent distension of the epidural veins) during coughing, moving CSF to the head, which returns to the spinal canal immediately postcoughing in a healthy subject but not in a patient with CMI, provided there is sufficient foramen magnum obstruction due to neural crowding.^{22,33-35} These studies also demonstrated that there was minimal if any pressure dissociation in these patients with CMI at rest before coughing or Valsalva.³³ While we did not calculate pressure gradients from our velocity data, our results confirmed both of these observations made by previous invasive pressure studies.^{34,35,41} First, a decrease in CSF flow after coughing in patients with CMI indicates that CSF circulation from the head to spine is impaired, a condition that would result in pressure dissociation. Second, a decrease in CSF flow after coughing was transient, lasting only a few seconds before returning to the resting levels in the relaxation period. This finding suggests that there is increased pressure dissociation in the postcoughing period due to further downward descent of cerebellar tonsils exaggerating neural crowding at the foramen magnum.²³ This exaggeration of neural crowding and further obstruction of CSF flow are believed to result in exacerbation of symptoms after coughing.^{23,32-35} Our observation thus strongly suggests that MR imaging assessment of CSF flow in CMI would be much more informative in assessing the CSF circulation abnormalities if performed with a physiologic challenge.

Our results provide the first evidence of differences in CSF flow in response to coughing in 2 groups of symptomatic patients with CMI, which were classified on the basis of symptoms and clinical findings. While this is a small exploratory study, it suggests that there is a higher degree of transient CSF flow impairment after coughing in patients with CMI with specific symptoms and objective findings—that is, more severe disease than in those with nonspecific symptoms. Furthermore, unlike invasive pressure monitoring, the method described here is noninvasive and has the potential to be used in studying many patients with CMI

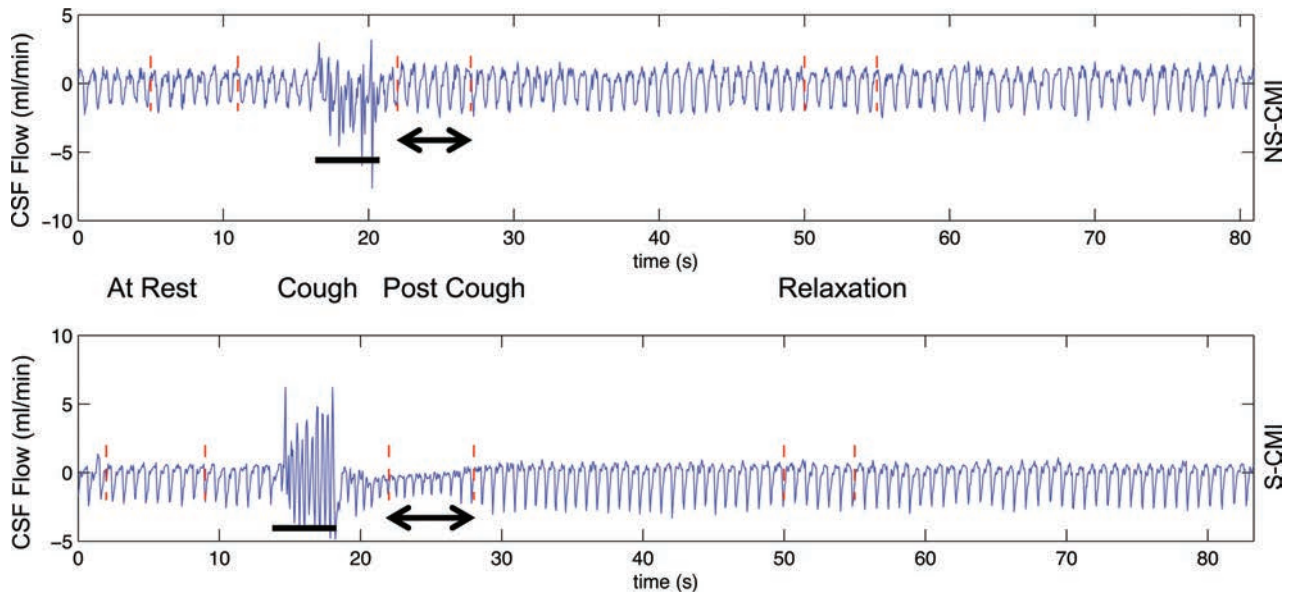


FIG 3. The effect of coughing on cardiac cycle–related CSF flow waveforms in different patients with CMI, one with nonspecific symptoms and one with specific symptoms. Left-to-right: resting, coughing (*underlined*), postcoughing (*underlined with double-headed arrows*), and relaxation waveforms are seen. In the patient with S-CMI (*lower waveform*), the CSF flow-pulsation magnitude in the immediate postcoughing period decreases to $\pm 50\%$ of the resting value before gradually returning to the resting level at relaxation. In contrast, in the patient with NS-CMI, the CSF flow-pulsation magnitude immediately postcoughing is not significantly different compared with that of the resting period. The x-axis indicates time in seconds; the y-axis, CSF flow rate, in milliliters per minute.

with different grades of disease severity and to follow-up patients treated with or without surgical decompression.

Several limitations of our exploratory study (and method) need to be addressed. First, the small sample size limits our ability to recommend it as an objective test for patients with CMI until further patient data are collected in a larger prospective study. However, even in this small group of patients, cough-associated changes in CSF flow were the only anatomic or physiologic parameter that demonstrated a statistically significant difference between patients with NS-CMI and S-CMI, highlighting their potential in objectively assessing disease severity in patients with CMI. Second, due to small sample size, we could only divide patients with CMI into 2 groups as has been done by many previous CMI studies. Given the wide variety of symptoms and clinical findings in CMI, we believe that dividing CMI disease severity into only 2 groups is a limitation that needs to be addressed in the future, including separate assessment of patients with CMI with syringomyelia to further elucidate its pathophysiology. Third, we did not quantitatively measure coughing effort by patients but asked them to cough as forcefully as possible, which could potentially introduce an additional variable that was not accounted for in our study. We have since developed a method to quantitatively assess cough effort during our MR imaging experiments to better evaluate CSF flow changes in individual patients. However, we believe cough effort to be less of an issue in the group comparison performed here. This is because patients with severe symptoms (S-CMI) are more likely to not cough forcefully due to fear of inducing pain than those with less severe symptoms (NS-CMI) and thus may have introduced a negative bias, if any, thus further enhancing our results. Fourth, due to the small sample size in this exploratory study, interobserver variability between the neurosurgeons classifying the patients and radiologists reading the MR imaging studies, respectively, was not ana-

lyzed, but in both situations, decisions were made by consensus. Finally, the pencil-beam sequence used here is currently only available in research mode on 1 vendor platform. If this method is to be used in routine clinical practice for CSF flow studies in patients with CMI, expanding it across different vendor platforms is required.

CONCLUSIONS

Our exploratory study suggests a potential future role for real-time physiologic measurement of CSF flow in response to coughing as an objective qualifier for clinical assessment in patients with CMI.

Disclosures: Ekkehard M. Kasper—UNRELATED: Board Membership: Editorial Boards of *Neurosurgery*, *Neurooncology*, others; Consultancy: Risk Management Foundation of The Harvard Medical Institutions, Comments: legal expert review as an external specialist; Expert Testimony: CRICO; Travel/Accommodations/Meeting Expenses Unrelated to Activities Listed: World Federation of Neurosurgical Societies Committee on Anatomy, Comments: For educational courses to which we are invited as a World Federation of Neurosurgical Societies committee, the venue will provide room and board. We pay for our own airfare. Yansong Zhao—UNRELATED: Employment: Philips Healthcare. Rafeeqe A. Bhadelia—RELATED: Grant: Conquer Chiari Foundation, Comments: money for MRI scans and analysis software.* *Money paid to the institution.

REFERENCES

1. Aboulezz AO, Sartor K, Geyer CA, et al. **Position of cerebellar tonsils in the normal population and in patients with Chiari malformation: a quantitative approach to MR imaging.** *J Comput Assist Tomogr* 1985;9:1033–36 CrossRef Medline
2. Elster AD, Chen MY. **Chiari I malformations: clinical and radiologic reappraisal.** *Radiology* 1992;183:347–53 CrossRef Medline
3. Meadows J, Kraut M, Guarnieri M, et al. **Asymptomatic Chiari Type I malformations identified on magnetic resonance imaging.** *J Neurosurg* 2000;92:920–26 Medline
4. Alden TD, Ojemann JG, Park TS. **Surgical treatment of Chiari I**

- malformation: indications and approaches.** *Neurosurg Focus* 2001; 11:E2 Medline
5. Alperin N, Sivaramakrishnan A, Lichtor T. **Magnetic resonance imaging-based measurements of cerebrospinal fluid and blood flow as indicators of intracranial compliance in patients with Chiari malformation.** *J Neurosurg* 2005;103:46–52 CrossRef Medline
 6. Baisden J. **Controversies in Chiari I malformations.** *Surg Neurol Int* 2012;3(Suppl 3):S232–37 CrossRef Medline
 7. Hofkes SK, Iskandar BJ, Turski PA, et al. **Differentiation between symptomatic Chiari I malformation and asymptomatic tonsillar ectopia by using cerebrospinal fluid flow imaging: initial estimate of imaging accuracy.** *Radiology* 2007;245:532–40 CrossRef Medline
 8. Sekula RF Jr, Arnone GD, Crocker C, et al. **The pathogenesis of Chiari I malformation and syringomyelia.** *Neurol Res* 2011;33: 232–39 CrossRef Medline
 9. Shaffer N, Martin BA, Rocque B, et al. **Cerebrospinal fluid flow impedance is elevated in Type I Chiari malformation.** *J Biomech Eng* 2014;136:021012 CrossRef Medline
 10. Voelker R. **Chiari conundrum: researchers tackle a brain puzzle for the 21st century.** *JAMA* 2009;301:147–49 CrossRef Medline
 11. Tubbs RS, Beckman J, Naftel RP, et al. **Institutional experience with 500 cases of surgically treated pediatric Chiari malformation type I.** *J Neurosurg Pediatr* 2011;7:248–56 CrossRef Medline
 12. Aliaga L, Hekman KE, Yassari R, et al. **A novel scoring system for assessing Chiari malformation type I treatment outcomes.** *Neurosurgery* 2012;70:656–64; discussion 664–65 CrossRef Medline
 13. Alperin N, Kulkarni K, Loth F, et al. **Analysis of magnetic resonance imaging-based blood and cerebrospinal fluid flow measurements in patients with Chiari I malformation: a system approach.** *Neurosurg Focus* 2001;11:E6 Medline
 14. Armonda RA, Citrin CM, Foley KT, et al. **Quantitative cine-mode magnetic resonance imaging of Chiari I malformations: an analysis of cerebrospinal fluid dynamics.** *Neurosurgery* 1994;35:214–23; discussion 223–24 CrossRef Medline
 15. Bhadelia RA, Bogdan AR, Wolpert SM, et al. **Cerebrospinal fluid flow waveforms: analysis in patients with Chiari I malformation by means of gated phase-contrast MR imaging velocity measurements.** *Radiology* 1995;196:195–202 CrossRef Medline
 16. Haughton VM, Korosec FR, Medow JE, et al. **Peak systolic and diastolic CSF velocity in the foramen magnum in adult patients with Chiari I malformations and in normal control participants.** *AJNR Am J Neuroradiol* 2003;24:169–76 Medline
 17. Hofmann E, Warmuth-Metz M, Bendszus M, et al. **Phase-contrast MR imaging of the cervical CSF and spinal cord: volumetric motion analysis in patients with Chiari I malformation.** *AJNR Am J Neuroradiol* 2000;21:151–58 Medline
 18. McGirt MJ, Nimjee SM, Floyd J, et al. **Correlation of cerebrospinal fluid flow dynamics and headache in Chiari I malformation.** *Neurosurgery* 2005;56:716–21; discussion 716–21 CrossRef Medline
 19. Oldfield EH, Muraszko K, Shawker TH, et al. **Pathophysiology of syringomyelia associated with Chiari I malformation of the cerebellar tonsils. Implications for diagnosis and treatment.** *J Neurosurg* 1994;80:3–15 CrossRef Medline
 20. Quigley MF, Iskandar B, Quigley ME, et al. **Cerebrospinal fluid flow in foramen magnum: temporal and spatial patterns at MR imaging in volunteers and in patients with Chiari I malformation.** *Radiology* 2004;232:229–36 CrossRef Medline
 21. Sansur CA, Heiss JD, DeVroom HL, et al. **Pathophysiology of headache associated with cough in patients with Chiari I malformation.** *J Neurosurg* 2003;98:453–58 CrossRef Medline
 22. Williams B. **Cerebrospinal fluid pressure changes in response to coughing.** *Brain* 1976;99:331–46 CrossRef Medline
 23. Williams B. **Cough headache due to craniospinal pressure dissociation.** *Arch Neurol* 1980;37:226–30 CrossRef Medline
 24. Heiss JD, Patronas N, DeVroom HL, et al. **Elucidating the pathophysiology of syringomyelia.** *J Neurosurg* 1999;91:553–62 CrossRef Medline
 25. Tachibana S, Iida H, Yada K. **Significance of positive Queckenstedt test in patients with syringomyelia associated with Arnold-Chiari malformations.** *J Neurosurg* 1992;76:67–71 CrossRef Medline
 26. Williams B. **On the pathogenesis of syringomyelia: a review.** *J R Soc Med* 1980;73:798–806 CrossRef Medline
 27. Iskandar BJ, Quigley M, Haughton VM. **Foramen magnum cerebrospinal fluid flow characteristics in children with Chiari I malformation before and after craniocervical decompression.** *J Neurosurg* 2004;101(2 Suppl):169–78 Medline
 28. Levy LM, Di Chiro G. **MR phase imaging and cerebrospinal fluid flow in the head and spine.** *Neuroradiology* 1990;32:399–406 CrossRef Medline
 29. McGirt MJ, Atiba A, Attenello FJ, et al. **Correlation of hindbrain CSF flow and outcome after surgical decompression for Chiari I malformation.** *Childs Nerv Syst* 2008;24:833–40 CrossRef Medline
 30. McGirt MJ, Nimjee SM, Fuchs HE, et al. **Relationship of cine phase-contrast magnetic resonance imaging with outcome after decompression for Chiari I malformations.** *Neurosurgery* 2006;59:140–46; discussion 140–46 CrossRef Medline
 31. Sakas DE, Korfiatis SI, Wayte SC, et al. **Chiari malformation: CSF flow dynamics in the craniocervical junction and syrinx.** *Acta Neurochir (Wien)* 2005;147:1223–33 CrossRef Medline
 32. Bhadelia RA, Madan N, Zhao Y, et al. **Physiology-based MR imaging assessment of CSF flow at the foramen magnum with a Valsalva maneuver.** *AJNR Am J Neuroradiol* 2013;34:1857–62 CrossRef Medline
 33. Bhadelia RA, Patz S, Heilman C, et al. **Cough-associated changes in CSF flow in Chiari I malformation evaluated by real-time MRI.** *AJNR Am J Neuroradiol* 2016;37:825–30 CrossRef Medline
 34. Williams B. **Simultaneous cerebral and spinal fluid pressure recordings, I: technique, physiology, and normal results.** *Acta Neurochir (Wien)* 1981;58:167–85 CrossRef Medline
 35. Williams B. **Simultaneous cerebral and spinal fluid pressure recordings, 2: cerebrospinal dissociation with lesions at the foramen magnum.** *Acta Neurochir (Wien)* 1981;59:123–42 CrossRef Medline
 36. Alperin N, Loftus JR, Ollivier CJ, et al. **MRI measures of posterior cranial fossa morphology and CSF physiology in Chiari malformation type I.** *Neurosurgery* 2014;75:515–22; discussion 522 CrossRef Medline
 37. Hardy CJ, Pearlman JD, Moore JR, et al. **Rapid NMR cardiography with a half-echo M-mode method.** *J Comput Assist Tomogr* 1991;15: 868–74 CrossRef Medline
 38. Maier SE, Hardy CJ, Jolesz FA. **Brain and cerebrospinal fluid motion: real-time quantification with M-mode MR imaging.** *Radiology* 1994;193:477–83 Medline
 39. Bhadelia RA, Bogdan AR, Kaplan RF, et al. **Cerebrospinal fluid pulsation amplitude and its quantitative relationship to cerebral blood flow pulsations: a phase-contrast MR flow imaging study.** *Neuroradiology* 1997;39:258–64 CrossRef Medline
 40. Bradley WG Jr, Scalzo D, Queralt J, et al. **Normal-pressure hydrocephalus: evaluation with cerebrospinal fluid flow measurements at MR imaging.** *Radiology* 1996;198:523–29 CrossRef Medline
 41. Alperin NJ, Lee SH, Loth F, et al. **MR-intracranial pressure (ICP): a method to measure intracranial elastance and pressure noninvasively by means of MR imaging: baboon and human study.** *Radiology* 2000;217:877–85 CrossRef Medline

Extent of Microstructural Tissue Damage Correlates with Hemodynamic Failure in High-Grade Carotid Occlusive Disease: An MRI Study Using Quantitative T2 and DSC Perfusion

A. Seiler, R. Deichmann, U. Nöth, A. Lauer, W. Pfeilschifter, O.C. Singer, and M. Wagner



ABSTRACT

BACKGROUND AND PURPOSE: Chronic hemodynamic impairment in high-grade carotid occlusive disease is thought to cause microstructural abnormalities that might be subclinical or lead to subtle symptoms including cognitive impairment. Quantitative MR imaging allows assessing pathologic structural changes beyond macroscopically visible tissue damage. In this study, high-resolution quantitative T2 mapping combined with DSC-based PWI was used to investigate quantitative T2 changes as a potential marker of microstructural damage in relation to hemodynamic impairment in patients with unilateral high-grade carotid occlusive disease.

MATERIALS AND METHODS: Eighteen patients with unilateral high-grade ICA or MCA stenosis/occlusion were included in the study. T2 values and deconvolved perfusion parameters, including relative CBF, relative CBV, and the relative CBF/relative CBV ratio as a potential indicator of local cerebral perfusion pressure, were determined within areas with delayed TTP and compared with values from contralateral unaffected areas after segmentation of normal-appearing hypoperfused WM and cortical regions. Hemispheric asymmetry indices were calculated for all parameters.

RESULTS: Quantitative T2 was significantly prolonged ($P < .01$) in hypoperfused tissue and correlated significantly ($P < .01$) with TTP delay and relative CBF/relative CBV reduction in WM. Significant correlations ($P < .001$) between TTP delay and the relative CBF/relative CBV ratio were found both in WM and in cortical areas.

CONCLUSIONS: Quantitative T2 can be used as a marker of microstructural tissue damage even in normal-appearing GM and WM within a vascular territory affected by high-grade carotid occlusive disease. Furthermore, the extent of damage correlates with the degree of hemodynamic failure measured by DSC perfusion parameters.

ABBREVIATIONS: AI = asymmetry index; CPP = cerebral perfusion pressure; q = quantitative; rCBF = relative CBF; rCBV = relative CBV

In patients with ICA and MCA occlusive disease, chronic hemodynamic compromise is associated with an increased risk of ischemic stroke¹⁻⁴ because it may lead to hemodynamic infarction and it presumably also predisposes the patient to embolic phenomena.⁵ Apart from focal neurologic symptoms due to acute

ischemia, chronic hemodynamic impairment in unilateral high-grade ICA stenosis or occlusion may be associated with measurable global cognitive impairment,^{6,7} even in patients without visible ischemic lesions on conventional MR images (“silent”).⁷ Pathophysiologically, these clinical findings seem to be related to microstructural changes, including diffuse demyelination, the loss of axons, and gliosis.^{6,8-12}

On conventional MR imaging, ipsilateral atrophy and signal increase on T2WI due to increased water content and gliotic changes have been described in severe chronic hypoperfusion.¹³ However, in many patients, no abnormalities are visible on conventional T2WI, though microstructural damage associated with stenosis-related chronic hypoperfusion might be reasonably assumed. Compared with conventional MR imaging, quantitative (q)MR imaging techniques are more sensitive to microstructural and metabolic tissue changes.^{14,15} In patients with diffuse chronic hypoxia (ischemic leukoaraiosis), quantitative MR imaging including qT2 revealed significant T2 prolongation in the normal-appearing WM, suggesting mi-

Received November 28, 2017; accepted after revision March 15, 2018.

From the Department of Neurology (A.S., W.P., O.C.S.), Brain Imaging Center (R.D., U.N.), and Institute of Neuroradiology (A.L., M.W.), Goethe University Frankfurt, Frankfurt, Germany.

Ralf Deichmann and Ulrike Nöth were supported by the Brain Imaging Center Bundesministerium für Bildung und Forschung (Germany) DLR 01GO0203, Deutsche Forschungsgemeinschaft (Germany) ZA 233/1-1.

Please address correspondence to Alexander Seiler, MD, Department of Neurology, Goethe University Frankfurt, Schleusenweg 2-16, 60528 Frankfurt, Germany; e-mail: Alexander.Seiler@kgu.de

Indicates open access to non-subscribers at www.ajnr.org

Indicates article with supplemental on-line table.

Indicates article with supplemental on-line photo.

<http://dx.doi.org/10.3174/ajnr.A5666>

crostructural damage.¹⁴ Therefore, qT2 might detect subtle changes, including microstructural damage in the territory of a chronically stenotic cerebral artery that is not visible on conventional MR imaging, and might be a promising imaging biomarker for microstructural changes related to chronic hypoperfusion.

Because these microstructural changes possibly depend on the degree of hemodynamic failure and cerebral perfusion pressure (CPP) impairment,⁸ it might be interesting to investigate the correlation between potential qT2 changes in the dependent territory and hemodynamic measures, including the CPP. By means of PET, the CBF/CBV ratio has been validated as an indicator of local CPP,¹⁶ and a negative correlation with DSC-based TTP delay has been demonstrated in patients with unilateral ICA or MCA stenosis/occlusion.¹⁷ Consequently, if this relationship can be reproduced, DSC-based relative (r)CBF/rCBV might be a suitable index for local CPP as well.

In this study, an advanced high-resolution qMRI technique combined with DSC perfusion imaging was used to explore qT2 changes in hypoperfused tissue in patients with high-grade ICA and MCA occlusive disease. The purpose was to evaluate the following: 1) whether qT2 mapping displays a significant increase of T2 values in chronically hypoperfused noninfarcted and normal-appearing tissue as a sign of microstructural damage, and 2) whether these changes of qT2 are related to measures of hemodynamic impairment, including autoregulatory capacity and CPP.

MATERIALS AND METHODS

Patients

Eighteen consecutive patients, some having been described previously,¹⁸ with unilateral symptomatic or asymptomatic high-grade stenosis or occlusion of the ICA or MCA were included. Inclusion criteria were the following: 1) Doppler sonography evidence of unilateral, >70% (NASCET criteria) high-grade extracranial ICA stenosis or ICA occlusion; or 2) Doppler sonography or MR angiographic evidence of a high-grade (>50%) unilateral intracranial ICA or proximal MCA stenosis/occlusion. Patients with relevant bilateral stenoses (contralateral stenosis of >50%) were not considered for inclusion in the study. The study was approved by the local institutional review board, and written informed consent was obtained from all patients before study enrollment.

MR Imaging Protocol

MR imaging measurements were performed on a 3T whole-body scanner (Magnetom Trio; Siemens, Erlangen, Germany) using the body coil of the scanner for radiofrequency transmission and an 8-channel phased array head coil for signal reception. The MR imaging examination included quantitative T2 mapping as well as DWI and PWI, MRA, and conventional T1WI and T2WI.

Anatomic imaging was based on a T1-weighted MPRAGE sequence with the following imaging parameters: TR/TE/TI = 2250/2.6/900 ms, FOV = 256 × 224 × 144 mm³, whole-brain coverage, isotropic spatial resolution = 1 mm, 22% oversampling in the slice-encoding (left-right) direction to avoid aliasing, bandwidth = 200 Hz/pixel, excitation angle = 9°, duration = 7 minutes 23 seconds. This dataset was used for tissue segmentation.

Quantitative T2 mapping was based on a fast spin-echo sequence with an echo-train length of 11 echoes per excitation, an

echo spacing of 17.1 ms, and the following imaging parameters: 50 axial slices with 2-mm slice thickness, no interslice gap, TR = 10 seconds, bandwidth = 100 Hz/pixel, 180° refocusing pulses, matrix size = 192 × 132 (readout × phase encoding), FOV = 240 × 165 mm², and in-plane resolution = 1.25 × 1.25 mm². For quantitative T2-mapping, 5 datasets were acquired with different TE values (17, 86, 103, 120, 188 ms), keeping all other acquisition parameters constant. The total duration was 11 minutes 50 seconds.

PWI was based on a gradient-echo EPI sequence with the following imaging parameters: TE = 35 ms, TR = 1500 ms, flip angle = 90°, FOV = 192 × 192 mm, matrix = 64 × 64, slice thickness = 4 mm, number of slices = 16, voxel size = 2.0 × 2.0 × 4.0 mm³, and acquisition time = 1 minute 15 seconds. The contrast agent (0.1 mmol/kg of Gd-DTPA, Magnevist; Bayer HealthCare Pharmaceuticals, Wayne, New Jersey) was injected into an antecubital vein using a power injector at a rate of 5 mL/s followed by a flush with 10 mL of saline.

Image Postprocessing and Analysis

Perfusion-weighted MR raw images were processed on a pixel-by-pixel basis to generate maps of the nondeconvolved TTP, rCBF, and rCBV. To determine the shape of the arterial input function, 2 experienced neuroradiologic readers manually selected 5–10 pixels in consensus over the proximal MCA in the unaffected hemisphere. For calculation of rCBF and rCBV maps, we used the model-independent (nonparametric) singular-value decomposition method described by Ostergaard et al.¹⁹

Further image postprocessing and analysis were performed with FMRIB Software Library tools (FSL, Version 5.0; <https://fsl.fmrib.ox.ac.uk/fsl>). All images were skull-stripped before coregistration. Quantitative T2 maps were linearly coregistered to the T1-weighted images. Because PWI parameter maps do not provide sufficient anatomic contrast for coregistration, we used the following: The first volume of the PWI time-series, which showed adequate anatomic contrast for coregistration, was extracted and coregistered to the T1-weighted image, saving the coregistration matrix. This matrix was applied to coregister TTP, rCBF, and rCBV parameter maps to the T1-weighted image. For coregistration of DWI maps, the first diffusion-weighted image ($b=0$, purely T2-weighted) was coregistered to the T1-weighted image. The coregistration matrix of this step was used for later coregistration of the diffusion-weighted image with $b=1000$ s/mm² to the T1-weighted image.

T1-weighted images were segmented with the FMRIB Automated Segmentation Tool (FAST; <https://fsl.fmrib.ox.ac.uk/fsl/fslwiki/FAST>),²⁰ yielding partial volume estimate maps for white matter, gray matter, and CSF. A lower partial volume estimate threshold of 0.95 was applied to both the WM and the GM maps.²¹ For segmentation of the cerebral cortex, voxels of non-cortical structures, including subcortical lesions or (enlarged) perivascular spaces misclassified as GM, were removed from the GM maps. Both the WM and cortex maps were binarized to receive tissue masks for the qT2 and PWI parameter maps (Fig 1, upper row, and Fig 2A).

Maps of rCBF and rCBV were processed voxelwise to calculate maps of the rCBF/rCBV ratio as possible indicators of local

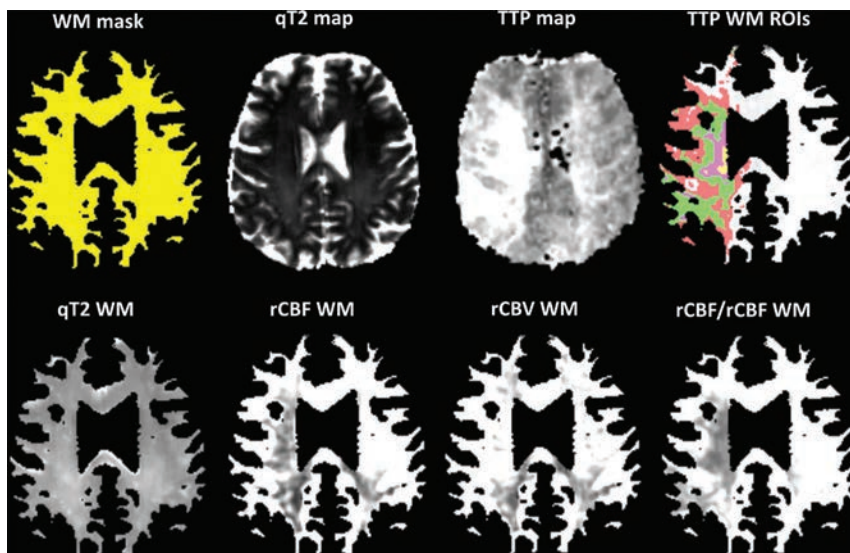


FIG 1. Illustration of image postprocessing and analysis in a patient with right-sided intracranial ICA stenosis. *Upper row:* WM mask obtained from segmentation of the T1-weighted image, skull-stripped qT2, and TTP maps. ROIs according to different TTP delay ranges for WM analysis are shown on the segmented image in the upper right corner: 0- to 2-second delay (red), 2- to 4-second delay (green), 4- to 6-second delay (purple), and 6- to 8-second delay (yellow). *Lower row:* Segmented qT2 and perfusion parameter maps for WM analysis. Note the reduction of rCBF and the rCBF/rCBV ratio in perfusion-delayed white matter.

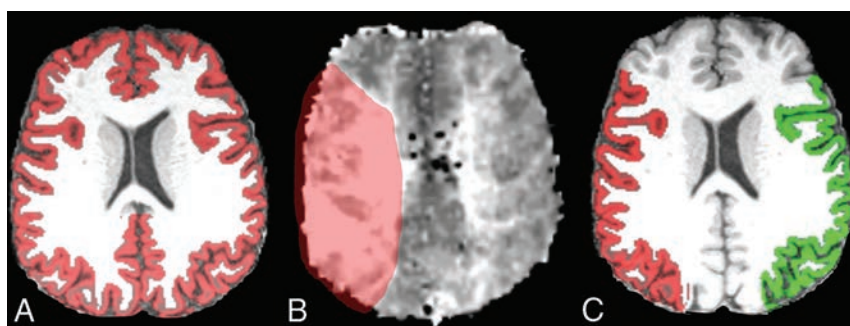


FIG 2. A, Skull-stripped T1-weighted image with an overlaid cortex mask. B, Enlarged TTP lesion mask (red) for definition of perfusion-delayed cortical areas. C, Perfusion-delayed cortical areas (red) and corresponding contralateral normoperfused cortex (green) overlaid on a T1-weighted image. Same patient as in Fig 1.

CPP.^{16,22} The binary WM and cortex masks were applied to the qT2 and PWI parameter maps to generate WM and cortex maps for each parameter (Fig 1, lower row). After the masking procedure, macroscopically visible lesions (including DWI lesions) were automatically removed from the respective parameter maps (On-line Figure). The second T2-weighted raw image (TE = 86 ms) from each patient was thoroughly inspected and manually corrected if necessary to exclude residual visible lesions or to avoid removing parenchyma beyond the edges of the lesions.

3D ROIs were defined on the basis of areas with TTP delay in the affected hemisphere. For WM, an elliptic periventricular ROI was placed in the unaffected hemisphere. The mean TTP plus 2 SDs was defined as the upper limit of normoperfusion and was used as a lower threshold for TTP maps. On the basis of this threshold, different degrees of TTP delay were determined by gradually increasing the threshold in intervals of 2 seconds (eg, 0–2 and 2–4 seconds, up to the maximum TTP delay) (Fig 1, upper row). For the cortical ribbon, the delineation of areas with

different degrees of TTP delay was not deemed feasible. Therefore, only cortical areas were included that depended, with an extremely high likelihood (considering all available imaging data including CTA/MRA and DSA to assess a potentially adjusted watershed area, the presence of communicating arteries, and so forth), on the stenosed/occluded artery and should have been affected by resulting perfusion abnormalities (Fig 2). Parameter values from WM areas with different ranges of TTP delay and from cortical areas were compared with values from corresponding contralateral unaffected areas by mirroring the ROIs to the contralateral side. To determine relative changes within hypoperfused tissue, we calculated a hemispheric asymmetry index (AI) for each parameter using the following equation^{23,24}:

$$AI = (R_i - R_c) / (R_i + R_c) \times 2 \times 100 (\%),$$

where R_i and R_c represent the ROI values in the ipsilateral and contralateral hemispheres, respectively. For a comparative morphometric measure, the volumes of affected WM and hypoperfused cortex (including visible lesions) were determined on the segmented T1-weighted images and compared with tissue volumes on the contralateral side. Before volumetric analysis, the tissue maps were linearly coregistered to standard space (Montreal Neurological Institute 152, 1 mm; <http://www.bic.mni.mcgill.ca/ServicesAtlases/>) using 6 *df* to minimize interpolation errors.

Statistical Analysis

Statistical analysis was performed using SPSS 22 (IBM, Armonk, New York). Because several parameters were not normally distributed (Kolmogorov-Smirnov test), we only used nonparametric statistical testing. Parameter values between corresponding ROIs (ipsilateral/contralateral hemispheres) were compared with the 2-sided Wilcoxon signed rank test. For evaluation of a parameter correlation, the 2-sided Spearman signed rank test was used. A $P < .05$ was considered statistically significant. Correction for multiple statistical testing was done by performing false discovery rate correction for all parameters. Data are given as mean \pm SD unless indicated otherwise.

RESULTS

The mean age of the patients (15 men, 3 women) was 57.7 ± 14.8 years (range, 28–83 years). Sites of stenosis and occlusion were the extracranial ICA ($n = 8$), the proximal MCA (M1 segment) ($n = 7$), and the intracranial ICA ($n = 3$). The right hemisphere was affected in 9 patients, while the other 9 patients had a left-sided pathology.

Demographic and clinical baseline characteristics of all patients

Patient No.	Age/Sex	Site of Stenosis/Occlusion	Affected Hemisphere
1	42/M	Extracranial ICA	Right
2	28/M	MCA MI	Left
3	49/M	Extracranial ICA	Left
4	36/M	MCA MI	Right
5	53/M	Intracranial ICA	Right
6	60/M	Extracranial ICA	Left
7	82/M	Extracranial ICA	Right
8	53/M	Extracranial ICA	Right
9	83/F	MCA MI	Left
10	62/M	Extracranial ICA	Right
11	53/F	MCA MI	Right
12	67/M	Intracranial ICA	Left
13	64/M	Extracranial ICA	Right
14	49/M	MCA MI	Left
15	50/M	MCA MI	Left
16	75/F	Extracranial ICA	Right
17	70/M	MCA MI	Left
18	62/M	Intracranial ICA	Left

Seven patients were recently symptomatic (stroke or TIA within the last 30 days before MR imaging), 6 had been formerly symptomatic (several years before MR imaging examination), and 5 patients had a completely asymptomatic vascular pathology. Demographic and clinical baseline characteristics for all patients are summarized in the Table. Four patients showed small (<10 cm³) ischemic lesions on DWI, which were removed from the parameter maps before further analysis as described above.

qT2 and Perfusion Parameters within Perfusion-Restricted Normal-Appearing WM

In normal-appearing WM with any TTP delay (>0 seconds, entire TTP lesion) ipsilateral to the vessel pathology, T2 values were significantly increased compared with corresponding contralateral normoperfused areas (110.08 ± 19.27 ms versus 106.39 ± 15.71 ms, AI = 3.07% ± 4.1%, *P* = .008). Perfusion parameters also showed significant changes within the entire TTP-delayed area with significant decreases of rCBF (AI = -15.57% ± 12.38%, *P* = .001) and an increase of rCBV (AI = 5.8% ± 9.68%, *P* = .041), resulting in a significant decrease of the rCBF/rCBV ratio (AI = -22.11% ± 11.94%, *P* < .001) compared with contralateral unaffected areas. These changes were coherent for the respective parameters at different degrees of perfusion delay, except for a low TTP delay of 0–2 seconds and a severe TTP delay of 6–8 seconds (On-line Table). Asymmetry indices increased for qT2 and decreased for the rCBF/rCBV ratio with the increasing TTP delay (On-line Table). AI for qT2 showed a strong positive correlation with the TTP delay (*r* = 0.595, *P* < .001) and a strong negative correlation with the AI for rCBF/rCBV (*r* = -0.352, *P* = .002), with the latter showing a negative correlation with the TTP delay (*r* = -0.570, *P* < .001) (Fig 3A–C).

qT2 and Perfusion Parameters within TTP-Delayed Cortical Areas

Similarly, in the TTP-delayed cortex, qT2 was significantly elevated in comparison with the corresponding contralateral cortical areas of the unaffected hemisphere (148.78 ± 37.46 ms versus 142.58 ± 31.18 ms, AI = 3.61% ± 5.02%, *P* = .007). Analogous to the WM ROIs, significant decreases of rCBF (AI = -7.35% ±

12.88%, *P* = .022) and significant increases of rCBV (AI = 11.24% ± 45.53%, *P* = .013) were detected, resulting in significant decreases of the rCBF/rCBV ratio (AI = -15.17% ± 13.41%, *P* < .001), compared with unaffected cortical areas (On-line Table). In contrast to WM, relative changes of T2 values in hypoperfused cortical areas did not correlate significantly with changes of perfusion parameters (AI qT2 versus TTP delay: *r* = 0.311, *P* = .21; AI qT2 versus AI rCBF/rCBV: *r* = -0.292, *P* = .256), while again a strong significant negative signed correlation was found between the rCBF/rCBV AI and TTP delay (*r* = -0.806, *P* < .001) (Fig 3D).

Volumetric Analysis

Volumes of affected WM and hypoperfused cortex did not differ significantly from volumes of the contralateral unaffected tissue (269.33 ± 25.5 cm³ versus 270.81 ± 27.29 cm³, *P* = .372 and 79.54 ± 20.5 cm³ versus 79.12 ± 20.16 cm³, *P* = .948). False discovery rate correction was performed for the respective parameters, and the corrected level of significance was *P* = .033.

DISCUSSION

This study revealed significantly increased qT2 values in perfusion-delayed normal-appearing WM and in cortical areas in patients with unilateral high-grade carotid occlusive disease compared with corresponding contralateral areas. In addition, these changes correlated with increasing hemodynamic failure as indicated by TTP delay, suggesting silent hypoperfusion-related microstructural tissue damage. Furthermore, the rCBF/rCBV ratio seems to be a promising parameter to assess CPP in chronic cerebral hypoperfusion.

In patients with high-grade carotid stenosis—even asymptomatic—qT2 showed a significant increase within normal-appearing GM and WM. This is in line with the literature findings, in which experimental studies revealed structural damage, including demyelination and axonal loss, in chronically hypoperfused brain parenchyma—in fact, the extent of structural damage correlated with the degree of perfusion impairment.⁸ In addition, glial activation has been demonstrated in experimentally induced chronic cerebral hypoperfusion.⁸ Gliosis in chronically hypoperfused tissue, which can be expected to cause prolongation of qT2 due to increased water content, may be caused by subtotal ischemic necrosis not leading to focal softening or cavitation (so-called “selective neuronal loss”).^{25,26} Hence, selective neuronal death may be one of the underlying causes of the significant prolongation of qT2 in normal-appearing hypoperfused tissue in this study. Furthermore, the qT2 increase in normal-appearing depending WM correlated significantly with the perfusion abnormalities depicted as perfusion delay on TTP maps, suggesting that the extent of tissue damage is related to the degree of perfusion delay. Most interesting, qT2 prolongation within hypoperfused tissue also showed a strong negative correlation with changes of the rCBF/rCBV ratio, which, for its part, correlated significantly with TTP delay (Fig 3A–C). By means of PET imaging, the CBF/CBV ratio has been validated as an index of local CPP,¹⁶ which itself is a function of mean arterial blood pressure. Because obtaining rCBF and rCBV via DSC MR imaging (a bolus-tracking technique) is subject to various sources of imprecision and is technically fun-

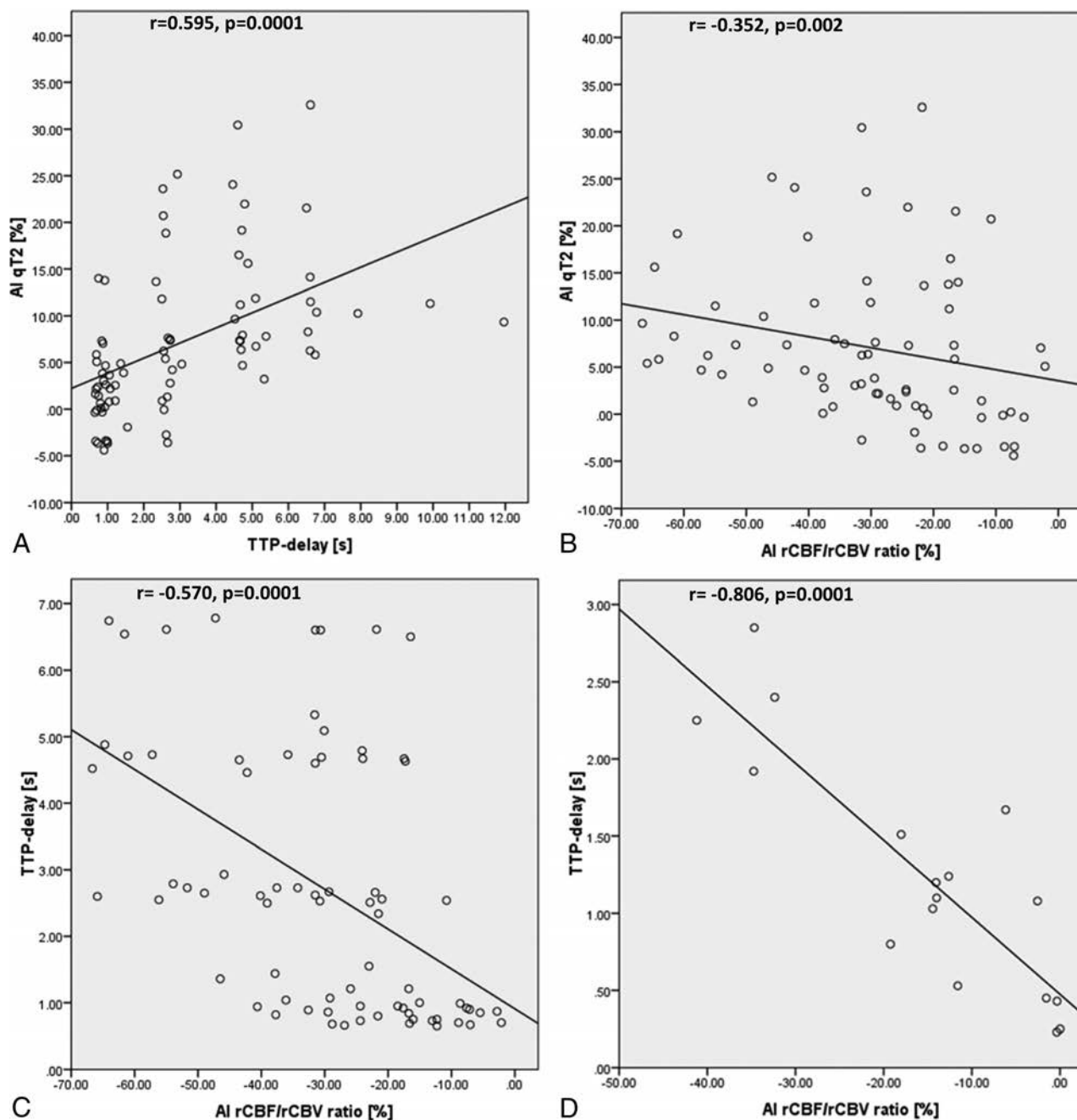


FIG 3. A–C, Scatterplots for seventy-four 3D WM ROIs, which were generated according to different degrees of TTP delay in all 18 patients. The number of data points per patient depends on the maximal extent of TTP delay in WM. A, The relationship between qT2 and TTP delay. B, The relationship between qT2 and the rCBF/rCBV ratio. C, The relationship between TTP delay and the rCBF/rCBV ratio. D, The relationship between TTP delay and the rCBF/rCBV ratio in hypoperfused cortex for all 18 patients (1 data point per patient). For qT2 values and perfusion parameters (except time-to-peak for which the mean TTP delay is given), the graphs display the mean hemispheric asymmetry indices. Lines were obtained from linear regression analysis.

damentally different from measuring perfusion with PET, MR imaging–derived rCBF/rCBV might not necessarily have the same significance. However, because TTP has been shown to correlate with PET-derived CBF/CBV,¹⁷ the finding of a significant relationship between the rCBF/rCBV ratio and TTP delay in this study supports the hypothesis that rCBF/rCBV obtained with DSC MR imaging could also reflect the local CPP. The significant correlation between qT2 and TTP as well as the rCBF/rCBV ratio suggests that pathologic alterations of hypoperfused WM are mainly related to the degree of local CPP compromise, which

determines the restriction of microvascular perfusion and oxygen supply and promotes microstructural tissue damage, even in normal-appearing tissue.

In cortical areas, the same changes of qT2 and perfusion parameters as in WM were detected, again indicating reduced perfusion pressure (On-line Table). Whereas a strong negative correlation between TTP delay and rCBF/rCBV was also found in the hypoperfused cortex, no significant correlation of qT2 increase with perfusion measures was detected. This difference between the cortex and WM might be explained by the anatomic struc-

ture of the respective supplying arterial vasculature. Because the perforating arteries supplying the deep WM are hardly collateralized, the extent of ischemic tissue damage depends on the severity of hemodynamic compromise.^{27,28} In contrast, a variable degree of leptomeningeal collateralization compensating for decreased perfusion can be expected in chronically hypoperfused cortex.²⁹ This might explain why the magnitudes of both TTP delay and rCBF/rCBV reduction within affected cortical areas are lower than in WM (On-line Table and Fig 3). On the other hand, the occurrence of embolism or microembolism, which is not necessarily directly related to perfusion abnormalities, might be more predominant as a mechanism of tissue damage in the cortex.³⁰

That volumetric quantification of normal-appearing WM and cortex did not reveal significant volume reduction of hypoperfused tissue excludes relevant partial volume effects from CSF, with a resulting increase of tissue water as the reason for the increase of T2 values observed in this study. The different underlying causes of microstructural changes in hypoperfused tissue, which may include a variety of pathologies, cannot be differentiated with qT2 mapping. Because microstructural changes in carotid occlusive disease have been shown to regress partly after stent placement⁶ or carotid endarterectomy,^{11,31} the underlying mechanisms might also comprise (partially) reversible conditions, though the pathophysiologic correlate for this finding remains currently unclear.

In summary, the results of this study suggest the presence of microstructural alterations that are not assessable using conventional MR imaging within chronically hypoperfused tissue in patients with carotid occlusive disease and exhausted autoregulation. In addition, our results might support the hypothesis that the DSC-derived rCBF/rCBV ratio could be used as an index of local CPP, comparable with TTP delay, as an appropriate indicator of hemodynamic failure in chronic cerebrovascular disease.

Limitations

This study has several limitations. First, perfusion values determined with DSC techniques only provide representative relative values, which must be compared with values from reference regions. Second, because this is not a longitudinal study, the temporal evolution of qT2 values and perfusion parameters and their possible response to reperfusion procedures was not evaluated. Third, although prolongation of qT2 has been described in chronic cerebral hypoperfusion and would be consistent with microstructural damage manifesting itself as gliosis and neuronal loss, a formal histologic validation of qT2 as a marker of microstructural tissue damage due to hypoperfusion is lacking. This should be pursued and further investigated in future studies. Additionally, the relationship between pathologic qT2 increases and clinical correlates such as cognitive performance must be investigated for the relevance in clinical practice. Finally, an investigation of qT2 changes in larger patient collectives with well-defined risk profiles and different statuses of reperfusion as well as a PET-based validation of MR imaging-based rCBF/rCBV as an index of CPP would be of interest.

CONCLUSIONS

Quantitative T2 mapping seems to detect microstructural damage in chronically hypoperfused but normal-appearing cortex and WM, which correlates with the degree of perfusion pressure impairment due to carotid occlusive disease. The rCBF/rCBV ratio and the nondeconvolved TTP determined with DSC MR imaging seem to be suitable for detecting reduced CPP and hemodynamic failure in these patients. After further research to elucidate the clinical correlates of these parameters and their response to reperfusion, these techniques could help to identify patients at risk of progressive cognitive decline who would potentially benefit from revascularization.

Disclosures: Alexander Seiler—UNRELATED: Grants/Grants Pending: Goethe University Frankfurt, Faculty of Medicine.* Ralf Deichmann—RELATED: Grant: support to the Brain Imaging Center Frankfurt, Comments: Bundesministerium für Bildung und Forschung (Germany) DLR 01GO0203, Deutsche Forschungsgemeinschaft (Germany) ZA 233/1–1*; UNRELATED: Consultancy: Wellcome Trust Centre for Neuroimaging at UCL, London, UK, Comments: consultant for MR imaging scanner procurement; Employment: University of Frankfurt; Grants/Grants Pending: Land of Hesse, Germany: LOEWE research grant "Neuronale Koordination Forschungsschwerpunkt Frankfurt," 2011–2013 Deutsche Forschungsgemeinschaft: "Imaging of damage and repair in MS patients—Impact of new lesions on network activity, Teilprojekt B5" 2012–2016, Comments: public funding*; Royalties: published book chapters: 1) R. Deichmann, "Principles of MRI and Functional MRI." In: *fMRI Techniques and Protocols*. M. Filippi, ed. Humana Press, Springer, Heidelberg, 2009; 2) R. Deichmann, U. Noeth, N. Weiskopf, "The Basics of Functional Magnetic Resonance Imaging." In: *EEG-fMRI*. C. Mulert, L. Lemieux, eds. Springer, Heidelberg, 2010 (so far, no royalties paid); Travel/Accommodations/Meeting Expenses Unrelated to Activities Listed, Comments: occasionally travel expenses for invited lectures given at nonprofit organizations. Ulrike Nöth—RELATED: Grant: support to Brain Imaging Center Frankfurt, Comments: Bundesministerium für Bildung und Forschung (Germany) DLR 01GO0203, Deutsche Forschungsgemeinschaft (Germany) ZA 233/1–1.* Waltraud Pfeilschifter—UNRELATED: Consultancy: Sanofi-Aventis; Grants/Grants Pending: Stryker Neurovascular, Boehringer Ingelheim, Medtronic*; Payment for Lectures Including Service on Speakers Bureaus: Stryker Neurovascular, Boehringer Ingelheim. *Money paid to the institution.

REFERENCES

1. Yamauchi H, Fukuyama H, Nagahama Y, et al. **Evidence of misery perfusion and risk for recurrent stroke in major cerebral arterial occlusive diseases from PET.** *J Neurol Neurosurg Psychiatry* 1996;61:18–25 CrossRef Medline
2. Yamauchi H, Fukuyama H, Nagahama Y, et al. **Significance of increased oxygen extraction fraction in five-year prognosis of major cerebral arterial occlusive diseases.** *J Nucl Med* 1999;40:1992–98 Medline
3. Derdeyn CP, Grubb RL Jr, Powers WJ. **Cerebral hemodynamic impairment: methods of measurement and association with stroke risk.** *Neurology* 1999;53:251–59 CrossRef Medline
4. Derdeyn CP, Videen TO, Yundt KD, et al. **Variability of cerebral blood volume and oxygen extraction: stages of cerebral haemodynamic impairment revisited.** *Brain* 2002;125:595–607 CrossRef Medline
5. Caplan LR, Hennerici M. **Impaired clearance of emboli (washout) is an important link between hypoperfusion, embolism, and ischemic stroke.** *Arch Neurol* 1998;55:1475–82 CrossRef Medline
6. Cheng HL, Lin CJ, Soong BW, et al. **Impairments in cognitive function and brain connectivity in severe asymptomatic carotid stenosis.** *Stroke* 2012;43:2567–73 CrossRef Medline
7. Bakker FC, Klijn CJ, Jennekens-Schinkel A, et al. **Cognitive impairment in patients with carotid artery occlusion and ipsilateral transient ischemic attacks.** *J Neurol* 2003;250:1340–47 CrossRef Medline
8. Shibata M, Ohtani R, Ihara M, et al. **White matter lesions and glial activation in a novel mouse model of chronic cerebral hypoperfusion.** *Stroke* 2004;35:2598–603 CrossRef Medline
9. Tatemichi TK, Desmond DW, Prohovnik I, et al. **Dementia associated with bilateral carotid occlusions: neuropsychological and**

- haemodynamic course after extracranial to intracranial bypass surgery. *J Neurol Neurosurg Psychiatry* 1995;58:633–36 CrossRef Medline
10. Shiraishi A, Hasegawa Y, Okada S, et al. **Highly diffusion-sensitized tensor imaging of unilateral cerebral arterial occlusive disease.** *AJNR Am J Neuroradiol* 2005;26:1498–504 Medline
 11. Sato Y, Ito K, Ogasawara K, et al. **Postoperative increase in cerebral white matter fractional anisotropy on diffusion tensor magnetic resonance imaging is associated with cognitive improvement after uncomplicated carotid endarterectomy: tract-based spatial statistics analysis.** *Neurosurgery* 2013;73:592–98; discussion 598–99 CrossRef Medline
 12. Meng X, Jun C, Wang Q, et al. **High b-value diffusion tensor imaging of the remote white matter and white matter of obstructive unilateral cerebral arterial regions.** *Clin Radiol* 2013;68:815–22 CrossRef Medline
 13. Sahin N, Solak A, Genc B, et al. **Dilatation of the Virchow-Robin spaces as an indicator of unilateral carotid artery stenosis: correlation with white matter lesions.** *Acta Radiol* 2015;56:852–59 CrossRef Medline
 14. Wagner M, Helfrich M, Volz S, et al. **Quantitative T2, T2*, and T2' MR imaging in patients with ischemic leukoaraiosis might detect microstructural changes and cortical hypoxia.** *Neuroradiology* 2015; 57:1023–30 CrossRef Medline
 15. Inglese M, Ge Y. **Quantitative MRI: hidden age-related changes in brain tissue.** *Top Magn Reson Imaging* 2004;15:355–63 CrossRef Medline
 16. Schumann P, Touzani O, Young AR, et al. **Evaluation of the ratio of cerebral blood flow to cerebral blood volume as an index of local cerebral perfusion pressure.** *Brain* 1998;121(Pt 7):1369–79 CrossRef Medline
 17. Kajimoto K, Moriwaki H, Yamada N, et al. **Cerebral hemodynamic evaluation using perfusion-weighted magnetic resonance imaging: comparison with positron emission tomography values in chronic occlusive carotid disease.** *Stroke* 2003;34:1662–66 CrossRef Medline
 18. Seiler A, Jurcoane A, Magerkurth J, et al. **T2' imaging within perfusion-restricted tissue in high-grade occlusive carotid disease.** *Stroke* 2012;43:1831–36 CrossRef Medline
 19. Ostergaard L, Weisskoff RM, Chesler DA, et al. **High resolution measurement of cerebral blood flow using intravascular tracer bolus passages, Part I: mathematical approach and statistical analysis.** *Magn Reson Med* 1996;36:715–25 CrossRef Medline
 20. Zhang Y, Brady M, Smith S. **Segmentation of brain MR images through a hidden Markov random field model and the expectation-maximization algorithm.** *IEEE Trans Med Imaging* 2001;20:45–57 CrossRef Medline
 21. Volz S, U, Jurcoane A, et al. **Quantitative proton density mapping: correcting the receiver sensitivity bias via pseudo proton densities.** *Neuroimage* 2012;63:540–52 CrossRef Medline
 22. Sette G, Baron JC, Mazoyer B, et al. **Local brain haemodynamics and oxygen metabolism in cerebrovascular disease: positron emission tomography.** *Brain* 1989;112(Pt 4):931–51 CrossRef Medline
 23. Powers WJ, Press GA, Grubb RL Jr, et al. **The effect of hemodynamically significant carotid artery disease on the hemodynamic status of the cerebral circulation.** *Ann Intern Med* 1987;106:27–34 CrossRef Medline
 24. Kado H, Kimura H, Tsuchida T, et al. **Abnormal magnetization transfer ratios in normal-appearing white matter on conventional MR images of patients with occlusive cerebrovascular disease.** *AJNR Am J Neuroradiol* 2001;22:922–27 Medline
 25. Lassen NA. **Incomplete cerebral infarction—focal incomplete ischemic tissue necrosis not leading to emolliation.** *Stroke* 1982;13: 522–23 CrossRef Medline
 26. Baron JC, Yamauchi H, Fujioka M, et al. **Selective neuronal loss in ischemic stroke and cerebrovascular disease.** *J Cereb Blood Flow Metab* 2014;34:2–18 CrossRef Medline
 27. Bisschops RH, Klijn CJ, Kappelle LJ, et al. **Association between impaired carbon dioxide reactivity and ischemic lesions in arterial border zone territories in patients with unilateral internal carotid artery occlusion.** *Arch Neurol* 2003;60:229–33 CrossRef Medline
 28. Derdeyn CP, Khosla A, Videen TO, et al. **Severe hemodynamic impairment and border zone—region infarction.** *Radiology* 2001;220: 195–201 CrossRef Medline
 29. Derdeyn CP, Shaibani A, Moran CJ, et al. **Lack of correlation between pattern of collateralization and misery perfusion in patients with carotid occlusion.** *Stroke* 1999;30:1025–32 CrossRef Medline
 30. Moriwaki H, Matsumoto M, Hashikawa K, et al. **Hemodynamic aspect of cerebral watershed infarction: assessment of perfusion reserve using iodine-123-iodoamphetamine SPECT.** *J Nucl Med* 1997; 38:1556–62 Medline
 31. Soinne L, Helenius J, Saimanen E, et al. **Brain diffusion changes in carotid occlusive disease treated with endarterectomy.** *Neurology* 2003;61:1061–65 CrossRef Medline

Prediction of Borderzone Infarction by CTA in Patients Undergoing Carotid Embolization for Carotid Blowout

B.-C. Lee, Y.-H. Lin, C.-W. Lee, H.-M. Liu, and A. Huang



ABSTRACT

BACKGROUND AND PURPOSE: Permanent common carotid artery and/or ICA occlusion is an effective treatment for carotid blowout syndrome. Besides postoperative thromboembolic infarction, permanent common carotid artery and/or ICA occlusion may cause borderzone infarction when the collateral flow to the deprived brain territory is inadequate. In this study, we aimed to test the predictive value of CTA for post-permanent common carotid artery and/or ICA occlusion borderzone infarction in patients with carotid blowout syndrome.

MATERIALS AND METHODS: In this retrospective study, we included 31 patients undergoing unilateral permanent common carotid artery and/or ICA occlusion for carotid blowout syndrome between May 2009 and December 2016. The vascular diameter of the circle of Willis was evaluated using preprocedural CTA, and the risk of borderzone infarction was graded as very high risk, high risk, intermediate risk, low risk, and very low risk.

RESULTS: The performance of readers' consensus on CTA for predicting borderzone infarction was excellent, with an area under receiver operating characteristic curve of 0.938 (95% confidence interval, 0.85–1.00). We defined very high risk, high risk, and intermediate risk as positive for borderzone infarction, the sensitivity, specificity, positive predictive value, and negative predictive value of CTA for borderzone infarction were 100% (7/7), 62.5% (15/24), 43.8% (7/16), and 100% (15/15), respectively. The interobserver reliability was excellent ($\kappa = 0.807$). No significant difference in the receiver operating characteristic curves was found between the 2 readers ($P = .114$).

CONCLUSIONS: CTA can be used to predict borderzone infarction after permanent common carotid artery and/or ICA occlusion by measuring the collateral vessels of the circle of Willis.

ABBREVIATIONS: AcomA = anterior communicating artery; A_z = area under the ROC curve; BTO = balloon test occlusion; CBS = carotid blowout syndrome; CCA = common carotid artery; PCO = permanent common carotid artery and/or ICA occlusion; PcomA = posterior communicating artery; ROC = receiver operating characteristic

Rupture of the carotid artery and its branches, referred to as carotid blowout syndrome (CBS), is an infrequent but dreaded complication of head and neck cancer, which occurs in up to 4.3% of patients.^{1–4} Patients with head and neck cancer who have radiation-induced necrosis, tumor recurrence, pharyngocu-

taneous fistulas, or wound complications are more prone to develop CBS.^{5,6} The emergency surgical management of CBS, which involves ligating the common carotid artery (CCA) or ICA, is a technically challenging procedure that is associated with high risk of cerebral ischemia.^{4,7,8} For a patient with CBS and a diseased CCA and/or ICA, permanent CCA and/or ICA occlusion (PCO) with coils is an effective treatment that produces better clinical outcomes compared with stent-graft placement⁹ and has been the standard treatment in our institution. Still, thromboembolic infarction and borderzone infarction occurred in approximately 20% of patients.⁹ Balloon test occlusion (BTO) is the optimal testing method that can simulate the collateral reserve of the circle of Willis, which is associated with hypoperfusion-related borderzone infarction after PCO.^{10–12} However, the suitability of BTO during emergent PCO for CBS is contentious, and the complication rate of BTO has been reported to be as high as 3.2%, which might be even higher for patients with CBS in whom heparin infusion is contraindicated.^{12,13}

Received December 18, 2017; accepted after revision March 24, 2018.

From the Department of Medical Imaging (B.-C.L., Y.-H.L., C.-W.L.), National Taiwan University Hospital and National Taiwan University College of Medicine, Taipei, Taiwan; Department of Radiology (H.-M.L.), Fu-Jen Catholic University Hospital, New Taipei, Taiwan; and Research Center for Adaptive Data Analysis (A.H.), National Central University, Jhongli, Taiwan.

This work was supported by the Ministry of Science and Technology (MOST 106-2218-E002-018) and the Ministry of Health and Welfare (MOHW107-TDU-B-212-123004) of Taiwan.

Please address correspondence to Chung-Wei Lee, MD, PhD, Department of Medical Imaging, National Taiwan University Hospital, No. 7, Chung-Shan South Rd, Taipei 100, Taiwan, R.O.C.; e-mail: rad.chungweilee@gmail.com

Indicates open access to non-subscribers at www.ajnr.org

Indicates article with supplemental on-line tables.

<http://dx.doi.org/10.3174/ajnr.A5672>

Because of the superior ability of CTA to detect an exposed artery compared with angiography, CTA has become a valuable tool for procedure planning in patients with CBS.¹⁴ The diameter of the collateral vessels in the circle of Willis can be measured on CTA using thin-sliced images with MIP and using MPR techniques.¹⁵ Therefore, we hypothesized that CTA can stratify the cerebral collateral reserve of the circle of Willis, permitting prediction of borderzone infarction. In this study, we aimed to estimate the predictive value of CTA for post-PCO borderzone infarction in patients with CBS.

MATERIALS AND METHODS

This retrospective study was approved by the institutional review board of National Taiwan University Hospital, and the requirement for informed consent was waived. The medical records of patients with CBS treated with PCO between May 2009 and March 2016 were retrieved and reviewed. The inclusion criteria were patients with a history of head and neck cancer, treated with an operation and/or chemotherapy and/or radiation therapy, having undergone unilateral PCO following CBS. There were 42 patients identified; 11 of them were excluded because of contralateral ICA occlusion ($n = 1$), ipsilateral extracranial intracranial bypass ($n = 1$), spontaneous ipsilateral ICA thrombosis after local compression ($n = 1$), prolonged (>5 minutes) cardiovascular resuscitation before the procedure ($n = 1$), no preprocedural CTA of the circle of Willis due to a clinical emergency ($n = 3$), and no available thin-slice (≤ 1 mm) CTA images for detailed evaluation of the circle of Willis ($n = 4$). No patient was identified as having a contralateral ICA, bilateral vertebral arteries, or basilar artery stenosis ($>50\%$). Finally, 31 patients were enrolled in our study.

CTA Imaging Protocol

The routine CTA protocol for CBS was as previously reported.¹⁴ In brief, a 64-detector row CT scanner (LightSpeed VCT; GE Healthcare, Milwaukee, Wisconsin) was used for CTA imaging, with 3 scanning phases (precontrast, arterial, and venous). The CTA protocol was as follows: 64×0.625 collimation, 0.516 pitch, 0.4-second rotation time, and 100 kV (peak). We used 200 mA for the precontrast phase and 400 mA for the arterial and venous phases. Dual injectors were used. The scanning range was between the aortic arch and the level of the lateral ventricles, and the timing of CTA was determined by the test-bolus technique. At a rate of 4 mL/s, the contrast material (60 mL) and a saline chaser (35 mL) were injected after a delay to generate the arterial phase, and the venous phase was obtained after another 30 seconds. The source images were reconstructed into 0.625- or 1-mm slice thicknesses in axial, coronal, and sagittal views.

Visibility of the Circle of Willis

The CTA images were evaluated for the following segments of the circle of Willis: the A1 and A2 segments of the anterior cerebral artery, the anterior communicating artery (AcomA), the P1 and P2 segments of the posterior cerebral artery, and the posterior communicating artery (PcomA). One radiologist (B.-C.L.) who did not participate in the evaluation of the circle of Willis graded the quality of CTA in 3 categories: excellent, indicating high-quality

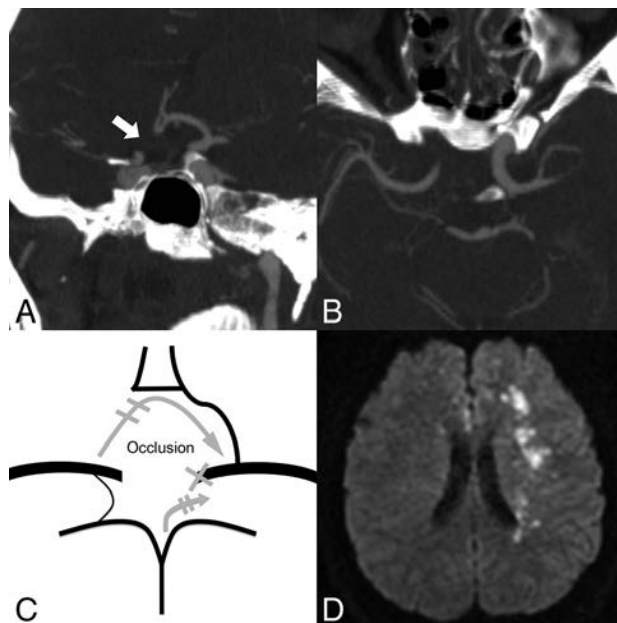


FIG 1. A 33-year-old man with nasopharyngeal carcinoma and left ICA blowout. *A*, No right A1 segment is detected on the coronal MIP (5 mm) image (white arrow). *B*, Only a hair-thin PcomA is detected on the axial MIP (5 mm) image. *C*, The narrowest portion of the anterior and posterior collateral vessels is aplastic, and the patient is grouped as very high risk. The recruited collateral flows after PCO are indicated by gray arrows. *D*, Diffusion-weighted imaging shows left borderzone infarction and bilateral anterior cerebral artery thromboembolic infarction on the same day after left ICA embolization.

ity delineation of the circle of Willis; fair, indicating slightly lower quality, but still useful for delineation of the circle of Willis; and poor, indicating suboptimal for evaluation of the circle of Willis.

Evaluation and Data Analysis

All CTA images (source images plus MIP images) were evaluated independently by 2 attending neuroradiologists (C.-W.L. and Y.-H.L. with 11 and 4 years of experience, respectively), blinded to patient identity and neurologic outcomes. MIP images were generated from subtracted arterial phase images. Different projections by MPR techniques were used for optimal demonstration of the target vascular portion. Stenosis on MIP images was estimated by visual inspection, and the readers could adjust the window width and level if needed.

After PCO, the circle of Willis redistributes blood flow via the AcomA and the ipsilateral PcomA to the occluded side of the brain. The blood flows from the contralateral ICA, goes along the contralateral A1 segment and the AcomA in an anterograde manner and then along the ipsilateral A1 segment in a retrograde manner, eventually supplying the ipsilateral MCA territory. Meanwhile, the recruitment of blood flow from the basilar artery goes through the ipsilateral P1 segment and PcomA to supply the ipsilateral MCA territory.

The narrowest portions of the vessels were presumed to dominate the collateral blood flow. Both readers classified the narrowest portion of the AcomA and bilateral A1 segments (forming the anterior collateral vessels), which dominate the collateral flow from the contralateral ICA after PCO, into aplastic ($<25\%$ of the ipsilateral A2 segment) (Fig 1A), hypoplastic (25%–50% of the

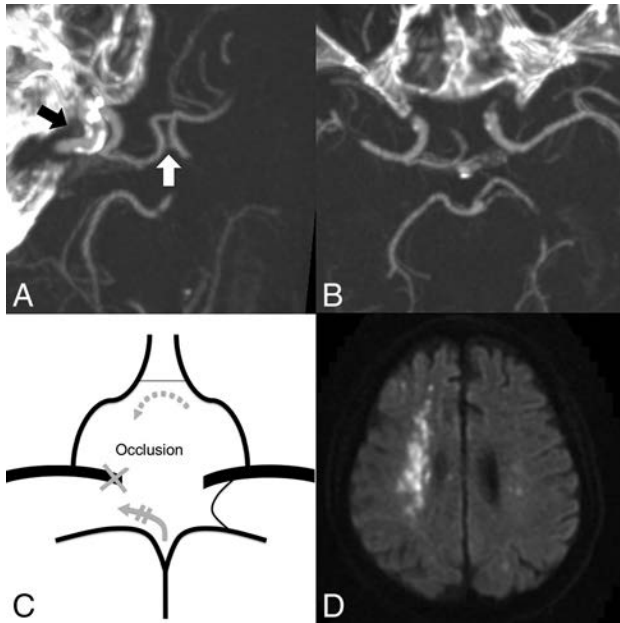


FIG 2. This 74-year-old man with nasopharyngeal carcinoma presented with massive hematemesis and epistaxis. *A*, Faint opacification of the AcomA (white arrow) is shown on the oblique MIP image (7 mm), which is hypoplastic. The target of embolization is the right ICA (black arrow) due to an ICA pseudoaneurysm (not shown). *B*, No right PcomA is detected on the axial MIP image (7 mm). *C*, This patient is interpreted as high risk because only 1 hypoplastic AcomA supplies the collateral flow (gray arrows). *D*, Right borderzone infarction and tiny left embolic infarctions developed 5 days after right ICA embolization (shown on diffusion-weighted imaging).

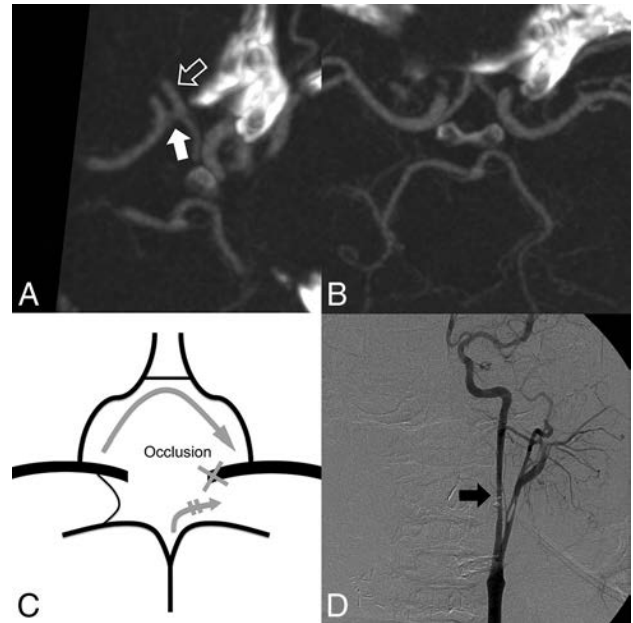


FIG 3. Images in a 36-year-old man with massive bleeding from a protruding tumor. *A*, Oblique MIP image (7 mm) shows that the AcomA (white arrow) diameter is $>50\%$ of the ipsilateral A2 artery (PCO side, hollow arrow). *B*, The left PcomA on the axial MIP image (5 mm) is aplastic. *C*, The patient is interpreted as low risk. The recruited collateral flows after PCO are indicated by gray arrows. *D*, Intraoperative angiography shows irregular narrowing of the diseased left ICA (black arrow). No neurologic deficit was detected after left PCO.

ipsilateral A2 segment) (Fig 2A), and patent ($>50\%$ of the ipsilateral A2 segment) (Figs 3A and 4A) segments. Likewise, the readers classified the narrowest portion of the ipsilateral PcomA and P1 segments (forming the posterior collateral vessels), which form the collateral flow from the basilar artery after PCO, into aplastic ($<25\%$ of the ipsilateral P2 segment) (Figs 1B, 2B, and 3B), hypoplastic (25%–50% of the ipsilateral P2 segment), and patent ($>50\%$ of ipsilateral P2 segment) (Fig 4B) segments. Steno-occlusive disease of the contralateral CCA and/or ICA and anatomic variants of the intracranial vasculature were also evaluated.

Both readers concluded their interpretation on collateral reserve, if disruption (ie, PCO) occurred, with a 5-point scale regarding the risk of borderzone infarction: very high risk, high risk, intermediate risk, low risk, and very low risk. If there was disagreement between the 2 readers, a consensus decision was made after discussion. In brief, assessment was as follows: The collateral reserve of the circle of Willis would be considered very high risk if both the anterior and posterior collateral vessels were aplastic (Fig 1), high risk if one was aplastic and the other was hypoplastic (Fig 2), intermediate risk if both were hypoplastic, low risk if one was patent and the other was aplastic (Fig 3), and very low risk if one was patent and the other was hypoplastic or patent (Fig 4).

PCO Protocol

Before every procedure, written informed consent was obtained from the patient and/or his or her family. All the PCO procedures were conducted in a biplane angiographic suite (Axiom Artis; Siemens, Erlangen, Germany). In our institution, PCO is the first-

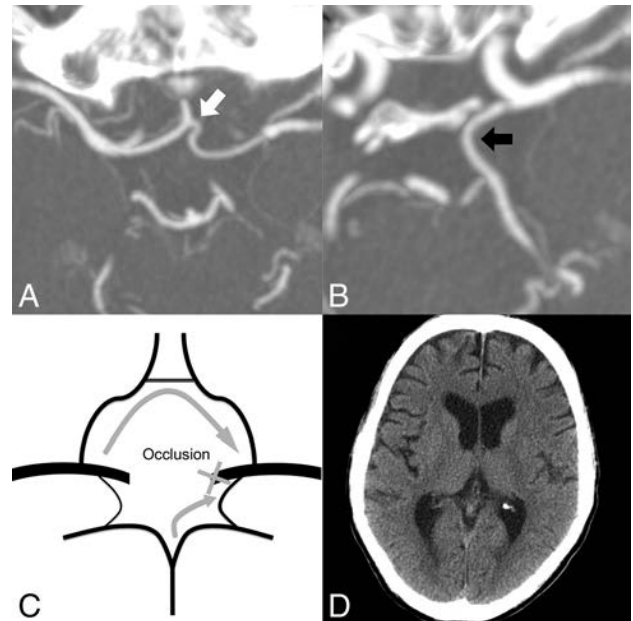


FIG 4. A 52-year-old man with hypopharyngeal cancer and bleeding from the exposed left carotid artery. *A*, Axial MIP image (7 mm) shows a well-opacified AcomA (white arrow), which is $>50\%$ of the ipsilateral (PCO side) A2 segment (not shown). *B*, An axial MIP image (7 mm) reveals the left PcomA (black arrow), which is considered patent. *C*, The patient is considered very low risk. The recruited collateral flows after PCO are indicated by gray arrows. *D*, No cerebral infarction was found on brain CT 14 days after the left ICA embolization.

line treatment for CBS with pathologic lesions located in the CCA and/or ICA. To save time and to prevent excessive bleeding from anticoagulant use, we did not perform BTO before embolization.

Likewise, we did not deploy stent grafts for CBS because long-term neurologic outcomes have not been shown to be superior to PCO^{9,16-18} and because poststenting antiplatelet and anticoagulant therapy is not preferred in CBS.

The timing of PCO was based on the clinical condition, CTA findings, and the willingness of the patient and/or family. Conservative managements, such as gauze packing, local compression, blood transfusion, fluid challenge, and/or tracheostomy were given if a patient refused PCO. The extent of PCO was planned according to the CTA images and correlated with angiography. The vertebral arteries and contralateral CCA were checked before the procedure ended. Platinum coils were used as the primary embolic agent, and vascular plugs were reserved for CCA occlusion. After PCO, we routinely elevated the systolic blood pressure to between 120 and 160 mm Hg to ensure sufficient brain perfusion.

Neurologic Outcomes

After PCO, patients were admitted to an intensive care unit and monitored closely for signs of developing neurologic deficits, changing blood pressure, and rebleeding. The severity of the neurologic deficit was determined according to the summary of the neurology and rehabilitation consultation notes during admission. One radiologist (B.-C.L.) identified borderzone infarction and other thromboembolic infarction within 1 month after embolization by CT or MR imaging¹⁹; both were available for all patients with neurologic deficits. Borderzone infarction with extension to territorial regions was grouped as borderzone infarction. Patients were followed after the initial CTA to the last hospital visit or death.

Statistical Analysis

All statistical analyses were performed with MedCalc statistical software (Version 15.4.0.0; MedCalc Software, Mariakerke, Belgium). Reserve ratings of very high risk, high risk, and intermediate risk were considered positive, and collateral reserve ratings of low risk and very low risk were considered negative, to determine the sensitivity and specificity. Receiver operating characteristic (ROC) analysis was performed, and sensitivities and specificities were calculated for the performance of readers when predicting neurologic outcome after PCO. The diagnostic performance (areas under the ROC curve, [A_z]) of CTA for different neurologic outcomes was compared by paired comparison of the ROC curves using the DeLong method.²⁰ The interobserver reliability was analyzed by the linear weighted- κ statistic, with a value of 0.61–0.80 indicating substantial agreement and a value of 0.81–1.00 indicating excellent agreement. For all statistical analyses, a *P* value < .05 was considered statistically significant.

RESULTS

The patients (*n* = 31, 4 women and 27 men) enrolled in our study had a mean age of 53.7 years (range, 33–79 years). The primary diagnosis was nasopharyngeal carcinoma in 41.9% (13/31) of patients, oropharyngeal cancer in 19.4% (6/31), oral cancer in 12.9% (4/31), hypopharyngeal cancer in 19.4% (6/31), laryngeal cancer in 3.2% (1/31), and thyroid cancer in 3.2% (1/31). The clinical characteristics of these patients are shown in On-line

Table 1. The quality of CTA was considered excellent in 28 patients (90.3%, 28/31) and fair in the other 3 patients (9.7%, 3/31). The fair ratings were because of the suboptimal timing of the arterial phase, which resulted in opacification of the cavernous sinus.

Accuracy of CTA for Predicting Neurologic Outcome

The stratified stroke risk in the cerebral collateral model is shown in the Table. All-cause stroke occurred in 10 (32.3%, 10/31) patients, with the pattern being borderzone infarction in 7 patients, left retinal artery infarction in 1 patient, right retinal artery infarction in 1 patient, and right anterior cerebral artery infarction in 1 patient. The right anterior cerebral artery infarction was caused by inadvertent coil migration to the ipsilateral anterior cerebral artery.

The diagnostic performance and interobserver agreement of the CTA ratings are shown in On-line Table 2. For predicting borderzone infarction, the ROC curve analysis demonstrated A_z values of 0.97, 0.938, and 0.914 for the experienced reader (C.-W.L.), the overall consensus, and the less-experienced reader (Y.-H.L.), respectively. No significant difference in the ROC curves was found between the 2 readers (*P* = .114). Based on the consensus results, the sensitivity, specificity, positive predictive value, and negative predictive value of CTA for borderzone infarction were 100% (7/7), 62.5% (15/24), 43.8% (7/16), and 100% (15/15), respectively. Based on our findings, patients with either patent anterior or posterior collateral vessels (forming low-risk and very low-risk classifications) were thought to have adequate collateral reserve to prevent borderzone infarction after PCO. Interobserver agreement was substantial for anterior and posterior collateral vessels (κ = 0.631) and was excellent for the collateral reserve (κ = 0.807). The A_z values of CTA were lower for all-cause stroke than for borderzone infarction for both readers and the consensus.

Technical Outcomes

Rebleeding episodes occurred in 5 (16.1%, 5/31) patients between days 3 and 64 after the initial PCO, and 4 of them required further endovascular treatment. One patient did not undergo further angiography because compact gauze packing was effective for bleeding control. The rebleeding occurred in the contralateral CCA in one case because of advanced tumor involvement. Of the other 3 cases, rebleeding occurred in the ipsilateral external carotid artery in 2 cases and the ipsilateral vertebral artery in 1 case.

Anatomic Variants of the Circle of Willis

A fetal origin of the posterior cerebral artery was found in 3 patients (left in 2, right in 1). However, no persistent carotid-vertebrobasilar anastomosis was found in the studied patients.

DISCUSSION

In the present study, we demonstrated that CTA could be used to predict borderzone infarction after PCO in patients with CBS. Our results showed that 1 patent anterior or posterior collateral vessel, regardless of the integrity of the remaining circle of Willis, would be enough to prevent borderzone infarction after PCO. Moreover, the reader's experience had no prominent effect on the

Assessment of the anterior and posterior collateral vessels and the collateral reserve

	Collateral Reserve	Anterior Collateral Vessels ^a		
		Patent	Hypoplastic	Aplastic
Posterior collateral vessels ^b	Patent	Very low risk	Very low risk	Low risk
	Hypoplastic	Very low risk	Intermediate risk	High risk
	Aplastic	Low risk	High risk	Very high risk

^a AcomA and bilateral A1.

^b Ipsilateral PcomA and P1.

ROC analysis, implying that the result may be generalized to less-experienced readers. This finding has not, to our knowledge, been reported previously, and it may expand to other conditions that require PCO, such as carotid artery cavernous fistulas, inoperable giant carotid artery aneurysms, or carotid trunk lacerations.

The collateral potential of the circle of Willis, which allows alternative routes for the cerebral circulation when the cerebral blood supply is decreased, was first described by Sir Thomas Willis in 1664.²¹ In patients undergoing PCO, diminished arterial pressure is expected at the postocclusive carotid artery, and neurologic manifestations can be highly variable; whereas some patients remain asymptomatic, others develop devastating borderzone infarctions in the deprived territory.⁹ The ability of the circle of Willis to recruit collaterals to the deprived part of the brain is crucial to stroke avoidance, similar to that seen with carotid disease caused by atherosclerotic occlusive disease.^{22,23} It has been shown that the existence of collateral flow from the PcomA was related to a lower incidence of borderzone infarctions in patients with unilateral ICA occlusion.¹¹ However, if the collateral blood flow cannot meet the demand of the deprived territory, borderzone infarction will still occur. Several other factors, such as coil migration and possible cerebral thromboembolism during coil deployment, might contribute to the development of thromboembolic infarction after PCO. However, such factors are more related to the technical aspect of endovascular treatment itself and are embolic in nature, so they cannot be predicted by our model, as shown by the finding that the A_z values of CTA were lower for all-cause stroke than for borderzone infarction.

BTO, which involves temporarily occluding the ICA under neurologic monitoring, is an established way of assessing the cerebral blood flow dependence on a particular ICA.¹² In patients who pass the BTO, the incidence of neurologic complications is 3.0%–6.7% after permanent ICA occlusion.²⁴ However, the total occlusion time needed for most BTO methods, which usually last 30–40 minutes, may not be tolerable for patients with CBS,²⁵ and BTO was reported to have a high false-negative rate of 5%–20% in previous studies.^{26,27} Recently, venous phase BTO, which measures the discrepancy of venous filling between both hemispheres during ICA occlusion, has been introduced and requires only 60–90 seconds of occlusion time.¹³ Although bilateral femoral cannulation is needed for venous phase BTO, the low complication rate (0%–0.7%) and its short examination time are promising. Another viable but less-studied method is transcranial Doppler sonography or contralateral carotid angiography with ipsilateral manual carotid compression, which can be performed within 1 minute.²⁸ However, most patients with CBS might have a large bleeding wound on the neck, which would be thickly packed to stop bleeding, or postirradiation fibrosis, which would make manual carotid compression difficult and incomplete. BTO is still the criterion standard when evaluating cerebral collateral

reserve under nonemergency clinical scenarios and can be considered during emergent PCO if venous phase BTO is used. Given the noninvasiveness and predictive value of CTA, our methods can serve as an initial risk-stratification tool during the preoperative evaluation, and BTO may be reserved for cases with undetermined results.

Carotid stent-graft deployment may preserve the cerebral perfusion in patients with CBS, potentially preventing borderzone infarction. However, we did not perform stent-graft deployment for CBS in a unilateral carotid artery because long-term neurologic outcome after stent placement in this setting has not been shown to be superior to PCO.^{9,16–18} The rates of stent-related complications, such as in-stent thrombosis, cerebral ischemia, and septic embolism, have been reported to approach 25%–50%, with neurologic complication rates of 10%–27.8%.^{9,29} The unacceptably high poststenting complication rates could be attributable to inadequate antiplatelet therapy during clinical emergencies and contamination from the exposed artery. Therefore, we did not consider that routine stent-graft deployment was justified in patients with CBS, though it might be beneficial if both the initial CTA and confirmative BTO were considered risky for borderzone infarction. Further prospective studies are needed to evaluate the long-term outcomes of stent grafts in patients with insufficient collateral circulations.

The present study had some limitations. We did not account for other less-frequent collateral flow to the embolized carotid trunk, such as persistent embryonic vessels or ophthalmic anastomoses from the ipsilateral external carotid artery, which may supply the ICA in a retrograde manner after PCO. These unaccounted collateral flows may explain why some high-risk patients ($n = 3$) did not develop borderzone infarction. However, the ophthalmic anastomoses are usually tiny and no persistent embryonic vessel was found in this study. Therefore, we believe that these unaccounted collaterals may only contribute to a small portion of brain perfusion after PCO. Another limitation was that evaluation of the stenotic portions of collateral vessels, which sometimes follow complex routes and form redundant loops, may be difficult using visual inspection by inexperienced readers. However, a vascular diameter of >0.6 mm can be confidently identified by combining source images, MIP, and MPR,³⁰ which allows stratification of collateral vessels using index A2 (mean, 2.4 mm) and P2 (mean, 2.1 mm) diameters.^{31,32} Also, readers only had to distinguish patent or nonpatent collateral vessels to obtain a 100% sensitivity for borderzone infarction according to our study results.

CONCLUSIONS

CTA was suitable for estimating the collateral reserve of the circle of Willis in patients with CBS, thereby predicting the occurrence of borderzone infarction after PCO. Further study is warranted to test whether this result can be generalized to other imaging modalities, such as MR angiography, or even become an alternative to BTO in other clinical scenarios.

ACKNOWLEDGMENTS

We thank Cheng-Li Lin for her help on statistical analysis.

Disclosures: Adam Huang—UNRELATED: Patents (Planned, Pending or Issued): I have a patent related to removing bone from CT angiography, but that patent has not been licensed to any company and it has not created any income.

REFERENCES

1. Cohen J, Rad I. **Contemporary management of carotid blowout.** *Curr Opin Otolaryngol Head Neck Surg* 2004;12:110–15 CrossRef Medline
2. Chaloupka JC, Putman CM. **Endovascular therapy for surgical diseases of the cranial base.** *Clin Plast Surg* 1995;22:417–50 Medline
3. Pereira J, Phan T. **Management of bleeding in patients with advanced cancer.** *Oncologist* 2004;9:561–70 CrossRef Medline
4. Maran AG, Amin M, Wilson JA. **Radical neck dissection: a 19-year experience.** *J Laryngol Otol* 1989;103:760–64 CrossRef Medline
5. McDonald MW, Moore MG, Johnstone PA. **Risk of carotid blowout after reirradiation of the head and neck: a systematic review.** *Int J Radiat Oncol Biol Phys* 2012;82:1083–89 CrossRef Medline
6. Chang FC, Luo CB, Lirng JF, et al. **Evaluation of the outcomes of endovascular management for patients with head and neck cancers and associated carotid blowout syndrome of the external carotid artery.** *Clin Radiol* 2013;68:e561–69 CrossRef Medline
7. Moore OS, Karlan M, Sigler L. **Factors influencing the safety of carotid ligation.** *Am J Surg* 1969;118:666–68 CrossRef Medline
8. Chaloupka JC, Putman CM, Citardi MJ, et al. **Endovascular therapy for the carotid blowout syndrome in head and neck surgical patients: diagnostic and managerial considerations.** *AJNR Am J Neuroradiol* 1996;17:843–52 Medline
9. Chang FC, Luo CB, Lirng JF, et al. **Endovascular management of post-irradiated carotid blowout syndrome.** *PLoS One* 2015;10:e0139821 CrossRef Medline
10. Kulik T, Kusano Y, Aronhime S, et al. **Regulation of cerebral vasculature in normal and ischemic brain.** *Neuropharmacology* 2008;55:281–88 CrossRef Medline
11. Hendrikse J, Hartkamp MJ, Hillen B, et al. **Collateral ability of the circle of Willis in patients with unilateral internal carotid artery occlusion: border zone infarcts and clinical symptoms.** *Stroke* 2001;32:2768–73 CrossRef Medline
12. Mathis JM, Barr JD, Jungreis CA, et al. **Temporary balloon test occlusion of the internal carotid artery: experience in 500 cases.** *AJNR Am J Neuroradiol* 1995;16:749–54 Medline
13. Sorteberg A. **Balloon occlusion tests and therapeutic vessel occlusions revisited: when, when not, and how.** *AJNR Am J Neuroradiol* 2014;35:862–65 CrossRef Medline
14. Lee CW, Yang CY, Chen YF, et al. **CT angiography findings in carotid blowout syndrome and its role as a predictor of 1-year survival.** *AJNR Am J Neuroradiol* 2014;35:562–67 CrossRef Medline
15. Katz DA, Marks MP, Napel SA, et al. **Circle of Willis: evaluation with spiral CT angiography, MR angiography, and conventional angiography.** *Radiology* 1995;195:445–49 CrossRef Medline
16. Simental A, Johnson JT, Horowitz M. **Delayed complications of endovascular stenting for carotid blowout.** *Am J Otolaryngol* 2003;24:417–19 CrossRef Medline
17. Kim HS, Lee DH, Kim HJ, et al. **Life-threatening common carotid artery blowout: rescue treatment with a newly designed self-expanding covered nitinol stent.** *Br J Radiol* 2006;79:226–31 CrossRef Medline
18. Gaba RC, West DL, Bui JT, et al. **Covered stent treatment of carotid blowout syndrome.** *Semin Intervent Radiol* 2007;24:47–52 CrossRef Medline
19. Mangla R, Kolar B, Almast J, et al. **Border zone infarcts: pathophysiologic and imaging characteristics.** *Radiographics* 2011;31:1201–14 CrossRef Medline
20. DeLong ER, DeLong DM, Clarke-Pearson DL. **Comparing the areas under two or more correlated receiver operating characteristic curves: a nonparametric approach.** *Biometrics* 1988;44:837–45 CrossRef Medline
21. Eastcott HH. **The beginning of stroke prevention by surgery.** *Cardiovasc Surg* 1994;2:164–69 Medline
22. Klijn CJ, Kappelle LJ, Tulleken CA, et al. **Symptomatic carotid artery occlusion: a reappraisal of hemodynamic factors.** *Stroke* 1997;28:2084–93 CrossRef Medline
23. Lima FO, Furie KL, Silva GS, et al. **The pattern of leptomeningeal collaterals on CT angiography is a strong predictor of long-term functional outcome in stroke patients with large vessel intracranial occlusion.** *Stroke* 2010;41:2316–22 CrossRef Medline
24. American Society of Interventional and Therapeutic Neuroradiology. **Carotid artery balloon test occlusion.** *AJNR Am J Neuroradiol* 2001;22:S8–9 Medline
25. Zussman B, Gonzalez LF, Dumont A, et al. **Endovascular management of carotid blowout.** *World Neurosurg* 2012;78:109–14 CrossRef Medline
26. Marshall RS, Lazar RM, Young WL, et al. **Clinical utility of quantitative cerebral blood flow measurements during internal carotid artery test occlusions.** *Neurosurgery* 2002;50:996–1004; discussion 1004–05 Medline
27. Schneweis S, Urbach H, Solymosi L, et al. **Preoperative risk assessment for carotid occlusion by transcranial Doppler ultrasound.** *J Neurol Neurosurg Psychiatry* 1997;62:485–89 CrossRef Medline
28. Hetzel A, von Reutern G, Wernz MG, et al. **The carotid compression test for therapeutic occlusion of the internal carotid artery: comparison of angiography with transcranial Doppler sonography.** *Cerebrovasc Dis* 2000;10:194–99 CrossRef Medline
29. Hakime A, Khoury E, Hameg A, et al. **Polytetrafluoroethylene-covered nitinol stent graft for treatment of carotid artery blowout syndrome in head and neck cancer patients.** *Laryngoscope* 2013;123:1670–75 CrossRef Medline
30. Skutta B, Fürst G, Eilers J, et al. **Intracranial stenooclusive disease: double-detector helical CT angiography versus digital subtraction angiography.** *AJNR Am J Neuroradiol* 1999;20:791–99 Medline
31. Kawashima M, Rhoton AL Jr, Tanriover N, et al. **Microsurgical anatomy of cerebral revascularization, Part II: posterior circulation.** *J Neurosurg* 2005;102:132–47 CrossRef Medline
32. Kawashima M, Rhoton AL Jr, Tanriover N, et al. **Microsurgical anatomy of cerebral revascularization, Part I: anterior circulation.** *J Neurosurg* 2005;102:116–31 CrossRef Medline

Clinical Significance of Intraplaque Hemorrhage in Low- and High-Grade Basilar Artery Stenosis on High-Resolution MRI

C. Zhu, X. Tian, A.J. Degnan, Z. Shi, X. Zhang, L. Chen, Z. Teng, D. Saloner, J. Lu, and Q. Liu



ABSTRACT

BACKGROUND AND PURPOSE: Intraplaque hemorrhage within intracranial atherosclerotic plaques identified by high-resolution MR imaging has been studied as a potential marker of stroke risk. However, previous studies only examined intracranial arteries with high-grade stenosis (degree of stenosis, >50%). This study aimed to ascertain the clinical relevance of intraplaque hemorrhage in patients with low- and high-grade stenotic basilar artery plaques.

MATERIALS AND METHODS: Patients with basilar artery stenosis ($n = 126$; mean age, 62 ± 10 years; 66 symptomatic and 60 asymptomatic) underwent high-resolution MR imaging. The relationship between imaging findings (intraplaque hemorrhage, contrast enhancement, degree of stenosis, minimal lumen area, and plaque burden) and symptoms was analyzed.

RESULTS: Intraplaque hemorrhage was identified in 22 patients (17.5%), including 21 (31.8%) symptomatic patients and 1 (1.7%) asymptomatic patient. Multivariate analysis showed that intraplaque hemorrhage was the strongest independent marker of symptomatic status (odds ratio, 27.5; 95% CI, 3.4–221.5; $P = .002$). Contrast enhancement was also independently associated with symptomatic status (odds ratio, 9.9; 95% CI, 1.5–23.6; $P = .016$). Stenosis, minimal lumen area, and plaque burden were not correlated with symptoms ($P > .05$). Intraplaque hemorrhage was present in both low- and high-grade stenotic basilar arteries (11.3% versus 16.3%, $P = .63$). Diagnostic performance values of intraplaque hemorrhage for patients with acute/subacute symptomatic stroke were the following: specificity, 98.3%; sensitivity, 31.8%; positive predictive value, 95.5%; and negative predictive value, 56.7%.

CONCLUSIONS: Intraplaque hemorrhage is present in both low- and high-grade stenotic basilar artery plaques and is independently associated with symptomatic stroke status. Intraplaque hemorrhage may identify high-risk plaque and provide new insight into the management of patient with stroke without significant stenosis.

ABBREVIATIONS: HR-MRI = high-resolution MR imaging; ICAD = intracranial atherosclerotic disease; IPH = intraplaque hemorrhage

Intracranial atherosclerotic disease (ICAD) is a major cause of stroke that has likely been underappreciated, in part due to challenges in detecting intracranial atherosclerotic plaque.¹ ICAD

may produce ischemia through multiple mechanisms, including the following: thrombotic occlusion, occlusion of small perforating arteries, plaque rupture leading to artery-to-artery embolization, and vessel luminal narrowing leading to hypoperfusion.² Current practice guidelines rely solely on the degree of stenosis (often $\geq 50\%$) of major intracranial arteries in determining management strategies. However, many authors have questioned this practice, especially given the high prevalence at postmortem examination of mild and moderate intracranial arterial stenosis in fatal stroke.^{2–6} Branch occlusive disease, in particular, has been underestimated and appears to constitute a more common cause of stroke.⁵ Other factors, including plaque composition, arterial hemodynamic features, and collateral status, have been proposed as alternative variables to better predict recurrent stroke risk.⁴

ICAD with ischemia caused by artery-to-artery embolization from plaque rupture may require more aggressive antiplatelet therapy to mitigate clot progression, whereas stenotic disease re-

Received January 10, 2018; accepted after revision March 29.

From the Department of Radiology and Biomedical Imaging (C.Z., D.S.), University of California, San Francisco, San Francisco, California; Department of Radiology (X.T., Z.S., X.Z., L.C., J.L., Q.L.), Changhai Hospital, Shanghai, China; Department of Radiology (A.J.D.), Children's Hospital of Philadelphia, Philadelphia, Pennsylvania; and Department of Radiology (Z.T.), University of Cambridge, Cambridge, UK.

Chengcheng Zhu and Xia Tian contributed equally to this work.

This work was supported by the National Natural Science Foundation of China (31470910) and National Institutes of Health grants R01HL114118, R01NS059944, and K99HL136883.

Paper previously presented, in part, at: Annual Meeting and Exhibition of the International Society for Magnetic Resonance in Medicine, May 7–13, 2016; Singapore.

Please address correspondence to Qi Liu, MD, Department of Radiology, Changhai Hospital, 168 Changhai Rd, Shanghai, China, 200433; e-mail: liuqimd@126.com

Indicates open access to non-subscribers at www.ajnr.org

<http://dx.doi.org/10.3174/ajnr.A5676>

sulting in hypoperfusion might benefit more from angioplasty.² Given these important distinctions in treatment selection for patients with ICAD based on stroke mechanism, the assessment of culprit plaque location and morphology is clinically relevant.² In the past decade, many advances have been made in visualizing large-vessel intracranial plaque morphology and composition using high-resolution MR imaging (HR-MRI).^{7,8} Expanded use of HR-MRI could result in the reclassification of many strokes previously termed cryptogenic and could improve clinical decision-making. A few studies have examined atherosclerotic plaque of the posterior circulation using HR-MRI with improved characterization of basilar artery ICAD.⁹⁻¹³

Intraplaque hemorrhage (IPH) occurs in atherosclerotic plaque and is attributed to fragile neovascularity with endothelial disruption that increases plaque wall stress, making plaque more vulnerable.¹⁴ IPH was first identified as a T1-weighted hyperintense signal in extracranial carotid plaque imaging,¹⁵ and subsequent articles have supported carotid IPH as a risk factor for recurrent stroke independent of stenosis.^{16,17} Preliminary work using intracranial HR-MRI showed a similar appearance of IPH within intracranial arteries in symptomatic ICAD.¹⁸ Xu et al¹⁹ observed T1-weighted hyperintense signal more often in symptomatic middle cerebral artery plaque than in asymptomatic plaques. More recently, in patients with basilar artery stenosis, HR-MRI has revealed IPH as more frequent in symptomatic patients than in asymptomatic patients (42.3% versus 21.4%), suggesting a risk for IPH with a relative risk of 1.64.¹²

These prior basilar artery HR-MRI studies have only imaged basilar artery plaque with high-grade stenosis. The primary aim of this study was to ascertain the presentation and clinical relevance of basilar artery IPH in both low- and high-grade stenotic basilar artery plaques. Given the frequency of nonstenotic ICAD in stroke and preliminary evidence supporting IPH as a risk factor, we hypothesize that IPH status might be useful in distinguishing acute/subacute symptomatic from chronic/asymptomatic basilar artery plaque regardless of the degree of stenosis.

MATERIALS AND METHODS

The authors declare that all supporting data are available within the article.

Study Population

This study was approved by the Changhai Hospital institutional review board with all patients providing written informed consent.

This was a prospective study. Patients with basilar artery atherosclerotic disease were recruited for this study between September 2013 and October 2016. The inclusion criteria were the following: 1) ischemic stroke or transient ischemic attacks in the basilar artery territory, and/or basilar artery stenosis of >30% on DSA, CTA, or MRA; and 2) >1 atherosclerotic risk factor, including hypercholesterolemia, hypertension, smoking, and diabetes mellitus. Exclusion criteria included the following: 1) coexistent unilateral or bilateral vertebral artery stenosis of >50% on MRA, 2) complete basilar artery occlusion, 3) dissection, 4) intracranial dolichoectasia, 5) nonatherosclerotic intracranial arterial disease (eg, inflammatory arteritis and congenital agenesis), 6) the pres-

ence of atrial fibrillation on 24-hour monitoring, and 7) clinical contraindications to MR imaging.

Symptomatic plaque was defined when conventional neuroimaging (FLAIR and diffusion-weighted images) demonstrated infarct within the basilar artery territory. Patients were classified into 2 groups based on their symptom presentation: 1) symptomatic ischemic stroke/TIA symptoms presenting <12 weeks before imaging; and 2) patients with asymptomatic basilar artery plaque without neuroimaging evidence of infarct.

Patients' clinical information including age, sex, diabetes, hypertension, smoking, hyperlipidemia, preadmission statin and aspirin use, ischemic coronary heart disease, and National Institutes of Health Stroke Scale score was collected.

MR Imaging Protocol

MR imaging was performed on a 3T whole-body MR imaging scanner (Skyra; Siemens, Erlangen, Germany) with a 20-channel phased array head and neck coil.

3D time-of-flight images were acquired in the axial plane (TR/TE = 21/3.43 ms, FOV = 181 × 200 mm, thickness = 0.7 mm, matrix = 331 × 384). 3D TOF images were reformatted using multiplanar reconstruction. HR-MRI was then performed in planes perpendicular to the basilar artery. The HR-MRI protocol included 3 sequences with 1 sequence repeated postcontrast (12 slices with 2-mm slice thickness; in-plane resolution = 0.4 × 0.3 mm, FOV = 100 × 100 mm, matrix = 256 × 320); precontrast T1-weighted fast spin-echo (TR/TE = 581/18 ms, echo-train length = 4, NEX = 4); T2-weighted FSE (TR/TE = 2890/46 ms, echo-train length = 20, NEX = 3); and postcontrast T1-weighted FSE. Inflow saturation bands were placed below the imaging slab for blood suppression. In addition, 12 coronal slices were scanned with similar scan parameters to help exclude the potential IPH-mimicking flow artifacts. Clinical DWI and FLAIR imaging were used for the identification of infarct.

Image Analysis

Stenosis value was measured independently on HR-MRI by 2 experienced radiologists (X.T. and Q.L., with 7 and 15 years' experience in neuroradiology) who were blinded to the patients' clinical information.²⁰ The stenosis value was calculated as $(1 - D_{\text{Stenosis}} / D_{\text{Normal}}) \times 100\%$, where D_{Stenosis} is the minimal lumen diameter at the site of maximal stenosis, and D_{Normal} is the lumen diameter at the site of the normal basilar artery (either distal or proximal to the stenosis site). The presence of fresh IPH was identified as >150% signal relative to nearby medial pterygoid muscles on precontrast T1-weighted images by the 2 radiologists independently, blinded to the patient's clinical information.¹² Because intraluminal thrombus/hematoma in intracranial dolichoectasia or dissection also exhibits hyperintense signal on precontrast T1-weighted images, we carefully excluded these conditions on the basis of their imaging features.^{21,22} Basilar dolichoectasia was identified if the basilar diameter was enlarged >4 mm and demonstrated a tortuous appearance on MRA.²¹ Dissection might appear with a dissection flap or double lumen or as a tapering vessel; intraluminal thrombus in dissection also usually involves a long segment.²² Acute or subacute thrombus demonstrates different morphology compared with IPH. Thrombus is

Table 1: Clinical characteristics and imaging findings of patients with low- and high-grade stenotic basilar artery plaque

	All (n = 126)	Low-Grade Stenosis (<50%, n = 46)	High-Grade Stenosis (≥50%, n = 80)	P Value
Age (mean) (yr)	61.5 ± 10.0	63.70 ± 9.4	60.3 ± 10.1	.07
Sex (male) (No.) (%)	82 (65.1%)	33 (71.7%)	49 (61.3%)	.23
Diabetes (No.) (%)	42 (33.3%)	15 (32.6%)	27 (33.8%)	.90
Smoking (No.) (%)	35 (27.8%)	13 (28.3%)	22 (27.5%)	.93
Hypertension (No.) (%)	101 (80.2%)	37 (80.4%)	64 (80.0%)	.96
Hyperlipidemia (No.) (%)	65 (51.6%)	18 (39.1%)	47 (58.8%)	.03 ^a
Coronary artery disease (No.) (%)	5 (4.0%)	3 (6.5%)	2 (2.5%)	.27
Preadmission aspirin use (No.) (%)	31 (24.6%)	9 (19.6%)	22 (27.5%)	.32
Preadmission statin use (No.) (%)	17 (13.5%)	4 (8.7%)	13 (16.3%)	.23
NIHSS score (median) (range)	1 (0–11)	2 (0–11)	0 (0–6)	<.001 ^a
Degree of stenosis (mean) (%)	52.6 ± 15.8	35.2 ± 9.7	62.6 ± 7.9	<.001 ^a
Enhancement percentage (mean)	17.4 ± 28.4	21.1 ± 33.1	15.3 ± 25.3	.27
Intraplaque hemorrhage (No.) (%)	22 (17.5%)	9 (19.6%)	13 (16.3%)	.63
Minimum lumen area (mean) (mm ²)	3.2 ± 2.7	5.1 ± 3.4	2.1 ± 1.3	<.001 ^a
Plaque burden (mean) (%)	84.0 ± 9.1	75.9 ± 8.2	88.6 ± 5.7	<.001 ^a
Symptomatic (No.) (%)	66 (52.4%)	28 (60.9%)	38 (47.5%)	.15

^a Statistically significant.**Table 2: Clinical characteristics and imaging findings of patients with different symptom stages**

	All (n = 126)	Symptomatic (n = 66)	Asymptomatic (n = 60)	P Value
Age (mean) (yr)	61.5 ± 10.0	61.7 ± 10.5	61.4 ± 9.4	.86
Sex (male) (No.) (%)	82 (65.1%)	50 (75.8%)	32 (53.3%)	<.001 ^a
Diabetes (No.) (%)	42 (33.3%)	23 (34.8%)	19 (31.7%)	.71
Smoking (No.) (%)	35 (27.8%)	25 (37.9%)	10 (16.7%)	<.001 ^a
Hypertension (No.) (%)	101 (80.2%)	52 (78.8%)	49 (81.7%)	.69
Hyperlipidemia (No.) (%)	65 (51.6%)	38 (57.6%)	27 (45.0%)	.16
Coronary artery disease (No.) (%)	5 (4.0%)	3 (4.5%)	2 (3.3%)	.73
Preadmission aspirin use (No.) (%)	31 (24.6%)	21 (31.8%)	10 (16.7%)	.06
Preadmission statin use (No.) (%)	17 (13.5%)	10 (15.2%)	7 (11.7%)	.57
NIHSS score (median) (range)	1 (0–11)	2 (0–11)	0 (0–4)	<.001 ^a
Degree of stenosis (mean) (%)	52.6 ± 15.8	52.4 ± 15.5	52.8 ± 16.1	.88
Enhancement percentage (mean)	17.4 ± 28.4	25.5 ± 26.1	8.5 ± 28.5	<.001 ^a
Intraplaque hemorrhage (No.) (%)	22 (17.5%)	21 (31.8%)	1 (1.7%)	<.001 ^a
Minimum lumen area (mean) (mm ²)	3.2 ± 2.7	3.7 ± 2.8	2.7 ± 2.6	.04 ^a
Plaque burden (mean) (%)	84.0 ± 9.1	83.6 ± 9.8	84.4 ± 8.2	.62

^a Statistically significant.

long and close to the lumen, while IPH is focal within plaque and is often eccentric to the lumen.

The lumen and outer wall boundary were manually segmented using CMRtools software (Cardiovascular Imaging Solutions, London, UK) on T2-weighted images. The reproducibility of this area measurement method was previously reported (measurement error for plaque area: 7.5%).²³

The contrast-enhancement percentage was measured at the slice of greatest enhancement, using adjacent gray matter (in a region of ~15 mm²) to normalize signal intensity. The contrast-enhancement percentage was calculated as $\{[\text{Signal of Plaque (Postcontrast)} / \text{Signal of Gray Matter (Postcontrast)}] / [\text{Signal of Plaque (Precontrast)} / \text{Signal of Gray Matter (Precontrast)}] - 1\} \times 100\%$. Plaque burden was measured on the maximal stenosis site and was defined as $(1 - \text{Lumen Area} / \text{Outer Area}) \times 100\%$.

Statistical Analysis

Normality assumptions were formally assessed using a Shapiro-Wilk test. Distributions were summarized using the mean ± SD or median (interquartile range). Categorical data were expressed as

counts or percentages. Continuous data were compared using either a Mann-Whitney *U* test or a Student *t* test. Categorical variables were analyzed using the Fisher exact test. Multivariate logistic regression analysis was used to determine the independent factors associated with acute/subacute symptoms. The intra-class correlation coefficient and Cohen κ coefficient were used to evaluate the agreement between 2 reviewers for the measurement of the degree of stenosis and the identification of IPH. A *P* value of < .05 was considered statistically significant. All *P* values were 2-sided. GraphPad Prism 5 software (GraphPad Software, San Diego, California) and R statistics (Version 3.1.3; www.r-project.org) were used for data analysis.

RESULTS

Patients, Demographics, and Imaging Findings

A total of 175 patients met the inclusion criteria. Forty-nine patients were excluded due to intracranial aneurysms (*n* = 28), Moyamoya disease (*n* = 3), vasculitis (*n* = 1), dissection (*n* = 6), coexistent vertebral artery stenosis >50% (*n* = 8), and bad image quality (*n* = 3). As a result, 126 patients were included in the final analysis (mean age, 61.5 ± 10.0 years; 82 males; mean degree of stenosis of 52.6% ± 15.8%). A total of 66 patients were symptomatic, and 60 were asymptomatic. Forty-six patients had a degree of stenosis of ≤50% (low-grade stenosis; range, 13.4%–48.7%), while 80 patients had a degree of stenosis of >50% (high-grade stenosis; range, 50.1%–80.3%). Demographic information and imaging findings are summarized in Tables 1 and 2 on the basis of the patients' degree of stenosis and symptom status.

IPH was identified in 22 patients (17.5%), including 21 symptomatic patients (31.8%) and 1 (1.7%) asymptomatic patient (Table 2). IPH appeared over a range of stenosis values (Table 1), and there was no difference in the presentation rate of the basilar arteries in low- and high-grade stenosis (19.6% versus 16.3%, *P* = .63). The IPH-to-muscle signal ratio was 2.10 ± 0.54 (range, 1.50–3.19). In these 21 patients with stroke with IPH, 15 had paramedian pontine infarct stroke and 6 had lacunar infarction stroke. Univariate and multivariate analyses of the parameters associated with symptoms are shown in Table 3. IPH was the strongest independent indicator of symptomatic status (odds ratio, 27.5; 95% CI, 3.4–221.5; *P* = .002). Contrast enhancement was also independently associated with symptomatic status (odds ratio, 9.9; 95% CI, 1.5–23.6; *P* = .016). Degree of stenosis, minimal lumen area, and plaque burden were not significantly associ-

Table 3: Univariate and multivariate analyses of the parameters associated with symptomatic status

Variable	Univariate Analysis		Multivariate Analysis	
	Odds Ratio (95% CI)	P	Odds Ratio (95% CI)	P
Sex (male)	2.7 (1.2–5.8)	<.001		
Smoking	3.0 (1.3–7.1)	<.001		
Enhancement percentage	13.0 (2.6–25.0)	<.001	9.9 (1.5–23.6)	.016
Intraplaque hemorrhage	27.5 (3.6–212.4)	.002	27.5 (3.4–221.5)	.002
Minimum lumen area	1.2 (1.0–1.4)	.04		

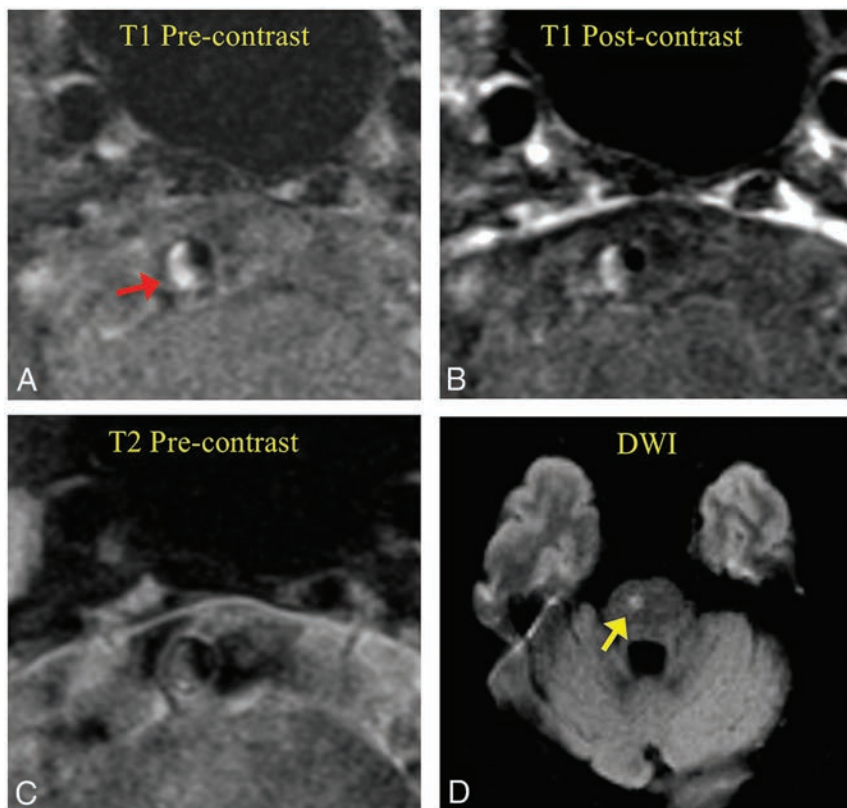


FIG 1. Intraplaque hemorrhage presenting in a low-grade stenotic basilar artery plaque (43% degree of stenosis) in an acute symptomatic female patient (65 years of age). *A*, T1-weighted black-blood MR imaging shows high signal (fresh IPH, red arrow) in the plaque. *B*, Postcontrast T1-weighted image shows slight enhancement of the plaque. *C*, T2-weighted image shows isointense signal of the plaque. *D*, DWI shows infarct in the brain stem (yellow arrow).

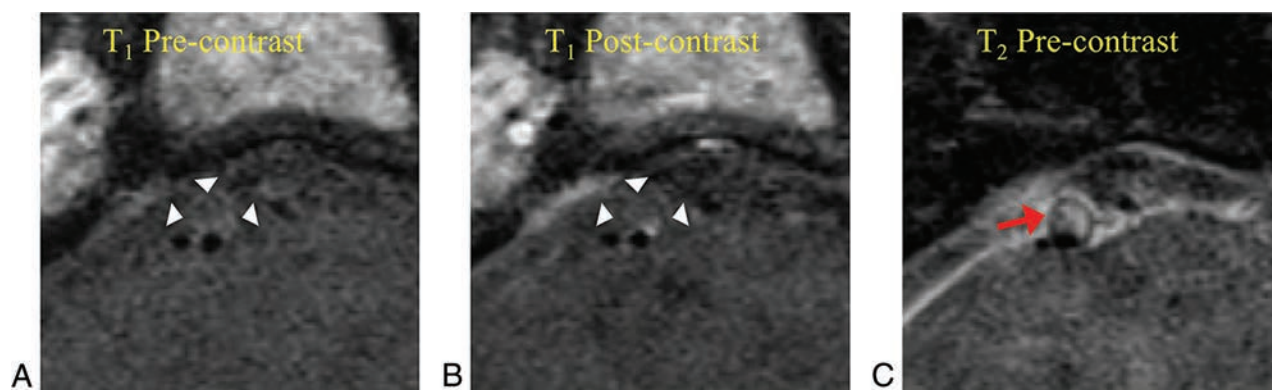


FIG 2. A high-grade stenotic basilar artery plaque (degree of stenosis, 73%) without intraplaque hemorrhage in an asymptomatic female patient (56 years of age). *A*, T1-weighted black-blood MR imaging shows isointense signal in the plaque. *B*, Postcontrast T1-weighted image shows enhancement of the plaque surface. *C*, T2-weighted image shows high signal of the plaque (red arrow).

ated with symptoms ($P > .05$). The presence of IPH was not associated with stenosis ($r = 0.16$, $P = .10$) or plaque burden ($r = 0.16$, $P = .11$). Representative basilar artery plaque images with and without IPH are shown in Figs 1–3.

The diagnostic performance of IPH for acute/subacute symptomatic patients with stroke is summarized in Table 4. IPH had a high specificity of 98.3% and a high positive predictive value of 95.5%; however, the sensitivity (31.8%) and negative predictive value (56.7%) were lower.

MR Imaging Measurements

Reproducibility

There was excellent interreader agreement for measuring the degree of stenosis (intraclass correlation coefficient = 0.97; 95% CI, 0.94–0.98) and for identification of IPH (96% agreement, $\kappa = 0.88$; 95% CI, 0.76–1.00).

DISCUSSION

This study adds to the growing literature that emphasizes the importance of intracranial plaque properties compared with the degree of luminal narrowing.² In this study, IPH was the only finding associated with stroke-symptom status, whereas contrast enhancement, degree of stenosis, minimal lumen area, and plaque burden were not associated with symptom status. Because IPH was present in both low- and high-grade stenotic basilar artery plaque with a high positive predictive value (95.5%) for symptomatic stroke, it is evident that symptomatic ischemia may be explained by factors other than stenosis resulting in

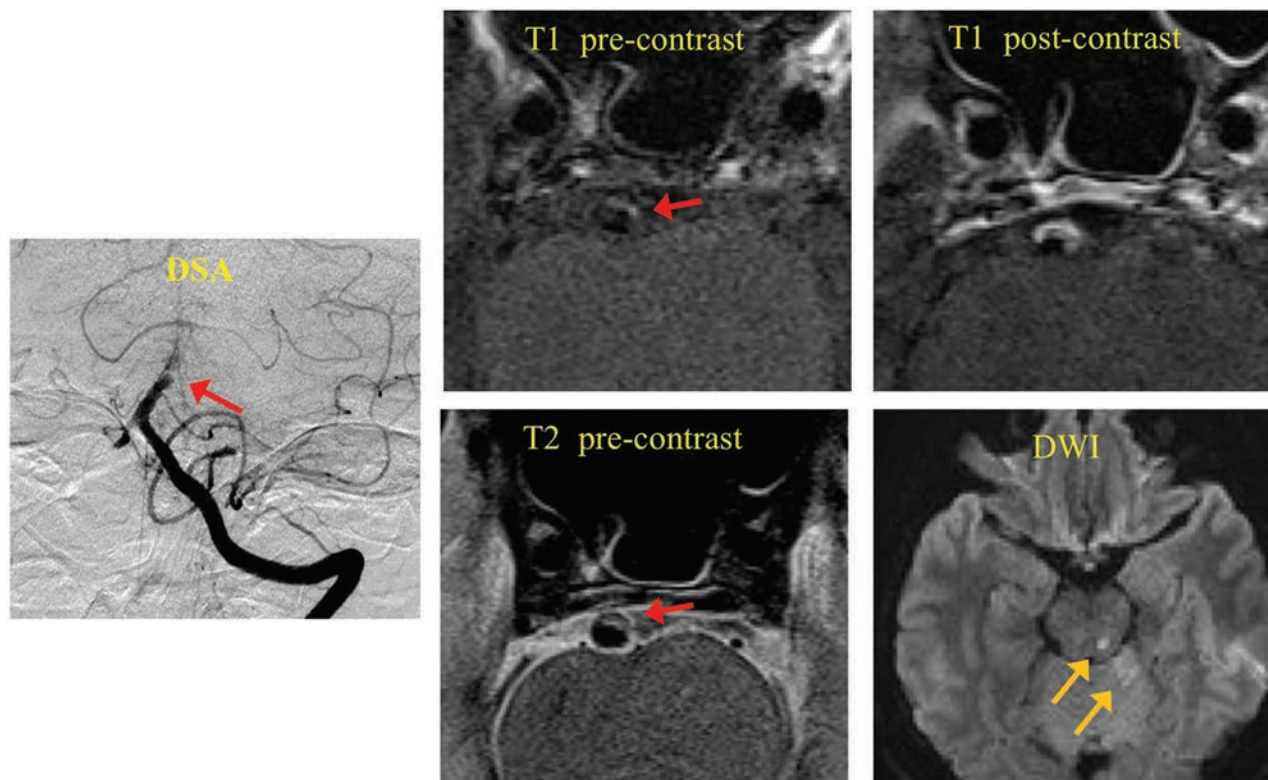


FIG 3. A symptomatic patient with infarctions distal to the location of basilar artery plaque. *Red arrows* show the location of the plaque. *Yellow arrows* show the location of infarctions on DWI. T1-weighted black-blood MR imaging shows high signal in the plaque (IPH). Postcontrast T1-weighted image shows strong enhancement of the plaque.

Table 4: Diagnostic performance of intraplaque hemorrhage in identifying symptomatic/asymptomatic basilar artery plaque

	IPH-Positive (n = 22)	IPH-Negative (n = 104)
Symptomatic	21	45
Asymptomatic	1	59
Diagnostic performance (%) (95% CI)		
Specificity	98.3 (91.1–100.0)	
Sensitivity	31.8 (20.9–44.4)	
PPV	95.5 (74.4–99.3)	
NPV	56.7 (52.6–60.8)	

Note:—PPV indicates positive predict value; NPV, negative predict value.

hypoperfusion. The presence of IPH likely indicates a high risk for artery-to-artery embolic occlusion following plaque rupture. In this conceptualization, future stroke risk for a smaller plaque with IPH is possibly greater than for a larger plaque with a stable fibrous cap.

A study of basilar artery ICAD in patients with at least 30% stenosis found T1-weighted hyperintense intraplaque signal in 8 of 38 cases (21%), which could indicate IPH, though the authors did not specifically term this finding IPH.⁹ The prevalence of basilar artery T1-weighted hyperintense signal reported by Huang et al⁹ (21%) was similar to that reported in the current study (19.6%). On the other hand, a study of 74 patients with >50% stenosis documented IPH in 42.3% of patients with an increased frequency in symptomatic patients.¹² The reason for this higher incidence of IPH may be related to the larger plaque size in these patients with a mean stenosis of 72.9%, though we did not observe a significant difference between IPH frequency in stenotic-versus-

nonstenotic plaque in our study.¹² Alternatively, patients in our study were younger than those of Yu et al,¹² with a difference in mean age of approximately 10 years between the populations in the 2 studies. IPH may occur more frequently with age, though this hypothesis is untested. The diagnostic performance of IPH in the aforementioned study was similar to that in the current study with relatively high specificity (79%) but low sensitivity (53%).¹² A study of IPH in other intracranial arteries has observed similar findings. IPH was significantly more frequent in symptomatic middle cerebral artery plaque than in asymptomatic plaque (19.6% versus 3.2%).¹⁹

While current management guidelines focus on stenosis, our work and that of others supports the use of identification of plaque properties to better indicate future stroke risk. Our study emphasizes the highly specific (98.3%) nature of IPH as an indicator of symptomatic stroke, implying that this represents unstable basilar artery atherosclerotic plaque. Unfortunately, IPH is not particularly sensitive (31.8%) to the presence of a symptomatic basilar artery. These observations likely reflect the multiple stroke mechanisms encountered in ICAD, in which IPH could predispose to artery-to-artery embolization with small-vessel occlusion and could cause branch occlusive disease affecting perforating arteries. On the other hand, some symptomatic strokes in this study could also be caused by stenotic basilar artery plaque leading to hypoperfusion. IPH was the best overall marker of symptomatic plaque with an odds ratio of 27.5. The findings of this study support the use of IPH in basilar artery atherosclerotic plaque as a better indicator of symptomatic plaque rather than stenosis or plaque burden alone.

Other intracranial plaque characteristics including contrast

enhancement and minimal lumen area have been associated with symptoms.^{24,25} We observed a similar relationship between contrast enhancement and symptom status in our study. A smaller study examining the basilar artery with contrast-enhanced HR-MRI observed wall enhancement in patients with recent infarction and also those who would go on to have ischemic events.²⁶ Another study of intracranial atherosclerotic disease also concluded that contrast enhancement was associated with culprit plaques with a substantial odds ratio of approximately 35.²⁵ Research suggests that the vasa vasorum evolves with age and demonstrates different distributions with less vasa vasorum in the intracranial vasculature and differing distributions within the cerebral vascular territories.²⁷ Theoretically, enhancement of the basilar artery wall could reflect physiologic enhancement of the vasa vasorum rather than pathologic plaque enhancement, which could reduce the specificity of vessel wall enhancement. An improved understanding of the vasa vasorum may enhance the specificity of basilar artery enhancement.

Further work is needed to histologically validate HR-MRI assessment of IPH, with only 1 case of histologically verified intracranial IPH demonstrated as T1-weighted hyperintense intraplaque signal on postmortem HR-MRI.²⁸ Due to the reliance on postmortem assessment of plaque, histologic validation of intracranial plaque imaging characteristics is more challenging than in the extracranial carotid artery plaque, which may be ascertained following endarterectomy. While a study of intracranial plaque characterization using ex vivo 3T HR-MRI in 53 postmortem specimens determined relaxation times for many plaque components, no IPH was encountered in these plaque specimens.²⁹ Therefore, IPH detection on HR-MRI largely infers plaque characteristics from existing extracranial atherosclerosis imaging literature.

Our results cannot directly confer causality of IPH in symptomatic stroke, and this cross-sectional study design cannot provide an assessment of future stroke risk. Prospective assessment of IPH and subsequent stroke risk would extend the clinical relevance of the findings of this study, and such data could be used in risk-assessment calculations. HR-MRI can also determine IPH timing and duration. Potentially, signal characteristics of IPH could provide information on the onset of hemorrhage, and serial examination of patients with ICAD exhibiting IPH could provide insight into its natural history. Moreover, serial assessment of intracranial IPH evolution while patients were on different pharmacologic therapies might potentially provide objective information regarding treatment efficacy.

In addition, there are technical limitations to our study. Our study used a standard 2D T1-weighted black-blood fast spin-echo sequence. The use of 3D sequences with higher resolution,³⁰ better T1-weighted contrast,³¹ and advanced blood-suppression techniques (such as diffusion preparation³² or variable flip angle train³⁰) could potentially improve the identification of IPH. However, the 3D high-resolution sequences can increase scan time, the use of diffusion preparation can reduce the signal-to-noise ratio and induce T2 contrast,³² and variable flip angle trains can induce blurring with a wider point-spread function.³⁰ All of these limitations will need to be accounted for in future clinical studies.

CONCLUSIONS

Evidence from this study suggests that IPH in the basilar artery found on HR-MRI identifies atherosclerotic lesions that are more likely to be symptomatic regardless of the degree of stenosis. This plaque property appears to be substantially associated with symptom status, whereas many other factors, including plaque size, contrast enhancement, and degree of stenosis, do not. In the future, the use of HR-MRI for the early detection of basilar artery IPH may allow clinicians to select individuals at greater risk of imminent stroke and help provide optimal therapeutic intervention.

Disclosures: Chengcheng Zhu—RELATED: Grant: National Institutes of Health—National Heart, Lung, and Blood Institute, Comments: supported by National Heart, Lung, and Blood Institute grant K99HL136883. Jianping Lu—RELATED: Grant: National Nature Science Foundation of China (No. 31470910).

REFERENCES

1. Gorelick PB, Wong KS, Bae HJ, et al. **Large artery intracranial occlusive disease: a large worldwide burden but a relatively neglected frontier.** *Stroke* 2008;39:2396–99 CrossRef Medline
2. Bodle JD, Feldmann E, Swartz RH, et al. **High-resolution magnetic resonance imaging: an emerging tool for evaluating intracranial arterial disease.** *Stroke* 2013;44:287–92 CrossRef Medline
3. Mazighi M, Labreuche J, Gongora-Rivera F, et al. **Autopsy prevalence of intracranial atherosclerosis in patients with fatal stroke.** *Stroke* 2008;39:1142–47 CrossRef Medline
4. Leng X, Wong KS, Liebeskind DS. **Evaluating intracranial atherosclerosis rather than intracranial stenosis.** *Stroke* 2014;45:645–51 CrossRef Medline
5. Ryoo S, Park JH, Kim SJ, et al. **Branch occlusive disease: clinical and magnetic resonance angiography findings.** *Neurology* 2012;78:888–96 CrossRef Medline
6. Adams HP Jr, Bendixen BH, Kappelle LJ, et al. **Classification of subtype of acute ischemic stroke: definitions for use in a multicenter clinical trial—TOAST. Trial of Org 10172 in Acute Stroke Treatment.** *Stroke* 1993;24:35–41 CrossRef Medline
7. Degnan AJ, Gallagher G, Teng Z, et al. **MR angiography and imaging for the evaluation of middle cerebral artery atherosclerotic disease.** *AJNR Am J Neuroradiol* 2012;33:1427–35 CrossRef Medline
8. Dieleman N, van der Kolk AG, Zwanenburg JJ, et al. **Imaging intracranial vessel wall pathology with magnetic resonance imaging: current prospects and future directions.** *Circulation* 2014;130:192–201 CrossRef Medline
9. Huang B, Yang WQ, Liu XT, et al. **Basilar artery atherosclerotic plaques distribution in symptomatic patients: a 3.0T high-resolution MRI study.** *Eur J Radiol* 2013;82:e199–203 CrossRef Medline
10. Klein IF, Lavallée PC, Mazighi M, et al. **Basilar artery atherosclerotic plaques in paramedian and lacunar pontine infarctions: a high-resolution MRI study.** *Stroke* 2010;41:1405–09 CrossRef Medline
11. Kim YS, Lim SH, Oh KW, et al. **The advantage of high-resolution MRI in evaluating basilar plaques: a comparison study with MRA.** *Atherosclerosis* 2012;224:411–16 CrossRef Medline
12. Yu JH, Kwak HS, Chung GH, et al. **Association of intraplaque hemorrhage and acute infarction in patients with basilar artery plaque.** *Stroke* 2015;46:2768–72 CrossRef Medline
13. Chung JW, Kim BJ, Choi BS, et al. **High-resolution magnetic resonance imaging reveals hidden etiologies of symptomatic vertebral arterial lesions.** *J Stroke Cerebrovasc Dis* 2014;23:293–302 CrossRef Medline
14. Huang X, Teng Z, Canton G, et al. **Intraplaque hemorrhage is associated with higher structural stresses in human atherosclerotic plaques: an in vivo MRI-based 3D fluid-structure interaction study.** *Biomed Eng Online* 2010;9:86 CrossRef Medline
15. Moody AR, Murphy RE, Morgan PS, et al. **Characterization of complicated carotid plaque with magnetic resonance direct thrombus**

- imaging in patients with cerebral ischemia. *Circulation* 2003;107:3047–52 CrossRef Medline
16. McNally JS, McLaughlin MS, Hinckley PJ, et al. **Intraluminal thrombus, intraplaque hemorrhage, plaque thickness, and current smoking optimally predict carotid stroke.** *Stroke* 2015;46:84–90 CrossRef Medline
 17. Altaf N, MacSweeney ST, Gladman J, et al. **Carotid intraplaque hemorrhage predicts recurrent symptoms in patients with high-grade carotid stenosis.** *Stroke* 2007;38:1633–35 CrossRef Medline
 18. Turan TN, Bonilha L, Morgan PS, et al. **Intraplaque hemorrhage in symptomatic intracranial atherosclerotic disease.** *J Neuroimaging* 2011;21:e159–61 CrossRef Medline
 19. Xu WH, Li ML, Gao S, et al. **Middle cerebral artery intraplaque hemorrhage: prevalence and clinical relevance.** *Ann Neurol* 2012;71:195–98 CrossRef Medline
 20. Liu Q, Huang J, Degan AJ, et al. **Comparison of high-resolution MRI with CT angiography and digital subtraction angiography for the evaluation of middle cerebral artery atherosclerotic stenotic disease.** *Int J Cardiovasc Imaging* 2013;29:1491–98 CrossRef Medline
 21. Lou M, Caplan LR. **Vertebrobasilar dilatative arteriopathy (dolichoectasia).** *Ann N Y Acad Sci* 2010;1184:121–33 CrossRef Medline
 22. Choi YJ, Jung SC, Lee DH. **Vessel wall imaging of the intracranial and cervical carotid arteries.** *J Stroke* 2015;17:238–55 CrossRef Medline
 23. Zhang X, Zhu C, Peng W, et al. **Scan-rescan reproducibility of high resolution magnetic resonance imaging of atherosclerotic plaque in the middle cerebral artery.** *PLoS One* 2015;10:e0134913 CrossRef Medline
 24. Teng Z, Peng W, Zhan Q, et al. **An assessment on the incremental value of high-resolution magnetic resonance imaging to identify culprit plaques in atherosclerotic disease of the middle cerebral artery.** *Eur Radiol* 2016;26:2206–14 CrossRef Medline
 25. Qiao Y, Zeiler SR, Mirbagheri S, et al. **Intracranial plaque enhancement in patients with cerebrovascular events on high-spatial-resolution MR images.** *Radiology* 2014;271:534–42 CrossRef Medline
 26. Lou X, Ma N, Ma L, et al. **Contrast-enhanced 3T high-resolution MR imaging in symptomatic atherosclerotic basilar artery stenosis.** *AJNR Am J Neuroradiol* 2013;34:513–17 CrossRef Medline
 27. Portanova A, Hakakian N, Mikulis DJ, et al. **Intracranial vasa vasorum: insights and implications for imaging.** *Radiology* 2013;267:667–79 CrossRef Medline
 28. Chen XY, Wong KS, Lam WW, et al. **High signal on T1 sequence of magnetic resonance imaging confirmed to be intraplaque haemorrhage by histology in middle cerebral artery.** *Int J Stroke* 2014;9:E19 CrossRef Medline
 29. Jiang Y, Zhu C, Peng W, et al. **Ex-vivo imaging and plaque type classification of intracranial atherosclerotic plaque using high resolution MRI.** *Atherosclerosis* 2016;249:10–16 CrossRef Medline
 30. Zhu C, Haraldsson H, Tian B, et al. **High resolution imaging of the intracranial vessel wall at 3 and 7 T using 3D fast spin echo MRI.** *MAGMA* 2016;29:559–70 CrossRef Medline
 31. Zhu DC, Vu AT, Ota H, et al. **An optimized 3D spoiled gradient recalled echo pulse sequence for hemorrhage assessment using inversion recovery and multiple echoes (3D SHINE) for carotid plaque imaging.** *Magn Reson Med* 2010;64:1341–51 CrossRef Medline
 32. Zhu C, Graves MJ, Yuan J, et al. **Optimization of improved motion-sensitized driven-equilibrium (iMSDE) blood suppression for carotid artery wall imaging.** *J Cardiovasc Magn Reson* 2014;16:61 CrossRef Medline

Mobile Stroke Unit Reduces Time to Image Acquisition and Reporting

 E.M. Nyberg,  J.R. Cox,  R.G. Kowalski,  D. Vela-Duarte,  B. Schimpf, and  W.J. Jones

ABSTRACT

SUMMARY: Timely administration of thrombolytic therapy is critical to maximizing the likelihood of favorable outcomes in patients with acute ischemic stroke. Although emergency medical service activation overall improves the timeliness of acute stroke treatment, the time from emergency medical service dispatch to hospital arrival unavoidably decreases the timeliness of thrombolytic administration. Our mobile stroke unit, a new-generation ambulance with on-board CT scanning capability, reduces key imaging time metrics and facilitates in-the-field delivery of IV thrombolytic therapy.

ABBREVIATIONS: EMS = emergency medical service; MSU = mobile stroke unit

Acute ischemic stroke is the fifth leading cause of mortality in the United States and remains the leading cause of morbidity and long-term disability, costing approximately \$33 billion per year.¹ The effectiveness of tPA in improving outcomes has been shown to be sensitive to the timeliness of drug delivery,² with a 20% decrease in the likelihood of a good outcome (defined by a modified Rankin Scale score of 0–2) at 90 days for every 30-minute delay in reperfusion.³ Besides decreasing the effectiveness of the drug, delays in care also preclude some patients from receiving thrombolytic therapy when the delays place patients outside the 4.5-hour treatment window. Currently, only 3%–5% of patients with acute ischemic stroke receive thrombolytic therapy, often due to the time-limited treatment window.⁴ Until recently, the time required for prehospital evaluation and transportation via emergency medical service (EMS) has generally been unavoidable. With the introduction of mobile stroke units (MSUs), the time required for transportation and repeat patient evaluation before IV tPA administration can be eliminated.

The purpose of this study was to compare pertinent imaging time metrics for patients imaged in the MSU with those imaged via the conventional pathway through the emergency depart-

ment. Specifically, we compared the time of EMS dispatch with the availability of CT images on a PACS and the time of EMS dispatch with the time of a radiology report provided to the neurologist between MSU and conventional pathway groups.

MATERIALS AND METHODS

Mobile Stroke Unit

Our MSU is a new-generation ambulance with an on-board CereTom CT scanner (NeuroLogica, Danvers, Massachusetts). CT images are transferred to the hospital-based PACS system via a Health Insurance Portability and Accountability Act–compliant, 4G network cloud-based system for a radiologist’s interpretation. Teleneurology capabilities allow real-time remote examination of the patient by a stroke neurologist. The on-board MSU team includes a stroke-trained nurse who can deliver tPA in the field under the direction of the remote stroke neurologist, as well as a CT technologist, paramedic, and an emergency medical technician.

Prehospital Stroke Alerts

Current stroke guidelines indicate that when an emergency medical technician suspects that a patient is having an acute ischemic stroke on prehospital assessment, that emergency medical technician should contact the receiving emergency department to alert them that the patient is a “prehospital stroke alert.” This results in a streamlined patient work-up on arrival to the emergency department. Every other week, if the EMS dispatcher suspects acute ischemic stroke based on the initial call, then our MSU is dispatched simultaneously with the standard EMS service in our region. If on arrival to the scene, the patient is deemed a potential tPA candidate, the MSU assumes control of the patient’s transport and care. If the patient is not a tPA candidate, the MSU leaves

Received February 4, 2018; accepted after revision March 27.

From the Departments of Radiology (E.M.N., J.R.C.) and Neurology (R.G.K., D.V.D., B.S., W.J.J.), University of Colorado, Aurora, Colorado.

A previous version of these data was presented at: Annual Meeting of the American Society of Neuroradiology and the Foundation of the ASNR Symposium, April 22–27, 2017; Long Beach, California.

Please address correspondence to Eric M. Nyberg, MD, Department of Radiology, University of Colorado, 12605 E 16th Ave, Aurora, CO 80045; e-mail: Eric.Nyberg@ucdenver.edu

<http://dx.doi.org/10.3174/ajnr.A5673>

Table 1: Mean times from dispatch to images viewable on PACS and dispatch to report

Time (min)	MSU		Control		Difference	P Value
	Mean	SD	Mean	SD		
PACS time	21	5.7	44	46.3	23	<.001
Report time	34	8.8	55	47.1	21	<.001

Table 2: Group differences in imaging times related to treatment benchmarks

Time	PACS Time			Report Time		
	MSU	Control	P Value	MSU	Control	P Value
<30 min	96%	40%	<.001	40%	4%	<.001
<1 hr	100%	90%	.057	100%	78%	<.001
>1 hr	0%	10%	.057	0%	18%	<.001

the scene and control of patient care defaults to the conventional EMS provider. On alternating weeks, the MSU is used in a neighboring metropolitan area.

Institutional review board permission for this study was obtained. Consecutive patients identified as prehospital stroke alerts during weeks when the MSU was operating locally from the prospectively maintained stroke alert data base were included. Control stroke-alert patients presenting from the same geographic region during weeks that the MSU was not running locally were selected from the data base on the basis of prehospital stroke-alert status and were matched for day of the week and time of day.

Time from the EMS dispatch to time of image availability in a PACS (PACS time) and time from EMS dispatch to time of a radiologist's verbal communication of results to the stroke neurologist (report time) were compared between the MSU and control patient groups. The difference between PACS time and report time represents the time during which the radiologist opens and interprets the CT scan and verbally communicates the findings via the dedicated physician-to-physician communication service (the "DocLine") of the hospital. Descriptive statistics between MSU and control patients were compared using a Student *t* test. Categorical group differences in meeting critical benchmarks were compared using a Fisher exact test.

RESULTS

Ninety-seven patients from January 2016 through September 2016 were included for analysis, including 47 consecutive patients imaged via the MSU and 50 control patients imaged via the conventional in-hospital pathway. Mean times of dispatch to images viewable on the PACS were 21 minutes and 44 minutes in MSU and control groups, respectively ($P < .001$). Mean times of dispatch to the radiology report were 34 minutes and 54 minutes, respectively ($P < .001$) (Table 1). SDs for both image and report times were smaller in the MSU group compared with controls.

Other key time metrics were also significantly shorter in the MSU group (Table 2). In the MSU group, images were visible on the PACS within 30 and 60 minutes in 98% and 100% of cases, respectively, compared with 40% and 90% of cases, respectively, in the control group. Similarly, in the MSU group, radiologists' reports were given to the stroke neurologist within 30 minutes and 60 minutes in 40% and 100% of cases, respectively, compared with only 4% and 78% in the control group. The MSU pathway was significantly more likely to get images to the PACS within 30

minutes and to provide a report within 60 minutes of dispatch compared with controls ($P < .001$). Mean differences between PACS time and report time between the MSU and control groups, 13 and 11 minutes, respectively, were similar. It is not surprising that CT interpretation and reporting are streamlined in both MSU and conventional stroke-alert pathways.

DISCUSSION

This study demonstrates the considerable impact that the MSU can have on key imaging metrics within the stroke-alert treatment pathway, and it is the first to demonstrate this impact in a US market. Walter et al⁵ performed a similar study in Homburg, Germany, also with week-on and week-off pseudorandomization.⁵ That study showed a reduction of PACS time by 41 minutes from 97 to 56 minutes. In both studies, the PACS time was reduced by roughly half (43% in the Homburg study and 52% in our study). The MSU facilitated provision of actionable reports within 60 minutes of dispatch, the so-called "golden hour," in 100% of patients compared with only 78% in the control group. Tighter SDs of image and report times in the MSU group suggest decreased variability and greater reliability of imaging and reporting within a given timeframe. Anecdotally, earlier CT results and examination by a neurologist facilitated by the MSU have been associated with commensurate improvements in the timeliness of tPA administration. However, the data describing the impact of the MSU on tPA utilization, expediency, and clinical outcomes are currently being collected and will be addressed in subsequent studies.

The mobile stroke unit may represent a paradigm shift in the treatment pathway for acute stroke and presents an opportunity to consider new ways in which health care can be delivered. There may be an even greater impact as the MSU is deployed to more widely distributed geographic regions. Patients from rural communities face distinct limitations and challenges in acute ischemic stroke care, some of which have been addressed by novel telestroke services.^{6,7} Patients from these communities not only contend with the decreased effectiveness of thrombolytic therapy resulting from delayed tPA administration secondary to the inherently longer travel times, but rural patients are also more often excluded from thrombolytic therapy entirely due to this delay. The MSU, it is hoped, should result in fewer patients being excluded from thrombolytic treatment due to time constraints. Thus, the MSU may represent an important step toward a more equitable distribution of health care delivery services across different demographic populations.

CONCLUSIONS

This study demonstrates the ability of a mobile stroke unit system to significantly reduce the time elapsed from EMS dispatch to the availability of CT acquisition and reporting. The MSU also significantly impacted the ability of a neurologist to receive an actionable radiology report within 60 minutes of dispatch. We expect that commensurate improvements in tPA delivery times and, ultimately, patient outcomes will be borne out in subsequent studies. Further additional questions will include the economic impact and cost effectiveness of the MSU in reducing the considerable cost that ischemic stroke inflicts on society.

Disclosures: William J. Jones—*RELATED: Grant: Benefits of Stroke Treatment Delivered using a Mobile Stroke Unit, Comments: Patient-Centered Outcomes Research Institute–funded, multicenter grant to study the effectiveness, including cost-effectiveness, of Mobile Stroke Units. Also, as site Principal Investigator for the BEST-MSU study, I, as well as the institution, get financial support from the BEST-MSU study*; Fees for Participation in Review Activities such as Data Monitoring Boards, Statistical Analysis, Endpoint Committees, and the Like: VOYAGER PAD, Comments: Independent Stroke Outcome Adjudicator for the Bayer Pharmaceuticals–sponsored VOYAGER PAD study. *Money paid to the institution.*

REFERENCES

1. Mozaffarian D, Benjamin EJ, Go AS, et al; Writing Group Members; American Heart Association Statistics Committee, Stroke Statistics Subcommittee. **On behalf of the American Heart Association Statistics Committee and Stroke Statistics Subcommittee. Heart disease and stroke statistics—2016 update: a report from the American Heart Association.** *Circulation* 2016;133:e38–360 CrossRef Medline
2. Lees KR, Bluhmki E, von Kummer R, et al; ECASS, ATLANTIS, NINDS and EPITHET rt-PA Study Group. **Time to treatment with intravenous alteplase and outcome in stroke: an updated pooled analysis of ECASS, ATLANTIS, NINDS, and EPITHET trials.** *Lancet* 2010;375:1695–703 CrossRef Medline
3. Mazighi M, Chaudhry SA, Ribo M, et al. **Impact of onset-to-reperfusion time on stroke mortality: a collaborative pooled analysis.** *Circulation* 2013;127:1980–85 CrossRef Medline
4. Cheng NT, Kim AS. **Intravenous thrombolysis for acute ischemic stroke within 3 hours versus between 3 and 4.5 hours of symptom onset.** *Neurohospitalist* 2015;5:101–09 CrossRef Medline
5. Walter S, Kostopoulos P, Haass A, et al. **Diagnosis and treatment of patients with stroke in a mobile stroke unit versus in hospital: a randomised controlled trial.** *Lancet Neurol* 2012;11:397–404 CrossRef Medline
6. Hess DC, Wang S, Hamilton W, et al. **REACH: clinical feasibility of a rural telestroke network.** *Stroke* 2005;36:2018–20 CrossRef Medline
7. Kulcsar M, Gilchrist S, George MG. **Improving stroke outcomes in rural areas through telestroke programs: an examination of barriers, facilitators, and state policies.** *Telemed J E Health* 2014;20:3–10 CrossRef Medline

Endovascular Treatment of Dural Arteriovenous Fistulas Using Transarterial Liquid Embolization in Combination with Transvenous Balloon-Assisted Protection of the Venous Sinus

D.F. Vollherbst, C. Ulfert, U. Neuberger, C. Herweh, M. Laible, S. Nagel, M. Bendszus, and M.A. Möhlenbruch



ABSTRACT

BACKGROUND AND PURPOSE: Sinus-preserving endovascular embolization was described as a promising treatment technique for dural arteriovenous fistulas. Our aim was to report our single-center experience in patients with dural arteriovenous fistulas who were treated with transarterial liquid embolization in combination with transvenous balloon-assisted protection of the affected venous sinus.

MATERIALS AND METHODS: A retrospective analysis of a prospectively collected data base was performed. Demographic and clinical data, angiographic features of the dural arteriovenous fistulas, procedural parameters, complications, treatment success, follow-up imaging, and clinical outcome were assessed.

RESULTS: Twenty-two patients were treated in 25 procedures. All patients were symptomatic, of whom 81.8% presented with tinnitus; 9.1%, with ocular symptoms; and 9.1%, with headache. Most fistulas were located at the transverse and/or sigmoid sinus. The most frequent fistula type was Cognard IIa+b (40.9%), followed by Cognard I (31.8%) and Cognard IIa (27.3%)/Borden I (59.1%), followed by Borden II (40.9%). The affected sinus could be preserved in all except for 1 patient in whom it was sacrificed in a second treatment procedure by coil embolization. The overall complete occlusion rate was 86.4%. The overall complication rate was 20%, with transient and permanent morbidity and mortality of 8%, 0%, and 0%, respectively. After a mean follow-up of 18 months, most patients (68.2%) achieved complete symptom remission, 27.3% showed symptom relief, and 4.6% had stable symptoms.

CONCLUSIONS: Transarterial liquid embolization of dural arteriovenous fistulas in combination with transvenous balloon-assisted protection of the venous sinus is feasible and safe and offers high rates of occlusion and of symptom remission.

ABBREVIATION: dAVF = dural arteriovenous fistula

Dural arteriovenous fistulas (dAVFs) are pathologic, usually acquired connections between dural arteries and dural venous sinuses or cortical veins, resulting in arteriovenous shunting of blood. The 2 major types of clinical presentation are either hemorrhage, with corresponding neurologic deficits, or venous hypertension, with the latter potentially resulting in a variety of symptoms, such as headache, pulsatile tinnitus, visual disturbances, cognitive decline, or seizures.¹

Endovascular treatment is considered effective for dAVFs.^{2,3} Various endovascular treatment techniques have been and are currently being used, using either a transarterial, transvenous, or combined approach.² The armamentarium of embolic agents in-

cludes liquid embolic agents, such as cyanoacrylates and ethylene-vinyl copolymers, coils, and particles.^{2,3} In special situations, transient occlusion with balloon catheters can be used as an adjunct to conventional transarterial or transvenous embolization. When applied on the arterial side, they can be used for reduction of the blood flow of the fistula, for enhancement of distal migration of the embolic agent while simultaneously reducing the amount of reflux, and for improvement of embolization control.⁴⁻⁷ In the venous system, balloon catheters can be used for protecting the venous sinuses and nontarget veins from unwanted embolization.^{6,8-10} In dAVFs with a high risk for venous nontarget embolization, especially fistulas at the transverse or sigmoid sinus, this aspect is of particular importance because nontarget embolization risks occlusion of functionally relevant venous drainage, potentially leading to venous congestion, venous infarction, or intracerebral hemorrhage.^{11,12} Transarterial embolization in combination with transvenous balloon protection is a promising approach for the effective treatment of dAVFs with prevention of nontarget emboliza-

Received January 15, 2018; accepted after revision March 5.

From the Departments of Neuroradiology (D.F.V., C.U., U.N., C.H., M.B., M.A.M.) and Neurology (M.L., S.N.), Heidelberg University Hospital, Heidelberg, Germany.

Please address correspondence to Markus A. Möhlenbruch, MD, Department of Neuroradiology, Heidelberg University Hospital, INF 400, 69120 Heidelberg, Germany; e-mail: markus.moehlenbruch@med.uni-heidelberg.de

<http://dx.doi.org/10.3174/ajnr.A5651>

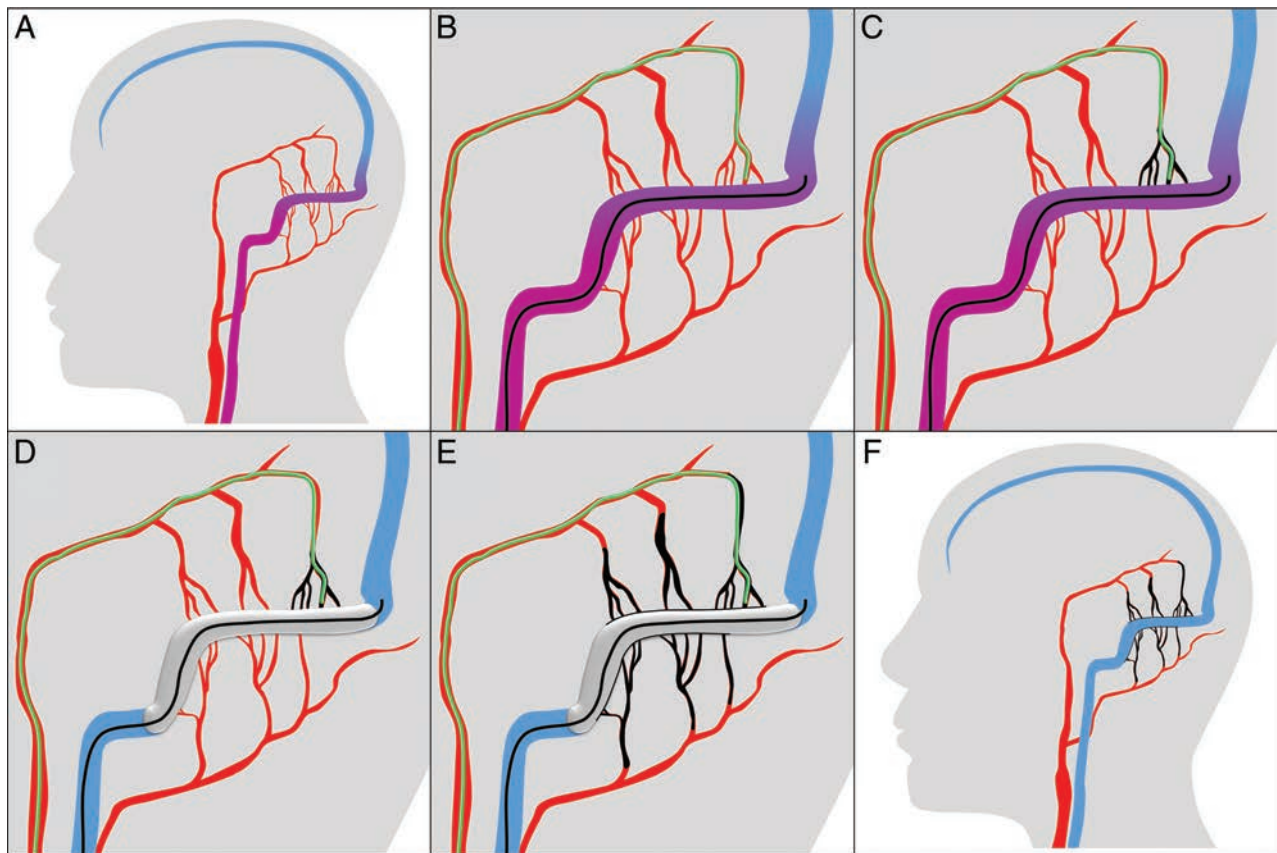


FIG 1. Schematic illustration of the treatment technique. *A*, The treatment technique is shown in the example of a Cognard I/Borden I dAVF located at the transverse and sigmoid sinuses with feeders from the occipital and middle meningeal arteries. *B*, After preinterventional diagnostic angiography, a balloon catheter (in black) is navigated into the affected sinus, and a microcatheter (in green) is navigated into the most promising feeder (in this example, the petrosquamosal branch of the middle meningeal artery). *C*, After superselective diagnostic angiographies via the microcatheter with and without balloon inflation, Onyx is injected under balloon deflation until the Onyx cast (in black) reaches the sinus. *D*, Subsequently, the balloon is inflated to prevent inadvertent embolization of the sinus and to enable retrograde embolization of the other arterial feeders. *E*, Onyx injection is continued under balloon inflation and deflation until embolization of all feeders is achieved. *F*, After the intervention, all feeding arteries are embolized and the sinus and the normal superficial veins (not shown) are preserved.

tion of the venous sinuses or normal superficial veins. So far, only a few studies on this technique with a relatively small number of patients are available.^{6,8,9,12,13}

The aim of this study was to report our consecutive single-center experience of patients with dAVFs who were treated with transarterial liquid embolization in combination with transvenous balloon-assisted protection of the venous sinus and to present the feasibility, effectiveness, and safety of this treatment technique.

MATERIALS AND METHODS

Clinical and Angiographic Analyses

Study approval and informed consent for data collection were provided by the local ethics committee and the patients, respectively.

A retrospective analysis of a prospectively maintained patient data base was performed to identify all subsequent patients with dAVFs who were treated with endovascular transarterial liquid embolization in combination with transvenous balloon-assisted protection of the venous sinus from January 2011 to November 2017.

Patient demographics, clinical presentation, and clinical follow-up were assessed and recorded by a board-certified neurolo-

gist, including preinterventional (on the day of the intervention) and postinterventional (at discharge and after 6 months) modified Rankin Scale scores. Angiographic features of the treated dAVFs were extracted, including location, type of fistula (according to the Cognard and Borden classifications^{14,15}), and territories and number of the feeding arteries, by 2 experienced neuroradiologists (D.F.V. and M.A.M. with 5 and 12 years of experience, respectively), one of whom had no involvement in the treatment. Procedural parameters, such as the number of procedures, number of embolization positions, and the preservation of the venous sinus were documented. Peri- and post-procedural complications were assessed and graded as asymptomatic complications, transient symptomatic complications, and symptomatic complications with permanent neurologic deficits. The initial complete angiographic occlusion rate was assessed after the last treatment procedure. Overall complete occlusion was defined as complete occlusion of the dAVF at the last follow-up examination, diagnosed with digital subtraction angiography, which was performed 6 months after the last treatment, and/or MR imaging, which was performed before discharge and during the follow-up.

Table 1: Patient demographics, clinical presentation, and angiographic features of the treated dAVFs^a

Patient demographics	
Total No. of patients	22
Patient age (yr)	55 ± 15
Male/female ratio	1:1
Clinical presentation	
Symptomatic patients	22 (100%)
Hemorrhage	1 (4.6%)
Preinterventional mRS	1 ± 1
dAVF location	
Transverse and/or sigmoid sinus	19 (86.4%)
Superior sagittal sinus	2 (9.1%)
Marginal sinus	1 (4.6%)
dAVF classification	
Cognard I	7 (31.8%)
Cognard IIa	6 (27.3%)
Cognard IIa+b	9 (40.9%)
Borden I	13 (59.1%)
Borden II	9 (40.9%)
Feeder territories	
Middle meningeal artery	21 (95.5%)
Occipital artery	21 (95.5%)
Internal carotid artery (dural branches)	19 (86.4%)
Vertebral artery (dural branches)	14 (63.6%)
Superficial temporal artery	11 (50.0%)
Other angiographic features	
Bilateral feeders	13 (59.1%)
No. of feeder territories	5 ± 2
≥20 Feeding arteries ^b	19 (86.4%)
<20 Feeding arteries ^b	3 (13.6%)

^a Data are presented as No. (relative frequency in %) or mean ± SD.

^b Feeding arteries with a length of ≥10 mm (measured from the dural sinus).

Patient Selection

Transarterial liquid embolization in combination with transvenous balloon-assisted protection of the affected venous sinus was chosen as the primary treatment technique in patients with patency and functioning of the affected sinus and location of the fistula point within the sinus wall. Contraindications for transvenous balloon-assisted protection of the sinus were nonpatency or nonfunctioning of the sinus (for example, due to high-grade stenosis or complete occlusion) or location of the fistula point in a sinus compartment, which can potentially be embolized selectively while preserving the sinus.¹⁶

Interventional Procedure

All interventions were performed with the patient under general anesthesia in a biplane angiography suite (Artis Q or Artis zee; Siemens, Erlangen, Germany). During the procedure, patients were anticoagulated using heparin to achieve an activated clotting time of >250 seconds. After puncture, a 6F introducer sheath was inserted into the right femoral artery and an 8F introducer sheath was inserted into the left femoral vein. Preinterventional bilateral diagnostic angiographies of the internal and external carotid arteries and of the vertebral arteries were performed. A schematic illustration of the treatment technique is shown in Fig 1. A compliant, dimethyl sulfoxide-compatible, venous remodeling balloon (Copernic RC, 8 × 80 or 10 × 80 mm; Balt Extrusion, Montmorency, France) was navigated via the transvenous route into the affected sinus covering the arterial feeders. Subsequently, a dimethyl sulfoxide-compatible microcatheter (Marathon microcatheter, Covidien, Irvine, California; or SONIC, Balt Extrusion)

was navigated into the most promising arterial feeder with the aim of achieving a distal position as close as possible to the fistula point.

Superselective diagnostic angiographies via the selected arterial feeder with and without balloon inflation were performed to assess the distribution into other arterial feeders and to determine the optimal embolization and balloon position. If one balloon was not sufficient for complete occlusion of the sinus or for complete coverage of the fistula, a second balloon was inserted. Afterward, transarterial embolization was performed using Onyx 18 (Covidien) under a roadmap technique. Simultaneously, the venous balloon was inflated and deflated with a maximum inflation time of 5 minutes. The balloon inflation pressure was manually adjusted to prevent migration of the embolic agent into the main sinus lumen and to simultaneously achieve retrograde penetration into the arterial feeders. After termination of the embolization procedure, diagnostic angiographies were performed via the feeder territories for treatment control.

RESULTS

Patient demographics, clinical presentation, and angiographic features of the treated dAVFs are summarized in Table 1.

Twenty-two patients diagnosed with dAVFs who were treated with endovascular transarterial liquid embolization in combination with transvenous balloon-assisted protection of the venous sinus from January 2011 to November 2017 were analyzed. All these patients were symptomatic, of whom 81.8% had tinnitus; 9.1%, ocular symptoms; 9.1%, headache; and 22.7%, other symptoms. One patient (4.6%) presented with an intracerebral hemorrhage. The fistulas were located at the transverse and/or sigmoid sinus (86.4%), the sagittal superior sinus (9.1%), or the marginal sinus (4.6%). Most treated fistulas were low-grade without cortical venous reflux (59.1%). According to the Cognard classification, the most frequent fistula type was IIa+b (40.9%), followed by I (31.8%) and IIa (27.3%). According to the Borden classification, the most frequent fistula type was I (59.1%), followed by II (40.9%). The middle meningeal artery, the occipital artery (both 95.5%), and dural branches of the internal carotid artery (86.4%) were the predominant arterial supplies.

Procedural parameters, treatment results, follow-up, and outcome are summarized in Table 2. An illustration of a representative case is shown in Fig 2.

Twenty-five treatment procedures were performed. In all patients, the treatment technique of the first procedure was transarterial Onyx embolization in combination with transvenous balloon protection. Two of the 3 patients who needed an additional treatment were again treated using the same technique, while for 1 patient, the second treatment consisted of coil embolization of the affected sinus. The reason for sinus occlusion in this patient was progressive thrombosis of the sinus, which was exclusively draining the fistula and was no longer involved in the normal venous drainage of the cranium. In 4 patients, 2 balloon catheters were required for adequate occlusion of the venous sinus or for complete coverage of the fistula. Most fistulas were embolized via the middle meningeal artery (80.0%); the second most frequently selected feeder was the occipital artery (24.0%).

The initial complete angiographic occlusion rate was 63.6%, followed by 5 more complete spontaneous occlusions during the

Table 2: Procedural parameters, treatment results, follow-up, and outcome^a

No. of treatment procedures	
Total No. of treatment procedures	25
1 treatment procedure per patient	19 (86.4%)
2 treatment procedures per patient	3 (13.6%)
Selected feeder for embolization	
Middle meningeal artery	18 (80.0%)
Occipital artery	5 (24.0%)
Others	2 (8.0%)
No. of embolization positions	
1	20 (80.0%)
≥2	5 (20.0%)
Complications	
Overall complications	5 (20.0%)
Asymptomatic complications	3 (12.0%)
Transient symptomatic complications	2 (8.0%)
Symptomatic complications with permanent neurologic deficits	0 (0%)
Follow-up	
Follow-up (mo)	18 ± 18
Postinterventional angiography available	17 (77.2%)
Postinterventional MRI available	22 (100%)
Angiographic outcome	
Initial complete angiographic occlusion	14 (63.6%)
Spontaneous occlusion after subtotal endovascular occlusion	5 (22.7%)
Time from last treatment to diagnosis of spontaneous occlusion (mo)	3.5 ± 6.0
Overall complete occlusion at last examination	19 (86.4%)
Residual fistula at last examination	3 (13.6%)
Clinical outcome	
Postinterventional mRS at discharge	1 ± 1
Postinterventional mRS 6 mo after treatment	1 ± 1
Complete symptom remission after treatment	15 (68.2%)
Symptom relief after treatment	6 (27.3%)
Stable symptoms after treatment	1 (4.6%)
Worsening of symptoms after treatment	0 (0%)

^aData are presented as No. (relative frequency in %) or mean ± SD.

follow-up period, resulting in an overall complete occlusion rate of 86.4%. One of the 3 patients with residual fistula on angiography had a low-grade fistula (Cognard IIa/Borden I) and showed complete symptom remission at the last clinical examination. The remaining 2 patients refused further treatment because of symptom relief. For the 5 patients with spontaneous occlusion after treatment, the mean time from treatment to diagnosis of spontaneous occlusion was 106 days, ranging from 7 days to 14 months.

After a mean follow-up of 18 months, most patients (68.2%) were free of symptoms, while 27.3% showed symptom relief and 4.6% had stable symptoms compared with the preinterventional status. Five patients still had symptoms (symptom relief for 4 patients and stable symptoms for 1 patient) despite complete occlusion of the fistula. These patients had nonpulsatile tinnitus ($n = 2$), headache ($n = 2$), and residual symptoms after severe venous congestion ($n = 1$). No patient died during the follow-up.

Postinterventional diagnostic angiography was performed in 77.2% of cases. From the patients without follow-up DSA, 3 patients refused further invasive diagnostic imaging because of complete symptom remission, and for 2 patients, follow-up DSA is still pending. Postinterventional MR imaging was performed in all patients.

Five procedure-related complications occurred, resulting in an overall complication rate of 20% (with respect to the number of treatment procedures). We recorded the following

complications: 2 small infarctions, 2 small subdural hemorrhages (most likely caused by vessel perforation during navigation of the microcatheter into the respective arterial feeder or during traction of the microcatheter after embolization), and 1 small intracerebral hemorrhage (<1 cm in diameter). In 1 patient with a small venous infarction, inadvertent embolization of the proximal part of the vein of Labbé could be identified as a suspected reason for the complication. For the small intracerebral hemorrhage, which was detected on a peri-interventional conebeam CT scan during the treatment of a patient with a Cognard IIa/Borden I dAVF, stasis in a small temporal vein, caused by the temporary balloon occlusion, could be identified as a suspected reason for the complication. Three complications were asymptomatic, and 2 complications were symptomatic. The 2 patients with symptomatic complications had headaches, which were declining until discharge and no longer present 6 months after treatment. No complication with permanent neurologic deficits was recorded. No procedure-related cranial neuropathies were observed.

DISCUSSION

Endovascular therapy has become the treatment of choice for most intracranial dAVFs and has considerably improved in recent years, which can—among other factors—be attributed to the introduction of new treatment techniques based on new devices, such as embolic agents, microcatheters, and balloon catheters.^{2,3,17} More recently, the strategy of neuroendovascular treatment aims to eliminate the respective pathology with preservation of the surrounding healthy vasculature. A promising technique for avoiding inadvertent occlusion of normal veins during transarterial embolization of dAVFs, which was first described by Shi et al¹³ in 2009, is the transient placement of a balloon in the affected venous sinus.^{6,8-10} The studies with the highest case numbers reporting this technique are those by Piechowiak et al⁶ and Ertl et al¹² in 2017. Piechowiak et al⁶ conducted a retrospective study of 9 patients with fistulas of the transverse and sigmoid sinuses who were treated using a technique that is similar to the technique described here. However, they used balloon assistance on both the venous and the arterial sides. Ertl et al¹² compared sinus-occluding and sinus-preserving endovascular treatment techniques for dAVFs, reporting on a subgroup of 11 patients treated with transarterial Onyx embolization combined with transvenous balloon-assisted protection of the venous sinus. In our retrospectively analyzed and prospectively maintained data base, 22 patients treated with transarterial liquid embolization in combination with transvenous balloon-assisted protection of the

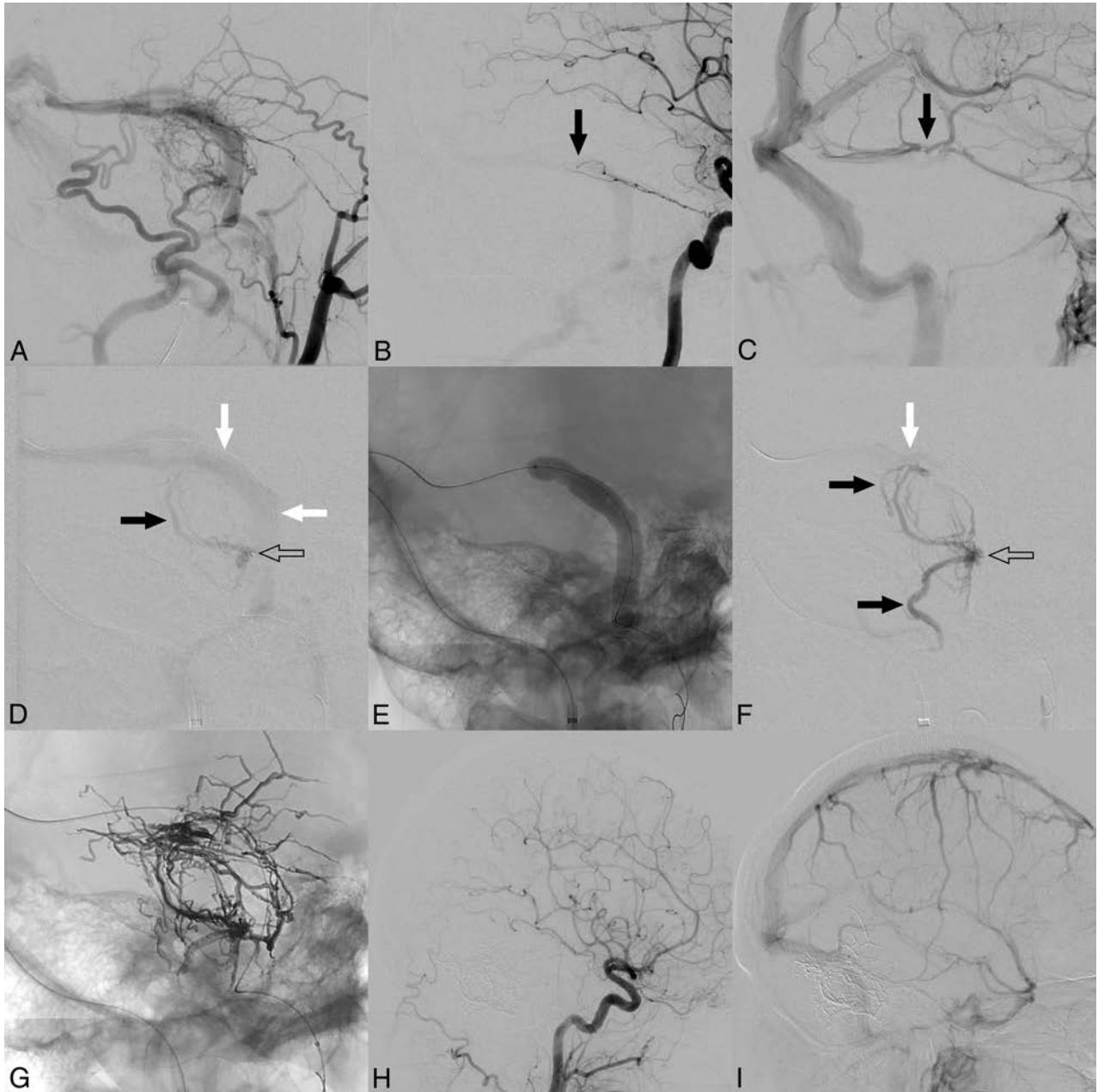


FIG 2. Illustration of a representative case. *A*, Right external carotid artery angiogram shows a Cognard IIa+b/Borden II dAVF located at the transverse and sigmoid sinuses with multiple feeding arteries out of numerous vascular territories. *B*, Right internal carotid artery angiogram shows dural branches of the internal carotid artery feeding the fistula (*black arrow*). *C*, Venous phase of *B*. Note the proximity of the fistula point (*black arrow* in *B*) to the junction of the vein of Labbé and of the inferior temporal veins into the sinus (*black arrow*). For successful treatment of the dAVF, the fistula point should be embolized while simultaneously preserving these veins. *D*, Superselective angiogram without balloon inflation via the feeder that was selected for embolization, the mastoid branch of the occipital artery (microcatheter tip marked with an *open arrow*). There is drainage via the sinus (*white arrows*) and only slight filling of the adjacent feeders (*black arrow*). *E*, Lateral x-ray shows the inflated balloon. *F*, Superselective angiogram after balloon inflation (microcatheter tip marked with an *open arrow*). Due to the temporary occlusion of the sinus, which shows only minimal enhancement at the edge of the balloon (*white arrow*) at the junction of the vein of Labbé and the inferior temporal veins (*C*), nearby feeders show marked filling of contrast agent (*black arrows*). The angiograms with the inflated balloon serve as a test injection to estimate the distribution of the subsequently injected liquid embolic agent. *G*, Onyx cast after embolization with distribution of the embolic agent in all feeding artery territories. Common carotid artery angiogram of the arterial (*H*) and venous (*I*) phases 6 months after treatment shows complete occlusion of the fistula and patency of the venous sinuses and the normal superficial veins.

venous sinus were analyzed, and the feasibility, effectiveness, and safety of this treatment technique were investigated.

Except for 1 patient in our study in whom the affected sinus was occluded by coil embolization, preservation of the sinus could be achieved in all procedures. In the above-mentioned studies, the

postinterventional patency of the respective sinus was not specifically reported.^{6,12,13}

The described embolization technique promotes the preservation of the normal venous structures. In addition, another major advantage of the technique is described here. Not only is the arte-

rial feeder through which the injection is performed being embolized but feeders from other arterial territories with connection to the respective sinus segment are also embolized in a retrograde manner by migration of embolic agent along the balloon and the sinus wall into the feeders. As a result, feeding arteries that are difficult or technically impossible to catheterize can be easily embolized and the number of arterial feeders to be catheterized can be reduced, potentially lowering the risk of periprocedural technical complications and also reducing the procedure time. Accordingly, in most cases in our study, only 1 embolization position was necessary for complete or near-complete embolization of the dAVFs. This is important because most of the dAVFs of the transverse and sigmoid sinuses have multiple feeders,¹⁸ as was the case in our series, in which 86% of the treated fistulas had >20 arterial feeding arteries. In this context, besides the facilitation of embolization of feeding arteries, this treatment technique also bears the risk of inadvertent embolization of cortical veins draining into the sinus. To prevent this complication, these veins must be carefully observed during the embolization, and if necessary, the balloon must be repositioned or another arterial feeder selected for embolization.

The overall complete occlusion rate of 86% in our series is comparable with the results of Piechowiak et al,⁶ who achieved complete occlusion or substantial flow reduction in 89% of patients treated with balloon-assistance on the arterial and venous sides. Similarly, Ertl et al¹² reported a complete occlusion rate of 71% for sinus-preserving endovascular treatments (not further subdivided with respect to the specific treatment technique).

Most of the fistulas in our series were low-grade without cortical venous reflux. For this type of fistula, the risk of bleeding is relatively low; therefore, substantial relief or complete remission of symptoms is the main aim of the treatment.¹⁹ The high rate of complete symptom remission and symptom relief of 95% in our study is in accordance with the results of recently published studies and underlines the effectiveness of endovascular embolization for the treatment of this type of dAVF.^{3,6,12}

A significantly lower complication rate for sinus-preserving than for sinus-occluding techniques has been reported in a recently published study (0% versus 33%), however, with a higher rate of permanent fistula occlusion for sinus-occluding techniques.¹² In our study, the overall complication rate was 20% without any permanent neurologic deficits. Of the 5 complications that occurred in the present study, 2 can be attributed to the balloon occlusion of the venous sinus: 1 case of venous infarction due to inadvertent embolization of the proximal part of the vein of Labbé (facilitated by the balloon occlusion) and 1 case of intracerebral hemorrhage due to stasis of a small temporal vein caused by the temporary balloon occlusion itself. For the second patient who developed a venous infarction, no specific reason could be identified; however, the 2 above-mentioned mechanisms might also have contributed to this complication. To prevent procedure-related complications, as mentioned above, special attention should be paid to cortical veins draining into the affected sinus because inadvertent occlusion of these structures (both by inadvertent embolization and by too long temporary balloon occlusion) can lead

to venous congestion and/or hemorrhage. The low rate of symptomatic complications is in line with data from other studies of sinus-preserving and sinus-occluding techniques with and without balloon-assistance.^{3,5,6,12,20}

A potential limitation of this study is its relative low case number. However, to the best of our knowledge, this is the largest study reporting on this treatment technique. Furthermore, the study was conducted in a single institution with retrospective analysis of prospectively maintained data, which is a potential limitation on the study findings.

CONCLUSIONS

Transarterial liquid embolization in combination with transvenous balloon-assisted protection of the venous sinus is feasible and safe for the treatment of dAVFs and offers high rates of complete occlusion and of complete symptom remission or relief. Further studies with higher case numbers and long-term follow-up are necessary to further assess the value of this treatment technique.

Disclosures: Dominik F. Vollherbst—UNRELATED: Travel/Accommodations/Meeting Expenses Unrelated to Activities Listed: MicroVention, Stryker*. Christian Ulfert—UNRELATED: Travel/Accommodations/Meeting Expenses Unrelated to Activities Listed: MicroVention, Stryker. Christian Herweh—UNRELATED: Consultancy: Brainomix, Oxford, UK, Comments: <€10,000. Simon Nagel—UNRELATED: Consultancy: Brainomix, Boehringer Ingelheim; Payment for Lectures Including Service on Speakers Bureaus: Pfizer, Medtronic, Bayer AG. Martin Bendszus—UNRELATED: Board Membership: Data and Safety Monitoring Board for Vascular Dynamics, Guerbet, Boehringer Ingelheim; Consultancy: Codman, Roche Diagnostics, Guerbet, Boehringer Ingelheim, Braun; Grants/Grants Pending: DFG, Hopp Foundation, Novartis, Siemens, Guerbet, Stryker, Covidien*; Payment for Lectures Including Service on Speakers Bureaus: Novartis, Roche Diagnostics, Guerbet, Teva Pharmaceutical Industries, Bayer AG, Codman. Markus A. Möhlenbruch—UNRELATED: Board Membership: Codman; Consultancy: Medtronic, MicroVention, Stryker; Payment for Lectures Including Service on Speakers Bureaus: Medtronic, MicroVention, Stryker. *Money paid to the institution.

REFERENCES

1. Gross BA, Du R. **The natural history of cerebral dural arteriovenous fistulae.** *Neurosurgery* 2012;71:594–602; discussion 602–03 CrossRef Medline
2. Rammos S, Bortolotti C, Lanzino G. **Endovascular management of intracranial dural arteriovenous fistulae.** *Neurosurg Clin N Am* 2014;25:539–49 CrossRef Medline
3. Gross BA, Albuquerque FC, Moon K, et al. **Evolution of treatment and a detailed analysis of occlusion, recurrence, and clinical outcomes in an endovascular library of 260 dural arteriovenous fistulas.** *J Neurosurg* 2017;126:1884–93 CrossRef Medline
4. Spiotta AM, Miranpuri AS, Vargas J, et al. **Balloon augmented Onyx embolization utilizing a dual lumen balloon catheter: utility in the treatment of a variety of head and neck lesions.** *J Neurointerv Surg* 2014;6:547–55 CrossRef Medline
5. Chiu AH, Aw G, Wenderoth JD. **Double-lumen arterial balloon catheter technique for Onyx embolization of dural arteriovenous fistulas: initial experience.** *J Neurointerv Surg* 2014;6:400–03 CrossRef Medline
6. Piechowiak E, Zibold F, Dobrocky T, et al. **Endovascular treatment of dural arteriovenous fistulas of the transverse and sigmoid sinuses using transarterial balloon-assisted embolization combined with transvenous balloon protection of the venous sinus.** *AJNR Am J Neuroradiol* 2017;38:1984–89 CrossRef Medline
7. Kim JW, Kim BM, Park KY, et al. **Onyx embolization for isolated type dural arteriovenous fistula using a dual-lumen balloon catheter.** *Neurosurgery* 2016;78:627–36 CrossRef Medline
8. Jittapiromsak P, Ikka L, Benachour N, et al. **Transvenous balloon-**

- assisted transarterial Onyx embolization of transverse-sigmoid dural arteriovenous malformation. *Neuroradiology* 2013;55:345–50 CrossRef Medline
9. Zhang Y, Li Q, Huang QH. Embolization of a superior sagittal sinus dural arteriovenous fistula under intrasinus balloon protection: a case report. *Interv Neuroradiol* 2015;21:94–100 CrossRef Medline
 10. Kerolus MG, Chung J, Munich SA, et al. An Onyx tunnel: reconstructive transvenous balloon-assisted Onyx embolization for dural arteriovenous fistula of the transverse-sigmoid sinus. *J Neurosurg* 2017 Nov 17:1–6. [Epub ahead of print] CrossRef Medline
 11. Choi BJ, Lee TH, Kim CW, et al. Reconstructive treatment using a stent graft for a dural arteriovenous fistula of the transverse sinus in the case of hypoplasia of the contralateral venous sinuses: technical case report. *Neurosurgery* 2009;65:E994–96; discussion E996 CrossRef Medline
 12. Ertl L, Brückmann H, Kunz M, et al. Endovascular therapy of low- and intermediate-grade intracranial lateral dural arteriovenous fistulas: a detailed analysis of primary success rates, complication rates, and long-term follow-up of different technical approaches. *J Neurosurg* 2017;126:360–67 CrossRef Medline
 13. Shi ZS, Loh Y, Duckwiler GR, et al. Balloon-assisted transarterial embolization of intracranial dural arteriovenous fistulas. *J Neurosurg* 2009;110:921–28 CrossRef Medline
 14. Cognard C, Gobin YP, Pierot L, et al. Cerebral dural arteriovenous fistulas: clinical and angiographic correlation with a revised classification of venous drainage. *Radiology* 1995;194:671–80 CrossRef Medline
 15. Borden JA, Wu JK, Shucart WA. A proposed classification for spinal and cranial dural arteriovenous fistulous malformations and implications for treatment. *J Neurosurg* 1995;82:166–79 CrossRef Medline
 16. Piske RL, Campos CM, Chaves JB, et al. Dural sinus compartment in dural arteriovenous shunts: a new angioarchitectural feature allowing superselective transvenous dural sinus occlusion treatment. *AJNR Am J Neuroradiol* 2005;26:1715–22 Medline
 17. Serulle Y, Miller TR, Gandhi D. Dural arteriovenous fistulae: imaging and management. *Neuroimaging Clin N Am* 2016;26:247–58 CrossRef Medline
 18. Nishijima M, Takaku A, Endo S, et al. Etiological evaluation of dural arteriovenous malformations of the lateral and sigmoid sinuses based on histopathological examinations. *J Neurosurg* 1992;76:600–06 CrossRef Medline
 19. Davies MA, Ter Brugge K, Willinsky R, et al. The natural history and management of intracranial dural arteriovenous fistulae, Part 2: aggressive lesions. *Interv Neuroradiol* 1997;3:303–11 CrossRef Medline
 20. Rangel-Castilla L, Barber SM, Klucznik R, et al. Mid and long term outcomes of dural arteriovenous fistula endovascular management with Onyx: experience of a single tertiary center. *J Neurointerv Surg* 2014;6:607–13 CrossRef Medline

Risk of Branch Occlusion and Ischemic Complications with the Pipeline Embolization Device in the Treatment of Posterior Circulation Aneurysms

 N. Adeb,  C.J. Griessenauer,  A.A. Dmytriw,  H. Shallwani,  R. Gupta,  P.M. Foreman,  H. Shakir,  J. Moore,  N. Limbucci,  S. Mangiafico,  A. Kumar,  C. Michelozzi,  Y. Zhang,  V.M. Pereira,  C.C. Matouk,  M.R. Harrigan,  A.H. Siddiqui,  E.I. Levy,  L. Renieri,  T.R. Marotta,  C. Cognard,  C.S. Ogilvy, and  A.J. Thomas



ABSTRACT

BACKGROUND AND PURPOSE: Flow diversion with the Pipeline Embolization Device is increasingly used for endovascular treatment of intracranial aneurysms due to high reported obliteration rates and low associated morbidity. While obliteration of covered branches in the anterior circulation is generally asymptomatic, this has not been studied within the posterior circulation. The aim of this study was to evaluate the association between branch coverage and occlusion, as well as associated ischemic events in a cohort of patients with posterior circulation aneurysms treated with the Pipeline Embolization Device.

MATERIALS AND METHODS: A retrospective review of prospectively maintained databases at 8 academic institutions from 2009 to 2016 was performed to identify patients with posterior circulation aneurysms treated with the Pipeline Embolization Device. Branch coverage following placement was evaluated, including the posterior inferior cerebellar artery, anterior inferior cerebellar artery, superior cerebellar artery, and posterior cerebral artery. If the Pipeline Embolization Device crossed the ostia of the contralateral vertebral artery, its long-term patency was assessed as well.

RESULTS: A cohort of 129 consecutive patients underwent treatment of 131 posterior circulation aneurysms with the Pipeline Embolization Device. Adjunctive coiling was used in 40 (31.0%) procedures. One or more branches were covered in 103 (79.8%) procedures. At a median follow-up of 11 months, 11% were occluded, most frequently the vertebral artery (34.8%). Branch obliteration was most common among asymptomatic aneurysms ($P < .001$). Ischemic complications occurred in 29 (22.5%) procedures. On multivariable analysis, there was no significant difference in ischemic complications in cases in which a branch was covered ($P = .24$) or occluded ($P = .16$).

CONCLUSIONS: There was a low occlusion incidence in end arteries following branch coverage at last follow-up. The incidence was higher in the posterior cerebral artery and vertebral artery where collateral supply is high. Branch occlusion was not associated with a significant increase in ischemic complications.

ABBREVIATIONS: PCA = posterior cerebral artery; PED = Pipeline Embolization Device; VA = vertebral artery

Flow diversion using the Pipeline Embolization Device (PED; Covidien, Irvine, California) has become an important treatment technique for intracranial aneurysms. Although the mechanism of action of this device is still not completely understood, it

is expected to initially reduce the intra-aneurysmal flow leading to aneurysm thrombosis and seal off the aneurysm from circulation by inducing neointimal coverage of the PED surface at the aneurysm neck.¹ When the PED spans an arterial branch, there is concern for branch occlusion and subsequent ischemic stroke. Among others, this concern had limited the Food and Drug Administration approval of PED use to the internal carotid artery below the level of the posterior communicating artery.² Since this decision, the PED has only been used reluctantly in the treatment of posterior circulation aneurysms where multiple branches supply the brain stem. A handful of studies have evaluated the off-

Received November 21, 2017; accepted after revision April 10, 2018.

From the Beth Israel Deaconess Medical Center (N.A., C.J.G., A.A.D., R.G., J.M., C.S.O., A.J.T.), Harvard Medical School, Boston, Massachusetts; Department of Neurosurgery (C.J.G.), Geisinger Medical Center, Geisinger Commonwealth School of Medicine, Danville, Pennsylvania; Department of Medical Imaging (A.A.D., Y.Z., V.M.P.), Toronto Western Hospital, University Health Network, Toronto, Ontario, Canada; Division of Diagnostic and Therapeutic Neuroradiology (A.A.D., A.K., T.R.M.), St. Michael's Hospital, Toronto, Ontario, Canada; Department of Neurosurgery (H. Shallwani, H. Shakir, A.H.S., E.I.L.), State University of New York at Buffalo, Buffalo, New York; Department of Neurosurgery (P.M.F., M.R.H.), University of Alabama at Birmingham, Birmingham, Alabama; Department of Interventional Neuroradiology (N.L., S.M., L.R.), University of Florence, Florence, Italy; Department of Diagnostic and Therapeutic Neuroradiology (C.M., C.C.), Toulouse University Hospital, Toulouse, France; and Department of Neurosurgery (C.C.M.), Yale School of Medicine, New Haven, Connecticut.

Please address correspondence to Ajith J. Thomas, MD, Beth Israel Deaconess Medical Center, Harvard University, 110 Francis St, Suite 3B, Boston, MA 02115; e-mail: athomas6@bidmc.harvard.edu

 Indicates article with supplemental on-line table.

<http://dx.doi.org/10.3174/ajnr.A5696>

label use of the PED in the treatment of posterior circulation aneurysms and reported a relatively high risk of ischemic complications, particularly in the treatment of fusiform aneurysms.³⁻⁹ In this study, we aimed to assess the association between branch coverage and occlusion incidence and its impact on ischemic complications.

MATERIALS AND METHODS

A retrospective review of prospectively maintained databases at 8 academic institutions in North America and Europe was performed from 2009 to 2016 to identify adult patients (18 years of age or older) with posterior circulation aneurysms treated consecutively with the PED. Both ruptured and unruptured aneurysms and all aneurysm shapes were included. Patients younger than 18 years of age were excluded. The following information was collected prospectively by the treating neurointerventionalists: patient demographics, aneurysm characteristics, platelet function test results, antiplatelet regimen, procedural details, angiographic and functional outcomes, and complications. Aneurysm measurements were obtained using digital subtraction angiography, except in cases of partially thrombosed aneurysms in which axial images were also analyzed. Institutional review board approval was obtained at all centers. The primary end point for the study was the occurrence of branch occlusion after placement of the PED across major posterior circulation branches. The secondary end point was the occurrence of ischemic complications following branch occlusion.

Procedure Details

Patients received aspirin, 325 mg daily, and clopidogrel, 75 mg daily, for 3–14 days before the intervention. Platelet function testing was routinely performed by some of the centers using whole-blood lumiaggregometry, light transmission aggregometry, or the VerifyNow P2Y12 assay (Accumetrics, San Diego, California). In those centers, clopidogrel nonresponders were identified on the basis of established cutoff values at the individual institutions and were guided by manufacturer's recommendations. If a patient was identified as a clopidogrel nonresponder, the choice to continue the same dose of clopidogrel, administer a 1-time 600-mg clopidogrel boost within 24 hours preprocedure, or switch to an alternative antiplatelet agent was at the discretion of the interventionist performing the procedure. All patients were anticoagulated with heparin throughout the procedure. Activated clotting time was used in most cases to guide heparin administration intraprocedurally, with a target of 250–300 seconds; typical dosing consisted of a 3000- to 5000-U bolus at the beginning of the procedure, with hourly dosing of 1000 U. The guide catheter and microcatheter used for PED deployment were at the discretion of the individual interventionalists. The deployment and apposition of the PED to the vessel wall were documented using fluoroscopy. Dual antiplatelet therapy was continued for at least 3 months after the procedure.

Branch Coverage and Obliteration

Branch coverage and occlusion following PED placement were assessed on procedural DSA and last follow-up imaging, respectively. Only complete branch occlusion was considered. MR an-

giography was used as a follow-up technique in 1 center, but DSA was used to confirm branch occlusion if suspected. Vessels assessed included the posterior inferior cerebellar artery, anterior inferior cerebellar artery, superior cerebellar artery, and posterior cerebral artery (PCA). In addition, if the PED crossed the ostia of the contralateral vertebral artery (VA), the long-term patency of the covered VA was also assessed. Because brain stem perforator vessels are too small to resolve on DSA, we did not attempt to assess them. However, if brain stem infarct occurred, the possibility of perforator infarcts was considered. When we assessed predictors of branch occlusion following coverage, each covered branch was considered as a separate entity.

Ischemic Complications

Ischemic complications occurring from the date of the procedure to last follow-up were included. Intraprocedural thromboembolic complications were identified on DSA as either thrombus formation, slow filling of a previously normally filling vessel, or vessel drop-out. Postprocedural ischemic complications were identified using a combination of clinical and radiographic findings. Postprocedural imaging was performed at the discretion of the treating physician and was only obtained due to clinical concern. Routine screening for clinically silent ischemic strokes was not performed. Only ischemic strokes in the territory of the treated vessel were included. An ischemic complication was considered symptomatic if the patient reported symptoms or signs attributable to an ischemic event; this included transient or resolving signs and symptoms.

Statistical Analysis

Statistical analysis was performed using SPSS 21.0 (IBM, Armonk, New York). In univariable analysis, variables were compared between groups with the Mann-Whitney test for numeric variables and the χ^2 test for categorical variables. Statistical significance was defined as $P < .05$. Multivariable logistic regression was performed on candidate predictor variables to identify variables independently associated with branch occlusion following coverage and thromboembolic complications following PED placement after controlling for potential confounders. Accounting for interactions and collinearity among variables was undertaken.

RESULTS

Patient and Aneurysm Characteristics

One-hundred twenty-nine consecutive patients (median age, 58 years; male/female ratio, 1:1.7) underwent 129 procedures to treat 131 posterior circulation aneurysms with the PED. Smoking and multiple aneurysms were encountered in 33.3% and 24.8% of procedures, respectively. Most patients presented with neurologic deficits caused by aneurysm rupture or direct neurovascular compression (55%). Incidental aneurysms were identified in 21.7% of procedures. Treatment of immediate (<24 hours) or acute (>24 hours and <2 weeks) aneurysmal SAH occurred in 14.0% and 5.4% of procedures, respectively. Most aneurysms were fusiform (40.5%) or saccular (37.4%) and were commonly located along the intracranial segment of the VA (35.1%) or the basilar artery (34.5%). The median maximum diameter was 12 mm, and a daughter sac was present in 19.8% of aneurysms. Platelet func-

Table 1: Baseline characteristics

Parameter	No.
No. of procedures	129
No. of aneurysms	131
No. of branches covered	228
Sex	
Female	82 (63.6%)
Male	47 (36.4%)
Median age (range) (yr)	58 (29–82)
Smoking ^a	40 (33.3%)
Multiple aneurysms	32 (24.8%)
Presenting symptoms	
Asymptomatic	28 (21.7%)
Headache/dizziness	30 (23.3%)
Neurologic deficit	71 (55%)
Subarachnoid hemorrhage	
Immediate (<24 hr)	18 (14.0%)
Acute (>24 hr and <2 wk)	7 (5.4%)
Remote (>2 wk)	14 (10.9%)
Pretreatment mRS	
0–2	101 (78.3%)
3–5	28 (21.7%)
Aneurysm shape	
Saccular	49 (37.4%)
Fusiform	53 (40.5%)
Dissecting	29 (22.1%)
Aneurysm location	
Vertebral artery	46 (35.1%)
PICA	10 (7.6%)
Vertebrobasilar artery	18 (13.6%)
Basilar artery	45 (34.5%)
SCA	4 (3.1%)
PCA	8 (6.1%)
Aneurysm measurements (median) (range) (mm)	
Maximal diameter	12 (2–73)
Neck size (for saccular aneurysms)	5.35 (2–15)
Daughter sac	26 (19.8%)
Prior treatment	
Endovascular	14 (10.7%)
Surgery	2 (1.5%)
Both	1 (0.8%)
Platelet function test	77 (59.7%)
Clopidogrel nonresponders	14 (18.2%)
Treatment of nonresponders	
Continue clopidogrel	8 (57.1%)
Switch to ticagrelor	5 (35.8%)
Other	1 (7.1%)

Note:—SCA indicates superior cerebellar artery.

^a Data are missing for 9 procedures.

tion testing was performed in 59.7% of procedures, and the incidence of clopidogrel nonresponders was 18.2% of those tested (Table 1).

Treatment Outcome

The median number of PEDs deployed was 1 (range, 1–14). Adjunctive coiling was used in 31% of procedures. Following PED placement, ≥ 1 branch was covered in 79.8% of procedures. At a median follow-up of 11 months (range, 172 months), complete or near-complete aneurysm occlusion ($\geq 90\%$) was achieved in 78.1% of aneurysms. Retreatment with endovascular techniques was necessary in 8.4% of aneurysms. At last follow-up, the mRS improved in 34.4% and worsened in 22.4%, inclusive of patients presenting with aneurysmal SAH. The overall mortality rate was 11.2% (Table 2).

Table 2: Outcome measures

Parameter	No.
No. of Pipelines deployed (median) (range)	1 (1–14)
Adjunctive coiling	40 (31%)
Procedures with covered branches	103 (79.8%)
No. of covered branches (median) (range)	2 (0–6)
Last angiographic follow-up (median) (range) (mo) ^a	11 (1–72)
Follow-up aneurysm occlusion rate ^a	
Complete (100%)	85 (66.4%)
Near-complete (90%–99%)	15 (11.7%)
Partial (<90%)	28 (21.9%)
Retreatment	
Endovascular	11 (8.4%)
Outcome of covered branches ^b	228
Occluded (overall)	25 (11%)
VA	23
Occluded	8 (34.8%)
PICA	49
Occluded	4 (8.2%)
AICA	78
Occluded	6 (7.7%)
SCA	61
Occluded	3 (4.9%)
PCA	17
Occluded	4 (23.5%)
Last clinical follow-up (median) (range) (mo) ^c	8 (0.3–72)
Posttreatment mRS ^c	
0–2	99 (79.2%)
3–5	12 (9.6%)
6 (Death)	14 (11.2%)
Follow-up mRS ^c	
Improved	43 (34.4%)
No change	54 (43.2%)
Worsened	28 (22.4%)
Ischemic complications	29 (22.5%)
Timing	
Intraprocedural	2 (1.6%)
Postprocedural	27 (20.9%)
Location	
Brain stem	13 (10.1%)
Cerebellum	13 (10.1%)
PCA territory	10 (7.8%)
Symptomatic	17 (13.2%)
Temporary	6 (4.7%)
Permanent	11 (8.5%)
Territory of ischemic complications	
Same as covered branch	21 (72.4%)
Different	8 (27.6%)

Note:—SCA indicates superior cerebellar artery.

^a Data were missing on 3 aneurysms.

^b Each covered branch was considered separately.

^c Data were missing on 4 procedures.

Predictors of Branch Occlusion and Ischemic Stroke following PED Placement

The rate of aneurysm occlusion following coverage was 11% (25/228). There was a higher branch occlusion incidence when the PED covered posterior circulation branches in asymptomatic patients with incidental aneurysms ($P < .001$). The VA (34.8%) and PCA (23.5%) were associated with a significantly higher incidence of occlusion compared with other posterior circulation branches ($P = .001$). There was an increased incidence of branch occlusion when ≥ 2 branches were covered in the same procedure, but this was not statistically significant ($P = .07$).

Ischemic complications occurred in 22.5% of procedures, while permanent symptomatic ischemic complications occurred

in 8.5%. On univariable analysis, the risk of ischemic complications was significantly higher when vascular branches were covered with the PED compared with cases with no branch coverage (26.2% versus 7.7%, $P = .04$). The territory of ischemia was the same as the covered branch in 72.4% of cases. Among the cases with covered branches, there was no significant difference in the incidence of ischemic complications regarding branch occlusion ($P = .16$) (Fig 1). All 3 cases in which branch occlusion was associated with an ischemic complication in the same territory involved the AICA (Fig 2). There was no significant difference in branch occlusion ($P = .018$) or ischemic complications ($P = .7$) per aneurysm morphology (Table 3 and On-line Table).

DISCUSSION

In this multicenter study, we report the fate of major posterior circulation branches after placement of PEDs in the treatment of intracranial aneurysms. In our study, 25 of 228 covered branches were obliterated following coverage (11%). The VA and PCA were associated with the highest incidence of vascular obliteration, while the superior cerebellar artery was associated with the lowest

incidence. Despite this variability, there was no significant difference in the incidence of ischemic complications based on the covered branch. The presence of a covered branch was associated with a significant increase in the incidence of ischemia on univariable analysis. However, it was not significant as an independent predictor, regardless of the number of covered branches. Intramural thrombosis was associated with a significant increase in ischemic complication incidence on multivariable analysis.

Treatment of Posterior Circulation Aneurysms Using the PED

Posterior circulation aneurysms are often associated with a higher incidence of morbidity and mortality compared with their anterior circulation counterparts; this is mainly related to higher rates of aneurysm rupture and neurovascular compression caused by large dolichoectatic aneurysms.^{10,11} Flow diversion using the PED has gained popularity as an off-label treatment option.³⁻⁹

Flow diverters are designed to seal aneurysms from the circulation by diverting blood flow away from the aneurysm, allowing intra-aneurysm thrombus formation followed by neointimal

growth across the neck of the aneurysm.¹ Intimal growth over the luminal surface of a flow-diversion device is expected to be seen as a tissue layer consisting of smooth muscle cells covered by endothelium (endothelialization), while thrombus organization is expected to be visualized in the form of smooth-muscle cell invasion and connective tissue formation within the clot.¹

Despite widespread reluctance to use the PED for treatment of posterior circulation aneurysms, a handful of studies have attempted to evaluate the safety and efficacy in this high-risk group of aneurysms. The incidence of thromboembolic complications in these studies ranged between 0% and 22.5%³⁻⁹ and was particularly high in fusiform aneurysms. A possible explanation for this

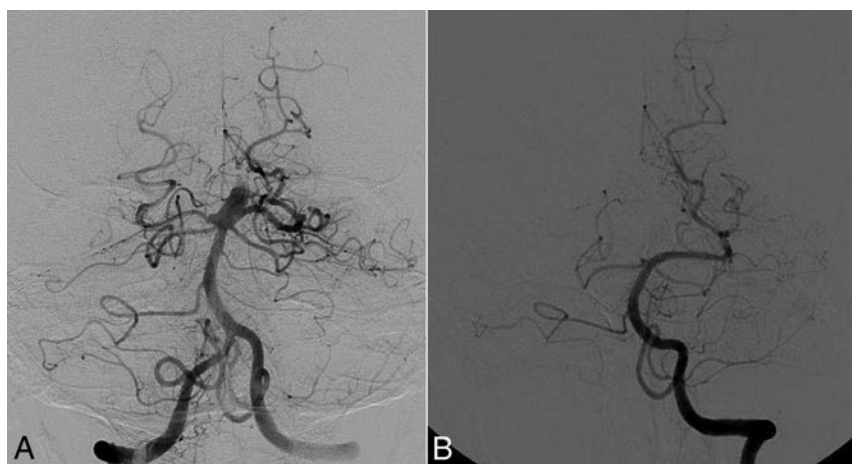


FIG 1. Digital subtraction angiography shows a basilar tip sacular aneurysm before treatment with the Pipeline Embolization Device (A). The PED was placed spanning the lower part of the basilar trunk into the left posterior cerebral artery. On 4-month follow-up (B), DSA shows complete aneurysm occlusion, along with complete occlusion of the right PCA. The anterior inferior cerebral arteries and superior cerebellar arteries remained patent. The patient remained neurologically intact.

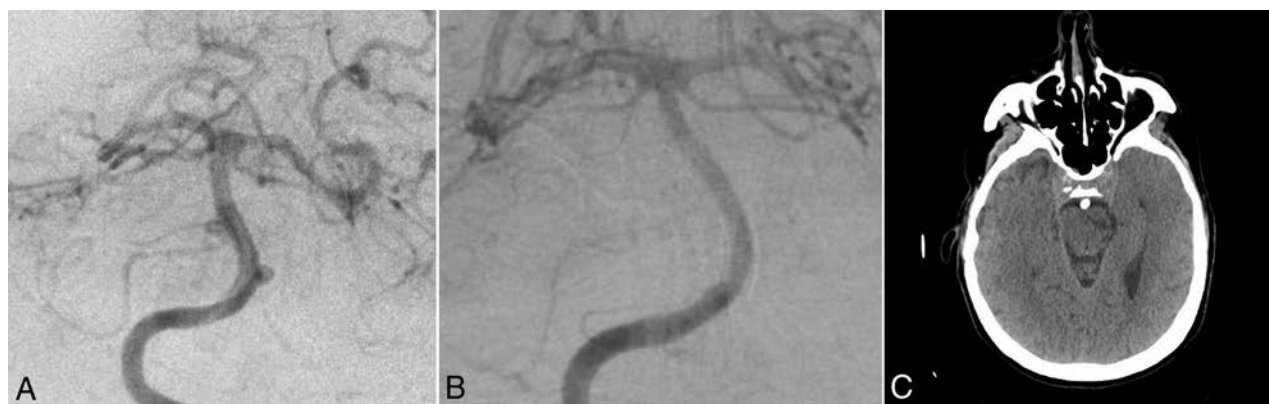


FIG 2. Digital subtraction angiography shows 2 basilar trunk sacular aneurysms before treatment with the Pipeline Embolization Device (A). The PED was placed spanning the AICA bilaterally. On follow-up DSA (B), there was complete occlusion of the left AICA. The patient had a symptomatic left-sided pontine stroke that remained symptomatic at 10-month follow-up (C).

Table 3: Predictors of branch occlusion following coverage

Parameter	Branch Occlusion (No.) (%)		P Value
	Not Occluded (n = 203)	Occluded (n = 25)	
Sex			
Female	108 (87.1%)	16 (12.9%)	.3
Male	95 (91.3%)	9 (8.7%)	
Median age (range) (yr)	59.5 (29–82)	61 (42–78)	.56
Smoking ^a			
Yes	53 (82.8%)	11 (17.2%)	.1
No	137 (90.7%)	14 (9.3%)	
Presenting symptoms			
Asymptomatic	32 (72.7%)	12 (27.3%)	<.001
Headache/dizziness	38 (88.4%)	5 (11.5%)	
Neurologic deficit	133 (94.3%)	8 (5.7%)	
Subarachnoid hemorrhage			
No	141 (87.6%)	20 (12.4%)	.36
Acute (<24 hr)	25 (96.2%)	1 (3.8%)	
Immediate (<2 wk)	11 (100%)	0%	
Remote (>2 wk)	26 (86.7%)	4 (13.3%)	
Pretreatment mRS			
0–2	160 (87.4%)	23 (12.6%)	.12
3–5	43 (95.6%)	2 (4.4%)	
Aneurysm shape			
Saccular	74 (84.1%)	14 (15.9%)	.18
Fusiform	89 (91.8%)	8 (8.2%)	
Dissecting	38 (92.7%)	3 (7.3%)	
Aneurysm measurements			
Maximal diameter			
<7 mm	32 (84.2%)	6 (15.8%)	.23
7–12 mm	50 (84.7%)	9 (15.3%)	
13–24 mm	52 (89.7%)	6 (10.3%)	
>24 mm	69 (94.5%)	4 (5.5%)	
Daughter sac			
Yes	45 (90%)	5 (10%)	.8
No	158 (88.8%)	20 (11.2%)	
Intra-aneurysmal thrombus			
Yes	68 (94.4%)	4 (5.6%)	.08
No	135 (86.5%)	21 (13.5%)	
Prior treatment			
No	174 (88.3%)	23 (11.7%)	.8
Endovascular	25 (92.6%)	2 (7.4%)	
Surgery	3 (100%)	0%	
Both	1 (100%)	0%	
Platelet function testing			
Yes	128 (85.3%)	22 (14.7%)	.01
No	75 (96.2%)	3 (3.8%)	
Clopidogrel responders ^b			
Yes	110 (86.6%)	17 (13.4%)	.3
No	18 (78.3%)	5 (21.7%)	
Adjunctive coiling			
Yes	75 (88.2%)	10 (11.8%)	.77
No	128 (89.5%)	15 (10.5%)	
No. of Pipelines deployed (median) (range)	1 (1–14)	1 (1–4)	.33
Length of procedure (median) (range) (min)	110 (22–410)	114 (32–271)	.8
Branch			
VA	15 (65.2%)	8 (34.8%)	.001
PICA	45 (91.8%)	4 (8.2%)	
AICA	72 (92.3%)	6 (7.7%)	
SCA	58 (95.1%)	3 (4.9%)	
PCA	13 (76.5%)	4 (23.5%)	
No. of covered branches in same procedure			
1	37 (97.4%)	1 (2.6%)	.07
≥2	166 (87.4%)	24 (12.6%)	

Note:—SCA indicates superior cerebellar artery.

^a Data are missing for 13 branches.

^b Among patients with platelet function testing.

finding was the higher likelihood of branch coverage when fusiform aneurysms were treated with the PED. Moreover, fusiform aneurysms can often be associated with intramural thrombosis,

and placement of the PED is particularly hazardous because critical perforators may only be supplied through tenuous channels crossing the thrombus.⁹ However, in this study, most ischemic complications were either temporary or asymptomatic, and only 8.5% of procedures were affected by permanent symptomatic ischemic complications.

Branch Coverage and Occlusion following PED Placement

Initial evaluation of the PED by Kallmes et al^{12,13} showed that despite placement of multiple overlapping flow-diversion devices in the rabbit aorta, lumbar branch vessels remained patent at follow-up. In an assessment of the patency of anterior circulation branches following PED placement, Rangel-Castilla et al¹⁴ reported a 15.8% branch occlusion following coverage. The occlusion rate was lowest in the anterior choroidal artery (0%) and almost equal in the ophthalmic artery (10.5%) and posterior communicating artery (10.7%). Both cases of anterior cerebral artery coverage ended with occlusion on last follow-up. Despite branch obliteration, the authors did not identify any clinical sequelae.¹⁴

Similar results were reported by separate studies on the fates of the ophthalmic artery,^{15–18} posterior communicating artery,¹⁹ and anterior choroidal artery.^{19,20} Brinjikji et al²¹ reported a 45% incidence of posterior communicating artery occlusion or diminished flow at last follow-up, but none of the patients showed clinical symptoms related to vessel obliteration. Most of these patients demonstrated diminished blood flow immediately following PED placement; this finding was significantly associated with a higher occlusion incidence at follow-up. Gawlitz et al²² reported using flow diverters to treat aneurysms in the middle cerebral artery bifurcation and anterior communicating artery complex. Of the covered branches, 10.5% (2/19) had completely occluded on last follow-up. Temporary symptomatic ischemic events in perforator territories occurred in 17.6% of cases, which were reversible in all cases within 24 hours. Follow-up MR imaging disclosed asymptomatic lacunar defects corresponding to covered perforating artery territories in 29.4%. The lack of symptoms was attributed to the supply of respective cortical territories by leptomeningeal collaterals in all cases.²²

The high incidence of occlusion of the ophthalmic artery and posterior communicating artery following flow-diverter coverage is attributed to the rich collateral supply from the external carotid artery and PCA, respectively. These collateral vessels might increase the tendency for proximal occlusion if a flow diverter causes some diminution of inflow and the distal anastomosis takes over the end-organ arterial supply.^{14,15} This collateral supply also explains the absence of clinical symptoms. On the contrary, terminal arteries without significant collateral supply, such as the anterior choroidal artery or middle cerebral artery perforators, are more likely to remain patent after coverage by a flow diverter. The pressure gradient across these arteries is more than that across vessels with a rich collateral supply, thus increasing the threshold for branch occlusion by a flow diverter.^{14,20}

Other considerations regarding the use of the PED for treatment of aneurysms near large branches include the branch that is incorporated into the neck of an aneurysm. In these cases, the use of the PED is controversial and often does not result in aneurysm occlusion. This outcome can be seen with flow diversion of pos-

terior communicating artery aneurysms and may be related to retrograde aneurysm filling.^{18,21}

In this series, the fate of major posterior circulation branches has been assessed for the first time in a large and diverse group of patients. Similar to the anterior circulation branches, major branching arteries including the PICA, AICA, and superior cerebellar artery had a low incidence of branch occlusion after coverage with the PED. However, following occlusion of these branches, the risk of ischemic complications might be high. In our series, all 3 cases in which branch occlusion was associated with ischemic complications in the same territory involved the AICA. The relatively high incidence of VA and PCA occlusion was thought to result from a rich collateral arterial supply and was not significantly associated with ischemic complications. Like the study of Puffer et al,¹⁵ the number of PEDs deployed was not found to have any significant relation to branch occlusion incidence. Moreover, there was no significant correlation between branch occlusion and thromboembolic events.

Limitations

The primary limitations are the retrospective study design and variability in the management and follow-up protocols of patients across centers. The inclusion of multiple institutions, however, improves the generalizability of the findings. Indications for using the PED for posterior circulation aneurysms were at the discretion of the participating institution. Immediate branch flow following PED placement was not assessed. The time of branch occlusion and the status of perforators, which is difficult to precisely detect on DSA, was also not assessed. Lack of consistent follow-up brain images could result in missed silent strokes. Moreover, MRA was used to assess the branch occlusion in a subset of patients, along with the limitations related to this imaging technique. The lack of significant association between branch coverage and end points of interest may be influenced by type II error.

CONCLUSIONS

This is the first study to evaluate the fate of posterior circulation branches covered by a PED with attention to the risk of ischemic complications. There was a low incidence of branch occlusion following coverage in most vessels. Moreover, there was no significant increase in the incidence of ischemic complications following branch occlusion compared with covered branches that remained patent. Intramural thrombosis was an independent predictor of ischemic complications.

Disclosures: Christophe Cognard—UNRELATED: Consultancy: Stryker, Medtronic, MicroVention. Elad I. Levy—UNRELATED: Board Membership: Acute Ischemic Stroke Clinical Advisory Board (Stryker), Advisory Board (NeXtGen Biologics), Advisory Board (MEDX), Advisory Board (Cognition Medical); Consultancy: Pulsar Vascular; Expert Testimony: Medical Malpractice, Comments: renders medical/legal opinion as an expert witness; Payment for Lectures Including Service on Speakers Bureaus: Medtronic, Abbott Vascular, Comments: honorarium for training and lectures (Medtronic), carotid training sessions for physicians (Abbott Vascular); Stock/Stock Options: Intratech Medical Ltd, NeXtGen Biologics, Neuravi/now Codman Neuro (Johnson & Johnson), sold April 2017. Thomas R. Marotta—UNRELATED: Consultancy: proctor for PED Medtronic; Patents (Planned, Pending or Issued): no money for eCLIPS/Evasc; Stock/Stock Options: eCLIPS/Evasc. Ajith J. Thomas—UNRELATED: Expert Testimony: CRICO, Comments: cerebrovascular disorders; OTHER RELATIONSHIPS: I am on the Data Safety Monitoring Board of the SCENT trial, a flow-diverter trial.* Adnan H. Siddiqui—UNRELATED: Consultancy: Amnis Therapeutics, Boston Scientific, Canon Medical Systems USA, Cerebrotech Medical Systems,

Cerenovus, Claret Medical, Corindus Vascular Robotics, EndoStream Medical, Guidepoint Global consulting, Imperative Care, Integra, MicroVention, Penumbra, Rapid Medical, Rebound Therapeutics Corp, Silk Road Medical, StimMed, Stryker, Three Rivers Medical Center, VasSol, W.L. Gore & Associates, Medtronic; Stock/Stock Options: Amnis Therapeutics, Apama Medical, Blinktbi, Buffalo Technology partners, Cardinal Health, Cerebrotech Medical Systems, Claret Medical, Cognition Medical, EndoStream Medical, Imperative Care, International Medical Distribution Partners, Rebound Therapeutics Corp, Silk Road Medical, StimMed, Synchron, Three Rivers Medical, Viseon Spine; Other: Cerenovus LARGE trial and ARISE II trial, MicroVention FRED Trial and CONFIDENCE study, MUSC POSITIVE trial, Penumbra Separator 3D trial, COM-PASS trial, INVEST trial, Comments: National Principal Investigator/Steering Committees. *Money paid to the institution.

REFERENCES

1. Szikora I, Turányi E, Marosfoi M. Evolution of flow-diverter endotelialization and thrombus organization in giant fusiform aneurysms after flow diversion: a histopathologic study. *AJNR Am J Neuroradiol* 2015;36:1716–20 CrossRef Medline
2. Nelson PK, Lylyk P, Szikora I, et al. The Pipeline Embolization Device for the intracranial treatment of aneurysms trial. *AJNR Am J Neuroradiol* 2011;32:34–40 CrossRef Medline
3. Chalouhi N, Tjoumakaris S, Dumont AS, et al. Treatment of posterior circulation aneurysms with the Pipeline Embolization Device. *Neurosurgery* 2013;72:883–89 CrossRef Medline
4. Albuquerque FC, Park MS, Abila AA, et al. A reappraisal of the Pipeline embolization device for the treatment of posterior circulation aneurysms. *J Neurointerventional Surg* 2015;7:641–45 CrossRef Medline
5. Ducruet AF, Crowley RW, Albuquerque FC, et al. Reconstructive endovascular treatment of a ruptured vertebral artery dissecting aneurysm using the Pipeline Embolization Device. *J Neurointerv Surg* 2013;5:e20 CrossRef Medline
6. Mazur MD, Kilburg C, Wang V, et al. Pipeline embolization device for the treatment of vertebral artery aneurysms: the fate of covered branch vessels. *J Neurointerv Surg* 2016;8:1041–47 CrossRef Medline
7. Phillips TJ, Wenderoth JD, Phatouros CC, et al. Safety of the Pipeline Embolization Device in treatment of posterior circulation aneurysms. *AJNR Am J Neuroradiol* 2012;33:1225–31 CrossRef Medline
8. Siddiqui AH, Abila AA, Kan P, et al. Panacea or problem: flow diverters in the treatment of symptomatic large or giant fusiform vertebral basilar aneurysms. *J Neurosurg* 2012;116:1258–66 CrossRef Medline
9. Dmytriw AA, Adeeb N, Kumar A, et al. Flow diversion for basilar apex aneurysms. *Neurosurgery* 2018 Feb 26. [Epub ahead of print]. CrossRef Medline
10. Flemming KD, Wiebers DO, Brown RD Jr, et al. The natural history of radiographically defined vertebral basilar nonsaccular intracranial aneurysms. *Cerebrovasc Dis* 2005;20:270–79 CrossRef Medline
11. Wiebers DO, Whisnant JP, Huston J, et al; International Study of Unruptured Intracranial Aneurysms Investigators. Unruptured intracranial aneurysms: natural history, clinical outcome, and risks of surgical and endovascular treatment. *Lancet* 2003;362:103–10 CrossRef Medline
12. Kallmes DF, Hanel R, Lopes D, et al. International retrospective study of the Pipeline Embolization Device: a multicenter aneurysm treatment study. *AJNR Am J Neuroradiol* 2015;36:108–15 CrossRef Medline
13. Kallmes DF, Ding YH, Dai D, et al. A new endoluminal, flow-disrupting device for treatment of saccular aneurysms. *Stroke* 2007;38:2346–52 CrossRef Medline
14. Rangel-Castilla L, Munich SA, Jaleel N, et al. Patency of anterior circulation branch vessels after Pipeline embolization: longer-term results from 82 aneurysm cases. *J Neurosurg* 2017;126:1064–69 CrossRef Medline
15. Puffer RC, Kallmes DF, Cloft HJ, et al. Patency of the ophthalmic artery after flow diversion treatment of paraclinoid aneurysms. *J Neurosurg* 2012;116:892–96 CrossRef Medline
16. Szikora I, Berentei Z, Kulcsar Z, et al. Treatment of intracranial aneurysms by functional reconstruction of the parent artery: the Bu-

- dapest experience with the Pipeline Embolization Device. *AJNR Am J Neuroradiol* 2010;31:1139–47 CrossRef Medline
17. Griessenauer CJ, Ogilvy CS, Foreman PM, et al. **Pipeline Embolization Device for small intracranial aneurysms: evaluation of safety and efficacy in a multicenter cohort.** *Neurosurgery* 2017;80:579–87 CrossRef Medline
 18. Griessenauer CJ, Ogilvy CS, Foreman PM, et al. **Pipeline Embolization Device for small paraophthalmic artery aneurysms with an emphasis on the anatomical relationship of ophthalmic artery origin and aneurysm.** *J Neurosurg* 2016;125:1352–59 CrossRef Medline
 19. Vedantam A, Rao VY, Shaltoni HM, et al. **Incidence and clinical implications of carotid branch occlusion following treatment of internal carotid artery aneurysms with the Pipeline Embolization Device.** *Neurosurgery* 2015;76:173–78; discussion 178 CrossRef Medline
 20. Brinjikji W, Kallmes DF, Cloft HJ, et al. **Patency of the anterior choroidal artery after flow-diversion treatment of internal carotid artery aneurysms.** *AJNR Am J Neuroradiol* 2015;36:537–41 CrossRef Medline
 21. Brinjikji W, Lanzino G, Cloft HJ, et al. **Patency of the posterior communicating artery after flow diversion treatment of internal carotid artery aneurysms.** *Clin Neurol Neurosurg* 2014;120:84–88 CrossRef Medline
 22. Gawlitza M, Januel AC, Tall P, et al. **Flow diversion treatment of complex bifurcation aneurysms beyond the circle of Willis: a single-center series with special emphasis on covered cortical branches and perforating arteries.** *J Neurointerv Surg* 2016;8:481–87 CrossRef Medline

Abnormal Blood Oxygen Level–Dependent Fluctuations in Focal Cortical Dysplasia and the Perilesional Zone: Initial Findings

L. Gupta, P.A.M. Hofman, R.M.H. Besseling, J.F.A. Jansen, and W.H. Backes

ABSTRACT

BACKGROUND AND PURPOSE: Focal cortical dysplasia is a common cause of intractable epilepsy for which neurosurgery is an option. Delineations of a focal cortical dysplasia lesion on structural brain images may not necessarily reflect the functional borders of normal tissue. Our objective was to determine whether abnormalities in spontaneous blood oxygen level–dependent fluctuations arise in focal cortical dysplasia lesions and proximal regions.

MATERIALS AND METHODS: Fourteen patients with focal cortical dysplasia–related epilepsy and 16 healthy controls underwent structural and resting-state functional MR imaging. Three known blood oxygen level–dependent measures were determined, including the fractional amplitude of low-frequency fluctuations, regional homogeneity, and wavelet entropy. These measures were evaluated in the lesion and perilesional zone and normalized to the contralateral cortex of patients with focal cortical dysplasia and healthy controls.

RESULTS: Patients showed significantly decreased fractional amplitude of low-frequency fluctuations and increased wavelet entropy in the focal cortical dysplasia lesion and the perilesional zone (≤ 2 cm) relative to the contralateral homotopic cortex and the same regions in healthy controls. Regional homogeneity was significantly increased in the focal cortical dysplasia lesion compared with the contralateral homotopic cortex and healthy controls.

CONCLUSIONS: Abnormalities in spontaneous blood oxygen level–dependent fluctuations were seen up to 2 cm distant from the radiologically visible boundary. It was demonstrated that functional boundaries go beyond structural boundaries of focal cortical dysplasia lesions. Validation is required to reveal whether this information is valuable for surgical planning and outcome evaluation of focal cortical dysplasia lesions and comparing current results with electrophysiologic analysis.

ABBREVIATIONS: BOLD = blood oxygen level–dependent; EEG = electroencephalography; fALFF = fractional amplitude of low-frequency fluctuations; FCD = focal cortical dysplasia; ReHo = regional homogeneity; WE = wavelet entropy

A focal cortical dysplasia (FCD) is a congenital malformation of cortical development and a frequent cause of intractable epilepsy in children and adults.¹ A complete resection of the epileptogenic zone is required to become seizure-free; therefore, an accurate visualization by neuroimaging is crucial for surgical planning. Histopathologic examination of surgical specimens has

demonstrated that 80% of patients who had a complete resection become seizure-free, compared with only 20% who had incomplete resections.² The most frequently mentioned cause of unsuccessful surgical treatment is invisibility of lesion boundaries on imaging modalities.³

The computer-aided diagnostic approach using morphologic characteristics such as focal cortical thickening or thinning, areas of focal brain atrophy, gray-white junction blurring, and increased signal on T2- and fluid-attenuated inversion recovery–weighted images assists in improving lesion detection.⁴ However, where the exact borders reside and whether the lesion and the perilesional zone are functionally normal or abnormal often remains unknown.^{5,6} Therefore, we proposed exploring a physiologic image contrast in FCD, in addition to the clinically used morphologic contrasts.

Simultaneous electroencephalography (EEG)-fMRI studies revealed that interictal epileptiform discharge–related hemodynamic changes were observed beyond the visible lesion on struc-

Received August 31, 2017; accepted after revision April 1, 2018.

From the Department of Radiology and Nuclear Medicine (L.G., P.A.M.H., R.M.H.B., J.F.A.J., W.H.B.) and School for Mental Health and Neuroscience (P.A.M.H., J.F.A.J., W.H.B.), Maastricht University Medical Center, Maastricht, the Netherlands; and Department of Electrical Engineering (R.M.H.B.), Eindhoven University of Technology, Eindhoven, the Netherlands.

This work was partly supported by a grant from the Dutch National Epilepsy Fund 10–08, and the study is registered in the Dutch Trial Registry (<http://www.trialregister.nl/trialreg/admin/rctview.asp?TC=2315>).

Please address correspondence to Walter H. Backes, PhD, Departments of Radiology and Nuclear Medicine, Maastricht University Medical Center (MUMC+), P.O. Box 5800, 6202 AZ Maastricht, the Netherlands; e-mail: w.backes@mumc.nl

<http://dx.doi.org/10.3174/ajnr.A5684>

Table 1: Patient characteristics

No.	Age/Sex	Seizure Frequency ^a	FCD Location	MRI Structural Image Findings
1	30/F	High	Right insula	Transmantle sign, gray-white matter blurring, cortical thickening, T2-FLAIR hyperintensity
2	29/F	High	Right superior frontal	Transmantle sign, gray-white matter blurring, cortical thickening, T2-FLAIR hyperintensity
3	33/M	Low	Right inferior frontal	Transmantle sign, gray-white matter blurring, T2-FLAIR hyperintensity
4	47/F	High	Right precentral	Transmantle sign, gray-white matter blurring, T2-FLAIR hyperintensity
5	21/M	Low	Left postcentral	Gray-white matter blurring, cortical thickening, T2-FLAIR hyperintensity
6	47/M	High	Left posterior cingulate	Transmantle sign, gray-white matter blurring, cortical thickening, T2-FLAIR hyperintensity
7	43/M	High	Left caudal middle frontal	Transmantle sign, gray-white matter blurring, cortical thickening, T2-FLAIR hyperintensity
8	26/M	Low	Left rostral middle frontal	Transmantle sign, gray-white matter blurring, cortical thickening, T2-FLAIR hyperintensity
9	21/F	Low	Caudal anterior cingulate	Transmantle sign, gray-white matter blurring, cortical thickening, T2-FLAIR hyperintensity
10	21/M	High	Right supramarginal	Transmantle sign, gray-white matter blurring, cortical thickening, T2-FLAIR hyperintensity
11	21/M	Low	Right insular	Transmantle sign, gray-white matter blurring, cortical thickening, T2-FLAIR hyperintensity
12	27/M	Low	Left precentral	Transmantle sign, gray-white matter blurring, cortical thickening, T2-FLAIR hyperintensity
13	54/M	High	Right rostral middle frontal	Transmantle sign, gray-white matter blurring, cortical thickening, T2-FLAIR hyperintensity
14	25/M	None	Left inferior parietal	Gray-white matter blurring, cortical thickening, T2-FLAIR hyperintensity

^a Seizure frequency: low, 1 per month; high, >1 per week.

tural MR imaging, and surgical outcomes were better using EEG-fMRI in addition to structural MR imaging and intracranial EEG.⁷ Electrophysiologic examinations have revealed epileptogenicity, not only in the lesion but also in perilesional areas.⁸ To our knowledge, no systematic imaging study has explored the physiology of the immediate vicinity of FCDs, which may be relevant for resection planning and outcome prediction.

Using resting-state functional MR imaging, we assessed the time signature of spontaneous blood oxygen level–dependent (BOLD) fluctuations in patients with FCD. We evaluated 3 known BOLD measures to characterize the spontaneous fluctuations: 1) the amplitude (fractional amplitude of low frequency fluctuations [fALFF]) as a measure of oscillation strength, 2) regional homogeneity (ReHo) as a measure of local signal similarity, and 3) wavelet entropy (WE) as a measure of disorder/order in BOLD time-series.

The same functional MR imaging dataset was previously used to show abnormalities in the spatial profile of functional connectivity of FCDs beyond the MR imaging–visible lesion.⁹ That study used a seed-based functional connectivity approach to determine the interregional correlations with remote brain regions, whereas in the current study, we characterized the intrinsic BOLD fluctuations in FCD lesions with local spatiotemporal measures (fALFF, ReHo, and WE). The objective of this study was to determine whether functional abnormalities arise in spontaneous BOLD fluctuations of FCD lesions and proximal regions in comparison with normal-appearing brain tissue.

MATERIALS AND METHODS

Subjects

The study was approved by the ethics committees of the 2 participating medical institutions. Informed written consent was obtained from all subjects. Fourteen patients with FCD-related epi-

lepsy were recruited (mean age, 32 ± 11 years; 10 men), as well as 16 age- and sex-matched healthy controls (mean age, 35 ± 9 years; 7 men). Structural MR images were rated by neuroradiologists with >20 years of experience. The clinical diagnosis was based on concordance among seizure semiology, EEG findings, and neuroimaging.¹ Briefly, this involved recurrent stereotyped seizures and focal interictal and/or ictal EEG abnormalities that coincided with an FCD-concordant lesion on MR imaging.¹⁰ Relevant imaging features included, among others, an abnormal gyral pattern, increased cortical thickness, the transmantle sign, and blurring of the gray-white matter interface.¹¹ None of the patients included in this study had dual pathology. Table 1 lists the lesion characteristics per patient. For 5 patients, surgery and histopathology information were also available, which further confirmed the diagnosis of FCD.

MR Imaging

All subjects underwent structural and functional MR imaging at 3T (Achieva; Philips Healthcare, Best, the Netherlands) using an 8-element receive-only head coil. Structural imaging involved a T1-weighted scan: 3D fast spoiled gradient-echo sequence; TE/TR/TI, 3.8/8.3/1022 milliseconds; voxel size, 1 × 1 × 1 mm³; duration, 7.5 minutes. In addition, a FLAIR sequence was used (3D turbo spin-echo; TE/TR/TI, 330/8000/2400 milliseconds; 0.4 × 0.4 mm² pixel size; 0.6-mm-thick axial slices; duration, 8 minutes). Functional MR imaging involved a BOLD T2*-weighted task-free scan, for which the participants were instructed to close their eyes, lie still, and think of nothing in particular. The settings were the following: single-shot echoplanar imaging sequence; TE/TR, 35/2000 milliseconds; 2 × 2 mm² pixel size; 4-mm thick axial slices; 195 dynamics; duration, 6.5 minutes.

Image Processing

Functional images were corrected for slice-timing differences and head displacements, coregistered to the anatomic template, and smoothed with an 8-mm kernel (full width at half maximum) using computational software (Statistical Parametric Mapping, SPM8; <http://www.fil.ion.ucl.ac.uk/spm/software/spm12>). Any signal drifts across time were corrected by removing the very-low-frequency components (<10 MHz) (FSL 3.0; <http://www.fmrib.ox.ac.uk/fsl>). To correct for physiologic fluctuations, we included the time-series from the CSF and white matter as covariates in the linear regression analysis.¹² Gray matter, white matter, and CSF voxels were segmented from the T1-weighted images (FreeSurfer software, Version 5.3.0; <http://surfer.nmr.mgh.harvard.edu>).

Fractional Amplitude of Low-Frequency Fluctuations

The signal time-series of each voxel was standardized and Fourier-transformed to the frequency domain, and the power spectrum was calculated in specific frequency sub-bands. The fALFF is computed per voxel as the ratio of the power spectrum in a specific sub-band (10–80 MHz) to the full range (0–250 MHz)¹³ (Resting-State fMRI Data Analysis Toolkit [REST], Version 1.8; <http://www.rfmri.org/REST>). This ratio helps to eliminate the confounding influence of the relatively strong signal of the pulsating CSF and physiologic noise.¹³ The fALFF was computed in 4 predefined frequency sub-bands: 10–27 MHz (slow-5), 27–73 MHz (slow-4), 73–198 MHz (slow-3), and 198–250 MHz (slow-2).¹⁴

Regional Homogeneity

The Kendall coefficient of concordance was used to calculate the ReHo of the time-series of a voxel with its 26 (immediate) neighbor voxels (REST Toolkit, Version 1.8) as proposed by Zang et al.¹⁵

ReHo measures the similarity in contiguous voxels of the time-series and was averaged over all gray matter voxels per ROI. While most functional imaging analysis methods rely on a priori knowledge of a signal model, ReHo is a voxel-by-voxel, data-driven approach that requires no prior knowledge of the experimental design.

Wavelet Entropy

The wavelet entropy is computed using the discrete wavelet transform of the time-series.¹⁶ Unlike the Fourier transform or short-time Fourier transform, the nonstationary components in the BOLD time-series are detected by the discrete wavelet transform (Daubechies-4 wavelet) by means of the convolution with the time-shifted and scaled mother wavelet function. The resulting sub-bands are squared and integrated across time to obtain the energy E_i per sub-band i , from which the WE over the sub-bands is calculated as $WE = -\sum p_i \ln p_i$, with $p_i = E_i / \sum E_i$, the relative energy per sub-band. WE is a measure of lack of structure, thus randomness, over the wavelet sub-band. A typical BOLD signal represents a frequency structure in which the energy roughly decreases as a function of frequency (sub-band) due to the low-pass nature of the blood signal. When the distribution of energy over frequency sub-bands becomes more equal (ie, more random), WE increases.¹⁷

Image Analysis

FCDs were manually marked on the structural images by an experienced neuroradiologist on FLAIR images. These ROIs were spatially transformed to the functional images. Three proximal regions of FCD were selected at a 1-, 2-, and 3-cm distance from the lesion border, as 1-cm-thick shells. To reduce physiologic variation, we used the entire normal-appearing cortex of the contralateral hemisphere for normalizing all BOLD measures. In healthy controls, the BOLD measures were obtained from the anatomic atlas regions that spatially corresponded to the lesions in patients (using FreeSurfer software).

Statistical Analysis

Region-averaged BOLD measures of the FCD lesions and the homotopic contralateral cortex were reported as absolute (ie, not normalized to the contralateral cortex) values. In addition, normalized values were given as a ratio between the region-averaged BOLD value (fALFF, ReHo, or WE) and the mean measure of all voxels in the entire normal-appearing cortex of the contralateral hemisphere.

The Student 2-sample t test was used to reveal any differences between the patients with FCD and control subjects. The paired t test was used for statistical assessment of the FCD region, proximal regions, and contralateral homotopic cortex. Statistical significance was inferred at $P < .05$.

A threshold was derived from the results of the healthy control group (reference value). This threshold served to determine which and how many patients had abnormal BOLD values (ie, beyond the 95% confidence intervals of the healthy control group) in the lesion and proximal regions.

RESULTS

Figure 1 shows an FCD lesion on a FLAIR image with cortical maps of fALFF, ReHo, and WE of the FCD lesion and proximal cortex. In this example, decreased fALFF, increased ReHo, and increased WE were observed in the FCD lesion and the proximal regions.

Absolute BOLD Measures

Table 2 lists the absolute BOLD measures. The fALFF of the FCD lesions was significantly lower and wavelet entropy was significantly higher than the contralateral homotopic cortex and the same region in the control subjects. ReHo showed no significant differences.

Normalized Fractional Amplitude of Low-Frequency Fluctuations

Figure 2 provides the fALFF as a function of frequency in the range of 10–250 MHz for the FCD lesion, proximal regions, and controls. Only for the slow-5 sub-band (10–27 MHz) was the amplitude of the FCD lesions significantly lower than for the control subjects ($P < .001$). For this sub-band, all 3 proximal regions showed lower amplitudes than in controls. The most distant shell at 3 cm showed a significantly higher fALFF than the more proximal regions (1 and 2 cm).

Patients showed a significantly lower normalized fALFF in the FCD lesion and the closer proximal regions (at 1 and 2 cm) rela-

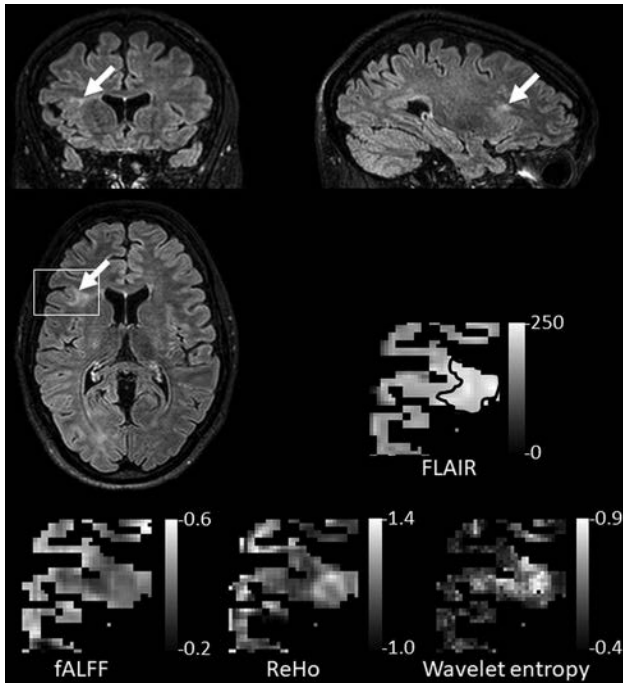


FIG 1. Sample orthogonal FLAIR images depicting an FCD lesion (arrows) of a 30-year-old woman. Inserts show the magnification of the lesion on FLAIR contrast and cortical parameter maps of fALFF, regional homogeneity, and wavelet entropy. Increased regional homogeneity, wavelet entropy, and decreased fALFF were observed in the FCD lesion and the immediate perilesional regions in comparison with the regions more distinct from the FCD. Only gray matter is visualized; white matter is masked out.

Table 2: Absolute BOLD measures in the FCD lesion, the contralateral homotopic cortex, and healthy controls^a

Absolute Measure	Lesion	Contralateral Homotopic Cortex	Controls
fALFF	0.327 ± 0.007 ^b	0.352 ± 0.008	0.358 ± 0.008
ReHo	0.348 ± 0.032	0.292 ± 0.031	0.310 ± 0.024
WE	1.245 ± 0.005 ^b	1.227 ± 0.004	1.227 ± 0.003

^a Data are mean ± standard error.

^b Significant differences ($P < .05$) with the contralateral homotopic cortex and the same region in controls, respectively.

tive to the contralateral homotopic cortex (FCD lesion: $P < .001$; proximal at 1 and 2 cm: $P < .02$) and the same regions in the control subjects (FCD lesion: $P < .001$; proximal at 1 and 2 cm: $P < .01$) (Table 3). Thirteen of 14 patients showed abnormal (lower) fALFF in the lesions, and 11 of these 13 patients showed abnormal fALFF up to 2 cm from the boundary (Table 4). Six patients showed abnormal fALFF in the contralateral homotopic cortex.

Normalized Regional Homogeneity

The normalized ReHo was significantly higher in FCD lesions compared with the contralateral homotopic cortex in patients ($P < .01$) and control subjects ($P < .01$). None of the proximal regions showed significant differences. The mean ReHo increased with the distance in the proximal regions (Table 3). Eleven of 14 patients showed abnormal (higher) ReHo in the lesion, and 5 of these patients showed abnormal ReHo up to 2 cm from the

boundary (Table 4). Four patients showed abnormal fALFF in the contralateral homotopic cortex.

Normalized Wavelet Entropy

The normalized WE for the FCD lesion and the closer proximal regions (at 1 or 2 cm) was significantly higher than the contralateral homotopic cortex (FCD lesion: $P < .01$; proximal at 1 and 2 cm: $P < .05$) and the same region in healthy controls (FCD lesion: $P < .01$; proximal at 1 and 2 cm: $P < .05$) (Table 3). Twelve of 14 patients showed abnormal (higher) WE in the lesion, and 10 of these patients showed abnormal WE up to 2 cm from the boundary (Table 4). Five patients showed abnormal WE in the contralateral homotopic cortex.

DISCUSSION

In this study, we set out to determine physiologic abnormalities of the BOLD signal time-series in FCD lesions of patients with epilepsy. The most suitable BOLD measures were obtained by normalizing lesion or perilesional values to the contralateral homotopic cortex. Patients with FCD showed significantly decreased oscillation amplitudes (normalized fALFF), decreased spatiotemporal heterogeneity (ie, increased normalized ReHo), and increased temporal heterogeneity (ie, increased normalized WE) in the FCD lesions compared with healthy controls. The most striking result was that abnormal BOLD fluctuations were also manifest in regions adjacent to the structurally visible borders of the lesions.

BOLD Abnormalities in FCD Lesions

Decreased BOLD amplitude (normalized fALFF) and increased temporal heterogeneity (increased normalized WE) suggest reduced neuronal activity or neurovascular coupling in the lesions. Suppression of activity in the FCD lesion was also previously reported in the intracranial EEG, where interrupted pseudoperiodic spikes were reported.¹⁸

There was also significantly increased normalized ReHo observed in patients with FCD lesions relative to healthy controls. This could be due to the lower amplitude, which also attenuates differences and randomness in BOLD signals within FCD lesions. The increase in normalized ReHo increases the similarity of the signals and thus increases ReHo.

Perilesional Functional Abnormalities

All 3 BOLD measures and the wavelet spectrum showed that the abnormalities extend beyond the visible lesion border on FLAIR images. An increase in normalized WE in the FCD lesion and the 2-cm perilesional zone was observed, indicating a more equalized frequency distribution over the sub-bands for the FCD lesion and the perilesional zone, which implies a less pronounced frequency structure. The normalized fALFF measure also showed reduction of activity, indicating that irregularities of the BOLD fluctuations in the perilesional zone may be related to some form of epilepsy-related activity of the impaired brain.^{7,19} However, from the current observations in patients with epilepsy, who were well-treated by medication and/or surgery, we cannot infer whether the perilesional activity acts as an epileptogenic or inhibitory mechanism.

Also previous electrophysiologic investigations showed that interictal epileptic discharges extend beyond the FCD visible le-

sion (ie, in perilesional regions).^{20,21} Urrestarazu et al²² reported that a very high rate of fast ripples in the EEG signal was observed in the perilesional area, which was adjacent to the seizure-onset area. The fast ripples in the perilesional zone might be an indicator of potential epileptogenicity, which Cohen-Gadol et al²³ suggested could possibly turn into a seizure focus after the removal of the primary seizure-onset zone. Other studies further suggested that removal of the entire lesion, including surrounding interictally active tissue, would be necessary to achieve long-term seizure relief.^{24,25}

The results indicated variability among patients because not all patients showed BOLD abnormalities up to 2 cm from the lesion boundaries and only a few patients showed abnormalities beyond 2 cm. This intersubject variation suggests that different pathologic mechanisms might be at work; for instance, excitotoxic effects could lead to variations in the BOLD signal. The variable findings may also reflect the heterogeneity of a clinical sample of patients with FCD, with variations in the frequency of epileptiform discharges and antiepileptic drug use. The results presented in this study are in line with the findings presented in a functional connectivity study, in which 11/14 patients (a similar number of patients showed abnormality using normalized fALFF and normalized WE) showed abnormality in FCD perilesional regions⁹ on the same dataset.

Note that because structural findings like the transmantle sign and gray-white matter blurring potentially infer an indeterminate lesion border, which may influence the exact values of the BOLD measures we obtained in individuals. In this study, we delineated

the lesion border on the hyperintensities of the FLAIR images, which were present for all subjects. It is unlikely that individual uncertainties in border definition would strongly influence our results because we present group average results.

Clinical Perspective

The most interesting finding of this study is that structural boundaries are not the same as functional boundaries obtained by the physiologic BOLD contrast for the FCD lesions. Reports indicate that on average, 62% of patients with cortical dysplasia are seizure-free after an operation.^{2,26} Our findings show that functional abnormalities, derived from spontaneous BOLD fluctuations, were seen up to 2 cm distant from the radiologically visible boundary of the FCD lesion. These findings could be critical information for surgery planning of FCD lesions.

Recent findings show that removing as much as possible of the aberrant cortex improves seizure-free outcome.² The presented BOLD method can possibly be used to help noninvasively assess the functional extent of FCD lesions and has the potential to unveil lesion areas that could be missed by structural MR imaging in a surgical work-up.

Study Considerations

Because the 2 brain hemispheres are intrinsically connected, the BOLD signal of the contralateral homotopic cortex is also likely to be affected by the abnormality caused by FCD. This abnormality was noticed because some patients showed increased normalized WE and decreased normalized fALFF in comparison with controls in the contralateral homotopic cortex.

Functional imaging has been linked to electrophysiology, in a previous study in which epileptiform spikes were mapped to the brain using simultaneously acquired EEG-fMRI.⁷ The current study results need to be verified by comparing BOLD measures on functional MR imaging data from patients who become seizure-free after an operation with measures of those who have recurrent seizures. Ideally, this comparison should be supplemented with histopathology according to the most recent classification,^{1,27} which we could not fully provide. Similarly, our findings on the abnormal BOLD fluctuations in the perilesional zone need to be evaluated against intracranial EEG recordings in suitable patient groups.

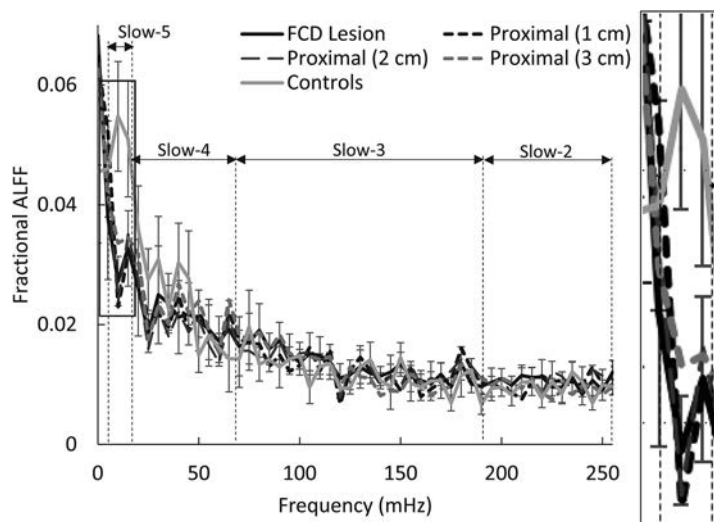


FIG 2. Fractional amplitude of low frequency fluctuations as a function of frequency in the range of 10–250 MHz. Only the lowest sub-band (ie, slow-5; 10–27 MHz, magnified) showed significantly lower amplitudes in the FCD lesion relative to the controls. Error bars represent the standard error of mean.

Table 3: The normalized BOLD measures in the FCD lesion, perilesional regions, contralateral homotopic region, and healthy controls^a

Normalized Measure	Lesion	Perilesional Zones			Contralateral Homotopic	Control Subjects
		1 cm	2 cm	3 cm		
fALFF	0.922 ± 0.016 ^b	0.941 ± 0.014 ^b	0.947 ± 0.014 ^b	0.981 ± 0.013	0.983 ± 0.012	1.005 ± 0.009
ReHo	1.206 ± 0.066 ^b	0.992 ± 0.032	0.991 ± 0.036	1.021 ± 0.034	1.023 ± 0.032	1.020 ± 0.022
WE	1.018 ± 0.004 ^b	1.013 ± 0.003 ^b	1.009 ± 0.003 ^b	1.003 ± 0.003	1.003 ± 0.002	1.002 ± 0.002

^aData are mean ± standard error. Normalized fALFF was significantly decreased, while WE was significantly higher in FCD lesions and perilesional zones (up to 2 cm) than in the contralateral homotopic cortex and control subjects. ReHo was significantly higher in FCD lesions. BOLD measures were normalized with the entire contralateral cortex.

^bSignificant differences ($P < .05$) with the contralateral homotopic cortex and the same region in controls, respectively.

Table 4: Number of patients with measures outside the 95% confidence interval of the normative (healthy control) values^a

Normalized Measure	Lesion	Perilesional Zone			Contralateral Homotopic Cortex
		1 cm	2 cm	3 cm	
fALFF	13 (93)	12 (86)	11 (79)	6 (43)	6 (43)
ReHo	11 (79)	5 (36)	5 (36)	4 (29)	4 (29)
WE	12 (86)	11 (79)	10 (71)	4 (29)	5 (36)

^aData are the number of patients (percentage).

CONCLUSIONS

In this study, it was shown that functional boundaries of FCD extend beyond boundaries visible on structural MR imaging. Our findings show that functional abnormalities, in terms of attenuated and more disordered BOLD fluctuations, were seen up to 2 cm away from the radiologically visible boundary of the lesion. This information could be critical for surgery planning of FCD lesions, which needs to be validated with intracranial EEG recordings, because BOLD findings in the lesional and perilesional areas could reflect metabolic/hemodynamic changes due to epileptic discharges.

Disclosures: Paul A.M. Hofman—RELATED: Grant: Dutch Epilepsy Fund, Comments: Project 10–8.* *Money paid to the institution.

REFERENCES

- Blümcke I, Thom M, Aronica E, et al. **The clinicopathological spectrum of focal cortical dysplasias: a consensus classification proposed by an ad hoc Task Force of the ILAE Diagnostic Methods Commission.** *Epilepsia* 2011;52:158–74 CrossRef Medline
- Hauptman JS, Mathern GW. **Surgical treatment of epilepsy associated with cortical dysplasia: 2012 update.** *Epilepsia* 2012;53(Suppl 4):98–104 CrossRef Medline
- Winston GP, Micallef C, Kendell BE, et al. **The value of repeat neuroimaging for epilepsy at a tertiary referral centre: 16 years of experience.** *Epilepsy Res* 2013;105:349–55 CrossRef Medline
- Yagishita A, Arai N, Maehara T, et al. **Focal cortical dysplasia: appearance on MR images.** *Radiology* 1997;203:553–59 CrossRef Medline
- Jiang YJ, Ang LC, Blume WT. **Extent of EEG epileptiform pattern distribution in “focal” cortical dysplasia.** *J Clin Neurophysiol* 2010; 27:309–11 CrossRef Medline
- Tassi L, Colombo N, Garbelli R, et al. **Focal cortical dysplasia: neuropathological subtypes, EEG, neuroimaging and surgical outcome.** *Brain* 2002;125(Pt 8):1719–32 Medline
- Thornton R, Vulliemoz S, Rodionov R, et al. **Epileptic networks in focal cortical dysplasia revealed using electroencephalography-functional magnetic resonance imaging.** *Ann Neurol* 2011;70:822–37 CrossRef Medline
- Hodozuka A, Tsuda H, Hashizume K, et al. **Focal cortical dysplasia: pathophysiological approach.** *Childs Nerv Syst* 2006;22:827–33 CrossRef Medline
- Besseling RMH, Jansen JFA, de Louw AJA, et al. **Abnormal profiles of**

- local functional connectivity proximal to focal cortical dysplasias.** *PLoS One* 2016;11:e0166022 CrossRef Medline
- Chassoux F, Landré E, Mellerio C, et al. **Type II focal cortical dysplasia: electroclinical phenotype and surgical outcome related to imaging.** *Epilepsia* 2012;53:349–58 CrossRef Medline
 - Hofman PAM, Fitt GJ, Harvey AS, et al. **Bottom-of-sulcus dysplasia: imaging features.** *AJR Am J Roentgenol* 2011;196:881–85 CrossRef Medline
 - Zou QH, Zhu CZ, Yang Y, et al. **An improved approach to detection of amplitude of low-frequency fluctuation (ALFF) for resting-state fMRI: fractional ALFF.** *J Neurosci Methods* 2008;172:137–41 CrossRef Medline
 - Zang YF, He Y, Zhu CZ, et al. **Altered baseline brain activity in children with ADHD revealed by resting-state functional MRI.** *Brain Dev* 2007;29:83–91 CrossRef Medline
 - Wang Z, Zhang Z, Liao W, et al. **Frequency-dependent amplitude alterations of resting-state spontaneous fluctuations in idiopathic generalized epilepsy.** *Epilepsy Res* 2014;108:853–60 CrossRef Medline
 - Zang Y, Jiang T, Lu Y, et al. **Regional homogeneity approach to fMRI data analysis.** *Neuroimage* 2004;22:394–400 CrossRef Medline
 - Rosso OA. **Entropy changes in brain function.** *Int J Psychophysiol* 2007;64:75–80 CrossRef Medline
 - Gupta L, Jansen JFA, Hofman PAM, et al. **Wavelet entropy of BOLD time series: an application to Rolandic epilepsy.** *J Magn Reson Imaging* 2017;46:1728–37 CrossRef Medline
 - Menezes Cordeiro I, von Ellenrieder N, Zazubovits N, et al. **Sleep influences the intracerebral EEG pattern of focal cortical dysplasia.** *Epilepsy Res* 2015;113:132–39 CrossRef Medline
 - Gotman J. **Epileptic networks studied with EEG-fMRI.** *Epilepsia* 2008;49(Suppl 3):42–51 CrossRef Medline
 - Tassi L, Colombo N, Cossu M, et al. **Electroclinical, MRI and neuropathological study of 10 patients with nodular heterotopia, with surgical outcomes.** *Brain* 2005;128:321–37 Medline
 - Palmini A, Gambardella A, Andermann F, et al. **Intrinsic epileptogenicity of human dysplastic cortex as suggested by corticography and surgical results.** *Ann Neurol* 1995;37:476–87 CrossRef Medline
 - Urrestarazu E, Chander R, Dubeau F, et al. **Interictal high-frequency oscillations (100–500 Hz) in the intracerebral EEG of epileptic patients.** *Brain* 2007;130:2354–66 CrossRef Medline
 - Cohen-Gadol AA, Ozduman K, Bronen RA, et al. **Long-term outcome after epilepsy surgery for focal cortical dysplasia.** *J Neurosurg* 2004;101:55–65 CrossRef Medline
 - Hader WJ, Mackay M, Otsubo H, et al. **Cortical dysplastic lesions in children with intractable epilepsy: role of complete resection.** *J Neurosurg* 2004;100(2 Suppl Pediatrics):110–17 CrossRef Medline
 - Alexandre V Jr, Walz R, Bianchin MM, et al. **Seizure outcome after surgery for epilepsy due to focal cortical dysplastic lesions.** *Seizure* 2006;15:420–27 CrossRef Medline
 - Phi JH, Cho BK, Wang C, et al. **Longitudinal analyses of the surgical outcomes of pediatric epilepsy patients with focal cortical dysplasia.** *J Neurosurg Pediatr* 2010;6:49–56 CrossRef Medline
 - Najm IM, Sarnat HB, Blümcke I. **Review: the International Consensus Classification of Focal Cortical Dysplasia—a critical update 2018.** *Neuropathol Appl Neurobiol* 2018;44:18–31 CrossRef Medline

Role of the Apparent Diffusion Coefficient as a Predictor of Tumor Progression in Patients with Chordoma

T. Sasaki, T. Moritani, A. Belay, A.A. Capizzano, S.P. Sato, Y. Sato, P. Kirby, S. Ishitoya, A. Oya, M. Toda, and K. Takahashi



ABSTRACT

BACKGROUND AND PURPOSE: Diffusion-weighted imaging may aid in distinguishing aggressive chordoma from nonaggressive chordoma. This study explores the prognostic role of the apparent diffusion coefficient in chordomas.

MATERIALS AND METHODS: Sixteen patients with residual or recurrent chordoma were divided postoperatively into those with an aggressive tumor, defined as a growing tumor having a doubling time of <1 year, and those with a nonaggressive tumor on follow-up MR images. The ability of the ADC to predict an aggressive tumor phenotype was investigated by receiver operating characteristic analysis. The prognostic role of ADC was assessed using a Kaplan-Meier curve with a log-rank test.

RESULTS: Seven patients died during a median follow-up of 48 months (range, 4–126 months). Five of these 7 patients were in the aggressive tumor group, and 2 were in the nonaggressive tumor group. The mean ADC was significantly lower in the aggressive tumor group than in the nonaggressive tumor group ($P = .002$). Receiver operating characteristic analysis showed that a cutoff ADC value of $1.494 \times 10^{-3} \times \text{mm}^2/\text{s}$ could be used to diagnose aggressive tumors with an area under the curve of 0.983 (95% CI, 0.911–1.000), a sensitivity of 1.000 (95% CI, 0.541–1.000), and a specificity of 0.900 (95% CI, 0.555–0.998). Furthermore, a cutoff ADC of $\leq 1.494 \times 10^{-3} \times \text{mm}^2/\text{s}$ was associated with a significantly worse prognosis ($P = .006$).

CONCLUSIONS: Lower ADC values could predict tumor progression in postoperative chordomas.

ABBREVIATION: RT = radiotherapy

Chordoma is a rare bone tumor arising from notochordal remnants in the skull base, spine, or sacrococcygeal region.¹ The 2013 World Health Organization classification of bone tumors identifies 3 subgroups of chordoma: classic chordoma not otherwise specified, chondroid, and dedifferentiated.¹ Dedifferentiated chordoma arises in a pre-existing low-grade chordoma and has the worst prognosis, so it is important to identify dedifferentiated or aggressive components when evaluating chordomas.²

DWI could potentially be used to distinguish chordoma from chondrosarcoma because the ADC values for chordoma are lower than those for chondrosarcoma.^{3,4} Moreover, the ADC values are lower in aggressive chordomas than in classic chordomas, suggesting that ADC may be useful for classifying chordomas into subcategories according to aggressiveness.⁴ Hanna et al⁵ suggested that a low T2 component in chordoma represented aggressive chordoma. Classic and chondroid chordomas contain stromal mucin and chondroid matrix, respectively, which produce an increased T2 signal and a higher ADC, whereas an aggressive tumor contains less stroma with high cellularity and a lower ADC.⁴ However, there is sparse literature describing the relationship between the MR imaging signal characteristics of chordoma and prognosis.

Surgical resection is the standard therapy for chordoma, though there have been recent advances in radiation therapy (RT).^{6–11} En bloc surgical resection with negative margins and no intraoperative spill is associated with a reduced rate of local recurrence. However, the location of the chordoma may limit the ability to perform a gross total resection.^{8,10} After the first surgical resection, adjuvant RT is often used to reduce the likelihood of recurrence and improve the prognosis.^{12,13}

Received September 11, 2017; accepted after revision March 10, 2018.

From the Departments of Radiology (T.S., T.M., A.B., A.A.C., S.P.S., Y.S.) and Pathology (P.K.), University of Iowa, Iowa City, Iowa; Asahikawa Medical University (T.S., S.I., A.O., M.T., K.T.), Asahikawa, Hokkaido, Japan; and Department of Radiology (T.M.), University of Michigan, Ann Arbor, Michigan.

This work was supported by the Japan Society for the Promotion of Science Grant-in-Aid for Scientific Research Grant No. JP15K19762 (T.S.).

Please address correspondence to Tomoaki Sasaki, MD, PhD, Department of Radiology, Asahikawa Medical University, 2-1-1-1 Midorigaoka-higashi, Asahikawa, Hokkaido 078-8510, Japan; e-mail: tomoaki3est@gmail.com

Indicates open access to non-subscribers at www.ajnr.org

Indicates article with supplemental on-line appendix.

Indicates article with supplemental on-line photos.

<http://dx.doi.org/10.3174/ajnr.A5664>

After an initial operation and RT, most patients undergo serial imaging to detect recurrence. It is important to recognize recurrence early to ensure adequate salvage therapy.^{6,13} Although radiologic evaluation is important in oncology, assessment of tumor progression or response to treatment is based on changes in the residual tumor size on imaging.¹⁴ ADC can identify further characteristics of many tumors with malignant potential.¹⁵

We hypothesized that recurrent or residual chordoma that acquires aggressive features with time also shows a decrease in the ADC value. The aim of this study was to explore the role of the ADC as a predictor of outcome in patients with chordomas.

MATERIALS AND METHODS

Study Population

This retrospective study was approved by the University of Iowa institutional review board. The need for informed consent was waived because of the retrospective nature of the research. We searched our data base from 2000 to 2016 using the search term “chordoma” and identified 31 patients (mean age, 46.0 ± 21.0 years; range, 7–88 years; 18 males, 13 females) with histopathologically proved chordoma. Five patients were diagnosed with chondroid chordoma, and 26, with classic chordoma. The primary sites of the chordomas were the clivus ($n = 16$), cervical spine ($n = 7$), thoracic spine ($n = 1$), lumbar spine ($n = 3$), sacrococcygeal region ($n = 3$), and subarachnoid space in the posterior fossa ($n = 1$). We included patients with residual or recurrent tumors after the initial therapies for analysis during follow-up periods. Thirteen of the 31 patients had no recurrent or residual tumor or did not undergo >1 MR imaging examination during the follow-up period, so they were excluded from the study. Eighteen of the 31 patients had residual or recurrent chordoma. A “residual tumor” was defined as an expansile mass in the operative bed with contrast enhancement that included high-signal components on T2-weighted imaging after incomplete resection without additional resection within 3 months from the first resection ($n = 12$). Because the first resection was performed to make a histologic diagnosis in some patients, a subsequent radical resection followed. A “recurrent tumor” was defined as a new expansile mass at or around the previous surgical site on MR imaging, which implied a residual tumor on histopathology ($n = 4$; On-line Fig 1). MR imaging data for 2 patients were inadequate for analysis because of artifacts or incomplete scan sequences, leaving 16 patients (mean age, 55.3 ± 19.8 years; range, 17–77 years; 12 males, 4 females) with longitudinal follow-up data available for analysis.

A pathologist reviewed the available pathologic material for the 16 patients and confirmed the diagnoses as chondroid chordoma ($n = 5$) and classic chordoma ($n = 11$): In 1 patient, the classic chordoma had aggressive features (necrosis, mitotic activity, and cellular pleomorphism), but they were not sufficient for it to be categorized as a dedifferentiated chordoma.

Gross total resection was reported at the first operation in 2 patients, and incomplete resection, in 14 patients. Thirteen of the 16 patients underwent postsurgical RT (photon RT in 11 patients;

radiation doses were unknown in 2 patients), 2 patients had no RT, and the treatment was unknown in 1 patient.

Analysis of MR Imaging Data

MR imaging examinations were performed using 1.5T MR imaging scanners (Magnetom Symphony, Avanto, or Espree; Siemens, Erlangen, Germany). The following parameters were used for the head: spin-echo T2-weighted imaging (TR, 3790–6270 ms; TE, 80–107 ms; FOV, 240 mm; matrix size, 256 × 240; slice thickness, 4–6 mm with 10%–20% interval gaps; parallel imaging factor, 2); precontrast and postcontrast fat-saturated T1-weighted imaging (TR, 413–587 ms; TE, 8.4–12 ms; FOV, 240 mm; matrix size, 256 × 240; slice thickness, 4–6 mm with 10%–20% interval gaps; parallel imaging factor, 2); and echo-planar DWI (TR, 2200–5600 ms; TE, 73–89 ms; FOV, 240 mm; matrix size, 128 × 128; slice thickness, 5 mm with 10%–20% interval gaps; b-value = 0 and 1000 s/mm²; 3 or 12 diffusion directions; parallel imaging factor, 3). The following parameters were used for the spinal and sacral regions: spin-echo T2-weighted imaging (TR, 4000–7280 ms; TE, 101–108 ms; FOV, 220 mm [mobile spine] to 300 [pelvis] mm; matrix size, 240 × 200; parallel imaging factor, 2); precontrast and postcontrast fat-saturated T1-weighted imaging (TR, 507–611 ms; TE, 6.6–9.5 ms; FOV, 220 mm [mobile spine] to 300 [pelvis] mm; matrix size, 220 × 200; slice thickness, 4–6 mm with 10%–20% interval gaps; parallel imaging factor, 2); and echo-planar DWI (TR, 4100–9300 ms; TE, 78–96 ms; FOV, 220 mm [mobile spine] to 300 [pelvis] mm; matrix size, 128 × 128–192 × 145; parallel imaging factor, 1–2; slice thickness, 5 mm with 10%–20% interval gaps; b-value = 0 and 1000 s/mm²; 3 diffusion directions). ADC maps were generated according to a monoexponential fitting model using commercially available software (Olea Sphere, Version 3.0; Olea Medical, La Ciotat, France).

During follow-up, all 16 patients underwent at least 2 MR imaging scans. The 2 MR imaging series were selected on the basis of the following rules: 1) The first MR imaging occurred at least 6 months after RT; 2) there was neither surgical resection nor RT between the first and second MR imaging; 3) DWI was available, in addition to at least T1- or T2-weighted images; and 4) if there were >2 MR imaging scans after the first MR imaging, the second MR imaging was selected as the scan that occurred approximately 1 year after the first MR imaging.

Two neuroradiologists independently outlined the ROI in freehand for the 2 MR imaging scans—that is, they outlined the whole volume of the chordoma on the ADC maps, while checking the coregistered T2-weighted and contrast-enhanced T1-weighted images, in addition to using Olea Sphere, Version 3.0, software to avoid cystic components and necrosis (On-line Fig 2). The mean ADC values and tumor volume were calculated on the basis of the summation of the ROIs.¹⁶ The volume change ratios were calculated using the following formula:

$$\text{Volume Change Ratio} = (\text{Vol}_{2\text{nd}} - \text{Vol}_{1\text{st}}) / \text{Vol}_{1\text{st}}$$

where Vol_{1st} is the tumor volume on the first MR imaging scan and Vol_{2nd} is the tumor volume on the second MR imaging scan.

We classified patients into 2 groups based on the volume change ratio and tumor growth rate. To assess the tumor

Table 1: Patient demographic and clinical characteristics^a

	Aggressive Tumor	Nonaggressive Tumor	P Value
No.	6	10	
Volume change ratio	14.4 ± 21.0 (-2.18–17.2)	0.463 ± 1.135 (-1.40–3.78)	.003
Doubling time (mo)	5.77 ± 4.03 (0.73–10.8)	NA	
Age at first operation (yr)	54.3 ± 9.9	45.8 ± 24.3	.713
Location of tumor (ratio of clival chordoma to all)	3/6	8/10	.299 ^b
Postsurgical RT radiation dose (Gy)	72.4 ± 33.5 (n = 4)	74.2 ± 10.9 (n = 7)	.927
Ratio of patients with postsurgical RT to all	4/6	9/10	.518 ^b
Time from first operation to first follow-up MRI (mo)	62.8 ± 53.3	71.4 ± 76.2	>.99
Time between the 2 follow-up MRIs (mo)	9.1 ± 5.2	18.3 ± 12.5	.022
No. of surgical resections at first follow-up MRI	2.00 ± 0.89	1.10 ± 0.32	.056
Sex (M/F)	5:1	7:3	>.99 ^b
Histopathology (ratio of classic chordoma to all chordomas)	6/6	5/10	.093 ^b
Mean ADC (×10 ⁻³ × mm ² /s)	1.055 ± 0.298 (0.78–1.37)	1.622 ± 0.139 (1.34–1.65)	<.001
Tumor volume (× 10 ³ × mm ³)	21.2 ± 37.4 (0–60.4)	3.44 ± 2.38 (0–7.46)	.492

Note:—NA indicates not applicable.

^aNumbers in the table represent mean ± SD. The numbers in parentheses indicate the 95% CIs.

^bP value was calculated by the Fisher exact test because the data were categorical.

growth rate, we calculated the tumor doubling time in patients with a positive volume change ratio (ie, growing tumors) using the Schwartz formula¹⁷:

$$\text{Doubling Time} = t \log 2 / [\log (\text{Vol}_{2\text{nd}} / \text{Vol}_{1\text{st}})],$$

where *t* is the time interval between the 2 MR imaging scans.

We defined growing tumors with a doubling time of <1 year as aggressive tumors and those with a doubling time of ≥1 year as nonaggressive tumors.

Statistical Analysis

Statistical analysis was performed with the Statistical Package for the Social Sciences, Version 22 for Windows (IBM, Armonk, New York). The tumor measurements were assessed for interobserver reliability using the intraclass correlation coefficient, and mean values were used for further evaluation. On the first postoperative MR imaging, we compared mean ADC values, tumor volume, patient age at the time of the first surgical resection, time interval between the surgical resection and the first MR imaging, time interval between the first and second MR imaging examinations, number of surgical resections, patient sex, histopathology, location of the tumor, and volume change ratio between the 2 groups using the Mann-Whitney *U* test or Fisher exact test. We assessed the cutoff ADC on the first MR imaging to predict aggressiveness and receiver operating characteristic analysis to assess outcomes in the aggressive tumor group. The optimal cutoff value in the receiver operating characteristic analysis was determined as a value to maximize the Youden index.¹⁸ Kaplan-Meier curves for survival were compared using log-rank tests with the following variables: the mean ADC cutoff value in the receiver operating characteristic analysis and the following items previously reported to be prognostic factors: age at the time of the first operation,¹⁹ number of previous surgical resections,^{19,20} tumor volume,^{2,19} histopathology,²¹ tumor location,² and adjuvant radiation therapy.¹⁶ The study end point was survival. The survival period was calculated as the duration from the first MR imaging scan to the date of death or last follow-up in the censored living patients. Moreover, a Kaplan-Meier curve with a log-rank test was performed as a reference at the second MR imaging in the 2 groups. A 2-tailed *P* value <.05 was statistically significant.

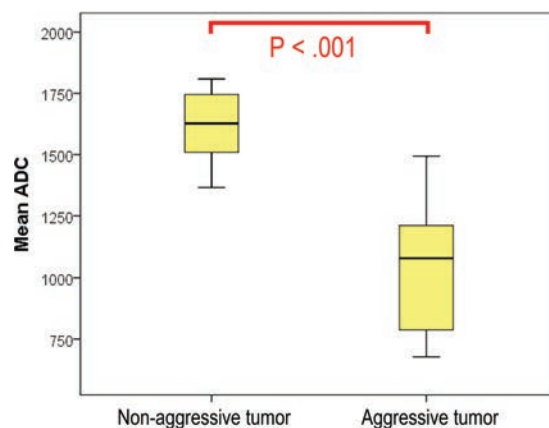


FIG 1. Comparison of mean ADC values between groups with different tumor-progression statuses. There was a significant difference between the 2 groups (*P* < .001).

RESULTS

Demographic, Clinical, and Radiographic Data

The intraclass correlation coefficients for interobserver reliability between the 2 readers were 0.922 (95% CI, 0.843–0.963) for the mean ADC and 0.974 (95% CI, 0.946–0.988) for the tumor volume. Six of the 16 patients had aggressive tumors, and 10 had nonaggressive tumors. Seven of the 16 patients died during the study period (5 were in the aggressive-tumor group and died of complications of their chordomas; 2 were in the nonaggressive tumor group and died of concurrent diffuse large B-cell lymphoma [*n* = 1] and an unknown cause [*n* = 1]). The patient characteristics are shown in Table 1.

The volume change ratios were significantly different between the 2 groups (*P* = .003). The mean ADC was significantly lower in the aggressive tumor group than in the nonaggressive tumor group (*P* < .001; Figs 1–3). The time interval between the 2 MR imaging examinations was significantly shorter in the aggressive tumor group than in the nonaggressive tumor group (*P* = .022).

Role of ADC in Predicting Aggressive Tumor at First MRI

Receiver operating characteristic analysis clearly distinguished the aggressive tumor group from the nonaggressive tumor group with a cutoff ADC of $1.494 \times 10^{-3} \times \text{mm}^2/\text{s}$, a sensitivity of 1.000

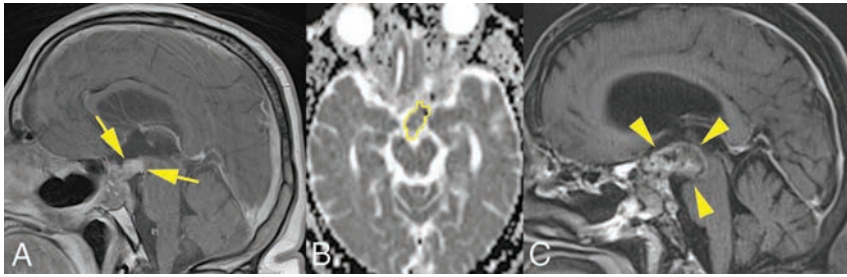


FIG 2. A 59-year-old man with a recurrent chordoma in the aggressive tumor group. A, Two years after the first surgery, contrast-enhanced T1-weighted imaging shows an expansile mass extending to the suprasellar region (arrows). B, The ROI outlined in yellow on the ADC map represents decreased water diffusivity ($ADC = 1.211 \times 10^{-3} \times \text{mm}^2/\text{s}$). C, Contrast-enhanced T1-weighted imaging obtained 8 months later shows an increase of the mass (volume change ratio, 1.67; arrowheads) with a doubling time of 5.5 months. The patient died of disease 15 months after the second MR imaging examination.

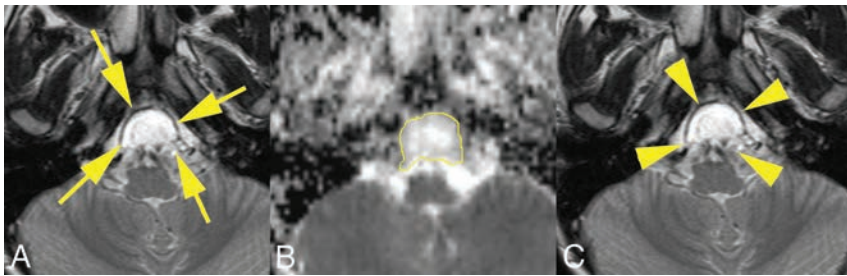


FIG 3. A 10-year-old boy with a residual chordoma in the nonaggressive tumor group. A, Three years after the first operation, T2-weighted imaging shows an expansile mass in the clivus (arrows). B, The ROI outlined in yellow on the ADC map represents increased water diffusivity ($ADC = 1.808 \times 10^{-3} \text{mm}^2/\text{s}$). C, The mass was stable on T2-weighted imaging obtained 13 months later (volume change ratio = 0.11; arrowheads) with a doubling time of 10.0 years. He was still alive 7 years after the second MR imaging.

Table 2: ROC plot analysis for ADC values differentiating an aggressive tumor from a nonaggressive tumor^a

	Aggressive Tumor
AUC (95% CI)	0.983 (0.911–1.000) ($P = .002$)
Cutoff ADC value ($\times 10^{-3} \times \text{mm}^2/\text{s}$)	1.494
Sensitivity	1.000 (0.541–1.000)
Specificity	0.900 (0.555–0.998)
Accuracy	0.938 (0.698–0.998)
PPV	0.857 (0.421–0.996)
NPV	1.000 (0.664–1.000)
Positive LR	10 (1.56–64.2)
Negative LR	0

Note:—ROC indicates receiver operating characteristic; AUC, area under the curve; LR, likelihood ratio; NA, not available; NPV, negative predictive value; PPV, positive predictive value.

^aNumbers in parentheses indicate 95% confidence intervals.

(95% CI, 0.541–1.000), a specificity of 0.900 (95% CI, 0.555–0.998), and a higher area under the curve of 0.983 ($P = .002$; 95% CI, 0.911–1.000; Table 2).

Predicting Survival for Patients with Chordoma

The median follow-up was 48 months (range, 4–126 months). The results for prognostic factors are shown in Table 3. The log-rank test revealed that an ADC below the cutoff of $\leq 1.494 \times 10^{-3} \times \text{mm}^2/\text{s}$ was associated with a significantly worse prognosis ($P = .006$, Fig 4A). The log-rank test for the 2 groups at the second MR imaging showed a significantly worse prognosis in the aggressive tumor group than in the nonag-

gressive tumor group ($P < .001$, Fig 4B). There was a significant association between ≥ 2 previous surgical resections and a worse prognosis ($P = .002$). The other variables did not contribute significantly to survival.

DISCUSSION

Our measurements showed that the interclass correlation coefficients were >0.8 , which indicated excellent interobserver reliability.²² In patients with residual postoperative chordoma, the tumor ADC values accurately predicted disease progression as defined by tumor volume change with time. This finding is consistent with that reported by Yeom et al,⁴ who suggested that poorly differentiated chordomas have a lower ADC value compared with conventional and chondroid chordomas. Aggressive chordoma has a worse prognosis and typically arises in a pre-existing low-grade lesion with or without previous radiation therapy.^{1,5,23–28} Thus, a lower ADC value in chordomas might correlate with aggressive growth. By measuring ADC coefficients of residual chordomas, we were able to retrospectively identify patients who went on to show tumor

progression >9 months later at the second follow-up MR imaging. Moreover, ADC measurement is less technically demanding for measuring tumor volumes.

Our Kaplan-Meier curves for survival using a log-rank test identified a lower ADC value and more surgical resections as significant prognostic factors. The ADC and the number of surgical resections could be confounder factors of each other for survival (On-line Fig 3). Most of the reports related to chordoma evaluated primary chordomas and recurrent chordomas en bloc, but we focused on residual or recurrent chordomas.^{21,29,30} Ailon et al⁶ suggested that further complete surgical resection can be considered for local recurrent chordoma, even if the management of recurrent chordoma is challenging and may be palliative. We supposed that follow-up MR imaging using ADC mapping could discriminate small chordomas with an aggressive potential from those without it; this discrimination could allow a short follow-up or early salvage therapy (further surgical resection) that would likely be successful or effective.

RT might affect MR imaging signal evaluation in residual or recurrent tumors.^{31–33} We did not find any correlation between the ADC values and RT dose or duration from RT to the first MR imaging (On-line Appendix). However, ADC values reflecting the response to treatment might be increased several days after RT or chemotherapy in various types of tumors.^{31–34} Given that ADC values correlate with cell density,³³ the treat-

ment response (with reduction of tumor cell volume) could elevate the ADC, while tumor progression (with proliferation of tumor cells) could decrease it. There is little information concerning MR imaging signal changes in chordomas after RT, particularly after proton or carbon ion RT. Proton or carbon ion RT might become an alternative therapy for unresectable chordoma in the future.^{20,35,36} We speculate that a reduced ADC during follow-up after RT might predict early recurrence.

Our study has several limitations. First, it was retrospective in nature and included a small population from a single institution. Chordoma is a rare low-grade tumor, so it is difficult to

perform large studies in patients with this tumor. Second, because of the long time intervals between datasets, the MR imaging scan parameters were different. Third, we were unable to evaluate the pathology of the tumors in those who died of disease to assess aggressiveness or dedifferentiation in those tumors. Fourth, the time interval between the 2 follow-up MR imaging scans differed between the 2 groups. Fifth, whether 1 year of doubling time was the most appropriate cutoff to separate the aggressive tumor group from the nonaggressive tumor group is unknown. Sixth, there were 2 patients with an unknown RT dose and 1 patient with an unknown RT history,

which might have affected the results for our small cohort. Finally, we did not show a significant role for RT in survival. The role of RT might be underestimated because high-dose RT is needed to reduce the risk of recurrence and improve patient prognoses.^{12,13,37} Further studies are needed to address these issues.

CONCLUSIONS

The mean ADC for recurrent or residual chordoma after the first operation could predict a subgroup with likely tumor progression and was significantly lower in the aggressive tumor group than in the nonaggressive tumor group. An $ADC \leq 1.494 \times 10^{-3} \text{ mm}^2/\text{s}$ could be predictive of the likelihood of rapid disease progression and a worse prognosis. In chordoma with a lower ADC, therefore, it may be prudent to recommend closer follow-up.

Table 3: Kaplan-Meier curves for survival using log-rank tests in patients with recurrent chordomas

Explanatory Variables	Total No.	No. of Events	P Value
Univariate models			
Age at first operation (yr)			.312
Younger than 60	10	5	
60 or older	6	2	
No. of surgical resections at first MRI			.002
1	11	3	
≥ 2	5	4	
Tumor volume			.957
$< 3 \times 10^3 \times \text{mm}^3$	10	4	
$\geq 3 \times 10^3 \times \text{mm}^3$	6	3	
Histopathology			.346
Chondroid chordoma	5	1	
Classic chordoma	11	6	
Tumor location			.507
Clivus	11	5	
Other sites	5 (C = 1, L = 2, S = 1, other = 1)	2	
Adjuvant radiation therapy			.172
None/unknown	3	2	
Done	13	5	
Mean ADC (for an aggressive tumor)			.006
$> 1.494 \times 10^{-3} \times \text{mm}^2/\text{s}$	10	2	
$\leq 1.494 \times 10^{-3} \times \text{mm}^2/\text{s}$	6	5	

Note:—C indicates cervical spine; L, lumbar spine; S, sacrum.

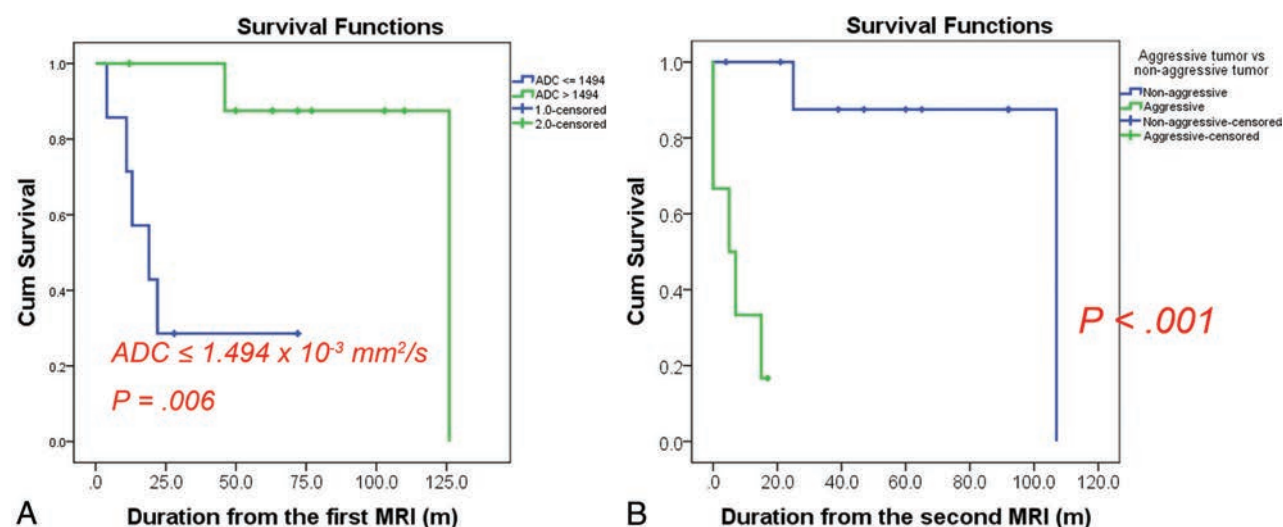


FIG 4. Kaplan-Meier curves using log-rank tests for survival. A, Graph shows 2 groups based on a cutoff ADC of $1.494 \times 10^{-3} \text{ mm}^2/\text{s}$ at the first MR imaging. The group with the lower ADC had a significantly worse prognosis ($P = .006$). B, Graph shows the tumor progression rate in the 2 groups at the second MR imaging. The prognosis was significantly worse in the aggressive tumor group than in the nonaggressive tumor group ($P < .001$). The cutoff ADC value could predict patients with a worse prognosis at the first MR imaging at a mean of 9.1 ± 5.2 months earlier than the second MR imaging. Cum indicates cumulative.

REFERENCES

1. Fletcher CD, Bridge JA, Hogendoorn P, et al. *WHO Classification of Tumours of Soft Tissue and Bone*. 4th ed. Lyon: IARC Press; 2013
2. Chugh R, Tawbi H, Lucas DR, et al. **Chordoma: the nonsarcoma primary bone tumor.** *Oncologist* 2007;12:1344–50 CrossRef Medline
3. Müller U, Kubik-Huch RA, Ares C, et al. **Is there a role for conventional MRI and MR diffusion-weighted imaging for distinction of skull base chordoma and chondrosarcoma?** *Acta Radiol* 2016;57:225–32 CrossRef Medline
4. Yeom KW, Lober RM, Mobley BC, et al. **Diffusion-weighted MRI: distinction of skull base chordoma from chondrosarcoma.** *AJNR Am J Neuroradiol* 2013;34:1056–61, S1 CrossRef Medline
5. Hanna SA, Tirabosco R, Amin A, et al. **Dedifferentiated chordoma: a report of four cases arising 'de novo.'** *J Bone Joint Surg Br* 2008;90:652–56 Medline
6. Ailon T, Torabi R, Fisher CG, et al. **Management of locally recurrent chordoma of the mobile spine and sacrum: a systematic review.** *Spine (Phila Pa 1976)* 2016;41(Suppl 20):S193–98 CrossRef Medline
7. Gokaslan ZL, Zadnik PL, Sciubba DM, et al. **Mobile spine chordoma: results of 166 patients from the AOSpine Knowledge Forum Tumor database.** *J Neurosurg Spine* 2016;24:644–51 CrossRef Medline
8. Boriani S, Saravanja D, Yamada Y, et al. **Challenges of local recurrence and cure in low grade malignant tumors of the spine.** *Spine (Phila Pa 1976)* 2009;34:S48–57 CrossRef Medline
9. Boriani S, Bandiera S, Biagini R, et al. **Chordoma of the mobile spine: fifty years of experience.** *Spine (Phila Pa 1976)* 2006;31:493–503 CrossRef Medline
10. York JE, Kaczaraj A, Abi-Said D, et al. **Sacral chordoma: 40-year experience at a major cancer center.** *Neurosurgery* 1999;44:74–79; discussion 79–80 CrossRef Medline
11. Chen KW, Yang HL, Lu J, et al. **Prognostic factors of sacral chordoma after surgical therapy: a study of 36 patients.** *Spinal Cord* 2010;48:166–71 CrossRef Medline
12. Hulén CA, Temple HT, Fox WP, et al. **Oncologic and functional outcome following sacrectomy for sacral chordoma.** *J Bone Joint Surg Am* 2006;88:1532–39 Medline
13. Pennicooke B, Laufer I, Sahgal A, et al. **Safety and local control of radiation therapy for chordoma of the spine and sacrum: a systematic review.** *Spine (Phila Pa 1976)* 2016;41(Suppl 20):S186–92 CrossRef Medline
14. Eisenhauer EA, Therasse P, Bogaerts J, et al. **New response evaluation criteria in solid tumours: revised RECIST guideline (version 1.1).** *Eur J Cancer* 2009;45:228–47 CrossRef Medline
15. Si MJ, Wang CS, Ding XY, et al. **Differentiation of primary chordoma, giant cell tumor and schwannoma of the sacrum by CT and MRI.** *Eur J Radiol* 2013;82:2309–15 CrossRef Medline
16. Kabolizadeh P, Chen YL, Liebsch N, et al. **Updated outcome and analysis of tumor response in mobile spine and sacral chordoma treated with definitive high-dose photon/proton radiation therapy.** *Int J Radiat Oncol Biol Phys* 2017;97:254–62 CrossRef Medline
17. Choe J, Lee SM, Lim S, et al. **Doubling time of thymic epithelial tumours on CT: correlation with histological subtype.** *Eur Radiol* 2017;27:4030–36 CrossRef Medline
18. Zukotynski KA, Vajapeyam S, Fahey FH, et al. **Correlation of 18F-FDG PET and MRI apparent diffusion coefficient histogram metrics with survival in diffuse intrinsic pontine glioma: a report from the Pediatric Brain Tumor Consortium.** *J Nucl Med* 2017;58:1264–69 CrossRef Medline
19. Bettgowda C, Yip S, Lo SL, et al; AOSpine Knowledge Forum Tumor. **Spinal column chordoma: prognostic significance of clinical variables and T (brachyury) gene SNP rs2305089 for local recurrence and overall survival.** *Neuro Oncol* 2017;19:405–13 CrossRef Medline
20. Park L, Delaney TF, Liebsch NJ, et al. **Sacral chordomas: impact of high-dose proton/photon-beam radiation therapy combined with or without surgery for primary versus recurrent tumor.** *Int J Radiat Oncol Biol Phys* 2006;65:1514–21 CrossRef Medline
21. Kayani B, Sewell MD, Tan KA, et al. **Prognostic factors in the operative management of sacral chordomas.** *World Neurosurg* 2015;84:1354–61 CrossRef Medline
22. Han X, Suo S, Sun Y, et al. **Apparent diffusion coefficient measurement in glioma: influence of region-of-interest determination methods on apparent diffusion coefficient values, interobserver variability, time efficiency, and diagnostic ability.** *J Magn Reson Imaging* 2017;45:722–30 CrossRef Medline
23. Kayani B, Sewell MD, Hanna SA, et al. **Prognostic factors in the operative management of dedifferentiated sacral chordomas.** *Neurosurgery* 2014;75:269–75; discussion 275 CrossRef Medline
24. Kim SC, Cho W, Chang UK, et al. **Two cases of dedifferentiated chordoma in the sacrum.** *Korean J Spine* 2015;12:230–34 CrossRef Medline
25. Makek M, Leu HJ. **Malignant fibrous histiocytoma arising in a recurrent chordoma: case report and electron microscopic findings.** *Virchows Arch A Pathol Anat Histol* 1982;397:241–50 CrossRef Medline
26. Halpern J, Kopolovic J, Catane R. **Malignant fibrous histiocytoma developing in irradiated sacral chordoma.** *Cancer* 1984;53:2661–62 Medline
27. Fukuda T, Aihara T, Ban S, et al. **Sacroccygeal chordoma with a malignant spindle cell component: a report of two autopsy cases with a review of the literature.** *Acta Pathol Jpn* 1992;42:448–53 Medline
28. Hruban RH, May M, Marcove RC, et al. **Lumbo-sacral chordoma with high-grade malignant cartilaginous and spindle cell components.** *Am J Surg Pathol* 1990;14:384–89 CrossRef Medline
29. Ruosi C, Colella G, Di Donato SL, et al. **Surgical treatment of sacral chordoma: survival and prognostic factors.** *Eur Spine J* 2015;24(Suppl 7):912–17 CrossRef Medline
30. Kayani B, Hanna SA, Sewell MD, et al. **A review of the surgical management of sacral chordoma.** *Eur J Surg Oncol* 2014;40:1412–20 CrossRef Medline
31. Hong X, Liu L, Wang M, et al. **Quantitative multiparametric MRI assessment of glioma response to radiotherapy in a rat model.** *Neuro Oncol* 2014;16:856–67 CrossRef Medline
32. Morse DL, Galons JP, Payne CM, et al. **MRI-measured water mobility increases in response to chemotherapy via multiple cell-death mechanisms.** *NMR Biomed* 2007;20:602–14 CrossRef Medline
33. Chenevert TL, Stegman LD, Taylor JM, et al. **Diffusion magnetic resonance imaging: an early surrogate marker of therapeutic efficacy in brain tumors.** *J Natl Cancer Inst* 2000;92:2029–36 CrossRef Medline
34. Jordan BF, Runquist M, Raghunand N, et al. **Dynamic contrast-enhanced and diffusion MRI show rapid and dramatic changes in tumor microenvironment in response to inhibition of HIF-1alpha using PX-478.** *Neoplasia* 2005;7:475–85 CrossRef Medline
35. Imai R, Kamada T, Araki N. **Carbon ion radiation therapy for unresectable sacral chordoma: an analysis of 188 cases.** *Int J Radiat Oncol Biol Phys* 2016;95:322–27 CrossRef Medline
36. Uhl M, Welzel T, Jensen A, et al. **Carbon ion beam treatment in patients with primary and recurrent sacroccygeal chordoma.** *Strahlenther Onkol* 2015;191:597–603 CrossRef Medline
37. Choy W, Terterov S, Kaprelian TB, et al. **Predictors of recurrence following resection of intracranial chordomas.** *J Clin Neurosci* 2015;22:1792–96 CrossRef Medline

MSVAT-SPACE-STIR and SEMAC-STIR for Reduction of Metallic Artifacts in 3T Head and Neck MRI

 T. Hilgenfeld,  M. Prager,  F.S. Schwinding,  M. Nittka,  P. Rammelsberg,  M. Bendszus,  S. Heiland, and  A. Juerchott

ABSTRACT

BACKGROUND AND PURPOSE: The incidence of metallic dental restorations and implants is increasing, and head and neck MR imaging is becoming challenging regarding artifacts. Our aim was to evaluate whether multiple-slab acquisition with view angle tilting gradient based on a sampling perfection with application-optimized contrasts by using different flip angle evolution (MSVAT-SPACE)-STIR and slice-encoding for metal artifact correction (SEMAC)-STIR are beneficial regarding artifact suppression compared with the SPACE-STIR and TSE-STIR in vitro and in vivo.

MATERIALS AND METHODS: At 3T, 3D artifacts of 2 dental implants, supporting different single crowns, were evaluated. Image quality was evaluated quantitatively (normalized signal-to-noise ratio) and qualitatively (2 reads by 2 blinded radiologists). Feasibility was tested in vivo in 5 volunteers and 5 patients, respectively.

RESULTS: Maximum achievable resolution and the normalized signal-to-noise ratio of MSVAT-SPACE-STIR were higher compared with SEMAC-STIR. Performance in terms of artifact correction was dependent on the material composition. For highly paramagnetic materials, SEMAC-STIR was superior to MSVAT-SPACE-STIR (27.8% smaller artifact volume) and TSE-STIR (93.2% less slice distortion). However, MSVAT-SPACE-STIR reduced the artifact size compared with SPACE-STIR by 71.5%. For low-paramagnetic materials, MSVAT-SPACE-STIR performed as well as SEMAC-STIR. Furthermore, MSVAT-SPACE-STIR decreased artifact volume by 69.5% compared with SPACE-STIR. The image quality of all sequences did not differ systematically. In vivo results were comparable with in vitro results.

CONCLUSIONS: Regarding susceptibility artifacts and acquisition time, MSVAT-SPACE-STIR might be advantageous over SPACE-STIR for high-resolution and isotropic head and neck imaging. Only for materials with high-susceptibility differences to soft tissue, the use of SEMAC-STIR might be beneficial. Within limited acquisition times, SEMAC-STIR cannot exploit its full advantage over TSE-STIR regarding artifact suppression.

ABBREVIATIONS: CCT-T = porcelain-fused-to-metal nonprecious alloy crown with titanium implant; MAVRIC = multiaquisition with variable resonance image combination; MSVAT-SPACE = multiple-slab acquisition with view angle tilting gradient based on SPACE; nSNR = normalized SNR; SEMAC = slice-encoding for metal artifact correction; SPACE = sampling perfection with application-optimized contrasts by using different flip angle evolutions; Z-T = monolithic zirconia crown with titanium implant

MR imaging has become a widely used technique for the head and neck area. Image quality, however, it is often impaired by metallic dental restorations and implant-supported prostheses.¹ MR image quality is affected by dental metals spoiling the

homogeneity of the static magnetic field (B_0)^{2,3} and by eddy currents in response to alternating gradients and radiofrequency magnetic fields.^{4,5} In the elderly, besides dental restoration materials, metallic implants and their crowns are a major source of artifacts. In Germany for instance, the prevalence of dental implants has increased 10-fold compared with 1997,⁶ which is caused by an increased patient life expectancy and a broadening of implant indications. Therefore, artifact reduction has become increasingly important in head and neck imaging.

To address the decreased image quality due to metallic implants, several sequences for metal artifact reduction were developed such as view angle tilting, slice-encoding for metal artifact correction (SEMAC), multiaquisition with variable resonance image combination (MAVRIC; GE Healthcare, Milwaukee, Wisconsin), the

Received October 15, 2017; accepted after revision March 30, 2018.

From the Department of Neuroradiology (T.H., M.P., M.B., S.H., A.J.) and Section of Experimental Radiology (M.P., S.H.), University of Heidelberg, Heidelberg, Germany; Department of Prosthodontics (F.S.S., P.R.), Heidelberg University Hospital, Heidelberg, Germany; and Siemens Healthcare (M.N.), Erlangen, Germany.

Tim Hilgenfeld and Marcel Prager contributed equally to this work.

The study was supported, in part, by Dietmar Hopp Stiftung (project no. 23011228).

Please address correspondence to Alexander Juerchott, MD, Department for Neuroradiology, University Hospital, Im Neuenheimer Feld 400, 69120 Heidelberg, Germany; e-mail: Alexander.Juerchott@med.uni-heidelberg.de

<http://dx.doi.org/10.3174/ajnr.A5678>

Parameters of all sequences

Sequence	TR/TE (ms)	Voxel		Readout Bandwidth			Slice-Encoding Steps or Oversampling (%)		Time (min:sec)
		Size (mm)	FOV (mm)	Matrix	(Hz/Px)	Slices	VAT		
SPACE-STIR	2500/131	0.55 × 0.55 × 0.55	140 × 124	256	501	72	55.6	No	14:02
MSVAT-SPACE-STIR	2500/199	0.55 × 0.55 × 0.55	140 × 84	256	528	72	55.6	Yes	06:04
TSE-STIR	5100/44	0.59 × 0.59 × 1.5	150 × 150	256	592	25	No	No	03:36
SEMACE-STIR	5100/45	0.59 × 0.59 × 1.5	150 × 150	256	592	25	4	Yes	06:19

Note:—VAT indicates view angle tilting.

multiple-slab acquisition with view angle tilting gradient based on a sampling perfection with application-optimized contrasts by using different flip angle evolutions (SPACE) sequence (MSVAT-SPACE; Siemens, Erlangen, Germany), and combinations of these techniques such as MAVRIC-SEMACE.⁷⁻¹² These new techniques for artifact reduction were predominantly developed and tested for orthopedic and neurosurgical applications.^{13,14} Until now, little attention has been paid to the head and neck area. Moreover, results of previous studies are of limited transferability because the amount of material, shape, and materials is different in the head and neck area compared with orthopedic or neurosurgical implants, and all these characteristics influence artifact size.

The combination of these pulse sequences with STIR-based fat suppression, as the most reliable fat-suppression technique in the presence of B_0 inhomogeneities,¹⁵ might be beneficial in cases with metallic dental materials and suspected osteomyelitis (evaluation of bone marrow edema), head and neck tumors (defining tumor margins), or injury of the inferior alveolar nerve (evaluation of nerve signal intensity).¹⁶ Furthermore, previous studies focused on the maximum achievable reduction of artifacts and an ideal comparison of pulse techniques (identical imaging parameters) at the expense of long acquisition times. This focus severely limits the implementation in routine protocols, especially because the head and neck area is extremely sensitive to motion artifacts due to breathing and swallowing. Therefore, we aimed to investigate how well these techniques perform within a limited acquisition time in the presence of commercially available dental implants with supported prostheses compared with standard sequences. To reach this goal, the main tasks were the following:

- 1) Quantify and compare metal-induced artifact volumes (signal loss and pileup) for 2 commercially available implant-supported prostheses using anisotropic (TSE-STIR, SEMACE-STIR) and isotropic (SPACE-STIR, MSVAT-SPACE-STIR) sequences

- 2) Compare image quality of all sequences qualitatively and quantitatively

- 3) Test the feasibility of all sequences in 5 volunteers with metallic dental materials and the sequence providing the best trade-off among artifact reduction, resolution, and image quality in 5 patients.

MATERIALS AND METHODS

MR Imaging and Sequences

A 3T MR imaging system (Magnetom Trio, a Tim system; Siemens), a 16-channel multipurpose surface coil (Variety; NORAS MRI Products; Höchberg, Germany) for the in vitro experiments, and a 15-channel surface coil (Mandibula; NORAS MRI Products) for the in vivo measurements were used.

The SEMACE prototype sequence applies additional phase-encoding steps in the slice direction to correct for distortions of the excited slice profile¹⁷ and also incorporates view angle tilting to correct for in-plane distortions.¹¹ The MSVAT-SPACE prototype sequence uses slab-selective excitation and refocusing radiofrequency pulses that allow interleaved multislab acquisitions.¹⁸

Because we aimed for both short acquisition times that allow clinical application and maximum artifact reduction of each specific sequence, individual sequence optimization ended with differences in sequence parameters but an identical, relatively short acquisition time. First, MSVAT-SPACE-STIR and SEMACE-STIR were optimized for artifact reduction in the presence of implants (eg, by changing the voxel size, readout bandwidth, slice oversampling, and number of slice-encoding steps). Second, the SNR was optimized for these 2 sequences (eg, by changing the turbo factor or number of averages). Third, standard sequences (SPACE-STIR, TSE-STIR) with imaging parameters as similar as possible to MSVAT-SPACE-STIR and SEMACE-STIR were implemented for comparison. Spectral coverage for off-resonance frequencies was slightly lower for MSVAT-SPACE-STIR (± 2.8 kHz) than for SEMACE-STIR (± 2.8 kHz). Due to restrictions in the prototype sequences, the bandwidths of inversion and excitation could not be perfectly matched (MSVAT-SPACE-STIR, 1/1.4 kHz; SEMACE-STIR, 1.72/1.4 kHz). For a reduction in scanning time, a generalized autocalibrating partially parallel acquisition was used in all sequences, and partial Fourier, for SPACE-STIR and MSVAT-SPACE-STIR. For SEMACE-STIR and TSE-STIR, a flip angle of 150° was used. Relevant parameters of all sequences are shown in the Table.

Evaluation of Artifact Volume

Besides the sizes and shape of materials, their magnetic susceptibility heavily influences the artifact volume. Schenck² classified 3 groups of materials because of their differences in magnetic susceptibility. To cover the worst- and best-case scenarios in a realistic setting, we used 2 commercially available implant-supported single crowns for the evaluation of artifact suppression. The single crowns of both prostheses were made of porcelain-fused-to-metal nonprecious alloy (CCT-T) and monolithic zirconia (Z-T), respectively. The CCT-T crown consisted of Cobalt (61%), Chrome (28%), and Tungsten (11%) and belongs to group 1, predicting large artifacts. In contrast, the crown of the Z-T sample consisted of Zirconia (92%) and belongs to group 3, resulting in no or only minimal artifacts. The implant body, abutment, and abutment screw of both implants were made of Titanium (diameter × length: 4.3 × 10 mm [CCT-T], 4.3 × 13 mm [Z-T]; Nobel-Replace; Nobel Biocare, Zurich, Switzerland).

Both samples were embedded in a mixture of semisynthetic fat (58.8%), water (40%), and macrogol-8-stearate (1.2%). Artifact volume (signal loss and pileup artifacts) was determined by a semiautomatic threshold-based process with AMIRA 3D software (FEI, Hillsboro, Oregon) as described before.¹⁹ Quantification of pileup artifacts was performed to serve as an indicator for slice distortions. In vitro results were compared with measured artifact areas in vivo in 5 volunteers with metallic dental materials. For each volunteer, the maximum artifact area was determined in 1 slice 3 times by 2 readers (reader 1 twice, reader 2 once). The results were averaged.

Qualitative Image Review

For analysis of image quality and to test the sequences in a realistic setting, we performed ex vivo measurements in 2 fresh porcine heads with inserted implant samples. For preparation of the implant site in the anterior section of the mandible, a pilot drill, 1.5 mm in diameter, and spiral drills, 2.8 and 3.5 mm in diameter, were used. Both implants were tested consecutively in both porcine heads. Positioning of the longitudinal axis of the implants, porcine teeth, and surface coil was like that in the in vivo situation. Two radiologists (both with 4 years' experience in head and neck imaging) independently assessed all images of the 2 porcine heads twice, with an interval of 2 months to exclude learning bias. Both readers were blinded to the type of sequence. Both observers were asked to identify 8 different anatomic structures of the mandible (cortical bone, trabecular bone, lamina dura, tooth root, pulp chamber, apical foramen, periodontal space, and enamel/dentin). A 5-point scale was used to assess the visibility of anatomic structures as described before.⁸ For visualization of anatomic structures, grade 5 indicated that the anatomic structure was not visible; grade 4, that <25% of the anatomic structure was visible; grade 3, visualization of 25%–50%; grade 2, visualization of 50%–75%; and grade 1, visualization of >75%.

Evaluation of motion artifacts in 5 patients was performed at 5 anatomic positions (lymph nodes in lymph node level II, submandibular gland, maxillary artery, inferior alveolar nerve, and masseter muscle). Evaluation of motion artifacts was performed as well on a 5-point scale: 5, anatomic structure not visible; 4, severe artifacts but contours could be delineated; 3, moderate artifacts that allow partial visibility of internal structures; 2, minor artifacts with good delineation of internal structures; and 1, no artifacts at all.

Quantitative Image Review

A phantom with 4 tubes (CRYO.S; Greiner Bio-One, Frickenhausen, Germany) containing water was used for normalized SNR (nSNR) measurements. Because a phased array radiofrequency coil was used, we determined the SNR by calculating the dynamic noise and the signal within the same ROI from 25 repetitions of each sequence.²⁰ Due to the long acquisition time of the conventional SPACE-STIR and the need for several repetitions of each sequence, evaluation of SNR in vivo was not possible. ROIs of 10 mm in diameter were placed manually in each of the 4 tubes in 1 slice. A Matlab script (MathWorks, Natick, Massachusetts) allowed copying the ROIs to the same position on MR images of

all sequences and repetitions. Due to the long acquisition time, signal drift had to be considered.²¹ Because signal drift was linear in all our measurements, we used linear regression to exclude the bias effects of signal drift. Finally, for a better comparability of SNR among different sequences, the SNR was normalized to voxel size and measurement time (nSNR, formula 1):

$$nSNR = \frac{\text{mean (SNR)}}{\sqrt{T} \times V}.$$

Formula 1: Calculation of *normalized SNR*; *mean (SNR)*, calculated SNR within the ROI; *T*, acquisition time in seconds; *V*, voxel volume in cubic millimeters.

Patient and Volunteer Recruitment

This observational, prospective study was approved by the institutional ethics committee (approval number S-452/2010; University of Heidelberg), and written informed consent was obtained from all participants. Artifact size of all sequences was evaluated in 5 volunteers with metallic dental materials disturbing the B₀. Furthermore, 1 sequence was tested in 5 patients presenting with various head and neck diseases (osteomyelitis, injury of the inferior alveolar nerve, jaw tumor, and drained abscess in the mandible), and motion artifacts were analyzed.

Statistical Analysis

Due to multiple comparisons, a 2-way analysis of variance with pair-wise post hoc Tukey tests was used for comparison of in vitro artifact volumes using SPSS 22 (IBM, Armonk, New York). Multiple comparisons of nSNR and in vivo artifact areas among all sequences for each volunteer were performed using a 1-way ANOVA with post hoc Tukey tests. Categorical data (visibility scores of image quality) were analyzed with the Fisher exact test after dichotomization of the scores into 2 groups ("good visibility," scores 1–2 and "unsatisfactory visibility," scores 3–5). The Cohen κ statistic (κ -value) was calculated to determine the inter- and intrarater agreement of image quality and interpreted as published before.²²

RESULTS

In Vitro Analysis

Quantification of artifact volume revealed only minor intrarater variability (mean, 1.6%; minimum, 0.1%; maximum, 5.5%) and minor interrater variability (mean, 1.1%; minimum, 0.1%; maximum, 2.8%).

Overall, artifact size of the CCT-T sample was significantly larger compared with the Z-T sample in all tested sequences ($P < .001$). The artifact volume of CCT-T was between 9.8 ± 1.4-fold (SEMACE-STIR, 2.7 versus 0.3 mL) and 26.4 ± 6.6-fold (SPACE-STIR, 12.9 versus 0.4 mL) larger than the artifact volume of Z-T (Fig 1).

Impact of Sequence Type on Artifact Volume

Comparing all STIR sequences with each other, we found a significant decrease of 71.5% ± 0.1% in artifact volume in MSVAT-SPACE-STIR compared with SPACE-STIR for the CCT-T sample ($P < .001$) and 69.7% ± 5.4% for the Z-T sample ($P < .001$, Figs 1 and 2). As a result, in vivo visibility of anatomic structures in direct proximity to a retainer and a dental filling

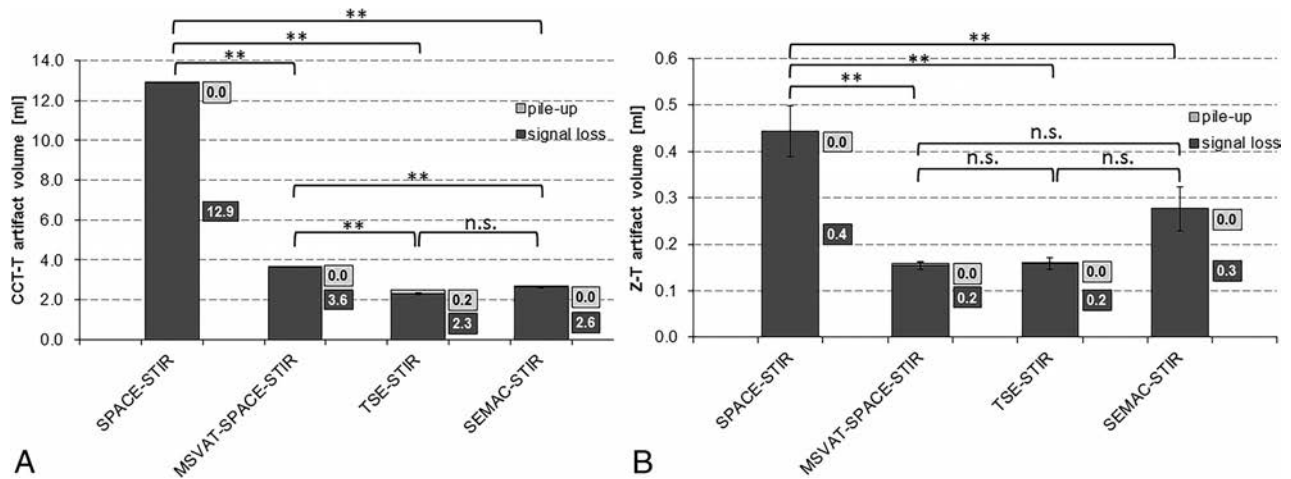


FIG 1. Artifact volumes (signal loss and pileup artifacts) of all sequences caused by the CCT-T (A) and the Z-T (B) samples (double asterisks indicate $P \leq .001$; numbers next to the bars indicate the volume of pileup and signal loss artifacts separately in milliliters). n.s. indicates not significant.

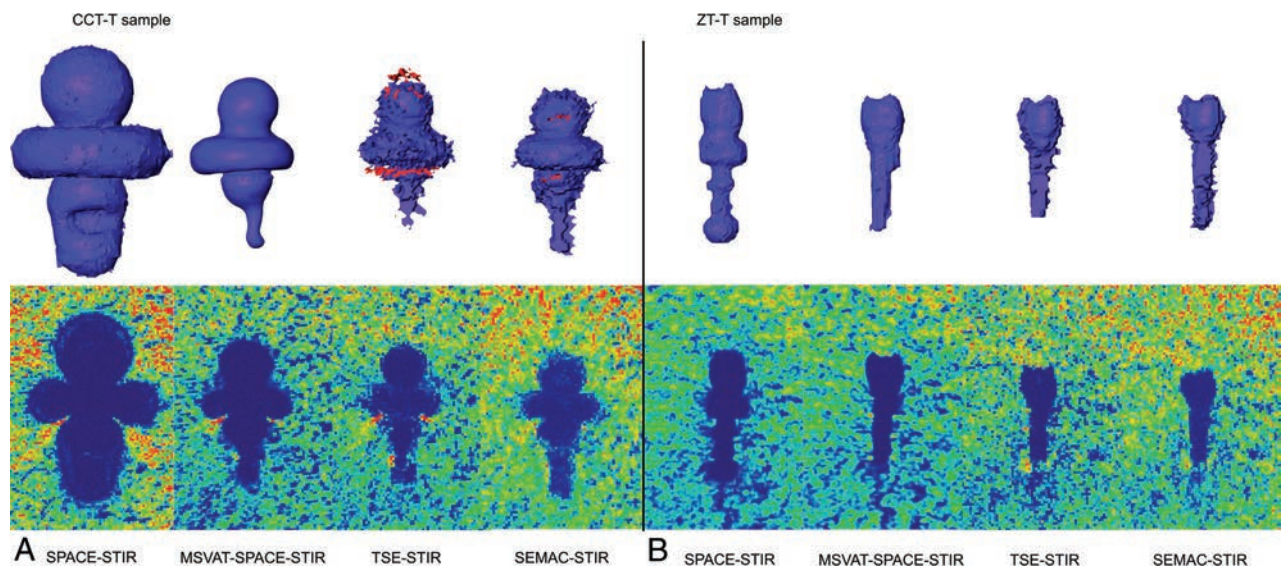


FIG 2. 3D rendering of artifacts and source images (blue, signal loss artifacts; red, pileup artifacts) of the CCT-T (A) samples and Z-T (B) samples for all evaluated sequences.

in the volunteers was improved in MSVAT-SPACE-STIR compared with standard SPACE-STIR (Fig 3). The smallest artifact volumes were observed for TSE-STIR and SEMAC-STIR followed by MSVAT-SPACE-STIR. In particular, the artifact volume of SEMAC-STIR was significantly smaller than the artifact volume of MSVAT-SPACE-STIR for the CCT-T sample ($P < .001$; 2.7 versus 3.7 mL) but not for the Z-T sample ($P = .974$; 0.3 versus 0.2 mL).

The amount of pileup artifacts, as an indicator of slice distortions, was dependent on the applied sequence type. The proportion between pileup artifact volume and overall artifact volume was lower for SPACE-STIR/MSVAT-SPACE-STIR (mean, $0.007\% \pm 0.0007\%/1.3\% \pm 0.004\%$ for the CCT sample) compared with TSE-STIR/SEMAC-STIR (mean, $7.8\% \pm 0.07\%/0.99\% \pm 0.04\%$). SEMAC-STIR significantly reduced the amount of pileup artifacts on overall artifact size for both samples ($P < .001$).

Evaluation of Image Quality

The nSNR of MSVAT-SPACE-STIR was higher than the nSNR of SPACE-STIR ($P < .001$, SNR increase of $22\% \pm 4.5\%$; Fig 4). No significant differences in nSNR were found between TSE-STIR and SEMAC-STIR. The nSNR of MSVAT-SPACE-STIR was 4.8 times higher in comparison with SEMAC-STIR ($P < .001$).

Interrater agreement for the assessment of image quality in porcine heads was good ($\kappa = 0.67$). Intrarater agreement was good for the first rater (κ -value = 0.77) and excellent for the second rater (κ -value = 0.86). No systematic differences in image quality were detected between SPACE-STIR and MSVAT-SPACE-STIR and TSE-STIR and SEMAC-STIR, respectively (Fig 5). Only the image quality of enamel/dentin was slightly better in TSE-STIR, SPACE-STIR, and MSVAT-SPACE-STIR compared with SEMAC-STIR ($P < .05$, $P < .001$, $P < .001$; Fig 5).

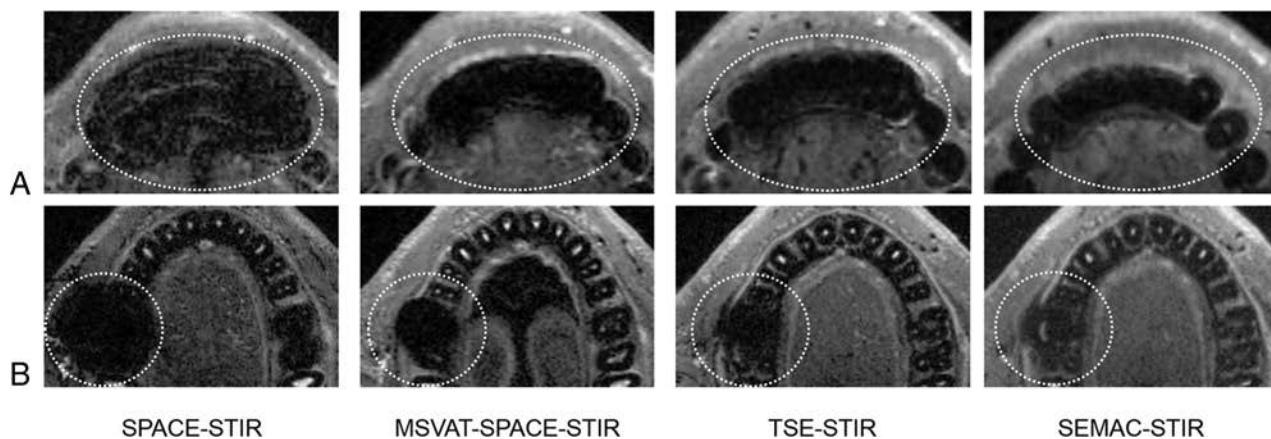


FIG 3. Comparison of all 4 STIR sequences in 2 volunteers with metallic dental materials. A, A patient with artifacts caused by a retainer (signal-loss artifact within *dashed lines*). B, A volunteer with artifacts caused by an amalgam filling. Note the decrease of artifact sizes in MSVAT-SPACE-STIR images compared with SPACE-STIR images in both examples. Minor differences can be noted between TSE-STIR and SEMAC-STIR images, as well.

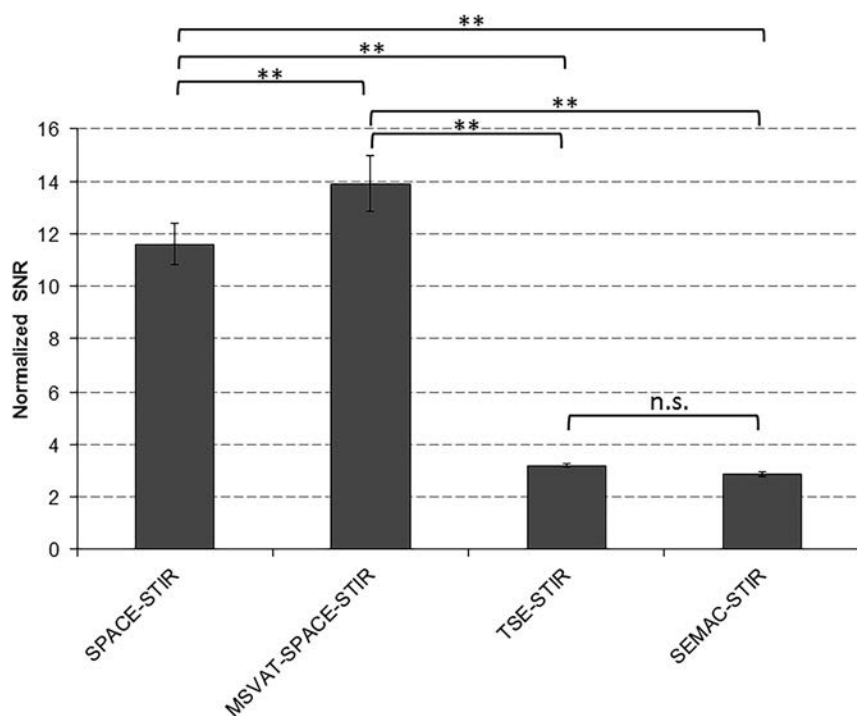


FIG 4. nSNR values of all used sequences. *Double asterisks* indicate $P \leq .001$. n.s. indicates not significant.

In Vivo Analysis

Finally, all 4 STIR sequences were tested in 5 volunteers with metallic dental restorations or retainers (Fig 3). When we compared all sequences, the largest artifact areas were observed in SPACE-STIR ($P < .001$). Furthermore, MSVAT-SPACE-STIR significantly reduced the artifact area in all volunteers compared with the SPACE-STIR sequence ($P < .001$; implant-supported crown, $35.7\% \pm 1\%$; retainer 1, $25.2\% \pm 0.3\%$; retainer 2, $54.3\% \pm 1.2\%$; metal abrasion, $36.2\% \pm 3.1\%$; amalgam filling, $60.4\% \pm 5.8\%$). The mean artifact reduction of MSVAT-SPACE-STIR was $42.3\% \pm 14.5\%$ compared with SPACE-STIR (Fig 3). In contrast, SEMAC-STIR significantly reduced the artifact area only for 1 volunteer with a retainer ($23.6\% \pm 1.4\%$; $P < .001$; Fig 3) compared with TSE-STIR. As

noted in the in vitro analysis, the smallest artifact areas were observed for TSE-STIR and SEMAC-STIR, followed by MSVAT-SPACE-STIR.

Because >30 minutes of acquisition time would have been needed for the 4 STIR sequences tested in vitro before, it was not possible to implement all sequences in clinical protocols. Because the visibility scores did not differ systematically and the results of artifact-reduction studies were dependent on the analyzed material, the nSNR and estimated size of artifacts in each patient were the decisive factors for sequence selection. Because none of the 5 randomly selected patients with head and neck pathologies presented with dental materials known to cause severe artifacts (eg, retainers), we chose to use MSVAT-STIR instead of SEMAC-STIR because of higher resolution, higher nSNR, and isotropic voxel size (Fig 6). In clinical application, no or only minor motion artifacts were observed by both raters (mean score of motion artifacts of both raters and all subjects, 1.3 ± 0.5 ; range over all subjects, 1.2 ± 0.4 to 1.6 ± 0.5).

DISCUSSION

In head and neck imaging, an increasing number of patients are presenting with metallic implants.⁶ This results in decreased image quality in the head and neck area and can even affect brain MR images.²³ Sufficient image quality, however, is essential, for example, for staging oral cavity cancers, detecting injury of the inferior alveolar nerve, or detecting bone marrow enhancement and edema in osteomyelitis. Thus, artifact-reduction techniques are becoming increasingly important for the head and neck area. Prior studies have evaluated the benefit of artifact-reduction tech-

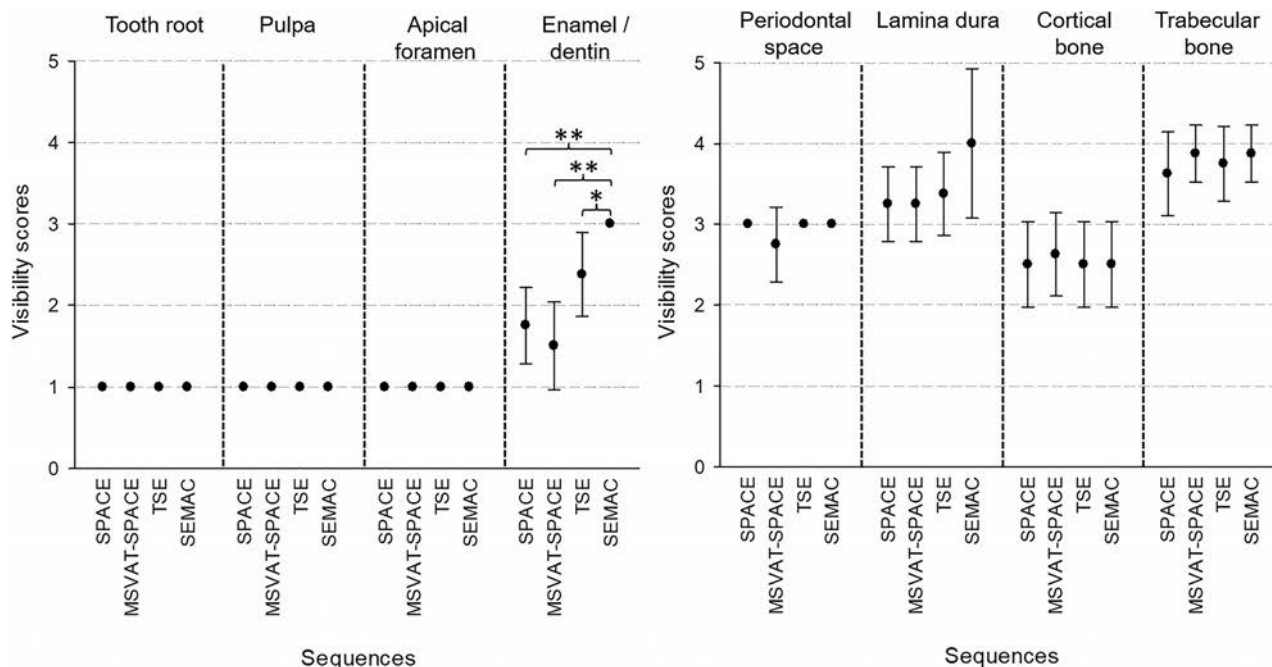


FIG 5. Mean visibility scores of in vitro images of the 8 anatomic structures in all STIR sequences. The asterisk indicates $P \leq .05$; double asterisks, $P \leq .001$.

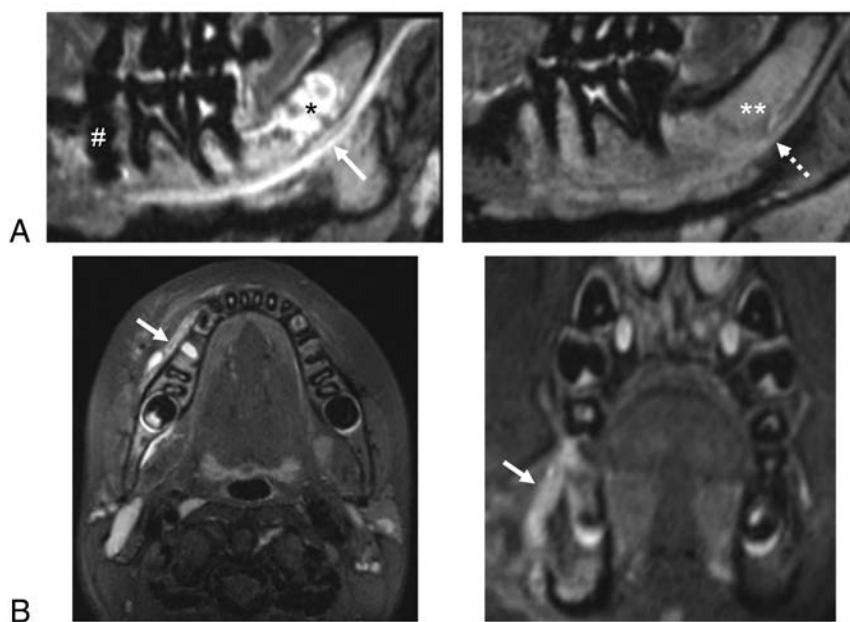


FIG 6. Two patients examined with MSVAT-SPACE-STIR. **A**, A 25-year-old woman with dysesthesia in the right mandible and chin after wisdom tooth extraction in the right mandible (asterisk indicates the extraction site). Increased signal intensity of the neurovascular bundle (white solid arrow) compared with the healthy side (white dashed arrow) in curved multiplane reconstructions of MSVAT-SPACE-STIR, suggesting nerve damage. Note the small amount of artifacts around the implant-supported crown (hash tag) and incomplete bone marrow conversion resulting in bright signal in STIR images on both sides (double asterisks). **B**, An 8-year-old child after drainage of an abscess in the right mandible with residual soft-tissue inflammation in the right lateral gingiva (white arrows in reformatted axial [left] and coronal [right] images).

niques for orthopedic and neurosurgical applications, but little attention has been paid to the head and neck area so far. Here, we demonstrate the advantages and disadvantages of MSVAT-SPACE-STIR and SEMAC-STIR in high-resolution head and

neck imaging, with special regards to short acquisition times in vitro and in vivo.

The MSVAT-SPACE-STIR sequence revealed a significant artifact reduction compared with the standard SPACE-STIR sequence in vivo and in vitro. No difference in artifact size was noted between MSVAT-SPACE-STIR and SEMAC-STIR for materials with lower magnetic-susceptibility difference compared with that of soft tissue. For materials with higher magnetic susceptibility, TSE-STIR and SEMAC-STIR showed the smallest artifact volumes. A significant reduction of distortions was observed by SEMAC-STIR compared with TSE-STIR. Combined artifact volume was not different between SEMAC-STIR and TSE-STIR in the in vitro analysis. In contrast, a small but statistically significant difference was observed in some volunteers, indicating a dependency of the results on material composition and material size.

Regarding MSVAT-SPACE-STIR, our results are consistent with the results of Ai et al,⁷ who reported a reduction of artifact volume for MSVAT-SPACE in T1-weighted images at 1.5T when imaging titanium screws. They observed a comparable degree of artifact reduction for titanium by comparing MSVAT-SPACE and conventional SPACE (up to 56% mean reduction in comparison with 70.5% in our study). However, the authors did not evaluate

the impact of 3T STIR imaging and, most important, dental restorations or implants, which are regularly encountered in clinical routine.

In contrast, a study by Zho et al²⁴ reported an artifact reduction of 80% by non-STIR SEMAC using a dental crown made of nickel and chromium. The apparently differing results can be explained by the difference in the number of slice-encoding steps, resulting in differences in spectral coverage and artifact volume, respectively. Higher numbers of slice-encoding steps increase the spectral coverage and thereby reduce the size of artifacts but increase the acquisition time at the same time. Zho et al used 36 slice-encoding steps in an acquisition time of 29 minutes. Such long acquisition times are not applicable to in vivo head and neck imaging because different weightings as well as pre- and post-contrast images are typically used in clinical protocols. An in vivo study of Lee et al¹³ noted only a minor artifact reduction of 17.8% using SEMAC-STIR instead of TSE-STIR for spine imaging. Once again, this can be explained by less spectral coverage in terms of slice-encoding steps compared with Zho et al but still more than we used in our study: 11 (Lee et al) versus 36 (Zho et al) versus 4 in our study. With our sequence parameters, however, an increase of slice-encoding steps from 4 to 11 would still have resulted in an acquisition time of >17 minutes, which precludes clinical use.

Since image quality was not systematically different among all tested sequences, we conclude that artifact reduction does not come at the expense of image quality. However, in the case of SEMAC-STIR, artifact reduction resulted in 75% increased acquisition time. Therefore, further acceleration techniques such as compressed sensing for the SEMAC sequence are desirable²⁵ to facilitate the clinical applicability of this technique. In contrast, MSVAT-SPACE-STIR significantly reduced overall artifact volume and decreased acquisition time by 57% compared with SPACE-STIR. In addition, the nSNR of MSVAT-SPACE-STIR was nearly 5 times higher than the nSNR of SEMAC-STIR. Furthermore, MSVAT-SPACE-STIR, unlike SEMAC-STIR, allowed isotropic image acquisition and multiplane reconstructions. In vivo application of MSVAT-SPACE-STIR resulted in high-quality 3D datasets with decreased artifact size.

We acknowledge some limitations of our study. The T1 relaxation times of the phantom are not identical to those in living tissue. This feature may result in vivo in other artifact volumes in STIR sequences as in our in vitro results. Furthermore, our phantom design allowed only evaluation of slice distortions in direct proximity of the signal loss. Because additional slice distortions can be expected beyond the signal loss as well, we probably underestimated the amount of slice-distortion reduction by MSVAT-SPACE-STIR and SEMAC-STIR. Finally, because of the small number of patients included, further research is necessary to determine which sequence is best in a patient population.

CONCLUSIONS

For optimized fat suppression in the presence of metallic dental implants for head and neck imaging, MSVAT-SPACE-STIR reduced artifact volume and acquisition time compared with the standard SPACE-STIR sequence while maintaining image quality. In addition, MSVAT-SPACE-STIR allowed a much higher resolution than SEMAC-STIR and offered the possibility of 3D

reconstructions. Within a clinically reasonable acquisition time, SEMAC-STIR reduced the amount of slice distortions, and, for some materials, artifact size as well compared with the optimized TSE-STIR sequence. Therefore, radiologists must decide between high-resolution 3D imaging (MSVAT-SPACE-STIR) and the smallest artifact size (SEMAC-STIR). SPACE-STIR is not recommended for head and neck MR imaging due to its vulnerability to susceptibility artifacts.

ACKNOWLEDGMENTS

The authors would like to thank Stefanie Sauer, PhD, a pharmacist at the Department of Pharmacy, Heidelberg University Hospital, for her contribution to the MR imaging phantom. Furthermore, we would like to thank NORAS MRI Products, especially Daniel Gareis, MSc, and Celik Turgay, MSc, for providing the two 16-channel multipurpose coils used in the present study.

Disclosures: Tim Hilgenfeld—*RELATED: Grant:* Dietmar-Hopp Foundation.* Marcel Prager—*RELATED: Grant:* Dietmar Hopp Foundation*. Mathias Nittka—*UNRELATED: Employment:* Siemens, Germany. Peter Rammelsberg—*UNRELATED: Board Membership:* GrindCare (Sunstar). *Comments:* Scientific Board, financial compensation only for travelling expenses; *Payment for Lectures Including Service on Speakers Bureaus:* ZMK Update, Oemus Media. Martin Bendszus—*UNRELATED: Board Membership:* Data and Safety Monitoring Board for Vascular Dynamics, Guerbet, Boehringer Ingelheim; *Consultancy:* Codman Neuro, Roche AG, Guerbet, Boehringer Ingelheim, B. Braun Medical; *Grants/Grants Pending:* German Research Foundation, Dietmar Hopp Foundation, Novartis, Siemens, Guerbet, Stryker, Covidien*. Sabine Heiland—*RELATED: Grant:* Dietmar Hopp Foundation*; *UNRELATED: Grants/Grants Pending:* German Research Foundation (SFB 1118)*. Alexander Juerchott—*RELATED: Grant:* Dietmar Hopp Foundation*. *Money paid to the institution.

REFERENCES

1. Lissac M, Metrop D, Brugirard J, et al. **Dental materials and magnetic resonance imaging.** *Invest Radiol* 1991;26:40–45 CrossRef Medline
2. Schenck J. **The role of magnetic susceptibility in magnetic resonance imaging: MRI magnetic compatibility of the first and second kinds.** *Med Phys* 1996;23:815–50 Medline
3. Lüdeke K, Röschmann P, Tischler R. **Susceptibility artefacts in NMR imaging.** *Magn Reson Imaging* 1985;3:329–43 CrossRef Medline
4. Camacho CR, Plewes DB, Henkelman RM. **Nonsusceptibility artifacts due to metallic objects in MR imaging.** *J Magn Reson Imaging* 1995;5:75–88 CrossRef Medline
5. Graf H, Steidle G, Martirosian P, et al. **Metal artifacts caused by gradient switching.** *Magn Reson Med* 2005;54:231–34 CrossRef Medline
6. Jordan RA, Micheelis W, Cholmakov-Bodechtel C, et al. *Fifth German Oral Health Study.* Köln: Deutscher Ärzte Verlag; 2016
7. Ai T, Padua A, Goerner F, et al. **SEMAC-VAT and MSVAT-SPACE sequence strategies for metal artifact reduction in 1.5T magnetic resonance imaging.** *Invest Radiol* 2012;47:267–76 CrossRef Medline
8. Lee YH, Lim D, Kim E, et al. **Usefulness of slice encoding for metal artifact correction (SEMAC) for reducing metallic artifacts in 3-T MRI.** *Magn Reson Imaging* 2013;31:703–06 CrossRef Medline
9. Koch KM, Brau AC, Chen W, et al. **Imaging near metal with a MAVRIC-SEMAC hybrid.** *Magn Reson Med* 2011;65:71–82 CrossRef Medline
10. Cho ZH, Kim DJ, Kim YK. **Total inhomogeneity correction including chemical shifts and susceptibility by view angle tilting.** *Med Phys* 1988;15:7–11 CrossRef Medline
11. Lu W, Pauly KB, Gold GE, et al. **SEMAC: slice encoding for metal artifact correction in MRI.** *Magn Reson Med* 2009;62:66–76 CrossRef Medline
12. Koch KM, Lorbiecki JE, Hinks RS, et al. **A multispectral three-dimensional acquisition technique for imaging near metal implants.** *Magn Reson Med* 2009;61:381–90 CrossRef Medline

13. Lee YH, Hahn S, Kim E, et al. **Fat-suppressed MR imaging of the spine for metal artifact reduction at 3T: comparison of STIR and slice encoding for metal artifact correction fat-suppressed T2-weighted images.** *Magn Reson Med Sci* 2016;15:371–78 CrossRef Medline
14. Sutter R, Ulbrich EJ, Jellus V, et al. **Reduction of metal artifacts in patients with total hip arthroplasty with slice-encoding metal artifact correction and view-angle tilting MR imaging.** *Radiology* 2012; 265:204–14 CrossRef Medline
15. Fleckenstein JL, Archer BT, Barker BA, et al. **Fast short-tau inversion-recovery MR imaging.** *Radiology* 1991;179:499–504 CrossRef Medline
16. Cox B, Zuniga JR, Panchal N, et al. **Magnetic resonance neurography in the management of peripheral trigeminal neuropathy: experience in a tertiary care centre.** *Eur Radiol* 2016;26:3392–400 Medline
17. Koch KM, Hargreaves BA, Pauly KB, et al. **Magnetic resonance imaging near metal implants.** *J Magn Reson Imaging* 2010;32:773–87 CrossRef Medline
18. Li G, Nittka M, Paul D, et al. **MSVAT-SPACE for fast metal implants imaging.** *Proceedings of the ISMRM* 2011;19:3171
19. Hilgenfeld T, Prager M, Schwindling FS, et al. **Artefacts of implant-supported single crowns: impact of material composition on artefact volume on dental MRI.** *Eur J Oral Implantol* 2016;9:301–08 Medline
20. Dietrich O, Raya JG, Reeder SB, et al. **Measurement of signal-to-noise ratios in MR images: influence of multichannel coils, parallel imaging, and reconstruction filters.** *J Magn Reson Imaging* 2007;26: 375–85 CrossRef Medline
21. Friedman L, Glover GH. **Report on a multicenter fMRI quality assurance protocol.** *J Magn Reson Imaging* 2006;23:827–39 CrossRef Medline
22. Landis J, Koch GG. **An application of hierarchical kappa-type statistics in the assessment of majority agreement among multiple observers.** *Biometrics* 1977;33:363–74 CrossRef Medline
23. Costa ALF, Appenzeller S, Yasuda C-L, et al. **Artifacts in brain magnetic resonance imaging due to metallic dental objects.** *Med Oral Patol Oral Cir Bucal* 2009;14:82 Medline
24. Zho SY, Kim MO, Lee KW, et al. **Artifact reduction from metallic dental materials in T1-weighted spin-echo imaging at 3.0 Tesla.** *J Magn Reson Imaging* 2013;37:471–78 CrossRef Medline
25. Fritz J, Ahlawat S, Demehri S, et al. **Compressed sensing SEMAC: 8-fold accelerated high resolution metal artifact reduction MRI of cobalt-chromium knee arthroplasty implants.** *Invest Radiol* 2016; 51:666–76 CrossRef Medline

Cerebral Perfusion Is Perturbed by Preterm Birth and Brain Injury

 E.S. Mahdi,  M. Bouyssi-Kobar,  M.B. Jacobs,  J. Murnick,  T. Chang, and  C. Limperopoulos



ABSTRACT

BACKGROUND AND PURPOSE: Early disturbances in systemic and cerebral hemodynamics are thought to mediate prematurity-related brain injury. However, the extent to which CBF is perturbed by preterm birth is unknown. Our aim was to compare global and regional CBF in preterm infants with and without brain injury on conventional MR imaging using arterial spin-labeling during the third trimester of ex utero life and to examine the relationship between clinical risk factors and CBF.

MATERIALS AND METHODS: We prospectively enrolled preterm infants younger than 32 weeks' gestational age and <1500 g and performed arterial spin-labeling MR imaging studies. Global and regional CBF in the cerebral cortex, thalami, pons, and cerebellum was quantified. Preterm infants were stratified into those with and without structural brain injury. We further categorized preterm infants by brain injury severity: moderate-severe and mild.

RESULTS: We studied 78 preterm infants: 31 without brain injury and 47 with brain injury (29 with mild and 18 with moderate-severe injury). Global CBF showed a borderline significant increase with increasing gestational age at birth ($P = .05$) and trended lower in preterm infants with brain injury ($P = .07$). Similarly, regional CBF was significantly lower in the right thalamus and midpons ($P < .05$) and trended lower in the midtemporal, left thalamus, and anterior vermis regions ($P < .1$) in preterm infants with brain injury. Regional CBF in preterm infants with moderate-severe brain injury trended lower in the midpons, right cerebellar hemisphere, and dentate nuclei compared with mild brain injury ($P < .1$). In addition, a significant, lower regional CBF was associated with ventilation, sepsis, and cesarean delivery ($P < .05$).

CONCLUSIONS: We report early disturbances in global and regional CBF in preterm infants following brain injury. Regional cerebral perfusion alterations were evident in the thalamus and pons, suggesting regional vulnerability of the developing cerebro-cerebellar circuitry.

ABBREVIATIONS: ASL = arterial spin-labeling; BI = brain injury; DLPF = dorsolateral prefrontal; GA = gestational age; IO = inferior occipital; MT = midtemporal; PM = premotor; PO = parieto-occipital; PT = preterm; T1b = blood longitudinal relaxation time

Preterm birth is a major public health concern, with an estimated worldwide incidence of about 9.6% of all births.¹ Preterm birth is associated with a high prevalence of brain injury (BI) and life-long neurodevelopmental morbidity, manifesting in up to 50% of school-age survivors.^{2,3} Overall prematurity-related

mortality has decreased in recent years; however, adverse neurodevelopment consequences often persist until later in life.⁴ Only a few structural brain injuries can be recognized in the early postnatal period (<7–10 days) by conventional transcranial sonography or MR imaging.⁵ However, most cases of prematurity-related BI lack structural changes; this feature highlights the importance of studying early disturbances in systemic and cerebral hemodynamics that may predispose to such brain injuries.⁶ Risk factors implicated in prematurity-related BI include alteration of cardiovascular autonomic control, immaturity of the cerebral hemodynamic mechanism, disturbed oxygenation, and vascular fragility.⁷ The onset and extent to which cerebral blood flow is disturbed following preterm birth remain poorly understood, in large part

Received December 23, 2017; accepted after revision March 23, 2018.

From the Developing Brain Research Program (E.S.M., M.B.-K., J.M., C.L.), Department of Diagnostic Imaging and Radiology; Department of Neurology (T.C.); and Department of Epidemiology and Biostatistics (M.B.J.), Children's Research Institute, Children's National Health System, Washington, DC; and Institute for Biomedical Sciences (M.B.-K.), George Washington University, Washington, DC.

This work was supported by the Canadian Institutes of Health Research (MOP-81116) and the National Institutes of Health (R01 HL116585-01).

Paper previously presented, in part, orally at: Annual Meeting of the Radiological Society of North America, November 22–December 2, 2016; Chicago, Illinois. A fellow research award was granted.

Please address correspondence to Catherine Limperopoulos, PhD, Developing Brain Research Laboratory, Departments of Diagnostic Imaging and Radiology, Children's National Health System, 111 Michigan Ave NW, Washington, DC 20010; e-mail: climpero@childrensnational.org

 Indicates open access to non-subscribers at www.ajnr.org

 Indicates article with supplemental on-line tables.

<http://dx.doi.org/10.3174/ajnr.A5669>

because of the lack of availability of reliable monitoring techniques that can directly and noninvasively measure CBF.

Several prior studies have assessed cerebral brain perfusion in the neonate using various techniques such as cerebral artery Doppler, near-infrared spectroscopy, PET, and xenon-enhanced CT.⁸⁻¹¹ These techniques lack anatomic detail, use indirect cerebral perfusion measurements, and/or have a risk of radiation or the need for intravenous contrast.¹²⁻¹⁴ Conversely, in the present study, we used the arterial spin-labeling (ASL) MR imaging technique, which has recently emerged as a promising noninvasive method for direct quantitative assessment of cerebral perfusion in high-risk neonates, including neonates with perinatal stroke¹⁵ or hypoxic-ischemic encephalopathy,¹⁶ without radiation risk or the need for intravenous contrast.^{13,17}

While several ASL-MR imaging studies have been reported in full-term neonates,^{13,18-24} only 4 studies have performed ASL-MR imaging in the preterm (PT) period (ie, third trimester of ex utero life), all of which included small sample sizes of preterm infants with no structural BI at the time of the MR imaging.^{12,25-27} To date, to our knowledge, no study has examined early CBF in PT infants during the third trimester of ex utero brain development to better ascertain the impact of early-life BI on cerebral perfusion.

The primary objective of our study was to compare global and regional CBF in PT infants with and without BI on conventional MR imaging during the third trimester of ex utero life using ASL-MR imaging. As a secondary objective, we examined the relationship between regional cerebral and cerebellar perfusion measures and the degree of BI. Last, we investigated clinical risk factors associated with preterm birth and their potential influence on cerebral perfusion.

MATERIALS AND METHODS

Subjects

In the context of a prospective study, we recruited PT infants (<1500 g and gestational age [GA] of 32 weeks or younger) admitted to the Children's National Medical Center in Washington, DC. PT infants with a known or suspected brain malformation, dysmorphic features, or congenital anomalies suggestive of a genetic syndrome, metabolic disorders, chromosomal abnormality, or CNS infection were excluded. PT infants were stratified into those with and without structural BI on conventional MR imaging. We further categorized PT infants by injury severity: 1) mild injury (grade I/II germinal matrix hemorrhage, punctate cerebellar hemorrhage, and/or mild cerebral white matter injury), and 2) moderate-severe injury (grade III germinal matrix hemorrhage, periventricular hemorrhagic infarction, and/or extensive cerebellar hemorrhage). Medical records were reviewed for all subjects. Specific demographic and clinical variables were extracted including birth weight, GA at birth, GA at MR imaging, sex, Apgar score at 1 and 5 minutes; medications such as pressors, diuretics, caffeine, corticosteroids, indomethacin; sedation 48 hours before MR imaging; resuscitation status such as the use of ventilatory support during the hospital stay; intubation in the 48 hours before MR imaging; patent ductus arteriosus ligation; sepsis; and method of delivery. All data were collected in compliance with Health Information Portability and Accountability Act regula-

tions and approved by the institutional review board (Children's National Health System). Informed consent was acquired from all infant guardians.

MR Imaging and Arterial Spin-Labeling Acquisition

PT infants underwent MR imaging on either 1.5T or 3T scanners (Discovery MR 750 and 450, respectively; GE Healthcare, Milwaukee, Wisconsin). PT infants with specific requirements for a temperature-controlled environment ($n = 50$, 64%) underwent MR imaging studies on a 1.5T scanner using an MR imaging-compatible incubator with 1-channel receiver and transmitter coils. All other PT infants ($n = 28$, 36%) underwent MR imaging studies on a 3T scanner using 8 receiver-only head coils.

Our acquisition protocol included axial 3D pseudocontinuous arterial spin-labeling with a spiral k -space trajectory, which was performed with the following scan parameters: TE/TR = 11/4300 ms, FOV = 24 cm, matrix size = 512×8 , section thickness = 3 mm, and scan time = 3:25 minutes. Anatomic T2-weighted images were acquired with either axial T2 periodically rotated overlapping parallel lines with enhanced reconstruction (TE/TR = 101.7/6313 ms, section thickness = 2 mm) and axial single-shot FSE (TE/TR = 160/1320 ms, section thickness = 2 mm) for a 1.5T scanner, or 3D Cube (GE Healthcare) images (TE/TR = 64/2500 ms, section thickness = 1 mm) for a 3T scanner. Images were reviewed by an experienced pediatric neuroradiologist (J.M) for evidence of BI and structural abnormalities.

Neonates were generally scanned without sedation. Sedation was used on a small subset ($n = 10$) for clinical indications. All PT infants underwent vital signs monitoring throughout the scan.

Data Analysis/ASL Processing

CBF maps were generated using FuncTool software (GE Healthcare) in milliliters/100 g/minute. The blood longitudinal relaxation time (T1b) was corrected to 1.7 seconds.¹² We then created a brain mask of the perfusion map, which was coregistered to anatomic T2-weighted images. Global CBF was calculated from the cerebral perfusion map using FSL software (<http://fsl.fmrib.ox.ac.uk/fsl/fslwiki>).

The coregistered CBF map and T2-weighted images were used for anatomic delineation and ROI placement to quantify regional CBF. ROIs were manually placed using ITK-SNAP software (Version 3.4.0; www.itksnap.org) and were calculated as an average value from both the left and right cerebral hemispheres for ROIs that did not show bilateral differences on paired t tests at $P < .05$. ROIs were drawn as a small square of 2–3 mm in the cerebral cortices in the dorsolateral prefrontal (DLPF), premotor (PM), primary motor, parieto-occipital (PO), midtemporal (MT), and inferior occipital (IO) regions.²⁸ Thalami, midpons, anterior and posterior vermis, dentate nuclei, and cerebellar hemispheres were also included (Figs 1 and 2). The mean volume of ROIs was 23.7–47.2 mm³ (average, 33.06 mm³). The DLPF, PM, primary motor, and PO ROIs were drawn at the level of centrum semiovale and central sulcus. The MT and IO ROIs were drawn at the level of temporal horns of the lateral ventricles. All ROIs were localized by evaluation of the images in 3 orthogonal planes. Intrarater and interrater reliability was assessed via intraclass correlation coefficients on a randomly selected group of 29 PT infants. The mean intraclass cor-

relation coefficients for intrarater reliability measurements ranged from 0.62 to 0.96 (median, 0.82), and for interrater measurements, they ranged from 0.74 to 0.95 (median, 0.90).

Statistical Analysis

Descriptive characteristics of PT infants with and without BI were compared using *t* tests for normally distributed continuous variables, the Wilcoxon-Mann-Whitney test for nonparametric continuous outcomes, and the χ^2 test for categorical outcomes. Associations between GA at birth and GA at MR imaging and all CBF

measures were evaluated using generalized linear regression. Differences in CBF by ROIs between PT infants with and without BI and by BI severity were evaluated using ANCOVA, adjusted for GA at birth. Additional adjustment for GA at MR imaging (postmenstrual age) was considered; however, GA at MR imaging was not significantly correlated with any ROIs considered. Finally, generalized linear models were constructed for prespecified medical risk factors and all brain regions, controlling for age at birth, to identify medical factors that may be indicative of region-specific decreased CBF. Categorical risk factors identified in <10% of the PT infants were excluded. These included indomethacin and corticosteroid use. Additional analysis controlling for BI status resulted in similar findings. A *P* value of < .05 was considered a significant cutoff.

RESULTS

Characteristics of the Cohort

We studied 82 PT infants, of whom 4 were excluded due to technical factors (poor quality T2 or ASL). The remaining 78 PT infants had MR imaging at a mean GA of 33.7 ± 2.1 weeks (range, 28.4–37.0 weeks). Of the 78 PT infants, 31 (40%) had structurally normal MR imaging findings (ie, no BI) and 47 (60%) had BIs, of which 18 were moderate-severe and 29 were mild. Descriptive characteristics are summarized in Table 1.

Global CBF Measurement of the Cohort

The adjusted average global CBF showed a borderline significant increase with advancing GA at birth ($P = .05$), controlling for GA at MR imaging. However, there was no significant difference in global CBF with GA at MR imaging, controlling for GA at birth. The estimated global CBF was 20.3 (95% CI, 18.4–22.3) for PT infants without BI and 18.0 (95% CI, 16.4–19.5) in PT infants with BI, adjusting for GA at birth, indicating that global CBF in PT infants with BI trended lower than in PT infants without BI ($P = .07$) (Table 2).

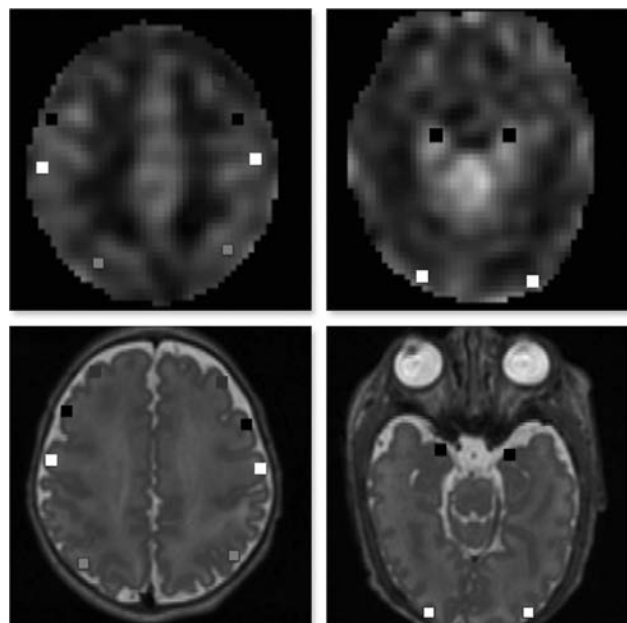


FIG 1. ROIs on axial 3D Cube (GE Healthcare) T2-weighted images (lower panel) coregistered with a corresponding CBF map (upper panel). ROI locations include DLPF, PM, primary motor, and PO cortical regions, respectively, (left panel) and MT and IO regions (right panel).

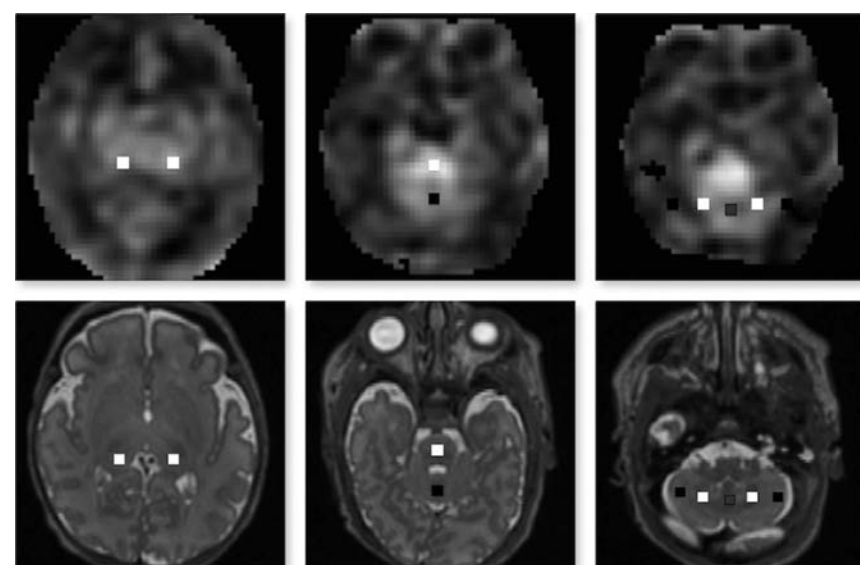


FIG 2. ROIs on axial 3D Cube (GE Healthcare) T2-weighted images (lower panel) coregistered with a corresponding CBF map (upper panel). ROI locations include thalamus regions (left panel), the midpons and anterior vermis (middle panel), and posterior vermis and bilateral dentate and cerebellar hemispheres (right panel).

Regional CBF Measurement of the Cohort

The adjusted regional CBF was significantly lower in PT infants with BI compared with those without BI in the right thalamus and midpons regions and trended lower in the MT, left thalamus, and anterior vermis regions (Table 2).

Regional CBF in PT infants with moderate-severe injury trended lower in the midpons, right cerebellar hemisphere, and dentate nuclei regions compared with PT infants with mild BI (Online Table 1).

Clinical Risk Factors Predicting CBF in the Cohort

Significant associations identified with generalized linear models for clinical risk factors and regional CBF are presented in Online Table 2. Our analysis showed that the presence of sepsis, use of

Table 1: Descriptive characteristics of the cohort (N = 78)

	PT without BI (n = 31)	PT with BI (n = 47)	P Value ^a
Birth GA (wk) ^b	28.2 ± 2.6 (22.9–32.0)	26.5 ± 2.6 (23.0–32.6)	.007
Birth weight (kg) ^b	1.1 ± 0.3 (0.4–1.5)	0.9 ± 0.3 (0.4–1.5)	.04
Days of life at MRI ^b	41.2 ± 17.6 (10.0–84.0)	49.1 ± 18.9 (15.0–93.0)	.07
Apgar score at 1 min ^c	6 (4, 2–9)	4 (4, 1–9)	.003
Apgar score at 5 min ^c	8 (3, 4–9)	7 (3, 3–9)	.005
Postmenstrual age at MRI (wk) ^b	34.0 ± 1.9 (30.9–36.9)	33.5 ± 2.19 (28.4–37.0)	.37
Weight at MRI (kg) ^b	1.7 ± 0.4 (0.8–2.7)	1.6 ± 0.5 (0.8–3.0)	.37
Female (No.) (%)	17 (54.8)	25 (53.2)	.89
Cesarean delivery (No.) (%)	23 (74.2)	28 (59.6)	.18

^a P value based on a t test for normally distributed continuous variables, the Wilcoxon-Mann-Whitney test for non-parametric continuous outcomes, and the χ^2 test for categorical outcomes.

^b Mean (range).

^c Median (interquartile range, range).

Table 2: Global and regional CBF between PT infants with brain injury and PT infants without injury, adjusted for GA at birth^a

Controlling for GA at Birth	PT without BI (n = 31)	PT with BI (n = 47)	P Value
Global CBF	20.3 (18.4–22.3)	18.0 (16.4–19.5)	.07
DLPF	16.7 (14.3–19.1)	14.8 (12.9–16.8)	.24
PM	21.7 (18.9–24.5)	19.4 (17.1–21.6)	.20
Primary motor	24.7 (21.8–27.7)	22.3 (19.9–24.6)	.21
PO	16.0 (13.5–18.5)	14.3 (12.3–13.3)	.31
MT	25.8 (22.9–29.0)	22.1 (19.7–24.7)	.07
IO	20.9 (17.8–24.0)	17.6 (15.1–20.1)	.11
Rt. thalamus	35.6 (31.1–40.2)	29.5 (25.8–33.2)	.04
Lt. thalamus	33.3 (28.6–38.1)	27.3 (23.5–31.1)	.06
Midpons	48.5 (41.6–55.3)	37.4 (31.8–43.1)	.02
Ant vermis	34.0 (28.2–39.8)	27.3 (22.5–32.0)	.08
Post vermis	32.4 (25.5–39.2)	27.8 (22.3–33.2)	.31
Rt. cerebellar hemisphere	21.0 (16.5–25.5)	19.0 (15.4–22.6)	.50
Lt. cerebellar hemisphere	22.8 (17.5–28.1)	22.0 (17.7–26.3)	.81
Dentate	30.6 (24.2–37.0)	29.0 (22.5–35.4)	.72

Note:—Rt. Indicates right; Lt., left; Ant, anterior; Post, posterior.

^a P value < .05 was considered significant. Data are means (95% confidence intervals).

ventilation, intubation in the 48 hours before MR imaging, and cesarean delivery were associated with lower global or regional CBF. However, pressor use was associated with higher CBF. Other risk factors explored were patent ductus arteriosus ligation, diuretic or caffeine use before MR imaging, and sedation 48 hours before MR imaging (On-line Table 3), though no significant associations were noted. Additional analysis controlling for BI status resulted in similar findings.

Influence of 1.5T versus 3T MR Imaging on CBF Measures

We adjusted our analyses for scanner type (1.5T versus 3T) and found no significant differences in global or regional CBF values for our cerebral regions or the vermis or dentate nuclei. Only cerebellar hemispheric CBF was significantly higher at 1.5T compared with 3T ($P = .03$).

DISCUSSION

In this prospective observational study, we report, for the first time, early disturbances in cerebral perfusion between PT infants with and without structural BI during the third trimester of ex utero development. We demonstrate that global CBF trended slightly lower in PT infants with BI compared with those without.

Regional CBF was significantly lower in the right thalamus and midpons and trended lower in the MT, left thalamus, and anterior vermis in PT infants with BI, suggesting regional vulnerability of the developing cerebro-cerebellar circuitry. These results collectively emphasize that perfusion effects in PT infants with BI and specifically moderate-severe injury are directed lower compared with those without BI. Finally, we reveal an association between lower regional CBF and the presence of sepsis, use of ventilation, intubation in the last 48 hours before the MR imaging, and cesarean de-

livery, after controlling for GA at birth.

Available data on cerebral perfusion using ASL-MR imaging in the neonatal period are limited, particularly available data with MR imaging studies performed during the preterm period (ie, third trimester of ex utero life) or those with prematurity-related brain injury. To date, most studies have been performed either in full-term infants or PT infants at term-equivalent age.^{13,17-24} Quantitative data on CBF in PT infants during the third trimester of development are scarce. To the best of our knowledge, only 4 studies have performed ASL-MR imaging at preterm age.^{12,25-27} Varela et al²⁵ scanned <10 PT infants without BI to quantify the ASL parameters and techniques. De Vis et al¹² scanned 6 PT infants, looking for cerebral perfusion changes with brain maturation. In another study by the same authors,²⁷ scanning of 18 PT infants was performed to assess hematocrit variability in the T1b and ASL measurements. Ouyang et al²⁶ reported higher global CBF and heterogeneous increases in regional CBF during the third trimester in 17 PT infants. Our data are in keeping with these findings; however, our study is the first to characterize quantitative regional CBF in PT infants with BI.

The mechanisms underlying disturbed CBF in PT infants are undoubtedly complex and likely multifactorial. In part, they may be related to the impact of PT birth on the alteration of cardiovascular autonomic control, which can manifest as variability in heart rate and blood pressure.⁷ Another potential mechanism may relate to immature cerebral hemodynamics, which increases the risk for cerebral hemorrhage and hypoxic-ischemic injury, especially in extremely premature infants.^{7,28} Increases in physiologic stress and metabolic demand, either in utero or during the early extrauterine life, may exceed the ability of the increase in cerebral blood flow.⁷

Our finding of decreased CBF in PT infants with BI corroborates a previous study by Lin et al,²⁹ using near-infrared spectroscopy and diffuse correlation spectroscopy imaging. However, ASL-MR imaging has an advantage over the previous method because it is a direct quantitative technique for assessing cerebral perfusion. Furthermore, it can be combined with other MR imaging techniques (spectroscopy, diffusion, and functional) to give a more comprehensive understanding of the pathophysiologic consequences of early hemodynamic disturbances.¹⁴

The decrease in regional CBF in the thalami, midpons, anterior vermis, and dentate nuclei in PT infants with BI suggests a

regional vulnerability of the developing cerebro-cerebellar circuitry. This circuitry includes multiple complex closed-loop circuits between the cerebral cortical regions and the cerebellum that control movement, language, and social processing.³⁰ The pivotal structures for this anatomic connection are located within the thalamus and brain stem regions, which represent areas with the highest perfusion during this critical preterm period of brain development. Limperopoulos et al³¹ reported a significant association between cerebellar injury in PT infants and impairment of regional volumetric growth in the contralateral cerebrum. Arcadiaz et al³² reported that ADC values in the brain stem and cerebellum can predict the outcomes of neonates with hypoxic-ischemic encephalopathy; this finding further emphasizes the importance of the cerebro-cerebellar connection.

Our analysis of medical risk factors and CBF was primarily exploratory. The potential effects of ventilation or intubation status on CBF are complex.³³ Other studies using near-infrared spectroscopy or intravenous ¹³³Xe reported a decrease in CBF in ventilated PT infants,³³ which is supported by our data. Most of the ventilated PT infants were on sedative medication at some point during their neonatal intensive care unit stay. It has been shown by van Alfen-van der Velden et al³⁴ that morphine is associated with increased cerebral blood volume, and midazolam, with a decrease in CBF velocity in ventilated PT infants. In our study, we examined the effect of sedative medication used up to 48 hours before MR imaging and found that there were no significant differences in CBF between PT infants who were sedated and those who were not sedated. This finding could be partly related to the small subset of PT infants receiving sedative medications in our cohort ($n = 10$).

There are several studies that report CBF/cerebral oxygenation differences according to the mode of delivery during the neonatal period.³⁵ Our data further support the notion that cesarean delivery may play a role in cerebral perfusion changes, with decreases in regional CBF noted. The effect of early-onset neonatal sepsis on CBF is complex and depends mainly on the changes in the cerebral autoregulatory mechanism.³⁶ Many of our neonates who had sepsis during their hospital stay have shown a decrease in regional CBF. Our data also demonstrate an increase in regional CBF in PT infants who had vasopressor medication during their first week of life before MR imaging, which further supports the finding that low-dose dopamine can result in a temporary elevation in CBF in PT infants.³⁷

Our study has several strengths: the largest sample size of PT infants scanned at preterm age of the third trimester of development using ASL-MR imaging to date, the inclusion of PT infants with various degrees of structural BI, and the examination of a variety of clinical factors that may influence perfusion. Acknowledging that ASL has been shown to change with GA, we controlled for GA at birth in our analysis.¹²

Our study also has some limitations, one of which is the use of generic T1b instead of a subject-specific T1 relaxation of the blood, which can be affected by hematocrit level.³⁸ The manual placement of the ROIs is another limitation because it is rater-dependent. However, we achieved good inter- and intrarater reliability measurements. The use of sedation at MR imaging in 10 PT infants may be another confounder to the study; however,

comparison analyses between PT infants with and without sedation demonstrated no statistically significant differences in global or regional CBF.

Furthermore, the use of different MR imaging field strengths (1.5T and 3T) is another potential limitation. However, the 2 groups (those studied on 1.5T versus 3T) may not be similar because those PT infants who needed an MR imaging incubator and a temperature-controlled environment due to their medical status were studied on the 1.5T scanner. Our results according to BI status were consistent across both scanners. In other words, the CBF measures in PT infants with BI were consistently lower compared with the PT infants without BI, and this finding is likely not due to scanner differences. Nevertheless, the best way to compare CBF measurement differences between a 1.5T versus 3T scanner would be to compare measurements in the same infants acquired on both scanners on the same day back to back. However, this was not possible in our study, given the acuity of illness of our cohort. Future work on the impact of MR imaging field strength on cerebral and cerebellar CBF measures is warranted.

Finally, the extent to which these early regional CBF disturbances impair subsequent cerebro-cerebellar development and connectivity and functional outcomes in survivors of preterm birth is an intriguing question that deserves further exploration.

CONCLUSIONS

We demonstrate that ASL provides a useful noninvasive tool for identifying early cerebral perfusion abnormalities in PT infants with BI. The ability to directly and noninvasively monitor CBF with ASL-MR imaging in the early postnatal period, when PT infants are at greatest risk for BI, is promising and may assist in identifying candidates for future therapeutic targets and measuring treatment effectiveness.

ACKNOWLEDGMENTS

We are thankful to all the families that participated in this study. We would like to thank Ms Caitlyn Loucas for her assistance in recruitment (Ms Loucas has no financial disclosure and no conflict of interest to report).

Disclosures: Marni B. Jacobs—*RELATED: Grant:* National Institutes of Health, *Comments:* work supported by the Clinical and Translational Science Institute Center Grant awarded to Children's National as part of the Biostatistics, Epidemiology, and Research Design Core*; *UNRELATED: Consultancy:* PATH, Inova Children's Hospital, *Comments:* consulting fees paid for scientific merit review (PATH) and statistical analysis (Inova); *Grants/Grants Pending:* Jain Foundation, ATyr Pharma, Department of Defense, *Comments:* biostatistician on grants related to neuromuscular disorders*; *Travel/Accommodations/Meeting Expenses Unrelated to Activities Listed:* Treat-NMD, *Comments:* Travel paid for scientific review panel for neuromuscular grant submissions. Catherine Limperopoulos—*RELATED: Grant:* National Institutes of Health RO1HL116585-01, Canadian Institutes of Health Research MOP-81116.*
*Money paid to the institution.

REFERENCES

1. Beck S, Wojdyla D, Say L, et al. **The worldwide incidence of preterm birth: a systematic review of maternal mortality and morbidity.** *Bull World Health Organ* 2010;88:31–38 [CrossRef Medline](#)
2. Hamilton BE1, Miniño AM, Martin JA, et al. **Annual summary of vital statistics: 2005.** *Pediatrics* 2007;119:345–60 [CrossRef Medline](#)
3. Ment LR, Vohr BR. **Preterm birth and the developing brain.** *Lancet Neurol* 2008;7:378–79 [CrossRef Medline](#)

4. Saigal S, Doyle LW. **An overview of mortality and sequelae of preterm birth from infancy to adulthood.** *Lancet* 2008;371:261–69 CrossRef Medline
5. Volpe JJ. **Intraventricular hemorrhage in the premature infant: current concepts, Part I.** *Ann Neurol* 1989;25:3–11 CrossRef Medline
6. Shalak L, Perlman JM. **Hemorrhagic-ischemic cerebral injury in the preterm infant: current concepts.** *Clin Perinatol* 2002;29:745–63 CrossRef Medline
7. Fyfe KL, Yiallourou SR, Wong FY, et al. **The development of cardiovascular and cerebral vascular control in preterm infants.** *Sleep Med Rev* 2014;18:299–310 CrossRef Medline
8. Shi Y, Jin R, Zhao J, et al. **Brain positron emission tomography in preterm and term newborn infants.** *Early Hum Dev* 2009;85:429–32 CrossRef Medline
9. Levene MI, Fenton AC, Evans DH, et al. **Severe birth asphyxia and abnormal cerebral blood-flow velocity.** *Dev Med Child Neurol* 1989;31:427–34 Medline
10. Peeples ES, Mehic E, Mourad PD, et al. **Fast Doppler as a novel bedside measure of cerebral perfusion in preterm infants.** *Pediatr Res* 2016;79:333–38 CrossRef Medline
11. Marin T, Moore J. **Understanding near-infrared spectroscopy.** *Adv Neonatal Care* 2011;11:382–88 CrossRef Medline
12. De Vis JB, Petersen ET, De Vries LS, et al. **Regional changes in brain perfusion during brain maturation measured non-invasively with arterial spin labeling MRI in neonates.** *Eur J Radiol* 2013;82:538–43 CrossRef Medline
13. Massaro AN, Bouyssi-Kobar M, Chang T, et al. **Brain perfusion in encephalopathic newborns after therapeutic hypothermia.** *AJNR Am J Neuroradiol* 2013;34:1649–55 CrossRef Medline
14. Calamante F, Thomas DL, Pell GS, et al. **Measuring cerebral blood flow using magnetic resonance imaging techniques.** *J Cereb Blood Flow Metab* 1999;19:701–35 CrossRef Medline
15. Watson CG, Dehaes M, Gagoski BA, et al. **Arterial spin labeling perfusion magnetic resonance imaging performed in acute perinatal stroke reveals hyperperfusion associated with ischemic injury.** *Stroke* 2016;47:1514–19 CrossRef Medline
16. Licht DJ, Wang J, Silvestre DW, et al. **Preoperative cerebral blood flow is diminished in neonates with severe congenital heart defects.** *J Thorac Cardiovasc Surg* 2004;128:841–49 CrossRef Medline
17. Deibler AR, Pollock JM, Kraft RA, et al. **Arterial spin-labeling in routine clinical practice, Part I: technique and artifacts.** *AJNR Am J Neuroradiol* 2008;29:1228–34 CrossRef Medline
18. De Vis JB, Hendrikse J, Petersen ET, et al. **Arterial spin-labeling perfusion MRI and outcome in neonates with hypoxic-ischemic encephalopathy.** *Eur Radiol* 2015;25:113–21 CrossRef Medline
19. Nagaraj UD, Evangelou IE, Donofrio MT, et al. **Impaired global and regional cerebral perfusion in newborns with complex congenital heart disease.** *J Pediatr* 2015;167:1018–24 CrossRef Medline
20. Wintermark P, Hansen A, Warfield SK, et al. **Near-infrared spectroscopy versus magnetic resonance imaging to study brain perfusion in newborns with hypoxic-ischemic encephalopathy treated with hypothermia.** *Neuroimage* 2014;85:287–93 CrossRef Medline
21. Wintermark P, Hansen A, Gregas MC, et al. **Brain perfusion in asphyxiated newborns treated with therapeutic hypothermia.** *AJNR Am J Neuroradiol* 2011;32:2023–29 CrossRef Medline
22. Tortora D, Mattei PA, Navarra R, et al. **Prematurity and brain perfusion: arterial spin labeling MRI.** *Neuroimage Clin* 2017;15:401–07 CrossRef Medline
23. Miranda MJ, Olofsson K, Sidaros K. **Noninvasive measurements of regional cerebral perfusion in preterm and term neonates by magnetic resonance arterial spin labeling.** *Pediatr Res* 2006;60:359–63 CrossRef Medline
24. Bouyssi-Kobar M, Murnick J, Brossard-Racine M, et al. **Altered cerebral perfusion in infants born preterm compared with infants born full term.** *J Pediatr* 2018;193:54–61.e2 CrossRef Medline
25. Varela M, Petersen ET, Golay X, et al. **Cerebral blood flow measurements in infants using look-locker arterial spin labeling.** *J Magn Reson Imaging* 2015;41:1591–600 CrossRef Medline
26. Ouyang M, Liu P, Jeon T, et al. **Heterogeneous increases of regional cerebral blood flow during preterm brain development: preliminary assessment with pseudo-continuous arterial spin labeled perfusion MRI.** *Neuroimage* 2017;147:233–42 CrossRef Medline
27. De Vis JB, Hendrikse J, Groenendaal F, et al. **Impact of neonate haematocrit variability on the longitudinal relaxation time of blood: implications for arterial spin labelling MRI.** *Neuroimage Clin* 2014;4:517–25 CrossRef Medline
28. Brew N, Walker D, Wong FY. **Cerebral vascular regulation and brain injury in preterm infants.** *Am J Physiol Regul Integr Comp Physiol* 2014;306:R773–86 CrossRef Medline
29. Lin PY, Hagan K, Fenoglio A, et al. **Reduced cerebral blood flow and oxygen metabolism in extremely preterm neonates with low-grade germinal matrix-intraventricular hemorrhage.** *Sci Rep* 2016;6:25903 CrossRef Medline
30. D’Mello AM, Stoodley CJ. **Cerebro-cerebellar circuits in autism spectrum disorder.** *Front Neurosci* 2015;9:408 CrossRef Medline
31. Limperopoulos C, Chilingaryan G, Guizard N, et al. **Cerebellar injury in the premature infant is associated with impaired growth of specific cerebral regions.** *Pediatr Res* 2010;68:145–50 CrossRef Medline
32. Arca-Diaz G, Re TJ, Drottar M, et al. **Can cerebellar and brainstem apparent diffusion coefficient (ADC) values predict neuromotor outcome in term neonates with hypoxic-ischemic encephalopathy (HIE) treated with hypothermia?** *PLoS One* 2017;12:e0178510 CrossRef Medline
33. Baenziger O, Jaggi JL, Mueller AC, et al. **Cerebral blood flow in preterm infants affected by sex, mechanical ventilation, and intrauterine growth.** *Pediatr Neurol* 1994;11:319–24 CrossRef Medline
34. van Alfen-van der Velden AA, Hopman JC, Klaessens JH, et al. **Effects of midazolam and morphine on cerebral oxygenation and hemodynamics in ventilated premature infants.** *Biol Neonate* 2006;90:197–202 CrossRef Medline
35. Pichler G, Schmolzer GM, Urlesberger B. **Cerebral tissue oxygenation during immediate neonatal transition and resuscitation.** *Front Pediatr* 2017;5:29 CrossRef Medline
36. Basu S, Dewangan S, Chandra Shukla R, et al. **Cerebral blood flow velocity in early-onset neonatal sepsis and its clinical significance.** *Eur J Pediatr* 2012;171:901–09 CrossRef Medline
37. Seri I, Rudas G, Bors Z, et al. **Effects of low-dose dopamine infusion on cardiovascular and renal functions, cerebral blood flow, and plasma catecholamine levels in sick preterm neonates.** *Pediatr Res* 1993;34:742–49 CrossRef Medline
38. Borogovac A, Asllani I. **Arterial spin labeling (ASL) fMRI: advances, theoretical constraints and experimental challenges in neurosciences.** *Int J Biomed Imaging* 2012;2012:818456 CrossRef Medline

β -Hydroxybutyrate Detection with Proton MR Spectroscopy in Children with Drug-Resistant Epilepsy on the Ketogenic Diet

J.N. Wright, R.P. Saneto, and S.D. Friedman

ABSTRACT

BACKGROUND AND PURPOSE: The ketogenic diet, including both classic and modified forms, is an alternative to antiepileptic medications used in the treatment of drug-resistant epilepsy. We sought to evaluate the utility of proton MR spectroscopy for the detection of β -hydroxybutyrate in a cohort of children with epilepsy treated with the ketogenic diet and to correlate brain parenchymal metabolite ratios obtained from spectroscopy with β -hydroxybutyrate serum concentrations.

MATERIALS AND METHODS: Twenty-three spectroscopic datasets acquired at a TE of 288 ms in children on the ketogenic diet were analyzed with LCModel using a modified basis set that included a simulated β -hydroxybutyrate resonance. Brain parenchymal metabolite ratios were calculated. Metabolite ratios were compared with serum β -hydroxybutyrate concentrations, and partial correlation coefficients were calculated using patient age as a covariate.

RESULTS: β -hydroxybutyrate blood levels were highly correlated to brain β -hydroxybutyrate levels, referenced as either choline, creatine, or *N*-acetylaspartate. They were inversely but more weakly associated with *N*-acetylaspartate, regardless of the ratio denominator. No strong concordance with lactate was demonstrated.

CONCLUSIONS: Clinical MR spectroscopy in pediatric patients on the ketogenic diet demonstrated measurable β -hydroxybutyrate, with a strong correlation to β -hydroxybutyrate blood levels. These findings may serve as an effective tool for noninvasive monitoring of ketosis in this population. An inverse correlation between serum β -hydroxybutyrate levels and brain tissue *N*-acetylaspartate suggests that altered amino acid handling contributes to the antiepileptogenic effect of the ketogenic diet.

ABBREVIATIONS: BHB = β -hydroxybutyrate; GABA = gamma-aminobutyric acid; KD = ketogenic diet; MAD = modified Atkins diet

The ketogenic diet (KD) is a high-fat, low-carbohydrate, low-protein diet developed in the 1920s as a treatment for epilepsy, in response to the observation that fasting decreased the incidence and severity of seizures.¹ Use of the KD was largely supplanted by the emergence of multiple highly effective antiepileptic medications throughout the subsequent decades.² More recently, there has been a resurgence of interest in the KD, especially for treatment of drug-resistant epilepsy in children. Clinical research has demonstrated that modified forms of the diet, including the modified Atkins diet (MAD)

and modified ratio formulations of the KD, are also effective in controlling seizures.³

The KD restricts intake of carbohydrates and protein, driving the production of ketone bodies from fat by the liver. This alteration in energetic substrates results in increased serum levels of β -hydroxybutyrate (BHB) and, to a lesser degree, acetone and acetoacetate. Brain parenchymal concentrations of ketone bodies have been shown to increase as a function of serum concentrations,⁴ modulated by the duration of hyperketonemia. Prolonged ketosis results in upregulation of the monocarboxylic acid transporter family of proteins that governs the active transport of ketone bodies from serum, resulting in increased steady-state brain tissue concentrations.⁵ Ketone bodies serve as the primary oxidative substrate for neurons during ketosis.⁶

The mechanisms by which the KD exerts its antiepileptogenic effect are not definitely known. Theories that have been advanced include the following: an anticonvulsant effect of ketone bodies; a shift in brain amino acid handling favoring increased synthesis of the inhibitory neurotransmitter gamma-

Received November 6, 2017; accepted after revision March 5, 2018.

From the Department of Radiology (J.N.W., S.D.F.) and Department of Neurology, Division of Pediatric Neurology (R.P.S.), University of Washington and Seattle Children's Hospital, Seattle, Washington.

Please address correspondence to Jason N. Wright, MD, Department of Radiology, M/S MA.7.220, Seattle Children's Hospital, PO Box 5371, Seattle, WA 98145; e-mail: jnixon@uw.edu

<http://dx.doi.org/10.3174/ajnr.A5648>

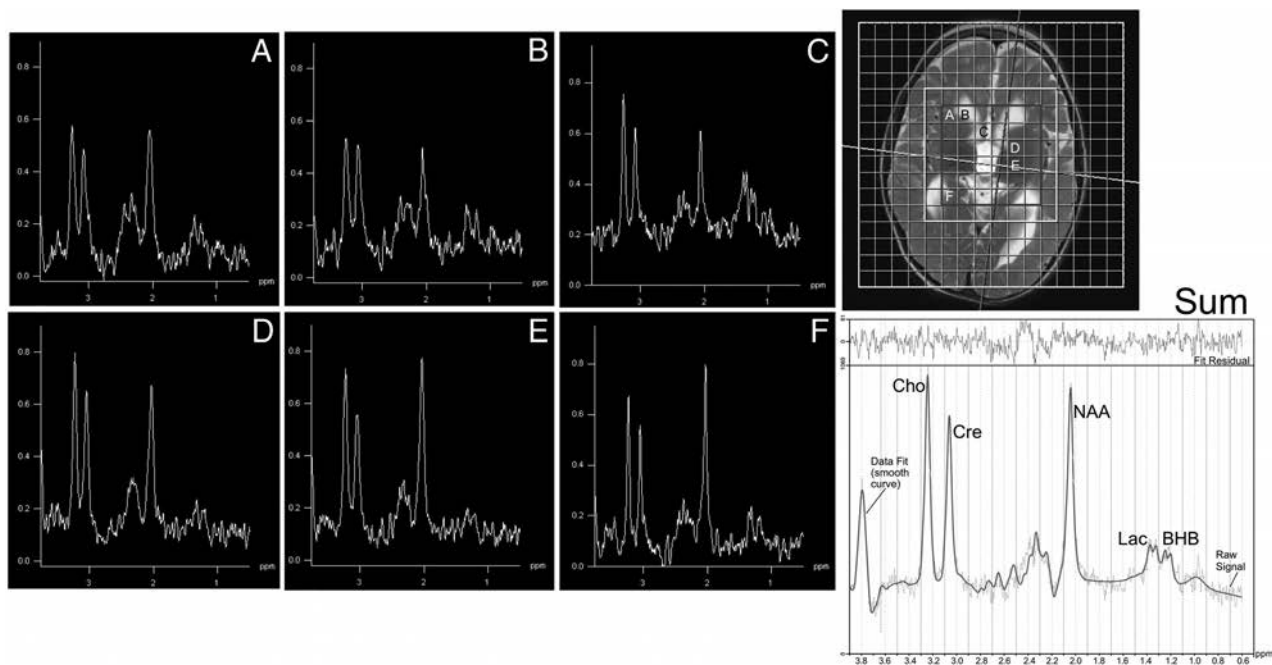


FIG 1. Voxel-of-interest (inner 8×8 matrix) and masked region (7×7 matrix) that retained spectra based on SNR, NAA, and adequate Cramér-Rao bounds. Across the brain (spectra labeled A–F, corresponding to labeled voxels in image at the upper right), 2 peaks comprising lactate and BHB are shown at 1.33 and 1.2 ppm, respectively, with lactate more prominent in voxels containing CSF in this patient with mitochondrial cytopathy. At the lower right, the composite spectrum from the masked region is shown, with the LCMoel fit overlaid.

aminobutyric acid (GABA); a direct consequence of glucose restriction; or an effect mediated by altered polyunsaturated fatty acid metabolism.⁷ Whatever the mechanism, steady-state blood levels of BHB have been shown to correlate with the degree of seizure control.⁸

Proton MR spectroscopy (^1H -MR spectroscopy) is a clinically available imaging technique by which tissue concentrations of metabolites can be noninvasively evaluated. Anecdotally, we have observed a resonance near 1.2 ppm on long-TE (288 ms) spectra in patients treated with the KD, tentatively attributed to BHB. There have been rare anecdotal reports of BHB detection by ^1H -MR spectroscopy in the brain parenchyma of children treated with the KD,^{9,10} with only 4 patients reported to date. We sought to evaluate the utility of ^1H -MR spectroscopy for the routine detection of BHB in a cohort of children treated with the KD for drug-resistant epilepsy and to correlate ^1H -MR spectroscopy metabolite ratios with BHB serum concentrations.

MATERIALS AND METHODS

Following institutional review board approval, we retrospectively identified 247 patients treated with the classic KD, a modified-ratio KD, or the MAD at our institution between 2006 and 2014. The classic KD used a ratio of 4:1, indicating a target dietary intake of 4 g of fat per gram of combined carbohydrate and protein. Patients were shifted to a modified-ratio formulation of the KD depending on clinical course and seizure response. The MAD, which limits carbohydrate intake to a maximum of 20 g per day, was used in some patients to increase tolerability and compliance.

Of the 247 patients, 38 underwent ≥ 1 ^1H -MR spectroscopy during their treatment, for a total of 49 MR spectroscopy datasets. Clinical data on patient age, epilepsy and seizure type, diet type, medications, serum BHB concentration, and lag in days between

blood testing and MR spectroscopy were recorded after retrospective chart review.

Data were further reduced to 23 spectra from 18 total patients in whom the lag between blood BHB sampling and MR spectroscopy was < 30 days. Medication histories were screened to exclude medications—including phenytoin and phenobarbital, known to contain propylene glycol or 1,2-propanediol—that generate a doublet resonance on ^1H -MR spectroscopy at 1.1 ppm, which could potentially confound results.

MR spectroscopy data were acquired axially for all subjects on a 3T Trio magnet (Siemens, Erlangen, Germany) with a multi-voxel point-resolved spectroscopy sequence acquisition centered on the basal ganglia (16×16 matrix with a VOI of 8×8 , TE = 288, TR = 1700, slice thickness = 15 mm, NEX = 2, time of acquisition = 5 minutes 16 seconds). Slab location was assigned in a standardized fashion per our clinical MR spectroscopy protocol, with generally equivalent anatomic sampling across patients (see Fig 1 for a sample slab position). Twenty-two of 23 MR spectroscopy examinations were performed with sedation, using either nitrous oxide/sevoflurane or propofol for induction and sevoflurane or propofol for maintenance.

Data were processed using LCMoel (Version 6.3; <http://www.lcmoel.com/>) to generate phase and frequency corrected spectra.¹¹ Spectral arrays were masked to exclude the outer row within the VOI, as well as any individual spectrum having *N*-acetylaspartate signal Cramér-Rao lower bounds of ≥ 15 , a typical criterion for spectral quality. The remaining voxels were summed to create a single composite spectrum for each subject.

The composite spectra were reprocessed in LCMoel with the addition of a simulated doublet centered at 1.2 ppm, correspond-

ing to the dominant BHB resonance produced by its methyl group ($-CH_3$) (see Fig 1 for a sample fitted summed spectrum). The additional low-amplitude multiplet resonances of BHB at 2.3–2.4 ppm and 4.1 ppm were not modeled.

Results were expressed as a ratio of tissue BHB concentration to commonly assessed brain metabolite concentrations, including NAA, creatine/phosphocreatine (Cr), choline-containing compounds (Cho), and lactate. Derived metabolite ratios were correlated to serum BHB concentrations, corrected for age in months at the time of MR spectroscopy acquisition.

Analyses were also performed on 3 exploratory datasets (one with a restricted sampling lag threshold of 14 days [$n = 13$], a second with an extended sampling lag threshold of 120 days [$n = 31$], and a third including all examinations regardless of sampling lag [$n = 49$]) to estimate the effect of sampling lag on the strength of correlations.

Statistical Analysis

Descriptive analyses were performed for all variables, with age at MR spectroscopy in months covaried for parametric Spearman correlations. Significance was set at $P < .05$, with the primary time point of interest being a lag of ≤ 30 days. Other lag intervals were analyzed to explore the strength of the correlation, with reported values not corrected for multiple comparisons and/or autocorrelation owing to overlapping samples with decreasing lags. Analyses were performed in SPSS 19 (IBM, Armonk, New York).

RESULTS

Clinical data for the 18 included patients are summarized in Table 1. Nineteen datasets were obtained from patients on the KD, and 4 were from patients treated with the MAD. Mean blood serum BHB concentrations were 35.2 ± 25.9 mg/dL (range, 0.2–81.3 mg/dL). The mean lag time between blood sampling and MR spectroscopy was 11.1 ± 9.7 days (range, 0–28 days).

Included spectra ($n = 23$) were acquired at a mean patient age of 54.0 ± 37.3 months (range, 1–129 months). In terms of spectral fit parameters, the mean SNR was 25.7 ± 6.3 (range, 12–36), and the mean full width at half maximum was 0.04 ± 0.01 (range, 0.02–0.06), with mean NAA Cramér-Rao lower bounds of 1.9 ± 0.6 (range, 1–3).

Using age as a covariate, we calculated correlation coefficients between blood levels and brain metabolites. They are reported in Table 2. BHB blood levels were strongly correlated to brain BHB levels (calculated correlation coefficient for blood BHB–BHB/NAA was $R = 0.81$ with $P < .001$; calculated correlation coefficient for blood BHB–BHB/Cr was $R = 0.80$ with $P < .001$) and inversely but more weakly related to NAA levels, regardless of the ratio denominator (calculated correlation coefficient for blood BHB–NAA/Cr was $R = -0.55$ with $P < .01$; calculated correlation coefficient for blood BHB–NAA–Cho was $R = -.44$ with $P < .04$). No

Table 1: Patient clinical data including underlying epilepsy syndrome, seizure type, and antiepileptic medications

Patient	Age (yr)	Epilepsy Syndrome ^{21–23}	Seizure Type	Medications
1	1	EE (Unclassified)	T	LEV
2	2	Metabolic (Mito)	TS	ZNS/LTG/LEV
2	7	Metabolic (Mito)	TS/GTC	ZNS/LTG/LEV/RFM
2	8	Metabolic (Mito)	TS/MY/GTC	ZNS/LTG/LEV/RFM
3	9	MAE	MY/AT/GTC	VPA/CLB/RFM
4	7	Metabolic (Mito)	MY/RFL	TPM
4	10	Metabolic (Mito)	MY/RFL	TPM/ZNS
5	7	EE (MCD)	T/AT/TS	VGB/LTG
6	2	Structural (MCD)	Focal	ZNS/TPM
7	1	Structural (Aicardi)	ES	VGB
8	6	Genetic (<i>SCN1A</i>)	MY/AT	LEV/ETX/CLN
9	6	Metabolic (Mito)	MY/AT	LEV/LTG/ETX/CLN
10	6	MAE	T/MY/TS	LTG
11	0.5	Genetic (<i>ATPIA3</i>)	Focal/SE	LEV
11	1	Genetic (<i>ATPIA3</i>)	SUB/MY	LTG/CLB
12	6	EE (unclassified)	AT/T/GTC	CLB
13	1	EE (unclassified)	ES	VGB
14	2	Metabolic (Mito)	ES	TPM
15	4	EE (LGS)	AT/T/AA	LTG/LEV/ZNS
16	1	EE (Unclassified)	ES	ZNS/LEV
17	5	Genetic (<i>DEAF 1</i>)	T/AT/GTC	LEV
18	1	Metabolic (Mito)	ES	ZNS

Note:—“Epilepsy Syndrome”: EE indicates epileptic encephalopathy; Mito, primary mitochondrial disease; MAE, myoclonic astatic epilepsy; MCD, malformation of cortical development; LGS, Lennox-Gastaut Syndrome; “Seizure Type”: T, tonic; TS, tonic spasms; GTC, generalized tonic-clonic; MY, myoclonic; AT, atonic; RFL, reflexive seizure; ES, epileptic spasms; SE, status epilepticus; AA, atypical absence; SUB, subclinical seizures; “Medications”: LEV, levetiracetam; ZNS, zonisamide; LTG, lamotrigine; RFM, rufinamide; CLB, clobazam; TPM, topiramate; VGB, vigabatrin; ETX, ethosuximide; CLN, clonazepam; VPA, valproic acid.

Table 2: Partial correlations of blood BHB concentration (mg/dL) and brain metabolite ratios derived from ¹H-MRS, using patient age in months as a covariate

Group	BHB/Cr	BHB/Cho	BHB/NAA	BHB/Lac	Cho/Cr	NAA/Cr	NAA/Cho	Lac/NAA	Lac/Cr
Lag ≤ 14 d ($n = 13$)									
R	.871	.898	.886	.507	-.287	-.645	-.540	.376	.253
Significance	.000	.000	.000	.092	.367	.024	.070	.228	.428
Lag ≤ 30 d ($n = 23$)									
R	.803	.814	.807	.538	-.165	-.553	-.443	.421	.334
Significance	.000	.000	.000	.010	.463	.008	.039	.051	.128
Lag ≤ 120 d ($n = 31$)									
R	.790	.802	.781	.484	-.312	-.658	-.515	.523	.423
Significance	.000	.000	.000	.008	.099	.000	.004	.004	.022
All ($N = 49$)									
R	.579	.588	.584	.393	-.170	-.387	-.312	.290	.162
Significance	.000	.000	.000	.006	.254	.007	.033	.048	.278

Note:—Lac indicates lactate.

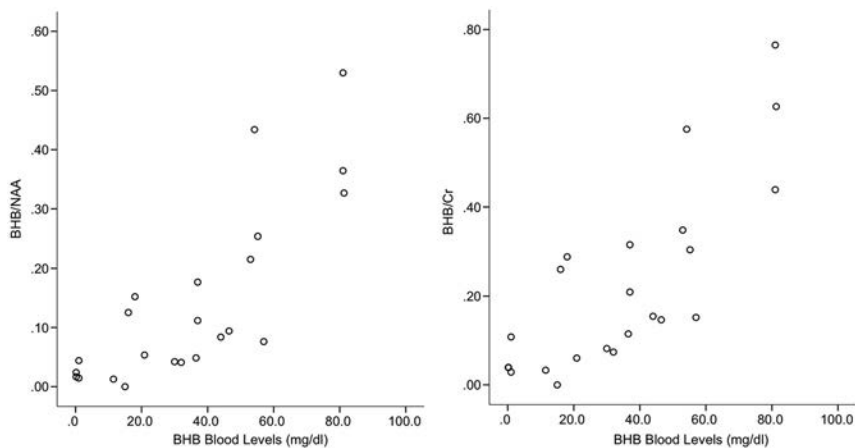


FIG 2. Scatterplot of blood serum BHB concentrations (milligrams/deciliter) versus brain BHB/NAA and BHB/Cr ratios demonstrates the strong associations between measures.

strong concordance with lactate was demonstrated. BHB/NAA and BHB/Cr plots versus blood BHB concentration for individual examinations are shown in Fig 2.

Results were calculated for the exploratory datasets, also reported in Table 2. For the dataset with a threshold lag of 14 days, the calculated correlation coefficient for blood BHB–BHB/NAA was $R = 0.89$ with $P < .001$. For the dataset with a threshold lag of 120 days, the calculated correlation coefficient for blood BHB–BHB/NAA was $R = 0.781$ with $P < .001$. When the entire cohort was included, blood BHB–BHB/NAA demonstrated an $R = 0.584$ with $P < .001$.

DISCUSSION

Prior reports have demonstrated ketone bodies by ^1H -MR spectroscopy in small numbers of mainly adult patients during prolonged fasting,^{4,12} diabetes,^{13,14} and BHB supplementation¹⁵ and in patients treated with the KD.^{9,10,12,16,17} To date, elevated BHB levels have been anecdotally reported in a only 4 children using ^1H -MR spectroscopy.^{9,10} In our cohort, we demonstrated routine detection of BHB in pediatric patients treated with the KD or a modified KD using long-TE multivoxel ^1H -MR spectroscopy performed at 3T.

High concordance between steady-state brain parenchymal BHB ratios and serum BHB levels was observed using a lag threshold between blood sampling and MR spectroscopy of 30 days (Fig 2). The strength of this correlation progressively increased as the lag threshold between blood BHB sampling and MR spectroscopy decreased, suggesting that the concordance reflects a true physiologic relationship. Results persisted when the lag threshold increased to 120 days, with a similar but weaker relationship demonstrated when the entire cohort was included, implying that BHB ratios are relatively stable with time in patients on the KD. These findings suggest that ^1H -MR spectroscopy might be an effective tool for noninvasive monitoring of ketosis in children on the KD, particularly when performed in conjunction with routine follow-up MR imaging.

In our cohort, seizure response dictated varying ratios of fat to carbohydrates and protein on the KD. Some patients required the MAD for compliance or tolerability concerns. The specific formulation of the diet did not appear to alter the correlation of brain

BHB ratios to serum BHB levels, though we had a relative paucity of children on the MAD. That the specific diet type did not appear to alter the observed correlation suggests that brain BHB levels may be correlated with serum BHB concentrations independent of the dietary mechanism used to achieve ketosis, be it increased fat ratio or carbohydrate restriction. Further evaluation of a cohort with larger subgroups of diet type would be useful to confirm this observation.

We demonstrated an inverse relationship between blood levels of BHB and brain NAA ratios, independent of patient age. This is in contrast to a prior animal study in rats with diabetic ketoacidosis, which found no significant difference

in NAA/Cr ratios between study and control animals using ^1H -MR spectroscopy performed at 7T with a TE of 132 ms.¹⁸ Our finding may reflect in vivo changes in amino acid handling that occur with prolonged ketosis in the KD.^{7,19} Increased acetyl-coenzyme A as a by-product of ketone body metabolism in the brain drives increased tricarboxylic acid cycling, resulting in increased conversion of cytosolic aspartate to glutamate. Aspartate serves as the precursor molecule for NAA, while glutamate is converted to the inhibitory neurotransmitter GABA. Thus, the observed decrease in NAA may serve as a marker for an increase in GABA production, one of the proposed mechanisms of seizure control in the KD. Further studies using an MR spectroscopy acquisition specifically tailored to interrogate brain GABA concentrations would be instructive, with specific evaluation of the relationship between serum BHB concentrations and both brain GABA ratios and the degree of seizure control.

Consistent with past studies using infusion samples, lactate ratios did not show significant correlation to BHB serum levels.⁴ This finding has the caveat that anything other than elevated lactate exists near the noise floor, which can preclude accurate association assessment. In 5/18 patients, mitochondrial cytopathy was the etiology of their drug-resistant epilepsy, contributing further uncertainty to ascribing lactate levels to dietary effects.

Of note, the ^1H -MR spectroscopy spectra included in our analyses were acquired with a TE of 288 ms, optimized for the detection of lactate. J-coupling for BHB is 6.3 Hz, suggesting that TEs of 160 ms (1/J) or 320 ms (2/J) would be more appropriate for optimization of BHB detection.¹⁰ Furthermore, this TE selection limits the evaluation of additional ketosis-related metabolites, including acetone and acetoacetate. Both metabolites have generally lower brain concentrations⁴ and shorter T2 relaxation times¹⁰ than BHB. Future work including short-echo data would be helpful to assess these metabolites.

An additional limitation of our methodology was inclusion of gray and white matter and CSF within the VOI. Tissue segmentation was not attempted, and the differential contributions of different tissue types to the composite spectra were not quantified. The presence of visually identifiable BHB peaks in parenchymal voxels suggests that the ketogenic diet metabolites are broadly

distributed across tissue types, consistent with the work of Pan et al.⁴ Future work would benefit from specific analysis of the contributions of different tissue types to the overall summed spectrum.

Our described methodology, preprocessing and summing a multivoxel dataset to increase the signal-to-noise ratio, allowed routine detection of BHB in brain parenchyma. Further work using same-day blood sampling; integrated tissue-type segmentation using an approach like localization by adiabatic selective refocusing,²⁰ which minimizes chemical shift artifacts; absolute metabolite quantification; as well as evaluation of longitudinal changes will be helpful to extend and refine these results.

CONCLUSIONS

We demonstrated routine detection of a brain parenchymal BHB using conventional ¹H-MR spectroscopy in the brains of pediatric patients with epilepsy treated with the KD. We further demonstrated a strong correlation between brain tissue BHB ratios and serum BHB concentrations, apparently independent of specific diet formulation. These findings suggest that ¹H-MR spectroscopy may be a useful noninvasive method of interrogating brain tissue BHB levels in patients on the KD or a modified KD protocol. The observation of an inverse correlation between brain tissue NAA levels and serum BHB levels may reflect altered amino acid handling induced by the KD, consistent with one of the proposed antiepileptic mechanisms of the KD.

REFERENCES

1. Wheless JW. **History of the ketogenic diet.** *Epilepsia* 2008;49(Suppl 8):3–5 CrossRef Medline
2. Brodie MJ. **Antiepileptic drug therapy the story so far.** *Seizure* 2010; 19:650–55 CrossRef Medline
3. Kim JA, Yoon JR, Lee EJ, et al. **Efficacy of the classic ketogenic and the modified Atkins diets in refractory childhood epilepsy.** *Epilepsia* 2016;57:51–58 CrossRef Medline
4. Pan JW, Rothman TL, Behar KL, et al. **Human brain beta-hydroxybutyrate and lactate increase in fasting-induced ketosis.** *J Cereb Blood Flow Metab* 2000;20:1502–07 CrossRef Medline
5. Pan JW, Telang FW, Lee JH, et al. **Measurement of beta-hydroxybutyrate in acute hyperketonemia in human brain.** *J Neurochem* 2001; 79:539–44 Medline
6. Owen OE, Morgan AP, Kemp HG, et al. **Brain metabolism during fasting.** *J Clin Invest* 1967;46:1589–95 CrossRef Medline
7. Bough KJ, Rho JM. **Anticonvulsant mechanisms of the ketogenic diet.** *Epilepsia* 2007;48:43–58 Medline
8. van Delft R, Lambrechts D, Verschuure P, et al. **Blood beta-hydroxybutyrate correlates better with seizure reduction due to ketogenic diet than do ketones in the urine.** *Seizure* 2010;19:36–39 CrossRef Medline
9. Novotny EJ, Rothman DL. **Observation of cerebral ketone bodies by proton nuclear magnetic resonance spectroscopy [abstract].** *Ann Neurol* 1996;40:285 CrossRef
10. Cecil KM, Mulkey SB, Ou X, et al. **Brain ketones detected by proton magnetic resonance spectroscopy in an infant with Ohtahara syndrome treated with ketogenic diet.** *Pediatr Radiol* 2015;45:133–37 CrossRef Medline
11. Provencher SW. **Estimation of metabolite concentrations from localized in vivo proton NMR spectra.** *Magn Reson Med* 1993;30: 672–79 CrossRef Medline
12. Schubert F, Meckle R, Ittermann B, et al. **Ketone bodies and glucose in human brain during ketogenic diet and fasting.** In: *Proceedings of the Annual Meeting and Exhibition of the International Society for Magnetic Resonance in Imaging*, Toronto, Ontario, Canada. May 30–June 5, 2015
13. Kreis R, Ross BD. **Cerebral metabolic disturbances in patients with subacute and chronic diabetes mellitus: detection with proton MR spectroscopy.** *Radiology* 1992;184:123–30 CrossRef Medline
14. Wootton-Gorges SL, Buonocore MH, Kuppermann N, et al. **Detection of cerebral {beta}-hydroxybutyrate, acetoacetate, and lactate on proton MR spectroscopy in children with diabetic ketoacidosis.** *AJNR Am J Neuroradiol* 2005;26:1286–91 Medline
15. Plecko B, Stoeckler-Ipsiroglu S, Schober E, et al. **Oral beta-hydroxybutyrate supplementation in two patients with hyperinsulinemic hypoglycemia: monitoring of beta-hydroxybutyrate levels in blood and cerebrospinal fluid, and in the brain by in vivo magnetic resonance spectroscopy.** *Pediatr Res* 2002;52:301–06 Medline
16. Seymour KJ, Bluml S, Sutherling J, et al. **Identification of cerebral acetone by 1H-MRS in patients with epilepsy controlled by ketogenic diet.** *MAGMA* 1999;8:33–42 Medline
17. Artzi M, Liberman G, Vaisman N, et al. **Changes in cerebral metabolism during ketogenic diet in patients with primary brain tumors: 1H-MRS study.** *J Neurooncol* 2017;132:267–75 CrossRef Medline
18. Glaser N, Ngo C, Anderson S, et al. **Effects of hyperglycemia and effects of ketosis on cerebral perfusion, cerebral water distribution, and cerebral metabolism.** *Diabetes* 2012;61:1831–37 CrossRef Medline
19. Yudkoff M, Daikhin Y, Nissim I, et al. **Brain amino acid metabolism and ketosis.** *J Neurosci Res* 2001;66:272–81 CrossRef Medline
20. Scheenen TW, Klomp DW, Wijnen JP, et al. **Short echo time 1H-MRSI of the human brain at 3T with minimal chemical shift displacement errors using adiabatic refocusing pulses.** *Magn Reson Med* 2008;59:1–6 CrossRef Medline
21. Berg AT, Berkovic SF, Brodie MJ, et al. **Revised terminology and concepts for organization of seizures and epilepsies: report of the ILAE Commission on Classification and Terminology, 2005–2009.** *Epilepsia* 2010;51:676–85 CrossRef Medline
22. Scheffer IE, Berkovic S, Capovilla G, et al. **ILAE classification of the epilepsies: position paper of the ILAE Commission for Classification and Terminology.** *Epilepsia* 2017;58:512–21 CrossRef Medline
23. Bernier FP, Boneh A, Dennett X, et al. **Diagnostic criteria for respiratory chain disorders in adults and children.** *Neurology* 2002;59: 1406–11 CrossRef Medline

Quantitative Assessment of Normal Fetal Brain Myelination Using Fast Macromolecular Proton Fraction Mapping

V.L. Yarnykh, I.Y. Prihod'ko, A.A. Savelov, and A.M. Korostyshevskaya



ABSTRACT

BACKGROUND AND PURPOSE: Fast macromolecular proton fraction mapping is a recently emerged MRI method for quantitative myelin imaging. Our aim was to develop a clinically targeted technique for macromolecular proton fraction mapping of the fetal brain and test its capability to characterize normal prenatal myelination.

MATERIALS AND METHODS: This prospective study included 41 pregnant women (gestational age range, 18–38 weeks) without abnormal findings on fetal brain MR imaging performed for clinical indications. A fast fetal brain macromolecular proton fraction mapping protocol was implemented on a clinical 1.5T MR imaging scanner without software modifications and was performed after a clinical examination with an additional scan time of <5 minutes. 3D macromolecular proton fraction maps were reconstructed from magnetization transfer-weighted, T1-weighted, and proton density-weighted images by the single-point method. Mean macromolecular proton fraction in the brain stem, cerebellum, and thalamus and frontal, temporal, and occipital WM was compared between structures and pregnancy trimesters using analysis of variance. Gestational age dependence of the macromolecular proton fraction was assessed using the Pearson correlation coefficient (r).

RESULTS: The mean macromolecular proton fraction in the fetal brain structures varied between 2.3% and 4.3%, being 5-fold lower than macromolecular proton fraction in adult WM. The macromolecular proton fraction in the third trimester was higher compared with the second trimester in the brain stem, cerebellum, and thalamus. The highest macromolecular proton fraction was observed in the brain stem, followed by the thalamus, cerebellum, and cerebral WM. The macromolecular proton fraction in the brain stem, cerebellum, and thalamus strongly correlated with gestational age ($r = 0.88, 0.80, \text{ and } 0.73; P < .001$). No significant correlations were found for cerebral WM regions.

CONCLUSIONS: Myelin is the main factor determining macromolecular proton fraction in brain tissues. Macromolecular proton fraction mapping is sensitive to the earliest stages of the fetal brain myelination and can be implemented in a clinical setting.

ABBREVIATIONS: GA = gestational age; GRE = gradient recalled-echo; MPF = macromolecular proton fraction; MT = magnetization transfer

Myelination is a fundamental physiologic process within the sequence of human brain maturation, which begins in the second trimester of pregnancy and continues for several postnatal

years.^{1,2} Pediatric myelination abnormalities may originate from various prenatal insults to the central nervous system, such as intoxications, infections, hypoxia/ischemia, and malnutrition.³ However, little is known about the clinical significance of myelination defects in the fetal brain due to the absence of clinically suitable imaging tools that could enable objective quantitative characterization of myelin development in utero.

Fast macromolecular proton fraction (MPF) mapping^{4,5} is a recently emerged quantitative MR imaging method for clinically targeted assessment of myelination in brain tissue. The MPF is a biophysical parameter describing the amount of macromolecular protons in tissues involved in cross-relaxation with free water

Received December 8, 2017; accepted after revision March 23, 2018.

From the Department of Radiology (V.L.Y.), University of Washington, Seattle, Washington; Research Institute of Biology and Biophysics (V.L.Y.), Tomsk State University, Tomsk, Russian Federation; and Institute "International Tomography Center" of the Siberian Branch of the Russian Academy of Sciences (I.Y.P., A.A.S., A.M.K.), Novosibirsk, Russian Federation.

The development of the imaging protocol and reconstruction software was supported by the Russian Science Foundation (Project No. 14-45-00040). Data acquisition and analysis were performed under support from the Ministry of Education and Science of the Russian Federation within the State Assignment Project No. 18.2583.2017/4.6. Drs Korostyshevskaya and Savelov received salary support from the Federal Agency for Scientific Organizations of the Russian Federation (Project No. 0333-2017-0003).

Paper previously presented, in part, at: Annual Meeting and Exhibition of the International Society for Magnetic Resonance in Medicine, April 22–27, 2017; Honolulu, Hawaii (abstract #806).

Please address correspondence to Vasily L. Yarnykh, PhD, Department of Radiology, University of Washington, 850 Republican St, Room 255, Seattle, WA 98109; e-mail: yarnykh@uw.edu; @yarnykh

Indicates open access to non-subscribers at www.ajnr.org

<http://dx.doi.org/10.3174/ajnr.A5668>

Table 1: Fast MPF mapping protocol parameters^a

Parameter	3D MT-Weighted ^b and Reference GRE	3D T1-Weighted GRE	3D PD-Weighted GRE
TR (ms)	32	20	20
TE (ms)	6.3 (6.1)	6.3 (6.1)	6.3 (6.1)
Flip angle	8°	20°	4°
FOV (mm ²)	250 × 250 (240 × 200)	250 × 250 (240 × 200)	250 × 250 (240 × 200)
Acquired/reconstructed in-plane resolution (mm ²)	1.5 × 1.5/0.8 × 0.8	1.5 × 1.5/0.8 × 0.8	1.5 × 1.5/0.8 × 0.8
Acquired/reconstructed section thickness (mm)	5/2.5	5/2.5	5/2.5
No. of acquired/reconstructed sections	12/24 (40/80)	12/24 (40/80)	12/24 (40/80)
EPI factor	9	9	9
No. of averages	2	2	2
Acquisition time (min:sec)	0:38 (1:55)	0:12 (0:36)	0:12 (0:36)

Note:—PD indicates proton density.

^aData in parentheses correspond to the parameters for adult brain scans if different from fetal ones.

^bStandard manufacturer's off-resonance saturation pulse (3-lobe sinc shape with Gaussian apodization) with the offset frequency of 1.1 kHz, effective flip angle of 520°, and duration of 15 ms was used in the MT-weighted sequence. Acquisition time includes both MT-weighted and reference images, which were sequentially acquired in a single scan using a standard manufacturer's option.

protons and causing the magnetization transfer (MT) effect.⁴ Animal studies have demonstrated close correlations between the MPF and myelin content.^{6–10} The fast method enabling whole-brain MPF mapping based on a single MT-weighted image⁴ showed promising clinical results in adult brain studies^{11,12} and has been histologically validated as an accurate quantitative tool for measuring demyelination.¹⁰ The single-point technique⁴ also allowed designing an ultrafast MPF mapping protocol for non-brain applications.¹³ In utero brain imaging is a promising area of MPF mapping applications where this method could identify the earliest brain tissue changes associated with myelin development and potentially lead to new diagnostic approaches aimed at detecting delayed myelination of the fetal brain. The objectives of this pilot study were to develop a fast clinically targeted technique for MPF mapping of the fetal brain in vivo and test its capability to characterize normal prenatal brain myelination.

MATERIALS AND METHODS

Study Population

This cross-sectional study was approved by the institutional ethics committee at the International Tomography Center of the Siberian Branch of the Russian Academy of Sciences. Written informed consent was obtained from all participants. The study population included 47 pregnant women referred for clinical fetal MR imaging for various indications. Patients were prospectively recruited between December 2015 and July 2017. Gestational age (GA) was determined from the last menstrual period and confirmed by prior sonographic examinations. An MPF mapping protocol with a total duration of about 5 minutes was executed after clinical MR imaging subject to the MR imaging facility time availability. All clinical MR imaging examinations were reviewed during the scanning session by a radiologist with 16 years' experience in pediatric and fetal MR imaging. The fetuses judged to have normal brain MR imaging findings or borderline abnormalities (mild ventriculomegaly and mega cisterna magna) were included in this study. Six cases were excluded due to unacceptable image quality caused by fetal motion. The final sample included 41 fetuses with a mean GA ± SD of 26.8 ± 5.9 weeks (range, 18–38 weeks). To verify the compatibility of MPF measurements using our protocol with previous studies,^{4,5,11,12} we also recruited 3 healthy adults (31- and 51-year-old men and a 50-year-old

woman). To study the effect of a possible noise bias on MPF measurements, we obtained an additional series of brain scans with variable SNRs from 1 healthy volunteer (a 47-year-old man).

MR Imaging Protocol

MR imaging was performed on a 1.5T scanner (Achieva; Philips Healthcare, Best, the Netherlands) with an 8-channel body coil for fetal examinations or a 16-channel neurovascular coil for adult brain scans. A fast 3D MPF mapping protocol was implemented using standard manufacturer's software with a multishot echo-planar imaging readout and included the following sequences: spoiled MT-weighted gradient recalled-echo (GRE); reference spoiled GRE without MT saturation; T1-weighted spoiled GRE; and proton-density-weighted spoiled GRE. Fetal and adult brain imaging protocol parameters are summarized in Table 1. To mitigate fetal motion artifacts, we repeated the above sequences in separate acquisition blocks from 2 to 4 times, followed by exclusion of motion-corrupted images (if present) and averaging of the rest of the data during postprocessing. Sample source images are illustrated in Fig 1. In the experiment with variable SNRs, the adult brain MPF mapping protocol (Table 1) was executed without the EPI readout and with increased spatial resolution (voxel size, 1.0 × 1.0 × 1.5 mm³). Different SNR levels were achieved by varying the receiver bandwidth with the actual values of 109, 217, 434, and 868 Hz/pixel.

Image Processing and Analysis

Source images were inspected for the presence of artifacts and misregistration. Only datasets without visible displacement of the fetal brain between scans and motion artifacts were included in subsequent processing. MPF maps were reconstructed from a single dataset in 9 cases (from 2 and 3 initially acquired datasets in 5 and 4 cases, respectively), from 2 datasets in 22 cases (from 2, 3, and 4 initially acquired datasets in 14, 6, and 2 cases, respectively), and from 3 datasets in 10 cases (from 3 and 4 initially acquired datasets in 7 and 3 cases, respectively). In 6 cases, no complete datasets suitable for reconstruction were obtained.

MPF maps were reconstructed using the single-point algorithm⁴ implemented in custom-written C-language software with the following values of the two-pool model parameter constraints: cross-relaxation rate constant $R = 19 \text{ s}^{-1}$; T2 of bound (macro-

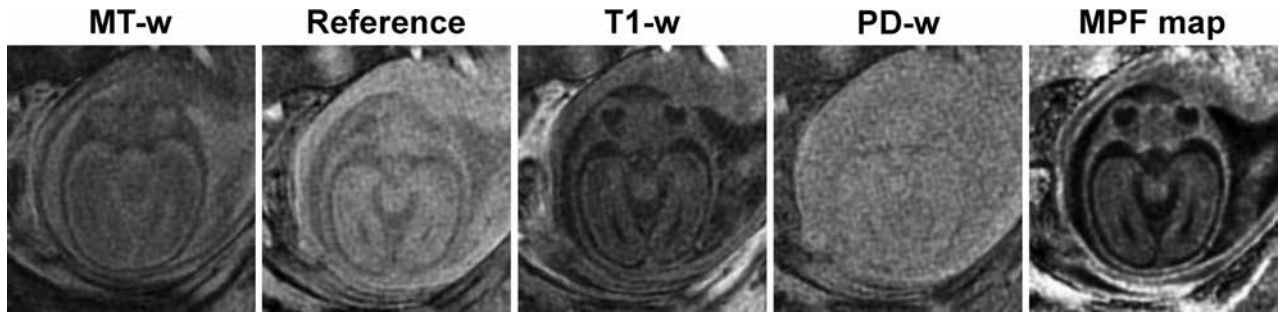


FIG 1. Sample source images (MT-weighted [MT-w], reference without saturation, T1-weighted [T1-w], and proton density–weighted [PD-w]) and a reconstructed MPF map obtained from the brain of a healthy 25-week fetus. Source data are presented after averaging the 3 consecutive image blocks. The MPF map is presented with a gray-scale range corresponding to MPF values from 0% to 10%.

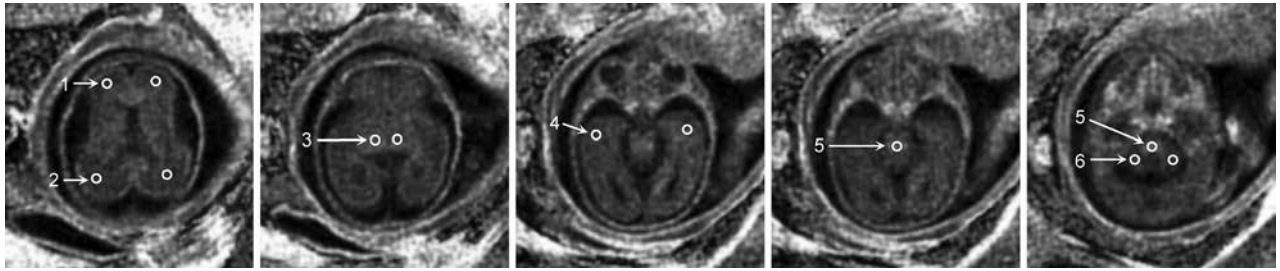


FIG 2. Selected transverse cross-sections of a 3D MPF map obtained from a healthy 25-week fetus with superimposed ROIs corresponding to the following brain structures: 1) frontal WM, 2) occipital WM, 3) thalamus, 4) temporal WM, 5) brain stem, and 6) cerebellum. All ROI measurements except for the brain stem were taken bilaterally and averaged. Brain stem measurements were obtained as a mean of 2 ROI values placed at the levels of the pons and medulla. The MPF map is presented with a gray-scale range corresponding to MPF values from 0% to 10%.

molecular) protons, $T_2^B = 10 \mu\text{s}$; and the product of the relaxation rate R1 and T2 of free water protons, $R_1 T_2^F = 0.055$. The parameters R and T_2^B were set according to the previous studies^{4,5} due to their independence of the magnetic field.¹⁴ The $R_1 T_2^F$ value for 1.5T was taken from the literature.¹⁵

MPF values were manually measured using ImageJ software (National Institutes of Health, Bethesda, Maryland) in circular ROIs placed within the following brain structures: brain stem, cerebellum, thalamus, and frontal, temporal, and occipital WM. The scheme of ROI placement is illustrated in Fig 2. The ROI area varied between 3.7 and 14.6 mm², depending on the brain and structure size. Care was taken in placing the thalamic ROIs to avoid inclusion of the germinal matrix. Additionally, the MPF was measured in the germinal matrix in a subset of cases where this structure was clearly identifiable. In adults, ROIs were placed in approximately similar positions to those in the fetal brain and had areas in a range of 16.7–36.1 mm².

Simulations and Measurements of the Noise Bias

To assess the effect of noise bias on MPF measurements, we fitted a series of simulated signal intensities with a variable added noise level using the single-point algorithm.⁴ Noiseless source data were generated using the matrix signal model⁴ for the MT-weighted intensities or the Ernst equation for other intensities. The noise bias was modeled by adding the noise term η to the signal in the form $S_n = \sqrt{S_0^2 + \eta^2}$, where S_n and S_0 are the signal intensities with and without noise, respectively. This approach is based on the Rician noise distribution and provides a good approximation for $\text{SNR} > 3$.¹⁶ The noise level was expressed as a fraction of the reference image intensity and uniformly added to other image

intensities (proton density-, T1-, and MT-weighted). Simulations were performed for the 4 tissue-specific datasets on the basis of actual MPF and T1 measurements, corresponding to adult frontal WM, adult GM (caudate nucleus), fetal frontal WM, and the fetal brain stem.

For all tissues, other model parameters (R , T_2^B , and $R_1 T_2^F$) were identical to the values listed above, and the proton density was set to unity. In all simulations, actual protocol parameters (Table 1) were used. To compare the results of simulations with experimental data, we measured the SNR and MPF values in the above anatomic structures for 1 adult and 1 fetal brain dataset with variable SNRs. The adult data were obtained with the variable receiver bandwidth as described above. The fetal dataset included the images obtained in the 3 consecutive acquisition blocks with the use of 1, 2, or all 3 data subsets for reconstruction of MPF maps. The SNR in the anatomic structures was calculated as $\text{SNR} = 0.7 S_{\text{ref}} / \sigma_n$, where S_{ref} is the signal intensity in the reference image, σ_n is the SD of background noise, and the coefficient 0.7 is the correction factor for the multichannel noise distribution¹⁷ applicable to both 8- and 16-channel coils.¹⁸

Statistical Analysis

Statistica software (StatSoft, Tulsa, Oklahoma) was used for all analyses. Normality of data was assessed with the Shapiro-Wilk test. Parametric analyses were used thereafter because no significant deviations from the normal distribution were found. The entire population was dichotomized into the second and third pregnancy trimester groups (GAs of 18–26.5 and 27–38 weeks, respectively). Repeated-measures ANOVA was used to compare the MPF between brain structures (within-subject factor) and tri-

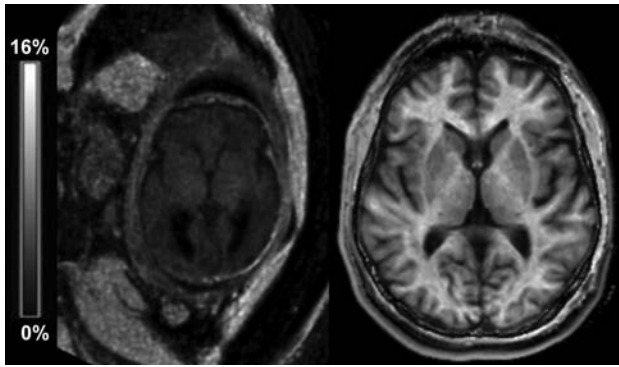


FIG 3. Sample transverse cross-sections of brain 3D MPF maps obtained from a healthy 36-week fetus (*left*) and a healthy adult volunteer (*right*) using the same clinical MR imaging scanner and protocol and presented with the same gray-scale range corresponding to the MPF between 0% and 16%.

mesters (between-subject factor) followed by post hoc tests with Bonferroni correction for multiple comparisons. Associations between MPF and GA were assessed using the Pearson correlation coefficient (r). Germinal matrix measurements were separately compared with other structures by paired t tests in a subset of subjects in whom the germinal matrix was identifiable. Adult data were not statistically analyzed due to a small sample size. Two-tailed tests were used in all analyses. P values $< .05$ were considered significant. Data are presented as means \pm SD where applicable.

RESULTS

MPF maps of the adult and fetal brains are compared in Fig 3. Sample brain MPF maps of fetuses of different GAs are shown in Fig 4. Results of MPF measurements across brain regions in the fetal and adult brains are listed in Table 2. MPF values in the fetal brain appeared extremely low compared with the adult brain (Fig 3 and Table 2). MPF maps of younger fetuses demonstrated slightly elevated values in the brain stem, germinal matrix, and cortical ribbon with a 3-layer supratentorial pattern (Fig 4A, -B). In older fetuses, a gradual increase of the MPF in the brain stem, cerebellum, thalamus, and striatum along with disappearance of the germinal matrix was visible (Fig 4C, -D).

ANOVA revealed highly significant effects of the pregnancy trimester ($F = 21.0, P < .001$), brain structure ($F = 126.1, P < .001$), and interaction between these factors ($F = 33.1, P < .001$) (Table 2). The MPF in the brain stem, cerebellum, and thalamus was significantly increased during the third trimester relative to the second one. The MPF in cerebral WM was similar during both trimesters. The MPF in the brain stem was significantly higher compared with other regions during both trimesters, except for the thalamus in the second trimester. MPF in cerebellar WM was similar to cerebral WM during the second trimester and became significantly higher in the third trimester. The MPF in the thalamus was significantly higher relative to both cerebral and cerebellar WM during both trimesters. No significant differences were found among frontal, temporal, and occipital WM in both trimesters.

The MPF in the brain stem, cerebellum, and thalamus significantly correlated with GA ($r = 0.88, 0.80, \text{ and } 0.73$, respectively; all $P < .001$) (Fig 5). No significant correlations were found for

frontal ($r = -0.13, P = .44$), temporal ($r = 0.28, P = .07$), and occipital ($r = -0.07, P = .66$) WM.

The germinal matrix was identified in 31 fetuses (GA range, 18–34 weeks) with a mean MPF of $3.83\% \pm 0.30\%$. This value was significantly larger ($P \leq .001$) than the MPF in all the above brain structures within the same subset of cases. No significant correlation between the MPF in the germinal matrix and GA was found ($r = 0.25, P = .18$).

The effect of the SNR in source images on the accuracy of MPF mapping is illustrated in Figs 6 and 7. Figure 6 shows the MPF maps of adult and fetal brains reconstructed from the datasets with different SNR levels. Figure 7 demonstrates simulated dependencies of the MPF on the SNR in the reference image with superimposed experimental measurements corresponding to the MPF maps presented in Fig 6. Although a reduced SNR resulted in visible propagation of noise into MPF maps (Fig 6), MPF measurements in the brain regions appeared nearly identical across a wide SNR range (Fig 7). Simulations suggest that the noise bias becomes apparent at very low SNRs and results in underestimation of MPF values (Fig 7). At the same time, for practically usable source images with SNR > 10 , the relative systematic errors caused by noise do not exceed 5%.

DISCUSSION

This study demonstrates the feasibility of fast fetal brain MPF mapping using a routine clinical MR imaging scanner. The notable finding of our research is a very low MPF in the fetal brain consistent with the absence or a small amount of myelin. Comparison between fetal and adult brain data shows that the MPF enables the largest dynamic range of maturation-dependent changes in brain tissues among quantitative MR imaging parameters available in the literature.^{19–22} Particularly, MPF in WM exhibits about a 5-fold increase from the fetus to adult, whereas the relaxation times T1,¹⁹ T2,¹⁹ and T2*²⁰ and the apparent diffusion coefficient^{21,22} are characterized by the 2- to 3-fold ranges of changes.

Despite a generally low level, the MPF in the fetal brain demonstrates substantial regional distinctions and different GA dependencies. Our observations are in good overall agreement with histologically established patterns of prenatal brain myelination^{1,2,23–25} and temporal changes in MR imaging signal intensities in vivo^{26–29} and ex vivo.^{30,31} The MPF in the structures with known prenatal myelination onset, such as the brain stem, cerebellum, and thalamus^{1,2,23–25} showed strong correlations with GA, whereas a steadily low MPF with no GA dependence was found in the WM of the cerebral hemispheres, which begins to myelinate around the middle of the first postnatal year.^{1,2} Elevated MPF in the brain stem observed in the second trimester agrees with the earliest myelination onset (around the 20th gestational week) in certain fiber tracts, such as the medial lemniscus and medial longitudinal fasciculus.^{1,23,24} A relatively high MPF and its correlation with GA in the thalamus are also in concordance with early myelination of this structure commencing at the 25th week.²⁵

While the myelin content provides the main determinant of the MPF in WM according to our results and other studies,^{6–10} subtle effects of other tissue properties on this parameter are also discernible. An increased MPF in the germinal matrix observed in

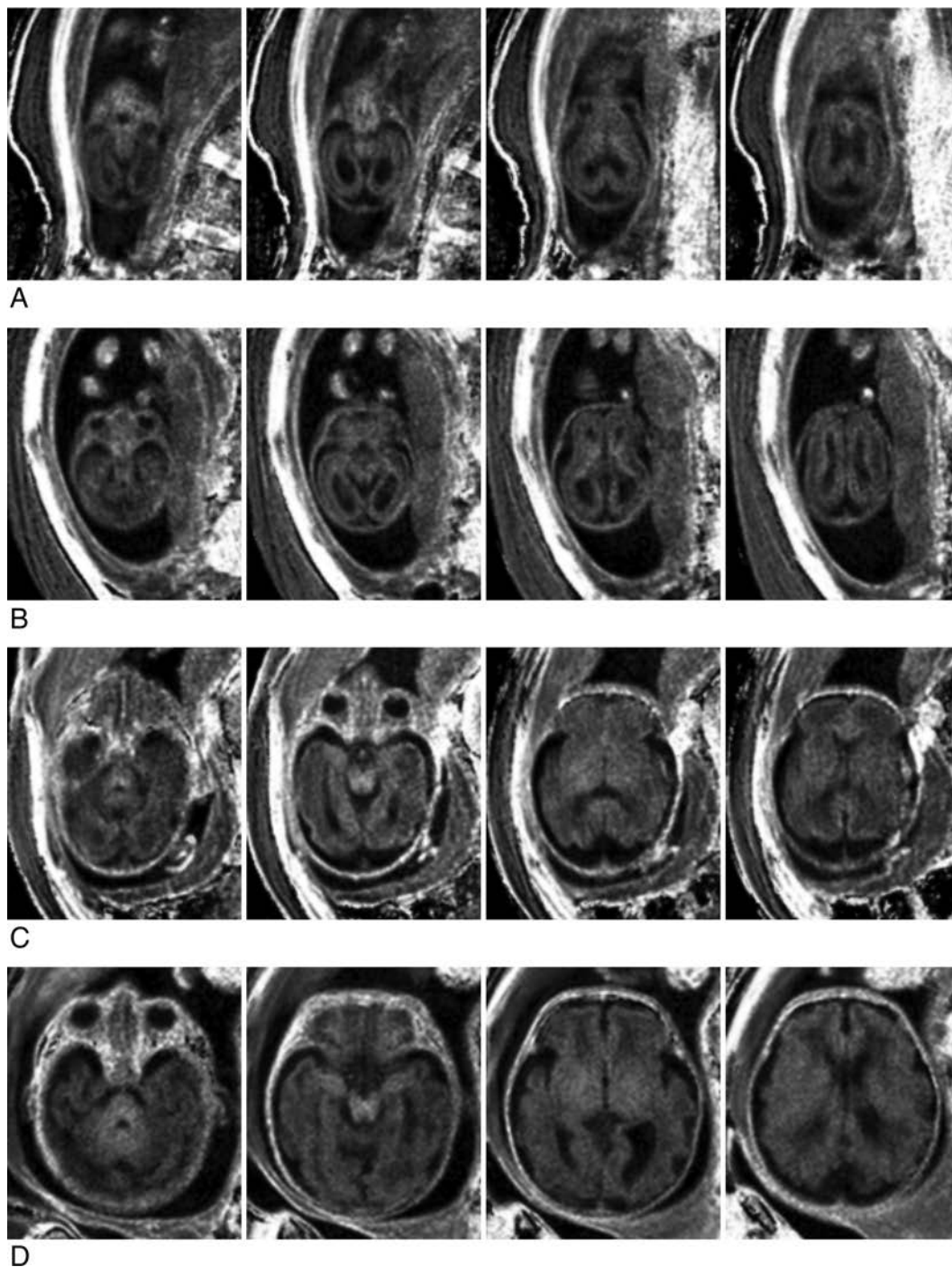


FIG 4. Sample transverse cross-sections of brain 3D MPF maps obtained from fetuses of different GAs: 19 weeks (A), 21 weeks (B), 29 weeks (C), and 36 weeks (D). Images of younger fetuses (A and B) show a 3-layer pattern in the supratentorial brain with an increased MPF in the germinal matrix and cortical ribbon compared with the intermediate layer. The brain stem appears hyperintense on all MPF maps (A–D). An increased MPF in the cerebellum, thalamus, and striatum becomes visible in older fetuses (C and D). WM of the cerebral hemispheres remains hypointense relative to both cortical and subcortical gray matter (C and D). MPF maps are presented with a gray-scale range corresponding to MPF values from 0% to 10%.

young fetuses suggests that unmyelinated brain tissue creates a low-signal background highlighting fine distinctions in the macromolecular content not related to myelin and probably associated with cellularity. Another explanation of elevated MPF in the germinal matrix could be the presence of collagen, characterized by an inherently large MPF¹³ and providing vessel wall support in this highly vascularized structure.³²

An important methodologic result of this study is the demonstration of the feasibility of fast MPF mapping with suboptimal sequence parameters and a low SNR. Prior human brain studies using the fast MPF mapping method^{4,5,11,12} used optimal MT saturation conditions (offset frequencies of ≥ 4 kHz⁴), very high SNR (> 100) in source images,⁴ and an optimized radiofrequency and gradient spoiling scheme.³³ In the manufacturer's product

sequence used in this work, the offset frequency is substantially lower (1.1 kHz) and spoiling implementation is suboptimal for quantitative measurements.^{3,3} Fetal images used for MPF mapping are also characterized by an inherently low SNR (around 10–25). Additionally, the software of routine clinical scanners does not contain specialized B_0 and B_1 field-mapping sequences; therefore, field corrections were not used in this study. Nevertheless, MPF measurements in the adult brain obtained with our protocol appeared in close overall agreement with the literature.^{4,5,11,12} Furthermore, our experimental data and simulations demonstrated a negligible noise bias in the MPF measurements

performed at the specified SNR levels. Taken together, these results suggest that the fast MPF mapping method is inherently robust with respect to the noise and instrumental errors and can be successfully deployed in a clinical setting.

This study has some limitations. First, MPF measurements in the adult brain were performed for illustrative purposes in a small number of participants and were not compared with those obtained with the optimized pulse sequences and protocol.^{4,5} Thus, a possible subtle bias in MPF measurements based on standard manufacturers' product sequences cannot be excluded and needs to be tested in future studies. Second, the constrained values of cross-relaxation parameters used in the single-point reconstruction algorithm⁴ were taken from previous studies in adults.^{4,15} While these values may potentially differ for the fetal brain, it is highly unlikely that improved constraints could change the main conclusions of this study regarding the extremely low MPF values in the fetal brain and their spatial-temporal behavior. Third, we did not use specialized image-processing procedures intended to mitigate fetal motion but rather relied on repeat data acquisition with subsequent exclusion of corrupted or misreg-

Table 2: Mean regional MPF values in the fetal and adult brain^a

Regional MPF (%)	Second Trimester Fetuses (18–26.5 GW, n = 23)	Third Trimester Fetuses (27–38 GW, n = 18)	Adults (n = 3)
Brain stem	3.30 ± 0.43	4.28 ± 0.45 ^b	10.60 ± 0.38
Cerebellum	2.32 ± 0.41 ^c	3.23 ± 0.53 ^{b,c,d}	12.28 ± 0.63
Thalamus	3.03 ± 0.48 ^d	3.74 ± 0.46 ^{b,c,d}	8.62 ± 0.21
Frontal WM	2.62 ± 0.34 ^{c,e}	2.36 ± 0.33 ^{c,d,e}	12.63 ± 0.54
Temporal WM	2.61 ± 0.17 ^{c,e}	2.63 ± 0.26 ^{c,d,e}	13.20 ± 0.24
Occipital WM	2.54 ± 0.30 ^{c,e}	2.41 ± 0.27 ^{c,d,e}	12.11 ± 0.45

Note:—GW indicates gestational weeks.

^aFetal data were compared between trimesters and structures using repeated-measures ANOVA. *P* values are Bonferroni-corrected for multiple pair-wise comparisons. No statistical comparisons were performed for the adult data.

^bSignificantly different from the second trimester (*P* < .001).

^cSignificantly different from the brain stem within the same trimester (*P* < .001).

^dSignificantly different from the cerebellum within the same trimester (*P* < .001).

^eSignificantly different from the thalamus within the same trimester (*P* < .001).

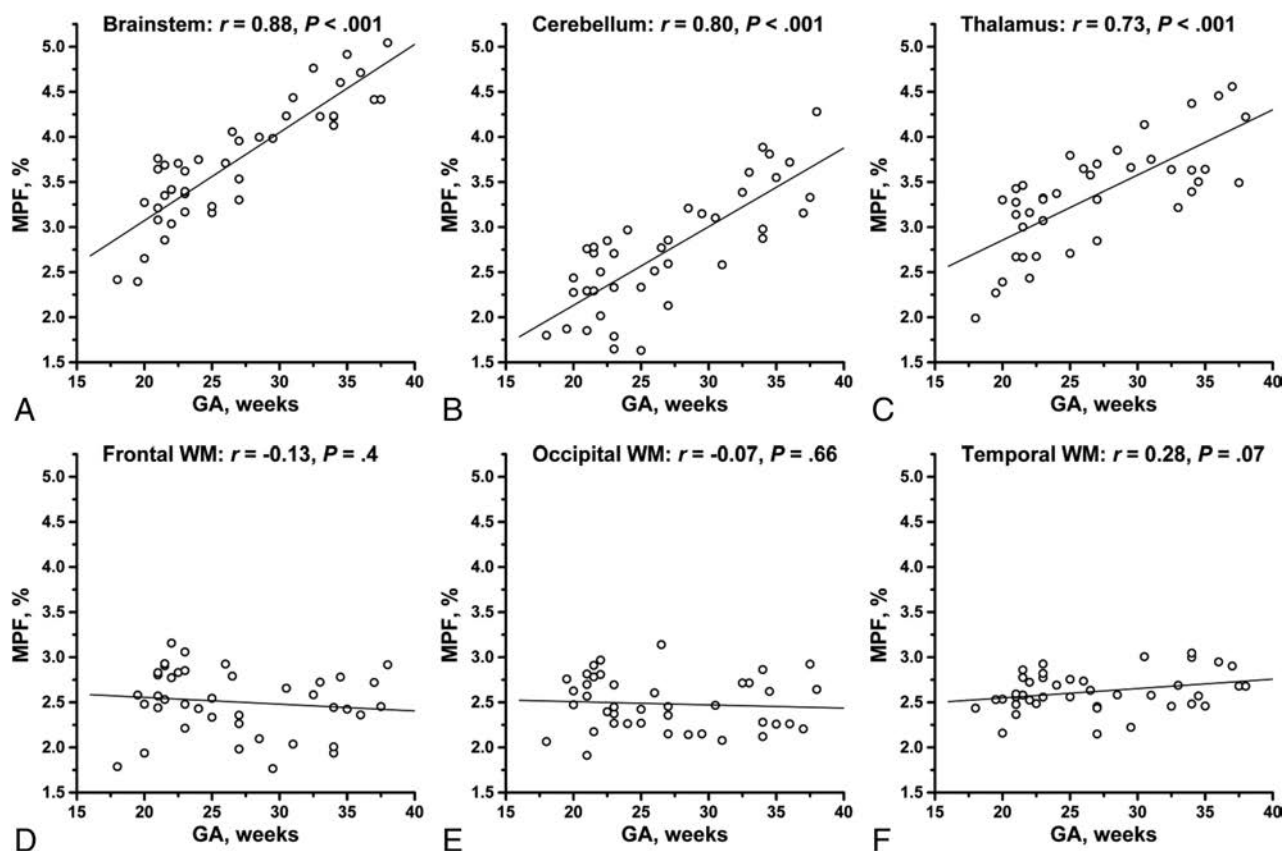


FIG 5. Scatterplots of MPF versus gestational age in the fetal brain structures: brain stem (A), cerebellum (B), thalamus (C), frontal WM (D), occipital WM (E), and temporal WM (F). The lines depict linear regression plots, and the numbers are Pearson correlation coefficients (*r*) and *P* values. The MPF in the brain stem, cerebellum, and thalamus (A–C) demonstrates strong significant correlations with GA. No significant correlations with GA are seen for frontal, occipital, and temporal WM (D–F).

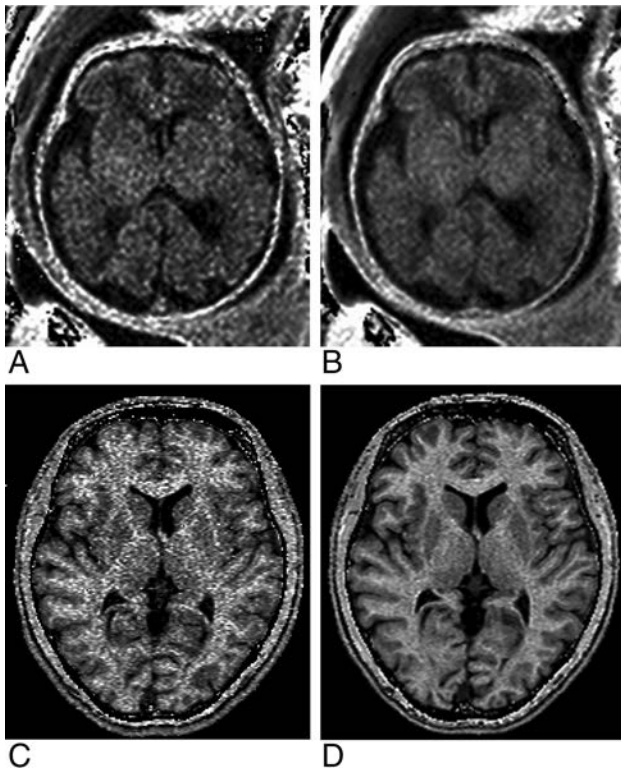


FIG 6. Sample MPF maps of the fetal (A and B) and adult (C and D) brains reconstructed from the datasets with different SNRs. Fetal MPF maps were reconstructed from 1 (A) and 3 (C) sets of source images. Adult MPF maps were reconstructed from the source images acquired with the receiver bandwidths of 868 (C) and 109 (D) Hz/pixel. Fetal and adult MPF maps are presented, with gray-scale ranges corresponding to MPF ranges of 0%–10% and 0%–20%, respectively.

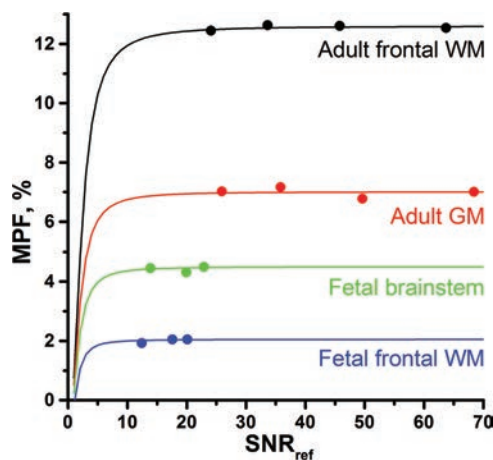


FIG 7. Simulated (lines) and experimental (dots) dependencies of the measured MPF on the SNR in source images expressed as functions of the reference image SNR (SNR_{ref}) based on the data exemplified in Fig 6. Simulated plots correspond to the actual MPF and T1 values measured in ROIs for adult frontal WM (MPF = 12.6%, T1 = 750 ms), adult GM in the caudate nucleus (MPF = 7.0%, T1 = 1230 ms), fetal brain stem (MPF = 4.5%, T1 = 1520 ms), and fetal frontal WM (MPF = 2.0%, T1 = 2340 ms). Adult MPF and SNR measurements were obtained from the datasets acquired with the receiver bandwidths of 868, 434, 217, and 109 Hz/pixel. Fetal measurements were obtained from the datasets containing 1, 2, and 3 averaged blocks of source images.

istered source images. The combination of MPF mapping with appropriate registration and motion-correction algorithms²⁰ may improve the performance and success rate of the method in future applications.

CONCLUSIONS

This study confirms that myelination is the main factor determining the MPF in brain tissues. Our results demonstrate that MPF mapping is sensitive to the earliest stages of myelin development in the fetal brain and can be implemented in a clinical setting. Potential clinical applications of fetal MPF mapping include various prenatal brain injuries and inherited myelinopathies for which this method may enable future studies of associations between fetal myelination abnormalities and postnatal neurodevelopment.

Disclosures: Vasily L. Yarnykh—RELATED: Grant: Russian Science Foundation, Ministry of Education and Science of the Russian Federation, Comments: Russian Science Foundation (Project No. 14-45-00040), Ministry of Education and Science of the Russian Federation (State Assignment Project No. 18.2583.2017/4.6).* Irina Y. Prihod'ko—RELATED: Grant: Federal Agency for Scientific Organizations (Russia).* Andrey A. Savelov—RELATED: Grant: Federal Agency for Scientific Organizations (Russia), Comments: grant 0333-2017-0003.* Alexandra M. Korostyshevskaya—RELATED: Grant: Federal Agency for Scientific Organizations of the Russian Federation (Project No. 0333-2017-0003). *Money paid to the institution.

REFERENCES

1. Yakovlev PI, Lecours AR. **The myelogenetic cycles of regional maturation of the brain.** In: Minkowski A, ed. *Regional Development of the Brain in Early Life.* Oxford: Blackwell; 1967:3–70
2. Kinney HC, Brody BA, Kloman AS, et al. **Sequence of central nervous system myelination in human infancy, II: patterns of myelination in autopsied infants.** *J Neuropathol Exp Neurol* 1988;47:217–34 CrossRef Medline
3. Rees S, Inder T. **Fetal and neonatal origins of altered brain development.** *Early Hum Dev* 2005;81:753–61 CrossRef Medline
4. Yarnykh VL. **Fast macromolecular proton fraction mapping from a single off-resonance magnetization transfer measurement.** *Magn Reson Med* 2012;68:166–78 CrossRef Medline
5. Yarnykh VL. **Time-efficient, high-resolution, whole brain three-dimensional macromolecular proton fraction mapping.** *Magn Reson Med* 2016;75:2100–06 CrossRef Medline
6. Underhill HR, Rostomily RC, Mikheev AM, et al. **Fast bound pool fraction imaging of the in vivo rat brain: association with myelin content and validation in the C6 glioma model.** *Neuroimage* 2011; 54:2052–65 CrossRef Medline
7. Samsonov A, Alexander AL, Mossahebi P, et al. **Quantitative MR imaging of two-pool magnetization transfer model parameters in myelin mutant shaking pup.** *Neuroimage* 2012;62:1390–98 CrossRef Medline
8. Thiessen JD, Zhang Y, Zhang H, et al. **Quantitative MRI and ultrastructural examination of the cuprizone mouse model of demyelination.** *NMR Biomed* 2013;26:1562–81 CrossRef Medline
9. Janve VA, Zu Z, Yao SY, et al. **The radial diffusivity and magnetization transfer pool size ratio are sensitive markers for demyelination in a rat model of type III multiple sclerosis (MS) lesions.** *Neuroimage* 2013;74:298–305 CrossRef Medline
10. Khodanovich MY, Sorokina IV, Glazacheva VY, et al. **Histological validation of fast macromolecular proton fraction mapping as a quantitative myelin imaging method in the cuprizone demyelination model.** *Sci Rep* 2017;7:46686 CrossRef Medline
11. Yarnykh VL, Bowen JD, Samsonov A, et al. **Fast whole-brain three-dimensional macromolecular proton fraction mapping in multiple sclerosis.** *Radiology* 2015;274:210–20 CrossRef Medline
12. Petrie EC, Cross DJ, Yarnykh VL, et al. **Neuroimaging, behavioral,**

- and psychological sequelae of repetitive combined blast/impact mild traumatic brain injury in Iraq and Afghanistan war veterans. *J Neurotrauma* 2014;31:425–36 CrossRef Medline
13. Yarnykh VL, Tartaglione EV, Ioannou GN. **Fast macromolecular proton fraction mapping of the human liver in vivo for quantitative assessment of hepatic fibrosis.** *NMR Biomed* 2015;28:1716–25 CrossRef Medline
 14. Naumova AV, Akulov AE, Khodanovich MY, et al. **High-resolution three-dimensional macromolecular proton fraction mapping for quantitative neuroanatomical imaging of the rodent brain in ultra-high magnetic fields.** *Neuroimage* 2017;147:985–93 CrossRef Medline
 15. Yarnykh VL, Yuan C. **Cross-relaxation imaging reveals detailed anatomy of white matter fiber tracts in the human brain.** *Neuroimage* 2004;23:409–24 CrossRef Medline
 16. Gudbjartsson H, Patz S. **The Rician distribution of noisy MRI data.** *Magn Reson Med* 1995;34:910–14 CrossRef Medline
 17. Constantinides CD, Atalar E, McVeigh ER. **Signal-to-noise measurements in magnitude images from NMR phased arrays.** *Magn Reson Med* 1997;38:852–57 CrossRef Medline
 18. The Association of Electrical Equipment and Medical Imaging Manufacturers. **Characterization of phased array coils for diagnostic magnetic resonance images.** NEMA Standards Publication MS 9-2008. Arlington: National Electrical Manufacturers Association; 2008:9–15. <http://www.nema.org/Standards/Pages/Characterization-of-Phased-Array-Coils-for-Diagnostic-Magnetic-Resonance-Images.aspx>. Accessed March 15, 2018
 19. Thayyil S, De Vita E, Sebire NJ, et al. **Post-mortem cerebral magnetic resonance imaging T1 and T2 in fetuses, newborns and infants.** *Eur J Radiol* 2012;81:e232–38 CrossRef Medline
 20. Blazejewska AI, Seshamani S, McKown SK, et al. **3D in utero quantification of T2* relaxation times in human fetal brain tissues for age optimized structural and functional MRI.** *Magn Reson Med* 2017;78:909–16 CrossRef Medline
 21. Righini A, Bianchini E, Parazzini C, et al. **Apparent diffusion coefficient determination in normal fetal brain: a prenatal MR imaging study.** *AJNR Am J Neuroradiol* 2003;24:799–804 Medline
 22. Schneider JF, Confort-Gouny S, Le Fur Y, et al. **Diffusion-weighted imaging in normal fetal brain maturation.** *Eur Radiol* 2007;17:2422–29 CrossRef Medline
 23. Gilles FH. **Myelination in the neonatal brain.** *Hum Pathol* 1976;7:244–48 CrossRef Medline
 24. Tanaka S, Mito T, Takashima S. **Progress of myelination in the human fetal spinal nerve roots, spinal cord and brainstem with myelin basic protein immunohistochemistry.** *Early Hum Dev* 1995;41:49–59 CrossRef Medline
 25. Hasegawa M, Houdou S, Mito T, et al. **Development of myelination in the human fetal and infant cerebrum: a myelin basic protein immunohistochemical study.** *Brain Dev* 1992;14:1–6 CrossRef Medline
 26. Girard N, Raybaud C, Poncet M. **In vivo MR study of brain maturation in normal fetuses.** *AJNR Am J Neuroradiol* 1995;16:407–13 Medline
 27. Wang Z, Chen J, Qin Z, et al. **The research of myelination of normal fetal brain with magnetic resonance imaging.** *Chin Med J (Engl)* 1998;111:71–74 Medline
 28. Chung HW, Chen CY, Zimmerman RA, et al. **T2-Weighted fast MR imaging with true FISP versus HASTE: comparative efficacy in the evaluation of normal fetal brain maturation.** *AJR Am J Roentgenol* 2000;175:1375–80 CrossRef Medline
 29. Abe S, Takagi K, Yamamoto T, et al. **Semiquantitative assessment of myelination using magnetic resonance imaging in normal fetal brains.** *Prenat Diagn* 2004;24:352–57 CrossRef Medline
 30. Brisse H, Fallet C, Sebag G, et al. **Supratentorial parenchyma in the developing fetal brain: in vitro MR study with histologic comparison.** *AJNR Am J Neuroradiol* 1997;18:1491–97 Medline
 31. Kostović I, Judas M, Rados M, et al. **Laminar organization of the human fetal cerebrum revealed by histochemical markers and magnetic resonance imaging.** *Cereb Cortex* 2002;12:536–44 CrossRef Medline
 32. Anstrom JA, Thore CR, Moody DM, et al. **Morphometric assessment of collagen accumulation in germinal matrix vessels of premature human neonates.** *Neuropathol Appl Neurobiol* 2005;31:181–90 CrossRef Medline
 33. Yarnykh VL. **Optimal radiofrequency and gradient spoiling for improved accuracy of T1 and B1 measurements using fast steady-state techniques.** *Magn Reson Med* 2010;63:1610–26 CrossRef Medline

Global and Widespread Local White Matter Abnormalities in Juvenile Neuronal Ceroid Lipofuscinosis

U. Roine, T.J. Roine, A. Hakkarainen, A. Tokola, M.H. Balk, M. Mannerkoski, L.E. Åberg, T. Lönnqvist, and T. Autti



ABSTRACT

BACKGROUND AND PURPOSE: Juvenile neuronal ceroid lipofuscinosis is a progressive neurodegenerative lysosomal storage disease of childhood. It manifests with loss of vision, seizures, and loss of cognitive and motor functions leading to premature death. Previous MR imaging studies have reported cerebral and cerebellar atrophy, progressive hippocampal atrophy, thalamic signal intensity alterations, and decreased white matter volume in the corona radiata. However, conventional MR imaging findings are usually normal at younger than 10 years of age. The purpose of our study was to investigate whether diffusion MR imaging could reveal changes in white matter microstructure already present at a younger age.

MATERIALS AND METHODS: We investigated global and local white matter abnormalities in 14 children with juvenile neuronal ceroid lipofuscinosis (mean age, 9.6 ± 3.4 years; 10 boys) and 14 control subjects (mean age, 11.2 ± 2.3 years; 7 boys). Twelve patients underwent follow-up MR imaging after 2 years (mean age, 11.4 ± 3.2 years; 8 boys). We performed a global analysis using 2 approaches: white matter tract skeleton and constrained spherical deconvolution–based whole-brain tractography. Then, we investigated local microstructural abnormalities using Tract-Based Spatial Statistics.

RESULTS: We found globally decreased anisotropy ($P = .000001$) and increased diffusivity ($P = .001$) in patients with juvenile neuronal ceroid lipofuscinosis. In addition, we found widespread increased diffusivity and decreased anisotropy in, for example, the corona radiata ($P < .001$) and posterior thalamic radiation ($P < .001$). However, we found no differences between the first and second acquisitions.

CONCLUSIONS: The patients with juvenile neuronal ceroid lipofuscinosis exhibited global and local abnormalities in white matter microstructure. Future studies could apply more specific microstructural models and study whether these abnormalities are already present at a younger age.

ABBREVIATIONS: AD = axial diffusivity; CLN3 = juvenile neuronal ceroid lipofuscinosis; CP = coefficient of planarity; FA = fractional anisotropy; MD = mean diffusivity; NCL = neuronal ceroid lipofuscinosis; RD = radial diffusivity; TBSS = Tract-Based Spatial Statistics

Juvenile neuronal ceroid lipofuscinosis (CLN3) is a rare, progressive neurodegenerative lysosomal storage disease, in which autofluorescent ceroid lipopigments accumulate in the lysosomes. The first clinical symptom, rapidly progressive vision fail-

ure leading to blindness, appears around 4–10 years of age.^{1–3} It is followed by deterioration in cognitive and motor functions, in which the cognitive decline becomes clearer around 8–12 years of age.¹ Other symptoms include ataxia, dysarthria, rigidity, and difficulty in initiating movement, and occasionally, there are pyramidal signs.¹ The patients start having epileptic seizures typically around 10 years of age.⁴ Psychiatric symptoms, such as depression and psychosis, are also common.⁵ Although the clinical course is variable, the disease eventually leads to premature death in the second or third decade of life.⁶

More than 400 mutations in 14 genes have been found in children with neuronal ceroid lipofuscinoses.^{7,8} The juvenile form is the most common, with a reported incidence of 2–7/100,000

Received November 22, 2017; accepted after revision April 11, 2018.

From the Department of Radiology (U.R., T.J.R., A.H., A.T., M.H.B., T.A.), HUS Medical Imaging Center, and Departments of Child Psychiatry (M.M.) and Psychiatry (L.E.Å.), University of Helsinki and Helsinki University Hospital, Helsinki, Finland; imec-Vision Lab (T.J.R.), Department of Physics, University of Antwerp, Wilrijk (Antwerp), Belgium; and Department of Child Neurology (T.L.), Children's Hospital, University of Helsinki and Helsinki University Hospital, Helsinki, Finland.

This work was supported by Noah's Hope/Hope 4 Bridget, the Thisbe and Noah Scott Foundation, the Batten Disease Support and Research Association, Finnish Brain Foundation, Paulo Foundation, and Emil Aaltonen Foundation.

Please address correspondence to Ulrika Roine, MD, HUS Medical Imaging Center, Radiology, University of Helsinki and Helsinki University Hospital, PL 22 (Haartmaninkatu 4), FI-00014 Helsingin Yliopisto, Finland; e-mail: ulrika.roine@helsinki.fi; @UlrikaRoine

Indicates article with supplemental on-line tables.

<http://dx.doi.org/10.3174/ajnr.A5687>

births in Scandinavia⁹ and 0.2–1.5/100,000 in Central Europe.^{10,11} In Canada, the estimated incidence is 0.6/100,000 births.¹² The disease is caused by the recessive inheritance of mutations in the *CLN3* gene located on chromosome 16p12, encoding a membrane protein CLN3.¹³

The presence of ocular abnormalities and vacuolated lymphocytes in peripheral blood is suggestive of the disease, and the diagnosis can typically be confirmed by *CLN3* mutation analysis.¹⁴

Conventional MR imaging findings are usually normal at younger than 10 years of age.¹⁵ Previous MR imaging studies have reported cerebral and cerebellar atrophy, progressive hippocampal atrophy, decreased gray matter volume in the dorsomedial part of the thalamus, and decreased white matter volume in the corona radiata in patients with CLN3.^{15–17} However, cerebral atrophy is mostly seen in patients older than 14 years of age, and cerebellar atrophy, even later.¹⁵ In a postmortem study, higher MR imaging signal intensity of the periventricular white matter was reported with histologically observed severe periventricular loss of myelin and gliosis.¹⁸ Thalamic alterations have been consistently found in several types of neuronal ceroid lipofuscinosis (NCL), including CLN1 (infantile NCL), CLN2 (classic late infantile NCL), CLN3 (juvenile NCL), CLN5 (Finnish-variant late infantile NCL), and CLN7 (Turkish-variant late infantile NCL).¹⁹ Decreased T2-weighted signal intensity in the thalamus was also reported in a retrospective study in 33% of 43 patients with NCL.²⁰ Of the 11 patients with CLN3, four had T2 hypointensity in the thalamus. Moreover, MR imaging and CT showed diffuse cerebral and cerebellar atrophy, and electroencephalography findings were abnormal in 90% of the patients.

Diffusion-weighted imaging is a noninvasive method that enables the investigation of the white matter microstructure in the brain.^{21,22} In an unrestricted space, the diffusion of water molecules is equal in all directions and is thus called “isotropic,” but in nerve fibers, the cell membranes restrict the diffusion of the molecules and the diffusion becomes anisotropic. Fractional anisotropy (FA) is the most commonly used index to quantify the degree of anisotropy.²³ Mean diffusivity (MD) or ADC is the average diffusivity over all directions, axial diffusivity (AD) describes the diffusivity along the nerve fiber, and radial diffusivity (RD), perpendicular to it.

DW-MRI has previously revealed increased ADC values in patients with late infantile NCL.²⁴ Furthermore, ADC values correlated with patient age and disease duration, but the correlation with the central nervous system disability scale was much weaker.

The aim of this study was to investigate global and local white matter abnormalities in CLN3. We hypothesized that DW-MRI would be more sensitive in detecting microstructural white matter abnormalities than conventional MR imaging. We investigated global white matter microstructure with 2 approaches: 1) by performing whole-brain tractography, ie, the reconstruction of the white matter tracts in the brain²⁵; and 2) by reconstructing a white matter tract skeleton.²⁶ With DTI-based tractography,^{27,28} it is not possible to detect crossing fibers.^{29,30} Thus, we used constrained spherical deconvolution–based tractography,^{25,31,32} which enables the reliable reconstruction of neural tracts through regions with complex (eg, crossing) fiber configurations,^{33–35}

present in most white matter voxels.³⁶ Finally, we used Tract-Based Spatial Statistics (TBSS; <http://fsl.fmrib.ox.ac.uk/fsl/fslwiki/TBSS>) to investigate local microstructural properties in the same subjects.²⁶

MATERIALS AND METHODS

Participants

We acquired DW-MRI data from 14 patients with CLN3 and 14 age-matched controls. Twelve of the 14 patients underwent follow-up MR imaging after 2 years on average. MR imaging was performed at the Helsinki University Central Hospital, Finland, from 2007 to 2014. During the first acquisition, the mean age of the patients was 9.6 ± 3.4 years, and during the second acquisition, it was 11.4 ± 3.2 years. The mean age of control subjects was 11.2 ± 2.3 years. The difference in age was not statistically significant between patients and controls in the first or second acquisition. Seventy-one percent of the patients were males in the first acquisition, and 67%, in the second acquisition. Fifty percent of the controls were males. In addition, we collected disease-severity information using the Unified Parkinson's Disease Rating Scale, Part III,³⁷ a clinician-scored monitored motor evaluation, from 13 of the 14 patients for the first acquisition and 11 of the 12 patients for the second acquisition. Only the youngest patient had visual function close to normal at the time of the first acquisition; the remainder were blind or almost blind.

The patients with CLN3 were diagnosed on the basis of their clinical symptoms, including deterioration of vision and typical ophthalmologic findings, and the diagnoses were confirmed by DNA analysis. Nine patients were homozygous for the main mutation (1.02kb deletion including amino acids in exons 7 and 8). Four patients were heterozygous for the major mutation and a minor mutation (3kb deletion including amino acids in exons 10–13). One patient was heterozygous for the main mutation and a single nucleotide mutation in exon 13. The symptoms of this patient differed from others because she was blind, but her cognitive profile was normal. Depending on the patient, symptomatic medication typical for the disease was in use, including citalopram, valproate, levetiracetam, and risperidone. In addition, most patients participated in a concurrent study testing simvastatin in CLN3 for 1–2 years. The patients were recruited from the Department of Child Neurology, Helsinki University Central Hospital, and the control subjects were healthy volunteers recruited for this study. The Ethics Committee for Gynaecology and Obstetrics, Pediatrics, and Psychiatry of the Hospital District of Helsinki and Uusimaa approved the research protocol, and a guardian of each participant signed a written informed consent form before the study.

Data Acquisition

The MR imaging data were acquired with an Achieva 3T machine (Philips Healthcare, Best, the Netherlands) with an 8-channel head coil, using a $2 \times 2 \times 2$ mm voxel size and 32 gradient orientations with diffusion-weighting of 1000 s/mm^2 . In addition, 1 non-DWI was acquired. The FOV was $224 \times 224 \times 160$ mm, and 80 axial slices were acquired. The TE was 59.5 ms, and TR was 10.809 seconds. T1-weighted anatomic 3D images were acquired with a resolution of $1 \times 1 \times 1$ mm. The FOV was

Table 1: Global microstructural differences between children with CLN3 and age-matched control group with both skeleton and tractography approaches

Measure	Control	CLN3 1st	CLN3 2nd	P Value ^a (CLN3 1st vs Control)	P Value ^a (CLN3 2nd vs Control)	P Value ^a (CLN3 1st vs CLN3 2nd)
FA (skeleton)	.328 ± .026	.297 ± .021	.288 ± .029	<.001 ^b	<.001 ^b	.95
FA (tractogram)	.271 ± .019	.233 ± .016	.224 ± .021	.000001 ^b	.000001 ^b	.82
MD (skeleton)	.965 × 10 ⁻³ ± .0582 × 10 ⁻³	1.011 × 10 ⁻³ ± .0806 × 10 ⁻³	1.057 × 10 ⁻³ ± .119 × 10 ⁻³	.01 ^b	.005 ^b	.89
MD (tractogram)	.957 × 10 ⁻³ ± .0506 × 10 ⁻³	1.036 × 10 ⁻³ ± .0882 × 10 ⁻³	1.108 × 10 ⁻³ ± .131 × 10 ⁻³	<.001 ^b	<.001 ^b	.43
AD (skeleton)	1.29 × 10 ⁻³ ± .0614 × 10 ⁻³	1.31 × 10 ⁻³ ± .0769 × 10 ⁻³	1.36 × 10 ⁻³ ± .112 × 10 ⁻³	.12	.04 ^b	.83
AD (tractogram)	1.22 × 10 ⁻³ ± .0506 × 10 ⁻³	1.28 × 10 ⁻³ ± .0803 × 10 ⁻³	1.34 × 10 ⁻³ ± .122 × 10 ⁻³	.008 ^b	<.001 ^b	.39
RD (skeleton)	.801 × 10 ⁻³ ± .0578 × 10 ⁻³	.859 × 10 ⁻³ ± .0849 × 10 ⁻³	.907 × 10 ⁻³ ± .126 × 10 ⁻³	.003 ^b	.002 ^b	.93
RD (tractogram)	.823 × 10 ⁻³ ± .0512 × 10 ⁻³	.917 × 10 ⁻³ ± .0927 × 10 ⁻³	.990 × 10 ⁻³ ± .136 × 10 ⁻³	<.001 ^b	<.001 ^b	.45
CP (skeleton)	.169 ± .0135	.163 ± .0125	.157 ± .0146	.04 ^b	.03 ^b	.73
CP (tractogram)	.141 ± .0113	.129 ± .00633	.126 ± .00866	<.001 ^b	<.001 ^b	.93

^a Age and sex were used as covariates.

^b Significant.

256 × 256 × 170 mm, TR was 8.3 ms, TE was 3.8 ms, and the flip angle was 8°. In addition, T2-weighted images were acquired with a resolution of 0.5 × 0.5 × 4.4 mm; for 8 of the 12 patients in the second acquisition, fluid-attenuated inversion recovery images were acquired with a resolution of 0.4 × 0.4 × 4.4 mm.

Visual Analysis

The size of the cerebral sulci and the ventricles was classified as normal, mildly enlarged, moderately enlarged, or severely enlarged. All signal intensity abnormalities were recorded. The mid-sagittal area of the corpus callosum was measured.³⁸

Global Microstructural Analysis

Whole-brain probabilistic tractography was performed to reconstruct fiber tracts with constrained spherical deconvolution in ExploreDTI (<http://exploredti.com/>).^{25,32,39} The DWIs were corrected for subject motion and eddy current and echo-planar imaging-induced distortions,^{40,41} after which the fiber orientation distribution functions were estimated with constrained spherical deconvolution.³² Spheric harmonics up to the fourth order were used in the estimation. Streamline tractography was then performed in native space for all subjects.²⁵ A seed point resolution of 1 × 1 × 1 mm, a fiber orientation distribution threshold of 0.1, a step size of 1 mm, and a maximum angle deviation of 45° were used. The minimum length of the fiber was set to 50 mm.

Finally, a streamline density-weighted mean FA value was calculated by weighting the FA value of all voxels with the number of streamlines passing through the voxel and dividing by the sum of all streamline counts. Mean values for MD, AD, RD, and the coefficient of planarity (CP) were calculated in the same way. CP can be used to quantify the degree of fiber complexity.⁴² A higher CP describes a more disc-shaped diffusion tensor, typically caused by crossing fibers.⁴³⁻⁴⁵

In addition, an FA skeleton was reconstructed for all subjects as introduced in TBSS.²⁶ The mean values for FA, MD, AD, RD, and CP were then calculated across the skeleton.

The relationship between disease severity and the global microstructural parameters was investigated by calculating correlations both with and without age and sex as covariates.

Statistical analyses were performed in SPSS (IBM, Armonk, New York) with a general linear model using age and sex as covariates. The homoscedasticity of the residuals was verified visually,

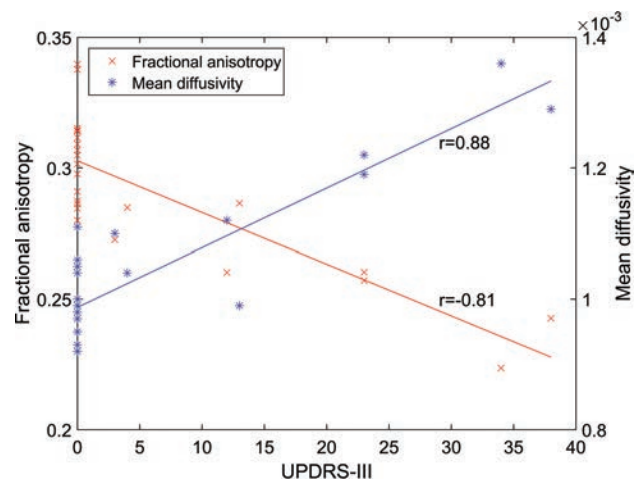


FIG 1. The relationship between disease severity measured by the Unified Parkinson's Disease Rating Scale (UPDRS), Part III, and fractional anisotropy (A) and mean diffusivity (B) calculated from the whole-brain white matter tract skeleton.

and the equality of error variances was confirmed using the Levene test. The significance threshold was $P < .05$.

Local Microstructural Analysis

The voxelwise microstructural analysis was performed using TBSS,²⁶ which belongs to the FMRIB Software Library tools (FSL; <http://www.fmrib.ox.ac.uk/fsl/>).⁴⁶ Subject motion and eddy current-induced distortions were corrected with the eddy tool (<https://fsl.fmrib.ox.ac.uk/fsl/fslwiki/eddy>),⁴⁷ after which the diffusion tensors were fitted. To reconstruct a mean FA skeleton, we transformed FA images into the subject space of the most representative subject by nonlinear registration based on free-form deformations and B-splines, after which a mean FA image of all subjects was calculated and thinned.²⁶ Finally, the individual subject's skeleton was projected onto the mean FA skeleton. For MD, AD, RD, and CP, we used the same nonlinear warps and projection vectors as used for FA images. Randomise (<http://fsl.fmrib.ox.ac.uk/fsl/fslwiki/Randomise>), a permutation program, was used for statistical testing of the voxelwise differences between patients and controls with 5000 permutations. Clusterlike structures in the data were enhanced with threshold-free cluster enhancement, and multiple correction for the family-wise error rate with a significance threshold of $P < .05$ was performed using permutation-based nonparametric testing.⁴⁸

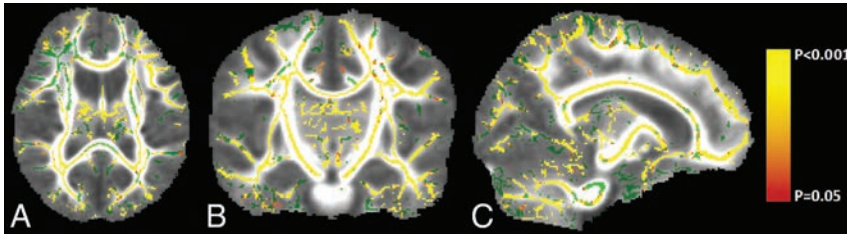


FIG 2. Tract-Based Spatial Statistics results for decreased fractional anisotropy in patients with juvenile neuronal ceroid lipofuscinosis visualized on axial (A), coronal (B), and sagittal (C) slices. The white matter tract skeleton is visualized in green, and the significant results are visualized from red ($P = .05$) to yellow ($P < .001$). Fractional anisotropy values are significantly ($P < .001$) decreased in many areas such as the corpus callosum, corticospinal tracts, corona radiata, and superior longitudinal fasciculi.

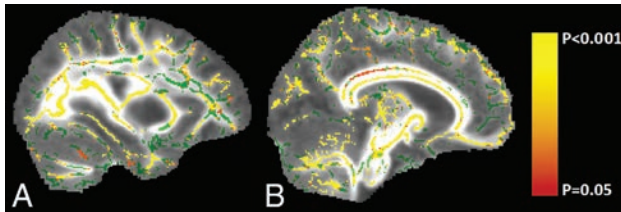


FIG 3. Decreased fractional anisotropy in patients with juvenile neuronal ceroid lipofuscinosis in, for example, the left posterior thalamic radiation ($P < .001$) and left posterior corona radiata ($P < .001$) on sagittal slices 58 (A) and 79 (B). The white matter tract skeleton is visualized in green, and significant results are visualized from red ($P = .05$) to yellow ($P < .001$).

RESULTS

Conventional MR Imaging Findings

Conventional MR imaging was considered normal in most subjects (On-line Table 1). The size of the ventricles was increased in 2 of the 14 patients during the first MR imaging and for 4 of the 11 patients during the second MR imaging. Thinning of the corpus callosum was observed in 2 of the 14 patients in the first MR imaging and 3 of the 11 patients in the second MR imaging.³⁸ Abnormal periventricular signal intensity was not present in the T1- or T2-weighted images. However, in FLAIR images, an increase in the periventricular signal intensity was observed for the 8 patients who underwent FLAIR in the second acquisition. The conventional MR imaging findings are further described in On-line Table 1.

Global Microstructural Analyses

We found significantly decreased FA and CP values and significantly increased AD, RD, and MD values in patients compared with the control group, as shown in Table 1. These differences were found with both the tractography and the skeleton approach. The largest relative difference was in the FA values using the tractography approach (-15% difference) ($P = .000001$).

We found significant differences in both acquisitions of patients with CLN3 compared with controls. However, there were no significant differences between the 2 acquisitions of the patients. The analyses between the 2 acquisitions were repeated without using age as a covariate, resulting in no significant differences. The effect of age was significant ($P = .006-.044$) for all dependent variables except for the CP tractogram.

Correlation analyses between the global microstructural parameters from the white matter skeleton and disease severity showed significant negative correlations for FA ($r = -0.81$, $P =$

$.000001$) and CP ($r = -0.66$, $P = .0005$), and significant positive correlations between the diffusivity parameters ($P < .0000001$) and disease severity. The relationships of FA and MD with respect to disease severity are shown in Fig 1. The correlation coefficients between the global microstructural parameters and disease severity are presented in On-line Table 2.

Local Microstructural Analysis

The local microstructural analysis performed with TBSS revealed widespread voxelwise decreases in FA as shown in

Fig 2, for example, in the corona radiata ($P < .001$) and posterior thalamic radiation ($P < .001$), as shown in Fig 3. In addition, MD, AD, and RD were increased and CP was decreased in many regions. The results for MD are shown in Fig 4.

DISCUSSION

In a visual analysis of conventional MR imaging of patients with CLN3, an increase in T2-weighted signal intensity of periventricular white matter may be observed, sometimes even before 10 years of age.¹⁸ Later, decreased white matter volume and increased white matter signal intensity due to gliosis can be seen.¹⁷ Related to the general brain atrophy, thinning of the corpus callosum is also present in CLN3.¹⁵

In this study, we investigated CLN3 for the first time with DW-MRI. For the global analyses, we used 2 different approaches, fiber tractography and white matter tract skeleton. We found widely distributed abnormalities in the white matter microstructure in patients with CLN3 compared with age-matched controls, and these abnormalities were seen at both the global and local level. However, there were no differences between the first and second acquisitions of patients with CLN3, suggesting that the microstructural changes do not progress rapidly and thus might be already present in early childhood.

More specifically, we found significantly decreased FA values in patients with CLN3 widely distributed across the whole brain. Intact cell membranes and dense packing of axons are the primary cause of anisotropic diffusion.²³ However, other properties such as myelination can also affect the degree of anisotropy.^{29,43} Because the complexity of the underlying white matter fiber structure can also affect the FA,²⁹ we compared the CP values between patients and controls. CP was decreased in patients with CLN3 compared with controls, suggesting that they would have a lower degree of crossing fibers than the controls. Thus, the lower FA in patients was not explained by more crossing fibers.

Increased MD in patients with CLN3 is in accordance with the previous DW-MRI study performed in patients with late infantile NCL, in which whole-brain ADC values correlated positively with age and disease severity, whereas in control subjects, ADC values decreased with age.²⁴ In another study, quantitative T2 values have been investigated in CLN2 and CLN3.⁴⁹ In patients with CLN2, there were elevated quantitative T2 values, but in CLN3, there were no differences in any of the white matter ROIs compared with controls. This finding suggests that DW-MRI is re-

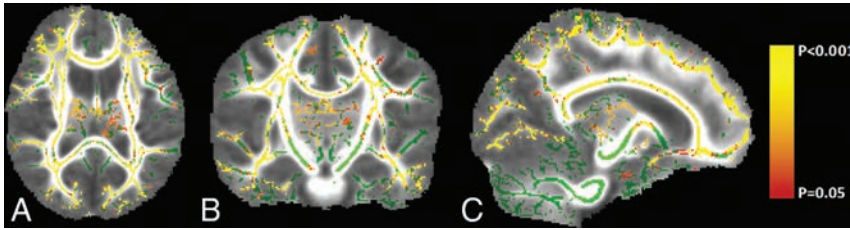


FIG 4. Tract-Based Spatial Statistics results for increased mean diffusivity in patients with juvenile neuronal ceroid lipofuscinosis visualized on axial (A), coronal (B), and sagittal (C) slices. The white matter tract skeleton is visualized in green, and the significant results are visualized from red ($P = .05$) to yellow ($P < .001$). Multiple areas but not as many as for fractional anisotropy (Fig 2) have significantly ($P < .001$) increased mean diffusivity values.

quired to detect the widespread microstructural changes in the white matter of patients with CLN3.

In addition, we looked at AD and RD values. Both AD and RD were increased in CLN3, but the absolute increase in RD (for the skeleton approach $+0.06$) was higher than in AD (for the skeleton approach $+0.02$), which is consistent with a decrease in FA.

Previous MR imaging findings suggest that there are thalamic alterations in lysosomal storage diseases, including CLN3.^{16–20} In our study, TBSS showed decreased FA in several tracts, including the anterior and posterior thalamic radiations. Decreased white matter volume in the corona radiata has been found earlier in CLN3.¹⁶ In our study, TBSS showed a decrease in FA in the posterior corona radiata. However, more specific analyses, such as a tractography reconstruction of the fiber bundles, potentially impaired in CLN3, could reveal more specific information about the microstructural and connectivity abnormalities than TBSS.

The patients with CLN3 underwent a follow-up MR imaging after 2 years. No significant differences between the 2 acquisitions of patients were found, suggesting that the microstructural changes do not progress rapidly in the prepubertal stage but might instead be present already in early childhood, though conventional MR imaging findings are usually normal in visual analysis at younger than 10 years of age.¹⁵

Limitations of this study include a relatively small sample size. However, we used several methods that produced similar results. In addition, we used constrained spherical deconvolution–based tractography in the global analyses, though its acquisition was suboptimal because the diffusion-weighting and the number of gradient orientations were relatively low.^{50,51} However, fiber crossings are present in most white matter³⁶ and can be reliably identified with constrained spherical deconvolution.^{32–35} Moreover, TBSS has limitations, for example, concerning the parameters selected by the user—that is, sensitivity, anatomic specificity, and restriction to only a part of the white matter voxels.⁵²

CONCLUSIONS

We found widespread microstructural white matter abnormalities in both acquisitions of patients with CLN3 compared with healthy controls. However, no significant differences were observed between the 2 acquisitions of the patients. Local microstructural abnormalities were investigated with TBSS, showing widespread abnormalities. In the future, more specific analyses are needed to investigate certain regions more thoroughly, such as the thalami, or white matter tracts related to those regions. Furthermore, the specific nature of the white

matter microstructural differences should be investigated with more detailed microstructural models.

Our results indicate that in patients with CLN3, the microstructural brain abnormalities are already present before 10 years of age and do not progress rapidly in the prepubertal stage. Considering that most of the conventional MR imaging findings manifest at an older age, we believe that specific microstructural abnormalities could also be revealed in other similar diseases using diffusion MR imaging.

Disclosures: Ulrika Roine—RELATED: Grant: Batten Disease Support and Research Association, Comments: \$50,000 funding from the foundation awarded to the University of Helsinki for this project.* Timo J. Roine—RELATED: Grant: Batten Disease Support and Research Association, Comments: Grant of \$50,000 awarded for this work to the University of Helsinki*; UNRELATED: Grants/Grants Pending: Emil Aaltonen Foundation, Finland, Comments: grant for a postdoctoral research project from December 2017 to November 2018 concerning the development and reproducibility of novel diffusion MRI analysis methods. Marja H. Balk—UNRELATED: Employment: HUS Medical Imaging Center, Comments: full-time job. Laura E. Åberg—UNRELATED: Employment: normal work in the Neuropsychiatric Clinic, Hospital District of Helsinki and Uusimaa. Tuula Lönnqvist—UNRELATED: Payment for Development of Educational Presentations: Actelion Pharmaceuticals Sverige AB, Comments: Lysosomal Storage Disease Academy in April 2017, Tampere, Finland. Taina Autti—RELATED: Grant: Batten Disease Support and Research Association.* *Money paid to the institution.

REFERENCES

- Santavuori P, Lauronen L, Kirveskari K, et al. **Neuronal ceroid lipofuscinoses in childhood.** *Suppl Clin Neurophysiol* 2000;53:443–51 CrossRef Medline
- Collins J, Holder GE, Herbert H, et al. **Batten disease: features to facilitate early diagnosis.** *Br J Ophthalmol* 2006;90:1119–24 CrossRef Medline
- Spalton DJ, Taylor DS, Sanders MD. **Juvenile Batten's disease: an ophthalmological assessment of 26 patients.** *Br J Ophthalmol* 1980; 64:726–32 CrossRef Medline
- Järvelä I, Autti T, Lamminranta S, et al. **Clinical and magnetic resonance imaging findings in Batten disease: analysis of the major mutation (1.02-kb deletion).** *Ann Neurol* 1997;42:799–802 CrossRef Medline
- Santavuori P, Linnankivi T, Jaeken J, et al. **Psychological symptoms and sleep disturbances in neuronal ceroid-lipofuscinoses (NCL).** *J Inherit Metab Dis* 1993;16:245–48 CrossRef Medline
- Jalanko A, Bräulke T. **Neuronal ceroid lipofuscinoses.** *Biochim Biophys Acta* 2009;1793:697–709 CrossRef Medline
- Miller JN, Chan CH, Pearce DA. **The role of nonsense-mediated decay in neuronal ceroid lipofuscinosis.** *Hum Mol Genet* 2013;22: 2723–34 CrossRef Medline
- Kousi M, Lehesjoki AE, Mole SE. **Update of the mutation spectrum and clinical correlations of over 360 mutations in eight genes that underlie the neuronal ceroid lipofuscinoses.** *Hum Mutat* 2012;33: 42–63 CrossRef Medline
- Uvebrant P, Hagberg B. **Neuronal ceroid lipofuscinoses in Scandinavia: epidemiology and clinical pictures.** *Neuropediatrics* 1997;28:6–8 CrossRef Medline
- Claussen M, Heim P, Knispel J, et al. **Incidence of neuronal ceroid-lipofuscinoses in West Germany: variation of a method for studying autosomal recessive disorders.** *Am J Med Genet* 1992;42:536–38 CrossRef Medline
- Cardona F, Rosati E. **Neuronal ceroid-lipofuscinoses in Italy: an epidemiological study.** *Am J Med Genet* 1995;57:142–43 CrossRef Medline
- MacLeod PM, Dolman CL, Chang E, et al. **The neuronal ceroid lipo-**

- fuscinoses in British Columbia: a clinical epidemiologic and ultrastructural study. *Birth Defects Orig Artic Ser* 1976;12:289–96 Medline
13. Lerner TJ, Boustanty RM, Anderson JW, et al. Isolation of a novel gene underlying Batten disease, CLN3: the International Batten Disease Consortium. *Cell* 1995;82:949–57 CrossRef Medline
 14. Williams RE, Aberg L, Autti T, et al. Diagnosis of the neuronal ceroid lipofuscinoses: an update. *Biochim Biophys Acta* 2006;1762:865–72 CrossRef Medline
 15. Autti T, Raininko R, Vanhanen SL, et al. MRI of neuronal ceroid lipofuscinosis, I: cranial MRI of 30 patients with juvenile neuronal ceroid lipofuscinosis. *Neuroradiology* 1996;38:476–82 CrossRef Medline
 16. Tokola AM, Salli EK, Åberg LE, et al. Hippocampal volumes in juvenile neuronal ceroid lipofuscinosis: a longitudinal magnetic resonance imaging study. *Pediatr Neurol* 2014;50:158–63 CrossRef Medline
 17. Autti T, Hämäläinen J, Åberg L, et al. Thalami and corona radiata in juvenile NCL (CLN3): a voxel-based morphometric study. *Eur J Neurol* 2007;14:447–50 CrossRef Medline
 18. Autti T, Raininko R, Santavuori P, et al. MRI of neuronal ceroid lipofuscinosis, II: postmortem MRI and histopathological study of the brain in 16 cases of neuronal ceroid lipofuscinosis of juvenile or late infantile type. *Neuroradiology* 1997;39:371–77 CrossRef Medline
 19. Autti T, Joensuu R, Aberg L. Decreased T2 signal in the thalami may be a sign of lysosomal storage disease. *Neuroradiology* 2007;49:571–78 CrossRef Medline
 20. Jadav RH, Sinha S, Yasha TC, et al. Clinical, electrophysiological, imaging, and ultrastructural description in 68 patients with neuronal ceroid lipofuscinoses and its subtypes. *Pediatr Neurol* 2014;50:85–95 CrossRef Medline
 21. Basser PJ, Mattiello J, LeBihan D. MR diffusion tensor spectroscopy and imaging. *Biophys J* 1994;66:259–67 CrossRef Medline
 22. Basser PJ, Mattiello J, LeBihan D. Estimation of the effective self-diffusion tensor from the NMR spin echo. *J Magn Reson B* 1994;103:247–54 CrossRef Medline
 23. Beaulieu C. The basis of anisotropic water diffusion in the nervous system: a technical review. *NMR Biomed* 2002;15:435–55 CrossRef Medline
 24. Dyke JP, Voss HU, Sondhi D, et al. Assessing disease severity in late infantile neuronal ceroid lipofuscinosis using quantitative MR diffusion-weighted imaging. *AJNR Am J Neuroradiol* 2007;28:1232–36 CrossRef Medline
 25. Jeurissen B, Leemans A, Jones DK, et al. Probabilistic fiber tracking using the residual bootstrap with constrained spherical deconvolution. *Hum Brain Mapp* 2011;32:461–79 CrossRef Medline
 26. Smith SM, Jenkinson M, Johansen-Berg H, et al. Tract-based spatial statistics: voxelwise analysis of multi-subject diffusion data. *Neuroimage* 2006;31:1487–505 CrossRef Medline
 27. Basser PJ, Pajevic S, Pierpaoli C, et al. In vivo fiber tractography using DT-MRI data. *Magn Reson Med* 2000;44:625–32 Medline
 28. Mori S, van Zijl PC. Fiber tracking: principles and strategies—a technical review. *NMR Biomed* 2002;15:468–80 CrossRef Medline
 29. Vos SB, Jones DK, Viergever MA, et al. Partial volume effect as a hidden covariate in DTI analyses. *Neuroimage* 2011;55:1566–76 CrossRef Medline
 30. Tournier JD, Mori S, Leemans A. Diffusion tensor imaging and beyond. *Magn Reson Med* 2011;65:1532–56 CrossRef Medline
 31. Tournier JD, Calamante F, Gadian DG, et al. Direct estimation of the fiber orientation density function from diffusion-weighted MRI data using spherical deconvolution. *Neuroimage* 2004;23:1176–85 CrossRef Medline
 32. Tournier JD, Calamante F, Connelly A. Robust determination of the fibre orientation distribution in diffusion MRI: non-negativity constrained super-resolved spherical deconvolution. *Neuroimage* 2007;35:1459–72 CrossRef Medline
 33. Tournier JD, Yeh CH, Calamante F, et al. Resolving crossing fibres using constrained spherical deconvolution: validation using diffusion-weighted imaging phantom data. *Neuroimage* 2008;42:617–25 CrossRef Medline
 34. Kristo G, Leemans A, Raemaekers M, et al. Reliability of two clinically relevant fiber pathways reconstructed with constrained spherical deconvolution. *Magn Reson Med* 2013;70:1544–56 CrossRef Medline
 35. Farquharson S, Tournier JD, Calamante F, et al. White matter fiber tractography: why we need to move beyond DTI. *J Neurosurg* 2013;118:1367–77 CrossRef Medline
 36. Jeurissen B, Leemans A, Tournier JD, et al. Investigating the prevalence of complex fiber configurations in white matter tissue with diffusion magnetic resonance imaging. *Hum Brain Mapp* 2013;34:2747–66 CrossRef Medline
 37. Movement Disorder Society Task Force on Rating Scales for Parkinson's Disease. The Unified Parkinson's Disease Rating Scale (UPDRS): status and recommendations. *Mov Disord* 2003;18:738–50 CrossRef Medline
 38. Toivainen-Salo S, Mäkitie O, Mannerkoski M, et al. Shwachman-Diamond syndrome is associated with structural brain alterations on MRI. *Am J Med Genet A* 2008;146A:1558–64 CrossRef Medline
 39. Leemans A, Jeurissen B, Sijbers J, et al. ExploreDTI: a graphical toolbox for processing, analyzing, and visualizing diffusion MR data. In: *Proceedings of the Scientific Meeting and Exhibition of the International Society for Magnetic Resonance in Medicine*, Honolulu, Hawaii. April 18–24, 2009;17:3537
 40. Leemans A, Jones DK. The B-matrix must be rotated when correcting for subject motion in DTI data. *Magn Reson Med* 2009;61:1336–49 CrossRef Medline
 41. Irfanoglu MO, Walker L, Sarlls J, et al. Effects of image distortions originating from susceptibility variations and concomitant fields on diffusion MRI tractography results. *Neuroimage* 2012;61:275–88 CrossRef Medline
 42. Westin CF, Maier SE, Mamata H, et al. Processing and visualization for diffusion tensor MRI. *Med Image Anal* 2002;6:93–108 CrossRef Medline
 43. Vos SB, Jones DK, Jeurissen B, et al. The influence of complex white matter architecture on the mean diffusivity in diffusion tensor MRI of the human brain. *Neuroimage* 2012;59:2208–16 CrossRef Medline
 44. Wiegell MR, Larsson HB, Wedeen VJ. Fiber crossing in human brain depicted with diffusion tensor MR imaging. *Radiology* 2000;217:897–903 CrossRef Medline
 45. Ennis DB, Kindlmann G. Orthogonal tensor invariants and the analysis of diffusion tensor magnetic resonance images. *Magn Reson Med* 2006;55:136–46 CrossRef Medline
 46. Smith SM, Jenkinson M, Woolrich MW, et al. Advances in functional and structural MR image analysis and implementation as FSL. *Neuroimage* 2004;23(Suppl 1):S208–19 CrossRef Medline
 47. Andersson JL, Sotiropoulos SN. Non-parametric representation and prediction of single- and multi-shell diffusion-weighted MRI data using Gaussian processes. *Neuroimage* 2015;122:166–76 CrossRef Medline
 48. Winkler AM, Ridgway GR, Webster MA, et al. Permutation inference for the general linear model. *Neuroimage* 2014;92:381–97 CrossRef Medline
 49. Paniagua Bravo A, Forkert ND, Schulz A, et al. Quantitative T2 measurements in juvenile and late infantile neuronal ceroid lipofuscinosis. *Clin Neuroradiol* 2013;23:189–96 CrossRef Medline
 50. Tournier JD, Calamante F, Connelly A. Determination of the appropriate b value and number of gradient directions for high-angular-resolution diffusion-weighted imaging. *NMR Biomed* 2013;26:1775–86 CrossRef Medline
 51. Toselli B, Tortora D, Severino M, et al. Improvement in white matter tract reconstruction with constrained spherical deconvolution and track density mapping in low angular resolution data: a pediatric study and literature review. *Front Pediatr* 2017;5:182 CrossRef Medline
 52. Bach M, Laun FB, Leemans A, et al. Methodological considerations on tract-based spatial statistics (TBSS). *Neuroimage* 2014;100:358–69 CrossRef Medline

Balanced Steady-State Free Precession Sequence (CISS/FIESTA/3D Driven Equilibrium Radiofrequency Reset Pulse) Increases the Diagnostic Yield for Spinal Drop Metastases in Children with Brain Tumors

K. Buch, P. Caruso, D. Ebb, and S. Rincon

ABSTRACT

BACKGROUND AND PURPOSE: Identification of spinal drop metastases is important in the staging and management of pediatric patients with primary brain tumors. Our aim was to assess the diagnostic utility of the balanced steady-state free precession (bSSFP) sequence (CISS/FIESTA/3D driven equilibrium radiofrequency reset pulse) for the detection of spinal drop metastases in pediatric patients with primary intracranial tumors.

MATERIALS AND METHODS: This was a retrospective study of 44 pediatric patients with primary intracranial tumors undergoing MR imaging spine evaluation for drop metastases before radiation treatment. All patients underwent a whole-spine MRI with both bSSFP and postcontrast T1WI sequences. Two neuroradiologists independently reviewed only the bSSFP sequence, then 1 week later only the postcontrast T1WI sequence.

RESULTS: Patients ranged from 1 to 18 years of age (mean, 7.1 ± 4.2 years) with 27 males and 17 females. The number of lesions per patient ranged from 1 to 13 and from 2 to 11 mm in size. Lesions suspicious for drop metastases were seen in 8 patients on the postcontrast T1WI (18%) compared with 10 patients on the bSSFP sequence (23%). Twenty-two drop metastases seen on the bSSFP sequence were not visible on the postcontrast T1WI, including nonenhancing drop metastases and multiple nodules of <3 mm. Interrater agreement was excellent for the bSSFP sequence (0.91) and the postcontrast T1 sequence (0.90).

CONCLUSIONS: The bSSFP sequence increased the diagnostic yield for the detection of drop metastases in pediatric patients with primary intracranial tumors and was particularly advantageous for small drop metastases (<3 mm) and nonenhancing metastases, and it decreased the number of false-positives. The bSSFP sequence may be an important adjunct to postcontrast T1WI for the evaluation of drop metastases.

ABBREVIATION: bSSFP = balanced steady-state free precession

Spinal cord imaging is considered standard of care for the staging and treatment planning of pediatric brain tumors. The inclusion of spinal imaging is particularly important for those tumors with a propensity for drop metastases. Identification of drop metastases can change radiation planning from focal radiation of the primary tumor bed to craniospinal radiation and may

mandate the intensification of both radiation and chemotherapy for appropriate treatment.¹

A balanced steady-state free precession (bSSFP) scan (CISS/FIESTA/3D driven equilibrium radiofrequency reset pulse) is a heavily fluid-weighted isotropic sequence. The bSSFP sequence is advantageous for spine imaging, given its superior contrast resolution, enabling sharp discrimination of CSF from the spinal cord and adjacent nerve roots, superior spatial resolution, and isotropy allowing triplanar reconstruction. The bSSFP sequence has been previously used, for example, for the evaluation of duplicated spinal nerve roots and a detailed assessment of spinal cord pathology, including diastematomyelia and syringomyelia.²⁻⁸ Most commonly, the bSSFP sequence has been used for the evaluation of vestibular schwannomas, given its superb fluid-to-soft tissue contrast and high spatial resolution.⁹⁻¹¹

The screening protocol for the detection of drop metastases at many institutions primarily consists of a postcontrast T1WI sequence through the entire spine. The purpose of this study was to

Received October 19, 2017; accepted after revision March 5, 2018.

From the Department of Neuroradiology (K.B., P.C., S.R.), Massachusetts General Hospital, Boston, Massachusetts; and Department of Pediatrics (D.E.), Pediatric Cancer Care Center, Massachusetts General Hospital for Children, Boston, Massachusetts.

Paper previously presented at: Annual Meeting of the American Society of Neuro-radiology and the Foundation of the ASNR Symposium, April 22–27, 2017; Long Beach, California.

Please address correspondence to Sandra Rincon, MD, Department of Neuroradiology, Massachusetts General Hospital Boston, 55 Fruit St, Boston, MA 02114; e-mail: srincon@partners.org

<http://dx.doi.org/10.3174/ajnr.A5645>

evaluate the diagnostic utility of the bSSFP sequence compared with conventional postcontrast T1WI for detection of drop metastases in pediatric patients with primary intracranial tumors.

MATERIALS AND METHODS

Study Design

This was a retrospective, institutional review board–approved study examining patients undergoing MR imaging of the spine for the surveillance of drop metastases performed between December 2010 and January 2017 at Massachusetts General Hospital. All pediatric patients with a diagnosis of a primary intracranial tumor included in this study were identified through a search of our Radiology Information System. All patients were referred for a routine clinical MRI for the detection of spinal drop metastases before radiation treatment. Inclusion criteria were patients 18 years of age or younger with a history of an intracranial neoplasm requiring screening for spinal drop metastases and a preradiation MRI that included a bSSFP sequence and a sagittal T1 postcontrast sequence of the entire spine. Exclusion criteria were patients with examinations degraded by technical or motion artifacts precluding a diagnostic assessment, patients with MRI examinations performed immediately following a brain operation to minimize the amount of postoperative hemorrhage and debris in the spinal canal, and patients with prior spinal radiation or resection of a spinal metastasis.

Medical Record Review

A search of the electronic medical record was performed on all patients in this study cohort by a second-year neuroradiology fellow. The electronic medical record was reviewed for the following: 1) basic demographic information including age and sex, 2) oncologic data including pathologic diagnosis, and 3) treatment history including prior surgery and chemotherapy.

Scanner Hardware

MRI examinations were performed on either a 1.5T Signa Excite HDx scanner (GE Healthcare, Milwaukee, Wisconsin) with an 8-channel spine coil or a 3T Tim Trio scanner (Siemens, Erlangen, Germany) with a 32-channel spine coil. All patients received the same intravenous gadolinium contrast agent, gadoterate meglumine. Spine imaging was performed immediately following the brain MRI without the administration of an additional dose of contrast.

Sequences reviewed included a bSSFP sequence of the cervicothoracic and thoracolumbar spine and a postcontrast sagittal T1 sequence with a similar FOV. The same imaging protocol was used for all patients regardless of age or histologic tumor type.

bSSFP (CISS) sequence parameters performed on the 3T Tim Trio scanner included TR/TE = 11.69/5.85 ms, NEX = 1, echo train = 1, matrix = 448 × 269, flip angle = 50°, slice thickness = 0.8 mm, slice spacing = 0 mm, cervicothoracic spine FOV = 15 × 3–5 × 199–220 mm (anterior-to-posterior × right-to-left × superior-to-inferior), thoracolumbar spine FOV = 15 × 3–5 × 199–220 mm (anterior-to-posterior × right-to-left × superior-to-inferior), voxel size = 0.55–0.58 mm³, with a scan time of approximately 5 minutes 20 seconds. For smaller children, the bSSFP sequence comprised two, 30-cm, superior-to-inferior seg-

ment slabs. With older and taller children, the bSSFP sequence comprised three, 30-cm, superior-to-inferior segment slabs.

Postcontrast T1 sequence parameters performed on the 3T Tim Trio scanner included TR/TE = 603/9.3 ms, NEX = 2, echo train = 3, matrix = 320 × 224, slice thickness = 3 mm, gap = 0 mm, cervicothoracic spine FOV = 4–7 × 3–5 × 220–240 mm (anterior-to-posterior × right-to-left × superior-to-inferior), thoracolumbar spine FOV = 4–7 × 3–5 × 210–240 mm (anterior-to-posterior × right-to-left × superior-to-inferior), with a scan time of approximately 3 minutes 15 seconds.

bSSFP (FIESTA) sequence parameters performed on the 1.5T Signa Horizon scanner included TR/TE = 5.288/2.044–5.948/2.22 ms, NEX = 1.5–4, echo train = 1, matrix = 448 × 256, flip angle = 65°, slice thickness = 0.8 mm, gap = 0.4 mm, cervicothoracic spine FOV = 15 × 3–5 × 220–280 mm (anterior-to-posterior × right-to-left × superior-to-inferior), thoracolumbar spine FOV = 15 × 3–5 × 220–280 mm (anterior-to-posterior × right-to-left × superior-to-inferior), voxel size = 0.55–0.58 mm³, with a scan time of approximately 5 minutes 40 seconds. For smaller children, the bSSFP sequence comprised two, 30-cm, superior-to-inferior segment slabs. With older and taller children, the bSSFP sequence comprised three, 30-cm, superior-to-inferior segment slabs.

Postcontrast T1WI performed on the 1.5T Signa Horizon scanner included TR/TE = 533.3/7.464 ms, NEX = 2, echo train = 3, matrix = 256 × 224, flip angle = 90°, slice thickness = 3 mm, gap = 0 mm, cervicothoracic spine FOV = 4–7 × 3–5 × 220–240 mm (anterior-to-posterior × right-to-left × superior-to-inferior), thoracolumbar spine FOV = 4–7 × 3–5 × 210–240 mm (anterior-to-posterior × right-to-left × superior-to-inferior), with a scan time of approximately 3 minutes 45 seconds.

Sedation for MR Imaging Examination

Patients younger than 6 years of age underwent sedation for the MRI examination to decrease motion artifacts and improve image quality. Sedation was administered by a pediatric anesthesiology team per our institutional protocol. For older children, we used video goggles and the aid of a dedicated child life specialist during the MRI acquisition to help decrease motion during the MRI examination.

Image Analysis

All preradiation spinal MRI studies obtained for treatment planning were reviewed. The bSSFP and sagittal postcontrast T1WI acquired during the examination were reviewed 1 week apart to reduce the risk of observer bias. All images were reviewed by a second-year neuroradiology fellow and a pediatric neuroradiology attending physician with >15 years' experience reading pediatric neuroimaging studies at our institution.

The presence of drop metastases and the number, size, and location, if applicable, were recorded by each of the 2 radiologists. If diffuse leptomeningeal disease was detected, this was recorded and no discrete measurements were performed.

Definitions of Lesions

A lesion was considered suspicious for a drop metastasis on the bSSFP sequence if it met the following criteria:

1) An extramedullary, intradural nodule measuring ≥ 1 mm that lay along nerve roots or the spinal cord and demonstrated smooth, round contours without a fluid-fluid level or the appearance of layering to suggest hemorrhage.

2) If there were small foci of abnormal signal intensity along the surface of the spinal cord and/or nerve roots, which did not meet the criteria of No. 1 above, these lesions were considered indeterminate.

Table 1: Demographic and clinical information for the 44-patient cohort

Patient Demographics	
Sex	
Male	27
Female	17
Age (yr)	
Mean	7.21
SD	4.24
Min	1
Max	18
Primary intracranial tumor type	
Medulloblastoma	15
Germinoma	11
Ependymoma	8
Astrocytoma	4
ATRT	3
Glioblastoma	2
Pineoblastoma	1

Note:—Min indicates minimum; max, maximum; ATRT, atypical rhabdoid tumor.

Table 2: Number of cases with nodules meeting the criteria for drop metastases (positive cases), cases with no evidence of drop metastases (negative cases), and cases with indeterminate findings^a

Sequence	Positive Cases	Negative Cases	Indeterminate Cases
bSSFP	10	34	0
Postcontrast T1WI	8	32	4

^a This classification was performed for both the bSSFP and postcontrast T1WI, which were evaluated independently.

A lesion was considered suspicious for a drop metastasis on the postcontrast T1WI if it met the following criteria:

- 1) An enhancing extramedullary, intradural nodule measuring ≥ 1 mm that lay along nerve roots or the spinal cord and demonstrated smooth, round contours and did not have the appearance of layering, which would suggest hemorrhage.
- 2) If there were small foci of enhancement that did not meet the criteria of No. 1 listed above, they were considered indeterminate.

Findings suggestive of diffuse leptomeningeal disease were defined as the following:

- 1) For the bSSFP sequence, diffuse nerve root thickening or nodularity and irregular contour of the spinal cord.
- 2) For the postcontrast T1WI, diffuse, abnormal enhancement and nodularity along the spinal cord and/or thickening of the nerve roots.

Findings suggestive of hemorrhage/debris, vascular structures, and flow artifacts were defined as the following:

- 1) Foci of signal in the thecal sac that either layered or appeared clearly separate from nerve roots were considered to represent hemorrhage/debris.
- 2) Tubular or linear structures along the surface of the spinal cord or adjacent to nerve roots were considered vascular structures.

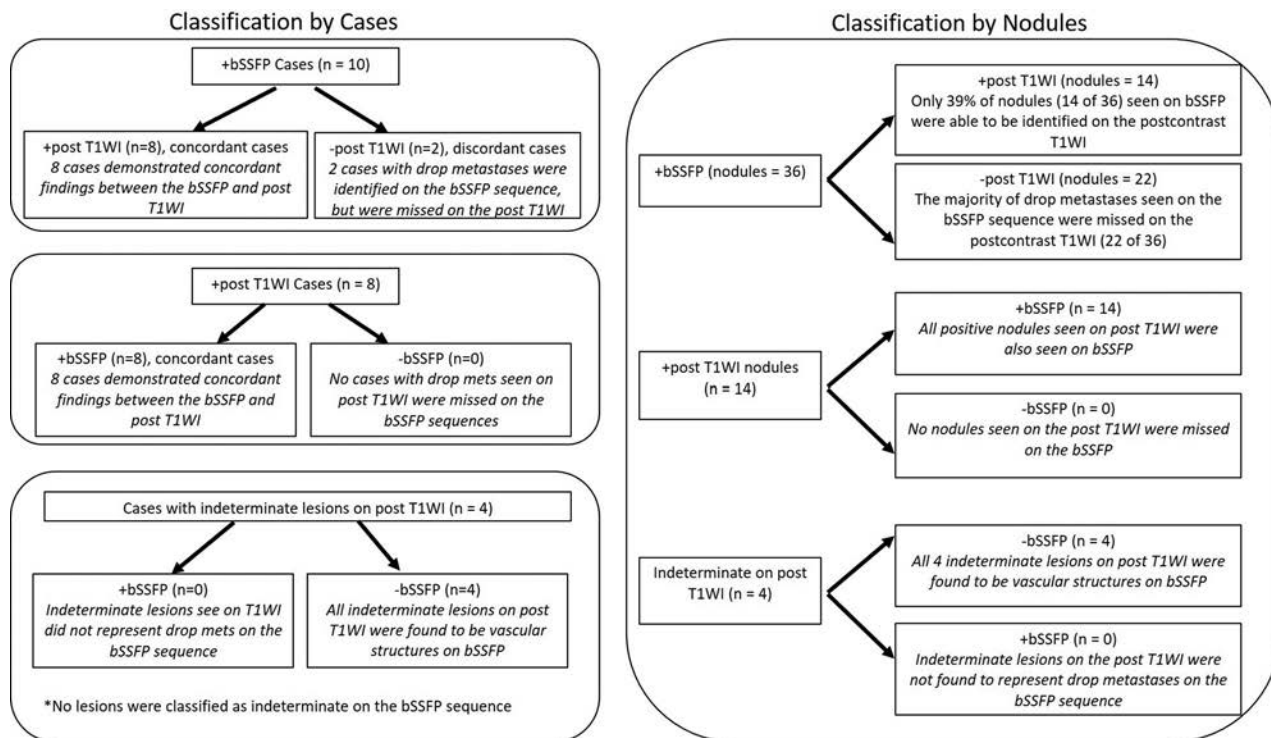


FIG 1. Classification by cases (left image) with positive, negative, and indeterminate findings on the bSSFP and postcontrast T1WI. Classification by nodules (right image) with positive, negative, and indeterminate findings.

3) Web-like, nonanatomic structures within the CSF were considered flow artifacts.

Indeterminate findings were those that did not meet the above criteria.

The results of the independently evaluated sequences (bSSFP and postcontrast T1WI) were compared.

A concordant case was defined as the following:

- 1) A case with a finding that was positive for drop metastasis on the bSSFP and positive on the postcontrast T1WI.
- 2) A case that was negative for the presence of drop metastases on the bSSFP and negative on the postcontrast T1WI.

A discordant case was defined as the following:

- 1) A case with a finding that was positive for drop metastasis on the bSSFP with no positive finding on the postcontrast T1WI.

Table 3: Total number of lesions, lesion size, and number of lesions of ≤ 3 mm detected on the bSSFP sequence compared with postcontrast T1WI

	bSSFP	Postcontrast T1WI	P Value
No. of lesions per patient			
Mean	6.3	2.1	.002
SD	3.9	1.2	
Min	2	1	
Max	13	4	
Lesion size (mm)			
Mean	3.9	4.9	.43
SD	4.6	6.8	
Min	1	1	
Max	25	24	
Lesions ≤ 3 mm			
Mean	3.9	1.2	.03
SD	2.1	1.7	

Note:—Min indicates minimum; max, maximum.

2) A case with a finding positive for drop metastasis on the post-contrast T1WI, and no positive finding on the bSSFP.

Interrater Assessment and Statistical Analysis

The level of interrater agreement between the 2 radiologists was assessed using a κ score. Discrepancies between the 2 radiologists were also reviewed by a third rater, a pediatric neuroradiology attending with >15 years' experience. Discrepancies between the number and size of drop metastases between the postcontrast T1WI and bSSFP sequence and the number of "missed" drop metastases were recorded. Basic descriptive statistics were used to evaluate significant differences in lesion size and number between the lesions detected on the bSSFP sequence compared with the postcontrast T1WI sequence.

RESULTS

Cohort Description

A total of 44 pediatric patients were included in this cohort, comprising 27 males and 17 females, ranging from 1 to 18 years of age (mean, 7.21 ± 4.24 years). Thirty patients were scanned on a 1.5T scanner, and 14 patients were scanned on a 3T scanner. Two examinations were excluded secondary to severe motion artifacts on the bSSFP sequence.

The most commonly encountered primary brain tumor pathologies were medulloblastoma ($n = 15$), germinoma ($n = 11$), and ependymoma ($n = 8$). A full list of primary intracranial tumor pathologies in this patient cohort is shown in Table 1.

bSSFP Evaluation

Lesions suggestive of drop metastases were detected on 10 bSSFP examinations, ranging from 2 to 13 lesions per examination (Table 2). On average, the number of drop metastases seen in an individual patient on the bSSFP sequence was 6.3 ± 3.9 . These lesions ranged from 1 to 25 mm (mean, 3.9 ± 4.6 mm) (Fig 1). Of



FIG 2. A 6-year-old boy with a history of medulloblastoma. Sagittal bSSFP images A and C demonstrate numerous nodular drop metastases (white arrows). B and D, Corresponding enhancing nodules along the cauda equina nerve roots. The axial bSSFP image (E) demonstrates a nodular drop metastasis along the cauda equina nerve roots (white arrow).

Table 4: Number of nodules seen on the bSSFP and postcontrast T1WI classified as positive nodules, indeterminate nodules, and discordant nodules^a

Nodule Classification	bSSFP	Postcontrast T1WI
Positive nodules	36	14
Indeterminate nodules	0	10
Discordant nodules	0	22

^aDiscordant or “missed” nodules are nodules not seen on the sequence being evaluated but present on the corresponding sequence. In this case, 22 nodules were not seen on postcontrast T1WI that were seen on the bSSFP sequence. No nodules were seen on the postcontrast T1WI but not the bSSFP sequence.

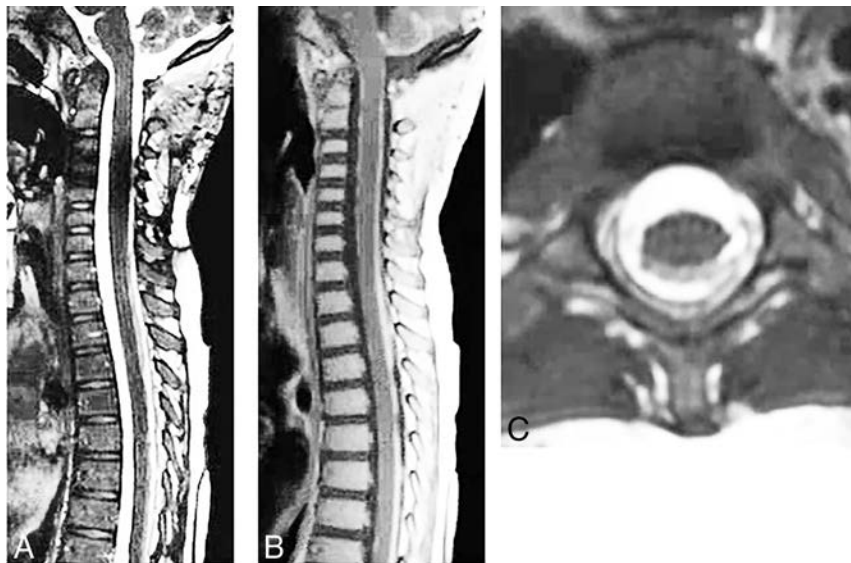


FIG 3. A 4-year-old boy with a history of medulloblastoma and diffuse leptomeningeal disease. The bSSFP image of the cervical spine (A) demonstrates subtle irregularity of the cervicothoracic spinal cord. Abnormal, confluent enhancement is more pronounced on the sagittal postcontrast T1WI of the cervicothoracic spine (B). The axial bSSFP image (C) demonstrates abnormal, crescentic signal abnormality along the dorsal spinal cord.

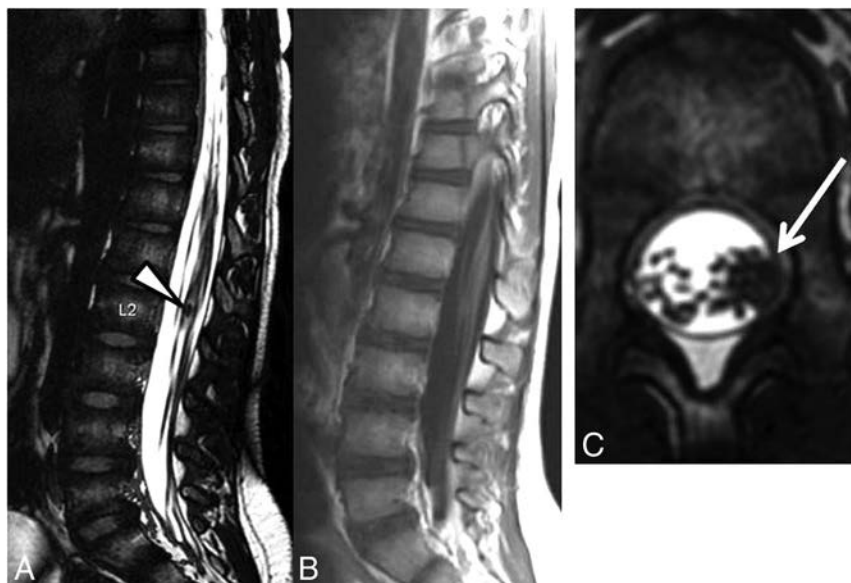


FIG 4. An 8-year-old boy with a history of germinoma. Sagittal bSSFP sequence (A) demonstrates a nodular drop metastasis within the cauda equina nerve roots (*white arrowhead*). No corresponding enhancement is seen on the postcontrast T1WI (B). The axial bSSFP sequence (C) demonstrates a nodular drop metastasis along the cauda equina nerve roots (*white arrow*) within the left lateral aspect of the thecal sac.

these spinal drop metastases, on average, a mean of 3.9 ± 2.1 lesions measured <3 mm as shown in Table 3. Thirty-six positive nodules were seen on the bSSFP sequence with no evidence of indeterminate or discordant nodules (Figs 1 and 2 and Table 4).

Sagittal Postcontrast T1WI Evaluation

Lesions suggestive of drop metastases were detected on 8 postcontrast T1WI scans (Figs 1 and 2 and Table 2). On average, the number of drop metastases seen in an individual patient on post-

contrast T1WI was 2.1 ± 1.2 . These lesions, on average, measured 4.9 ± 6.8 mm as shown in Table 3. Of these lesions, on average, 1.2 ± 1.7 lesions measured <3 mm as shown in Table 3. Fourteen positive nodules were identified on postcontrast T1WI. Ten indeterminate nodules were seen on postcontrast T1WI, for which additional imaging was recommended for further characterization (Fig 1 and Table 4).

Comparison of bSSFP and Postcontrast T1WI

Most drop metastases appeared as discrete, rounded nodules along the surface of the spinal cord and/or along the cauda equina nerve roots; however, in 3 patients, diffuse leptomeningeal disease was noted and was seen on both the postcontrast T1WI and the bSSFP sequence (Fig 3).

The postcontrast T1WI sequence identified fewer positive lesions ($n = 14$) suspicious for drop metastases compared with those seen on the bSSFP sequence ($n = 36$) (Fig 1). Twenty-two positive lesions were seen on the bSSFP sequence, which were not visualized on the postcontrast T1WI. These lesions were found in, among others, a patient with nonenhancing drop metastases related to a nonenhancing primary intracranial tumor (ependymoma) and a patient with multiple, small, <3 -mm nodules (Figs 4 and 5).

In 4 cases, indeterminate lesions were seen on postcontrast T1WI, which warranted additional imaging for classification. Comparison of the postcontrast T1WI with the corresponding bSSFP sequences, revealed these indeterminate lesions were consistent with vascular structures (Fig 1).

Among cases with positive nodules identified on both postcontrast T1WI and bSSFP sequences, there were 2 cases in which only 1 nodule was seen on the

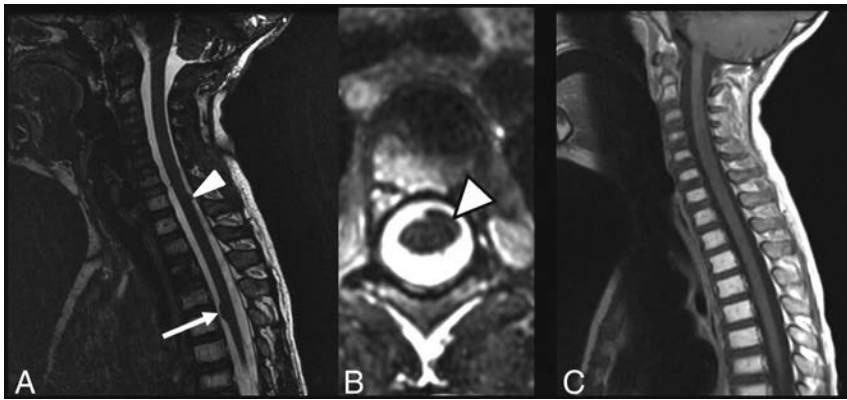


FIG 5. A 7-year-old boy with a history of ependymoma. A, Sagittal bSSFP sequence demonstrates a dominant, ventral spinal metastasis at the T5 level (*white arrow*) with multiple, additional, smaller metastases (*white arrowhead*). B, Axial bSSFP sequence at the T5 level demonstrates a left ventral metastasis (*white arrowhead*). C, Postcontrast T1WI in the same patient does not demonstrate abnormal enhancement or detectable drop metastases.

postcontrast T1WI, whereas multiple nodules were seen on the bSSFP sequence. This finding is clinically significant because the detection of additional nodules may change treatment from targeted radiation therapy of a single lesion to craniospinal radiation for the treatment of multiple lesions.

Statistically significant differences were seen between the number of drop metastases detected on the bSSFP sequence compared with postcontrast T1WI ($P = .03$), with a greater number of lesions detected per patient on the bSSFP sequence at 6.3 versus 2.1 detected on postcontrast T1WI.

While, on average, drop metastases measured slightly larger on the postcontrast T1WI (4.9 mm) compared with the bSSFP sequence (3.9 mm), this difference was not statistically significant ($P = .43$). Lesions measuring ≤ 3 mm were more frequently seen on the bSSFP sequence, including 27 lesions compared with 17 lesions identified on postcontrast T1WI. This difference was statistically significant ($P = .03$).

Interrater agreement was excellent for the bSSFP sequence (0.91) and the postcontrast T1WI (0.90).

DISCUSSION

The results of this study demonstrate proof of concept that the bSSFP sequence can enhance the detection of spinal drop metastases in pediatric patients with primary intracranial tumors. The bSSFP sequence is particularly advantageous for small drop metastases and nonenhancing metastases and decreases the number of false-positives.

The bSSFP sequence offers distinct advantages over traditional, standard postcontrast T1WI for drop metastases, including better spatial resolution; better contrast resolution; triplanar reformats, which obviate direct axial images and can thus reduce scan time; and the detection of nonenhancing drop metastases in cases of a nonenhancing or minimally enhancing primary brain tumor. These advantages facilitate the detection of nodular metastases insinuating along spinal nerve roots; decrease the rate of indeterminate lesion classification, which may potentiate additional follow-up imaging; and render the bSSFP sequence superior to the postcontrast T1WI for detection of nonenhancing drop metastases.

The bSSFP sequence demonstrated an improved ability to de-

tect nodular drop metastases measuring < 3 mm. In 2 patients, a single drop metastasis was seen on the postcontrast T1WI; however, on the bSSFP sequence, additional smaller drop metastases were identified. This finding is clinically significant because it may change treatment from targeted radiation therapy of a single lesion to craniospinal radiation for these patients.

In 1 patient, nodules were detected on the bSSFP sequence, but not on the postcontrast T1WI. A review of the pretreatment MR imaging showed that the primary brain tumor, an ependymoma, was nonenhancing. This finding exemplifies an advantage of the bSSFP sequence over conventional postcontrast T1WI where primary tumors and their

drop metastases may not enhance.

The diagnostic yield of bSSFP was greater than that of the postcontrast T1WI with 6.3 lesions per patient seen on the bSSFP sequence compared with 2.1 lesions per patient on the postcontrast T1WI, and this level reached statistical significance ($P = .002$).

One important consideration with the bSSFP sequence is awareness of the appearance of leptomeningeal metastases. In 3 of 44 patients, diffuse leptomeningeal disease was detected on postcontrast T1WI as avid enhancement along the surface of the spinal cord. On the bSSFP sequence, this finding appeared as subtle irregularity and distortion of the spinal cord contour. These cases highlight the occasional difficulty of detecting spinal leptomeningeal disease on the bSSFP sequence, which may present as subtle contour distortion and minimal irregularity.

Because of the findings in this study, we continue to advocate the use of postcontrast T1WI of the spine but recommend inclusion of the bSSFP sequence in staging evaluations. The combination of these 2 sequences offers patients the greatest detection of both focal drop metastases and diffuse leptomeningeal disease in the spine.

Although, on average, bSSFP imaging of the entire spine requires an additional 10 minutes of acquisition time, in our experience, this additional scan time is offset by the elimination of axial T1WI because the sagittal, isotropic bSSFP may be reformatted in the axial plane and thus may replace axial postcontrast T1WIs.

We found that the bSSFP sequence, when used as an adjunct to the conventional postcontrast T1WI, decreased the number of prominent vessels misclassified as potential drop metastases, reducing the risk of inaccurate tumor staging and incorrect risk-group assignment.

This study has limitations. The sample size was relatively small. Second, not all imaging was performed on the same MR imaging scanner platform with patients scanned on both 1.5T and 3T scanners. This heterogeneity in the scanning platform is not ideal because 3T imaging may detect a higher number of drop metastases compared with 1.5T imaging. In this study, the bSSFP and postcontrast T1WI of the same patient, which were directly compared with each other, were always performed on the same Tesla-strength scanner. Specifically, there were no instances in

which a bSSFP sequence obtained on a 1.5T scanner was directly compared with a postcontrast T1WI performed on a 3T scanner, and vice versa. Last, there is no histopathologic confirmation for the determination of drop metastases. For this study, a constellation of the imaging findings and clinical assessment was used to determine the presence of spinal metastases. We think that this method for determining spinal drop metastases is scientifically sound, and we recognize that obtaining histopathologic confirmation of drop metastases in most cases is not feasible clinically.

CONCLUSIONS

The bSSFP sequence is a valuable adjunct for the evaluation of drop metastases in pediatric patients with primary intracranial tumors. As demonstrated in this study, the bSSFP sequence is particularly advantageous over conventional postcontrast T1WI for identifying nonenhancing drop metastases and small metastatic lesions ≤ 3 mm. In addition, the bSSFP sequence can help decrease the rate of false-positives due to the presence of vascular structures that may be mistaken for drop metastases on the post-contrast T1WI.

REFERENCES

1. Tai P, Dubey A, Salim M, et al. **Diagnosis and management of spinal metastasis of glioblastoma.** *Can J Neurol Sci* 2015;42:410–13 CrossRef Medline
2. Ijiri K, Hida K, Yano S, et al. **Traumatic spinal-cord herniation associated with pseudomeningocele after lower-thoracic nerve-root avulsion.** *Spinal Cord* 2009;47:829–31 CrossRef Medline
3. Nayman A, Ozbek S. **Redundant nerve root syndrome of the cauda equina: the benefits of 3D CISS MRI sequence.** *Spine J* 2015;15:e31 CrossRef Medline
4. Nemoto O, Fujikawa A, Tachibana A. **Three-dimensional fast imaging employing steady-state acquisition MRI and its diagnostic value for lumbar foraminal stenosis.** *Eur J Orthop Surg Traumatol* 2014;24(Suppl 1):S209–14 CrossRef Medline
5. Ramli N, Cooper A, Jaspan T. **High resolution CISS imaging of the spine.** *Br J Radiol* 2001;74:862–73 CrossRef Medline
6. Roser F, Ebner FH, Danz S, et al. **Three-dimensional constructive interference in steady-state magnetic resonance imaging in syringomyelia: advantages over conventional imaging.** *J Neurosurg Spine* 2008;8:429–35 CrossRef Medline
7. Hashiguchi K, Morioka T, Yoshida F, et al. **Feasibility and limitation of constructive interference in steady-state (CISS) MR imaging in neonates with lumbosacral myeloschisis.** *Neuroradiology* 2007;49:579–85 CrossRef Medline
8. McCormack EJ, Egnor MR, Wagshul ME. **Improved cerebrospinal fluid flow measurements using phase contrast balanced steady-state free precession.** *Magn Reson Imaging* 2007;25:172–82 CrossRef Medline
9. Abele TA, Besachio DA, Quigley EP, et al. **Diagnostic accuracy of screening MR imaging using unenhanced axial CISS and coronal T2WI for detection of small internal auditory canal lesions.** *AJNR Am J Neuroradiol* 2014;35:2366–70 CrossRef Medline
10. Ozgen B, Oguz B, Dolgun A. **Diagnostic accuracy of the constructive interference in steady state sequence alone for follow-up imaging of vestibular schwannomas.** *AJNR Am J Neuroradiol* 2009;30:985–91 CrossRef Medline
11. Yoshida T, Sone M, Naganawa S, et al. **Accuracy of 3.0 Tesla magnetic resonance imaging in the diagnosis of intracochlear schwannoma.** *Auris Nasus Larynx* 2011;38:551–54 CrossRef Medline

MRI-Based Methods for Spinal Cord Atrophy Evaluation: A Comparison of Cervical Cord Cross-Sectional Area, Cervical Cord Volume, and Full Spinal Cord Volume in Patients with Aquaporin-4 Antibody Seropositive Neuromyelitis Optica Spectrum Disorders

C. Chien, A.U. Brandt, F. Schmidt, J. Bellmann-Strobl, K. Ruprecht, F. Paul, and M. Scheel



ABSTRACT

BACKGROUND AND PURPOSE: Measures for spinal cord atrophy have become increasingly important as imaging biomarkers in the assessment of neuroinflammatory diseases, especially in neuromyelitis optica spectrum disorders. The most commonly used method, mean upper cervical cord area, is relatively easy to measure and can be performed on brain MRIs that capture cervical myelon. Measures of spinal cord volume (eg, cervical cord volume or total cord volume) require longer scanning and more complex analysis but are potentially better suited as spinal cord atrophy measures. This study investigated spinal cord atrophy measures in a cohort of healthy subjects and patients with aquaporin-4 antibody seropositive neuromyelitis optica spectrum disorders and evaluated the discriminatory performance of mean upper cervical cord cross-sectional area compared with cervical cord volume and total cord volume.

MATERIALS AND METHODS: Mean upper cervical cord area, cervical cord volume, and total cord volume were measured using 3T MRIs from healthy subjects ($n = 19$) and patients with neuromyelitis optica spectrum disorders ($n = 30$). Group comparison and receiver operating characteristic analyses between healthy controls and patients with neuromyelitis optica spectrum disorders were performed.

RESULTS: Mean upper cervical cord area, cervical cord volume, and total cord volume measures showed similar and highly significant group differences between healthy control subjects and patients with neuromyelitis optica spectrum disorders ($P < .01$ for all). All 3 measures showed similar receiver operating characteristic–area under the curve values (mean upper cervical cord area = 0.70, cervical cord volume = 0.75, total cord volume = 0.77) with no significant difference between them. No associations among mean upper cervical cord cross-sectional area, cervical cord volume, or total cord volume with disability measures were found.

CONCLUSIONS: All 3 measures showed similar discriminatory power between healthy control and neuromyelitis optica spectrum disorders groups. Mean upper cervical cord area is easier to obtain compared with cervical cord volume and total cord volume and can be regarded as an efficient representative measure of spinal cord atrophy in the neuromyelitis optica spectrum disorders context.

ABBREVIATIONS: AQP4-Ab+ = aquaporin-4 antibody seropositive; CCV = cervical cord volume; EDSS = Expanded Disability Status Scale; MUCCA = mean upper cervical cord area; NMOSD = neuromyelitis optica spectrum disorders; SCA = spinal cord atrophy; TCV = total cord volume

Several imaging biomarkers have been established in treatment trials for neuroinflammatory diseases. The most prominent example is T2 lesion count and/or volume in multiple sclerosis.¹ In neuromyelitis optica spectrum disorders (NMOSD), no such imaging biomarkers have been established yet. In most patients with NMOSD, standard brain MR imaging shows only nonspe-

cific lesions.^{2,3} However NMOSD has a predilection for affecting the optic nerves and spinal cord.⁴⁻⁶

Spinal cord atrophy (SCA) can appear after longitudinally extensive transverse myelitis⁷⁻⁹ and has therefore been suggested as an imaging biomarker for disease severity and treatment response in NMOSD. Previous studies have demonstrated that SCA can be associated with longer disease duration and more severe disability and can potentially indicate poor prognosis in NMOSD.^{10,11}

The SCA measurement most commonly used is the mean upper cervical cord area (MUCCA). It is measured as the cross-

Received December 3, 2017; accepted after revision March 13, 2018.

From the NeuroCure Clinical Research Center (C.C., A.U.B., F.S., J.B.-S., F.P. M.S.) and Departments of Neurology (F.S., K.R., F.P.) and Neuroradiology (M.S.), Charité–Universitätsmedizin Berlin, Berlin, Germany; and Experimental and Clinical Research Center (J.B.-S., F.P.), Max Delbrück Center for Molecular Medicine and Charité–Universitätsmedizin Berlin, Berlin, Germany.

F. Paul and M. Scheel were equally contributing senior authors.

The data collection and analyses for this study were funded by the Deutsche Forschungsgemeinschaft, German Research Foundation (grant No. Exc 257).

Please address correspondence to Friedemann Paul, MD, NeuroCure Clinical Research Center, Charité–Universitätsmedizin Berlin, Charitéplatz 1, 10117 Berlin, Germany; e-mail: friedemann.paul@charite.de

Indicates open access to non-subscribers at www.ajnr.org

<http://dx.doi.org/10.3174/ajnr.A5665>

sectional area of the spinal cord at the level between the C2 and C3 vertebrae.¹²⁻¹⁵ Although longitudinally extensive transverse myelitis predominantly affects the cervical and upper thoracic spinal cord, the lower thoracic and lumbar cord in patients with NMOSD is often affected as well.^{16,17} Hence, the main disadvantage of MUCCA is that though it can be easily obtained and measured, it covers only a very small fraction of the spinal cord. Therefore, quantification of the total cord volume (TCV) is theoretically beneficial for a more precise assessment of SCA.

The main disadvantage of assessing TCV is that it requires extra scan time and a more complex and time-consuming analysis procedure. As a compromise between MUCCA and TCV quantification, cervical cord volume (CCV) could be measured.

In theory, TCV should best discriminate between patients with NMOSD and healthy control subjects and should also show a stronger association with clinical measures of disability. Our hypothesis was that TCV best reflects full SCA. Our study compares the discriminatory power of MUCCA, CCV, and TCV between patients with NMOSD and a healthy control group and investigates associations of MUCCA, CCV, and TCV with clinical disability measures.

MATERIALS AND METHODS

Patients and Subjects

Clinical, demographic, and MR imaging data from 30 patients with NMOSD and 19 healthy control subjects were included (Table 1) in this study. These data were acquired from an ongoing longitudinal prospective observational cohort study, which was approved by the local ethics committee.

All patients and subjects provided written informed consent. The study was conducted in accordance with the Declaration of Helsinki in its current applicable version and applicable country-specific laws.

All patients had a definite diagnosis of NMOSD according to current panel criteria⁷ and were aquaporin-4 antibody seropositive (AQP4-Ab+).¹⁸ We limited the patient cohort to those with AQP4-Ab+ NMOSD only, to ensure a homogeneous patient cohort with a comparable mechanism of spinal cord damage. All patients with AQP4-Ab+ NMOSD except for 2 (93%) had an attack history of myelitis. Clinical assessments consisted of the Expanded Disability Status Scale (EDSS), averaged timed 25-foot walk test time, and the averaged 9-hole peg test time.

MR Imaging Acquisition

All MR imaging scans were performed on a 3T (Magnetom Trio Tim; Siemens, Erlangen, Germany) scanner. The MR imaging protocol for this study included the following: 1) a T1-weighted 3D magnetization prepared rapid acquisition of gradient echo brain MR imaging ($1 \times 1 \times 1 \text{ mm}^3$ resolution, TR = 1900 ms, TE = 3.03 ms, in-plane resolution = $1 \times 1 \text{ mm}$) including the upper cervical cord, and 2) sagittally oriented 2D T2-weighted sequences (slice thickness = 2 mm, gap size = 0.2 mm, TR = 3500 ms, TE = 101 ms, in-plane resolution = $1.2 \times 0.9 \text{ mm}$) at the cervical, thoracic, and lumbar levels.

Spinal Cord Analysis

All spinal cord measurements were performed with Jim software (Version 7.0; <http://www.xinapse.com/home.php>). Jim software applies a semiautomatic active surface model, which is based on spinal cord surface parametrization, yielding reproducible measurements of cord cross-sectional areas. This method is also applicable in full spinal cord segmentation of 2D multislice T2-weighted MRI, giving volume measurements of specified spinal cord regions such as the cervical cord or full spinal cord.¹⁹ Because this method has been validated for area and volumetric measurements in both research and clinical settings, we chose the Jim software for this study.²⁰⁻²²

Mean Upper Cervical Cord Area

MUCCA was measured in 3D MPRAGE images by averaging the cross-sectional areas from 5 consecutive slices. Following standard convention, the C2–C3 intervertebral space was used as a horizontal reference level for the middle slice.¹²

Table 1: Demographics and clinical characteristics

	HCS	Patients with NMOSD	P Value
No.	19	30	—
Sex (F/M) (% female)	16:3 (84%)	27:3 (90%)	.56 ^a
Mean age (range) (yr)	41.6 (24–68)	46.5 (18–70)	.23 ^b
Median EDSS score (range)	—	3.8 (0–6.5)	—
Mean disease duration (range) (yr)	—	5.7 (0.5–18.5)	—

Note:—HCS indicates healthy controls.

^a χ^2 .

^b Two-sample *t* test.

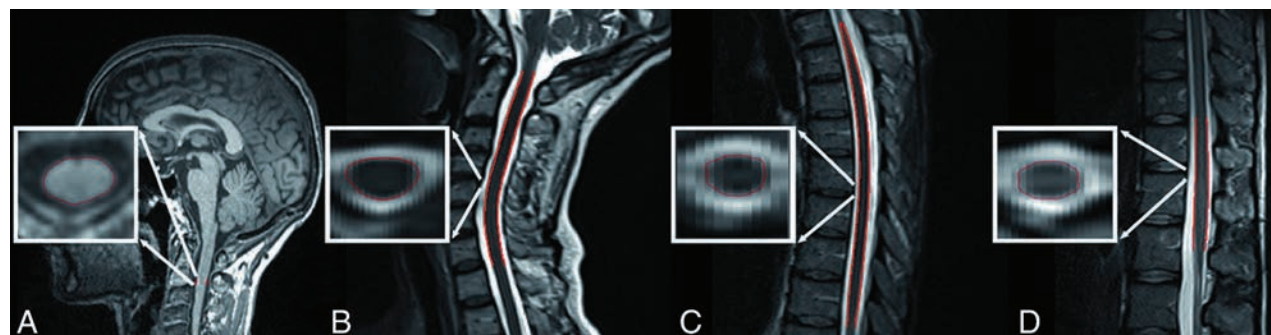


FIG 1. Sample segmentation of MUCCA (A), CCV (B), the thoracic spinal cord (C), and the lumbar spinal cord (D). TCV is calculated from the sum of B, C, and D.

Cervical Cord Volume

CCV was measured in a cervical spinal cord 2D T2-weighted sagittal MR imaging sequence. Images were reoriented to the axial orientation and interpolated with multiplanar reconstruction. The centerline of the cord was manually marked at 4 levels along the spinal cord from the tip of the dens to the rostral border of the T1 vertebral body. Subsequent automatic volumetric analysis of the cervical spinal cord was measured with the active surface model as implemented in Jim 7.0 software.

Total Cord Volume

TCV was measured using spinal cord sagittal 2D T2-weighted MR imaging sequences at 3 different levels: cervical, thoracic, and lumbar. All preprocessing by reorientation, multiplanar reconstruction, and centerline indication was the same as with the CCV. Therefore, the volumetric analysis of the full spinal cord required segmentation into 3 parts: 1) the cervical cord from the tip of the dens to the rostral border of the T1 vertebral body, 2) the thoracic cord from the rostral border of the T1 vertebral body to the T11 vertebral body rostral border, and 3) the lumbar cord from the T11 vertebral body rostral border to the conus tip. The TCV was calculated by adding all segmented volumes together.

Figure 1 shows a sample segmentation performed with the active surface model for MUCCA, CCV, and the thoracic and lumbar cords.

Statistical Analysis

Proportional group differences in sex were tested with a χ^2 test. For group comparison of continuous measurements (age, MUCCA, CCV, TCV), a Welch 2-sampled *t* test was used.

Association analysis of MUCCA, CCV, and TCV with each

other and with clinical performance measures (averaged timed 25-foot walk and dominant and nondominant hand 9-hole peg test times) was performed with the Pearson correlation test and for EDSS with the Spearman rank correlation test. Further group discriminatory performance was evaluated with receiver operating characteristic analysis including area under the curve comparison using the DeLong method.²³

All statistical analyses and plots were produced using R software (<http://www.r-project.org/>)²⁴ with the tidyverse,²⁵ ggpubr,²⁶ and pROC packages.²⁷

RESULTS

Demographics

Table 1 shows the demographic data of the study cohort. No significant differences were found between groups in sex or age.

Group Comparison and Receiver Operating Characteristic Analysis

Table 2 and Figs 2 and 3 summarize the group comparison analysis and spinal cord association analyses between patients with NMOSD and healthy controls for MUCCA, CCV, and TCV. All 3 measures show a clear and significant difference between each group and significant associations with each other.

Differentiation between healthy control and NMOSD group spinal cord measures are evident, as shown in Fig 2. MUCCA, CCV, and TCV have comparable area under the curve values in the receiver operating characteristic analysis, as shown in Fig 4. Area under the curve values were tested for a statistically significance difference using the DeLong method,²³ yielding no increased performance of any spinal cord measure over the other.

Table 2: Spinal cord measurements

Spinal Cord Measure	HCS (Mean ± SD)	Patients with NMOSD (Mean ± SD)	T Statistic; P Value
MUCCA (mm ²)	73.3 ± 5.51	68.5 ± 7.06	2.70; .009 ^a
CCV (mL)	7.52 ± 0.92	6.61 ± 0.96	3.33; .002 ^a
TCV (mL)	20.1 ± 2.37	17.6 ± 2.21	3.69; <.001 ^a

Note:—HCS indicates healthy controls.

^aStatistical difference from HCS (*P* < .01).

Associations with Clinical Disability

Associations of MUCCA, CCV, and TCV with the EDSS and the pyramidal functional system score of the EDSS²⁸ all showed nonsignificant associations (Fig 5 and Table 3). No spinal cord measures showed significant associa-

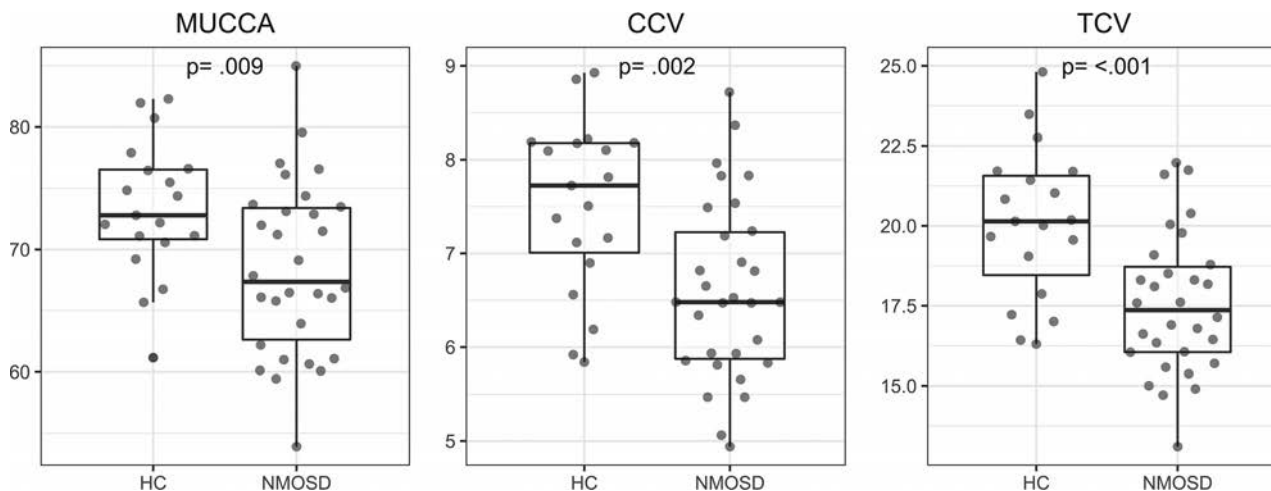


FIG 2. Group differences between healthy control (HC) subjects and patients with NMOSD for MUCCA in square millimeters, CCV and TCV, in milliliters.

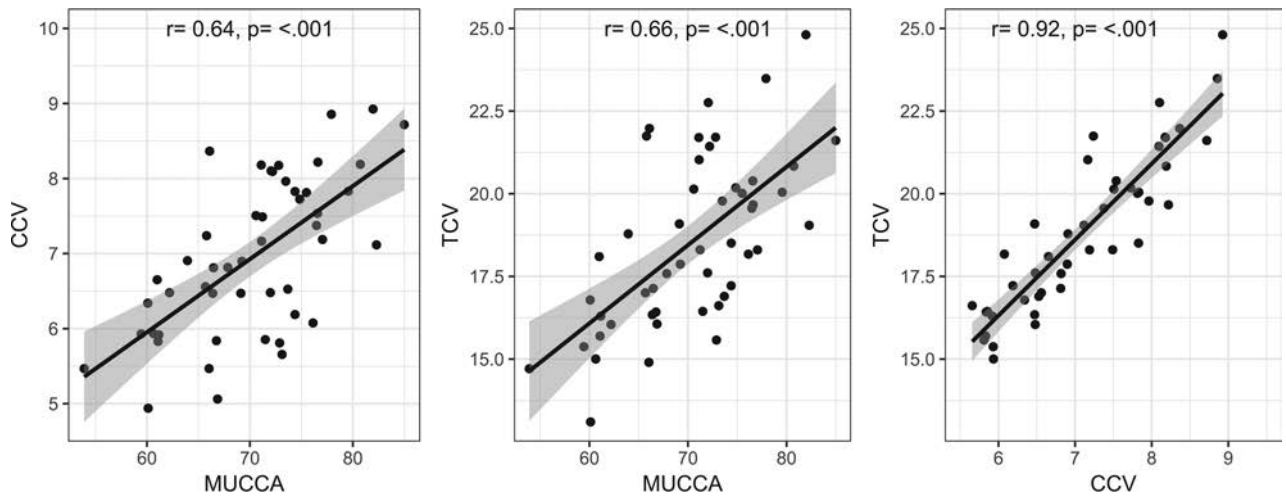


FIG 3. Pearson correlation tests of each spinal cord measure for healthy controls and patients with NMOSD combined. MUCCA is shown in square millimeters; CCV and TCV, in milliliters.

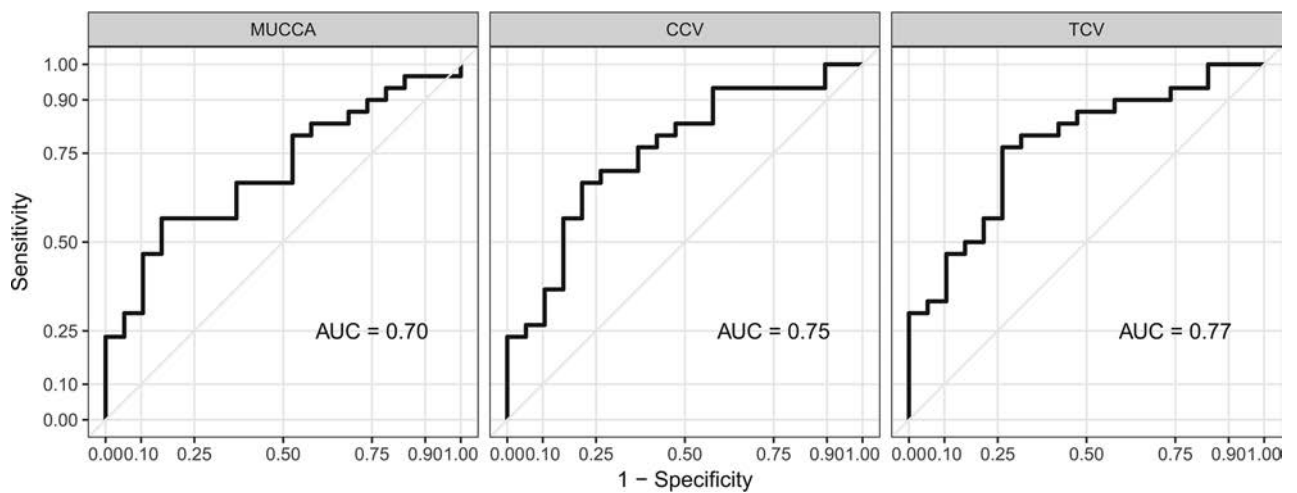


FIG 4. Receiver operating characteristic analysis for MUCCA, CCV, and TCV indicates good sensitivity (true-positive fraction) and specificity (false-positive fraction) for spinal cord atrophy measures in NMOSD. AUC indicates area under the curve.

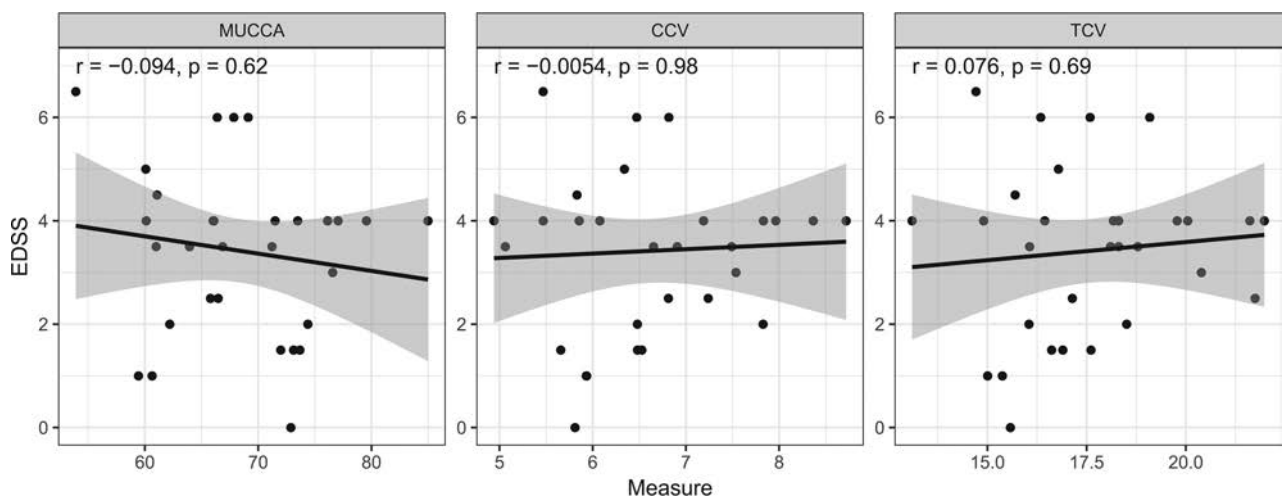


FIG 5. Associations of each spinal cord measure with the Expanded Disability Status Scale score. The x-axis shows measurements for MUCCA in square millimeters, CCV and TCV, in milliliters.

Table 3: Associations of spinal cord measurements with clinical disability

Spinal Cord Measure	Pyramidal Functional System Score ^a	Average Timed 25-Foot Walk ^b	9-Hole Peg Test ^b	
			Average Dominant Hand	Average Nondominant Hand
MUCCA	$R = -0.31, P = .1$	$R = -0.22, P = .25$	$R = -0.009, P = .97$	$R = -0.12, P = .56$
CCV	$R = -0.058, P = .76$	$R = -0.20, P = .30$	$R = -0.085, P = .67$	$R = 0.005, P = .98$
TCV	$R = 0.016, P = .93$	$R = -0.13, P = .50$	$R = 0.046, P = .82$	$R = 0.13, P = .50$

^a Nonparametric Spearman rank correlation coefficient.

^b Pearson correlation test.

tions with the averaged timed 25-foot walk or 9-hole peg tests (Table 3).

DISCUSSION

This study investigated 3 different MR imaging–based SCA measures for discriminatory performance in a cohort of patients with NMOSD and healthy control subjects. We demonstrated that all 3 types of quantification could significantly differentiate these 2 groups. In a receiver operating characteristic analysis, all measures showed similar area under the curve values in the range of 0.70–0.77, in which TCV had the highest value on a descriptive level. In a statistical comparison, these values were not significantly different. MUCCA, CCV, and TCV did not correlate with clinical disability, as measured by the EDSS, the pyramidal functional system score, and the averaged timed 25-foot walk and 9-hole peg tests.

The observed significant difference in MUCCA between groups is in line with results from other studies.^{29,30}

The area under the curve values obtained from receiver operating characteristic analysis for these 3 measures indicate that MUCCA, CCV, and TCV are not sufficiently sensitive or specific to be deemed clinically relevant diagnostic biomarkers in NMOSD.³¹ We believe that measuring MUCCA longitudinally could still indicate whether SCA or cord damage occurred.³²

The similar performance of MUCCA compared with CCV and TCV could be because the cervical and upper thoracic cord levels are most commonly affected in patients with NMOSD.^{20,33} Also, all fibers of the thoracic and lumbar spinal cord eventually converge, passing through the cervical cord. Hence, the cervical portion will reflect the overall damage even from lower segments.

Our results showed no clinical associations with the spinal cord measures we investigated. The literature on the associations of clinical disability with spinal cord measures is mixed for NMOSD.

Two studies from the same group found very strong associations of MUCCA with clinical measures in MS and NMOSD.^{29,34} One other spinal cord study in NMOSD observed some non-lesion-related damage and demonstrated a significant correlation of MUCCA with the patient-determined disease steps, but did not report any statistical tests with EDSS.³⁰

This discrepancy with our results could be due to ethnic, demographic, or cohort-selection differences. Another reason for this finding could be that the EDSS was developed for multiple sclerosis and might not be an ideal instrument reflecting NMOSD disease severity.³⁵

We chose not to apply normalization to all spinal cord measures because no consensus has been reached on how to normalize SCA measures.^{36–39} Performing spinal cord measurements using different types of MR imaging sequences may require different

normalization methods, which we did not investigate in this study.

Measurement of MUCCA, CCV, and TCV could be influenced by inflammation of the spinal cord, yielding larger values than the true cross-sectional areas. None of the patients in our cohort were imaged during an acute myelitis phase. Thus, no patient MRIs exhibited edema in any part of the myelon, which may have affected the spinal cord measurements.

Some limitations apply to our study. The study was performed in a relatively small sample of patients with AQP4-Ab+ only. We conducted this study in NMOSD because we expected a relatively strong difference in SCA measures compared with a healthy control group. We have limited this study cohort to patients with AQP4-Ab disease only to keep the patient cohort homogeneous, so damage mechanisms should be similar. Where the addition of patients with AQP4-Ab seronegativity would include patients with myelin oligodendrocyte glycoprotein antibody seropositivity, likely with different damage in the spinal cord.^{40,41} The main purpose of our study was to compare 3 possible measures of SCA and investigate whether the additional effort of full spinal cord analysis performs better than a simple MUCCA approach. Thus, we did not evaluate spinal cord lesion load or location in this study.

We are aware that sagittally oriented MR images are not ideal for detailed analysis of the spinal cord. Full spinal cord MR imaging is usually acquired in a sagittal orientation because larger portions of the spinal cord can be imaged compared with an axial orientation. Axially acquired spinal cord images would have been advantageous due to fewer partial volume effects. When one looks at the axial slices in Fig 1, it becomes clear that image resolution in the 2D axial plane is coarse. However, the active surface model used by the Jim software smooths out voxels and interpolates the slice spacing. It does not remove the spacing; rather, it fills in the gaps using an average from the signal coming from the contributing slices on either side. Thus, we believe the discrepancy between 3D and 2D images is minimized and the partial volume errors are decreased by this method.¹⁹ Moreover, the acquisition of axial images over the full spinal cord would have required excessively long scan times, and our results would not be comparable with the standard clinical setting.⁴²

There has been sparse research into MR imaging biomarkers for patients with NMOSD. Those who have investigated deep gray matter and white matter tracts have shown little discernable difference between patients with AQP4-Ab+ NMOSD and healthy controls.^{43,44} Thus, the decrease in spinal cord measures found in this study and others shows that SCA could be a suitable imaging biomarker in these patients.

Emerging quantitative MR imaging methods of white and gray matter segmentation in the spinal cord are now becoming clini-

cally available.^{8,20,39,45} Further studies will be required to show whether these new measures can better characterize SCA in the NMOSD context.

CONCLUSIONS

MUCCA shows similar performance for SCA evaluation in comparison with CCV and TCV. The hypothetical benefit of a more complete volumetric measurement could not be confirmed in our study. Therefore, in our opinion, MUCCA is an efficient and representative surrogate parameter for SCA analysis, at least in the context of patients with AQP4-Ab+ NMOSD.

MUCCA has 2 advantages: 1) being relatively easy to acquire, without the need for a dedicated spine sequence because 3D T1-weighted cerebral images can be used for MUCCA measurement; and 2) the measurement is relatively simple and quick to perform. The pathogenesis of SCA in NMOSD is still poorly understood, and the disease is difficult to study due to its rarity. It is, thus, of great advantage to have an efficient and easy-to-standardize method in future longitudinal studies. Our study demonstrates that MUCCA measurements are a good representative marker of whole spinal cord SCA in patients with NMOSD.

ACKNOWLEDGMENTS

We thank all the patients and healthy control subjects for their participation. We would also like to acknowledge our MR imaging technicians, Cynthia Kraut and Susan Pikol, for their assistance in this research.

Disclosures: A.U. Brandt—UNRELATED: Board Membership: Motognosis; Consultancy: Biogen, Comments: Vision Study; Payment for Lectures Including Service on Speakers Bureaus: Teva Pharmaceutical Industries; Patents (Planned, Pending, or Issued), Comments: ocular coherence tomography analysis, perceptive computing, MS biomarkers; Stock/Stock Options: Motognosis. J. Bellmann-Strobl—UNRELATED: Payment for Lectures Including Service on Speakers Bureaus, Comments: payment for lectures on fatigue in 2016 and pregnancy and MS in 2017; Travel/Accommodations/Meeting Expenses Unrelated to Activities Listed, Comments: travel grants in 2015, 2016, and 2017. Klemens Ruprecht—RELATED: Grant: KKNMS (Competence Network Multiple Sclerosis) Bundesministerium für Bildung und Forschung, Comments: research grant; UNRELATED: Grants/Grants Pending: Novartis Pharmaceuticals, Merck Serono, Comments: research grants. Friedemann Paul—UNRELATED: Board Membership: Guthy Jackson Charitable Foundation—International Clinical Consortium.* *Money paid to the institution.

REFERENCES

1. Filippi M, Rocca MA, Ciccarelli O, et al; MAGNIMS Study Group. **MRI criteria for the diagnosis of multiple sclerosis: MAGNIMS consensus guidelines.** *Lancet Neurol* 2016;15:292–303 CrossRef Medline
2. Pittock SJ, Lennon VA, Krecke K, et al. **Brain abnormalities in neuromyelitis optica.** *Arch Neurol* 2006;63:390–96 CrossRef Medline
3. Kim HJ, Paul F, Lana-Peixoto MA, et al; Guthy-Jackson Charitable Foundation NMO International Clinical Consortium & Biorepository. **MRI characteristics of neuromyelitis optica spectrum disorder: an international update.** *Neurology* 2015;84:1165–73 CrossRef Medline
4. Asgari N, Flanagan EP, Fujihara K, et al. **Disruption of the leptomeningeal blood barrier in neuromyelitis optica spectrum disorder.** *Neurol Neuroimmunol Neuroinflamm* 2017;4:e343 CrossRef Medline
5. Schmidt F, Zimmermann H, Mikolajczak J, et al. **Severe structural and functional visual system damage leads to profound loss of vision-related quality of life in patients with neuromyelitis optica spectrum disorders.** *Mult Scler Relat Disord* 2017;11:45–50 CrossRef Medline
6. Oertel FC, Kuchling J, Zimmermann H, et al. **Microstructural visual system changes in AQP4-antibody-seropositive NMOSD.** *Neurol Neuroimmunol Neuroinflamm* 2017;4:e334 CrossRef Medline
7. Wingerchuk DM, Banwell B, Bennett JL, et al; International Panel for NMO Diagnosis. **International consensus diagnostic criteria for neuromyelitis optica spectrum disorders.** *Neurology* 2015;85:177–89 CrossRef Medline
8. Pekcevik Y, Mitchell CH, Mealy MA, et al. **Differentiating neuromyelitis optica from other causes of longitudinally extensive transverse myelitis on spinal magnetic resonance imaging.** *Mult Scler* 2016;22:302–11 CrossRef Medline
9. Akaishi T, Nakashima I, Sato DK, et al. **Neuromyelitis optica spectrum disorders.** *Neuroimaging Clin N Am* 2017;27:251–65 CrossRef Medline
10. Wang Y, Wu A, Chen X, et al. **Comparison of clinical characteristics between neuromyelitis optica spectrum disorders with and without spinal cord atrophy.** *BMC Neurol* 2014;14:246 CrossRef Medline
11. Stevenson VL, Leary SM, Losseff NA, et al. **Spinal cord atrophy and disability in MS: a longitudinal study.** *Neurology* 1998;51:234–38 CrossRef Medline
12. Losseff NA, Webb SL, O’Riordan JI, et al. **Spinal cord atrophy and disability in multiple sclerosis: a new reproducible and sensitive MRI method with potential to monitor disease progression.** *Brain* 1996;119(Pt 3):701–08 CrossRef Medline
13. Daams M, Weiler F, Steenwijk MD, et al. **Mean upper cervical cord area (MUCCA) measurement in long-standing multiple sclerosis: relation to brain findings and clinical disability.** *Mult Scler* 2014;20:1860–65 CrossRef Medline
14. Liu Z, Yaldizli Ö, Pardini M, et al. **Cervical cord area measurement using volumetric brain magnetic resonance imaging in multiple sclerosis.** *Mult Scler Relat Disord* 2015;4:52–57 CrossRef Medline
15. Liu Y, Lukas C, Steenwijk MD, et al. **Multicenter validation of mean upper cervical cord area measurements from head 3D T1-weighted MR imaging in patients with multiple sclerosis.** *AJNR Am J Neuroradiol* 2016;37:749–54 CrossRef Medline
16. Jarius S, Ruprecht K, Kleiter I, et al; in cooperation with the Neuromyelitis Optica Study Group (NEMOS). **MOG-IgG in NMO and related disorders: a multicenter study of 50 patients, part 2—epidemiology, clinical presentation, radiological and laboratory features, treatment responses, and long-term outcome.** *J Neuroinflammation* 2016;13:280 CrossRef Medline
17. Sato DK, Callegaro D, Lana-Peixoto MA, et al. **Distinction between MOG antibody-positive and AQP4 antibody-positive NMO spectrum disorders.** *Neurology* 2014;82:474–81 CrossRef Medline
18. Zekeridou A, Lennon VA. **Aquaporin-4 autoimmunity.** *Neurol Neuroimmunol Neuroinflamm* 2015;2:e110 CrossRef Medline
19. Horsfield MA, Sala S, Neema M, et al. **Rapid semi-automatic segmentation of the spinal cord from magnetic resonance images: application in multiple sclerosis.** *Neuroimage* 2010;50:446–55 CrossRef Medline
20. Kim G, Khalid F, Oommen VV, et al. **T1- vs. T2-based MRI measures of spinal cord volume in healthy subjects and patients with multiple sclerosis.** *BMC Neurol* 2015;15:124 CrossRef Medline
21. Castellano A, Papinutto N, Cadioli M, et al. **Quantitative MRI of the spinal cord and brain in adrenomyeloneuropathy: in vivo assessment of structural changes.** *Brain* 2016;139(Pt 6):1735–46 CrossRef Medline
22. Cawley N, Tur C, Prados F, et al. **Spinal cord atrophy as a primary outcome measure in phase II trials of progressive multiple sclerosis.** *Mult Scler* 2017 May 1. [Epub ahead of print] CrossRef Medline
23. Hajian-Tilaki K. **Receiver operating characteristic (ROC) curve analysis for medical diagnostic test evaluation.** *Caspian J Intern Med* 2013;4:627–35 Medline
24. R Core Team. R version 3.4.1. 2014. <http://www.R-project.org/>.
25. Wickham H. *Tidyverse: Easily Install and Load the “Tidyverse.”* November 14, 2017. <https://CRAN.R-project.org/package=tidyverse>. Accessed April 27, 2018
26. Kassambara A. *ggpubr: “ggplot2” Based Publication Ready Plots.*

- November 14, 2017. <https://cran.r-project.org/web/packages/ggpubr/index.html>. Accessed April 27, 2018
27. Robin X, Turck N, Hainard A, et al. **pROC: an open-source package for R and S+ to analyze and compare receiver operating characteristic curves.** *BMC Bioinformatics* 2011;12:77 CrossRef Medline
 28. Ontaneda D, Cohen JA, Amato MP. **Clinical outcome measures for progressive MS trials.** *Mult Scler* 2017;23:1627–35 CrossRef Medline
 29. Liu Y, Wang J, Daams M, et al. **Differential patterns of spinal cord and brain atrophy in NMO and MS.** *Neurology* 2015;84:1465–72 CrossRef Medline
 30. Ventura RE, Kister I, Chung S, et al. **Cervical spinal cord atrophy in NMOSD without a history of myelitis or MRI-visible lesions.** *Neurol Neuroimmunol Neuroinflamm* 2016;3:e224 CrossRef Medline
 31. Skates SJ. **A statistical challenge: developing tests for biomarker utility specific to the intended use.** *J Natl Cancer Inst* 2014;106:dju076 CrossRef Medline
 32. Chen W, Samuelson FW, Gallas BD, et al. **On the assessment of the added value of new predictive biomarkers.** *BMC Med Res Methodol* 2013;13:98 CrossRef Medline
 33. Wang Y, Wang Y, Tan S, et al. **Spinal cord atrophy in neuromyelitis optica spectrum disorders.** *Mult Scler Relat Disord* 2016;8:9–10 CrossRef Medline
 34. Liu Y, Duan Y, Huang J, et al. **Different patterns of longitudinal brain and spinal cord changes and their associations with disability progression in NMO and MS.** *Eur Radiol* 2018;28:96–103 CrossRef Medline
 35. Cree BA, Bennett JL, Sheehan M, et al. **Placebo-controlled study in neuromyelitis optica: ethical and design considerations.** *Mult Scler* 2016;22:862–72 CrossRef Medline
 36. Healy BC, Arora A, Hayden DL, et al. **Approaches to normalization of spinal cord volume: application to multiple sclerosis.** *J Neuroimaging* 2012;22:e12–19 CrossRef Medline
 37. Oh J, Seigo M, Saidha S, et al. **Spinal cord normalization in multiple sclerosis.** *J Neuroimaging* 2014;24:577–84 CrossRef Medline
 38. Kearney H, Yiannakas MC, Abdel-Aziz K, et al. **Improved MRI quantification of spinal cord atrophy in multiple sclerosis.** *J Magn Reson Imaging* 2014;39:617–23 CrossRef Medline
 39. Papinutto N, Schlaeger R, Panara V, et al. **Age, gender and normalization covariates for spinal cord gray matter and total cross-sectional areas at cervical and thoracic levels: a 2D phase sensitive inversion recovery imaging study.** *PLoS One* 2015;10:e0118576 CrossRef Medline
 40. Zamvil SS, Slavin AJ. **Does MOG Ig-positive AQP4-seronegative optico-spinal inflammatory disease justify a diagnosis of NMO spectrum disorder?** *Neurol Neuroimmunol Neuroinflamm* 2015;2:e62 CrossRef Medline
 41. Jarius S, Ruprecht K, Kleiter I, et al; in cooperation with the Neuromyelitis Optica Study Group (NEMOS). **MOG-IgG in NMO and related disorders: a multicenter study of 50 patients, Part 1: frequency, syndrome specificity, influence of disease activity, long-term course, association with AQP4-IgG, and origin.** *J Neuroinflammation* 2016;13:279 CrossRef Medline
 42. Ozturk A, Aygun N, Smith SA, et al. **Axial 3D gradient-echo imaging for improved multiple sclerosis lesion detection in the cervical spinal cord at 3T.** *Neuroradiology* 2013;55:431–39 CrossRef Medline
 43. Finke C, Heine J, Pache F, et al. **Normal volumes and microstructural integrity of deep gray matter structures in AQP4+ NMOSD.** *Neurol Neuroimmunol Neuroinflamm* 2016;3:e229 CrossRef Medline
 44. Pache F, Zimmermann H, Finke C, et al. **Brain parenchymal damage in neuromyelitis optica spectrum disorder: a multimodal MRI study.** *Eur Radiol* 2016;26:4413–22 CrossRef Medline
 45. Dupont SM, De Leener B, Taso M, et al. **Fully-integrated framework for the segmentation and registration of the spinal cord white and gray matter.** *Neuroimage* 2017;150:358–72 CrossRef Medline

A Qualitative and Quantitative Correlation Study of Lumbar Intervertebral Disc Degeneration Using Glycosaminoglycan Chemical Exchange Saturation Transfer, Pfirrmann Grade, and T1- ρ

O. Togao, A. Hiwatashi, T. Wada, K. Yamashita, K. Kikuchi, C. Tokunaga, J. Keupp, M. Yoneyama, and H. Honda

ABSTRACT

BACKGROUND AND PURPOSE: Glycosaminoglycan chemical exchange saturation transfer (gagCEST) imaging allows the direct measurement and mapping of glycosaminoglycans. In this study, we aimed to evaluate the usefulness of gagCEST imaging in the quantitative assessment of intervertebral disc degeneration in a comparison with Pfirrmann grade and T1- ρ measurements.

MATERIALS AND METHODS: Ninety-six lumbar intervertebral discs in 24 volunteers (36.0 ± 8.5 years of age, 21 men and 3 women) were examined with both gagCEST imaging and T1- ρ measurements. The gagCEST imaging was performed at 3T with a saturation pulse with 1.0-second duration and the B₁ amplitude of 0.8 μ T followed by imaging by a 2D fast spin-echo sequence. The Z-spectra were obtained at 25 frequency offsets from -3 to $+3$ ppm (step, 0.25 ppm). A point-by-point B₀ correction was performed with a B₀ map. The gagCEST signal and T1- ρ values were measured in the nucleus pulposus in each intervertebral disc. The Pfirrmann grades were assessed on T2-weighted images.

RESULTS: The gagCEST signal at grade I ($5.36\% \pm 2.79\%$) was significantly higher than those at Pfirrmann grade II ($3.15\% \pm 1.40\%$, $P = .0006$), grade III ($0.14\% \pm 1.03\%$, $P < .0001$), grade IV ($-1.75\% \pm 2.82\%$, $P < .0001$), and grade V ($-1.47\% \pm 0.36\%$, $P < .0001$). The gagCEST signal at grade II was significantly higher than those of grade III ($P < .0001$), grade IV ($P < .0001$), and grade V ($P < .0001$). The gagCEST signal was significantly correlated negatively with Pfirrmann grade ($P < .0001$) and positively correlated with T1- ρ ($P < .0001$).

CONCLUSIONS: GagCEST imaging could be a reliable and quantitative technique for assessing intervertebral disc degeneration.

ABBREVIATIONS: CEST = chemical exchange saturation transfer; GAG = glycosaminoglycan; gagCEST = CEST imaging of GAGs; IVD = intervertebral disc; MTR_{asym} = asymmetry of the magnetization transfer ratio; PG = proteoglycans; WASSR = water saturation shift referencing

Low back pain represents the second leading cause of disability worldwide, being a major welfare and economic problem.¹ Degeneration of intervertebral discs (IVDs) is one of the leading causes of low back pain, accounting for 26%.² Surgical treatment such as spinal fusion has been performed in severe IVD degeneration, but more recently, early-stage IVD degeneration may be treated with emerging regenerative medicine therapy such as cell

therapy or growth factor therapy.³⁻⁵ Under such circumstances, noninvasive and quantitative imaging methods are desirable for the sensitive detection of early changes of IVD degeneration and for monitoring both the severity of the degeneration and the therapeutic response to such treatments.

Early degeneration of IVD is characterized by biochemical changes, including a loss of proteoglycans (PGs), dehydration, and collagen degeneration, of which the loss of PGs is the earliest and most remarkable phenomenon.^{6,7} The loss of PGs occurs predominantly in the nucleus pulposus, which decreases the ability of discs to distribute load forces.⁸ PGs consist of a core protein and ≥ 1 covalently attached glycosaminoglycan (GAG) chain. The GAGs are long unbranched polysaccharides that consist of repeating disaccharide units. PGs and GAGs are the platform of cartilage matrix, and they play crucial roles in the maintenance of the mechanical function of diarthrodial joints and IVDs.

Currently, conventional T1- and T2-weighted MR images are used to assess the severity of IVD degeneration in the clinical work-up. The Pfirrmann grade uses the signal intensity and height of discs on T2-weighted images to qualitatively evaluate

Received January 1, 2018; accepted after revision March 9.

From the Department of Clinical Radiology (O.T., A.H., K.Y., K.K., H.H.), Graduate School of Medical Sciences, Kyushu University, Fukuoka, Japan; Division of Radiology (T.W., C.T.), Department of Medical Technology, Kyushu University Hospital, Fukuoka, Japan; Philips Research (J.K.), Hamburg, Germany; and Philips Japan (M.Y.), Tokyo, Japan.

This work was supported by JSPS KAKENHI grant No. JP17K10410.

Paper previously presented at: Annual Meeting of the Radiological Society of North America, November 29–December 4, 2015; Chicago, Illinois.

Please address correspondence to Akio Hiwatashi, MD, PhD, Department of Clinical Radiology, Graduate School of Medical Science, Kyushu University, 3-1-1 Maidashi, Higashi-ku, Fukuoka 812-8582, Japan; e-mail: hiwatashi@radiol.med.kyushu-u.ac.jp

<http://dx.doi.org/10.3174/ajnr.A5657>

IVD degeneration on the basis of the 5-point scale.⁹ This grading system is simple and readily applicable but can be subjective when categorizing the degree of degeneration. So far, several quantitative MR imaging techniques to objectively evaluate the IVD degeneration have been reported. It was reported that the relaxation times T1, T2, and T1- ρ ; the magnetic transfer ratio; and diffusion coefficient measured by diffusion-weighted MR imaging could be quantitative imaging biomarkers for assessing the IVD matrix composition, integrity, and biomechanics.¹⁰⁻¹³

Conventional T2-weighted MR imaging can detect dehydration, collagen degeneration, and morphologic changes but not the loss of PGs or GAGs. It was reported that the loss of PGs can be detected by T1- ρ measurements.^{10,14,15} T1- ρ is the spin-lattice relaxation time in the rotating frame, which is associated with slow motional interactions between macromolecules and bulk water. T1- ρ is measured using a low B₁ field created by spin-lock pulses. Previous studies showed that T1- ρ is correlated with the PG content in the nucleus pulposus¹⁶ and that T1- ρ has a wider dynamic range compared with T2 relaxation time measurements for quantitative assessment of IVD.¹¹ However, the clinical applicability of T1- ρ imaging is limited by the long scan time and the high specific absorption rate required by multiple and long spin-lock pulses.

Chemical exchange saturation transfer (CEST) imaging has drawn considerable attention in the field of molecular imaging as a novel contrast mechanism in MR imaging.¹⁷ CEST contrast is achieved by applying a saturation pulse at the resonance frequency of a slow-intermediate exchanging proton site (eg, -NH, -OH) of endogenous or exogenous agents, and the resulting saturated spin is transferred to bulk water via a chemical exchange.¹⁷⁻¹⁹ The CEST imaging of GAGs (ie, gagCEST) is 1 subset of the endogenous CEST imaging techniques introduced by Ling et al.²⁰ GagCEST imaging leverages the proton exchange between the hydroxyl protons (-OH) in GAG units and bulk-water protons. Hydroxyl protons in GAGs have the frequency shift at around 1 ppm downfield of the bulk water peak, and the CEST effect at this frequency reflects the concentration or exchange rate of hydroxyl protons included in GAGs.

This method allows the direct measurements and mapping of GAGs in vivo, unlike other methods, and is considered one of the most clinically feasible methods among several CEST imaging techniques. The feasibility of this method for imaging human lumbar IVDs at 3T was demonstrated,^{21,22} but the quantitative performance of this method in vivo has not yet been evaluated. The purpose of the present study was to evaluate the usefulness of gagCEST imaging in the quantitative assessment of IVD degeneration in comparison with Pfirrmann grade and T1- ρ measurements.

MATERIALS AND METHODS

Subjects

Twenty-four volunteers were recruited for the study: 21 men and 3 women; mean age, 36.0 \pm 8.5 years; range, 26–58 years; in their 20s, $n = 6$; 30s, $n = 10$; 40s, $n = 7$, 50s, $n = 1$. All subjects were adult volunteers recruited from medical staff working in the hospital, and exclusion criteria included history of severe back pain for which the subject sought medical help, prior spine surgery or

interventions of any kind, disc herniation, spinal canal stenosis, congenital spine disorders, scoliosis, or fractures. Ten subjects with mild or moderate back pain that was tolerable without any medical treatments were included. The symptoms and histories were self-reported by the volunteers. In the examinations, all subjects were confirmed to have no spinal diseases except for IVD degeneration and mild bulging discs. No subjects had spinal canal stenosis or foraminal stenosis. A total of 96 IVDs at L2–3, L3–4, L4–5, and L5–S1 were analyzed. The IVD at L1–2 was not included in the B₀ shimming because of the difficulty in conducting homogeneous shimming over the large area. The study was approved by the institutional review board of Kyushu University Hospital, and written informed consent was obtained from all subjects.

MR Imaging

MR imaging was performed on a 3T clinical scanner (Achieva 3.0TX; Philips Healthcare, Best, the Netherlands) equipped with a second-order shim, using the posterior part of a 32-channel cardiac coil for signal reception and 2-channel parallel transmission via the body coil for radiofrequency transmission. The acquisition software was modified to alternate the operation of the 2 transmission channels during the radiofrequency saturation pulse. The alternate activation of the 2 transmission channels enables long quasicontinuous radiofrequency saturation up to 5 seconds beyond the 50% duty cycle of a single radiofrequency amplifier.²³

Because all imaging pulses within a parallel transmission-based sequence use both amplifiers together in a standard way, there are no restrictions regarding the choice of MR image types (spin-echo/gradient-echo) because the full radiofrequency power range is available.²⁴ The acquisition software was also modified to allow a special radiofrequency shimming for the saturation homogeneity of the alternated saturation pulse.²³ Following the second-order B₀ shimming, 2D gagCEST imaging was conducted on a single slice corresponding to a midsagittal section of the lumbar spine, which was identified on multislice T2-weighted images using a saturation pulse with a duration of 1 second (50 ms \times 20 elements) with sinc-Gaussian-shaped pulses and a saturation power level corresponding to B₁ = 0.8 μ T.

To obtain a Z-spectrum, we repeated imaging at 25 saturation frequency offsets from $\omega = -3$ to +3 ppm with a step of 0.25 ppm as well as 1 far-off-resonant frequency ($\omega = -1560$ ppm) for signal normalization. The Z-spectrum shows the frequency-dependent saturation effects visualized by plotting the water saturation normalized by the signal without saturation as a function of saturation frequency.¹⁹

The other imaging parameters were as follows: fast spin-echo readout with driven equilibrium refocusing; echo-train length = 128, sensitivity encoding factor = 2, TR = 5500 ms, TE = 6 ms, matrix = 168 \times 167, slice thickness = 5 mm, FOV = 250 \times 250 mm, number of averages = 1, scan time = 2 minutes 34 seconds for 1 Z-spectrum with 25 saturation frequency offsets. A B₀ map for off-resonance correction was acquired separately with a 2D gradient-echo sequence (TR = 24 ms, TE = 8.1 ms, dual-echo, Δ TE = 10 ms, 16 averages, 1 minute 5 seconds) in the same geometry as that used for the gagCEST imaging, and this B₀ map was used for a point-by-point B₀ inhomogeneity correction.²⁴

For the T1- ρ mapping, T1- ρ prepared images using the 3D gradient-echo sequence were obtained in the sagittal plane with the following parameters: TR = 4.7 ms, TE = 2.4 ms, FOV = 230 × 230 mm, matrix = 128 × 128, slice thickness = 5 mm, flip angle = 35°, spin-lock pulses = 1/25/50/75/90 ms, spin-lock pulse frequency = 500 Hz, number of slices = 3, total scan time = 15 minutes. A low flip angle was used, but it did not affect the T1- ρ contrast because a shot interval of 6000 ms was set between each slice acquisition and the k -space was filled using low-to-high ordering. T2-weighted images in the sagittal planes were obtained with the following parameters: TR = 2815 ms, TE = 77 ms, FOV = 250 × 250 mm, slice thickness = 4 mm, number of slices = 13, matrix size = 320 × 242, number of acquisitions = 2, echo-train length = 21, and scan time = 2 minutes 35 seconds. The middle of the imaging slab for T1- ρ was set to correspond to the midsagittal section of the lumbar spine, which was identified on multislice T2-weighted images and was used for the gagCEST imaging.

Image Analyses

GagCEST Image Analysis. GagCEST imaging analysis was performed with the software program ImageJ (Version 1.43u; National Institutes of Health, Bethesda, Maryland). A dedicated ImageJ plug-in was built to analyze the Z-spectra and asymmetry of the magnetization transfer ratio (MTR_{asym}), equipped with a correction function for B_0 inhomogeneity using interpolation among the Z-spectral image data.²⁴ The local B_0 field shift in hertz was obtained from the B_0 map, which was created from dual-echo gradient-echo images ($\Delta TE = 10$ ms) according to the following equation: $\Delta B_0(x) = [Phase[TE2](x) - Phase[TE1](x)] / (TE2 - TE1) \times 2 \times \pi$, where $Phase[TEi](x)$ indicates the phases of the images with the TEs of TE1 or TE2 at position x in the radian, and TE1 and TE2 are given in seconds.²⁴ The $\Delta B_0(x)$ is the resulting B_0 map measured in hertz. Each voxel was corrected in image intensity for the nominal saturation frequency offset by Lagrange interpolation among the neighboring Z-spectral images. This procedure corresponds to a frequency shift along the saturation frequency offset axis according to the measured B_0 shift.

The Z-spectrum is a plot of signal intensity of bulk water as a function of the saturation frequency offset with respect to bulk water. The Z-spectrum was calculated as S_{sat}/S_0 , where S_{sat} and S_0 are the signal intensities obtained with and without selective saturation, respectively. To reduce these undesired contributions from the conventional magnetization transfer effect and the direct saturation of bulk water, we performed an asymmetry analysis of the Z-spectrum with respect to the water frequency as MTR_{asym} ²⁴:

$$MTR_{asym} = \frac{S_{sat}(-\alpha) - S_{sat}(+\alpha)}{S_0},$$

where $S_{sat}(-\alpha)$ and $S_{sat}(+\alpha)$ are the signal intensities obtained at $-\alpha$ and $+\alpha$ ppm, respectively. The gagCEST signal was defined as the mean of the MTR_{asym} from +0.5 to +1.5 ppm calculated as MTR_{asym} (3.5 ppm). An ROI (typical size = 50–75 mm²) was manually drawn by a board-certified neuroradiologist (O.T., with 17 years of experience) on one of the raw images to include the entire nucleus pulposus with reference to the T2-weighted images, avoiding obvious imaging artifacts.

T1- ρ Measurements. The T1- ρ maps were generated on a pixel-by-pixel basis using a custom-written software program in the IDL programming language (RSI, Boulder, Colorado) by mono-exponential fitting:

$$S(TSL) = S_0 \times \exp(-TSL / T1\rho),$$

where S_0 and $S(TSL)$ denote the equilibrium magnetization and the T1- ρ prepared magnetization with the spin-lock time (TSL), respectively. The ROIs used for the gagCEST measurements were copied and pasted onto the T1- ρ maps. Fine adjustments were made manually to correct slight locational differences.

Pfirrmann Grades. We classified the severity of the subjects' IVD degeneration into 5 grades with the Pfirrmann grading system, based on the structure, the distinction of the nucleus pulposus and annulus, the signal intensity, and the height of the IVD on the T2-weighted images.⁹ The Pfirrmann grade was determined by the consensus of 2 board-certified neuroradiologists (K.Y. with 15 years, and A.H., with 19 years of experience, respectively).

Statistical Analysis

All values are expressed as mean \pm SD. All comparisons were performed using a linear mixed-effects model, which accounts for multiple measurements per subject. In this model, subject identification was used as a random effect. The T1- ρ values or gagCEST signals were compared among the Pfirrmann grades using the linear mixed-effects model followed by the Bonferroni multiple comparison test. All statistical analyses were performed with commercially available software packages (GraphPad Prism software 5.0, GraphPad Software, San Diego, California; JMP13, SAS Institute, Cary, North Carolina). P values $< .05$ were considered significant.

RESULTS

The number of IVDs classified as Pfirrmann grades was as follows: grade I, $n = 29$; grade II, $n = 36$; grade III, $n = 11$; grade IV, $n = 16$; and grade V, $n = 4$.

Changes of Z-Spectra and MTR_{asym} in IVD Degeneration

The Z-spectra for each Pfirrmann grade showed that the IVDs with degeneration (ie, Pfirrmann grades III, IV, and V) had broader Z-spectra compared with the IVDs without degeneration (ie, Pfirrmann grades I and II) (Fig 1A). The MTR_{asym} for each Pfirrmann grade showed that MTR_{asym} reached its maximum value at 0.70 ppm in the grade I IVDs, 0.96 ppm in the grade II IVDs, and 0.96 ppm in the grade III IVDs, all of which were within the range of the frequency of hydroxyl protons (Fig 1B). The MTR_{asym} decreased as the grade advanced and approached the null at grade III; the values became negative at grades IV and V.

T1- ρ and GagCEST Signal per Pfirrmann Grade

The T1- ρ and gagCEST signal for each Pfirrmann grade are shown in Fig 2. The T1- ρ for the grade I IVDs (121.0 ± 13.8 ms) was significantly longer than those of the grade II (111.0 ± 11.5 ms, $P = .0023$), grade III (75.3 ± 7.8 ms, $P < .0001$), grade IV (65.0 ± 5.2 ms, $P < .0001$), and grade V IVDs (69.0 ± 6.4 ms, $P < .0001$). The T1- ρ for grade II was significantly longer than those for

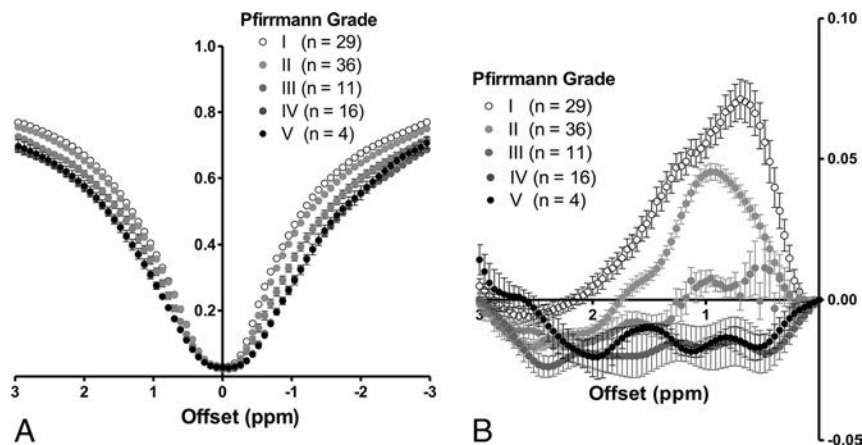


FIG 1. A, Z-spectra for each Pfirrmann grade. The IVDs with degeneration (Pfirrmann grades III, IV, and V) have broader Z-spectra compared with those without degeneration (Pfirrmann grades I and II). B, MTR_{asym} for each Pfirrmann grade. MTR_{asym} reaches its maximum value at 0.70 ppm in the 29 grade I IVDs, 0.96 ppm in the 36 grade II IVDs, and 0.96 ppm in the 11 grade III IVDs. The MTR_{asym} decreases as the grade advances and approaches the null at grade III; it shows negative values at grades IV ($n = 16$) and V ($n = 4$).

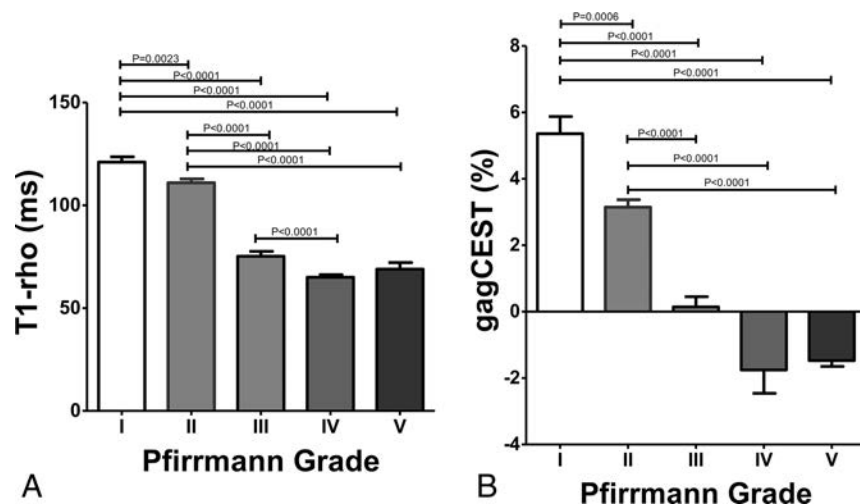


FIG 2. A, $T1-\rho$ (millisecond) at each Pfirrmann grade. $T1-\rho$ at grade I is significantly longer than those at grades II–V. $T1-\rho$ at grade II is significantly longer than those at grades III–V. $T1-\rho$ at grade III is significantly longer than at grade IV. B, GagCEST signal (percentage) at each Pfirrmann grade. The gagCEST signal at grade I is significantly higher than those at grades II–V. The GagCEST at grade II is significantly higher than those of grades III–V.

grades III–V ($P < .0001$, each). The $T1-\rho$ for grade III was significantly longer than for grade IV ($P < .0001$). $T1-\rho$ for grade I showed the widest variability in the measurements, which ranged from 101.1 to 157.0 ms. The gagCEST signal for the grade I IVDs ($5.36\% \pm 2.79\%$) was significantly higher than those for grade II ($3.15\% \pm 1.40\%$, $P = .0006$), grade III ($0.14\% \pm 1.03\%$, $P < .0001$), grade IV ($-1.75\% \pm 2.82\%$, $P < .0001$), and grade V ($-1.47\% \pm 0.36\%$, $P < .0001$). The gagCEST signal of grade II was significantly higher than those for grades III–V ($P < .0001$, each). Figure 3 shows a representative case with IVD degeneration. This IVD with degeneration (Pfirrmann grade IV) at L4–5 shows a shortened $T1-\rho$ and a lower gagCEST signal compared with the IVDs without degeneration (Pfirrmann grade I or II). The gagCEST for grade I showed the widest variability in the measurements, which ranged from -2.41% to 11.0% .

Relationship between the Pfirrmann Grade and $T1-\rho$ or the gagCEST Signal

The comparisons between the Pfirrmann grade and $T1-\rho$ or the gagCEST signal are shown in Fig 4. Significant inverse relationships were observed between the Pfirrmann grade and $T1-\rho$ ($P < .0001$) and between the Pfirrmann grade and gagCEST ($P < .0001$). The IVDs with more severe degeneration showed a shorter $T1-\rho$ and lower gagCEST signal.

Relationship between $T1-\rho$ and the gagCEST Signal

The correlation between $T1-\rho$ and the gagCEST signal is shown in Fig 5. A significant positive relationship ($P < .0001$) between $T1-\rho$ and the gagCEST signal was observed. The IVDs with a shorter $T1-\rho$ showed a lower gagCEST signal.

DISCUSSION

The results of this study demonstrate that the gagCEST signal in lumbar IVDs was correlated with both the qualitative visual assessment on T2-weighted images and the quantitative $T1-\rho$ measurement of IVD degeneration. There have been only a few studies that evaluated the degeneration of lumbar IVDs with gagCEST imaging in vivo at 3T.^{22,25,26} Haneder et al²² reported that the gagCEST signals of the nucleus pulposus were significantly lower in degenerative IVDs (mean Pfirrmann III and IV, 2.66 ± 2.48 and 1.47 ± 5.23) than in nondegenerative IVDs (mean Pfirrmann I and II, 7.06 ± 5.12 and 8.85 ± 4.47 ; $P < .001$), and they observed a significant correlation between the gagCEST signal and the Pfirrmann grades ($r = -0.449$).

Our present findings are consistent with those of the Haneder et al²² study, though some differences were observed in the measurements between the 2 studies. Such differences could be attributed to the different imaging schemes, especially regarding the saturation pulses or the postprocessing methods, including B_0 inhomogeneity correction. Compared with the weak linear correlation ($r = 0.299$) between the T2 values and gagCEST signals in their study, a stronger correlation was observed between the gagCEST signal and the $T1-\rho$ values ($r = 0.72$) in our study. This may be because $T1-\rho$ directly reflects the GAG content and thus can be more sensitive than T2 to the degeneration of IVDs. However, because we did not measure T2 values, the direct comparison between T2 and $T1-\rho$ values is necessary to confirm the higher sensitivity of $T1-\rho$ in a further study.

Several other interesting observations were made in our study: First, the Z-spectra were broader in the IVDs with degeneration

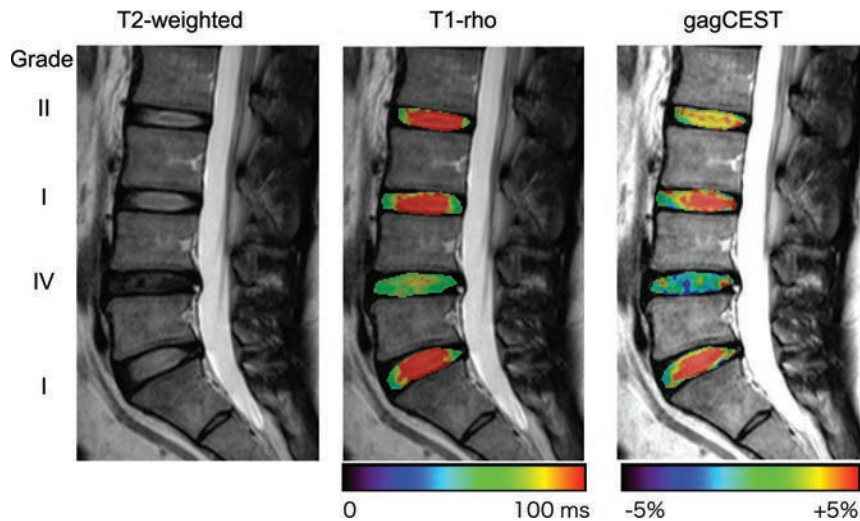


FIG 3. A representative case with IVD degeneration. This IVD with Pfirrmann grade IV degeneration at L4–5 shows a shortened T1- ρ and lower gagCEST signal compared with the other IVDs without degeneration (Pfirrmann grade I or II).

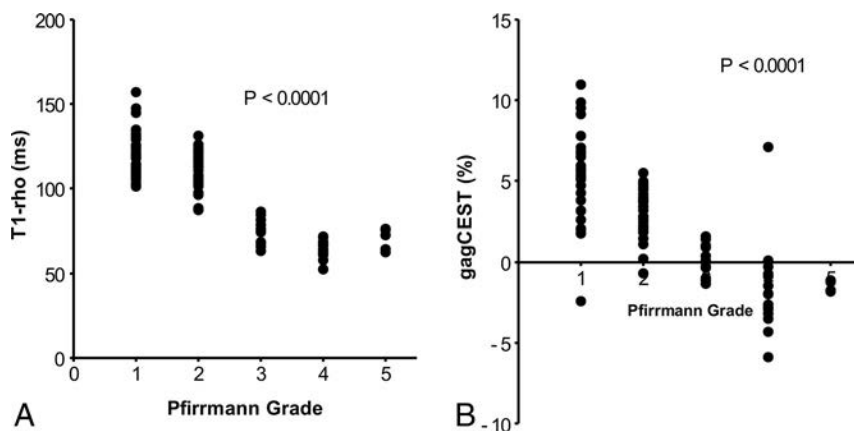


FIG 4. The relationship between the Pfirrmann grade and T1- ρ (A) or the gagCEST signal (B). Significant inverse relationships are observed between the Pfirrmann grade and T1- ρ and between the Pfirrmann grade and the gagCEST.

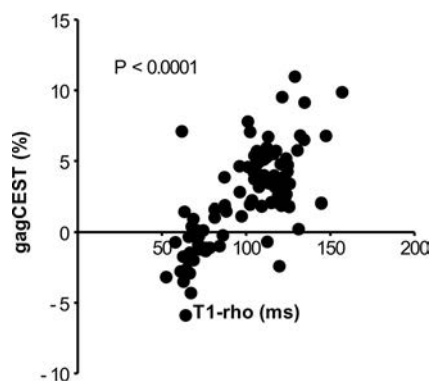


FIG 5. The relationship between T1- ρ and the gagCEST signal. A significant positive relationship is observed between the 2 parameters.

(grades III–V) compared with those without degeneration (grades I and II). This finding could be due to the reduced water content and collagen degeneration, which could result in T2 shortening and an increased magnetization transfer effect in the degenerative IVDs.

Second, the MTR_{asym} and gagCEST showed negative values in the IVDs with severe degeneration (ie, grades IV and V). The negative values might indicate that most of the CEST effects from hydroxyl protons included in the GAGs disappeared and the intrinsic nuclear Overhauser effect became dominant in the measured signals. Ling et al²⁰ showed that the nuclear Overhauser effect from the carbon-hydrogen bonds and *N*-acetyl groups of GAG gives rise to the magnetization transfer mechanism at -1.0 ppm and -2.6 ppm with respect to the bulk water. The nuclear Overhauser effect at -1.0 ppm could lead to the negative value of MTR_{asym} at 1.0 ppm when the CEST effects were reduced.

Third, although both T1- ρ and gagCEST were changed according to the degree of IVD degeneration, the percentage change between Pfirrmann grades I and II was larger in gagCEST (-57%) than in T1- ρ (-8%). This result might indicate that gagCEST imaging can sensitively detect the loss of GAGs at an early stage of IVD degeneration. Furthermore, both T1- ρ and gagCEST for Pfirrmann grade I showed the widest variability among all grades, though no obvious degeneration was identified on T2-weighted images. This finding may reflect that the T1- ρ and gagCEST could sensitively detect early degenerative changes that were not visible on T2-weighted images. Further investigations including histopathologic assessments are necessary to prove this theory.

From a technical point of view, the correction of B_0 inhomogeneity in the postprocessing is of great importance in gagCEST imaging because the resonance frequency of exchangeable protons (around 1 part per million) is critically close to that of bulk water; thus, even a small B_0 field difference and a resulting shift in the Z-spectrum may cause a large change in MTR_{asym} . Kim et al^{21,27} demonstrated the efficacy of the B_0 correction method called “water saturation shift referencing (WASSR)” in gagCEST imaging of lumbar IVDs. The advantages of WASSR include the centering of the Z-spectrum with polynomial fitting in a relatively short scan time, subhertz accuracy, and identical field reference conditions with CEST imaging due to the use of the same acquisition scheme. We alternatively used the correction with a separately acquired B_0 map obtained from the phase images of a dual-echo gradient-echo sequence.²⁴ This scan also can be acquired in a short time (approximately 1 minute) and easily implemented on clinical scanners.

B_0 shift correction using a B_0 map is a simple and robust method because this centering method is not affected by the magnetization transfer effect and direct saturation of water.²⁴ The

utility of B_0 map–based B_0 inhomogeneity correction proved to be accurate and reproducible.²⁴ However, the accuracy of a B_0 map in gagCEST imaging could be largely affected by ΔTE .²⁸ Wei et al²⁸ demonstrated that the dual gradient-echo method with longer ΔTE values (>8 ms) has an excellent correlation with the Z-spectrum method for gagCEST imaging at 3T. In the present study, the ΔTE was set at 10 ms, which might contribute to the accurate B_0 correction without the WASSR method.

There were limitations in this study. A reference for the absolute concentration/content of GAGs in IVDs was lacking because no specimens were obtained from the subjects. Instead, T1- ρ was used as an image-based reference standard for GAG content. The number of subjects was relatively small—especially those with degenerative IVDs—because all subjects were recruited as volunteers. The gagCEST images were obtained in a single sagittal slice; an axial slice for each IVD was not obtained to reduce the total scan time. Therefore, the distribution of GAGs in the axial plane in each IVD was not evaluated. 3D volume coverage with an efficient self- B_0 -correcting CEST method using fast spin-echo Dixon imaging is now available and is expected to overcome this issue.^{29,30} The imaging features commonly evaluated on T2-weighted images are not always related to the patient’s clinical symptoms. It is common to see IVD degeneration in asymptomatic patients, and vice versa. The discrepancy might be partly due to the inability of T2-weighted images to detect PGs and GAGs in IVDs. Therefore, to date, therapeutic interventions have not been based solely on imaging findings. At this moment, it is not clear whether the loss of the gagCEST signal is associated with a patient’s current symptoms or can predict future symptom development because there is no criterion standard to evaluate early IVD degeneration. The relationship between gagCEST imaging findings and the current or future symptoms in patients with IVD degeneration will be investigated in larger cohorts in further studies.

CONCLUSIONS

Our present findings demonstrated that the gagCEST signals of IVDs were reduced as degeneration progressed. The gagCEST signal was correlated with the Pfirrmann grades and the T1- ρ values in IVD degeneration. GagCEST imaging could be a reliable and quantitative imaging technique for assessing IVD degeneration. This method could be of great utility for the detection of the early degeneration of IVDs and for monitoring the therapeutic response to emerging regeneration therapies.

Disclosures: Jochen Keupp—UNRELATED: Employment: Philips Research. Masami Yoneyama—UNRELATED: Employment: Philips Japan.

REFERENCES

- Allegri M, Montella S, Salici F, et al. **Mechanisms of low back pain: a guide for diagnosis and therapy.** *F1000Res* 2016;5:1530 CrossRef Medline
- Manchikanti L, Singh V, Pampati V, et al. **Evaluation of the relative contributions of various structures in chronic low back pain.** *Physician* 2001;4:308–16 Medline
- Phillips FM, An H, Kang JD, et al. **Biologic treatment for intervertebral disc degeneration: summary statement.** *Spine (Phila Pa 1976)* 2003;28:S99 Medline
- Vadalà G, Sowa GA, Kang JD. **Gene therapy for disc degeneration.** *Expert Opin Biol Ther* 2007;7:185–96 CrossRef Medline
- Carl A, Ledet E, Yuan H, et al. **New developments in nucleus pulposus replacement technology.** *Spine J* 2004;4(6 Suppl):325S–29S Medline
- Adams MA, Roughley PJ. **What is intervertebral disc degeneration, and what causes it?** *Spine (Phila Pa 1976)* 2006;31:2151–61 CrossRef Medline
- Lyons G, Eisenstein SM, Sweet MB. **Biochemical changes in intervertebral disc degeneration.** *Biochim Biophys Acta* 1981;673:443–53 CrossRef Medline
- Urban JP, McMullin JF. **Swelling pressure of the intervertebral disc: influence of proteoglycan and collagen contents.** *Biorheology* 1985; 22:145–57 CrossRef Medline
- Pfirrmann CW, Metzdorf A, Zanetti M, et al. **Magnetic resonance classification of lumbar intervertebral disc degeneration.** *Spine (Phila Pa 1976)* 2001;26:1873–78 CrossRef Medline
- Li X, Cheng J, Lin K, et al. **Quantitative MRI using T1 ρ and T2 in human osteoarthritic cartilage specimens: correlation with biochemical measurements and histology.** *Magn Reson Imaging* 2011; 29:324–34 CrossRef Medline
- Blumenkrantz G, Zuo J, Li X, et al. **In vivo 3.0-Tesla magnetic resonance T1rho and T2 relaxation mapping in subjects with intervertebral disc degeneration and clinical symptoms.** *Magn Reson Med* 2010;63:1193–200 CrossRef Medline
- Antoniu J, Epure LM, Michalek AJ, et al. **Analysis of quantitative magnetic resonance imaging and biomechanical parameters on human discs with different grades of degeneration.** *J Magn Reson Imaging* 2013;38:1402–14 CrossRef Medline
- Paul CPL, Smit TH, de Graaf M, et al. **Quantitative MRI in early intervertebral disc degeneration: T1rho correlates better than T2 and ADC with biomechanics, histology and matrix content.** *PLoS One* 2018;13:e0191442 CrossRef Medline
- Menezes NM, Gray ML, Hartke JR, et al. **T2 and T1rho MRI in articular cartilage systems.** *Magn Reson Med* 2004;51:503–09 CrossRef Medline
- Takayama Y, Hatakenaka M, Tsushima H, et al. **T1 ρ is superior to T2 mapping for the evaluation of articular cartilage denaturalization with osteoarthritis: radiological-pathological correlation after total knee arthroplasty.** *Eur J Radiol* 2013;82:e192–98 CrossRef Medline
- Johannessen W, Auerbach JD, Wheaton AJ, et al. **Assessment of human disc degeneration and proteoglycan content using T1rho-weighted magnetic resonance imaging.** *Spine (Phila Pa 1976)* 2006; 31:1253–57 CrossRef Medline
- Ward KM, Aletras AH, Balaban RS. **A new class of contrast agents for MRI based on proton chemical exchange dependent saturation transfer (CEST).** *J Magn Reson* 2000;143:79–87 CrossRef Medline
- Woods M, Woessner DE, Sherry AD. **Paramagnetic lanthanide complexes as PARACEST agents for medical imaging.** *Chem Soc Rev* 2006;35:500–11 CrossRef Medline
- van Zijl PC, Yadav NN. **Chemical exchange saturation transfer (CEST): what is in a name and what isn't?** *Magn Reson Med* 2011;65: 927–48 CrossRef Medline
- Ling W, Regatte RR, Navon G, et al. **Assessment of glycosaminoglycan concentration in vivo by chemical exchange-dependent saturation transfer (gagCEST).** *Proc Natl Acad Sci U S A* 2008;105:2266–70 CrossRef Medline
- Kim M, Chan Q, Anthony MP, et al. **Assessment of glycosaminoglycan distribution in human lumbar intervertebral discs using chemical exchange saturation transfer at 3 T: feasibility and initial experience.** *NMR Biomed* 2011;24:1137–44 CrossRef Medline
- Haneder S, Apprich SR, Schmitt B, et al. **Assessment of glycosaminoglycan content in intervertebral discs using chemical exchange saturation transfer at 3.0 Tesla: preliminary results in patients with low-back pain.** *Eur Radiol* 2013;23:861–68 CrossRef Medline

23. Keupp J, Baltes C, Harvey P, et al. **Parallel RF transmission based MRI technique for highly sensitive detection of amide proton transfer in the human brain at 3T.** In: *Proceedings of the Annual Meeting and Exhibition of the International Society for Magnetic Resonance in Medicine*, Montréal, Québec, Canada. May 7–13, 2011;19:710
24. Togao O, Hiwatashi A, Keupp J, et al. **Scan-rescan reproducibility of parallel transmission based amide proton transfer imaging of brain tumors.** *J Magn Reson Imaging* 2015;42:1346–53 CrossRef Medline
25. Müller-Lutz A, Schleich C, Pentang G, et al. **Age-dependency of glycosaminoglycan content in lumbar discs: a 3T gagCEST study.** *J Magn Reson Imaging* 2015;42:1517–23 CrossRef Medline
26. Schleich C, Müller-Lutz A, Matuschke F, et al. **Glycosaminoglycan chemical exchange saturation transfer of lumbar intervertebral discs in patients with spondyloarthritis.** *J Magn Reson Imaging* 2015; 42:1057–63 CrossRef Medline
27. Kim M, Gillen J, Landman BA, et al. **Water saturation shift referenc-**
ing (WASSR) for chemical exchange saturation transfer (CEST) ex-
periments. *Magn Reson Med* 2009;61:1441–50 CrossRef Medline
28. Wei W, Jia G, Flanigan D, et al. **Chemical exchange saturation transfer MR imaging of articular cartilage glycosaminoglycans at 3 T: accuracy of B0 field inhomogeneity corrections with gradient echo method.** *Magn Reson Imaging* 2014;32:41–47 CrossRef Medline
29. Keupp J, Eggers H. **CEST-DIXON MRI for sensitive and accurate measurement of amide proton transfer in humans at 3T.** In: *Proceedings of the Annual Meeting of the International Society for Magnetic Resonance in Medicine and European Society for Magnetic Resonance in Medicine and Biology*. Stockholm, Sweden. May 1–7, 2010
30. Togao O, Keupp J, Hiwatashi A, et al. **Amide proton transfer imaging of brain tumors using a self-corrected 3D fast spin-echo Dixon method: comparison with separate B0 correction.** *Magn Reson Med* 2017;77:2272–79 CrossRef Medline

Efficacy and Safety of Percutaneous Microwave Ablation and Cementoplasty in the Treatment of Painful Spinal Metastases and Myeloma

M.A. Khan, G. Deib, B. Deldar, A.M. Patel, and J.S. Barr

ABSTRACT

BACKGROUND AND PURPOSE: Painful spinal metastases are a common cause of cancer-related morbidity. Percutaneous ablation presents an attractive minimally invasive alternative to conventional therapies. We performed a retrospective review of 69 patients with 102 painful spinal metastases undergoing microwave ablation and cementoplasty to determine the efficacy and safety of this treatment.

MATERIALS AND METHODS: Procedures were performed between January 2015 and October 2016 with the patient under general anesthesia using image guidance for 102 spinal metastases in 69 patients in the following areas: cervical ($n = 2$), thoracic ($n = 50$), lumbar ($n = 34$), and sacral ($n = 16$) spine. Tumor pathologies included the following: multiple myeloma ($n = 10$), breast ($n = 27$), lung ($n = 12$), thyroid ($n = 6$), prostate ($n = 5$), colon ($n = 4$), renal cell ($n = 3$), oral squamous cell ($n = 1$), and adenocarcinoma of unknown origin ($n = 1$). Procedural efficacy was determined using the visual analog scale measured preprocedurally and at 2–4 weeks and 20–24 weeks postprocedure. Tumor locoregional control was assessed on follow-up cross-sectional imaging. Procedural complications were recorded to establish the safety profile.

RESULTS: The median ablation time was 4 minutes 30 seconds \pm 7 seconds, and energy dose, 4.1 \pm 1.6 kJ. Median visual analog scale scores were the following: 7.0 \pm 1.8 preprocedurally, 2 \pm 1.6 at 2–4 weeks, and 2 \pm 2.1 at 20–24 weeks. Eight patients died within 6 months following the procedure. Follow-up imaging in the surviving patients at 20–24 weeks demonstrated no locoregional progression in 59/61 patients. Two complications were documented (S1 nerve thermal injury and skin burn).

CONCLUSIONS: Microwave ablation is an effective and safe treatment technique for painful spinal metastases. Further studies may be helpful in determining the role of microwave ablation in locoregional control of metastases.

ABBREVIATIONS: MWA = microwave ablation; ODI = Oswestry Disability Index; Pre = preprocedure; RT = radiation therapy; VAS = visual analog scale

Bone metastases are common in patients with advanced cancer and are the greatest contributor to cancer-related pain, with severe pain in up to 75% of patients with bone metastases. This pain is often unremitting and may severely affect the patient's quality of life.¹ Patients with metastatic disease are often undertreated for pain.^{2–4} Various treatment options exist for patients with painful spinal metastases, including surgery, radiation therapy, and percutaneous interventions. Historically, radiation therapy has been the standard of care for painful osseous metastases. However, approximately 40% of treated patients do not experience adequate pain relief.^{5,6} In addition, almost half of the re-

maining patients have recurrent pain at a median of 16 weeks following treatment.⁵

Management of metastatic spine disease requires multidisciplinary input. Treatment options include not only continually evolving medical therapy regimens, surgical techniques, and radiation technologies but also emerging minimally invasive interventions. Treatment recommendations should be based on collaborative recommendations of specialists as outlined by the Metastatic Spine Disease Multidisciplinary Working Group, which has provided a consensus document detailing the evidence supporting their algorithms.⁷

Image-guided ablative therapies demonstrate potential advantages compared with surgery and radiation therapy, including reduced morbidity, lower procedural cost, suitability for real-time imaging guidance, the ability to perform therapy in an outpatient setting, synergy with other cancer treatments, repeatability, and short procedural time.^{8–10} Ablation (alone or in combination with cementoplasty) can achieve a number of objectives: palliative pain control, skeletal stabilization, and tumor control. In most

Received November 10, 2017; accepted after revision March 6, 2018.

From the Department of Radiology (M.A.K., G.D.), Johns Hopkins University, Baltimore, Maryland; St. George's University of London (B.D.), London, UK; Departments of Radiology (A.M.P.) and Orthopedics (J.S.B.), University of Mississippi Medical Centre, Jackson, Mississippi.

Please address correspondence to Gerard Deib, MD, Johns Hopkins Hospital and Health System, 601 N Caroline St, Baltimore, MD 21287; e-mail: gdeib1@jhmi.edu; @gerarddeib

<http://dx.doi.org/10.3174/ajnr.A5680>

cases, an improvement in quality of life and prevention of morbidity would be the primary goals, rather than tumor control, especially in sick patients with limited life expectancy and poor functional status, who are often poor surgical candidates.¹¹

An ever-expanding array of percutaneous ablation technologies is being used in the treatment of painful neoplastic lesions. These modalities include cryoablation, ethanol ablation, laser ablation, MRI-guided focused sonography ablation, and radiofrequency ablation.^{8,10-12}

Microwave ablation (MWA) offers several potential advantages over other ablative modalities that may increase its effectiveness in the treatment of tumors, including larger tumor ablation volumes with a single probe, faster ablation times, improved convection profile, and optimal heating of necrotic masses. MWA has consistently higher intratumoral temperatures than other heat-based therapies. Like cryoablation, MWA can be performed with multiple applicators.¹³⁻¹⁶ However, MWA is a relatively new innovation, and literature demonstrating its clinical efficiency in treating spinal tumors is relatively sparse, with only 2 retrospective studies published to date (describing 20 and 37 lesions in 17 and 35 patients, respectively).^{17,18} The authors therefore aimed to present a larger retrospective series to demonstrate the efficacy and safety of microwave ablation and cementoplasty.

In our practice, polymethylmethacrylate is administered following ablation of spinal tumors. This is to prevent pathologic fractures (either because of metastatic disease directly or following ablative therapy), which may be a significant source of further pain from metastatic disease. In addition to alleviating pain, this may be helpful in preventing associated morbidities such as progressive kyphosis and respiratory compromise or damage to adjacent spinal nerve roots.

The authors report the results of a retrospective review to evaluate the safety and efficacy of MWA and cementoplasty for treating painful spinal metastases. To our knowledge, this series represents the largest study yet published in the literature and serves to confirm or refute findings from previously published smaller series.

We hypothesized that MWA ablation and cementoplasty would result in markedly reduced pain scores. We further hypothesized that a substantial proportion of our patients would demonstrate no evidence of disease progression on 6-month follow-up cross-sectional imaging.

The purpose of this study was to determine whether treatment of metastatic disease to the vertebral body with MWA and cementoplasty would significantly decrease visual analog scale (VAS) pain scores at 6 months. The secondary purpose of this study was to determine disease progression in the treated vertebral body in patients with oligometastatic disease at 6 months with cross-sectional imaging.

MATERIALS AND METHODS

Full Johns Hopkins Hospital institutional review board approval was obtained for retrospective analysis. Informed consent for the study was waived and Health Insurance Portability and Accountability Act compliance was guaranteed. Medical records, including demographics and pain scores, were obtained and reviewed.

Efficacy of treatment was defined by accomplishing primary and secondary objectives. The primary objective was pain reduc-

tion after microwave ablation and cementoplasty. The secondary objective was effective disease control, based on the absence of locoregional disease progression on follow-up cross-sectional imaging evaluation. Complications were reviewed in this cohort of patients to assess the safety of the procedure.

Patient Information

A search was performed using the keywords “microwave ablation,” “cementation,” “cementoplasty,” “kyphoplasty,” and “vertebroplasty” on all files in the Electronic Medical Record of our institution from January 2015 to October 2016. On the basis of this search and application of the inclusion and exclusion criteria detailed below, appropriate records were accessed.

A total of 105 patients were found in the search of our institution. These patients had all been screened at the multidisciplinary conference. After we applied the inclusion and exclusion criteria, 69 patients (36 men, 33 women) with spinal metastases treated with microwave ablation and cementoplasty from January 2015 to October 2016 were included in this retrospective review. The mean age of the patients was 56.

Inclusion Criteria

We included the following:

A) Patients with intractable pain (VAS > 4) from solitary or multiple sites of disease that resulted in a return visit to the oncologist (intractable pain was defined as unrelenting pain despite treatment with narcotic anesthesia).

B) Patients who either

- 1) Had persistent or recurrent pain after radiation therapy (RT),
- 2) Were not candidates for RT,
- 3) Had declined RT,
- 4) Had tumor considered percutaneously accessible by imaging.

Exclusion Criteria

We excluded the following:

A) Patients with an alternative explanation for pain based on correlation between clinical presentation and spine MR imaging,

B) Concurrent systemic illness,

C) Tumors with retropulsion of the posterior cortices, epidural extension, and/or cord compression,

D) Patients who had tumors whose margins approximated nerve roots or the spinal canal.

Twenty-eight patients who had undergone prior radiation therapy with continued pain were included in the study.

All patients had prior cross-sectional imaging (CT, MR imaging, and/or PET/CT). Sixty-nine patients had complete assessment of their pain in the interventional radiology clinic of our department using the visual analog scale pain score preprocedurally and at 2–3 weeks ($n = 69$) and 20–24 weeks ($n = 61$) post-procedure. In addition, 52 patients were assessed using the Oswestry Disability Index (ODI) score chart before the procedure and at similar intervals following it, with 17 patients refusing to use the ODI preset questionnaire for ODI determination.

Patients had been deemed appropriate for image-guided ablation and cementation in the multidisciplinary conference after discussion and review of cross-sectional imaging, which included a combination of CT, PET/CT, and MR imaging. All cross-

tional studies were evaluated by a noninterventionalist, board-certified, fellowship-trained neuroradiologist and were subsequently reviewed by a board-certified, fellowship-trained spine interventional radiologist at the multidisciplinary tumor board.

On the basis of cross-sectional CT imaging, lesions were classified into 65 lytic, 13 sclerotic, and 24 mixed lytic/sclerotic. The tumor area ranged between 0.75 to 15.0 cm² (mean, 3.6 ± 2.2 cm²) based on CT and MR imaging review by the interventional radiologist. Figure 1 demonstrates an example of a lytic osseous metastasis in a patient with metastatic breast carcinoma.

Procedural Details

Microwave ablation was performed using the AveCure microwave ablation system (MedWaves, San Diego, California) under CT (16-slice Somatom Sensation; Siemens, Erlangen, Germany) or fluoroscopic (Axiom Artist dBA Bi-Plane; Siemens) guidance. Most procedures were performed as outpatient procedures (*n* = 63; 91.3%) with 4-hour postprocedural observation. Patients whose lesions were within 5 mm of nerve roots (*n* = 6; 8.7%) were observed for 23 hours. All procedures were performed with the patient under general anesthesia and prone. Lesions were measured in 3 planes on cross-sectional imaging before the procedure. These measurements were then used as a basis for calculating the volume (and correlating energy deposition and time parameters) for ablation as detailed in Table 1. The cross-sectional imaging

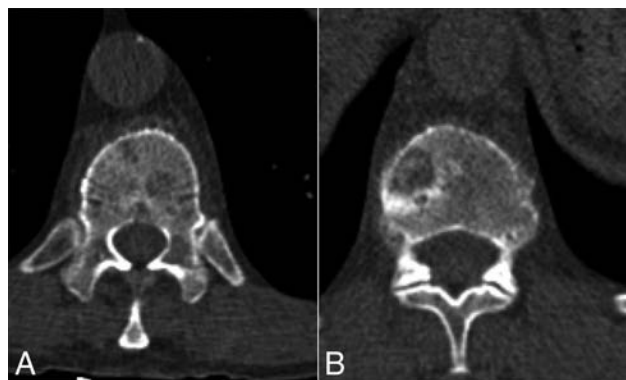


FIG 1. Axial CT images with the patient supine demonstrate lytic osseous metastasis in the T11 (A) and T12 (B) vertebral bodies in a 60-year-old woman with metastatic breast carcinoma.

was used in procedural planning, including making note of the proximity of tumoral margins to critical anatomic landmarks.

Local anesthesia (lidocaine hydrochloride 1%) was administered with a 3.5-inch 22-g spinal needle used to infiltrate the periosteum to ease the postprocedural pain followed by soft-tissue blunt dissection. An 11-g iVAS access cannula (Stryker Neurovascular, Kalamazoo, Michigan) was inserted via a posterior or posterolateral approach (either transpedicular or transcostovertebral) under image guidance and was positioned at the proximal edge of the tumor. A 13-g hand drill was then coaxially inserted into the tumor and advanced to its anterior edge. Once this position was confirmed, core biopsies were obtained and sent to the laboratory.

Subsequently, a single 14- or 16-g AveCure microwave ablation antenna (MedWaves, 1.8-mm, 20-cm-long) was coaxially inserted into the tumor. Placement of the hand drill and the ablation antenna is demonstrated in Fig 2. The size of the ablation antenna was determined on the basis of the calculated target lesion size, with the ablation zone calculated as 2 mm beyond the actual size of the target lesion to achieve adequate control. To calculate the appropriate cut-off temperature and energy deposition, we took the following approach: anteroposterior, lateral, and transverse measurements of the probe position relative to the vertebral margins. These measurements were then used to determine the appropriately sized antenna. Energy in kilojoules and temperature in centigrade were subsequently calculated using the vendor's standard algorithm. The team was then able to achieve these end points with our ablation.

A 13-g Trovex curved needle (Stryker) was used to access lesions along the posterior aspect of vertebral body; then, a 16-g 90-cm flexible AveCure microwave antenna (Medwaves) was advanced into an adequate position for ablation. An automated drill (11-g Arrow On-Control; Teleflex, Morrisville, North Carolina) and a biopsy cannula were used to access mixed and dense sclerotic lesions with subsequent placement of the microwave probe.

For fluoroscopically guided procedures in which there was a small ablation, conebeam CT (InSpace Dyna CT; Siemens) was performed to confirm the antenna position through the lesion. Where there were large lesions encompassing two-thirds of the vertebral body, a bipedicular approach was used with overlapping ablation zones. For CT-guided procedures, the antenna position was always confirmed under CT. The burn size was overestimated by only 2 mm in all directions in patients with oligometastatic disease (to achieve better disease control). However, the accuracy

Table 1: Tabular results of Mann-Whitney U paired tests between VAS and ODI data collected Pre and at 2–4 and 20–24 weeks, respectively

Table Analyzed	Mann-Whitney Test of VAS Pre–2/4 weeks	Mann-Whitney Test of VAS Pre–20/24 weeks	Mann-Whitney Test of ODI Pre–2/4 weeks	Mann-Whitney Test of ODI Pre–20/24 weeks
Column B versus Column A	VAS 2–4 weeks	VAS 20–24 weeks	ODI 2–4 weeks	ODI 20–24 weeks
Mann-Whitney test	VAS Pre	VAS Pre	ODI Pre	ODI Pre
<i>P</i> value	<.0001	<.0001	<.0001	<.0001
Sum of ranks in columns A and B	5526, 1978	5478, 2025	2665, 1252	2672, 1244
Mann-Whitney <i>U</i>	86.5	134	261.5	254
Median of column A	7, <i>n</i> = 61	7, <i>n</i> = 61	46, <i>n</i> = 44	46, <i>n</i> = 44
Median of column B	2, <i>n</i> = 61	2, <i>n</i> = 61	24, <i>n</i> = 44	24, <i>n</i> = 44
Difference: actual	–5	–5	–22	–22
Difference: Hodges-Lehmann	–5	–5	–22	–22
Exact 95.01% CI of difference	–5 to –4	–5 to –4	–28 to –16	–28 to –16

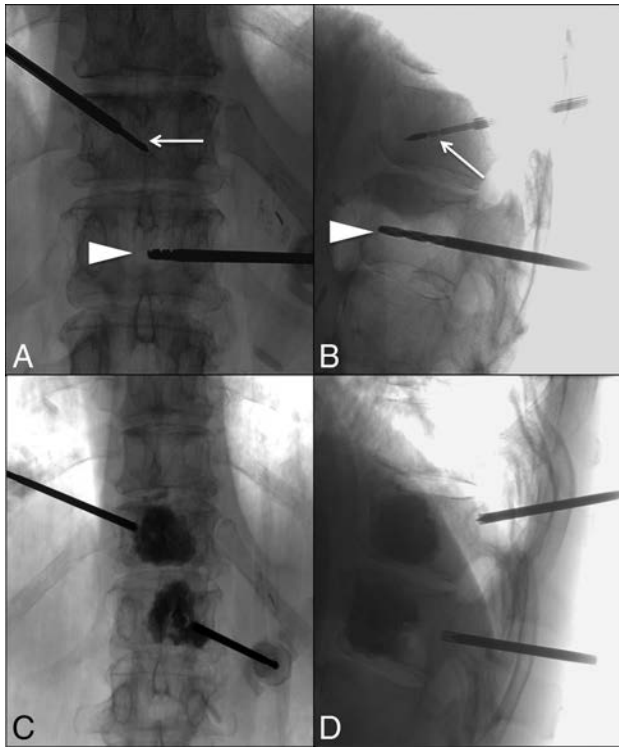


FIG 2. Intraoperative anteroposterior (A) and lateral (B) fluoroscopic images of T11- and T12-level microwave ablation. A microwave ablation probe (arrow) and a manual drill (arrowhead) have been advanced through access cannulas into the anterior aspect of the T11 and T12 vertebral bodies, respectively. Anteroposterior (C) and lateral (D) fluoroscopic images of the T11 and T12 vertebral bodies post-microwave ablation and cement augmentation. The access cannulas have been retracted into the pedicles.

of the gross extent of induced coagulation was limited by both spatial and contrast resolution to approximately 2–3 mm, and imaging findings are only a rough guide to the success of the ablation therapy because microscopic foci of residual disease cannot be expected to be identified with standard imaging.

Thermocouples were not placed in our series because lesions with a breach of the posterior cortex were excluded from the study, but whenever the ablation zone was close to the neural element (<5 mm), we used repeat short ablation cycles to control diffusion of the heat zone without decreasing the effectiveness of ablation, a technique used by the spine interventionalist.¹⁹ However, use of thermocouples and somatosensory evoked potentials/motor-evoked potentials monitoring is advised to avoid thermal injury to the spinal cord or spinal nerves in cases in which these structures are approximated. We used hydrodissection in 1 patient with tumor close to the S1 nerve root with instillation of saline around the nerve.

Vertebral cement augmentation was performed for all lytic and mixed osseous tumors ($n = 89$) after technically successful ablation, which was defined by the ability to place the microwave antenna successfully in the center of the lesion and achieve the target ablation power based on the size of the target lesion. No cementation was performed for purely sclerotic lesions. Patients were observed for 3–4 hours in the post anesthesia care unit for any immediate postprocedural complications. Patients were contacted 24–48 hours following their procedures to inquire about

their well-being. Any patients who reported new symptoms were brought into the clinic and reviewed.

Statistical Analysis

Mann-Whitney U tests and graphs were constructed for both ODI and VAS data preprocedurally, against data at 2–4 weeks and 3–6 months, respectively. The data consisted of the following: 69 patients with VAS and 52 patients with ODI scores obtained preprocedurally, at 2–4 weeks, and 20–24 weeks. Ablation time, temperature, energy, and duration of exposure were included as predictors in all models. Marginal plots were then constructed from the mixed models to visually compare the effects of predictors on outcomes. All statistical analyses were completed with GraphPad Prism software 7.0 (GraphPad Software, San Diego, California).

RESULTS

Technically successful ablations were achieved in 100% of patients. Technical success was defined as achieving a temperature of >80°C, with deposition of calculated energy based on the size of the target lesion with minimal-to-no reverse power.

The median ablation time was 4:30 ± 0.07 minutes (range, 3:00–10:34 minutes). The median energy dose received was 3.9 ± 1.6 kJ, and power was 13.28 ± 3.75 W. The preprocedural median VAS score was 7.0 ± 1.8. The median postprocedural VAS scores were 2 ± 1.6 at 2–4 weeks and 2 ± 2.1 at 20–24 weeks. A 4-point reduction in the VAS score was considered effective.

Follow-up imaging with CT of the chest, abdomen, and pelvis ($n = 34$) and PET/CT imaging²⁰ at 6 months ($n = 61$) demonstrated stable disease in 59/61 patients (96.7%). There were 2 procedure-related complications (2.9%) (S1 nerve thermal injury with the patient having severe pain radiating to the leg in an S1 distribution with three-fifths motor strength, and a skin burn over the target lesion). Eight patients died within 6 months of the procedure.

The median Oswestry Disability Index was 46 ± 17.9 preprocedurally and 24 ± 17.1 and 24 ± 18.8 at 2–4 weeks and 20–24 weeks postprocedurally, respectively. Box-and-whisker plots for VAS and ODI scores are shown in Fig 3.

A median difference of -22 ± 12.8 and -5 ± 2.0 ODI and VAS points, respectively, was observed in the interval between preprocedure (Pre) and 3–6 months postprocedure. Most of the treated patients reported a decreased dosage or frequency of narcotic analgesic use. Changes in the VAS score are demonstrated in Fig 4. Tabular results of Mann-Whitney U paired tests between VAS and ODI data collected preprocedure and at 2–4 and 20–24 weeks are detailed in Table 1.

Locoregional control at 20–24 weeks was achieved in all patients in the subgroup in our series who had oligometastatic disease ($n = 22$). Locoregional control was defined as stable disease at the treated level using a combination of conventional CT, PET/CT, and spine MR imaging. For the patient to be deemed stable, the imaging study was required to demonstrate the ablation zone encompassing the targeted area of tumor with no evidence of disease progression at the treated site.

Descriptive statistics showing quartiles, median, mean, SD, standard error of the mean, confidence intervals, and mean ranks for each dataset are detailed in Table 2.

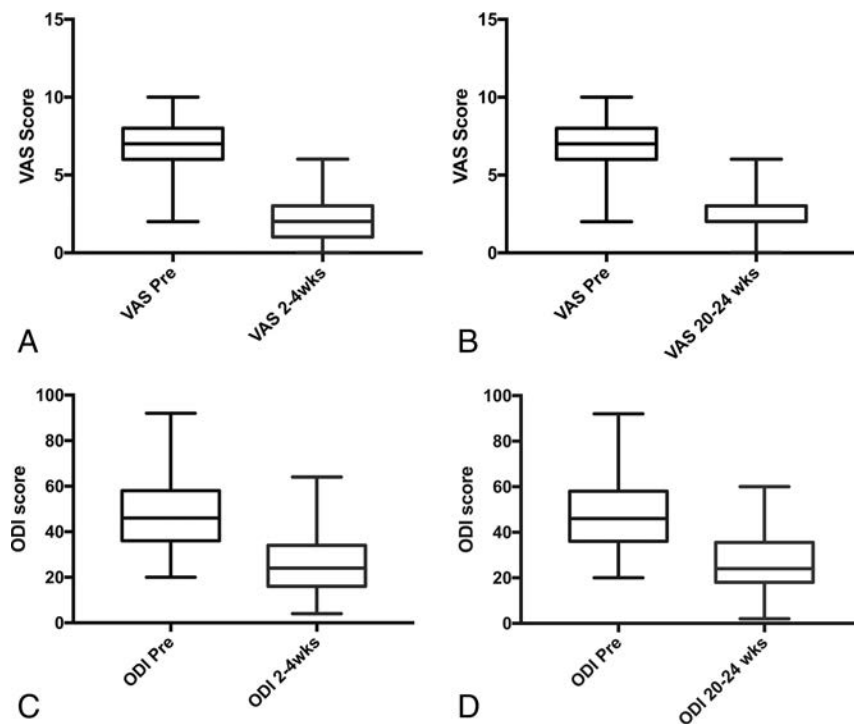


FIG 3. A, Box-and-whisker plots for VAS Pre and 2- to 4-week datasets. B, Box-and-whisker plots for VAS Pre and 20- to 24-week datasets. C, Box-and-whisker plots for ODI Pre and 2- to 4-week datasets. D, Box-and-whisker plots for ODI Pre and 20- to 24-week datasets.

DISCUSSION

As overall survival of cancer patients improves and medical imaging becomes increasingly ubiquitous, the number of patients with osseous metastases continues to grow. Microwave ablation represents a relatively new technique in the minimally invasive armamentarium that will likely play an increasing role in the palliative and potentially curative treatment of patients with painful spinal metastases. With this in mind, we reviewed results of microwave ablation and cementoplasty at our institution in the context of the existing scientific literature.

Microwave ablation of tumor cells is primarily achieved using electromagnetic methods, resulting in tumor destruction using devices with frequencies ranging between 900 and 2500 MHz. Electromagnetic microwaves heat matter by agitating water molecules in the affected and surrounding tissue, producing friction and heat, which induce cellular death via coagulation necrosis.⁹ Microwave ablation is more effective in high-impedance tissues like bone because poor thermal conduction in bone is a limiting factor in radiofrequency ablation. Osseous relative permeability and low conduction help microwaves penetrate deeper and are more effective in thermal ablation compared with radiofrequency ablation.

Radiofrequency ablation, cryoablation, MRI-guided focused ultrasound, and microwave are all being used in clinical practice to treat patients with painful osseous lesions, particularly metastases, for both pain relief and as a useful adjunct therapy for local tumor control.^{8,10-12} The heating of tissues is typically much faster and more precise with microwave ablation and causes better and complete coagulation necrosis.²¹

Clinical evidence for microwave ablation in the spine has been limited to some small series. In a retrospective study, Kastler et

al¹⁷ reported successfully treating 20 spinal metastases (17 patients) with MWA (with cementoplasty in 9 cases). They reported pain relief in 16 of 17 patients, with significant pain reduction 1 day, 1 week, 1 month, 3 months, and 6 months after ablation without any major complications.

In a second retrospective study, Pusceddu et al¹⁸ reported MWA of 37 osseous metastases (35 patients), which included spinal lesions in 12 patients. Local tumor control was achieved in all patients, and significant pain palliation, 1 week, 1 month, and 6 months after ablation (and 1 year after ablation in surviving patients at that time point). They also reported improved walking ability and no major complications.

In a prospective study, Aubry et al²² reported MWA of 16 bone and soft-tissue lesions in 13 patients. They reported an average necrosis rate of 85% at the first follow-up, and an 80% overall success rate; half of these patients were considered complete responders. Local control of the disease persisted with time,

though residual disease progressed slowly. Time to recurrence in this study was 7.2 months.

The results of the current study recapitulate the findings in these prior works, with immediate pain reduction obtained in 94% (65/69) of these procedures, maintained for 6 months.

Primary Outcome: Pain Relief

This series affirms that microwave ablation is a feasible and effective procedure for pain relief in patients with refractory painful spinal metastases. Immediate pain reduction was obtained in 94% (65/69) of these procedures and maintained for >6 months.

Reduction in pain from ablation procedures is thought to be attributable to a combination of proposed mechanisms: destruction of pain nerve fibers in the periosteum and bone cortex with reduced pain transmission; reduction in the size of the tumor burden and volume with reduced transmission of pain via the nerve endings; and decreased osteoclastic activity and coagulative necrosis of the tumor cells with a resultant decrease in the production of nerve-stimulating cytokines such as interleukins and α -tumor necrosis factor.²³

There is a significantly increased risk of pathologic fracture following radiation therapy, particularly following stereotactic beam radiation therapy or stereotactic radiosurgery, with a reported incidence of between 15% and 40%.^{24,25} Fractures most commonly occur several weeks after radiation and typically involve lytic lesions.²⁶ Thus, prophylactic stabilization of these lesions before RT may be useful. Despite the current lack of level 1 evidence to support this practice, we commonly perform vertebral augmentation before RT to prevent fracture-associated morbidities at our institutions.

Structural Stabilization

Patients with widely metastatic disease are often systemically unwell and are unable to tolerate prolonged conservative management and all it entails.²⁷ Consequently, these patients benefit greatly from early stabilization of fractures, with a lower requirement for bed rest, bracing, and anesthesia.²⁸ Even patients with chronic pain from unhealed fractures lasting longer than 12 months can benefit.²⁰

In patients with metastatic disease, surgical decompression has been shown to provide a reasonable long-term ambulatory benefit. Early evaluation for surgical stabilization is therefore recommended, particularly in patients who are young and/or highly functional and have a reasonable long-term prognosis.^{29,30} However, invasive surgery may be inappropriate for frail patients with complex tumors. In addition, prolonged postoperative recovery can delay systemic therapy.³¹

In this group of patients, in whom surgical decompression or fixation or both are inappropriate, there is strong evidence that percutaneous vertebral augmentation can achieve pain relief and functional improvement in both osteoporotic and pathologic fractures.

Cementoplasty (vertebroplasty when performed in the spine and sacroplasty in the sacrum), the injection of polymethylmethacrylate cement, stabilizes axial-loading areas of bone. This stabilization is important because vertebral body collapse after tumor ablation alone has been shown to occur in up to 60% of patients in the first year following ablation when not combined with cementoplasty support.³² Cementoplasty alone does not provide sufficient strength across areas of bone that experience significant shear or torsional stress. Traditionally, screw fixation would be required to account for such forces. New image-guided percutaneous interventions are currently being developed to facilitate reinforcement in these areas, sometimes termed “osteosynthesis.”³³

Vertebral augmentation has been shown to have acceptably low complication rates, quicker recovery times than surgery, and minimal disruption to adjunctive therapies, including chemotherapy and radiation.^{28,34} Patients are typically able to bear weight within a few

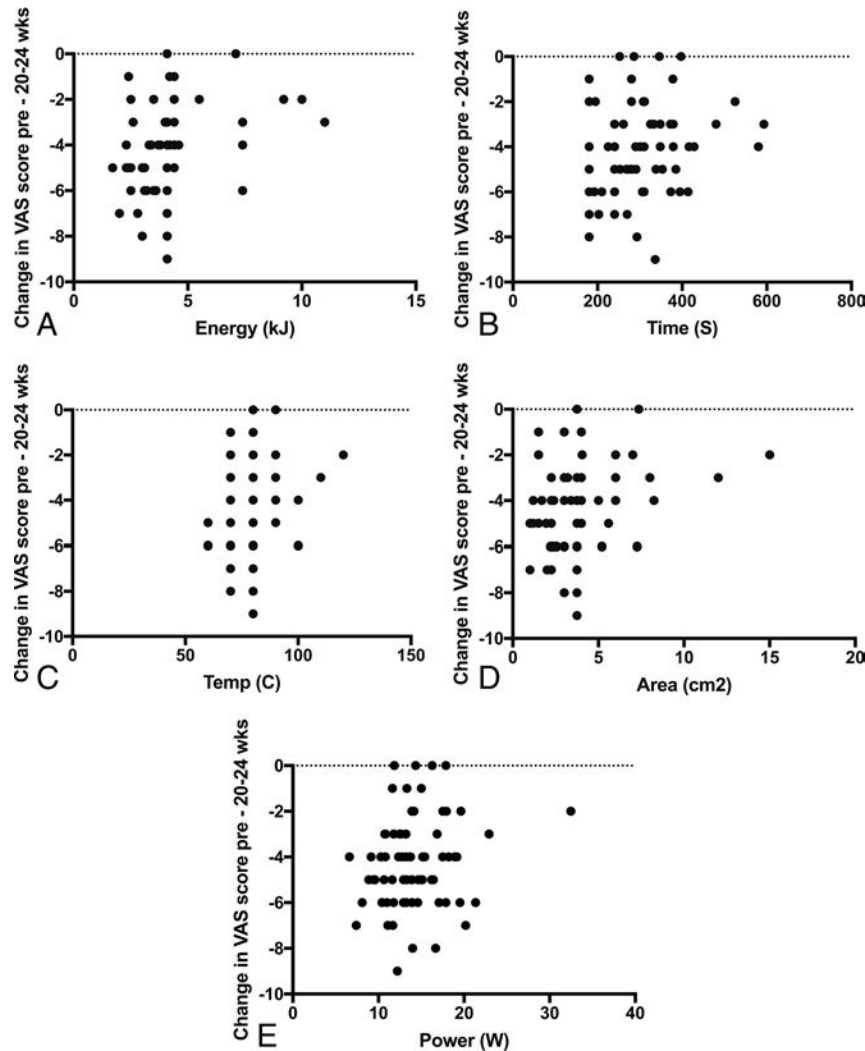


FIG 4. Comparing the change in VAS scores from preprocedure to 20–24 weeks postprocedure with ablation energy.

Table 2: Descriptive statistics showing quartiles, median, mean, SD, SEM, confidence intervals, and mean ranks for each dataset

	VAS Pre	VAS 2–4 Weeks	VAS 20–24 Weeks	ODI Pre	ODI 2–4 Weeks	ODI 20–24 Weeks
No. of values	61	61	61	44	44	44
Minimum	2	0	0	20	4	2
25% Percentile	6	1	2	36	16	18
Median	7	2	2	46	24	24
75% Percentile	8	3	3	58	34	35.5
Maximum	10	6	6	92	64	60
Mean	6.869	2.098	2.443	48.5	25.64	25.86
SD	1.737	1.338	1.522	16.37	13.78	13.18
SEM	0.2224	0.1713	0.1949	2.469	2.077	1.988
Lower 95% CI	6.424	1.756	2.053	43.52	21.45	21.86
Upper 95% CI	7.314	2.441	2.833	53.48	29.83	29.87
Mean ranks	90.58	32.42	33.2	60.56	28.44	28.27

Note:—SEM indicates standard error of the mean.

Table 3: Tumor area as defined by largest dimensions in the x and y planes

	Energy (kJ)	Temperature (°C)	Area (cm ²)	Time (s)	Power (W)
No. of values	102	102	102	102	102
Minimum	1.2	60	0.75	120	6.609
25% Percentile	2.7	70	2.25	237.5	11.22
Median	4.1	80	3.57	269.5	13.28
75% Percentile	4.1	80	3.813	336.5	15.61
Maximum	11	120	15	634	32.47
Mean	3.892	77.84	3.586	286.1	13.78
SD	1.604	9.584	2.218	94.41	3.75
SEM	0.1588	0.949	0.2197	9.348	0.3713
Lower 95% CI	3.577	75.96	3.15	267.6	13.04
Upper 95% CI	4.207	79.73	4.022	304.6	14.52
Mean ranks	235.2	478.5	207.6	580.5	374.8

Note:—SEM indicates standard error of the mean.

hours after the procedure and are usually able to engage in physical therapy the following day to minimize further deconditioning. Given the rapid recovery time and absence of large surgical wounds, adjunctive chemotherapy and RT can be rapidly pursued with minimal interruption. With the development of effective adjunctive therapies, tumor regression may often invoke local instability. Vertebral augmentation may therefore also be used to offer stability to vulnerable lesions.

Our findings lend credence to the idea that microwave ablation (in combination with cementoplasty) is effective in achieving effective and durable pain relief and demonstrates an excellent adverse effect profile. Patients who had tumors whose margins approximated nerve roots or the spinal canal were excluded from this study. When these patients are treated, somatosensory-evoked potentials/motor-evoked monitoring is advised to ensure safety.

Secondary Outcome: Tumor Control

Oligometastatic disease is a unique pathologic state in which patients have limited disseminated disease that may potentially be curable. This model is gaining increasing support within the oncology community and provides justification for treating these patients with an aggressive approach (surgery or embolization).³⁵ While many patients have isolated osseous metastases,³⁴ surgical resection of osseous lesions is uncommon, likely due to morbidity of the operation. Stereotactic radiation therapy for oligometastases is an active area of investigation, showing promising early results.³⁶⁻³⁸ A few series of image-guided ablation of limited metastatic disease have recently been published, including both exclusively osseous metastases and mixed disease.^{12,39-42}

Limited series in the literature show promising local control rates with oligometastatic disease.^{19,43-46} In 1 series, percutaneous thermal ablation of metastatic spine lesions could achieve a reasonable rate of curative therapy (up to 67% at 1 year¹²). This result was achieved in a select subgroup of small, solitary lesions within the vertebral body without significant cortical destruction or posterior element involvement.

Tumor areas in patients in this study are detailed in Table 3. There was a small subset of patients in this study with oligometastatic disease (20/67). Cross-sectional imaging at 20–24 weeks demonstrated no evidence of locoregional progression. Further

long-term follow-up would be required to compare this cohort with those described in the literature.

Definitive criteria to select appropriate patients for ablation of oligometastases have not yet been established. Most of the published series include patients with ≤ 5 sites of metastases. Image-guided ablation is usually used in nonsurgical candidates or in those who develop metastases in a previously irradiated field.

Limitations of the Study

The study was performed retrospectively on the basis of data from a single institution. Thus, a higher level of evidence could be achieved by performing a prospective, multicenter trial. A definitive record of the patients' medical anesthesia was not kept, which would have potentially provided additional qualification of the effectiveness of therapy. Tumor ablation zones were measured and recorded as areas (rather than volumes). Although this approach may be slightly less accurate, it reflects our current clinical practice and that of several centers with whom we collaborate.

CONCLUSIONS

Microwave ablation is a promising, safe, and effective treatment for osseous tumors, resulting in both a reduction in pain and a degree of locoregional control of the disease process.

ACKNOWLEDGMENTS

We are grateful to David Yousem for manuscript revision and mentoring.

Disclosures: Jennifer S. Barr—UNRELATED: Board Membership: Musculoskeletal Transplant Foundation, Comments: member of medical board of trustees; money for my services goes to my institution into a resident funding for books/activities.* *Money paid to the institution.

REFERENCES

- Coleman RE. Clinical features of metastatic bone disease and risk of skeletal morbidity. *Clin Cancer Res* 2006;12:6243s–49s CrossRef Medline
- Cleeland CS, Gonin R, Hatfield AK, et al. Pain and its treatment in outpatients with metastatic cancer. *N Engl J Med* 1994;330:592–96 CrossRef Medline
- Kirou-Mauro AM, Hird A, Wong J, et al. Has pain management in cancer patients with bone metastases improved? A seven-year review at an outpatient palliative radiotherapy clinic. *J Pain Symptom Manage* 2009;37:77–84 CrossRef Medline
- Pierik JG, IJzerman MJ, Gaakeer MI, et al. Pain management in the emergency chain: the use and effectiveness of pain management in patients with acute musculoskeletal pain. *Pain Med* 2015;16:970–84 CrossRef Medline
- Chow E, Zeng L, Salvo N, et al. Update on the systematic review of palliative radiotherapy trials for bone metastases. *Clin Oncol (R Coll Radiol)* 2012;24:112–24 CrossRef Medline
- Sze WM, Shelley M, Held I, et al. Palliation of metastatic bone pain: single fraction versus multifraction radiotherapy—a systematic review of randomised trials. *Clin Oncol (R Coll Radiol)* 2003;15:345–52 Medline
- Wallace AN, Robinson CG, Meyer J, et al. The metastatic spine disease multidisciplinary working group algorithms. *Oncologist* 2015; 20:1205–15 CrossRef Medline
- Goldberg SN, Gazelle GS, Mueller PR. Thermal ablation therapy for focal malignancy: a unified approach to underlying principles, techniques, and diagnostic imaging guidance. *AJR Am J Roentgenol* 2000;174:323–31 CrossRef Medline
- Simon CJ, Dupuy DE, Mayo-Smith WW. Microwave ablation: prin-

- principles and applications.** *Radiographics* 2005;25:S69–83 CrossRef Medline
10. Dupuy DE, Goldberg SN. **Image-guided radiofrequency tumor ablation: challenges and opportunities—part II.** *J Vasc Interv Radiol* 2001;12:1135–48 CrossRef Medline
 11. Kurup AN, Callstrom MR. **Increasing role of image-guided ablation in the treatment of musculoskeletal tumors.** *Cancer J* 2016;22:401–10 CrossRef Medline
 12. Deschamps F, Farouil G, Ternes N, et al. **Thermal ablation techniques: a curative treatment of bone metastases in selected patients?** *Eur Radiol* 2014;24:1971–80 CrossRef Medline
 13. Skinner MG, Iizuka MN, Kolios MC, et al. **A theoretical comparison of energy sources—microwave, ultrasound and laser—for interstitial thermal therapy.** *Phys Med Biol* 1998;43:3535–47 CrossRef Medline
 14. Stauffer P, Rossetto F, Prakash M, et al. **Phantom and animal tissues for modelling the electrical properties of human liver.** *Int J Hyperthermia* 2003;19:89–101 CrossRef Medline
 15. Shock SA, Meredith K, Warner TF, et al. **Microwave ablation with loop antenna: in vivo porcine liver model.** *Radiology* 2004;231:143–49 CrossRef Medline
 16. Wright AS, Lee FT Jr, Mahvi DM. **Hepatic microwave ablation with multiple antennae results in synergistically larger zones of coagulation necrosis.** *Ann Surg Oncol* 2003;10:275–83 CrossRef Medline
 17. Kastler A, Alnassan H, Aubry S, et al. **Microwave thermal ablation of spinal metastatic bone tumors.** *J Vasc Interv Radiol* 2014;25:1470–75 CrossRef Medline
 18. Pusceddu C, Sotgia B, Fele RM, et al. **Treatment of bone metastases with microwave thermal ablation.** *J Vasc Interv Radiol* 2013;24:229–33 CrossRef Medline
 19. Kujak JL, Liu PT, Johnson GB, et al. **Early experience with percutaneous cryoablation of extra-abdominal desmoid tumors.** *Skeletal Radiol* 2010;39:175–82 CrossRef Medline
 20. Brown DB, Gilula LA, Sehgal M, et al. **Treatment of chronic symptomatic vertebral compression fractures with percutaneous vertebroplasty.** *AJR Am J Roentgenol* 2004;182:319–22 CrossRef Medline
 21. Lubner MG, Brace CL, Hinshaw JL, et al. **Microwave tumor ablation: mechanism of action, clinical results, and devices.** *J Vasc Interv Radiol* 2010;21:S192–203 CrossRef Medline
 22. Aubry S, Dubut J, Nueffer JP, et al. **Prospective 1-year follow-up pilot study of CT-guided microwave ablation in the treatment of bone and soft-tissue malignant tumours.** *Eur Radiol* 2017;27:1477–85 CrossRef Medline
 23. Botsa E, Mylona S, Koutsogiannis I, et al. **CT image guided thermal ablation techniques for palliation of painful bone metastases.** *Ann Palliat Med* 2014;3:47–53 CrossRef Medline
 24. Jawad MS, Fahim DK, Gerszten PC, et al; on behalf of the Elekta Spine Radiosurgery Research Consortium. **Vertebral compression fractures after stereotactic body radiation therapy: a large, multi-institutional, multinational evaluation.** *J Neurosurg Spine* 2016;24:928–36 CrossRef Medline
 25. Rose PS, Laufer I, Boland PJ, et al. **Risk of fracture after single fraction image-guided intensity-modulated radiation therapy to spinal metastases.** *J Clin Oncol* 2009;27:5075–79 CrossRef Medline
 26. Cunha MV, Al-Omair A, Atenafu EG, et al. **Vertebral compression fracture (VCF) after spine stereotactic body radiation therapy (SBRT): analysis of predictive factors.** *Int J Radiat Oncol Biol Phys* 2012;84:e343–49 CrossRef Medline
 27. Gold D. **The clinical impact of vertebral fractures: quality of life in women with osteoporosis.** *Bone* 1996;18(3 Suppl):185S–89S CrossRef Medline
 28. Berenson J, Pflugmacher R, Jarzem P, et al; Cancer Patient Fracture Evaluation (CAFE) Investigators. **Balloon kyphoplasty versus non-surgical fracture management for treatment of painful vertebral body compression fractures in patients with cancer: a multicentre, randomised controlled trial.** *Lancet Oncol* 2011;12:225–35 CrossRef Medline
 29. Leithner A, Gruber G, Hochegger M, et al. **Comparison of seven preoperative prognostic scoring systems for spinal metastases.** *Orthopaedic Proceedings* 2010;92-B(Suppl V):602–03
 30. Schoenfeld AJ, Le HV, Marjoua Y, et al. **Assessing the utility of a clinical prediction score regarding 30-day morbidity and mortality following metastatic spinal surgery: the New England Spinal Metastasis Score (NESMS).** *Spine J* 2016;16:482–90 CrossRef Medline
 31. Piccioli A, Spinelli MS, Maccauro G. **Impending fracture: a difficult diagnosis.** *Injury* 2014;45:S138–41 CrossRef Medline
 32. Wallace AN, Greenwood TJ, Jennings JW. **Radiofrequency ablation and vertebral augmentation for palliation of painful spinal metastases.** *J Neurooncol* 2015;124:111–18 CrossRef Medline
 33. Deschamps F, de Baere T, Hakime A, et al. **Percutaneous osteosynthesis in the pelvis in cancer patients.** *Eur Radiol* 2016;26:1631–39 CrossRef Medline
 34. Clark W, Bird P, Gonski P, et al. **Safety and efficacy of vertebroplasty for acute painful osteoporotic fractures (VAPOUR): a multicentre, randomised, double-blind, placebo-controlled trial.** *Lancet* 2016;388:1408–16 CrossRef Medline
 35. Weichselbaum RR, Hellman S. **Oligometastases revisited.** *Nat Rev Clin Oncol* 2011;8:378–82 CrossRef Medline
 36. Lo SS, Teh BS, Mayr NA, et al. **Stereotactic body radiation therapy for oligometastases.** *Discov Med* 2010;10:247–54 Medline
 37. Milano MT, Katz AW, Muhs AG, et al. **A prospective pilot study of curative-intent stereotactic body radiation therapy in patients with 5 or fewer oligometastatic lesions.** *Cancer* 2008;112:650–58 CrossRef Medline
 38. Salama JK, Hasselle MD, Chmura SJ, et al. **Stereotactic body radiotherapy for multisite extracranial oligometastases: final report of a dose escalation trial in patients with 1 to 5 sites of metastatic disease.** *Cancer* 2012;118:2962–70 CrossRef Medline
 39. Barral M, Auperin A, Hakime A, et al. **Percutaneous thermal ablation of breast cancer metastases in oligometastatic patients.** *Cardiovasc Intervent Radiol* 2016;39:885–93 CrossRef Medline
 40. Littrup PJ, Bang HJ, Currier BP, et al. **Soft-tissue cryoablation in diffuse locations: feasibility and intermediate term outcomes.** *J Vasc Interv Radiol* 2013;24:1817–25 CrossRef Medline
 41. Solomon LA, Munkarah AR, Vorugu VR, et al. **Image-guided percutaneous cryotherapy for the management of gynecologic cancer metastases.** *Gynecol Oncol* 2008;111:202–07 CrossRef Medline
 42. Welch BT, Callstrom MR, Carpenter PC, et al. **A single-institution experience in image-guided thermal ablation of adrenal gland metastases.** *J Vasc Interv Radiol* 2014;25:593–98 CrossRef Medline
 43. McMenomy BP, Kurup AN, Johnson GB, et al. **Percutaneous cryoablation of musculoskeletal oligometastatic disease for complete remission.** *J Vasc Interv Radiol* 2013;24:207–13 CrossRef Medline
 44. Bang HJ, Littrup PJ, Currier BP, et al. **Percutaneous cryoablation of metastatic lesions from non-small-cell lung carcinoma: initial survival, local control, and cost observations.** *J Vasc Interv Radiol* 2012;23:761–69 CrossRef Medline
 45. Bang HJ, Littrup PJ, Goodrich DJ, et al. **Percutaneous cryoablation of metastatic renal cell carcinoma for local tumor control: feasibility, outcomes, and estimated cost-effectiveness for palliation.** *J Vasc Interv Radiol* 2012;23:770–77 CrossRef Medline
 46. Ilaslan H, Schils J, Joyce M, et al. **Radiofrequency ablation: another treatment option for local control of desmoid tumors.** *Skeletal Radiol* 2010;39:169–73 CrossRef Medline

Celebrating 35 Years of the AJNR
July 1983 edition

Intracranial Cavernous Hemangiomas: Neuroradiologic Review of 36 Operated Cases

Mario Savoiardo¹
Liliana Strada
Angelo Passerini

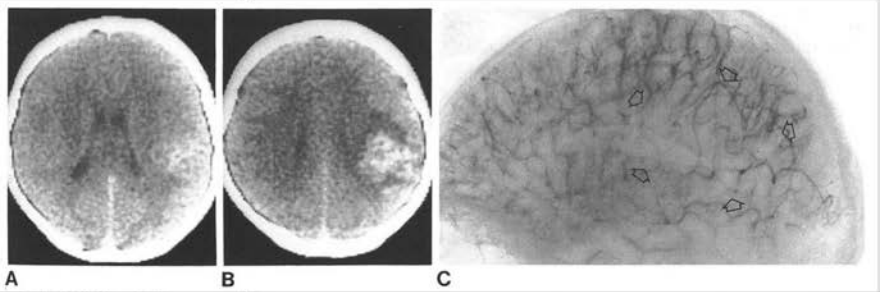
Neuroradiologic studies in 36 cases of hemangiomas were reviewed. Radiologic examinations. Angiography, performed in with absent or moderate mass effect. Cases mentioned in single case reports, were tomography (18 cases) usually demonstrate without significant mass effect and also combination of a long clinical history of focal angiographic findings should suggest the cases of so-called spontaneous hematomas. Angiography should be repeated after a cavernous hemangioma or other cryptic v

Cavernous hemangiomas of the brain are composed of thin-walled sinusoids have no elastic membrane, no muscle, parenchyma.

Their frequency seemed to be quite undiagnosed during life; however, in Cormick et al. [1] in 1968 demonstrated cerebral vascular malformation after a. Furthermore, the possibility of diagnosing (CT) has increased their recognition. Radiologic studies performed in a series of operated on at the Istituto Neurologico and surgical aspects of the first part of this series (14 patients) were reported by Giombini and Morello [2], and preliminary neuroradiologic review has also been reported [3].

Materials and Methods

Thirty-six cases of ICH were reviewed. There were 20 in cavernous hemangiomas (55 cases), being almost equal. The most common clinical cases). Focal neurologic symptoms acute, caused by (six cases), however, in the history of focal epilepsy. Removal of an intracranial later during the second he symptoms was 4.3 years.



Received October 19, 1982; accepted after revision January 28, 1983.
All authors: Department of Neurosurgery, Istituto Neurologico, Via Cavour 11, 20133, Milan, Italy. Address reprint requests to M. Savoiardo.
AJNR 4:889-892, July/August 1983
0195-6108/83/0404-0889\$02.00
© American Roentgen Ray Society

Comparative Advantages of Small- and Large-Dose Metrizamide Myelography

Livia Selti-Bohman^{1,2}
John R. Benton¹

A series of myelographies performed with a smaller than customary dose of metrizamide was compared with a series using the larger customary dose. There was a heartening drop in the incidence of headache and vomiting resulted from there was a heartening drop in the incidence of psychoneurosis. The difference in diagnostic quality between the two series resulted from the fact that the smaller dose was injected close to the site of main interest, but total spinal myelography with the low dose is often inadequate.

Metrizamide has become the contrast agent of choice for because it is simple to use, provides superior anatomic detail in conjunction with computed tomography (CT), and does not [1-5]. However, many are reluctant to use metrizamide myelography because of justifiable concern over acute headache, vomiting, mental and neurologic disorders, and correlation between complications and the total dose of metrizamide [1, 6]. We have been interested in determining metrizamide myelography can be significantly reduced by those customarily employed without sacrificing diagnostic quality.

Subjects, Methods, and Results

Metrizamide, as distributed in North America, is packaged in two packages, hereafter called the large dose, is intended to be used in 10 ml of contrast medium. The smaller package, hereafter called the small dose, is intended to be used primarily for metrizamide myelography. The volume of contrast medium for reconstruction of this small dose varies from 6 ml (300 mg I/ml) to 10 ml (300 mg I/ml) in this study, myelography was performed using either the small dose or the large dose, in which case at least the available dose was used. Of the 290 cervical and/or lumbar myelograms, 137 were obtained with the large dose and 153 with the small dose. Assignment of patients to the two groups was not arbitrary, it compromise the quality of studies. The large dose was generally used in large, obese, and had unfavorable spinal curvatures or suspicion of total spinal myelography was needed. The small dose patients, children, and for those in whom only one region of the spine was of interest. As the study progressed, it became apparent that the small dose patients other than large persons needing total spinal myelography use of the two dosages shifted. All myelographies termed lumbar were performed with the large dose, and the contrast material was not run above the thoracic level. Cervical studies performed by lateral C2-C7 punctures, while cervical studies were performed by a lumbar injection of the metrizamide and volumes of metrizamide used for the low-dose studies



This article appears in the July/August 1983 issue of AJNR and the October 1983 issue of AJNR.
Received August 9, 1982; accepted after revision November 17, 1982.
¹Department of Radiological Sciences, UCLA School of Medicine, Center for Health Sciences, Los Angeles, CA 90024. Address reprint requests to J. R. Benton.
²Present address: Department of Radiology, St. Vincent's Hospital, Los Angeles, CA 90057.
AJNR 4:889-892, July/August 1983
0195-6108/83/0404-0889\$02.00
© American Roentgen Ray Society

Is Gd-DTPA Necessary in Clinical Practice for Peripheral Nerve Injury?

We read with interest the article published in the *American Journal of Neuroradiology* by Hill et al¹ concerning the enhancement characteristics at 4.7T of the sciatic nerve of rats after injury. The purpose of this article was to provide a reliable high-resolution diagnostic method to judge the severity of trauma; in the clinical setting, this would guide future microsurgery repair. Sequences realized were axial T1-weighted gradient-echo with fat saturation before and after 0.1 mmol/kg of intravenous Gd-DTPA and axial T2-weighted rapid acquisition relaxation excitement with fat saturation, in addition to dynamic contrast-enhanced T1-weighted gradient-echo imaging with fat saturation and spectroscopy sequences.

Finding a reliable noninvasive diagnostic tool to determine the severity and injury of a nerve has a real impact in daily clinical practice because this type of lesion is very disabling and generally occurs in younger patients. An increase in uptake is expected after 7 days as mentioned by the authors because that is when the blood-nerve barrier permeability increases.

In our opinion, it would be interesting if the authors had compared the abnormalities visible with the contrast agent with the T2-weighted rapid acquisition relaxation excitement with fat saturation, for example, size, tumefaction, inhomogeneity of signal, and so forth, as well as validated it with histology first to create models of the type and severity of lesions. In the end, they could have recognized, for example, whether the most inhomogeneous lesions are those that more readily regenerate. Second, it would have been useful to establish whether the same findings were present in both sequences. Due to accumulation of the paramagnetic

contrast agent in the basal ganglion,^{2,3} as recently demonstrated, there has been a tendency to use fewer paramagnetic contrast agents, so the implementation of these results in clinical practice would be difficult.

Finally, ultra-high fields are beginning to be used with volunteers and patients for the analysis of peripheral nerves. We are currently in the validation and learning phase and now know that it is possible to delineate not only the nerve itself but also almost microscopic structures. We believe this finding will also allow us to classify the grade of injury and help determine which lesions have a better prognostic value.

REFERENCES

1. Hill BJ, Padgett KR, Kalra V, et al. **Gadolinium DTPA enhancement characteristics of the rat sciatic nerve after crush injury at 4.7T.** *AJNR Am J Neuroradiol* 2018;39:177–83 [CrossRef Medline](#)
2. Kanda T, Ishii K, Kawaguchi H, et al. **High signal intensity in the dentate nucleus and globus pallidus on unenhanced T1-weighted MR images: relationship with increasing cumulative dose of a gadolinium-based contrast material.** *Radiology* 2014;270:834–41 [CrossRef Medline](#)
3. Ramalho J, Castillo M, AlObaidy M, et al. **High signal intensity in globus pallidus and dentate nucleus on unenhanced T1-weighted MR images: evaluation of two linear gadolinium-based contrast agents.** *Radiology* 2015;276:836–44 [CrossRef Medline](#)

● M.I. Vargas

Division of Neuroradiology
Department of Imaging and Medical Information Sciences
Geneva University Hospital
Geneva, Switzerland

● O. Ipek

Ecole Polytechnique Federale de Lausanne
Center for Biomedical Imaging
Lausanne, Switzerland

<http://dx.doi.org/10.3174/ajnr.A5637>

REPLY:

Thank you very much for your interest and insight regarding our study. We agree that any potential clinical implementation of contrast-enhanced MR neurography for trauma would require a thoughtful risk-benefit analysis. However, the current widespread use and established safety profile of Gd-DTPA would be conducive to implementation. Regarding our noncontrast data, at your suggestion, we performed ROI-based SNR measurements on our T2-weighted sequences using the same approach described in the original article.

Between days 3 and 7, forceps-injured nerves did indeed demonstrate higher T2 signal compared with clip-injured nerves, both when comparing mean SNR of each group ($P = .02$) and when directly comparing injured nerves with their contralateral, non-operative counterparts ($P = .04$). This difference was best de-

tected using the contralateral, normal nerve as an internal control: Using this methodology, we found that forceps-injured nerves demonstrated 44% more T2 signal, while clip-injured nerves demonstrated 31% more T2 signal.

We agree that the relationship between T2 signal changes and Gd-DTPA enhancement warrants further investigation. Potentially, a multiparametric approach including T2 signal hyperintensity, enhancement data, and diffusion tractography would yield the greatest prognostic value.

 **B. Hill**

Department of Radiology
Miller School of Medicine

 **K. Padgett**

Departments of Radiology and Radiation Oncology, Miller School of Medicine
Department of Biomedical Engineering, College of Engineering

 **V. Karla**

Miller School of Medicine

 **R. Quencer**

Department of Radiology
Miller School of Medicine, University of Miami
Miami, Florida

<http://dx.doi.org/10.3174/ajnr.A5661>

Neuroimaging in Dengue Seropositive Cases

We read the publication “Brain Imaging in Cases with Positive Serology for Dengue with Neurologic Symptoms: A Clinicoradiologic Correlation” with a great interest.¹ Vanjare et al¹ concluded, “Although not specific, dengue infection has imaging findings that can be used to narrow down the differential list and help in prognostication.” We would like to share ideas and experiences from tropical Indochina on this finding. In fact, neurologic problems due to dengue are possible, but the brain imaging is usually not specific and might contribute little to the clinical diagnosis and management.² Regardless of brain imaging findings, poor neurologic signs and symptoms are usually related to poor outcome.³ With similar positive brain imaging findings (presence of diffusion restriction and hemorrhagic foci in the brain parenchyma), worse prognosis is reported in patients with overt encephalitis symptoms.⁴ Nevertheless, the important determinant for good outcome is the appropriate clinical management by fluid-replacement therapy.² In the previous study in Thailand, the cases with fatal dengue hemorrhagic fever usually had no pos-

itive brain imaging findings, and there was no prognostic advantage of brain imaging in patients with dengue.⁵

REFERENCES

1. Vanjare HA, Mannam P, Mishra AK, et al. **Brain imaging in cases with positive serology for dengue with neurologic symptoms: a clinicoradiologic correlation.** *AJNR Am J Neuroradiol* 2018;39:699–703 CrossRef Medline
2. Wiwanitkit V. **Dengue fever: diagnosis and treatment.** *Expert Rev Anti Infect Ther* 2010;8:841–45 CrossRef Medline
3. Misra UK, Kalita J, Mani VE, et al. **Central nervous system and muscle involvement in dengue patients: a study from a tertiary care center.** *J Clin Virol* 2015;72:146–51 CrossRef Medline
4. Wasay M, Channa R, Jumani M, et al. **Encephalitis and myelitis associated with dengue viral infection clinical and neuroimaging features.** *Clin Neurol Neurosurg* 2008;110:635–40 CrossRef Medline
5. Wiwanitkit V. **Magnitude and pattern of neurological pathology in fatal dengue hemorrhagic fever: a summary of Thai cases.** *Neuropathology* 2005;25:398 CrossRef Medline

● P. Sookaromdee

TWAS Medical Center
Bangkok Thailand

● V. Wiwanitkit

Department of Community Medicine
DY Patil University
Pune, India

<http://dx.doi.org/10.3174/ajnr.A5646>

REPLY:

We thank Dr Pathum Sookaromdee and Professor Viroj Wiwanitkit for their interest in our recent publication.¹ The authors have stated that the brain imaging findings in cases with dengue infection are nonspecific and are of little help in diagnosis, management, or prognostication.

To the best of our knowledge, our study is the single largest dataset that includes positive cases of dengue infection with neurologic symptoms attributed to the brain involvement. All these cases have undergone cranial imaging. Our study demonstrates imaging features that may help to clinically raise the possibility of arboviral infections and also help in prognostication. The data published in this study show significant association with poor clinical outcome, which is defined as death or the presence of neurologic deficits at discharge with involvement of the thalami and cerebellar peduncles and the presence of diffusion restriction and micro-/macrohemorrhages.

Reference articles 2, 3, and 5 used by the authors have little radiologic data, if any, to support their argument. Reference article 4 includes description of 6 cases, a small number to draw any conclusions.

<http://dx.doi.org/10.3174/ajnr.A5658>

Clinical differentiation between dengue-related encephalopathy and encephalitis is difficult because almost all such cases have significant metabolic derangement. The outcome related to encephalitis is likely to be poorer compared with encephalopathy, and imaging has an important role in this differentiation. By demonstrating brain parenchymal involvement, one would have additional evidence to favor encephalitis over encephalopathy and thus a guide to prognostication. Given improved medical management of metabolic derangement and multiple-organ dysfunctions as seen with severe dengue, the role of imaging to help in management (to rule out large hemorrhages) and prognostication cannot be overemphasized.

REFERENCE

1. Vanjare HA, Mannam P, Mishra AK, et al. **Brain imaging in cases with positive serology for dengue with neurologic symptoms: a clinicoradiologic correlation.** *AJNR Am J Neuroradiol* 2018;39:699–703
CrossRef Medline

 H.A. Vanjare

 S. Mani

Department of Radiology
Christian Medical College
Vellore, India

Common Origin of Brachiocephalic and Left Common Carotid Arteries: Proposal of New Terminology

There is recent renewed interest in studying the aortic arch variants, fueled, at least in part, by suggestions that they might play a role in aortic pathologies.^{1,2} The human aortic arch has several branching patterns, reflecting its complex embryologic development. The most common or the standard is a 3-vessel pattern (Fig 1A), with a reported prevalence between 65% and 86%³; the first branch is the brachiocephalic trunk, followed by the left common carotid artery and then the left subclavian artery.

The most common aortic arch variant by far is a 2-vessel branching pattern: The first branch is a common origin of the brachiocephalic trunk and left common carotid artery, and the second branch is the left subclavian artery (Fig 1B), or, less commonly, the left common carotid artery takes origin from the brachiocephalic trunk.¹ The reported prevalence of this variant is between 7% and 26%, with the highest prevalence in African and South American populations.³ This variant has been historically termed the “bovine” arch, yet the origin of this term is not clear.⁴ Despite several critiques,^{4,5} this term is still in wide use in radiologic and surgical reports and journal publications,^{1,2} mainly because it is familiar and shorter than the full anatomic description. Another term, the “ovine arch,” is used in some institutions to describe the same variant, though far less commonly.⁵ Both terms are known to be misnomers, and this aortic arch variant is not the typical aortic branching pattern in cattle or sheep.^{4,5}

The “bicarotid trunk/truncus bicaroticus” is a third name for the common origin of the brachiocephalic trunk and left common carotid artery.⁶ However, in our opinion, this term should be reserved for other 3-vessel branching variants in which there is a separate origin of a normal site or an aberrant right subclavian artery in combination with a common trunk for both carotid arteries and a separate origin for the left subclavian artery (Fig 1C).

A fourth name for the same variant, the “common brachiocephalic trunk,” is sometimes used. This term is short but less popular and is clearly anatomically deficient. Last, a fifth name was proposed, “common origin of innominate and carotid arteries,”⁵ which is not a misnomer but is still long and lacks familiarity.

Moreover, the association of this variant with a separate aortic origin of the left vertebral artery constitutes a different branching

variant, which was termed a combined “bovine” arch and direct origin of the left vertebral artery,³ despite being a 3- rather than the 2-vessel branching pattern suggested by the term “bovine” (Fig 1D). Another rare variant that we recently encountered is a right aortic arch with a common origin of the left brachiocephalic trunk and right common carotid artery, causing confusion about the terminology and raising the question of whether it could be termed a “reverse bovine” arch (Fig 1E).

To summarize, the most common variant of the human aortic arch branching pattern has 5 different confusing terms in use. Therefore, we propose naming the common origin of the brachiocephalic trunk and left common carotid artery the “brachio-bicephalic” trunk. This term is short enough and more anatomically correct, with familiarity and resemblance to the original name of the brachiocephalic trunk. Additionally, it is appropriate to use when combined with a direct origin of the left vertebral artery and could be labeled “left” when this variant is present in a right-sided aortic arch.

REFERENCES

1. Hornick M, Moomiaie R, Mojibian H, et al. **‘Bovine’ aortic arch: a marker for thoracic aortic disease.** *Cardiology* 2012;123:116–24 [CrossRef Medline](#)
2. Moorehead PA, Kim AH, Miller CP, et al. **Prevalence of bovine aortic arch configuration in adult patients with and without thoracic aortic pathology.** *Ann Vasc Surg* 2016;30:132–37 [CrossRef Medline](#)
3. Popieluszko P, Henry BM, Sanna B, et al. **A systematic review and meta-analysis of variations in branching patterns of the adult aortic arch.** *J Vasc Surg* 2017 Aug 30. pii: S0741–5214(17)31788–3 [Epub ahead of print] [CrossRef Medline](#)
4. Layton KF, Kallmes DF, Cloft HJ, et al. **Bovine aortic arch variant in humans: clarification of a common misnomer.** *AJNR Am J Neuroradiol* 2006;27:1541–42 [Medline](#)
5. Katz JC, Chakravarti S, Ko HH, et al. **Common origin of the innominate and carotid arteries: prevalence, nomenclature, and surgical implications.** *J Am Soc Echocardiogr* 2006;19:1446–48 [CrossRef Medline](#)
6. Reinshagen L, Vodiskar J, Mühler E, et al. **Bicarotid trunk: how much is “not uncommon”?** *Ann Thorac Surg* 2014;97:945–49 [CrossRef Medline](#)

● A.M. Tawfik

● D.M. Sobh

● N.M. Batouty

Department of Diagnostic and Interventional Radiology
Faculty of Medicine, Mansoura University
Mansoura, Egypt

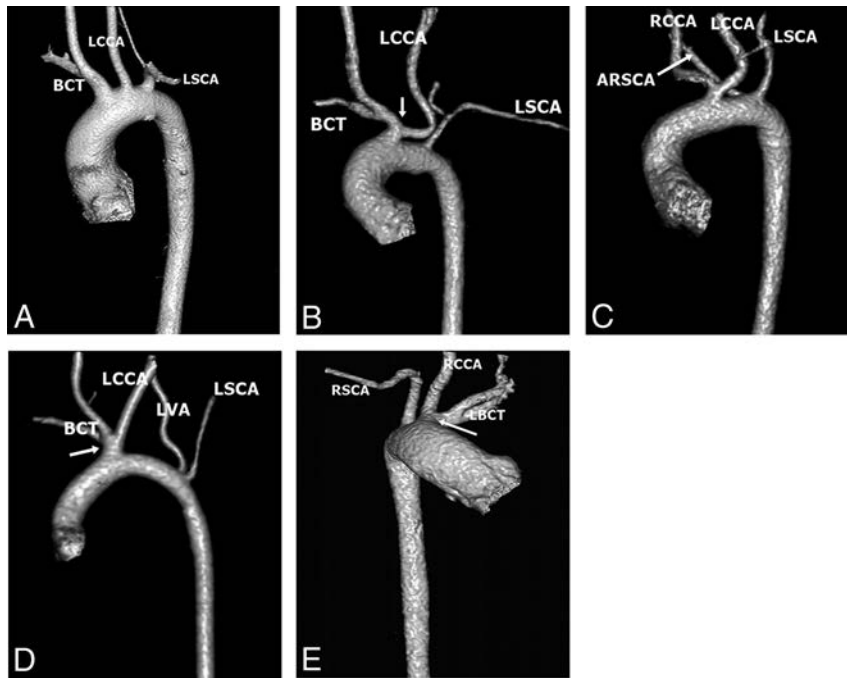


FIG 1. Volume-rendered CT of some aortic arch variants. *A*, Left aortic arch with normal branching pattern. *B*, Left aortic arch with a common origin (*arrow*) of the brachiocephalic trunk and left common carotid artery. *C*, Left aortic arch with separate origins of an aberrant right subclavian (*arrow*), and the left subclavian arteries and a common trunk for both carotid arteries. *D*, Left aortic arch with a common origin (*arrow*) of the brachiocephalic trunk and left common carotid artery and a separate origin of the left vertebral and left subclavian arteries. *E*, Right aortic arch with a common origin (*arrow*) of the left brachiocephalic trunk and the right common carotid artery. LCCA indicates left common carotid artery; RSCA, right subclavian artery; LSCA, left subclavian artery; RCCA, right common carotid artery; LBCT, left brachiocephalic trunk; ARSCA, aberrant right subclavian artery; LVA, left vertebral artery; BCT, brachiocephalic trunk.

ON-LINE APPENDIX

Overview of Convolutional Neural Networks

CNNs are an adaption of the traditional artificial neural network architecture whereby banks of 2D convolutional filter parameters and nonlinear activation functions act as a mapping function to transform a multidimensional input image into a desired output.¹ The banks of 2D convolutional operation are defined by

$$C_l = \sum_k x_k W_{kl} + b_l,$$

where the l th convolutional output C_l is the result of convolution between the k th input feature map x_k , and the l th subparameters w_{kl} and b_l are the l th additive bias terms. Because each convolutional layer acts on a total of k input feature maps, each parameter of size $i \times j$ consists of a total of $i \times j \times k \times l$ parameters, in which l is the number of output feature maps.

Each convolutional operation is then followed by a nonlinear activation function, σ . In this study, the rectified linear activation function was used, given well-documented advantages, including stable gradients at the extreme values of optimization.² The rectified linear operation is defined simply by

$$x_l = \sigma(C_l) = \max(C_l, 0),$$

where the l th activation map x_l represents the convolutional output C_l described above with the threshold at zero. Stacking serial convolutional and nonlinear activation functions allows a CNN to model high-order complex feature representations in a mathematically efficient form.

Convolutional Neural Network: Architectural Details

A customized CNN based on the popular ResNet was designed for classification of mutation status, comprising 4 residual blocks (On-line Figure). Batch normalization is used between the convolutional and rectified linear layers to limit drift of layer activations during training.³ Dropout at 50% was applied to all convolutional and fully connected layers to limit overfitting and add stochasticity to the training process.^{4,5} Feature maps were downsampled from the previous layer by convolutions with a stride length of 2 instead of max pooling, thus allowing the network to learn downsampling parameters and facilitating preservation of gradients during backpropagation.⁶ The number of activation channels in deeper layers was progressively increased from 8 to 16 to 32 to 64, reflecting increased feature complexity. The final single-dimensional feature vector was obtained through use of a global average pool applied to the penultimate $4 \times 4 \times 64$ convolutional feature map instead of implementing a costly, high-parameter intermediate fully convolutional layer.

Final classification error was determined using a softmax cross-entropy loss function, defined by

$$y = - \sum_c (x_{lc} - \log \sum_{d=1}^D e^{x_{ld}}),$$

where the loss, y , is calculated by subtracting the l th activation map of the ground truth class, c , with the sum of the softmax normalized (exponential function) values of the remaining class dimensions, D .

Data Augmentation

Real-time data augmentation was applied to all input images during the training process. This included the following: 1) addition of a random offset i on the interval of $(-0.5$ and $0.5)$ to the whole image; 2) arbitrary removal of an entire channel within the input in 50% of training cases; and 3) application of a random 3×3 affine transformation matrix independently to each input channel, resulting in stochastic application of image scaling, rotation, translation, and shear. "Channels" refer to 1 of the 4 input modalities (ie, T2, FLAIR, and so forth). Given a 2D affine matrix,

$$\begin{bmatrix} s_1 & t_1 & r_1 \\ t_2 & s_2 & r_2 \\ 0 & 0 & 1 \end{bmatrix},$$

the random affine transformation was initialized with random uniform distributions of interval $s_1, s_2 \in (0.8, 1.2)$, $t_1, t_2 \in (-0.3, 0.3)$, and $r_1, r_2 \in (-16, 16)$.

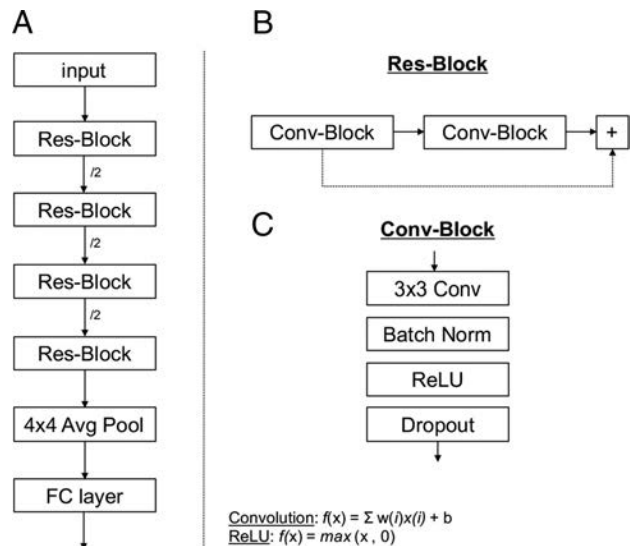
Implementation Details

Training was implemented using the Adam optimizer, an algorithm for first-order gradient-based optimization of stochastic objective functions, based on adaptive estimates of lower-order moments.⁷ Parameters were initialized using the heuristic described by He et al.⁸ L2 regularization was implemented to prevent over-fitting of data by limiting the squared magnitude of the convolutional weights. To account for training dynamics, the learning rate was annealed and the mini-batch size is increased whenever training loss plateaus. Furthermore a normalized gradient algorithm was employed to allow for locally adaptive learning rates that adjust according to changes in the input signal.⁹ Software code for this study was written in Python 3.5 using the open-source TensorFlow r1.0 library (Apache 2.0 license).¹⁰ Experiments were performed on a GPU-optimized workstation with a single NVIDIA GeForce GTX Titan X (12GB, Maxwell architecture).

REFERENCES

1. LeCun Y, Bengio Y. **Convolutional networks for images, speech, and time-series.** In: Arbib MA, ed. *The Handbook of Brain Theory and Neural Networks*. Cambridge: MIT Press; 1998:255–58
2. Nair V, Hinton GE. **Rectified linear units improve restricted Boltzmann machines.** In: *Proceedings of the 27th International Conference on Machine Learning*. Haifa, Israel: Omnipress; 2010:807–14
3. Ioffe S, Szegedy C. **Batch normalization: accelerating deep network training by reducing internal covariate shift.** *PMLR* 2015;37:448–56
4. Srivastava N, Hinton G, Krizhevsky A, et al. **Dropout: a simple way to prevent neural networks from overfitting.** *J Mach Learn Res* 2014;15:1929–58
5. Baldi P, Sadowski P. **The dropout learning algorithm.** *Artif Intell* 2014;210:78–122 [CrossRef Medline](#)
6. Springenberg JT, Dosovitskiy A, Brox T, et al. **Striving for simplicity: the all convolutional net.** *CoRR* 2014;abs/1412.6806. <https://arxiv.org/abs/1412.6806>. Accessed August 30, 2017
7. Kingma DP, Ba J. **Adam: a method for stochastic optimization.** *CoRR* 2014;abs/1412.6980. <https://arxiv.org/abs/1412.6980>. Accessed August 30, 2017
8. He K, Zhang X, Ren S, et al. **Delving deep into rectifiers: surpassing human-level performance on ImageNet classification.** In: *Proceedings of the 2015 IEEE International Conference on Computer Vision*, Santiago, Chile. December 7–13, 2015:1026–34 [CrossRef](#)

9. Mandic DP. **A generalized normalized gradient descent algorithm.** *IEEE Signal Process Lett* 2004;11:115–18 CrossRef
10. Abadi M, Agarwal A, Barham P, et al. **TensorFlow: large-scale machine learning on heterogeneous distributed systems.** *CoRR* 2015; abs/1603.04467. <https://arxiv.org/abs/1603.04467>. Accessed August 30, 2017



ON-LINE FIGURE. A, Summary of residual neural network architecture. Four residual blocks are used, subsampling the feature map 3 times through convolutions with a stride of 2 (demarcated by /2 in the figure). B, Each residual block consists of 2 serial 3×3 convolutional blocks; the latter is mapped to the former via an additional operation. C, Each convolutional block consists of a 3×3 convolution, batch normalization, a rectified linear nonlinearity, and 50% drop-out.

On-line Table 1: Study and patient characteristics of the included studies

Author, Year of Publication	Institution	Duration of Patient Recruitment	Study Design	Consecutive Enrollment	Reference Standard	No. of Patients	High-Grade Glioma (No.)	High-Grade Glioma (%)	Histology (WHO Grade)	Mean Age (yr)	Age Range (yr)	Male/Female
Bauer et al, 2015 ³	Cedars-Sinai Medical Center, Los Angeles, California	2013.6–2014.6	Retrospective	NA	Histopathology	23	13	56.5	Glioblastoma (grade IV)	NA	32–78	14:9
Bette et al, 2016 ⁴	Technische Universität München, Munich, Germany	NA	Retrospective	Yes	Histopathology	294	165	56.1	Glioblastoma (grade IV)	NA	NA	NA
Byrnes et al, 2011 ⁵	St. George's University of London, London, UK	2004.3–2006.1	Prospective	NA	Histopathology	28	16	57.1	Glioblastoma (grade IV)	60	27–76	21:7
Caravan et al, 2017 ⁶	Emergency County Hospital, Cluj-Napoca, Romania	2015.8–2016.12	Retrospective	NA	NA	52	25	48.1	Glioblastoma (grade IV)	NA	NA	NA
Chen et al, 2013 ⁷	University of Maryland Medical Center, Baltimore, Maryland	NA	NA	NA	Histopathology	51	26	51.0	Glioblastoma (grade IV)	58	NA	28:23
Han et al, 2015 ⁸	The First Affiliated Hospital of Xiamen University, Fujian, China	2010.7–2012.12	Retrospective	Yes	Histopathology	40	22	55.0	High-grade glioma (grade III, IV)	53.5 (median)	21–81	24:16
Holly et al, 2017 ⁹	Louisiana State University Health Sciences Center, Shreveport, Louisiana	NA	Retrospective	NA	Histopathology	84	40	47.6	High-grade glioma (grade III, IV)	57.2	26–82	48:36
Lee et al, 2011 ¹⁰	Toronto Western Hospital, Toronto, Ontario, Canada	2004.1–2006.6	Retrospective	Yes	Histopathology	73	38	52.1	Glioblastoma (grade IV)	57.5	29–83	41:32
Lemercier et al, 2014 ¹¹	Hospital Universitario y Politécnico la Fe, Valencia, Spain	2010.12–2012.8	Retrospective	NA	Histopathology	40	20	50.0	Glioblastoma (grade IV)	60.6	NA	26:14
Miquelini et al, 2016 ¹²	Hospital Italiano de Buenos Aires, Buenos Aires, Argentina	2009.7–2014.9	Retrospective	NA	Histopathology	84	42	50.0	Glioblastoma (grade IV)	62.8	NA	42:42
Server et al, 2009 ¹³	Ullevaal University Hospital, University of Oslo, Oslo, Norway	NA	Prospective	NA	Histopathology	82	59	72.0	High-grade glioma (grade III, IV)	61.8	25–88	NA
Tan et al, 2015 ¹⁴	Shanxi Medical University, Taiyuan City, China	2012.1–2014.3	Retrospective	NA	Histopathology or clinical diagnosis	51	31	60.8	High-grade glioma (grade III, IV)	58	39–77	NA
Wang et al, 2014 ¹⁵	Hospital of the University of Pennsylvania, Philadelphia, Pennsylvania	2006.6–2012.2	Retrospective	NA	Histopathology	221	128	57.9	Glioblastoma (grade IV)	59.8	24–90	124:97
Zhao et al, 2015 ¹⁶	The First Affiliated Hospital, Sun Yat-Sen University, Guangzhou, Guangdong Province, China	2012.11–2013.9	Prospective	Yes	Histopathology	20	15	75.0	High-grade glioma (grade III, IV)	NA	NA	NA

Note:—WHO indicates World Health Organization; NA, not available.

On-line Table 2: MRI characteristics of the included studies

Author, Year of Publication	Magnet Strength	Vendor	Scanner	Head Coil	MRI Technique	B-Value (s·mm ⁻²)	ROI Placement	Parameter	Cutoff Value	No. of Readers	Reader Experience (yr)	Blinding to Reference Standard
Bauer et al, 2015 ³	3T	Siemens ^a	Skyra	NA	DTI/DSC/DCE	1000	Enhancing tumor, perienhancing area	FA, MD	Perienhancing MD = 132×10^{-6} mm ² /s	NA	NA	NA
Bette et al, 2016 ⁴	3T	Philips ^b	Achieva, Ingenia, Verio	DTI	DTI	NA	Enhancing tumor	FA	NA	3 Neuroradiologists	2, 5, 6	Yes
Byrnes et al, 2011 ⁵	1.5T	GE ^c	Signa	DTI	DTI	1000	Enhancing tumor, perienhancing area	FA, MD	Binary logistic regression	1 Neurosurgeon	7	NA
Caravan et al, 2017 ⁶	1.5T	Siemens, GE	Magnetom Symphony Tim Upgrade, Optima 360	8	DWI	1000	Enhancing tumor, perienhancing area	ADC	Perienhancing ADC = 1.332×10^{-3} mm ² /s	1 Neuroradiologist, 1 medical student	9, 0	Yes
Chen et al, 2013 ⁷	3T	Siemens	Tim Trio	NA	DTI/DSC	1000	Enhancing tumor, perienhancing area	FA	Bayesian diagnostic system	NA	NA	NA
Han et al, 2015 ⁸	3T	Siemens	Magnetom Verio Tim	8	DWI	1000, 3000	Enhancing tumor, perienhancing area	Mean ADC _{min}	Perienhancing mean ADC _{min} = 1.316×10^{-3} mm ² /s	2 Neuroradiologists	7, 6	Yes
Holly et al, 2017 ⁹	1.5T	GE	NA	NA	DTI	NA	Enhancing tumor, perienhancing area	FA, MD	Perienhancing FA = 0.24, MD = 0.0001 mm ² /s	NA	NA	NA
Lee et al, 2011 ¹⁰	1.5T	GE	Signa EchoSpeed	Std coil	DWI	1000	Enhancing tumor, perienhancing area	Minimum ADC, ADC ratio	Perienhancing minimum ADC = 1.302×10^{-3} mm ² /s	1 Neuroradiologist	NA	Yes
Lemercier et al, 2014 ¹¹	1.5T, 3T	GE	Signa HDxt 1.5T, Signa HDxt 3T	Std coil	DWI	NA	Enhancing tumor, perienhancing area	Gradient of ADC in peritumoral edema	NA	1 Radiologist	NA	Yes
Miquelini et al, 2016 ¹²	1.5T	Siemens, Philips	Magnetom Avanto, Magnetom Essenza, Achieva	NA	DWI	NA	Perienhancing area	Minimal ADC at the apparently normal peritumoral white matter	707.5	1 Researcher	5	Yes
Server et al, 2009 ¹³	1.5T	Siemens	Magnetom Sonata	NA	DWI	500, 1000	Enhancing tumor, perienhancing area	Combination of 4 parameters (mean ADC of tumor, and minimum, maximum, and mean ADC tumor ratio)	0.716 (Logistic regression fitted-value)	1 Neuroradiologist	NA	Yes
Tan et al, 2015 ¹⁴	3T	GE	Signa HDxt	8	DTI/DKI	1000, 2000	Enhancing tumor, perienhancing area	FA, MD	Perienhancing MD = 1.89	2 Neuroradiologists	13, 6	Yes
Wang et al, 2014 ¹⁵	3T	Siemens	Tim Trio	12	DTI	1000	Enhancing tumor, perienhancing area	FA, MD	Logistic regression model	2 Neuroradiologists	10, 9	NA
Zhao et al, 2015 ¹⁶	3T	Siemens	Magnetom Verio	12	DWI/DCE	500, 1000	Enhancing tumor, perienhancing area	ADC	Perienhancing ADC = 1.357×10^{-3} mm ² /s	2 Radiologists	Experienced	NA

Note:—DCE indicates dynamic contrast-enhanced imaging; DKI, diffusional kurtosis imaging; Std, standard; NA, not available.

^a Erlangen, Germany.

^b Philips Healthcare, Best, the Netherlands.

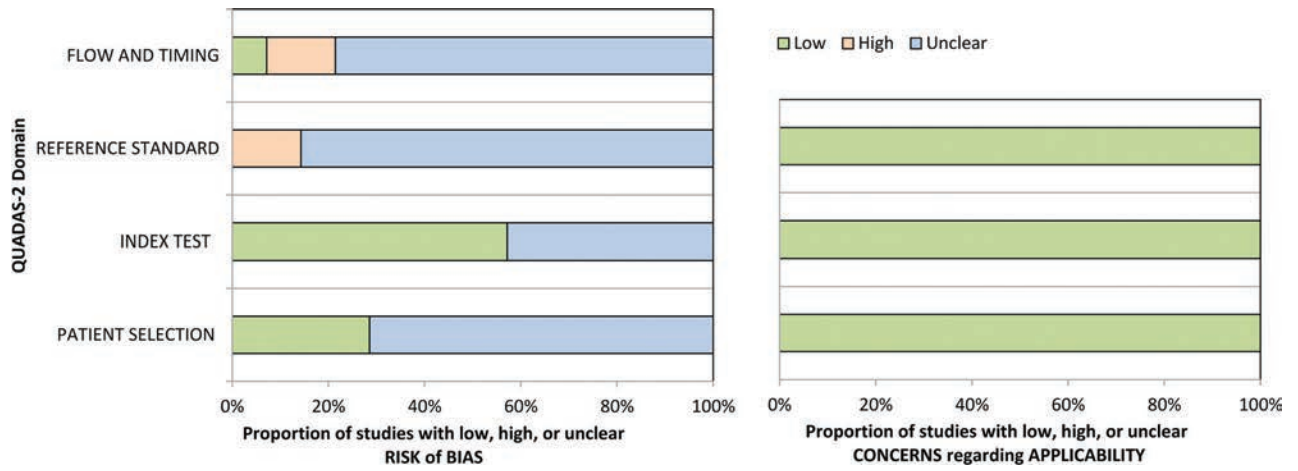
^c GE Healthcare, Milwaukee, Wisconsin.

On-line Table 3: The weight of each study for pooled sensitivity and specificity

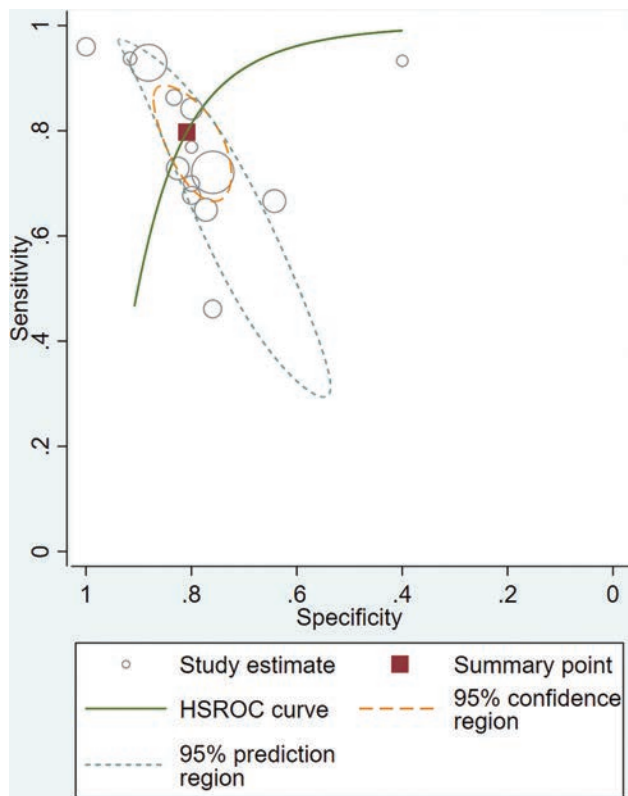
Author, Year of Publication	Weight (Sensitivity)	Weight (Specificity)
Bauer et al, 2015 ³	5.5%	3.3%
Bette et al, 2016 ⁴	10.9%	17.4%
Byrnes et al, 2011 ⁵	3.1%	2.0%
Caravan et al, 2017 ⁶	3.2%	1.1%
Chen et al, 2013 ⁷	8.3%	7.6%
Han et al, 2015 ⁸	5.8%	4.8%
Holly et al, 2017 ⁹	9.1%	10.6%
Lee et al, 2011 ¹⁰	7.7%	8.7%
Lemercier et al, 2014 ¹¹	7.2%	5.8%
Miquelini et al, 2016 ¹²	9.1%	12.0%
Server et al, 2009 ¹³	9.6%	6.0%
Tan et al, 2015 ¹⁴	8.5%	5.8%
Wang et al, 2014 ¹⁵	8.9%	12.1%
Zhao et al, 2015 ¹⁶	3.1%	2.6%

On-line Table 4: Results of multiple subgroup analyses

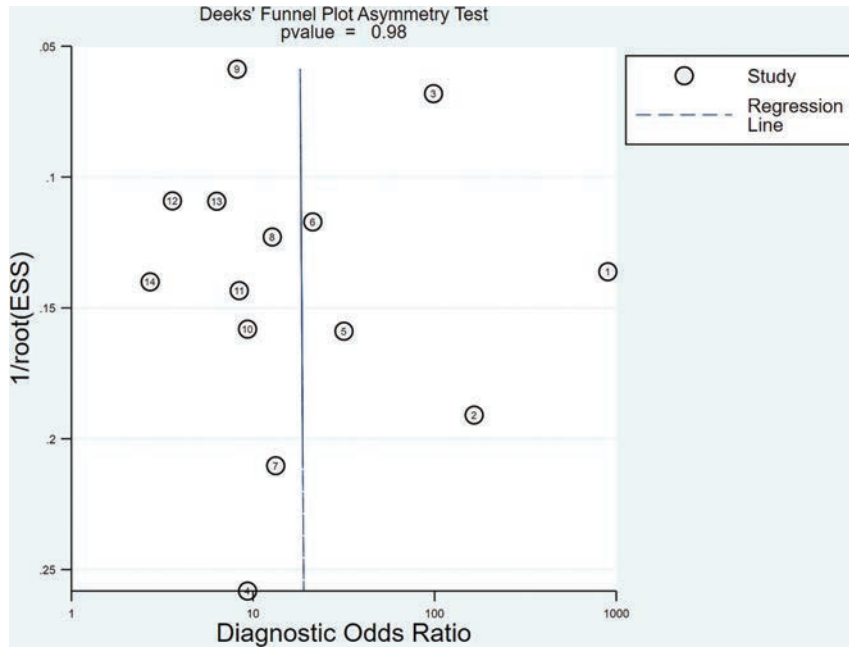
Subgroup	Meta-Analytic Summary Estimates	
	Sensitivity (95% CI)	Specificity (95% CI)
DWI (<i>n</i> = 7)	81.4% (70.6%–88.9%)	81.8% (69.5%–89.9%)
DTI (<i>n</i> = 7)	77.0% (62.3%–87.1%)	80.3% (73.5%–85.7%)
Glioblastoma only (<i>n</i> = 7)	82.2% (71.9%–89.3%)	81.4% (74.8%–86.6%)
Both glioblastoma and anaplastic astrocytoma (<i>n</i> = 7)	76.8% (61.4%–87.4%)	81.2% (69.9%–88.9%)
Enhancing tumor (<i>n</i> = 6)	72.6% (63.4%–80.3%)	77.0% (71.7%–81.6%)
Perienhancing area (<i>n</i> = 8)	80.1% (69.1%–87.9%)	81.0% (70.6%–88.3%)
FA (<i>n</i> = 6)	70.8% (61.0%–79.0%)	74.5% (69.0%–79.3%)
MD (<i>n</i> = 4)	84.5% (71.7%–92.1%)	81.3% (72.0%–88.1%)
Perienhancing ADC or MD (<i>n</i> = 6)	84.7% (73.6%–91.6%)	84.0% (71.8%–91.6%)



ON-LINE FIG 1. Grouped bar charts showing the risk of bias and concerns on the applicability according to QUADAS-2.



ON-LINE FIG 2. Hierarchic summary receiver operating characteristic curve of the diagnostic performance of DWI and DTI for differentiating high-grade glioma from solitary brain metastasis.



ON-LINE FIG 3. Deeks funnel plot. The *P* value of .98 suggests that the likelihood of publication bias is low.

On-line Table 1: Breakdown of susceptibility map datasets collected across the subject groups^a

Group	Total Sessions	Total Sessions Collected (by Visit)			Individualized Sessions Collected (No. of Subjects)						
		1 (24 hr)	2 (8 days)	3 (6 mo)	1-2-3	1-2	1-3	2-3	1	2	3
Injured	61/81	21	23	17	13	6	1	2	1	2	1
Control	68/81	26	23	19	16	7	2	0	1	0	1

^a Data-loss breakdown: Two of the 56 subjects (1 injured and 1 control) did not complete any MRI scans. From the remaining 54 subjects, 136 of a maximum of 162 QSM sets were included in the present analysis. Fifteen of 26 missing sets were due to subjects missing ≥ 1 of the 3 time-point imaging sessions. Four of 26 missing sets were due to scanner errors or raw data-saving failures. Seven of 26 missing sets were due to quality control failure, as described in the "Materials and Methods" section. The only notable deviation of subject participation between the groups is at the 24-hour imaging time point. This discrepancy is expected, due to the additional challenges in bringing in concussed subjects within 24 hours of their injuries. The only missing data point in the 24-hour control set is due to a quality control failure. The right half of the table outlines the collection of longitudinal data points across the subjects (ie, 13 injured and 16 control subjects attended all 3 imaging sessions).

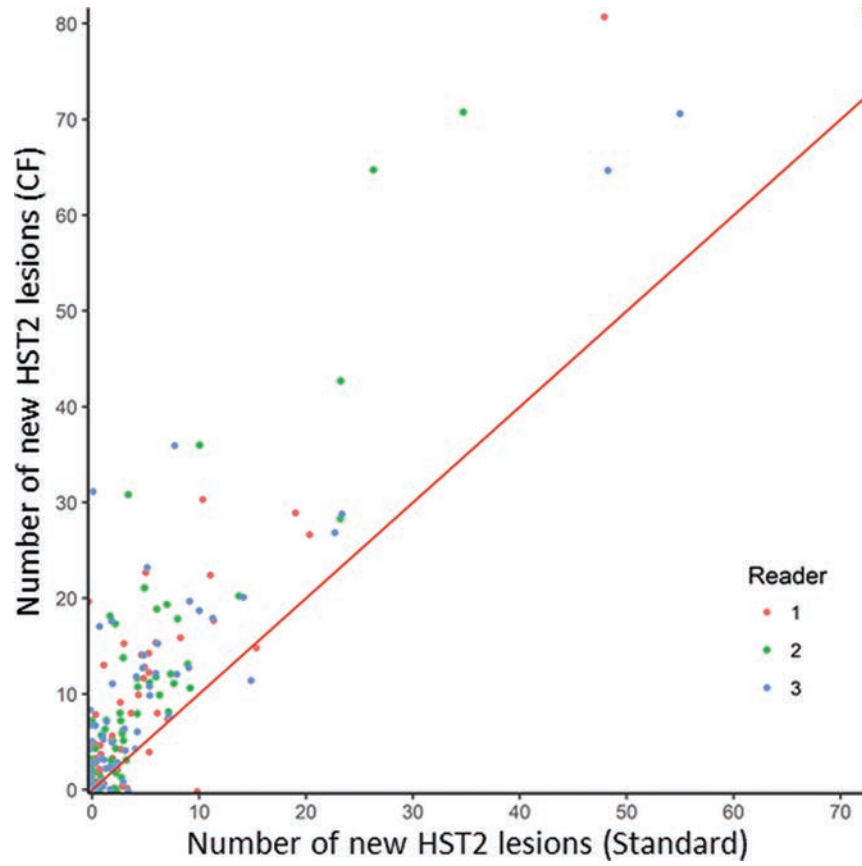
On-line Table 2: Selective cohort statistics computed at each time point using subjects who had susceptibility maps that were included in the present analysis^a

Metric	Control												Injured												P
	24 Hours				8 Days				6 Months				24 Hours				8 Days				6 Months				
	No.	Mean (95% CI)	No.	Mean (95% CI)	No.	Mean (95% CI)	No.	Mean (95% CI)	No.	Mean (95% CI)	No.	Mean (95% CI)	No.	Mean (95% CI)	No.	Mean (95% CI)	No.	Mean (95% CI)	No.	Mean (95% CI)	No.	Mean (95% CI)			
Age (yr)	26	18.0 (17.3–18.6)	23	18.1 (17.4–18.7)	18	17.9 (17.0–18.7)	21	17.1 (17.0–18.4)	23	18.8 (17.2–18.4)	17	17.5 (16.6–18.2)	23	18.8 (17.2–18.4)	17	17.5 (16.6–18.2)	23	18.8 (17.2–18.4)	17	17.5 (16.6–18.2)	23	18.8 (17.2–18.4)	17	17.5 (16.6–18.2)	.53
Weight (lbs)	26	72.0 (70.9–73.0)	23	71.6 (70.5–72.7)	18	72.1 (70.8–73.4)	21	71.2 (69.8–72.6)	23	71.7 (70.2–73.1)	17	71.7 (70.0–73.5)	23	71.7 (70.2–73.1)	17	71.7 (70.0–73.5)	23	71.7 (70.2–73.1)	17	71.7 (70.0–73.5)	23	71.7 (70.2–73.1)	17	71.7 (70.0–73.5)	.96
Height (in)	26	202.2 (186.4–218.1)	23	197.3 (182.1–212.5)	18	199.6 (180.9–218.4)	21	215.1 (190.6–239.6)	23	221.3 (197.0–245.6)	17	216.4 (186.4–246.4)	23	221.3 (197.0–245.6)	17	216.4 (186.4–246.4)	23	221.3 (197.0–245.6)	17	216.4 (186.4–246.4)	23	221.3 (197.0–245.6)	17	216.4 (186.4–246.4)	.09
Y.I.S. (yr)	26	8.2 (7.1–9.3)	23	8.5 (7.5–9.6)	18	8.0 (6.6–9.4)	21	8.9 (7.3–10.6)	23	9 (7.6–10.4)	17	8.1 (6.6–9.5)	23	8.9 (7.3–10.6)	17	8.1 (6.6–9.5)	23	9 (7.6–10.4)	17	8.1 (6.6–9.5)	23	9 (7.6–10.4)	17	8.1 (6.6–9.5)	.61
G.P.A.	26	3.3 (3.1–3.4)	23	3.3 (3.1–3.4)	18	3.3 (3.1–3.5)	20	3.2 (2.9–3.4)	23	3.1 (2.9–3.4)	16	3.1 (2.8–3.5)	23	3.2 (2.9–3.4)	16	3.1 (2.8–3.5)	23	3.1 (2.9–3.4)	16	3.1 (2.8–3.5)	23	3.1 (2.9–3.4)	16	3.1 (2.8–3.5)	.33
SAC	26	26.1 (25.3–26.9)	23	27.5 (26.9–28.2)	18	27.3 (26.4–28.2)	21	24.5 (23.3–25.7)	23	26.9 (25.8–28.0)	16	26.9 (25.7–28.0)	23	24.5 (23.3–25.7)	16	26.9 (25.7–28.0)	23	26.9 (25.8–28.0)	16	26.9 (25.7–28.0)	23	26.9 (25.8–28.0)	16	26.9 (25.7–28.0)	.03 ^b
BESS	25	12.3 (10.5–14.2)	22	10.1 (8.0–12.2)	18	11.9 (9.8–14.1)	18	14.1 (11.9–16.3)	23	11.8 (9.7–13.8)	17	11.8 (9.6–14.1)	23	14.1 (11.9–16.3)	17	11.8 (9.6–14.1)	23	11.8 (9.7–13.8)	17	11.8 (9.6–14.1)	23	11.8 (9.7–13.8)	17	11.8 (9.6–14.1)	.2
SCAT	26	3.0 (1.8–4.1)	23	1.9 (0.6–3.2)	18	2.3 (0.8–3.8)	21	27.2 (19.3–35.2)	23	5.3 (1.7–8.8)	17	1.2 (0.4–2.0)	23	27.2 (19.3–35.2)	17	1.2 (0.4–2.0)	23	5.3 (1.7–8.8)	17	1.2 (0.4–2.0)	23	5.3 (1.7–8.8)	17	1.2 (0.4–2.0)	<.001 ^b
RTP (days)	NA	NA	NA	NA	NA	NA	NA	NA	NA	17	14.9 (11.5–18.4)	20	14.9 (11.5–18.4)	13	14.4 (10.6–18.1)	NA	14.6 (11.6–17.4)	14	14.4 (10.6–18.1)	NA	14.6 (11.6–17.4)	13	14.4 (10.6–18.1)	NA	
P.SRC (total No.)	26	8	23	7	18	5	12	23	14	23	10	10	23	14	10	10	14	10	10	10	10	10	10	10	.05

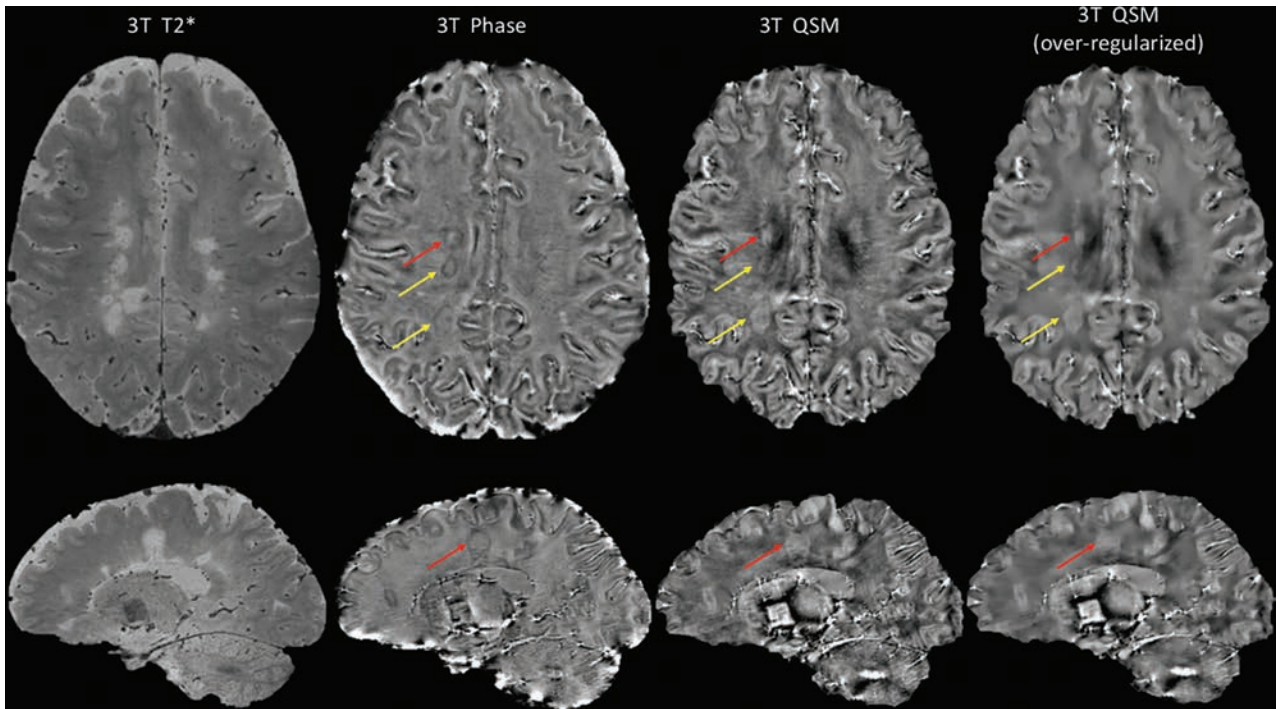
Note:—Y.I.S. indicates years in sport; G.P.A., academic grade point average on a 4.0-point scale; P.SRC, number of previous sports-related concussions; NA, not applicable; BESS, Balance Error Scoring System.

^a The number of subjects analyzed for each metric varied depending on the intersection of susceptibility map inclusion and availability of metric data for the subject. The final 3 columns provide time-point-resolved group statistical test P values (2-tailed t tests for all metrics except for P.SRC, which used a Mann-Whitney U test). Of note, none of the cohort statistics, when intersected with QSM data inclusion at each time point, show different results from the general statistics presented in Tables 2 and 3.

^b Significant.



ON-LINE FIGURE. Projection of the number of new HST2 lesions for each reader. Results are shown according to the CF method (on the y axis) or the standard one (on the x axis). The *red line* represents a similar detection rate for both techniques.



ON-LINE FIGURE. Comparison between phase and QSM images with different parameters for regularization at 3T MR imaging. MS lesions with paramagnetic rims (*yellow arrows*) are easier to detect on phase (hypointense) than on QSM (hyperintense) images. QSM images are typically smoothed; this process can result in a loss of conspicuity for rims. *Red arrows* indicate the same rim lesion on axial and sagittal reformations.

On-line Table 1: Scanner types and imaging parameters^a

	NMOSD	MS
Brain MR imaging		
Scanner type		
1.5T	54 (68.4)	42 (48.3)
3T	25 (31.6)	45 (51.7)
Manufacturer		
Toshiba ^b	13 (16.5)	3 (3.4)
Siemens ^c	22 (27.8)	21 (24.1)
GE ^d	22 (27.8)	29 (33.3)
Philips ^e	22 (27.8)	34 (39.1)
T2-weighted axial image		
Slice thickness (mm) ^f	5.2 ± 0.7	5.1 ± 0.7
Sequence parameters (FSE)		
TR ^g	2770–6014	3500–6220
TE ^g	78–110	80–110
ETL ^g	7–27	6–20
Spinal cord MR imaging		
Scanner type		
1.5T	56 (82.4)	53 (79.1)
3T	12 (17.6)	14 (20.9)
Manufacturer		
Toshiba	8 (11.8)	9 (13.4)
Siemens	26 (38.2)	22 (32.8)
GE	20 (29.4)	20 (29.9)
Philips	14 (20.6)	16 (23.9)
T2-weighted sagittal image		
Slice thickness (mm) ^f	3.6 ± 0.5	3.7 ± 0.7
Sequence parameters (FSE)		
TR ^g	2000–5000	2200–5179
TE ^g	85–131	81–131
ETL ^g	4–55	11–55
Optic nerve MR imaging		
Scanner type		
1.5T	29 (69)	8 (57.1)
3T	13 (31)	6 (42.9)
Manufacturer		
Toshiba	2 (4.8)	1 (7.1)
Siemens	15 (35.7)	8 (57.1)
GE	14 (33.3)	5 (35.7)
Philips	11 (26.2)	0 (0)
Orbital coronal image		
Slice thickness (mm) ^f	3.7 ± 0.9	3.8 ± 0.7
Sequence		
STIR image	31 (73.8)	8 (57.1)
FLAIR image	7 (16.7)	2 (14.3)
T2-weighted image	4 (9.5)	4 (28.6)

Note:—ETL indicates echo-train length.

^a Unless otherwise indicated, data in parentheses are percentages.

^b Toshiba Medical Systems, Tokyo, Japan.

^c Erlangen, Germany.

^d GE Healthcare, Milwaukee, Wisconsin.

^e Philips Healthcare, Best, the Netherlands.

^f Data are mean ± SD.

^g Data are range.

On-line Table 2: Summary of available MR imaging sequences for each analysis

Summary
For brain analysis
Quantitative analyses
Counting the number of lesions, measuring the maximum diameter, and identifying the location
Axial T2-weighted FSE images
Evaluation of the morphologic features and signs
T2-weighted FSE images (along with FLAIR and/or T1-weighted images with/without gadolinium enhancement if these imaging examinations were performed)
For spinal cord analysis
Quantitative analyses
Counting the number of lesions
Sagittal T2-weighted FSE images and axial T2-weighted FSE or gradient-echo images
Measuring the longitudinal length and identifying the spinal cord distribution
Sagittal T2-weighted FSE images
Measuring the transverse maximum diameter and identifying the intramedullary location
Axial T2-weighted FSE or gradient-echo images
Evaluation of the morphologic features
Sagittal T2-weighted FSE images and axial T2-weighted FSE or gradient-echo images
For optic nerve analysis
Identifying the location and evaluation of the morphologic features
Orbital coronal STIR, FLAIR, or T2-weighted images

On-line Table 3: Number and size of brain lesions for rater 2^a

Quantitative Analyses	NMOSD (n = 79)	MS (n = 87)	P Value ^b
Total No. of lesions	1064	1869	
Per patient	5 (1–17, 0–129)	12 (4–28, 0–123)	.002
Diameter (mm)	4.7 (3.7–6.6, 3.0–50)	5.4 (4.1–7.4, 3.0–50)	<.001
In each region (mm)			
PVWM	6.2 (4.3–8.4, 3.0–35)	6.2 (4.8–8.5, 3.0–50)	.32
DWM	4.5 (3.6–6.0, 3.0–23)	4.9 (3.8–6.5, 3.0–24)	.001
SCWM	4.5 (3.6–6.7, 3.0–31)	5.2 (4.0–6.9, 3.0–28)	.012
DGM	5.7 (3.7–8.0, 3.0–50)	5.3 (4.3–6.6, 3.0–17)	.59
BS	5.8 (4.6–7.2, 3.0–21)	5.4 (4.4–7.1, 3.2–16)	.68
Cerebellum	5.3 (5.1–8.0, 5.1–8.0)	5.6 (4.0–8.0, 3.0–20)	.84

^a Data are medians, with interquartile range, and total range in parentheses.

^b Mann-Whitney *U* test.

On-line Table 4: Number, size, and location of spinal cord lesions for rater 2^a

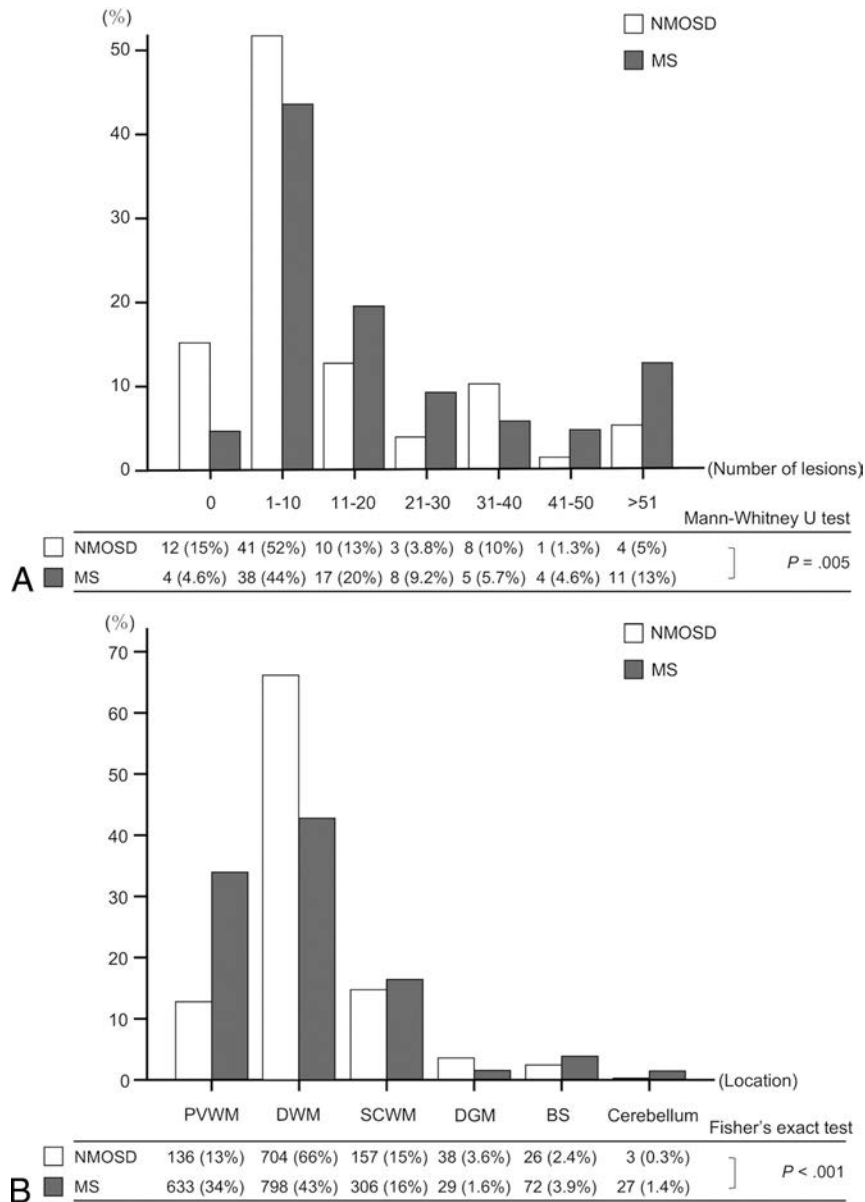
Quantitative Analyses	NMOSD (n = 57)	MS (n = 55)	P Value ^c
Total No. of lesions	105	160	
Per patient	1 (1–3, 0–7)	2 (1–4, 0–9)	.042
Longitudinal length (mm)	26 (9.0–69, 2.0–460)	10 (6.9–15, 2.2–109)	<.001
In cervical region (mm)	15 (8.0–37, 2.0–147)	10 (6.0–16, 2.2–70)	.009
In thoracic region (mm)	38 (10–78, 3.9–460)	9.0 (7.3–14, 3.4–109)	<.001
Transverse diameter (mm)	3.7 (2.6–5.6, 1.3–14)	4.0 (3.0–5.0, 1.3–10)	.72
In cervical region (mm)	4.6 (2.3–7.2, 1.5–14)	4.7 (3.4–6.1, 1.3–10)	.83
In thoracic region (mm)	3.5 (2.6–5.1, 1.3–9.1)	3.3 (2.7–4.3, 1.3–8.9)	.34
Intramedullary location ^b			
Central	65 (61.9)	68 (42.5)	.001 ^d
Peripheral	18 (17.1)	59 (36.9)	
Both	22 (21)	33 (20.6)	

^a Unless otherwise indicated, data are medians, with interquartile range and total range in parentheses.

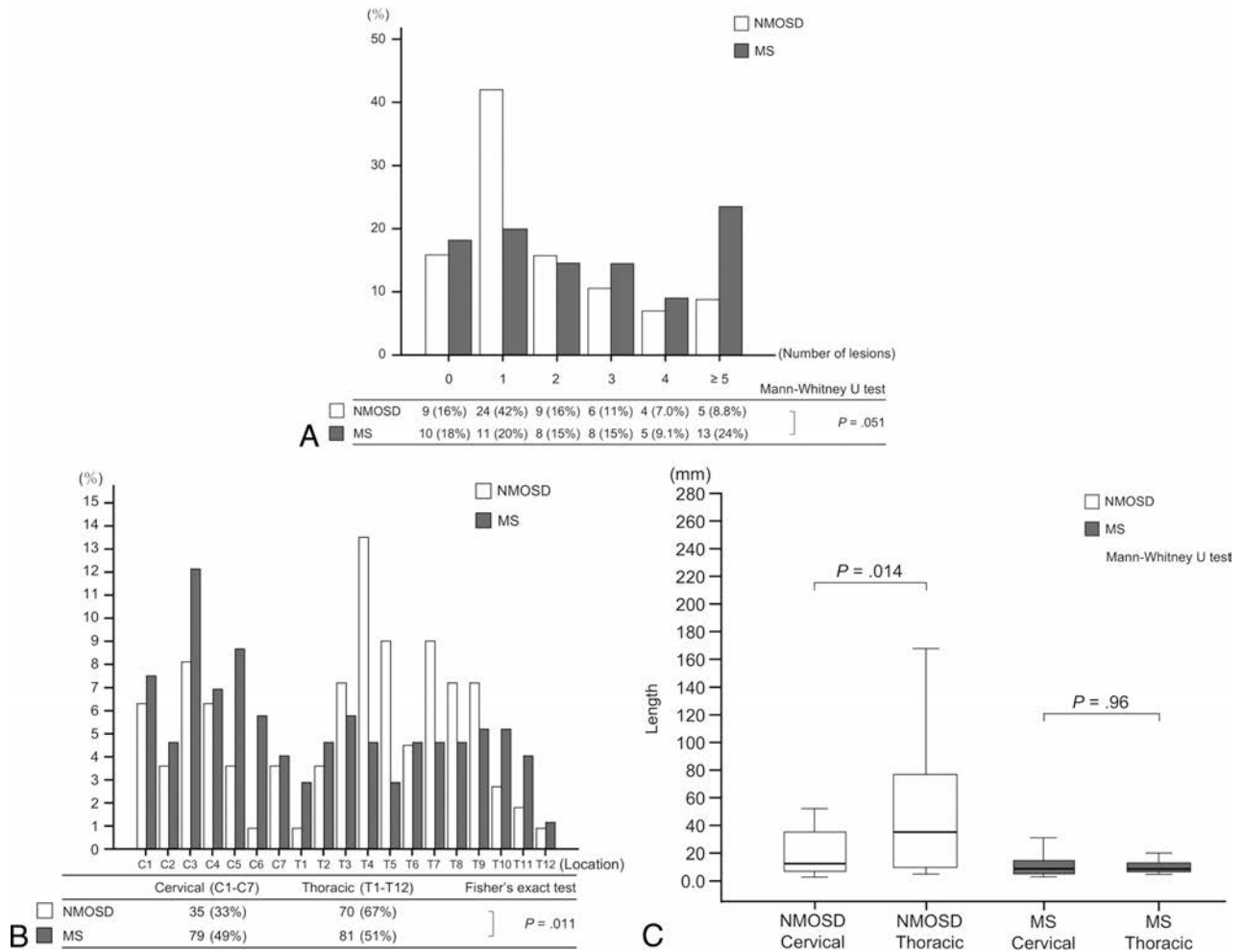
^b Data in parentheses are percentages.

^c Mann-Whitney *U* test.

^d Fisher exact test.



ON-LINE FIG 1. Bar graphs show the proportion of patients classified by the number of lesions in bins of 10 lesions (A) and the distribution of brain lesions categorized by location (PVWM, DWM, SCWM, DGM, BS, cerebellum) (B) for rater 2. A total of 1064 brain lesions in 79 patients with NMOSD and 1869 brain lesions in 87 patients with MS are identified. A, The proportion of patients is significantly different between NMOSD and MS ($P = .005$). More patients with NMOSD have no brain lesions of ≥ 3 mm, and a tendency for patients with MS to have more brain lesions than those with NMOSD is found. B, The distribution of lesions categorized by location is significantly different between NMOSD and MS ($P < .001$). DWM lesions (66%) are more frequent than PVWM lesions (13%) in NMOSD, whereas the difference in the frequencies of lesions in PVWM (34%) and DWM (43%) is small in MS.



ON-LINE FIG 2. Graphs show the proportion of patients classified according to the number of spinal cord lesions (A), the distribution and proportion of spinal cord lesions (B), and the length of spinal cord lesions in each location (C) for rater 2. A total of 105 spinal cord lesions in 57 patients with NMOSD and 160 spinal cord lesions in 55 patients with MS are identified. A, No significant difference is found in the number of lesions between NMOSD and MS ($P = .051$). Forty-eight (84%) patients with NMOSD and 45 (82%) patients with MS have ≥ 1 spinal cord lesion. B, Bimodal distributions of lesions are present in both NMOSD and MS, but the peak of the distribution in NMOSD is high in thoracic regions, whereas the variation and peaks of the distribution are relatively smaller in MS than in NMOSD. The proportion of lesions categorized into cervical or thoracic regions is significantly different between NMOSD and MS ($P = .011$). More thoracic lesions (67%) than cervical lesions (33%) are present in NMOSD, whereas the difference in the frequencies of cervical (49%) and thoracic lesions (51%) is small in MS. C, In NMOSD, thoracic lesions are significantly longer than cervical lesions ($P = .014$), whereas in MS, the length is not significantly different between cervical and thoracic lesions ($P = .96$).

On-line Table 1: Sequence parameters for 7T MRI

Sequence	TOF-MRA	MPRAGE
FOV (mm ²)	168 × 199	270 × 236
Matrix	896 × 756	384 × 336
Resolution (mm ²)	0.22 × 0.22	0.7 × 0.7
Slice thickness (mm)	0.41	0.7
TR (ms)	20	2500
TE (ms)	4.34	1.54
Flip angle	18°	7°
Bandwidth (Hz/pixel)	95	570
Acquisition time	6 min 22 sec	6 min 13 sec

On-line Table 2: Clinical characteristics

Patient No.	Lesions of Sporadic Moyamoya Angiopathy	Age at Examination (yr)	Age at Symptom Onset (yr)	Symptoms		Associated Symptoms	STA-MCA Bypass Surgery
				Symptoms	Symptoms		
1	Bilateral	23	23	Stroke, TIA		Cleft palate	Bilateral
2	Bilateral	46	45	Recurrent strokes, TIAs, seizures, headaches		Arterial hypertension	Bilateral
3	Unilateral	26	21	Recurrent strokes, TIA, headaches		Depression	Unilateral
4	Unilateral	26	24	Stroke		Hyperthyroidism	Unilateral
5	Bilateral	35	28	Recurrent strokes, TIAs, seizures		Cleft palate, livedo racemosa, arterial hypertension	Bilateral
6	Bilateral	29	20	Recurrent strokes, TIAs, choreatic movements, headaches		Hypothyroidism	Bilateral
7	Bilateral	58	34	Recurrent strokes, TIAs, seizures, hemorrhage, headaches		Depression, lung sarcoidosis, hypothyroidism	Bilateral
8	Bilateral	42	33	Stroke, headaches		Arterial hypertension	Bilateral
9	Bilateral	38	38	TIAs, vertigo, headaches		Depression	Unilateral
10	Bilateral	35	35	TIAs		Arterial hypertension	Unilateral
11	Bilateral	25	8	Stroke, ICH, headaches		Arterial hypertension since childhood	Bilateral
12	Bilateral	25	14	TIAs, stroke		Arterial hypertension	Bilateral
13	Bilateral	30	28	Recurrent strokes		Depression	Bilateral
14	Bilateral	56	55	TIAs, stroke		Depression	Bilateral
15	Bilateral	50	41	Recurrent strokes		Arterial hypertension multiple hernias	Bilateral

Note:—STA indicates superficial temporal artery; ICH, intracerebral hemorrhage.

On-line Table 3: Patient demographics and scoring of delineation of collateral pathways to cortical vessels^a

Patient No.	No.	Age (yr)	Sex	Side	Bypass Surgery	Suzuki Grading	Striate/Choroidal Arteries to Medullary-Cortical Arteries			Striate/Choroidal Arteries to Pericallosal Arteries		
							DSA	TOF	MPRAGE	DSA	TOF	MPRAGE
1	1	23	M	R	Pre	III	3	5	5	1	5	2
	2			L	Pre	III	4	4	4	2	4	3
	3	24	M	R	Post	III	3	5	4	1	5	3
	4			L	Post	III	4	4	4	2	5	3
2	5	46	M	R	Post	III	1	4	1	1	1	1
	6			L	Post	III	1	1	1	1	1	1
3	7	26	F	R	Pre	II	1	1	1	1	1	1
4	8	35	F	L	Post	III	1	1	1	1	1	1
5	9	34	F	R	Pre	III	1	4	1	1	1	1
	10			L	Pre	IV	1	3	1	1	1	1
	11			R	Post	III	1	4	1	1	1	1
	12			L	Post	IV	1	1	1	1	1	1
6	13	29	F	R	Pre	III	1	5	1	1	1	1
	14			L	Pre	III	5	5	1	3	4	1
7	15	58	F	R	Post	II	1	1	1	1	1	1
	16			L	Post	II	1	1	1	1	1	1
8	17	42	F	R	Post	III	1	1	1	1	1	1
	18			L	Post	III	5	5	1	4	5	1
9	19	38	F	R	Pre	III	4	5	1	1	1	1
	20			L	Pre	II	1	1	1	1	1	1
10	21	35	F	R	Pre	III	1	1	1	1	1	1
	22			L	Pre	III	1	1	1	1	1	1
11	23	26	F	R	Pre	III	5	5	2	1	1	1
	24			L	Pre	IV	5	5	5	1	1	1
12	25	19	F	R	Pre	II	1	1	1	1	1	1
	26			L	Post	IV	5	5	3	5	5	1
13	27	30	M	R	Post	IV	1	1	1	5	5	1
	28			L	Post	III	5	5	2	3	5	1
14	29	56	F	R	Post	II	1	1	1	1	1	1
	30			L	Pre	II	1	1	1	1	1	1
15	31	50	M	R	Pre	III	1	1	1	1	1	1
	32			L	Post	III	1	1	1	1	1	1

Note:—R indicates right; L, left; Pre, before; Post, after; No., running number of evaluated brain hemispheres.

^aRating: 5 = excellent, collateral networks obviously detected with clear identification of the vessel course and high vessel-tissue contrast; 4 = good, collateral networks well-detected with lower vessel-tissue contrast; 3 = moderate, collateral networks partially invisible but still adequate for diagnosis; 2 = poor, collateral connections scarcely demonstrated but sufficient to presume their existence; 1 = no collateral networks detected. Suzuki grading: stage I = narrowing of the carotid fork—narrowed ICA bifurcation; stage II = initiation of the Moyamoya—dilated ACA, MCA and narrowed ICA bifurcation with Moyamoya change; stage III = intensification of the Moyamoya—further increase in Moyamoya change of the ICA bifurcation and narrowed ACA and MCA; stage IV = minimization of the Moyamoya—Moyamoya change reducing with occlusive changes in ICA and tenuous ACA and MCA; stage V = reduction of the Moyamoya—further decrease in Moyamoya change with occlusion of ICA, ACA and MCA; stage VI = disappearance of the Moyamoya—ICA essentially disappeared with supply of brain from ECA.

On-line Table 4: Patient demographics and delineation scoring of collateral pathways to major trunk vessels^a

Patient No.	No.	Age (yr)	Sex	Side	Bypass Surgery	Suzuki Grading	Chorooidal Arteries and Ant/Post Thalamostriate Arteries				Intrastratial Arteries				Intrathalamic Arteries				Moyamoya Vessels in the Basal Cistern			
							DSA	TOF	MPRAGE	DSA	TOF	MPRAGE	DSA	TOF	MPRAGE	DSA	TOF	MPRAGE	DSA	TOF	MPRAGE	
1	1	23	M	R	Pre	III	5	5	4	5	5	4	5	5	4	5	5	4	5	5	4	
	2			L	Pre	III	5	5	4	5	5	4	5	5	4	5	5	4	5	5	4	
	3	24	M	R	Post	III	5	5	3	5	5	3	5	5	3	5	5	4	5	5	3	
	4			L	Post	III	5	5	3	5	5	3	5	5	3	5	5	3	5	5	4	
2	5	46	M	R	Post	III	3	3	1	1	1	1	1	1	1	5	5	3	5	5	4	
	6			L	Post	III	1	1	1	1	1	1	1	1	1	1	1	1	1	1	3	
3	7	26	F	R	Pre	II	1	1	1	1	1	1	1	1	1	1	1	1	1	1	4	
4	8	35	F	L	Post	III	5	5	4	1	1	1	1	1	1	1	1	1	1	1	4	
5	9	34	F	R	Pre	IV	4	3	1	1	1	4	5	5	4	1	1	1	1	1	4	
	10			L	Pre	IV	4	3	1	1	1	4	5	5	4	1	1	1	1	1	4	
	11			R	Post	III	4	3	1	1	1	4	5	5	4	1	1	1	1	1	4	
	12			L	Post	IV	4	3	1	1	1	4	5	5	4	1	1	1	1	1	4	
6	13	29	F	R	Pre	III	5	5	3	5	5	3	5	5	2	3	5	1	1	1	4	
	14			L	Pre	III	5	5	3	5	5	3	5	5	1	3	5	1	1	1	4	
7	15	58	F	R	Post	II	1	1	1	1	1	1	1	1	1	1	1	1	1	1	2	
	16			L	Post	II	1	1	1	1	1	1	1	1	1	1	1	1	1	1	2	
8	17	42	F	R	Post	III	4	5	1	1	1	1	5	5	3	1	1	1	1	1	4	
	18			L	Post	III	4	5	1	1	1	1	5	5	3	1	1	1	1	1	4	
9	19	38	F	R	Pre	III	1	1	1	1	1	1	1	1	1	1	1	1	1	1	3	
	20			L	Pre	II	1	1	1	1	1	1	1	1	1	1	1	1	1	1	3	
10	21	35	F	R	Pre	III	4	4	1	1	1	5	5	5	2	1	1	1	1	1	4	
	22			L	Pre	III	4	4	1	1	1	5	5	5	2	1	1	1	1	1	4	
11	23	26	F	R	Pre	III	5	5	1	1	1	5	5	5	3	1	1	1	1	1	1	
	24			L	Pre	IV	1	1	1	1	1	5	5	5	3	1	1	1	1	1	1	
12	25	19	F	R	Pre	II	1	1	1	1	1	1	1	1	1	1	1	1	1	1	1	
	26			L	Post	IV	5	5	1	1	1	4	5	5	2	4	1	1	1	1	1	
13	27	30	M	R	Post	IV	5	5	2	1	1	5	5	5	3	1	1	1	1	1	3	
	28			L	Post	III	1	1	1	1	1	5	5	5	3	1	1	1	1	1	2	
14	29	56	F	R	Post	II	1	1	1	1	1	1	1	1	1	1	1	1	1	1	1	
	30			L	Pre	II	1	1	1	1	1	1	1	1	1	1	1	1	1	1	1	
15	31	50	M	R	Pre	III	4	1	1	1	1	5	5	4	1	1	1	1	1	1	3	
	32			L	Post	III	4	1	1	1	1	3	3	3	1	1	1	1	1	1	4	

Note:—Ant/Post indicates anterior/posterior; No., running number of evaluated brain hemispheres.

^a Rating: 5 = excellent, collateral networks obviously detected with clear identification of the vessel course and high vessel-tissue contrast; 4 = good, collateral networks well-detected with lower vessel-tissue contrast; 3 = moderate, collateral networks were partially invisible but still adequate for diagnosis; 2 = poor, collateral connections scarcely demonstrated but sufficient to presume their existence; 1 = no collateral networks detected. Suzuki grading: stage I = narrowing of the carotid fork—narrowed ICA bifurcation; stage II = initiation of the Moyamoya—dilated ACA, MCA and narrowed ICA bifurcation with Moyamoya change; stage III = intensification of the Moyamoya—further increase in Moyamoya change of the ICA bifurcation and narrowed ACA and MCA; stage IV = minimization of the Moyamoya—Moyamoya change reducing with occlusive changes in ICA and tenuous ACA and MCA; stage V = reduction of the Moyamoya—further decrease in Moyamoya change with occlusion of ICA, ACA and MCA; stage VI = disappearance of the Moyamoya—ICA essentially disappeared with supply of brain from ECA.

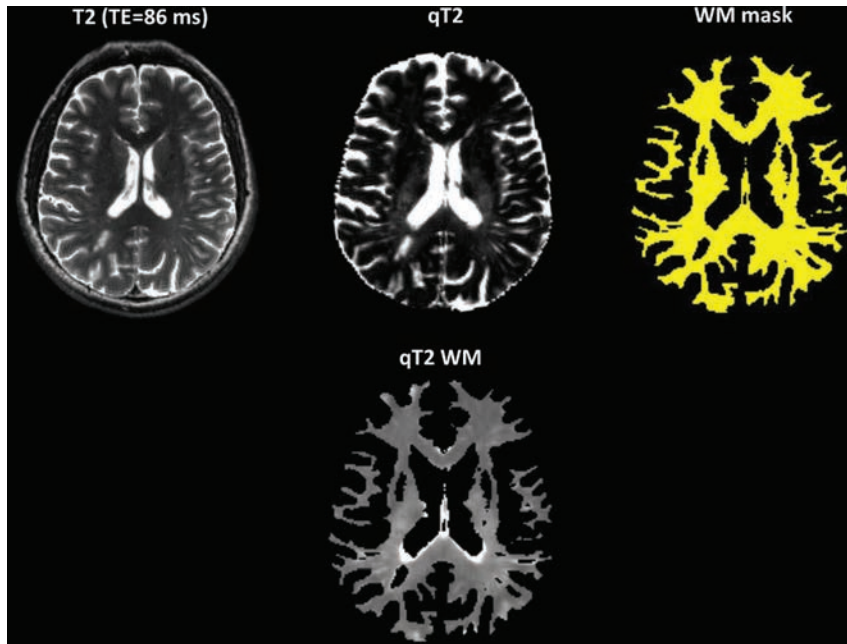
On-line Table: Mean values ± SD and AIs for qT2 and perfusion parameters in WM and cortical areas with TTP delay ipsilateral to the stenosis/occlusion and corresponding contralateral areas^a

ROI	qT2 (ms)		TTP Delay (s)	rCBF/rCBV (a.u.)		rCBF (a.u.)		rCBV (a.u.)					
	Ipsi	Contra		AI (%)	Ipsi	Contra	AI (%)	Ipsi	Contra	AI (%)			
WM													
>0-second delay	110.08 ± 19.27	106.39 ± 15.71	1.37 ± 1.03	3.07 ± 4.41	9.61 ± 15.7	11.28 ± 18.09	-22.11 ± 11.94	143.8 ± 76.9	167.9 ± 88.7	-15.75 ± 12.38	6 ± 4.4	5.7 ± 3.9	5.8 ± 9.68
P value	.008				<.001				.001			.04 ^b	
0- to 2-second delay	110.19 ± 24.59	108.55 ± 26.06	0.79 ± 0.12	1.61 ± 4.37	21.74 ± 14.96	26.17 ± 17.91	-19.01 ± 11.42	150.5 ± 77.2	169.2 ± 84.8	-12.61 ± 12.81	8.1 ± 3.1	7.5 ± 2.6	5.83 ± 10.74
P value	.184				<.001				.005			.052	
2- to 4-second delay	120.76 ± 22.71	110.18 ± 12.06	2.65 ± 0.17	8.21 ± 8.86	16.26 ± 11.26	23.58 ± 16.01	-37.3 ± 15.05	123.2 ± 81	160.6 ± 113.4	-23.84 ± 21.31	8.5 ± 3.4	7.7 ± 2.7	7.37 ± 11.4
P value	.001				<.001				.001			.02	
4- to 6-second delay	131.45 ± 35.3	115.29 ± 30.43	4.78 ± 0.26	12.82 ± 7.77	16.57 ± 11.85	23.75 ± 15.72	-38.52 ± 16.75	170.7 ± 106.6	212 ± 159.2	-20.66 ± 29.07	11.1 ± 4	9.8 ± 3.5	12.77 ± 19.13
P value	<.001				.001				.015			.02	
6- to 8-second delay	119.51 ± 13.12	104.09 ± 6.38	6.77 ± 0.44	13.42 ± 8.6	11.96 ± 4.65	17.76 ± 5.19	-41.04 ± 18.35	149.6 ± 94.3	183.2 ± 77.4	-26.13 ± 51.02	12 ± 4	10.6 ± 3.6	11.24 ± 45.53
P value	.008				.012				.401			.575	
Cortex	148.78 ± 37.46	142.58 ± 31.18	1.43 ± 1.14	3.61 ± 5.02	18.01 ± 8.91	20.89 ± 9.88	-15.17 ± 13.41	199.7 ± 78.4	219.6 ± 91.5	-7.35 ± 12.88	11.8 ± 3.3	11.1 ± 2.8	11.24 ± 45.53
P value	.007				<.001				.022			.013	

Note:—Ipsi indicates ipsilateral; Contra, contralateral; a.u., arbitrary units.

^a Perfusion parameter values are given in arbitrary units as exported by the scanner-processing software.

^b Not significant after correction for multiple comparisons.



ON-LINE FIGURE. Illustration of the masking procedure for white matter. The second T2-weighted image (TE = 86 ms) shows a hyperintense lesion in the right parieto-occipital white matter, which can also be seen on the quantitative T2 map. Note that after we applied the white matter mask based on the partial volume estimate (lower threshold = 0.95) to the quantitative T2 map, this lesion and other T2-hyperintense structures, including prominent perivascular spaces, are removed from the resulting white matter map. Furthermore, parts of the basal ganglia, which are visible in the T2-weighted images, are not included in the white matter mask.

On-line Table 1: Summary of patient characteristics, clinical presentation, CTA findings, treatment, and neurologic outcome in 31 patients with CBS

Patient No./Sex/Age (yr)	Cancer Type	Clinical Presentation	CTA Findings ^a	Location of PCO	Neurologic Outcome/mRS
Nasopharynx					
1/M/74	Nasopharyngeal cancer	Epistaxis/oral bleeding	1, 2, 4, 5	Right ICA	Right borderzone infarction/3
2/M/41	Nasopharyngeal cancer	Epistaxis/oral bleeding	1, 2, 4	Right CCA	Asymptomatic/0
3/M/58	Nasopharyngeal cancer	Epistaxis/oral bleeding	1, 2, 4, 5	Right ICA	Asymptomatic/0
4/M/33	Nasopharyngeal cancer	Epistaxis	1, 3	Left ICA	Left borderzone infarction/3
5/F/79	Nasopharyngeal cancer	Epistaxis	3	Left ICA	Left borderzone infarction/4
6/M/61	Nasopharyngeal cancer	Oral bleeding	1, 3, 4	Left ICA	Left borderzone infarction/4
7/M/67	Nasopharyngeal cancer	Epistaxis	1, 2, 3, 4, 5	Right CCA	Right ACA infarction/4
8/M/63	Nasopharyngeal cancer	Epistaxis	2, 4	Left ICA	Asymptomatic/0
9/F/39	Nasopharyngeal cancer	Epistaxis/oral bleeding	1, 2, 3, 5	Left ICA-ECA	Asymptomatic/0
10/M/52	Nasopharyngeal cancer	Epistaxis	2, 4, 5	Right ICA	Asymptomatic/0
11/M/58	Nasopharyngeal cancer	Epistaxis	1, 2, 4, 5	Left ICA	Asymptomatic/0
12/M/55	Nasopharyngeal cancer	Cough with sputum	1, 2, 4, 5	Left ICA	Asymptomatic/0
13/F/44	Nasopharyngeal cancer	Epistaxis	1, 2, 3, 4, 5	Right ICA	Asymptomatic/0
Oropharynx					
14/M/50	Oropharyngeal cancer	Oral bleeding	1	Left ICA	Left borderzone infarction/3
15/F/67	Oropharyngeal cancer	Oral bleeding	1, 2, 4, 5	Right ICA-CCA	Asymptomatic/0
16/M/54	Oropharyngeal cancer	Oral/exposed tumor bleeding	1, 2, 3, 5	Right ICA-CCA	Asymptomatic/0
17/M/46	Oropharyngeal cancer	Oral bleeding	1, 2, 4, 5	Right ICA	Asymptomatic/0
18/M/47	Oropharyngeal cancer	Oral bleeding	1, 2, 4, 5	Right ICA	Right borderzone infarction/2
19/M/67	Oropharyngeal cancer	Epistaxis/oral bleeding	1, 2, 5	Left ICA-CCA	Asymptomatic/0
Oral cavity					
20/M/61	Oral cancer	Neck wound bleeding	1, 2, 5	Left ICA-ECA	Asymptomatic/0
21/M/41	Oral cancer	Buccal wound bleeding	1, 2, 3, 5	Left ICA	Asymptomatic/0
22/M/48	Oral cancer	Buccal wound bleeding	1, 2, 4, 5	Left ICA-CCA	Asymptomatic/0
23/M/36	Oral cancer	Buccal wound bleeding	1, 2, 5	Left ICA-ECA-CCA	Asymptomatic/0
Hypopharynx					
24/M/45	Hypopharyngeal cancer	Neck wound bleeding	1, 2, 5	Left ICA-ECA-CCA	Left retinal artery infarction/1
25/M/41	Hypopharyngeal cancer	Neck wound bleeding	1, 2, 4, 5	Right CCA	Asymptomatic/0
26/M/52	Hypopharyngeal cancer	Neck wound bleeding	1, 2, 5	Left ICA	Asymptomatic/0
27/M/59	Hypopharyngeal cancer	Neck wound bleeding	1, 2, 5	Right CCA	Right borderzone infarction/4
28/M/60	Hypopharyngeal cancer	Tracheostomy bleeding	1, 2, 3, 5	Right ICA-CCA	Asymptomatic/0
29/M/51	Hypopharyngeal cancer	Epistaxis/oral bleeding	1, 2, 4, 5	Right ICA-CCA	Asymptomatic/0
Others					
30/M/53	Laryngeal cancer	Epistaxis/oral bleeding	1, 2, 5	Left CCA	Asymptomatic/0
31/M/64	Thyroid cancer	Oral bleeding	1, 2, 3, 5	Right CCA	Right retinal infarction/1

Note:—ACA indicates anterior cerebral artery; ECA, external carotid artery.

^a 1) viable perivascular tumor, 2) perivascular tissue or tumor necrosis, 3) contrast extravasation, 4) pseudoaneurysm formation, and 5) exposed artery.

On-line Table 2: The performance of CTA for predicting stroke after PCO

	κ	A_z Value (95% CI)	Sensitivity (%)	Specificity (%)	PPV (%)	NPV (%)
Collateral reserve of the circle of Willis	0.807					
Borderzone infarction						
Reader 1		0.97 (0.915–1)	100 (7/7)	70.8 (17/24)	50 (7/14)	100 (17/17)
Reader 2		0.914 (0.809–1)	100 (7/7)	62.5 (15/24)	43.8 (7/16)	100 (15/15)
Consensus		0.938 (0.85–1)	100 (7/7)	62.5 (15/24)	43.8 (7/16)	100 (15/15)
All-cause stroke						
Reader 1		0.767 (0.555–0.978)	70 (7/10)	66.7 (14/21)	50 (7/14)	82.4 (14/17)
Reader 2		0.702 (0.482–0.923)	70 (7/10)	57.1 (12/21)	43.8 (7/16)	80 (12/15)
Consensus		0.721 (0.5–0.943)	70 (7/10)	57.1 (12/21)	43.8 (7/16)	80 (12/15)

Note:—NPV indicates negative predictive value; PPV, positive predictive value.

On-line Table: Predictors of ischemic complications

Parameter	No Complications (n = 100)	Complications (n = 29)	P Value	
			Univariable	Multivariable
Sex				
Female	66 (80.5%)	16 (19.5%)	.29	—
Male	34 (72.3%)	13 (27.7%)		
Median age (range) (yr)	58 (29–78)	54 (29–82)	.86	—
Smoking ^a				
Yes	36 (90%)	4 (10%)	.02	OR, 0.2; 95% CI, 0.05–0.7; P = .01
No	57 (71.3%)	23 (28.8%)		
Presenting symptoms				
Asymptomatic	23 (82.1%)	5 (17.9%)	.2	—
Headache/dizziness	26 (8.7%)	4 (13.3%)		
Neurologic deficit	51 (71.8%)	20 (28.2%)		
Subarachnoid hemorrhage				
No	69 (75.8%)	22 (24.2%)	.17	—
Acute (<24 hr)	6 (100%)	0%		
Immediate (<2 wk)	13 (92.9%)	1 (7.1%)		
Remote (>2 wk)	12 (66.7%)	6 (33.3%)		
Pretreatment mRS				
0–2	81 (80.2%)	20 (19.8%)	.17	—
3–5	19 (67.9%)	9 (32.1%)		
Aneurysm location				
VA	38 (84.4%)	7 (15.6%)	.48	—
Vertebrobasilar artery	13 (72.2%)	5 (27.8%)		
PICA	8 (88.9%)	1 (11.1%)		
Basilar artery	32 (69.6%)	14 (30.4%)		
SCA	2 (66.7%)	1 (33.3%)		
PCA	7 (87.5%)	1 (12.5%)		
Aneurysm shape				
Saccular	36 (76.6%)	11 (23.4%)	.7	—
Fusiform	38 (74.5%)	13 (25.5%)		
Dissecting	24 (82.8%)	5 (17.2%)		
Aneurysm measurements				
Maximal diameter				
<7 mm	18 (81.8%)	4 (18.2%)	.11	—
7–12 mm	38 (88.4%)	5 (11.6%)		
13–24 mm	27 (69.2%)	12 (30.8%)		
>24 mm	17 (68%)	8 (32%)		
Daughter sac				
Yes	21 (80.8%)	5 (19.2%)	.66	—
No	79 (76.7%)	24 (23.3%)		
Intra-aneurysmal thrombus				
Yes	25 (64.1%)	14 (35.9%)	.02	OR, 2.7; 95% CI, 0.9–7.8; P = .06
No	75 (83.3%)	15 (16.7%)		
Prior treatment				
No	84 (75%)	28 (25%)	.37	—
Endovascular	13 (92.9%)	1 (7.1%)		
Surgery	2 (100%)	0%		
Both	1 (100%)	0%		
Platelet function testing				
Yes	64 (83.1%)	13 (16.9%)	.06	—
No	36 (69.2%)	16 (30.8%)		
Clopidogrel responders ^b				
Yes	54 (85.7%)	9 (14.3%)	.2	—
No	10 (71.4%)	4 (28.6%)		
Adjunctive coiling				
Yes	33 (82.5%)	7 (17.5%)	.36	—
No	67 (75.3%)	22 (24.7%)		
No. of Pipelines deployed (median) (range)	1 (1–14)	2 (1–9)	.03	OR, 1.1; 95% CI, 0.9–1.4; P = .4
Length of procedure (median) (range) (min)	104 (22–360)	145 (42–410)	.04	OR, 1; 95% CI, 0.9–1.01; P = .1
Branch status				
Covered	76 (73.8%)	27 (26.2%)	.04	OR, 2.6; 95% CI, 0.5–12.4; P = .24
Not covered	24 (92.3%)	2 (7.7%)		
No. of covered branches				
≤2	47 (71.2%)	19 (28.8%)	.43	—
>2	29 (78.4%)	8 (21.6%)		
Covered branches status				
Occluded	18 (85.7%)	3 (14.3%)	.16	—
Not occluded	58 (70.7%)	24 (29.3%)		

Note:—SCA indicates superior cerebellar artery.

^a Data are missing in 9 procedures.

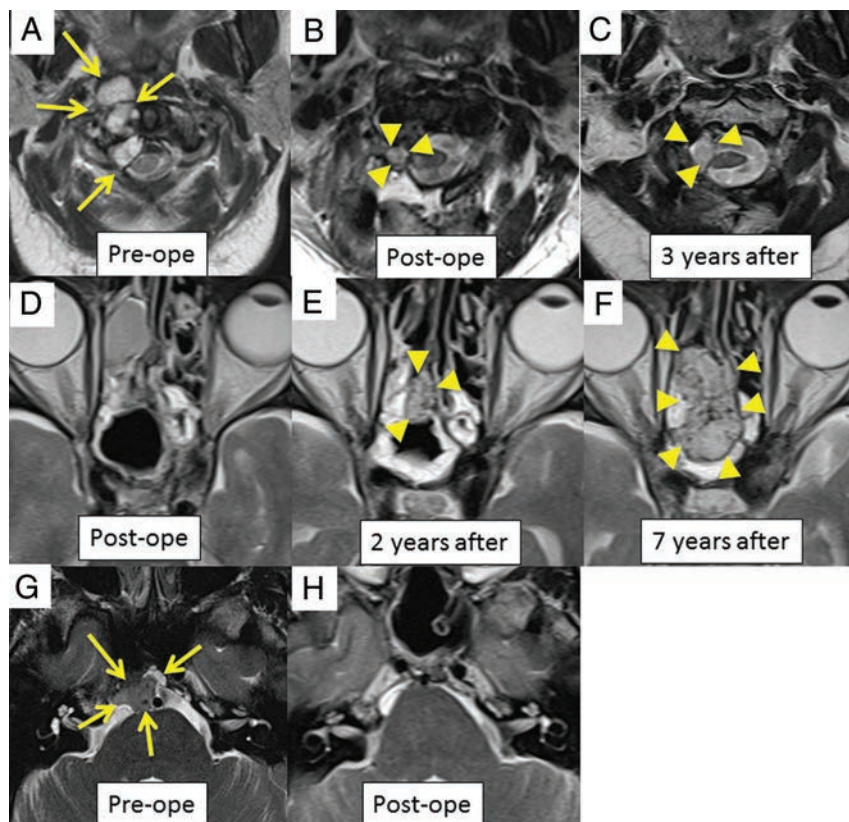
^b Among patients with platelet function testing.

ON-LINE APPENDIX

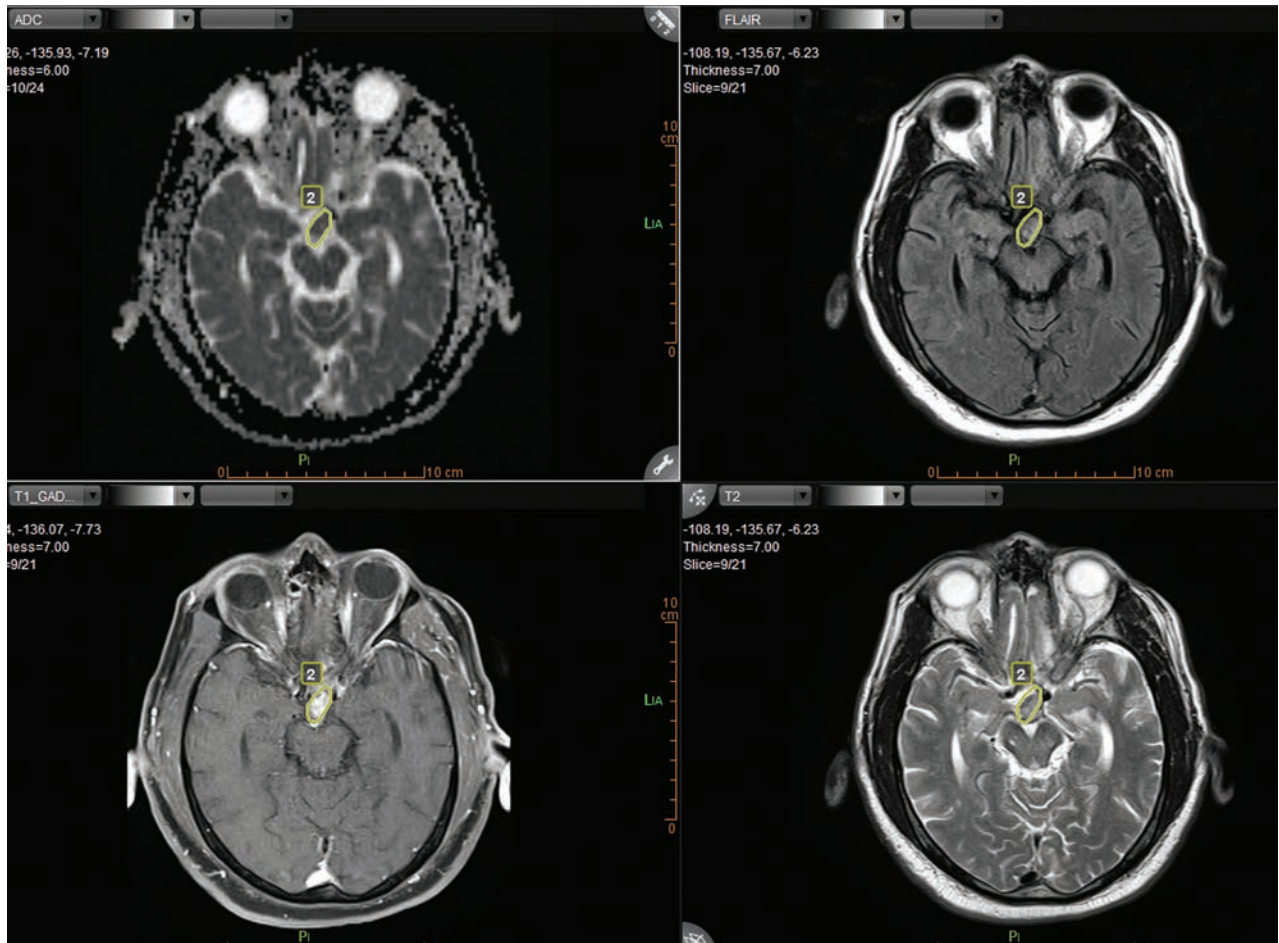
Supplemental data: Correlation between apparent diffusion coefficient and adjuvant radiation therapy.

Methods: We calculated Pearson correlation coefficients between the mean ADC at the first MR imaging scan and radiation dose and the interval from the RT to the first MR imaging in 11 patients.

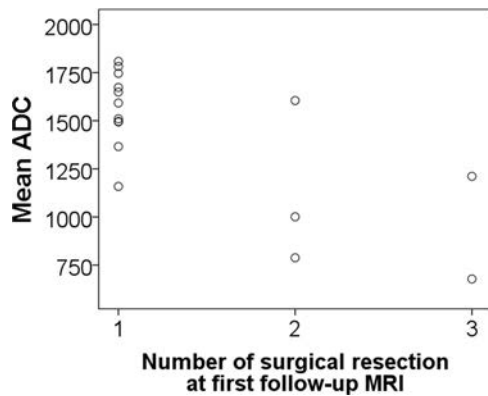
Result: There were no significant correlations between the ADC and radiation dose ($r = -0.119, P = .724$) or between the ADC and the interval between RT and the first MR imaging scan ($r = -.433, P = .160$).



ON-LINE FIG 1. Examples of residual and recurrent chordomas and no recurrence. A–C, Residual chordoma. A, An expansile mass was observed on the right side of the C2 spine preoperatively (arrows). B, A small expansile mass was observed adjacent to the resection site (arrowheads). C, The mass had increased in size 3 years after the resection (arrowheads). D–F, Recurrent chordoma. There was no residual tumor in the operation bed (D), but 2 years later, an expansile nodule appeared at the site (E, arrowheads), which increased in size 5 years after the recurrence (F, arrowheads). G–H, No recurrence or residual tumor. G, An expansile tumor arose in the clivus (arrows), and a subsequent image (H) showed neither residual tumor nor recurrence. Ope indicates operation.



ON-LINE FIG 2. Example of tumor measurements. Snapshot showing ADC measurements of a tumor by Olea Sphere. When drawing an ROI surrounding a tumor in one sequence, the software tool automatically copies the ROI to other images.



ON-LINE FIG 3. Correlation between ADC and the number of surgical resections at first MR imaging scan. Methods: We calculated the Pearson correlation coefficients between the mean ADC and the number of surgical resections at the first MR imaging. Result: There was a significant correlation between the ADC and the number of surgical resections ($r = -.718, P = .002$). The ADC and the number of surgical resections could be confounder factors of each other for survival. Moreover, the number of surgical resections was equivalent to the number of recurrences, which supported the hypothesis of this study that recurrent and residual chordoma might acquire aggressive features with time with a decreased ADC value. Some poorly differentiated chordomas arise in a pre-existing low-grade lesion with or without previous treatment.^{1,5,23-28}

On-line Table 1: Global and regional CBF by brain injury severity (mild BI versus moderate-severe injury), adjusted for GA at birth^a

Controlling for GA at Birth	PT with Mild BI (n = 29, 61.7%)	PT with Moderate-Severe BI (n = 18, 38.3%)	P Value
Global CBF	18.9 (17.0–20.8)	16.4 (13.9–18.9)	.12
DLPF	15.4 (12.9–17.8)	14.0 (10.8–17.1)	.49
PM	20.2 (17.3–23.0)	18.0 (14.3–21.7)	.35
Primary motor	23.6 (20.6–26.5)	20.1 (16.2–23.9)	.15
PO	15.4 (12.9–17.9)	12.5 (9.3–15.8)	.16
MT	23.2 (20.3–26.5)	20.0 (16.2–24.6)	.23
IO	18.3 (15.2–21.4)	16.4 (12.3–20.6)	.48
Rt. thalamus	29.7 (25.1–34.3)	29.0 (22.8–35.2)	.85
Lt. thalamus	29.6 (24.9–34.3)	23.3 (17.2–29.5)	.11
Midpons	40.8 (34.0–47.7)	30.9 (21.5–40.3)	.09
Ant vermis	30.1 (24.2–36.0)	22.4 (14.7–30.1)	.11
Post vermis	30.6 (24.1–37.1)	21.8 (12.4–31.2)	.12
Rt. cerebellar hemispheres	21.4 (17.1–25.7)	14.2 (8.2–20.3)	.06
Lt. cerebellar hemispheres	22.9 (17.7–28.2)	20.2 (12.8–27.5)	.54
Dentate	31.8 (24.7–38.9)	19.0 (6.0–32.0)	.08

Note:—Rt. indicates right; Lt., left; Ant, anterior; Post, posterior.

^aData are means (95% confidence intervals).

On-line Table 2: Clinical risk factors and CBF, adjusted for GA at birth^a

Risk factor (No.) (%) / Region	β	Yes (Positive Risk Factor)	No (Negative Risk Factor)	P Value
Sepsis (40) (51.3)				
Posterior vermis	−9.30	24.80	34.10	.03
Right cerebellar hemisphere	−6.73	16.40	23.13	.02
Left cerebellar hemisphere	−6.11	19.24	25.35	.07
Dentate	−8.99	24.76	33.75	.05
Ventilation (63) (80.8)				
Right thalamus	−7.87	30.41	38.28	.03
Left thalamus	−7.09	28.33	35.42	.06
Midpons	−14.48	39.27	53.75	.01
Pressors (16) (20.5)				
DLPF	4.75	19.35	14.60	.008
PM	3.55	23.14	19.59	.09
PO	1.85	17.54	14.35	.09
Intubation (48 hr) (9) (11.5)				
Global CBF	−4.03	15.36	19.39	.05
DLPF	−4.57	11.54	16.10	.06
PM	−5.30	15.63	20.93	.07
Primary motor	−5.85	18.08	23.94	.05
PO	−6.98	8.83	15.81	.006
IO	−6.35	13.33	19.68	.05
Right thalamus	−9.47	23.58	33.05	.05
Midpons	−22.06	22.48	44.55	.002
Ant vermis	−19.97	12.13	32.11	.001
Post vermis	−19.57	12.69	32.26	.003
Right cerebellar hemisphere	−13.89	7.63	21.52	.002
Left cerebellar hemisphere	−14.29	9.80	24.10	.007
Dentate nuclei	−17.62	18.84	31.46	.03
Delivery method (cesarean delivery) (51) (65.4)				
Right thalamus	−7.82	29.20	37.02	.007
Left thalamus	−9.62	26.36	35.98	.001
Midpons	−9.73	38.73	48.46	.03
Ant vermis	−9.51	26.75	36.26	.01
Right cerebellar hemisphere	−5.38	18.04	23.42	.06

Note:—Ant indicates anterior; Post, posterior.

^aCategoric measures with “Yes” indicate mean CBF values in PT infants with a clinical risk factor versus “No” without a risk factor for the specified risk factors and perfusion regions, except for delivery method in which the comparison is having cesarean delivery versus vaginal delivery.

On-line Table 3: CBF measures by sedation within 48 hours status, adjusted for GA at birth^a

Controlling for GA at Birth	No Sedation (n = 68, 87.2%)	Sedation (n = 10, 12.8%)	P Value
Global CBF	18.91 (17.61–20.21)	19.01 (15.59–22.43)	.96
DLPF	15.81 (14.23–17.39)	14.00 (9.84–18.15)	.42
PM	20.56 (18.71–22.41)	18.67 (13.79–23.54)	.47
Primary motor	23.22 (21.27–25.18)	23.50 (18.36–28.64)	.92
PO	15.58 (13.64–16.91)	13.17 (8.87–17.47)	.37
MT	23.29 (21.12–25.46)	26.08 (20.41–31.75)	.37
IO	18.91 (16.84–20.98)	19.13 (13.72–24.55)	.94
Rt. thalamus	29.75 (21.66–37.85)	32.27 (29.17–35.37)	.57
Lt. Thalamus	29.52 (26.33–32.72)	30.85 (22.45–39.26)	.77
Mid pons	42.60 (37.85–47.35)	37.54 (25.21–49.86)	.45
Anterior vermis	30.79 (26.87–34.72)	24.82 (14.62–35.02)	.28
Posterior vermis	30.59 (26.16–35.02)	22.33 (10.32–34.35)	.20
Rt. cerebellar hemispheres	20.22 (17.29–23.16)	16.86 (8.97–24.75)	.43
Lt. cerebellar hemispheres	22.90 (19.42–26.37)	18.34 (8.99–27.70)	.37
Dentate nuclei	30.45 (25.74–35.17)	24.54 (11.41–37.66)	.40

Note:—Rt. indicates right; Lt., left.

^aData are means (95% confidence intervals).

On-line Table 1: Conventional MRI findings in children with CLN3 during the first and second MRI acquisitions

Subject	1st MRI			2nd MRI			
	Age (yr)	Ventricles	Surface Area (cm ²) of Corpus Callosum	Age (yr)	Ventricles ^a	Sulci ^a	Surface Area (cm ²) of Corpus Callosum
1	7.1	0	4.0	9.2	0	0	3.9
2	6.0	0	4.0	8.2	0	0	3.8
3	10.6	0	4.2				
4	7.5	0	2.8	9.5	0	0	2.7
5	8.0	0	3.9	10.0	1	1	3.6
6	11.2	0	5.1				
7	9.9	1	3.1	12.0	1	1	2.8
8	13.9	0	4.5	16.2	0	1	3.5 ^b
9	15.9	2	2.7 ^b	18.2	3	3	2.2 ^b
10	11.5	0	3.3 ^b	13.6	1	0	3.3 ^b
11	8.5	0	3.7	10.8	0	0	4.7
12	7.1	0	4.7	9.3	0	0	4.7
13	4.6	0	3.1	6.8	0	0	3.5
14	12.6	0	5.0				

^a Ventricles and sulci: 0, normal; 1, slightly enlarged; 2, moderately enlarged; 3, severely enlarged.

^b Visually noticeable thinning of the corpus callosum.

On-line Table 2: Correlation coefficients (*r*) and their statistical significance (*P* values) between the Unified Parkinson's Disease Rating Scale, Part III scores and whole-brain microstructural properties

Covariates	Correlation	Fractional Anisotropy		Mean Diffusivity		Radial Diffusivity		Axial Diffusivity		Coefficient of Planarity	
		Skeleton	Tractogram	Skeleton	Tractogram	Skeleton	Tractogram	Skeleton	Tractogram	Skeleton	Tractogram
None	Pearson <i>r</i>	-0.81	-0.77	0.88	0.91	0.90	0.91	0.83	0.91	-0.66	-0.79
	<i>P</i> value	1.5E-06 ^a	9.6E-06 ^a	1.0E-08 ^a	7.3E-10 ^a	3.5E-09 ^a	9.5E-10 ^a	7.1E-07 ^a	6.7E-10 ^a	4.8E-04 ^a	3.7E-06 ^a
	Spearman <i>r</i>	-0.77	-0.73	0.73	0.72	0.75	0.73	0.65	0.73	-0.78	-0.83
Age and sex	<i>P</i> value	9.7E-06 ^a	5.8E-05 ^a	4.7E-05 ^a	6.6E-05 ^a	2.3E-05 ^a	4.5E-05 ^a	6.7E-04 ^a	4.7E-05 ^a	5.8E-06 ^a	5.5E-07 ^a
	Pearson <i>r</i>	-0.54	-0.32	0.60	0.69	0.64	0.67	0.45	0.71	-0.30	-0.40
	<i>P</i> value	.010 ^a	.15	.0033 ^a	4.3E-04 ^a	.0014 ^a	6.5E-04 ^a	.037 ^a	2.4E-04 ^a	.18	.067

^a Significant.